ULTRASONIC WAVE PROPAGATION IN CONCENTRATED EMULSIONS AND ENCAPSULATED EMULSIONS

By

Yinghui Chen

A thesis submitted to the University of Nottingham

For the degree of Doctor of Philosophy

Applied Ultrasonics Laboratory

School of Electrical and Electronic Engineering

University of Nottingham

June 2007

Abstract

Ultrasonic spectrometry has potential for monitoring chemical processes on line; an important application is the detection of the suspended particle size distribution (PSD) in emulsions. Measured ultrasonic wave attenuation as a function of frequency is compared to the predictions of an adaptive wave propagation model to obtain an estimate of the PSD. Current models are based either on scattering physics, heat transfer, or hydrodynamics, or on a combination of these. Most models give good prediction of attenuation for dilute and semi-dilute systems, but they are known to break down at high dispersed phase concentrations and for very small (10s of nm) particles. The limits of applicability are not known in a formal sense.

The principal aim and contribution to knowledge of this research is to formally determine the limits of existing theory and to set out which model or models are appropriate for use with emulsions with large or very small particles (nano-emulsion), and at small and large concentrations of dispersed phase. The second aim is to answer the same question for the case of encapsulated emulsions in which the droplets are encapsulated in a thin polymer shell.

The project combines computational methods based on analytic theories of wave propagation with a comprehensive experimental programme.

Acknowledgements

Firstly, I would like to sincerely thank my supervisor, Professor Richard Challis, for his excellent supervision, encouragement and leadership throughout the period of my Ph.D research, and for his example of hard work and commitment. Also, I would like to thank the other members in the Applied Ultrasonics (AU) Laboratory for the useful advice they have given me. Dr. Andrew Holmes has shown endless patience in experimental measurements whenever I met problems. Dr Valerie Pinfield gave me a lot of help in mathematics, physics and coding.

Outside university, I would like to show my appreciation to Professor Povey and his staff in the Procter Department of Food Science at the University of Leeds, who provided me most of the emulsions used in the experiments. I also would like to give my thanks to Dr. Fowles of the Dow AgroSciences Company, UK, who provided me the encapsulated emulsions.

Thanks for my family and my friends, who have been extremely understanding and supportive of me in many ways too numerous to mention during my study in UK. Thanks for my dear parents, to whom this thesis is rightly dedicated. I take this opportunity to thank you one and all. You encouragement and support over the years have been greatly appreciated.

Finally, to other students like me studied in school of engineering, who have given me hope that science and engineering do have a future.

Table of Contents

List of Figures

List of Tables

Glossary List of Symbols

In the ECAH model and HHM model:

1 Dispersed phase

2 Continuous phase

3 Effective medium

In Anson-Chivers shell model:

1 Surrounding medium

2 Shell medium

3 The core medium

Other symbols used in this thesis if it is not emphasised its definition will be given as below:

i	$\sqrt{-1}$
f	Frequency
ω	Angular frequency, $\omega = 2\pi f$
T	Absolute temperature
N	The number of particles in unit volume
λ	Wavelength
R	Coordinate radius
$r,\ r_s$	Suspended particle radius and shell radius, respectively
ρ	Density
η	Shear viscosity
μ	Shear modulus, $\mu = -i\omega\eta$
α	Attenuation coefficient of compressional wave

α_s	Attenuation coefficient of shear wave
c	The compressional wave speed
c_s	The shear wave speed $c_s = \sqrt{\frac{\mu}{\rho}}$
c_0	Speed of sound for spherical compressional wave in elastic isotropic solid $c_0 = \sqrt{\frac{\lambda + \frac{2}{3}\mu}{\rho}}$
β	Complex waenumber $\beta = \frac{\omega}{c} + i\alpha$
β_T	Thermal volume expansion coefficient
κ	Thermal conductivity
σ	Thermometric conductivity $\sigma = \frac{\kappa}{\rho C_P}$
χ	Adiabatic compressibility
γ	Ratio of specific heats $\gamma = C_p / C_v$
ϕ	Volume fraction of the suspended particles
d	The average particle surface-surface distance
δ_T, δ_S	Skin depth of thermal and viscous waves, respectively
S, S_h	Momentum transfer factor, and irreversible heat transfer term
b_c , b_t	Thermal terms defined by Allegra and Hawley
g , G	Thermal terms defined by Epstein and Carhart
k_c, k_t, k_s	The wavenumber of compressional, thermal and shear waves, respectively

a_c, a_t, a_s	Particle radius times the wavenumber of compression, thermal and shear waves, respectively
$x_{c_j}, x_{s_j}, x_{t_j}$	Particle radius times the wavenumber of compression, thermal and shear waves, respectively
$y_{c_j}, y_{s_j}, y_{t_j}$	Shell radius times the wavenumber of compression, thermal and shear waves, respectively
$\phi_c, \phi_t, \mathrm{A}_\psi$	The wave potential of compressional, thermal and shear waves, respectively
A_0, A_1, A_2	Zero, first, second order scattering coefficients
A_n, B_n, C_n	Partial amplitude of compression, thermal and shear waves in the continuous phase
$A_n^{'}, B_n^{'}, C_n^{'}$	Partial amplitude of compression, thermal and shear waves in the suspended particle
θ	Angle with respect to the incident wave vector
$f(\theta)$	Far field scattering amplitude
$j_n(z), h_n(z)$	Spherical Bessel and Hankel function of order n with a complex argument z
$P_n(\cos\theta)$	Legendre polynomial of order n
$P_n^1(\cos\theta)$	Associated Legendre polynomial of order n
U	The specific internal energy
p	Pressure
P_{ij}	Viscous stress tensor
$\mathbf{u}$	The velocity vector of a volume element

x_i	The Cartesian coordinate
T_{x_i}, T_{y_i}	Wavenumber terms

Bold type denotes a vector

Chapter 1 Introduction

The term *emulsion* refers to a mixture of materials in which some liquid particles, the dispersed phase, are suspended in a second liquid, known as the continuous phase. Many products exist as emulsions or will have passed through the emulsion state during their manufacturing process; examples are: food products such as milk, yoghurt, and sauces, agricultural sprays, pharmaceutical products, lubricants and fuels, and paints, inks and pigments. Emulsions are made by adding liquid drops into another liquid, and using a high-shear rate mixing machine to produce a wide range of particle sizes, typically around 10 nm to 1 μm in radius. The physical chemistry of the internal structures of emulsions is complicated, and the information required from any given test varies greatly across the many combinations of products and industrial processes. However, the most basic information that needs to be sought is the particle size distribution (PSD) of the dispersed phase, because many product properties, including shelf life, depend on this. There is thus a requirement to characterize emulsions in terms of their PSD and gross concentrations.

There is currently a vast range of well established techniques to achieve this: optical scattering, electrical conductivity, neutron and X-ray scattering, and ultrasonic methods. Ultrasonic methods are attractive, particularly when the dispersed phase concentrations are too high for optical techniques to work, or when the physical conditions and/or environment are inappropriate for electrical methods. Also, many widely used techniques of particle characterization require large dilutions of the sample to be made before

measurements can be taken. This dilution in itself may mask or even destroy any particulate structure that is being investigated; in principle, an ultrasonic method would not require such dilution.

The most frequently used ultrasonic spectrometry is the ultrasonic attenuation spectrometry. In this method, ultrasonic attenuation is measured as a function of frequency and compared to a prediction of the same function using a mathematical model of wave propagation that takes account of PSD. The model is adapted on PSD until its output matches the measured attenuation in a least mean squared error sense. At the point of smallest error the PSD input to the model is taken to represent the PSD of the test material. It is therefore crucial that the wave propagation model properly represents the physics of wave propagation in the emulsion.

Current models are based either on scattering physics, heat transfer, or hydrodynamics, or on combination of these. Most models give good prediction of attenuation for dilute and semi-dilute systems, but they are known to break down at high dispersed phase concentrations and for very small (10s of nm) particles. The limits of applicability are not known in a formal sense. The principal aim and contribution to knowledge of this research is to formally determine the limits of existing theory and to set out which model or models are appropriate for use with emulsions with large or very small particles (nano-emulsion), and at small and large concentrations of dispersed phase. The second aim is to answer the same question for the case of encapsulated emulsions in which the droplets are encapsulated in a thin polymer shell. The project combines computational methods based on analytic theories of wave propagation with a comprehensive experimental programme.

There are three issues to be addressed in this thesis:

1. What is the extent of the validity of the approximations to the 'scattering' models of Epstein and Carhart (1953) and Allegra and Hawley (1972). The reason for this exercise is that the so-called ECAH model involves difficult, intense and poorly conditioned computations which could be avoided if approximations were found to be valid.

2. Are there theoretical models that exist that can predict attenuation (and phase velocity) as functions of frequencies for an emulsion system with high volume fraction of dispersed phase, given accurate physical parameters for the materials involved? And can this model be used to correctly calculate PSD in a concentrated emulsion?

3. In some situations, there is a need to use a shell to cover the suspended particles, to control the release rate of active chemicals in the droplet phase. We seek a theoretical model for wave propagation in encapsulated emulsions which can predict the attenuation and phase velocity, as functions of frequency.

In general, models which simulate the ultrasonic attenuation and phase velocity within two phase media can be grouped into two categories. Scattering models consider the transmission and reflection of waves at the boundary interface between the dispersed phase particle and the continuous phase. Coupled phase models are derived from a consideration of mass continuity and the conservation of momentum when one phase moves with respect to the other, combined with thermal interactions between phases. In

this project it was decided not to seek new wave propagation models, largely because the questions outlined above have not been comprehensively answered for the existing ones. The task, then, was to comprehensively examine existing propagation models with a view to determining their applicability for emulsion characterization in a general sense and the determination of PSD in particular.

Within the framework of this opening discussion, the structure of this thesis is as follows. After a brief introduction of the background to this study, we present the most widely used model for emulsions and suspensions — the Epstein and Carhart and Allegra and Hawley theory (the ECAH model). Since the ECAH model may break down at high particle concentrations for emulsions with small particle sizes, we then present two further models in chapter 3, which can be used in concentrated emulsions: Hemar (1997) , Herrmann et al (1996) and McClements et al (1999) model (HHM model) and the coupled phase model developed by Evans and Attenborough (1996, 1997, 2002). Then the comprehensive shell model of Anson and Chivers (1993) is examined in chapter 4 and applied to encapsulated emulsions. A software package was developed to implement the Anson-Chivers model in a general sense — it would be used for any combination of the physical properties of the mixture phases and therefore was applicable to both solid and liquid materials in either phase.

Carefully controlled experiments on a variety of emulsions were required in order to test the validity of the various theoretical models outlined above. The experimental procedures are described in chapter 5. The Applied Ultrasonics Laboratory at Nottingham does not have expertise in the

preparation of emulsions and so these were supplied by Professor Povey and his staff, at the University of Leeds, and by Dr. Fowles of Dow AgroSciences, UK. I am greatly indebted to these two gentlemen for such an important contribution to this project. The transportation of emulsions from one site to another (Leeds to Nottingham) is associated with some risk that the lapsed time and the mechanical agitation of the emulsions could lead to a change in their properties. For this reason the emulsions from Leeds were based on 1-bromohexadecane droplets because these were density-matched with the aqueous continuous phase. The results of the programme therefore, formally, only apply to density-matched emulsions. The results of the modelling and experiments are presented in chapter 6 and discussed in summary in chapter 7. Chapter 8 summarises the work overall, and gives conclusions and recommendations for future work.

Chapter 2 Theories of Ultrasonic Wave Propagation in Emulsions

2.1 Introduction

Many natural and processed materials, such as foods, pharmaceuticals, cosmetics and agrochemicals, exist either partly or wholly as emulsions. The appearance, rheology, and stability of emulsions are largely determined by the properties of the droplets they contain, such as their size and concentration, and by the interaction between the dispersed and continuous phase. Consequently, there is a strong demand for analytical techniques which can be used to measure these properties. Measurements of ultrasonic compression wave attenuation and phase velocity are related to such properties and have potential for on-line applications.

Since Lord Rayleigh (1877, Strutt, 1896) published "The Theory of Sound", there has been considerable scientific interest in the propagation of ultrasonic waves in various media. This chapter provides a review of theories for acoustic wave propagation in particulate mixtures, especially for emulsion systems.

Of the sections that follow, section 2.2 describes the earlier theories of ultrasound propagation in emulsions. Section 2.3 gives a detailed account of the more comprehensive theory of acoustic wave propagation in particulate mixtures — the theory of Epstein and Carhart (1953) and Allegra and Hawley (1972), which is now known as the ECAH model. The limitations to the

ECAH model are discussed in section 2.4, where it is explained why and how the ECAH model breaks down for high volume concentration systems.

2.2 Basic theory of ultrasound propagation

The first theoretical investigations into the propagation of sound through disperse systems were conducted in the late 19th century (Challis, 1998). Since then an extremely large amount of work has been done to understand the sound attenuation in suspensions of particles. Stokes (1845) examined the viscous losses owing to shear viscosity, and Kirchoff (1868) quantified the losses owing to heat conduction. Rayleigh (1871, 1894) further developed the work of Stokes and Kirchoff and also investigated the physics of attenuation caused by suspended particles using light or sound of a wavelength longer (by a factor of approximately ten or greater) than the diameter of the particles. This is the so-called fourth power law in which the scattered wave amplitude A_s of a wave of wavelength λ scattered in any direction making an angle θ with the incident wave A_i, is inversely proportional to the fourth power of the wavelength (Rayleigh, 1894):

$$A_s \propto A_i \frac{1+\cos^2\theta}{\lambda^4} \tag{2.1}$$

Rayleigh represented mathematically the disturbance of a plane wave by a small particle by using a partial wave expansion. He concluded that the magnitude of the zero-order term is a function of the compressibility difference between the particle and suspending fluid; the particle acting in the manner of a pulsating sphere (a monopole radiator). The first-order term is a function of the density difference and represents the particle acting as a dipole

radiator. The characteristic of the first-order term is caused by viscous drag opposing the relative motion of the particle with respect to its surrounding medium. On the basis of Rayleigh's theory, Sewell (1910) derived an expression for the attenuation of sound caused by inelastic, immovable particles suspended in a gas. Lamb (1945) refined Sewell's expression to remove the restriction that the particles be immovable, and defined an expression for the scattered wave potential.

Up to the 1940's a great deal of research was undertaken to investigate and quantify the intrinsic acoustic losses in fluids and solids but it was not until 1947 that the first practically useful model for calculating acoustic phase velocity in a dispersion of particles was published by Urick (1947). He derived equations for the attenuation and velocity of sound propagating through a dispersion by using a simple effective-medium approach. This treats a dispersion as an equivalent homogeneous medium of modified physical properties in order to calculate the velocity using Wood's Equation (Wood, 1941).

$$c = \sqrt{\frac{1}{\chi_{eff}\rho_{eff}}} \tag{2.2}$$

where χ_{eff} and ρ_{eff} are the volume-weighted averages of the density and adiabatic compressibility of the two phases. This equation also provides a simple way to calculate the compressibility of the suspended phase given the sound speed and particle density. It works well in the long wavelength limit, but is limited in that it is wholly independent of frequency, and can break down at high dispersed phase volume fractions. In addition it is inaccurate for particles with significantly contrasting properties with respect to the

continuous phase due to the effects of scattering, thermal and viscous phenomena. Following this work, Urick and Ament (1949) developed a model which used a single equation to express the complex wave number of an effective medium from which both attenuation and phase velocity could be derived. It offers a useful method to calculate the frequency and particle-size dependent attenuation and phase velocity as long as the following assumptions are true:

a. The particles are spherical, compressible and mobile.

b. Absorption by the continuous phase is negligible.

c. Multiple scattering of energy is negligible.

d. The particles occupy negligible volume.

e. Thermal losses are negligible.

However, the subject of the last assumption, thermal losses, was shown by Isakovich (1948) to be a significant source of attenuation for mixtures where the densities of the particles and the continuous phase do not contrast greatly. The thermal losses due to two phases of a mixture heat-up differently in response to the compression cycle in the wave. Biot (1962) devised a model for the sound velocity in a porous elastic solid containing a viscous liquid. He considered the average motions of the solid and liquid phases separately, and obtained two sound velocities, one for a fast compression wave and the other for a slow wave. Johnson and Plona (1982) considered Biot's model and derived a similar equation for sound speed as that of Urick.

The theories outlined in the last paragraph assume that the suspensions are dilute and most are limited in applicability to mixtures where the density contrast between the particles and the surrounding phase is small. This is the

case for liquid-in-liquid emulsions and suspensions of polymeric particles in liquids, where the combined effects of compressibility and thermal contrast are dominant. However, for most materials more comprehensive theories are required to quantify the effects of their physical properties on ultrasonic wave attenuation and phase velocity.

2.3 The Epstein-Carhart and Allegra-Hawley theory

A significant proportion of current research into the modeling of acoustic loss mechanisms can be categorized into two distinct approaches: scattering models and coupled phase models. The former will be discussed in this chapter, and the coupled phase model will be discussed in chapter 3. The basis of the scattering model is the wave interaction at a single spherical particle suspended in an infinite liquid medium through which a plane wave is propagating (Povey, 1997). The wave scattered at the surface of the object, regardless of its initial shape, will tend towards planar at infinite distance away from the object (figure 2.1). A receiver located at an infinite distance away from the scatterer will receive both the transmitted wave and the scattered wave in superposition. The total effect of a number of scatterers is then obtained simply by adding their combined effects together. Because of the spherical nature of the scatterer and the sphericity of the boundary conditions, the scattered wave potential may be expanded in spherical harmonics by using appropriate radial and angular functions (Povey, 1997).

The basis for scattering theory was laid in the 19th century by Lord Rayleigh (Strutt, 1896), and his work has been built on over the years by many workers. Some of the important models in the application of partial wave

analysis to acoustical scattering include the calculation of the scattering coefficients of a fluid droplet suspended in a fluid continuum (Epstein and Carhart, 1953), and the experiment and theory in both emulsions (hexadecane in water) and suspensions (polystyrene spheres in water) by Allegra and Hawley (1972).

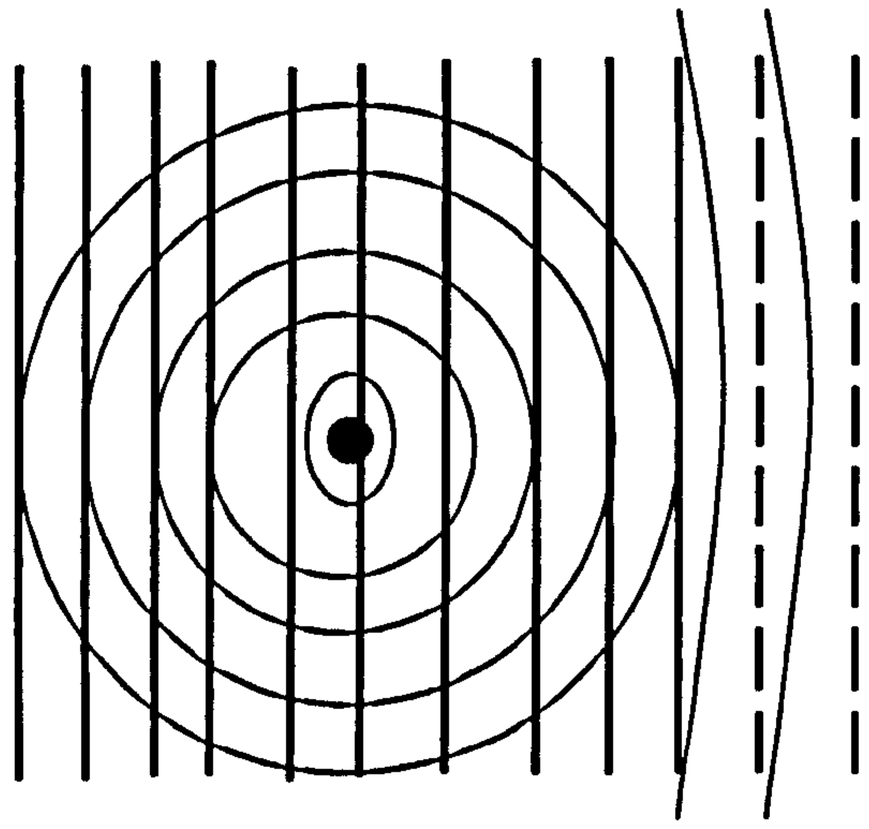

Figure 2.1. Schematic of spherically symmetric scattered wave, tending toward plane at an infinite distance. (Povey (1997), figure 4.3)

Epstein (1941) refined the Sewell-Lamb (1910) scattering equation to remove the restriction that the particle be incompressible. He considered spherical particles suspended in the surrounding fluid; the particle could be rigid, an elastic solid, or a viscous fluid, thus providing for both emulsions and suspensions. Compression and shear (transverse) wave equations were derived for the continuous and disperse phases respectively. In response to an incident compression wave both compression and transverse waves were diffracted from the particle boundary. For elastic solid or viscous liquid particles, waves of both types were excited inside the particle, whereas for rigid solid spheres the interaction was limited to reflection only. In the liquid continuous phase and inside the fluid particle the transverse mode took the form of a rapidly decaying shear wave, also known as a viscous wave. Solution of the boundary

equations around the particle with continuity of radial and tangential displacements (for solid particles) or velocity (for fluid particles) and stresses gave an expression for radiation scattered away from the particle. More details of this solution will be given below where we consider Epstein's later work. Epstein's expression for attenuation in atmospheric fogs was similar to that obtained earlier by Sewell (1910), but the expression for attenuation in suspensions and emulsions with a liquid continuous phase depended strongly on the densities of the two phases and was very different from Sewell's result. Later Epstein found that the discrepancy resulted from second order scattering effects which he neglected in his derivation. Whilst he did not consider it at this stage, his later work showed that thermal transport effects would be highly significant for a mixture where the densities of the two phases did not differ greatly.

Eleven years after this work Epstein collaborated with Carhart (Epstein and Carhart, 1953) and introduced thermal transport effects into the theory of compression wave propagation in particulate mixtures. This has proved to have had a major effect on the understanding of attenuation mechanisms in emulsions. The basic assumptions were that the suspended droplets were elastic and were free to move with respect to the surrounding fluid; they were much smaller than the compression wavelength and distributed randomly in space. The volume fraction of droplets was assumed to be very low, which implied large distances between droplets and therefore the interactions of thermal and viscous wave with neighbouring particles could be neglected. It was further assumed that no relaxation processes were associated with the

passage of the wave. They concluded that the total attenuation could be regarded as the sum of the viscous attenuation and thermal attenuation:

$$\alpha = \alpha_{viscous} + \alpha_{thermal} \tag{2.3}$$

Thermal attenuation is generated by the pulsation of the droplet. As the droplet pulsates, its temperature also fluctuates periodically because of pressure-temperature coupling. This leads to heat flow across the interface between the droplet and the surrounding liquid. Because the heat flow out of the droplet is more than the heat flow into the droplet within a compression-expansion cycle, some of the ultrasonic energy is converted to heat. Viscous attenuation is caused by the oscillating to-and-fro motion of the suspended particles relative to the continuous phase due to the density difference. This motion is damped by viscous drag imposed by the surrounding liquid. These frictional losses are referred to as viscoinertial absorption.

Twenty years later Allegra and Hawley (1972) extended the application of the Epstein and Carhart model to dispersions of solid (as well as liquid) particles in a liquid continuous phase. The combined (ECAH) theory really applies only to dilute systems, where scattering from a single particle does not affect neighbouring particles. Modifications to the theory are required when the propagation medium can no longer be regarded as dilute, and these will be discussed in chapter 3.

There were some long standing algebraic errors in the ECAH model and these have been corrected by Challis *et al* (1998). They also showed how the model could be applied to solid in solid composites and finally demonstrated that it was equivalent to the model of Ying and Truell (1956), which had been specifically focussed on the solid-in-solid system. The Challis formulation

enabled the effects of thermal phenomena in solid-in-solid suspension to be investigated (Challis *et al*, 1998).

2.3.1 ECAH field equations

The ECAH model can be used for both fluid and solid particles suspended in a fluid continuous phase. This thesis is mainly concerned with liquid-in-liquid emulsions, and so the following equations are based on the Epstein and Carhart theory. For the case of solid particles, the following relationship can be used:

$$\mu = -i\omega\eta \tag{2.4}$$

where ω denotes angular frequency, μ denote shear modulus and η denotes viscosity.

The conservation laws (conservation of mass, momentum and energy) were used as the basis of the ECAH model. These equations are well known and so will not be repeated in this thesis; interested readers are referred to Epstein and Carhart (1953). The acoustic field equations were then obtained by linearizing the conservation equations:

$$\frac{\partial \rho}{\partial t} + \rho \nabla \cdot \mathbf{u} = 0 \tag{2.5}$$

$$\rho \frac{\partial \mathbf{u}}{\partial t} + \nabla p - N\eta \nabla\left(\nabla \cdot \mathbf{u}\right) + \eta \nabla \times \nabla \times \mathbf{u} = 0 \tag{2.6}$$

$$\rho \frac{\partial U}{\partial t} + p \nabla \cdot \mathbf{u} = \nabla \cdot (\kappa \nabla T) \tag{2.7}$$

where $N = \frac{4}{3}\left(1 + \frac{\mu}{2\eta}\right)$, ρ denotes mass density, U is the specific internal energy, p is the pressure, $\boldsymbol{u}$ is the velocity vector of a volume element, κ is the

thermal conductivity, and T is the absolute temperature. Two variables, pressure $p(\rho, T)$ and specific internal energy $U(\rho, T)$, incorporate pressure-temperature relationships into the system of equations. Because $\boldsymbol{u}$ is a vector in three dimensional space, equations 2.5, 2.6 and 2.7 can be separated into seven equations in seven unknowns, and $\boldsymbol{u}, \rho, \mu, p$ and T, and rearranged to give:

$$\frac{\partial^2 \mathbf{u}}{\partial t^2} - \frac{c^2}{\gamma}\nabla^2 \mathbf{u} + \frac{\eta}{\rho}\cdot\nabla^2 \dot{\mathbf{u}} + \frac{\eta}{\rho}\cdot\nabla\times\nabla\times\dot{\mathbf{u}} = -\frac{-c^2\beta}{\gamma}\nabla\dot{T} \tag{2.8}$$

$$\frac{(\gamma-1)}{\beta}\nabla\cdot\mathbf{u} + \dot{T} = \gamma\sigma\nabla^2 T \tag{2.9}$$

where γ is the ratio of specific heats C_p / C_v, c is the adiabatic velocity of sound defined as equation 2.2, and σ is the thermometric conductivity and given by $\sigma = \dfrac{\kappa}{\rho C_p}$.

2.3.2 The ECAH wave equation

The wave equations were obtained by de-coupling the field equations into three ordinary differential equations. These differential equations can be solved separately to get the three wave potentials: two scalar potentials compressional ϕ_c and thermal ϕ_t, and a vector potential shear A_ψ, as follows:

$$(\nabla^2 + k_c^2)\phi_c = 0,$$

$$(\nabla^2 + k_s^2)\mathrm{A}_\psi = 0,$$

$$(\nabla^2 + k_t^2)\phi_t = 0, \tag{2.10}$$

where k is the wavenumber, which is given by:

$$k_c = \frac{\omega}{c}(1 + i\alpha), \quad (\alpha << \frac{\omega}{c}) \tag{2.11}$$

$$k_t = (1+i)\sqrt{\frac{\omega\rho C_p}{2\kappa}} \tag{2.12}$$

$$k_s = (1+i)\sqrt{\frac{\omega\rho}{2\eta}}, \tag{2.13}$$

The wavenumbers in equations 2.11 and 2.12 are equally applicable to a viscous fluid or elastic solid, as is equation 2.13 when the equivalence of equation 2.4 is invoked.

2.3.3 Spherical harmonics

Partial wave analysis, in which each wave potential is described by a sum of waves of different angular (spherical, dumbbell, etc.) and radial dependencies, permits the various components of the wave to be independently matched at the particle boundary. Omitting the time variation, the incident plane wave can be written in terms of all the possible angular (Legendre polynomials, $P_n(\cos\theta)$) and spherical (Bessel and Hankel functions, $j_n(k_c r)$ and $h_n(k_c r)$) variations out of which it can be constructed, in a somewhat similar manner to the way in which a wave can be written as the sum of its Fourier components. In these analyses the spherical coordinate system is used, with the origin at the centre of a spherical scatterer and coordinates (R,θ,ψ), whereas R is distance from the origin, θ is the angle with respect to the propagation direction of the incident wave and ψ is zenith angle. The analysis is generally done in the frequency domain. An incident plane wave is expressed in spherical coordinates as:

$$\phi_0 = \sum_{n=0}^{\infty} i^n (2n+1) j_n(k_c R) P_n(\cos\theta) \tag{2.14}$$

where n is the order of polynomial, and $i=\sqrt{-1}$. The plane incident wave ϕ_0 is represented in this way so that each of the partial wave orders of the incident wave can be matched with the respective components of the scattered wave at the spherically symmetrical particle boundary. The scattered waves produced at the particle boundary can be written in a form similar to the incident wave:

$$\phi_{c2}=\sum_{n=0}^{\infty} i^n(2n+1)A_n h_n(k_{c2}R)P_n(\cos\theta)=\sum_{n=0}^{\infty}\phi_{c2n} \quad \text{(the scattered compression wave)}$$

$$\phi_{t2}=\sum_{n=0}^{\infty} i^n(2n+1)B_n h_n(k_{t2}R)P_n(\cos\theta) \quad \text{(the scattered thermal wave)}$$

$$A_{\psi 2}=\sum_{n=0}^{\infty} i^n(2n+1)C_n h_n(k_{s2}R)P_n^1(\cos\theta) \quad \text{(the scattered shear wave)}$$

$$\phi_{c1}=\sum_{n=0}^{\infty} i^n(2n+1)A_n' j_n(k_{c1}R)P_n(\cos\theta) \quad \text{(the transmitted compression wave)}$$

$$\phi_{t1}=\sum_{n=0}^{\infty} i^n(2n+1)B_n' j_n(k_{t1}R)P_n(\cos\theta) \quad \text{(the transmitted thermal wave)}$$

$$A_{\psi 1}=\sum_{n=0}^{\infty} i^n(2n+1)C_n' j_n(k_{s1}R)P_n^1(\cos\theta) \quad \text{(the transmitted shear wave)}$$

(2.15)

where $j_n(kR)$ is the spherical Bessel function of the first kind; it is defined at the origin and therefore used to represent inwards travelling transmitted waves which pass though zero radius (see appendix 1.1); $h_n(kR)$ is the Hankel function, which is the third kind of spherical Bessel function. The Hankel function is defined at infinity and therefore used to represent reflected waves travelling outwards towards infinity (see appendix 1.1). The arguments of the Bessel and Hankel functions take the form of particle radius times

wavenumber products for six wave types in the system — compression, shear and thermal waves inside and outside the particles. $P_n(x)$ and $P_n^1(x)$ are Legendre polynomials and associated Legendre polynomials of the first kind, both of order n, respectively (see appendix 1.1). The subscripts 1 and 2 denote dispersed phase and continuous phase, respectively.

The zero-order scattered acoustic mode (ϕ_{c0}) represents the result of the particle pulsation, arising from the temperature difference and the compressibility difference between the particle and its suspending fluid. It is spherically symmetric. The first- order mode (ϕ_{c1}) represents the movement of the particle backwards and forwards in the direction of the incident wave. In the long wavelength limit ($kr << 1$), the series in the incident wave potential can usually be truncated at the first-order, and partial wave analysis is ideal for the analysis of acoustic propagation in this limit (Povey, 1997).

2.3.4 Boundary conditions

When a plane compressional wave is incident upon a sphere of radius r in a continuous suspending medium, the sphere translates some of the compressional energy into thermal and viscous waves, which gives rise to compressional, shear and thermal waves travelling from the surface of the sphere both outwards into the suspending medium and the inwards into the sphere (see figure 2.2).

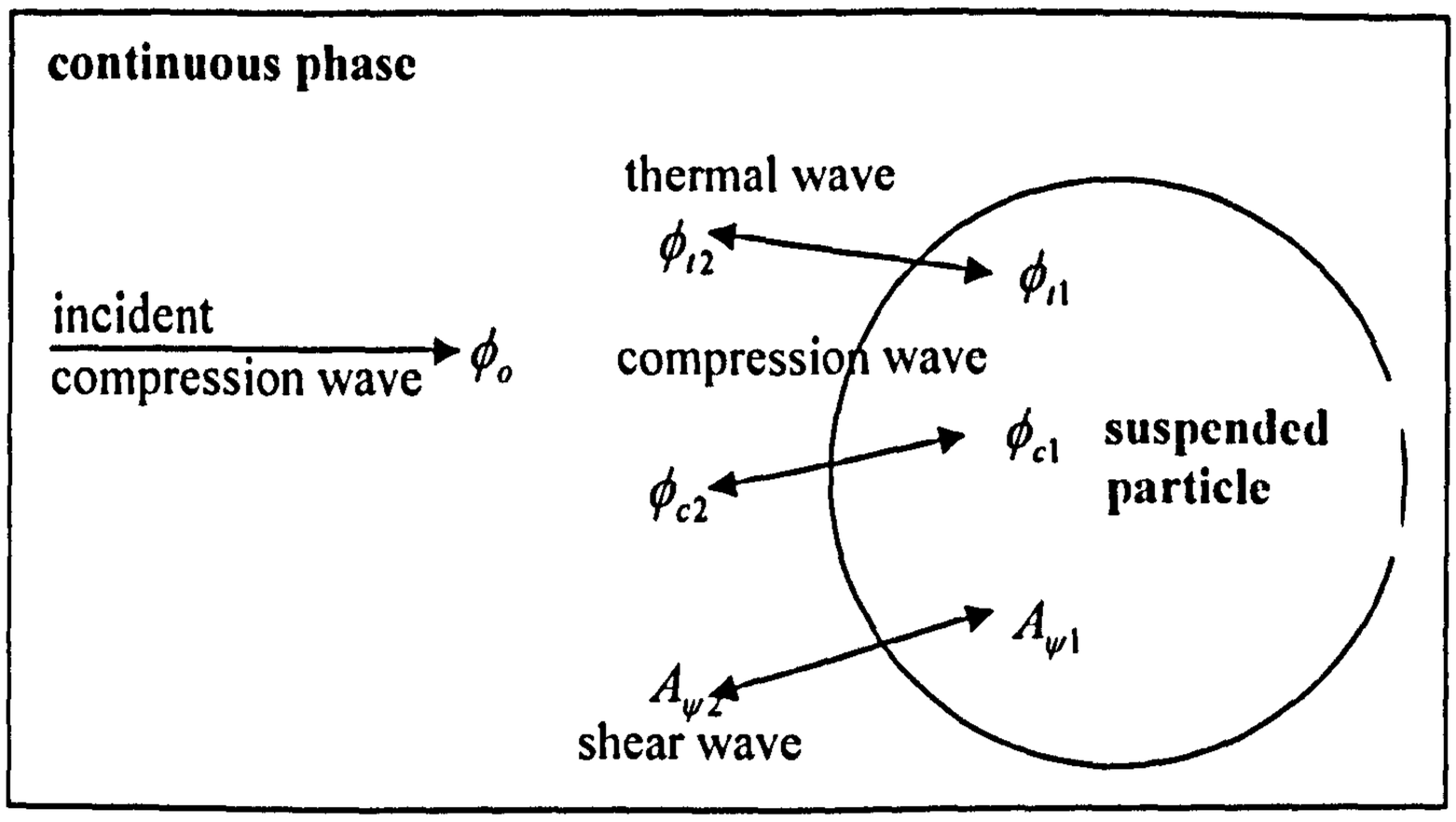

Figure 2.2. Schematic illustration of the translation of an incident wave into scattered and transmitted compressional, shear, and thermal wave (based on Tebbutt (1996)).

At the surface of the suspended particles, the velocity and stress components, and the temperature and heat flow are continuous. Following Epstein and Carhart and Allegra and Hawley, for axial symmetry, these boundary conditions can be written as:

$$v_{R2} = v_{R1}, \quad v_{\theta 2} = v_{\theta 1} \text{ (continuity of radial and angular velocity)}$$

$$T_2 = T_1 \quad \text{(continuity of temperature)}$$

$$\kappa_2 \frac{\partial T_2}{\partial R} = \kappa_1 \frac{\partial T_1}{\partial R} \text{ (continuity of heat flux)}$$

$$P_{RR2} = P_{RR1}, \quad P_{R\theta 2} = P_{R\theta 1} \text{ (continuity of compressive and shear stress)} \qquad \textbf{(2.16)}$$

where R denotes radial direction and θ is the tangential direction.

To obtain the boundary conditions at the particle surface, physical quantities such as temperature and stress must be expressed in terms of wave potential. The fluid velocity, temperature, and stress are given by Epstein and Carhart for the situation of liquid particles suspended in the fluid continuous phase:

$$v_R = -\frac{\partial \phi}{\partial R} + \frac{1}{R \sin\theta} \frac{\partial \phi}{\partial \theta}(A_\psi \sin\theta)$$

$$v_\theta = -\frac{1}{R}\frac{\partial \phi}{\partial \theta} - \frac{1}{R}\frac{\partial (RA_\psi)}{\partial R}$$

$$T = g\phi_c + G\phi_t$$

$$P_{RR} = (i\omega\rho + 2\eta k_c^2)\phi_c + (i\omega\rho + 2\eta k_t^2)\phi_t + 2\eta\left\{\frac{\partial^2 \phi}{\partial R^2} + \frac{1}{\sin\theta}\frac{\partial}{\partial \theta}\left[\left(\frac{A_\psi}{R^2} - \frac{1}{R}\frac{\partial A_\psi}{\partial r}\right)\sin\theta\right]\right\}$$

$$P_{R\theta} = \eta\left\{-\frac{\partial}{\partial \theta}\left(\frac{1}{R}\frac{\partial \phi}{\partial R} - \frac{\phi}{R^2}\right) - \left(\frac{\partial^2 A_\psi}{\partial R^2} - \frac{2A_\psi}{R^2}\right) + \frac{1}{R^2}\frac{\partial}{\partial \theta}\left[\frac{1}{\sin\theta}\frac{\partial}{\partial \theta}(A_\psi \sin\theta)\right]\right\} \quad \textbf{(2.17)}$$

where $\phi = \phi_0 + \phi_c + \phi_t$ for continuous phase and $\phi = \phi_c + \phi_t$ for dispersed phase, the thermal terms g, G are given by:

$$g = \frac{-i\omega(\gamma - 1)}{\beta c^2}$$

$$G = \frac{-\rho C_P}{\beta \kappa} \quad \textbf{(2.18)}$$

For the case of the solid-in-liquid suspension, Allegra and Hawley used alternative thermal terms b_c, b_t to replace the g, G terms. Challis *et. al.* (1998) investigated both Epstein and Carhart and Allegra and Hawley boundary equations, and obtained relationships between the thermal factors for solid and fluid particles.

2.3.5 General equations for emulsions and suspensions

The boundary condition equations can be obtained from equations 2.16 and 2.17, where terms of equal order in the series expansions are equated because of the orthogonality property of the spherical harmonics, and can be

deleted from both sides of the equation. The following set of equations define the boundary conditions for fluid particles in a liquid medium in the order of radial velocity, tangential velocity, temperature, heat flux, radial stress component, and tangential stress component, respectively. These equations ensure that the corresponding physical quantities are continuous across the scatterer boundary.

$$a_{c2}j_n'(a_{c2}) + A_n a_{c2}h_n'(a_{c2}) + B_n a_{t2}h_n'(a_{t2}) - C_n n(n+1)h_n(a_{s2})$$

$$= A_n' a_{c1}j_n'(a_{c1}) + B_n' a_{t1}j_n'(a_{t1}) - C_n' n(n+1)j_n(a_{s1}) \quad \textbf{(2.19 a)}$$

$$j_n(a_{c2}) + A_n h_n(a_{c2}) + B_n h_n(a_{t2}) - C_n\left[h_n(a_{s2}) + a_{s2}h_n'(a_{s2})\right]$$

$$= A_n' j_n(a_{c1}) + B_n' j_n(a_{t1}) - C_n'\left[j_n(a_{s1}) + a_{s1}j_n'(a_{s1})\right] \quad \textbf{(2.19 b)}$$

$$g_2[j_n(a_{c2}) + A_n h_n(a_{c2})] + G_2 B_n h_n(a_{t2}) = g_1 A_n' j_n(a_{c1}) + G_1 B_n' j_n(a_{t1}) \quad \textbf{(2.19 c)}$$

$$\kappa_2\{g_2[a_{c2}j_n'(a_{c2}) + A_n a_{c2}h_n'(a_{c2})] + G_2 B_n a_{t2}h_n'(a_{t2})\}$$

$$= \kappa_1\{g_1 A_n' a_{c1}j_n'(a_{c1}) + G_1 B_n' a_{t1}j_n'(a_{t1})\} \quad \textbf{(2.19 d)}$$

$$\eta_2\{[(a_{s2}^2 - 2a_{c2}^2)j_n(a_{c2}) - 2a_{c2}^2 j_n''(a_{c2})] + A_n[(a_{s2}^2 - 2a_{c2}^2)h_n(a_{c2}) - 2a_{c2}^2 h_n''(a_{c2})]$$

$$+ B_n[(a_{s2}^2 - 2a_{t2}^2)h_n(a_{t2}) - 2a_{t2}^2 h_n''(a_{t2})] + C_n 2n(n+1)[a_{s2}h_n'(a_{s2}) - h_n(a_{s2})]\}$$

$$= \eta_1 A_n'[(a_{s1}^2 - 2a_{c1}^2)j_n(a_{c1}) - 2a_{c1}^2 j_n''(a_{c1})] + B_n'[(a_{s1}^2 - 2a_{t1}^2)j_n(a_{t1}) - 2a_{t1}^2 j_n''(a_{t1})]$$

$$+ C_n' 2n(n+1)[a_{s1}j_n'(a_{s1}) - j_n(a_{s1})] \quad \textbf{(2.19 e)}$$

$$\eta_2\{a_{c2}j_n'(a_{c2}) - j_n(a_{c2}) + A_n[a_{c2}h_n'(a_{c2}) - h_n(a_{c2})] + B_n[a_{t2}h_n'(a_{t2}) - h_n(a_{t2})]$$

$$-(C_n/2)[a_{s2}^2 h_n''(a_{s2}) + (n^2+n-2)h_n(a_{s2})]\} = \eta_1\{A_n'[a_{c1}j_n'(a_{c1}) - j_n(a_{c1})]$$

$$+ B_n'[a_{t1}j_n'(a_{t1}) - j_n(a_{t1})] - (C_n'/2)[a_{s1}^2 j_n''(a_{s1}) + (n^2+n-2)j_n(a_{s1})]\} \quad \textbf{(2.19 f)}$$

Using the relationship in equation 2.4 we can get the boundary equations for solid particles in a fluid medium. The solution of this set of equations for each order n produces a value for the single-particle scattering coefficient A_n

of that order. The equations 2.19b and 2.19f are related to the tangential velocity and the tangential stress boundary condition respectively, they are invalid for $n=0$ because the angular function factor ($P_n^1(\cos(\theta))$) is identically zero for any arguments ($P_0^1=0$). Besides this, Epstein and Carhart pointed out in their paper that for $n=0$, the C_n and $C_n^{'}$ terms do not appear in the remaining equations, that is, the viscous waves should not enter into the spherically symmetric $n=0$ term (Epstein and Carhart, 1953). So the problem simplifies to four equations and four unknown at $n=0$.

2.3.6 Matrix form of the boundary equations

Equations 2.19 can be transposed into matrix format such that they take the form of $Mx=C$. The matrix equation 2.20 is based on Challis *et al* (1998) for fluid particles.

$$[M]_{EC}\begin{bmatrix} A_n \\ B_n \\ C_n \\ A_n^{'} \\ B_n^{'} \\ C_n^{'} \end{bmatrix} = -\begin{bmatrix} a_{c2}j_n^{'}(a_{c2}) \\ j_n(a_{c2}) \\ \eta_2(j_n(a_{c2})a_{s2}{}^2 - 2a_{c2}^2 j_n^{''}(a_{c2})) \\ \eta_2[a_{c2}j_n^{'}(a_{c2}) - j_n(a_{c2})] \\ g_2 j_n(a_{c2}) \\ \kappa_2 a_{c2} g_2 j_n^{'}(a_{c2}) \end{bmatrix} \tag{2.20}$$

Because the 6×6 matrix M_{EC} (see appendix 1.2 for details) and the vector on the right hand side are explicitly known, the system can be solved for the column vector of the complex scattering coefficients $A_n, B_n, C_n, A_n^{'}, B_n^{'}, C_n^{'}$ in directions other than the propagation direction for each order n. Acoustic attenuation in emulsions arises from energy scattered by the sphere to infinity, as well as the energy absorbed in the vicinity of the suspended particle. The

viscous and thermal waves that are produced at the boundary are damped near the interface and do not contribute to the scattered energy at a long distance away. Therefore, the observed attenuation is defined by the coefficient A_n of the scattered compressive waves. Hence it is only the coefficient A_n which needs to be evaluated in order to get the attenuation.

2.3.7 Solving the matrix

Inspection of matrix $[M]_{EC}$ reveals that a number of elements possess n as a multiplicand. Therefore, this matrix equation can be reduced to a 4×4 one when $n=0$. Pinfield showed that thermal terms can be neglected for $n>0$ (Pinfield, 2007), and by neglecting the thermal terms, the equation again can be simplified to a 4×4 one when $n=1$. But the solution becomes more difficult for $n\geq2$. Many methods can be used to find the solutions to such matrix equations (Tebbutt, 1996, O'Neill, 1998). The principal difference between these methods lies in their degree of sophistication, their mathematical complexity, and their computational cost. The matrix in equation 2.20 is ill conditioned because on the same row of the matrix some elements become exponentially large while others become exponentially small at the same time. Tebbutt (1996) and O'Neill (1998) have given detailed solutions for this matrix equation.

2.3.8 Single scattering model

Epstein and Carhart and Allegra and Hawley only calculate the attenuation of a plane compression wave by a single suspended sphere. The total attenuation contains the part due to the scattering losses and also due to

absorption in the vicinity of the particle, not the absorption alone. They derived an expression for the total energy attenuated by a dispersion of many spheres by representing the total velocity potential at infinity in terms of incoming and outgoing waves on a single sphere, and it was summed over the total number of particles per unit volume. The energy difference carried by these waves is the energy absorbed by the dispersion. In this way, the attenuation is found to be determined by the coefficients of the reflected compressional wave. The following equation is an approximation to attenuation obtained by approximating the square root of a complex number (Challis, 1998):

$$\alpha = -\frac{3\phi}{2k_c^2 r^3}\sum_{n=0}^{\infty}(2n+1)\mathrm{Re}(A_n) \qquad (2.21)$$

where ϕ is the volume fraction of the suspended material, and α is the attenuation for the pressure wave. This expression implies that only the real part of A_n directly contributes to the attenuation.

In 1961, Foldy derived an expression for the cumulative effect of a number of scatterers randomly dispersed in a volume.

$$\frac{\beta^2}{k_c^2} = 1 - \frac{3i\phi}{k_c^3 r^3}\sum_{n=0}^{\infty}(2n+1)A_n \qquad (2.22)$$

where β is the complex wavenumber of the dispersion., which is defined as: $\beta = \frac{\omega}{c} + i\alpha$. Foldy's equation considered only the forward scattering, i.e. $\theta = 0$ for scattering amplitude $f(\theta) = \frac{1}{ik}\sum_{n=0}^{\infty}(2n+1)A_n P_n(\cos\theta)$, which gives the scattered amplitude as a function of angle with respect to the propagation

axis, in a dilute dispersion of point scatterers, with coherent re-scattering assumed to be negligible.

As discussed in section §2.3.7, in the long wavelength region, only the lowest orders of A_n make a significant contribution to the attenuation, although, at larger values of $k_c r$, higher orders become more significant and must be included in the calculated scattered field. O'Neill (1998) has explored the convergence of A_n, demonstrating the maximum number of partial wave orders required to the wavenumber parameter $k_c r$ was $n \cong 1.05 k_c r + 4$, rounded off the nearest integer. However this result has not been substantiated in further work. Pinfield (1996) demonstrated that the limit of partial wave orders is determined by the incident wave magnitude for the various orders which limits the amount of scattered field of the same order. The number of partial wave orders required is defined by the number of wave orders needed to describe the incident field for a particle of a given radius. A more accurate value about the maximum number of partial wave orders was obtained by Pinfield by investigating the behaviour of the Bessel and Hankel functions with increasing of order n, for a fixed value of $k_c r$, the approximate result was $n \approx k_c r + 4$ (Pinfield, 2007).

2.3.9 Multiple scattering model

The above single scattering model is limited to very dilute systems where the proportion of acoustic field incident on a particle which has been scattered by other particles is very small. However, in the case of a high concentration of scatterers, the individual particles are no longer immersed in the

undisturbed initial acoustic field, but in this field combined with the acoustic field scattered by the surrounding particles. The proportion of the incident field which is due to all other scatterers may become significant as concentration increases. A wave is therefore redirected more than once in a process called multiple scattering. Figure 2.3 illustrates the multiple scattering effects for an emulsion system as an incident wave passes through it. We can see from this figure that a wave incident on a particle is scattered by it; this scattered wave, together with the original incident wave, impinges on an adjacent particle and is scattered again. The computation of the phase and amplitude relationships at each stage of this multiple scattering process (first, second, third scattering and so on) is important (Povey, 1997).

Waterman and Truell (1961) extended Foldy's equation, incorporating the work of Urick and Ament (1949). They developed an approximation for complex wavenumber based on a series of concatenated slabs of scattering material:

$$\frac{\beta^2}{k_c^2} = 1 - \frac{3i\phi}{k_c^3 r^3}\sum_{n=0}^{\infty}(2n+1)A_n + \frac{9\phi^2}{4k_c^6 r^6}\left[\left(\sum_{n=0}^{\infty}(2n+1)A_n\right)^2 - \left(\sum_{n=0}^{\infty}(-1)^n(2n+1)A_n\right)^2\right] \tag{2.23}$$

Their approximation takes into consideration both forward ($\theta = 0$) and backward scattering ($\theta = \pi$) from each dispersed particle. The first two terms of equation 2.23 are the same as equation 2.22. The last term, in the square of volume fraction, accounts for the backward scattering, which proved to be important for concentrated systems. Fikioris and Waterman (1964) later corrected a problem in their derivation of this result. Lloyd and Berry (1967) extended this model on the basis that the validity of the concatenated slab

approximation, they pointed out that Waterman and Truell's derivation was based on an erroneous integration. Instead they approached the problem from the point of view of the density of energy states in a medium, resulting in the acoustic wavenumber. It has been found to produce reliable results in many systems and has been widely adopted as the correct form for multiple scattering theory. Lloyd and Berry's result for the complex wavenumber is:

$$\frac{\beta^2}{k_c^2} = 1 - \frac{3i\phi}{k_c^3 r^3}(A_0 + 3A_1 + 5A_2) - \frac{27\phi^2}{k_c^6 r^6}\left(A_0 A_1 + \frac{10}{3}A_0 A_2 + 11 A_1 A_2\right) - \frac{54\phi^2}{k_c^6 r^6}\left(A_1^2 + \frac{115}{21}A_2^2\right) \tag{2.24}$$

The result presented here is terminated after the second-order scattering terms, since these are usually sufficient in the long wavelength region. The Lloyd and Berry's result agrees with that obtained by Firkioris and Waterman up to the first-order scattering mode at which it is frequently truncated.

Figure 2.4 shows the simulations based on ECAH model and ECAH modifications by Foldy (equation 2.22), Waterman and Truell (equation 2.23) and Lloyd and Berry (equation 2.24) for a 25% 1-bromohexadecane oil-in-water emulsion, together with our experimental measurement. We note that in this case there is no significant difference between the three formulations, because the density contrast between the suspended particles and continuous phase is very small, the zero-order term being dominant. The higher order terms are very small, due to the cross multiplications. All three models are in good agreement with experimental data.

It should be noted that equations 2.22 to 2.24 apply to suspensions of particles that are monodisperse, whereas the majority of particulate mixtures of industrial significance are polydiperse. If we use the monodisperse formula

to simulate a polydisperse mixture, there will be discrepancy between modelled and experimental data. Figure 2.5a shows the particle size distribution (PSD) of 25% v/v 1-bromohexadecane oil-in water emulsion, and 2.5b shows the experimental attenuation together with the simulations based on this PSD and on the mean radius alone. Thus it is important to modify the ECAH theory to include the particle size distribution effects. Challis *et al* (1998) suggest a distribution of particle size in the form of a histogram with J ($j = 1$ to J) discrete sizes R_j. The partial wave attenuation coefficients A_n are calculated for each of the J size bins, each represented by a dispersed phase volume fraction ϕ_j and a particle radius r_j, and summed to give the complex wavenumber thus:

$$\frac{\beta^2}{k_c^2} = 1 - \sum_{j=1}^{J} \frac{3i\phi_j}{k_c^3 r_j^3} \sum_{n=0}^{\infty} (2n+1) A_{nj} - \sum_{j=1}^{J} \frac{27\phi_j^2}{k_c^6 r_j^6} \left(A_{0j} A_{1j} + \frac{10}{3} A_{0j} A_{2j} + 11 A_{1j} A_{2j} \right) - \sum_{j=1}^{J} \frac{54\phi_j^2}{k_c^6 r_j^6} \left(A_{1j}^2 + \frac{115}{21} A_{2j}^2 \right) \tag{2.25}$$

Whilst this appears to work well (figure 2.5b), it must be noted that it is a gross approximation to the underlying physics. It assumes that waves scattered from particles of a given size, only re-scatter at particles of the same size, whereas in practice the scattering patterns are expected to be much more complex.

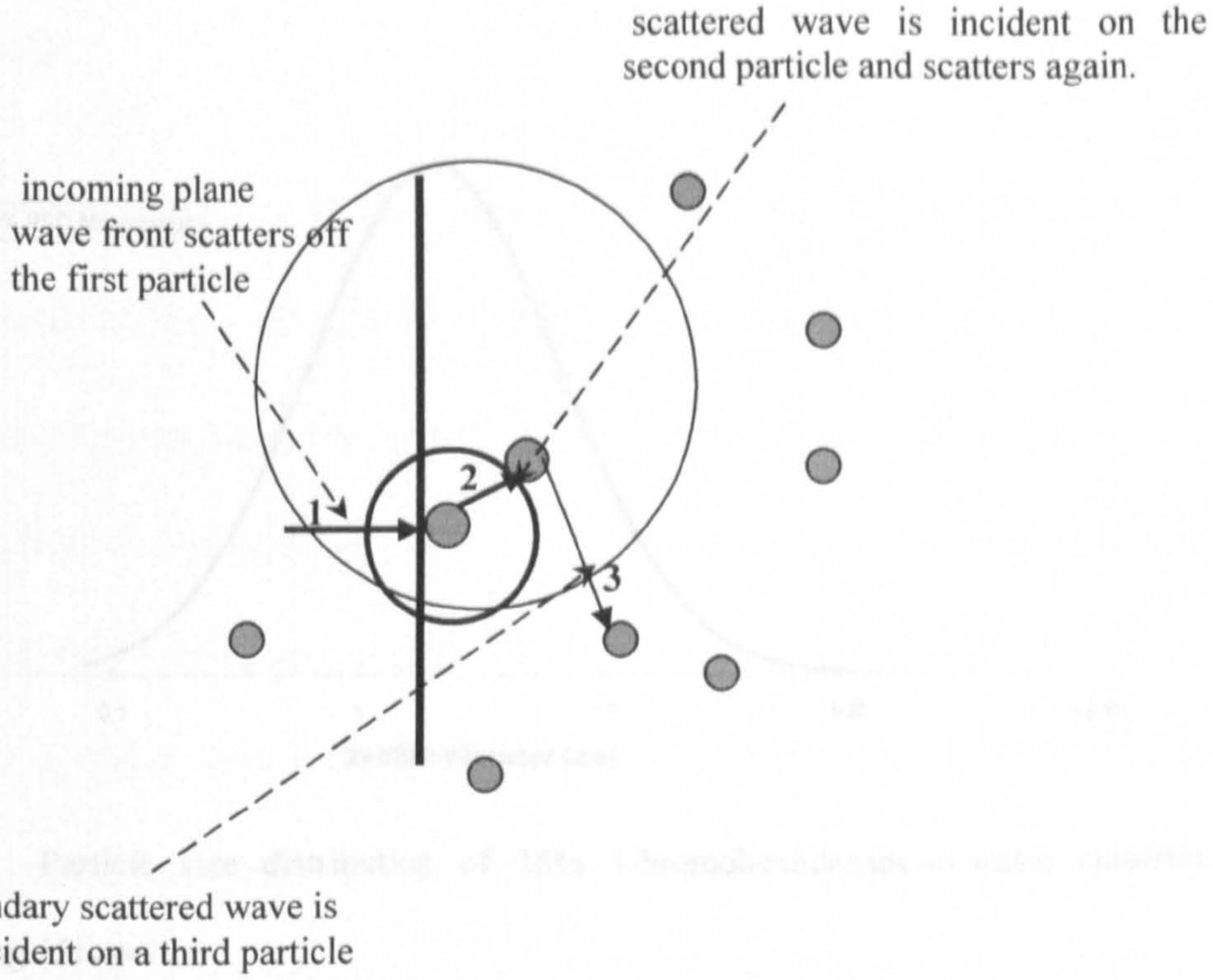

Figure 2.3. Multiple scattering of a plane wave by several particles (based on Povey, 1997, figure 4.4).

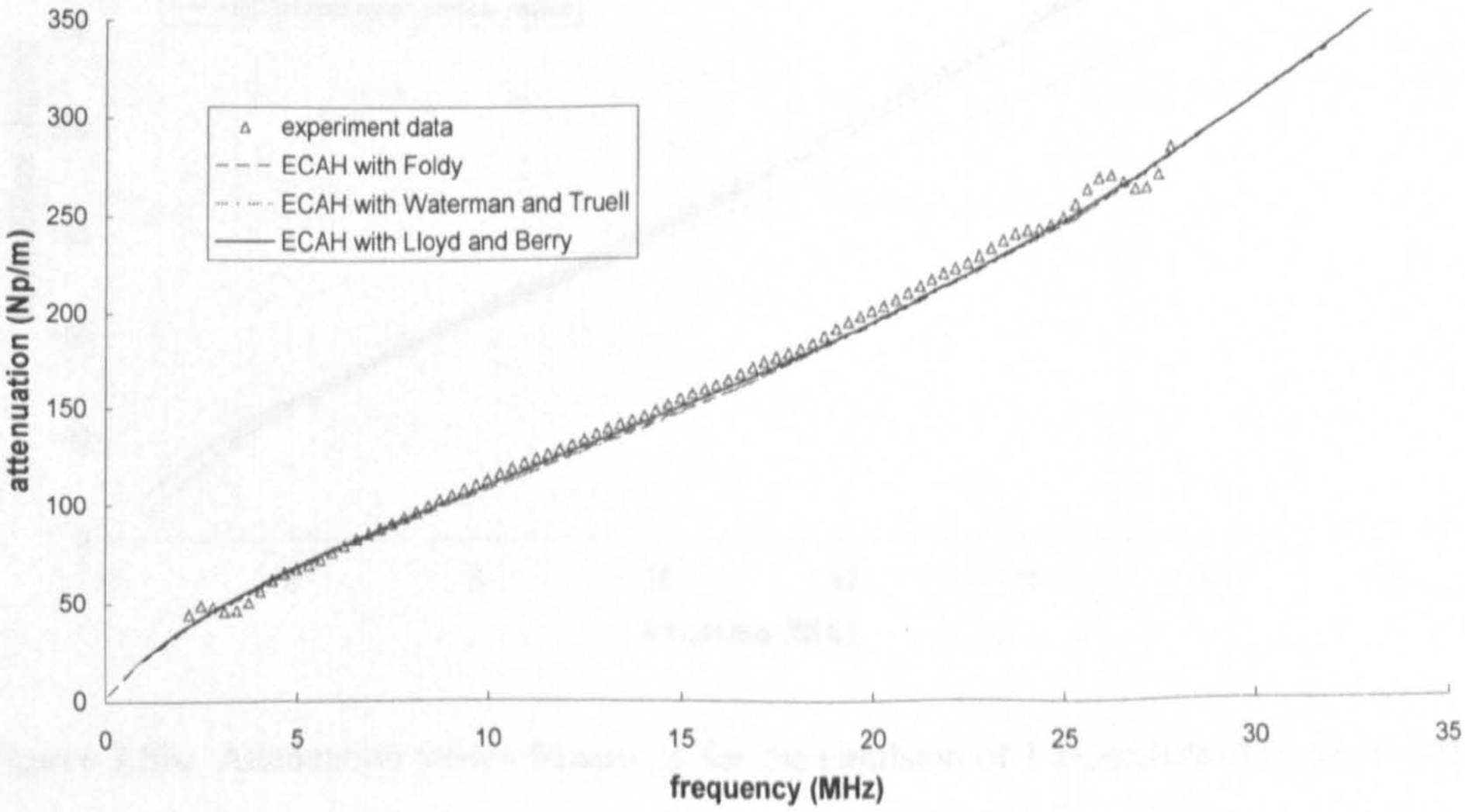

Figure 2.4. Comparison of the experimental attenuation for 25% 1-bromohexadecane emulsions of 1.2μm particle radius with the simulation data on the basis of ECAH model adopted by Foldy (broken line), Waterman and Truell (dash line) and Lloyd and Berry (solid line).

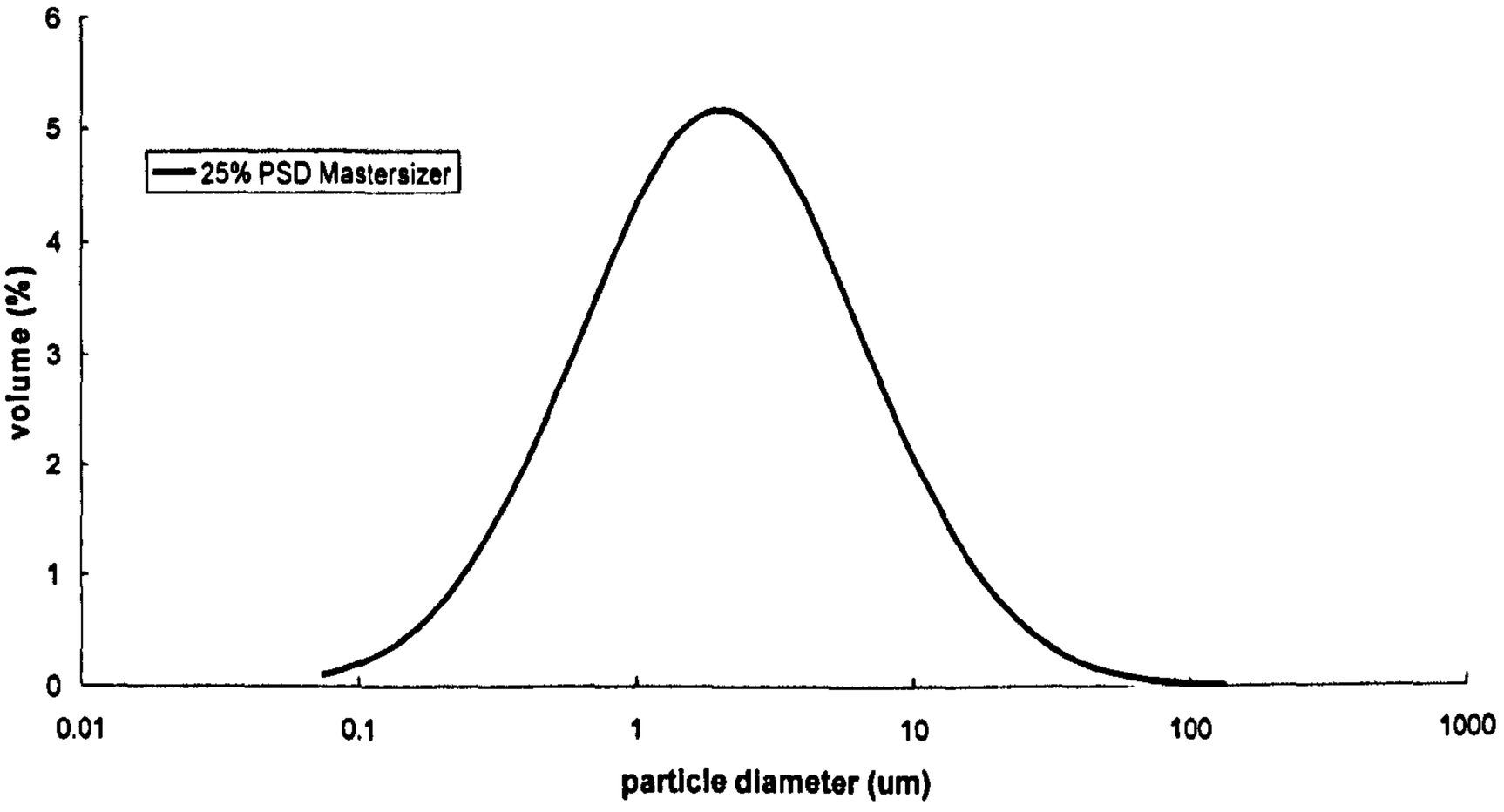

Figure 2.5a. Particle size distribution of 25% 1-bromohexadecane-in-water emulsion calculated using *Mastersizer*.

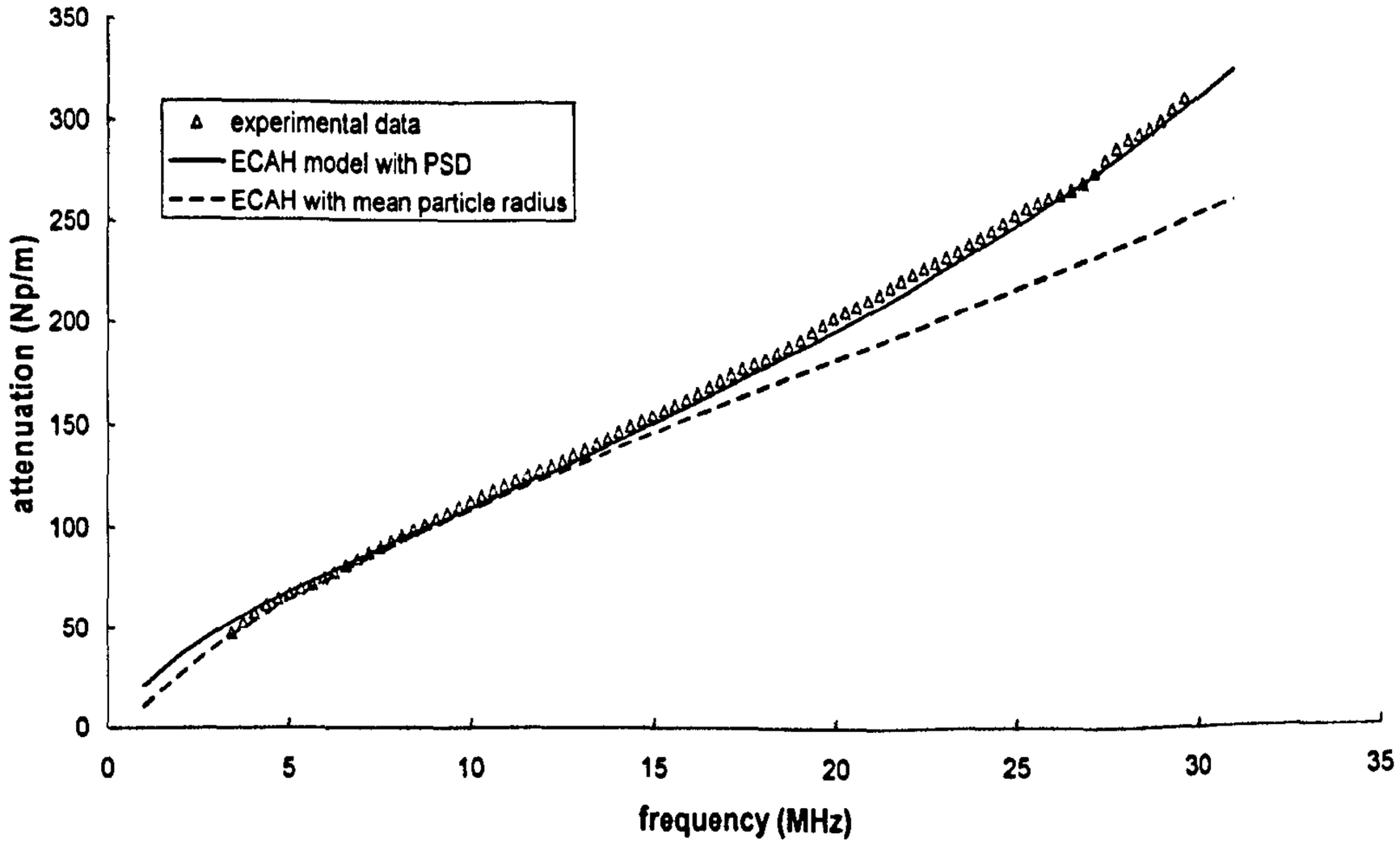

Figure 2.5b. Attenuation versus frequency for the emulsion of 1-bromohexadecane-in-water. Comparison of experimental data (dots) with ECAH model using the particle size distribution shown in figure 2.5a (solid line) and ECAH model using the mean particle radius (broken line).

2.3.10 Explicit expressions for low order scattering coefficients

An alternative way to calculate the theoretical attenuation is to use the explicit solution of the zero and first order attenuation coefficients A_0 and A_1. These explicit expressions were first derived by Epstein and Carhart (1953) for the case of a liquid-in-liquid system and then extended by Allegra and Hawley (1972) to the solid-in-liquid system. Within the long wavelength limit, the equations for A_0 and A_1 terms can be simplified by using limiting forms for the Bessel and Hankel functions, and the solution provides an opportunity to avoid the potential errors of computation associated with the full ECAH model. The analytical results also illuminate the physical phenomena that contribute to attenuation.

Epstein and Carhart obtained the following explicit expression for scattering coefficients for suspensions of liquid particles in a liquid continuum, and Allegra and Hawley obtained the same result some years later:

$$A_0 = -i\frac{a_{c2}}{3}\left(a_{c2}^2 - \frac{\rho_2}{\rho_1}a_{c1}^2\right) - ia_c\frac{g_2}{G_2}\left(1-\frac{\rho_2 b_{c1}}{\rho_2 b_{c2}}\right)\frac{H_1}{H_2} \tag{2.26}$$

$$A_1 = \frac{-ia_{c2}^3\left(\frac{\rho_2}{\rho_1}-1\right)\left[h_2(a_{s2})Q(a_{s1}) - \frac{\eta_2}{\eta_1}a_{s2}h_1(a_{s2})j_2(a_{s1})\right]}{3\times\left[3\frac{\rho_2}{\rho_1}h_2(a_{s2}) + 2\left(\frac{\rho_2}{\rho_1}-1\right)h_0(a_{s2})\right]Q(a_{s1}) - \frac{\eta_2}{\eta_1}a_{s2}h_1(a_{s2})j_2(a_{s1})\left(\frac{\rho_2}{\rho_1}+2\right)} \tag{2.27}$$

Where $H_1 = a_{t2}h_1(a_{t2})\left[1-\frac{\kappa_1 G_2}{\kappa_2 G_1}\right]$

$$H_2 = h_0(a_{t2}) - \frac{\kappa_2 a_{t2}}{\kappa_1 a_{t1}}\frac{h_1(a_{t2})}{j_1(a_{t1})}j_0(a_{t1})$$

$$Q(a_{s1}) = a_{s1} j_1(a_{s1}) - 2\left(1 - \frac{\eta_{s2}}{\eta_{s1}}\right) j_2(a_{s1}) \tag{2.28}$$

In long wavelength limit, since the compression wavenumber-radius products a_{c2} and a_{c1} are much less than one, the Hankel function, $h_n(x)$ and Bessel function, $j_n(x)$ with arguments a_{c2} and a_{c1} can be replaced by the first terms in their Taylor series. Approximate expressions for the low order Hankel and Bessel functions ($n = 0,1,2$) can be written as follows:

$$h_0(x) = -\frac{ie^{ix}}{x},\ h_1(x) = -\frac{e^{ix}}{x}\left(1 + \frac{i}{x}\right),\ h_2(x) = i\frac{e^{ix}}{x}\left(1 + \frac{3i}{x} - \frac{3}{x^2}\right);$$

$$j_0(x) = \frac{\sin x}{x},\quad j_1(x) = \frac{1}{x}\left(\frac{\sin x}{x} - \cos x\right),$$

$$j_2(x) = \frac{1}{x}\left[\left(\frac{3}{x^2} - 1\right)\sin x - \frac{3}{x}\cos x\right] \tag{2.29}$$

Alternative expressions for the scattering coefficients A_0 and A_1 for the case of liquid particles suspended in a liquid continuous phase were derived by Pinfield (1996) and Povey (1997). Their approximation has a simpler form for A_1 compared with the one obtained by Epstein and Carhart, since it only needs the basic thermal and acoustic parameters, and does not include the Hankel and Bessel function. But it gives the same result as the one derived by Epstein and Carhart. In their approximation, they used the conditions for the limiting values of the attenuation coefficient suggested by Pinfield (1997):

$$A_0 = -\frac{ia_{c2}\left(a_{c2}^2 - a_{c1}^2\dfrac{\rho_1}{\rho_2}\right)}{3} - ia_{c2}^3(\gamma - 1)\left(1 - \frac{\beta_1 C_{p2}\rho_2}{\beta_2 C_{p1}\rho_1}\right)^2 \frac{H}{a_{t2}^2}$$

$$A_1 = \frac{ia_{c2}^3(\rho_1 - \rho_2)(1 + T + iS)}{9(\rho_1 + \rho_2 T + iS\rho_2)} \tag{2.30}$$

Where $H = \left[\frac{1}{1 - i a_{t2}} - \frac{\kappa_2}{\kappa_1} \cdot \frac{\tan(a_{t1})}{\tan(a_{t1}) - a_{t1}} \right]^{-1}$ **(2.31 a)**

$$S = \frac{9}{4 a_{s2}} \left(1 + \frac{1}{a_{s2}} \right) \qquad \textbf{(2.31 b)}$$

$$\gamma = \frac{C_p}{C_v}; \quad T = \frac{1}{2} + \frac{9\delta}{4r}; \quad \delta = \sqrt{\frac{2\mu}{\rho\omega}}. \qquad \textbf{(2.31 c)}$$

Allegra and Hawley (1972) gave the approximations for solid particles suspended in the liquid continuum, which had a much more complex form than the expressions for liquid particles in liquid continuous phase; however, since these are not relevant to emulsions, they will not be included here.

The explicit expressions for the scattering coefficients will be used to predict the attenuation for comparison with the result obtained from the full ECAH model by solving the complex matrix equation. Expressions of this type are widely employed for the reason that they avoid the computational complexity associated with the full matrix solution. They are only accurate in the long wavelength limit, but it is not known what is the maximum value of $k_c r$ to remain valid. One of the aims of this project is examine the range of conditions over which these explicit expressions can be used to replace the full ECAH model.

2.3.11 Physical significance of scattering coefficients

The long wavelength limiting and explicit solutions help to identify the physical processes represented by the various scattered partial wave modes. The coefficient A_n represents the amplitude of the compression wave field diffracted by a suspended particle. Each A_n is associated with a spatial

distribution expressed by a spherical Hankel function and a Legendre polynomial, each of order n. Monopole symmetry is implied by $n=0$, dipole symmetry by $n=1$, and so on.

The zero-order scattering coefficient, A_0 (equation 2.30), can be separated into two parts. The first part, denoted as A_{01}, ($A_{01} = -\frac{ia_{c2}\left(a_{c2}^2 - a_{c1}^2 \frac{\rho_1}{\rho_2}\right)}{3}$) is unaffected by thermal effects and depends on the difference of compressibility between the two phases. The second part, A_{02}, ($A_{02} = -ia_{c2}^3(\gamma_2 - 1)\left(1 - \frac{\beta_1 \rho_2 C_{p2}}{\beta_2 \rho_1 C_{P1}}\right)^2$) is related to thermal scattering because it contains the thermal term $\left(1 - \frac{\beta_1 \rho_2 C_{p2}}{\beta_2 \rho_1 C_{P1}}\right)^2$, which results from the acylic differences in temperature between the particles and the surrounding phase. The larger this term, the greater effect of thermal scattering will be.

The first-order or dipole contribution to the attenuation described by the coefficient A_1 is related to visco-inertial scattering, which occurs when droplets have a different density from the surrounding fluid. In the presence of a compressional wave the difference in inertia between particles and fluid causes the particles to oscillate to and fro with respect to the continuous phase. This oscillation is damped by the viscosity of the surrounding fluid. As seen in equation 2.27 for the case of liquid particles in liquid continuous phase, the attenuation from this mechanism depends on the density difference between the suspended matter and that of the suspending fluid.

For a small density difference (such as 1-bromohexadecane, polystyrene), the particles move at the same speed as the molecules of suspending fluid, so

the energy loss is very small; for large density difference (such as silica or iron in water), the relative motion becomes greater with larger losses occurring. In emulsions or suspensions with low density contrast between the two phases (i.e. $0.8 \leq \frac{\rho_1}{\rho_2} \leq 1.2$), the thermal effect plays an important role, so A_0 is the dominant term compared with high order term of A_n. Figure 2.6a shows the attenuation calculated using the coefficients of A_0 and A_1 alone, together with the total attenuation by using the sum of them. It has been calculated for a 12.5% 1-bromohexadecane oil-in-water emulsion with a particle radius of 1.2 μm, the density ratio of water to 1-bromohexadecane is around 0.997. It is clear that A_0 is the dominant term in the whole attenuation. Figure 2.6b shows the dominance of A_1 for high density contrast suspensions of silica in water, the density ratio of silica to water is around 2.2.

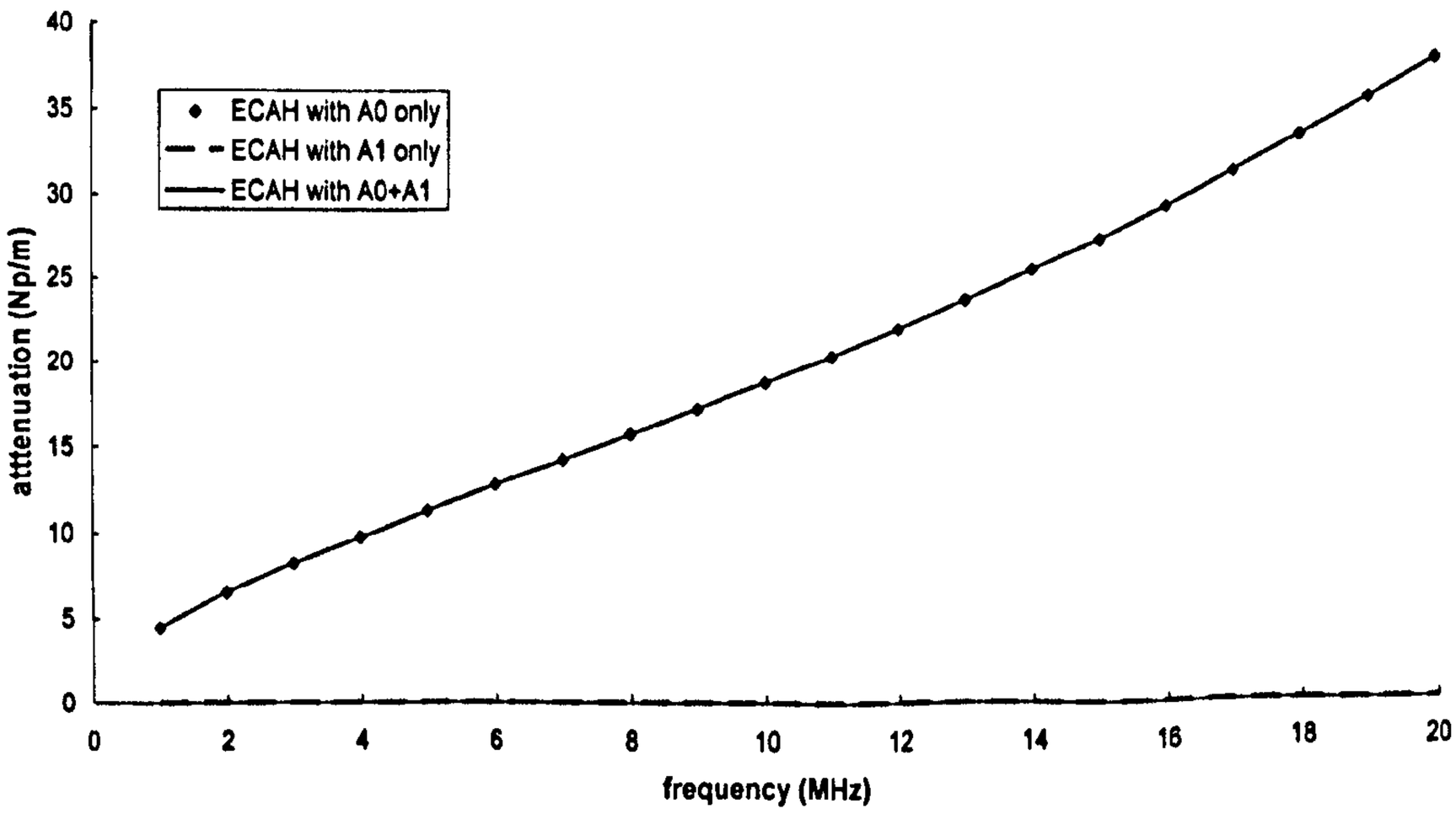

Figure 2.6a. Contribution of the ECAH attenuation coefficients A_0 and A_1 to the whole attenuation in emulsion: 12.5% 1-bromohexdecane with mean radius of 1.2 μm. The dots is for A_0 term only, broken line is for A_1 term only, solid line is for $A_0 + A_1$.

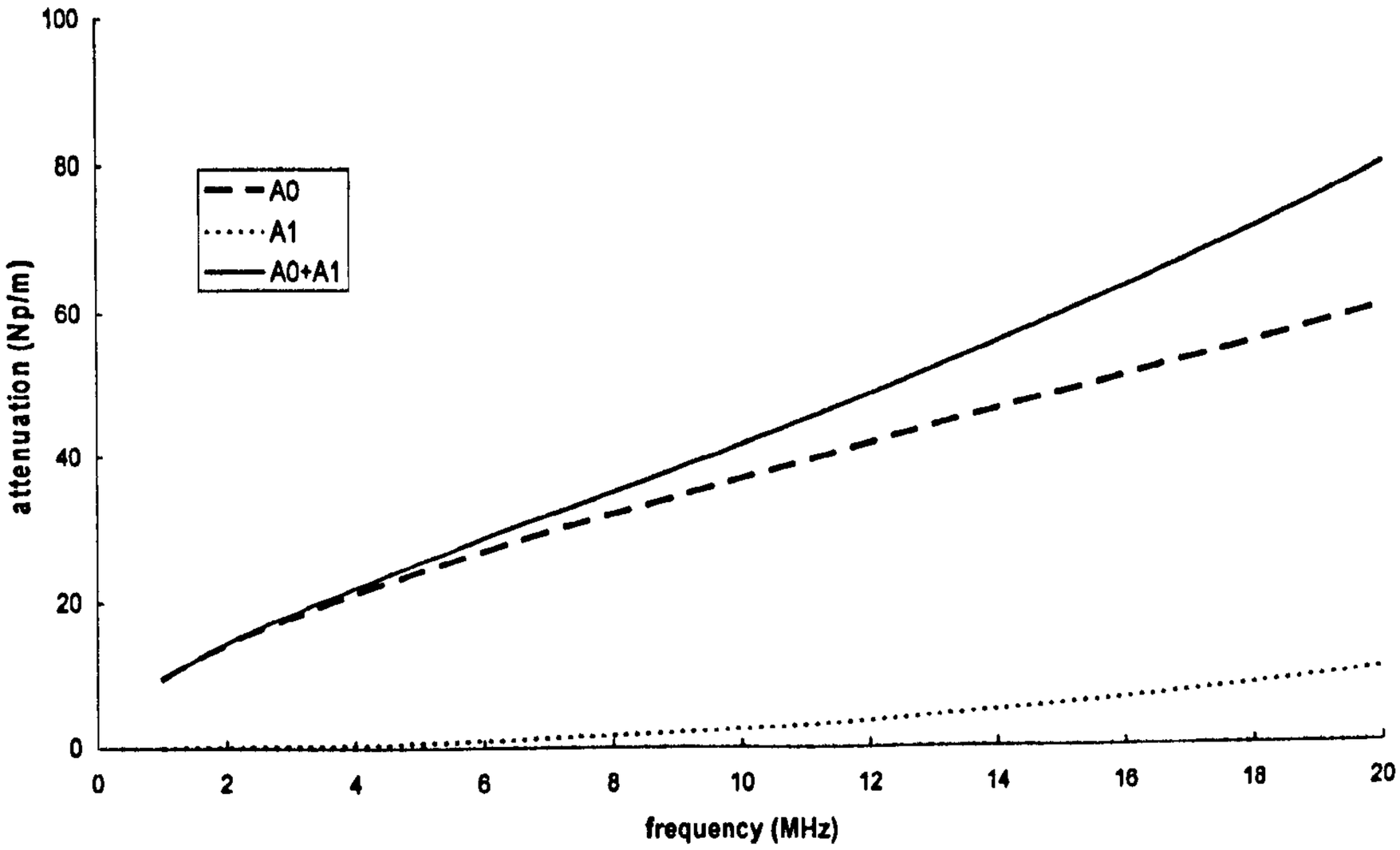

Figure 2.6b. Contribution of the ECAH attenuation coefficients A_0 and A_1 to the whole attenuation in suspension: 4.1% silica-in-water with mean radius of 0.16μm. The dash line is for A_1 term only, broken line is for A_0 term only, solid line is for $A_0 + A_1$.

Compared with the A_0 and A_1 terms, each higher-order term of $A_n (n \geq 2)$ contains an additional factor of a_c^2, and it is this that enables us to neglect the higher-order terms in the long wavelength limit because $a_c << 1$. Besides, as we mentioned in section §2.3.8, the maximum number of orders depends on $k_c r$.

In general the effects of visco-inertial and thermal scattering are intermingled, but in the long wavelength limit and for the dilute systems, we can calculate their effects independently and then add them together (see equation 2.3). Examination of the approximate expressions in equations 2.26 and 2.27 reveal that thermal scattering is associated with the A_0 term, whilst visco-inertial scattering is associated with the A_1 term (Ahuja, 1973). We

therefore separate the contributions of the thermal and visco-inertial scattering to the overall attenuation, and obtain:

$$\alpha_{th} = -\frac{3}{2}\frac{\phi \mathrm{Re}(A_0)}{k_c^2 r^3} \tag{2.32}$$

$$\alpha_{vis} = -\frac{3}{2}\frac{\phi \mathrm{Re}(3A_1)}{k_c^2 r^3} \tag{2.33}$$

Figure 2.7 was plotted to demonstrate the practical significance of the thermal and visco-inertial scattering mechanisms using equations 2.32 and 2.33. Attenuation per wavelength $\alpha\lambda$ is plotted against $\sqrt{fr}$, since this term is proportional to the terms of product of wavenumber and radius, which determine the magnitude of thermal and visco-inertial scattering. The magnitude of visco-inertial attenuation depends on the density difference between the particles and surrounding fluid, and its maximum value occurs when the viscous skin depth ($\delta_s = \sqrt{2\upsilon/\omega}$) is approximately equal to the particle radius, in figure 2.7 it is negligible. Similar arguments apply to the thermal attenuation, the maximum value occurs when the thermal skin depth ($\delta_t = \sqrt{2\sigma/\omega}$) is approximately equal to the particle radius. In this figure, the excess attenuation was used, which is defined as the difference between overall attenuation and that caused by intrinsic absorption alone:

$$\Delta\alpha = \alpha - (1-\phi)\alpha_2 - \phi\alpha_1$$

where α_1 and α_2 are the intrinsic attenuation of the dispersed phase and continuous phase, respectively.

In the emulsion, the excess attenuation is the sum of thermal and viscous attenuation.

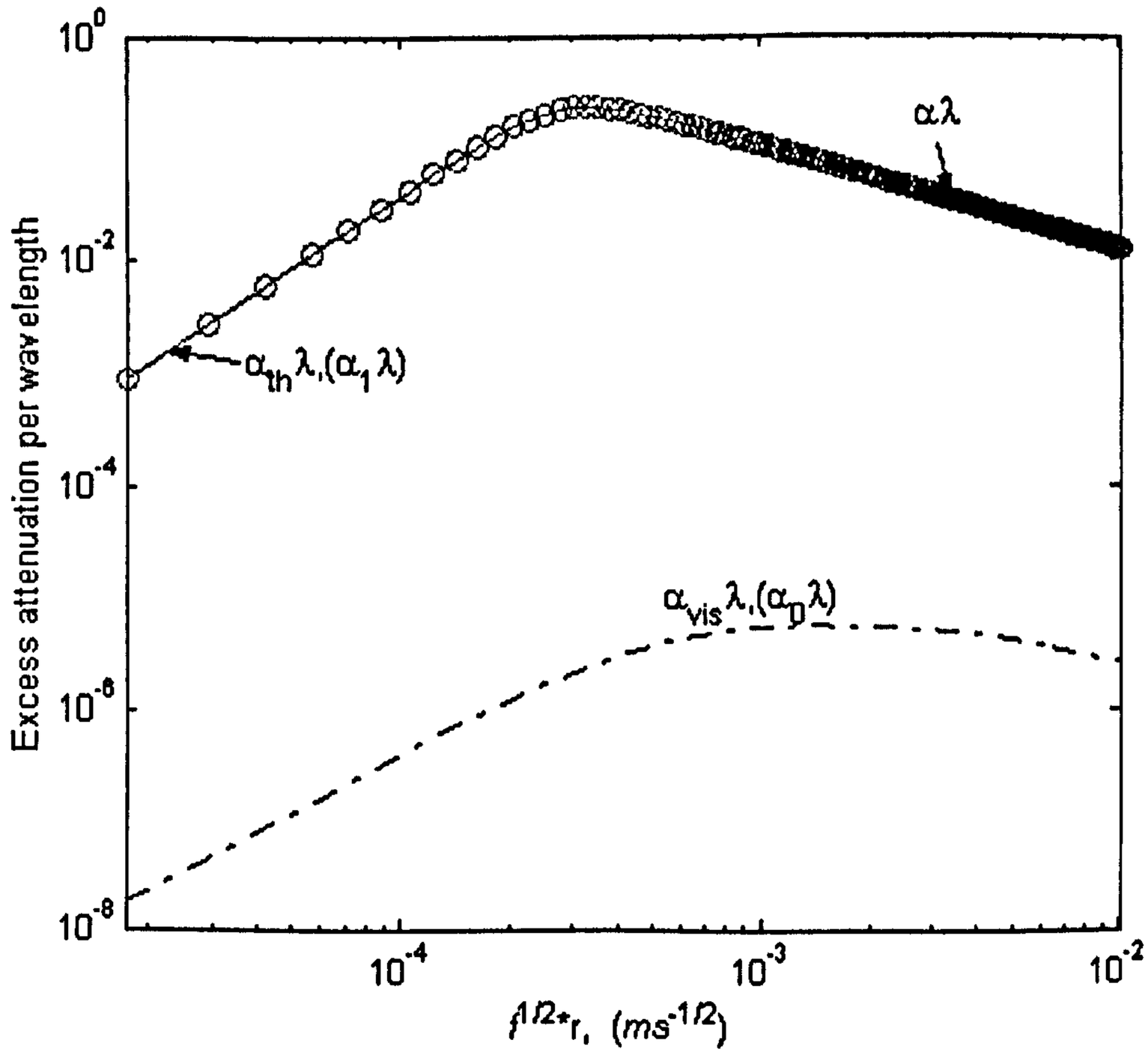

Figure 2.7. Variation of $\alpha_{vis}\lambda$ and $\alpha_{th}\lambda$ with for 1-bromohexadecane-in-water using equations 2.32 and 2.33.

2.4 Failure of theory at high concentrations

The acoustic analysis of suspensions and emulsions by the ECAH model is difficult at high particle concentrations. In this case, the particle or droplets can no longer be assumed to behave as individual isolated objects, and a simple linear superposition of isolated-particle behaviour is no longer adequate. The nonlinear increase of sound attenuation with particle concentration is due to two kinds of multiple-particle effects that become more significant at higher concentrations. First of all, the redirection of the acoustic wave between the particles leads to multiple scattering, where each particle is immersed in an overall field of primary and secondary waves instead of in the undisturbed

initial compressional wave. Secondly, particle-particle interactions lead to a modified intrinsic behaviour of individual particles. The response of a given particle to a certain excitation is different whether the particle is surrounded by an infinitely large homogeneous medium or by a medium interspersed by other particles. In the case of high concentration emulsions, because of the typically relatively small particle separation, the particle-particle interactions become a major source of nonlinearity and are thus one of the principal concerns of this thesis.

In the long wavelength limit, the principal form of attenuation in emulsions with low density contrast is the thermal transport which occurs between a droplet and its surroundings (McClements and Povey, 1989). The extent of these thermal losses depends on the difference in thermal properties between the droplet and its surroundings. The ECAH theory assumes that a single particle is surrounded by an infinite medium, i.e. there is no interaction between neighbouring droplets, so that the heat generated by one droplet flows directly into the continuous phase. However, in the following three situations, the thermal (or shear) wave generated by a droplet may propagate into its neighbouring droplets, as illustrated in figure 2.8. First of all, at high particle concentrations, the inter-particle distance is getting smaller. Secondly, for emulsions with small particle sizes, the inter-particle distance is getting smaller as well. And thirdly, at low frequencies, the thermal or shear wavelength is getting longer. Typically, these effects result in a deviation between ECAH model and the experiment data.

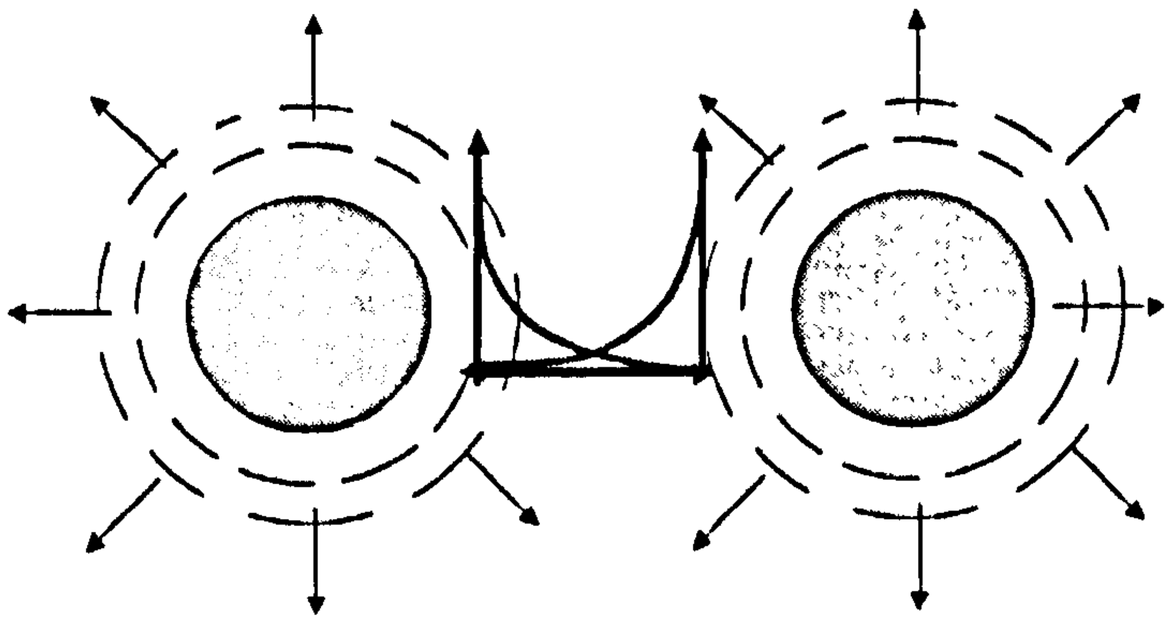

Figure 2.8. Thermal wave overlap effects in the emulsions (top); shear wave overlap effects in the suspensions (bottom), based on Challis et al (2005).

The limit at which thermal overlap becomes significant can be estimated from the average surface-surface distance between neighbouring particles. If the droplets are supposed to be spherical and randomly dispersed, then the average distance d separating the surfaces of two neighbouring particles as given by Herrmann (1996) is:

$$d \approx r\left(\sqrt[3]{\frac{4\pi}{3\phi}} - 2\right) \tag{2.34}$$

where r is the radius of the suspended droplet, and ϕ is the disperse volume fraction. This quantity is related to the length of the secondary waves around each particle, since in the case of d being small, the secondary waves may interfere, which will affect the intrinsic particle behaviour. To quantify the length of the secondary waves, the concept of skin depth was introduced.

Thermal skin depth is defined as the distance for the temperature in the surrounding fluid to decrease to $1/e$ of its value at the interface, which can be written as:

$$\delta_T = \sqrt{\frac{2\kappa}{\omega\rho C_p}} \tag{2.35}$$

where κ is the thermal conductivity and C_p is the specific heat capacity. Similarly, the shear skin depth as:

$$\delta_s = \sqrt{\frac{2\eta}{\omega\rho}} \tag{2.36}$$

Therefore, particle-particle interactions are significant if there is not enough interparticle space for the corresponding boundary layers, that is, thermal wave overlap happens when $\delta_T \geq d/2$ (or shear wave overlap happens when $\delta_s \geq d/2$). Figure 2.9 illustrates half the average surface-surface distance $\frac{d}{2}$, thermal skin depth δ_T and shear skin depth δ_s as a function of frequency for a range of concentrations, assuming the particle radius is 0.1 μm. The horizontal lines indicate the half average particle separation at different concentrations using equation 2.34. For example, at 20% v/v, the grey shadow indicates that there is thermal overlapping effect when frequency is less than 5.5 MHz, where the thermal skin depth is larger than the half particle distance, and when the frequency is less than 32 MHz, shear overlapping occurred, as the yellow shadow area indicates. It is apparent from this figure that for a fixed particle size, the overlapping becomes more pronounced at high particle concentration, which means d is small, or at low frequencies, where δ_T or δ_S is larger. As can also be seen in figure 2.9, the

thermal skin depth in aqueous dispersions is generally smaller than the viscous one ($\delta_T \approx 0.4\delta_S$). In systems where thermal losses are dominant, overlapping between boundary layers and corresponding nonlinearities therefore occur at higher particle concentrations.

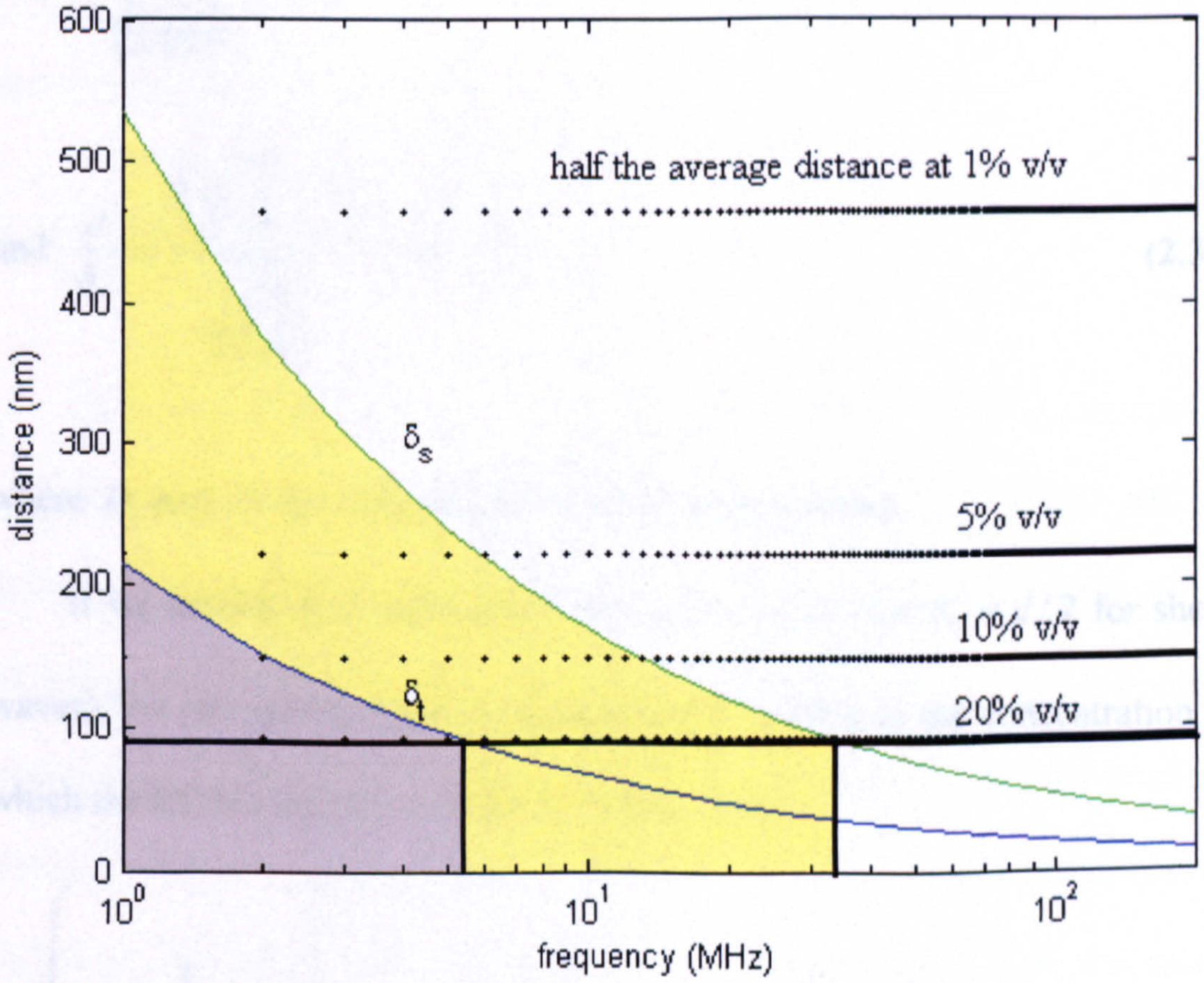

Figure 2.9. The viscous and thermal boundary layers in an aqueous phase, plotted as δ_T (blue line) and δ_S (green line) using equations 2.35 and 2.36. The half of averages separations between neighbouring particles are indicated as horizontal lines for several values of the particle volume fraction, assuming a particle radius of 0.1μm (equation 2.34). For d below δ_T (or δ_S) (the shade areas), particle interactions may arise.

From equation 2.34 we know that the average surface-surface distance d is proportional to the suspended particle radius r at a given ϕ. Therefore the ratio of distance to thermal skin depth d/δ_T (or the ratio of distance to shear

shin depth d/δ_S) becomes a function of the product of radius and the square root of frequency ($\sqrt{fr}$):

$$\frac{d}{\delta_T} = \frac{r\left(\sqrt[3]{\frac{4\pi}{3\phi}} - 1\right)}{\sqrt{\frac{2\kappa}{2\pi f\rho C_p}}} = D_1 \cdot \sqrt{fr} \tag{2.37}$$

$$\text{and } \frac{d}{\delta_s} = \frac{r\left(\sqrt[3]{\frac{4\pi}{3\phi}} - 1\right)}{\sqrt{\frac{2\eta}{2\pi f\rho}}} = D_2 \cdot \sqrt{fr} \tag{2.38}$$

where D_1 and D_2 are constants given the volume fraction.

If we assume that interactions start at $\delta_T = d/2$ (or $\delta_S = d/2$ for shear waves), we can get the critical volume fraction, which is the concentration at which the ECAH model is expected to break down:

$$\phi > \left(\frac{1}{1+\sqrt{\frac{\kappa}{\pi f r^2 \rho C_P}}}\right)^3 \tag{2.39}$$

We can conclude that, in a dilute emulsion system, the half distances between any two particles will be larger than the thermal skin depth: $d/2 > \delta_T$, so thermal wave can die away unaffected by other thermal waves scattered by adjacent particles. However, in concentrated emulsion systems, where the particles are close together, or at low value of frequency or with small particle sizes, where the thermal skin depth is larger than the half distance between droplets ($\delta_T \geq d/2$), thermal interactions will occur. This relationship effectively accounts for the fact that measurements of the attenuation are

always lower than those predicted by ECAH scattering theories at high droplet concentrations.

A model by which the effects of thermal overlap can be accounted for has been proposed by McClements *et al* (Hemar et al,1997, Herrmann et al, 1996 McClements et al, 1999), where a core shell was invoked, and this will be discussed in detail in chapter 3.

2.5 Conclusion

This chapter has given a brief introduction to the so-called scattering models for acoustic attenuation in particulate dispersions, following the formulations of Epstein and Carhart and Allegra and Hawley, known as the ECAH model. Generally the ECAH model when used to simulate ultrasonic measurements gives very good agreement with experimental results in dilute mixtures. At high concentrations of dispersed phase the ECAH model, even including multiple scattering, may break down and predict a greater attenuation than observed experimentally — the dependence of the attenuation on concentrations becomes non-linear. The breakdown is believed to be due to overlapping of evanescent wave fields scattered by suspended particles in close proximity — thermal wave fields in the case of emulsion, and viscous wave fields in the case of suspensions. The need for an alternative model for the high concentration case has been expressed by many at least a decade ago (McClements and Povey, 1989, Hemar, 1997). The solution has not yet been applied to solid in liquid systems (see Challis *et al* 2005), but a possible solution for emulsions with low density contrast between the two phases has been suggested by Hemar (1997), Herrmann (1998) and McClements et al

(1999) (HHM model). The principal questions in this thesis concern the validity of wave propagation models for emulsions — dilute and concentrated — and it is for this reason that HHM's model for thermal overlap will be discussed in detail in the next chapter.

Chapter 3 Extended Theories for Concentrated Emulsions

3.1 Introduction

The ECAH theory of the ultrasonic wave propagation in dilute systems is now well-established and was discussed in the last chapter. This approach gives excellent agreement with experimental measurements in dilute emulsions, but recent studies showed that, at high particle concentrations, say 15%, the ECAH model fails to explain quantitatively the ultrasonic attenuation (Hemar, 1997, McClements et al, 1999). It over-predicts the attenuation data compared with the experiment measurement, especially for small particle sizes and for low frequencies. This discrepancy has been attributed to the interactions between the decaying fields of evanescent waves scattered from particles in close proximity. In this chapter, we will present two relatively new models, which deal with the wave propagation in concentrated emulsion and suspension systems. The aim here is to establish once and for all what the limits of the unmodified ECAH theory actually are, and then to examine in detail the applicability of the new models. Ultimately we wish to know what model to use in procedures for dispersed phase particle sizing by means of ultrasound.

Section 3.2 introduces a HHM model, which was initially suggested by Hemar *et al* (1997) and extended by McClements et al (1999) to include intrinsic absorption as well as multiple scattering effects. Its authors propose

that this model can be used for high concentration emulsions because it accounts for the thermal wave interaction between particles.

A relative new-comer to wave propagation models is the coupled phase model of Evans and Attenborough (1996, 2002), which has the advantage that it avoids computations of matrix functions but nevertheless includes thermal coupling between phases. It has considerable potential for use in particle sizing operates, but its validity in the content of emulations of various concentrations and particle sizes remains to be established. It is for this reason that it is included in this study.

3.2 The Hemar, Herrmann and McClements model (HHM model)

In the long wavelength regime, the dominant part of the attenuation in emulsions with low density contrast between the dispersed phase and continuous phase is the heat flow which occurs between a suspended particle and its surroundings in the presence of an ultrasonic wave. The basic scattering theory, ECAH theory, assumes that there are no overlaps of thermal waves between neighbouring particles, so that heat generated by one particle flows directly into the continuous phase. In practice, the heat generated by a particle may be propagated into a neighbouring particle, therefore the temperature difference between any given particle and its surroundings is reduced, and thus leads to a decrease in the attenuation. This explains why the measurements of the attenuation coefficient of emulsions are lower than the scattering theory predicts at high concentrations.

The HHM model was developed by Hemar (1997), Herrmann (1998) and McClements *et al* (1999), the aim of which was to account for the interactions between thermal waves at high concentrations.

Hemar *et al* (1997) first proposed the idea of the HHM model to compensate the interaction between particles in concentrated emulsions. Figure 3.1 shows the conventional scattering model (left) and the HHM model (right). We can see that in the conventional scattering model, the droplet is assumed to be surrounded by pure continuous phase. In the HHM model, on the other hand, we imagine a shell of continuous phase surround the particle, which can be treated as a new particle with larger diameter. Outside the shell, there is an effective medium, whose properties are determined by the composition of both the disperse and continuous phases.

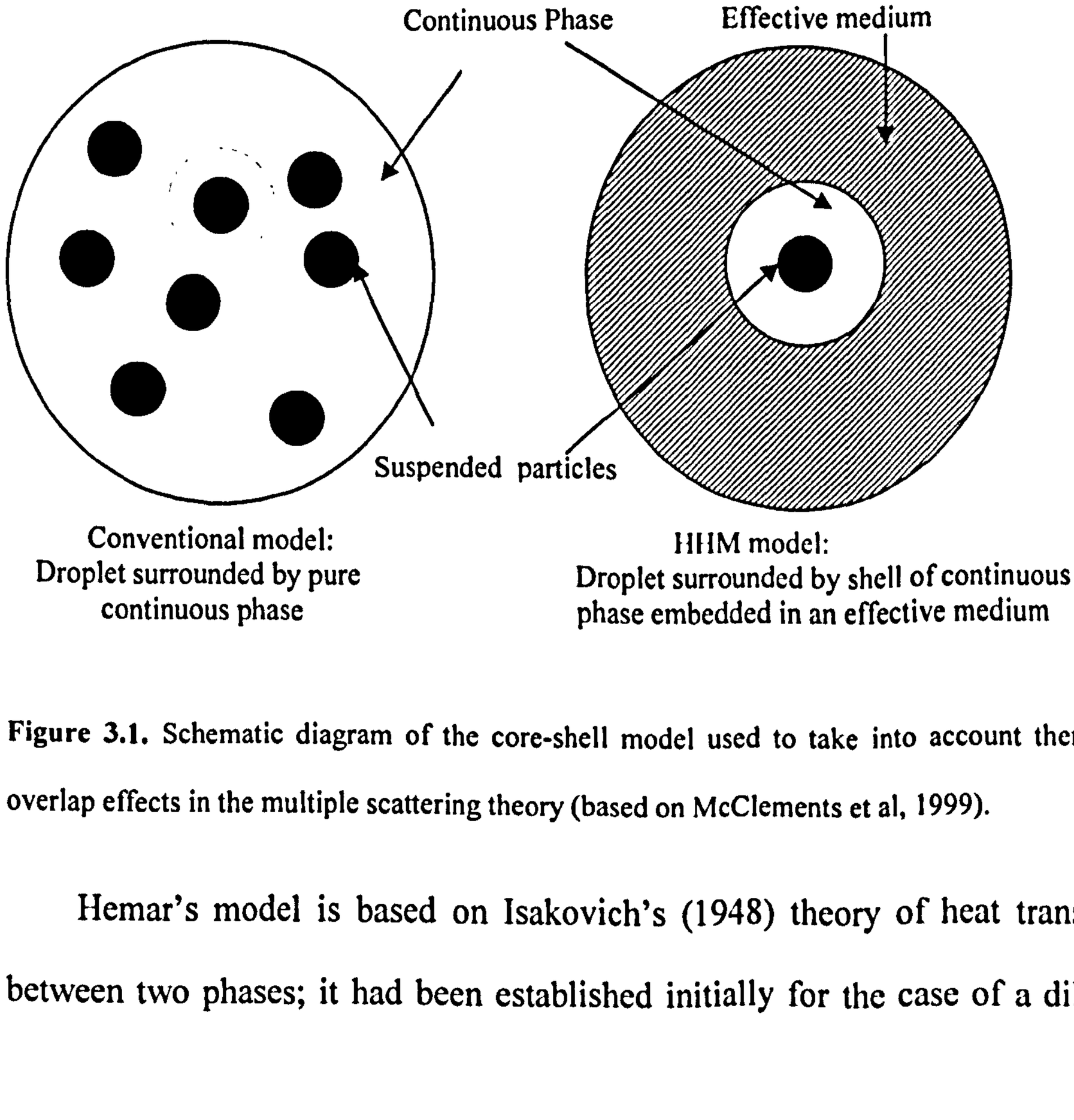

Figure 3.1. Schematic diagram of the core-shell model used to take into account thermal overlap effects in the multiple scattering theory (based on McClements et al, 1999).

Hemar's model is based on Isakovich's (1948) theory of heat transfer between two phases; it had been established initially for the case of a dilute

emulsion system. The complex wavenumber of the mixture was given by Isakovich:

$$\left(\frac{\beta}{k}\right)^2 = 1 + i\frac{3\phi}{\omega r^2}\frac{T}{\chi_3}\left(\frac{\beta_{T1}}{\rho_1 C_{P1}} - \frac{\beta_{T2}}{\rho_2 C_{P2}}\right)^2 H \qquad \textbf{(3.1)}$$

$$\text{where } H = \left[\frac{1}{\kappa_1[n_1 r/\tanh(n_1 r) - 1]} + \frac{1}{\kappa_2(1+n_2 r)}\right]^{-1} \qquad \textbf{(3.2)}$$

and χ_3 is the volume averaged adiabatic compressibility of the emulsions, which determined by the value of the adiabatic compressibility of both dispersed phase and continuous phase ($\chi_3 = \phi\chi_1 + (1-\phi)\chi_2$);

$$n_j = (1-i)\sqrt{\frac{\omega_j \rho_j C_{pj}}{2\kappa_j}} \text{ (j=1,2);}$$

κ is the thermal conductivity and r is the suspended particle radius. The subscripts 1 and 2 refer to the dispersed phase and continuous phase, respectively.

Hemar modified Isakovich's wavenumber equation (equation 3.1) by using a new thermal term H to replace equation 3.2 in his model. Thus this new equation took into consideration of the thermal overlap effects between the particles.

$$H = \kappa_1\kappa_2 \frac{n_1 r - \tanh(n_1 r)}{E\cdot C + F\cdot D}\left[2\kappa_3 \frac{g_2 - g_3}{g_1 - g_2} n_2 r_s (n_3 r_s + 1) + C(1+n_2 r) + D(1-n_2 r)\right] \qquad \textbf{(3.3)}$$

$$\text{where } g_j = \frac{\beta_{Tj}}{\rho_j C_{Pj}} \qquad \textbf{(3.4 a)}$$

$$n_j = (1-i)\sqrt{\frac{\omega_j \rho_j C_{Pj}}{2\kappa_j}} \qquad \textbf{(3.4 b)}$$

$$C = e^{n_2(r_s - r)}[\kappa_2(n_2 r_s - 1) + \kappa_3(n_3 r_s - 1)] \quad \textbf{(3.4 c)}$$

$$D = e^{-n_2(r_s - r)}[\kappa_2(n_2 r_s + 1) - \kappa_3(n_3 r_s + 1)] \quad \textbf{(3.4 d)}$$

$$E = \kappa_1 n_1 r + [\kappa_2(n_2 r + 1) - \kappa_1]\tanh(n_1 r) \quad \textbf{(3.4 e)}$$

$$F = \kappa_1 n_1 r - [\kappa_2(n_2 r - 1) + \kappa_1]\tanh(n_1 r) \quad \textbf{(3.4 f)}$$

It is easily verified that the above expression reduces to equation 3.2 both for high frequencies and for low concentrations (in these two cases the term C tends to infinity whilst the term D tends to zero because $n_j r_s$ goes to infinity). However, Hemar's model is limited because it ignores intrinsic absorption in both the particles and the continuous phase, multiple scattering caused by ϕ^2 term and visco-inertial effects, although the multiple scattering may be very small and visco-inertial effects may not be very important for low density contrast emulsions. McClements *et al* (1999) demonstrated how the ECAH scattering theory could be modified to incorporate Hemar's expression. By using Lloyd and Berry (1967) multiple scattering expression (the higher order terms are neglected in the following equation):

$$\left(\frac{\beta}{k_c}\right)^2 = 1 - \frac{3i\phi}{k_c^3 r^3}(A_0 + 3A_1) - \frac{27\phi^2}{k_c^6 r^6}(A_0 A_1 + 2A_1^2) \quad \textbf{(3.5)}$$

Following Hemar's idea, McClements et al modified the zero-order of the scattering coefficient A_0, i.e. the monopole term, to include the thermal wave overlap effects:

$$A_0 = -\frac{ia_{c2}}{3}\left(a_{c2}^2 - a_{c1}^2\frac{\rho_1}{\rho_2}\right) - \frac{ia_{c2}^3(\gamma_2 - 1)}{b_2^2}\left(1 - \frac{\beta_{T1}C_{P2}\rho_2}{\beta_{T2}C_{P1}\rho_1}\right)^2 H_{new} \quad \textbf{(3.6)}$$

Equation 3.6 shows that the first part of A_0 term is unchanged, but the second part, which is dominated by the thermal effects, was modified to get a

new term H_{new} to account for thermal wave overlap effects. This term is analogous to Hemar's expression, but with:

$$H_{new} = H\frac{\chi_2}{\chi_3\kappa_2} \tag{3.7}$$

Again, χ_3 is the volume averaged adiabatic compressibility of the emulsions as defined above.

Now the shell thickness is set to the average distance between the droplets in the emulsion, so the radius of shell is given by:

$$r_s = \frac{r}{\sqrt[3]{\phi}} \tag{3.8}$$

where r is the suspended particle radius, and ϕ is the volume fraction of the dispersed particles. It means that the larger the volume fraction is, the smaller the shell thickness will be; that is to say that at higher droplet concentrations, the environment of a particle will appear to be same as the particle–continuous phase mixture, rather than continuous phase alone.

It is to be emphasized that the HHM model does not require any other supposition or adjustable parameter, and it is claimed that it describes correctly what happens at low frequency, where the effective medium approximation has been shown to be adequate, as well as at high frequency, where the range of the thermal wave may be smaller than the distance between droplets. The effective medium, denoted by the subscript 3, is described by the following physical constants:

$$\rho_3 = \phi\rho_1 + (1-\phi)\rho_2 \tag{3.9}$$

$$\beta_3 = \phi\beta_1 + (1-\phi)\beta_2 \tag{3.10}$$

$$\rho_3 C_{p3} = \phi\rho_1 C_{p1} + (1-\phi)\rho_2 C_{p2} \tag{3.11}$$

The thermal conductivity, which cannot simply be obtained as a volume average, has been given by Torquato (1985) for a random dispersion of hard spheres:

$$\kappa_3 = \kappa_2 \frac{1+2\phi\gamma-2(1-\phi)\varsigma\gamma^2}{1-\phi\gamma-2(1-\phi)\varsigma\gamma^2} \tag{3.12}$$

where $\gamma = \frac{\kappa_1-\kappa_2}{\kappa_1+2\kappa_2}$ and $\varsigma = 0.21068\phi - 0.04693\phi^2$

The result of HHM model offers the possibility of an accurate prediction of the ultrasonic attenuation in emulsions up to 50%. In this project a number of computations were done to show the difference between the traditional scattering theory (ECAH model) and HHM model for different concentrates of corn oil-in-water emulsions, and the results are shown in figures 3.2 and 3.3 (the thermo-physical properties of these materials was shown in table 3.1). We also show experimental results for comparison with the two models. The mean radius of the suspended particles is around 120 nm in figure 3.2, and the volume fraction is between 5% and 50%. Figure 3.2 shows that in the fairly dilute system ($\phi \le 20\%$), the ECAH model predicts the same result as the HHM model, and both of these two models gave good agreements with the experiment data, especially at lower frequencies; but at higher droplet concentrations, for example, $\phi \ge 30\%$ the ECAH model began to overpredict the attenuation compared with the experimental data, whereas the HHM model still closely follows the experimental data even at 50% v/v, especially for lower frequencies.

As has been discussed in chapter 2, when the frequency is sufficiently high and when the particle size is sufficiently large, the spacing between the

droplets will be greater than the thermal skin depth ($d >> \delta_T$), and the thermal term H in equation 3.7 tends to give the same value as the one in equation 2.31a. The two models then tend to give the same result, which can be seen from figure 3.3, which shows the attenuation spectra for corn oil-in-water emulsions with volume fraction from 5% to 50%, here the mean particle radius is 600 nm. The ECAH model gave a reasonable prediction compared with the experimental results up to 40% v/v. At 50%, the ECAH model slightly overpredicted the attenuation data. The HHM model is in good agreement with the experimental data for all concentrations. At 40% v/v, and at 10 MHz, the calculated average particle–particle surface distance is $d = 0.12$ μm, and thermal skin depth is $\delta_T = 0.06$ μm from equation 2.34 and 2.35, so it is clear that the interparticle distance is twice as the thermal skin depth. When the particle concentration decreases, the interparticle distance will increase and the thermal skin depth will decrease at higher frequencies, leading to these being no thermal wave overlap effect, which explains why the ECAH model remains applicable.

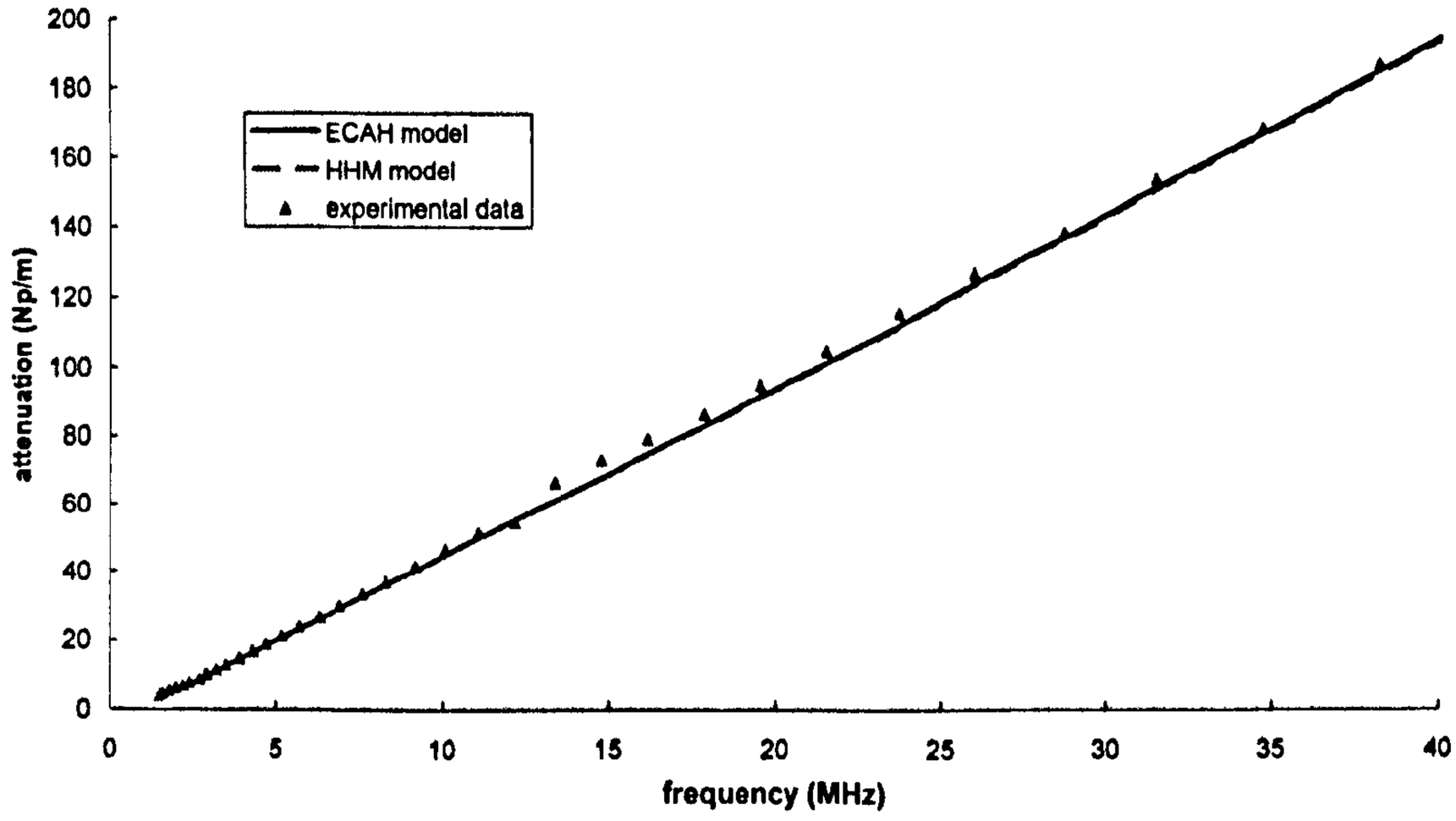

Figure 3.2a. Comparison of predicted and measured attenuation spectra for 5% corn oil-in-water emulsions with mean droplet radius of 120 nm. The triangles are experimental measurements, the solid line is computed using the ECAH model, and the broken line is computed using HHM model.

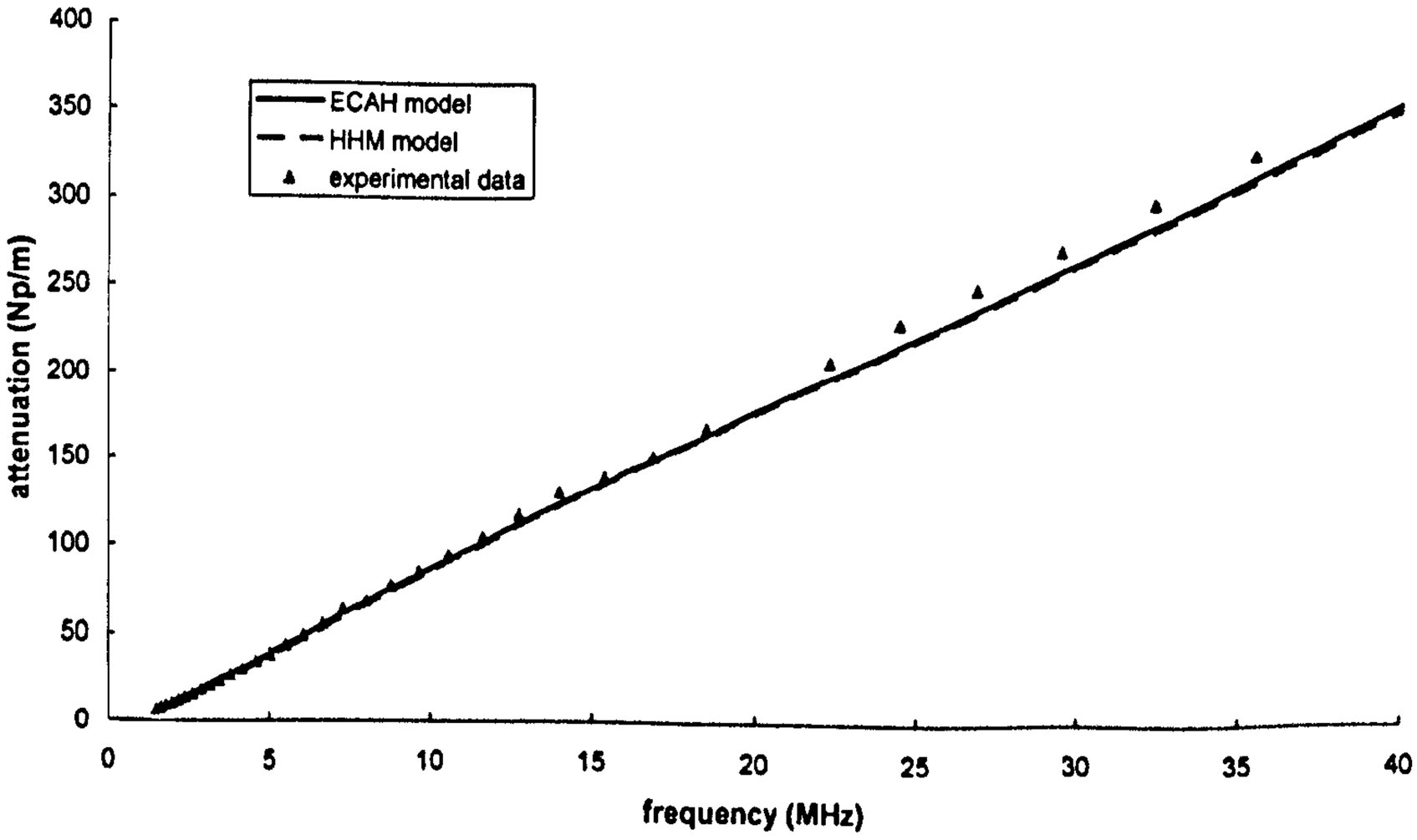

Figure 3.2b. Comparison of predicted and measured attenuation spectra for 10% corn oil-in-water emulsions with mean droplet radius of 120 nm. Line descriptions are the same as in figure 3.2a.

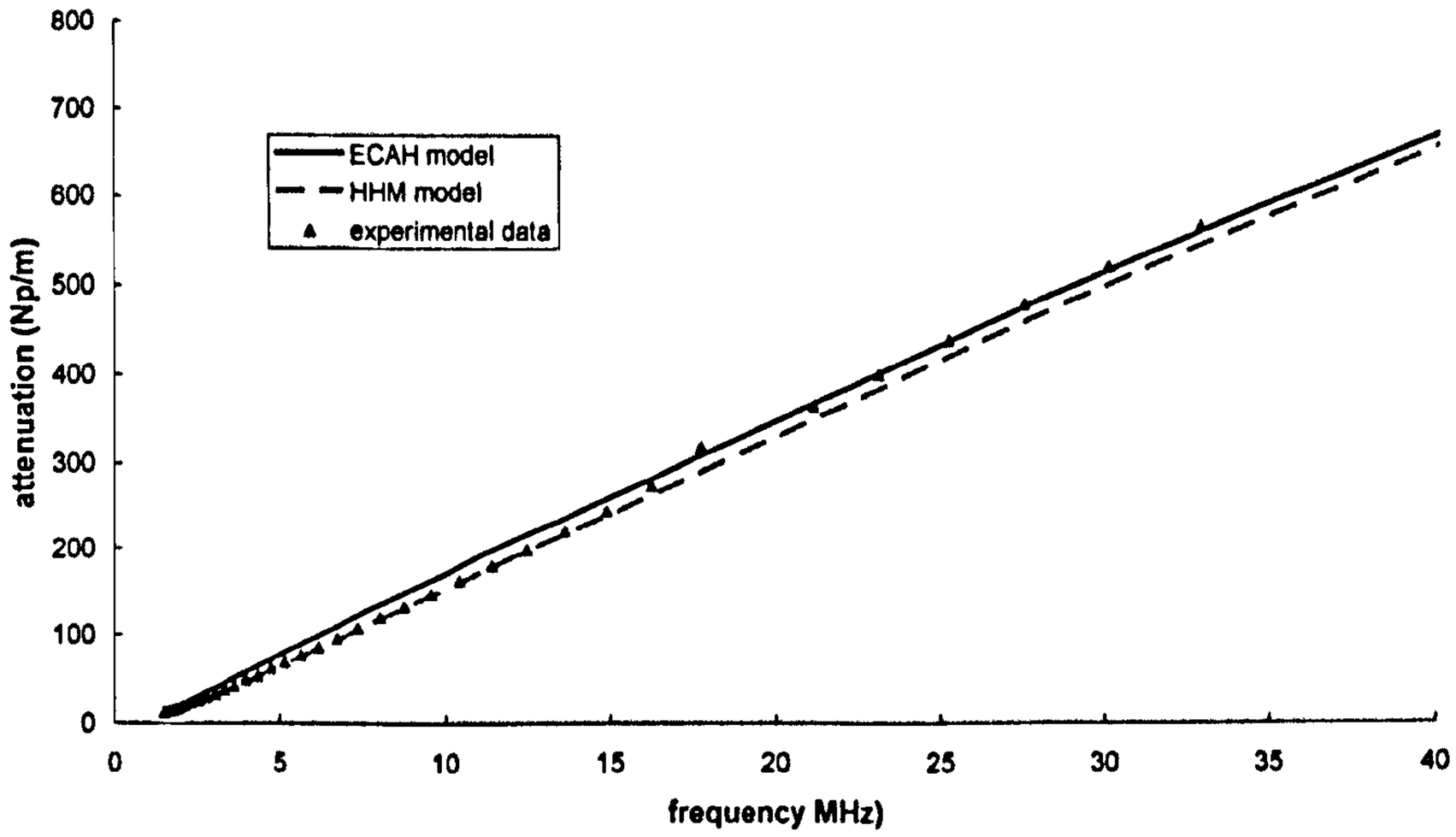

Figure 3.2c. Comparison of predicted and measured attenuation spectra for 20% corn oil-in-water emulsions with mean droplet radius of 120 nm. Line descriptions are the same as in figure 3.2a.

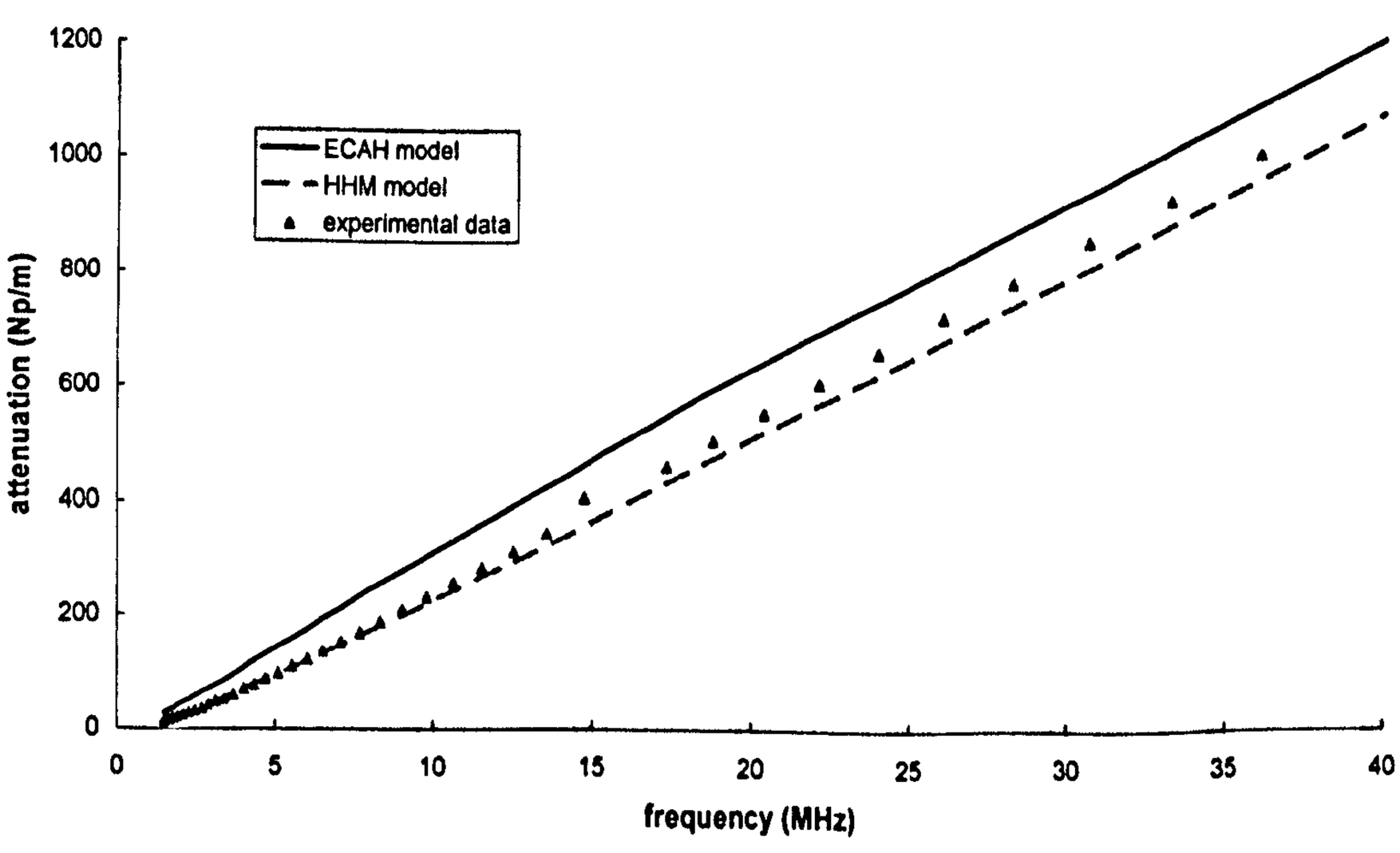

Figure 3.2d. Comparison of predicted and measured attenuation spectra for 40% corn oil-in-water emulsions with mean droplet radius of 120 nm. Line descriptions are the same as in figure 3.2a.

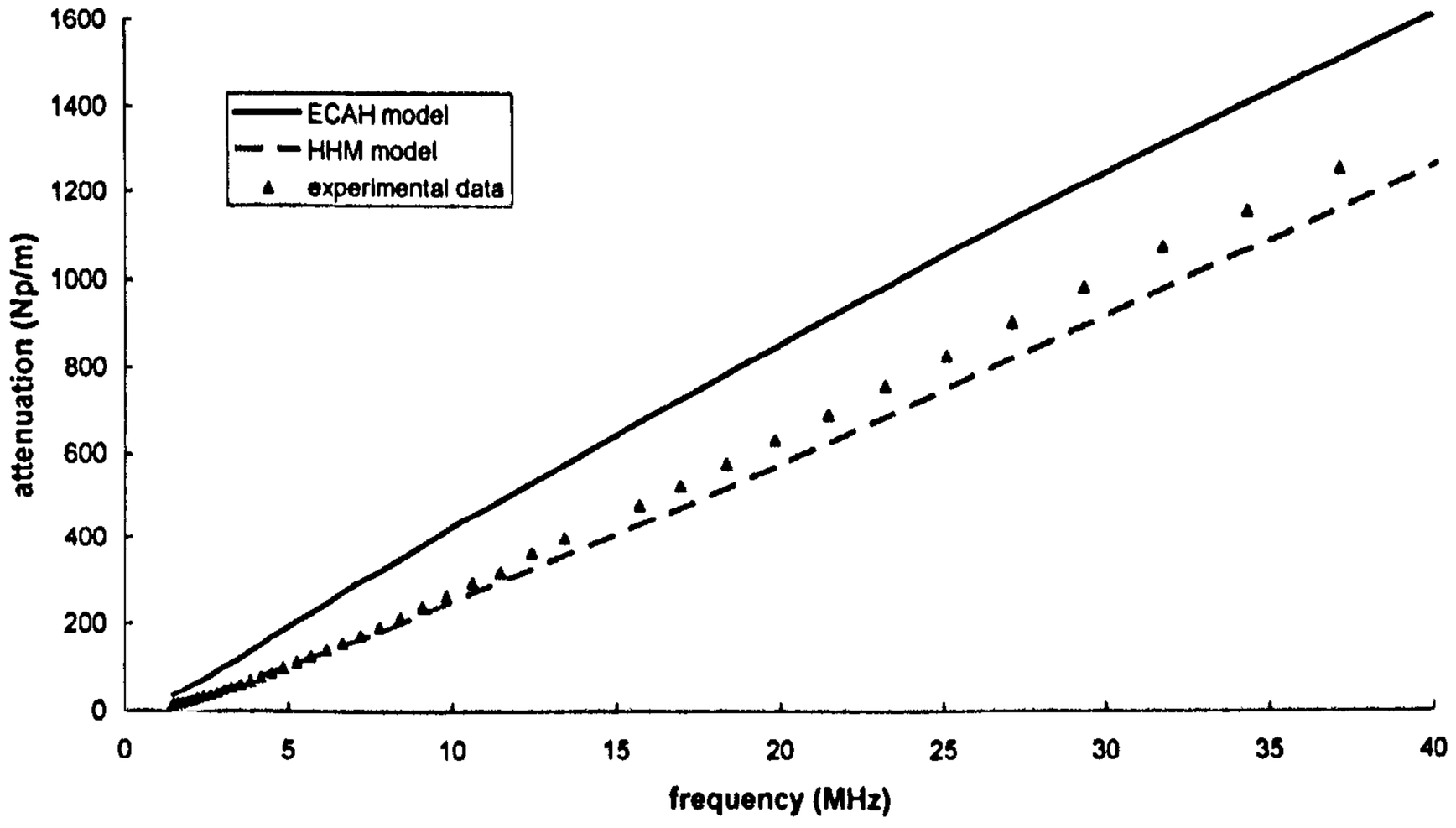

Figure 3.2e. Comparison of predicted and measured attenuation spectra for 50% corn oil-in-water emulsions with mean droplet radius of 120 nm. Line descriptions are the same as in figure 3.2a.

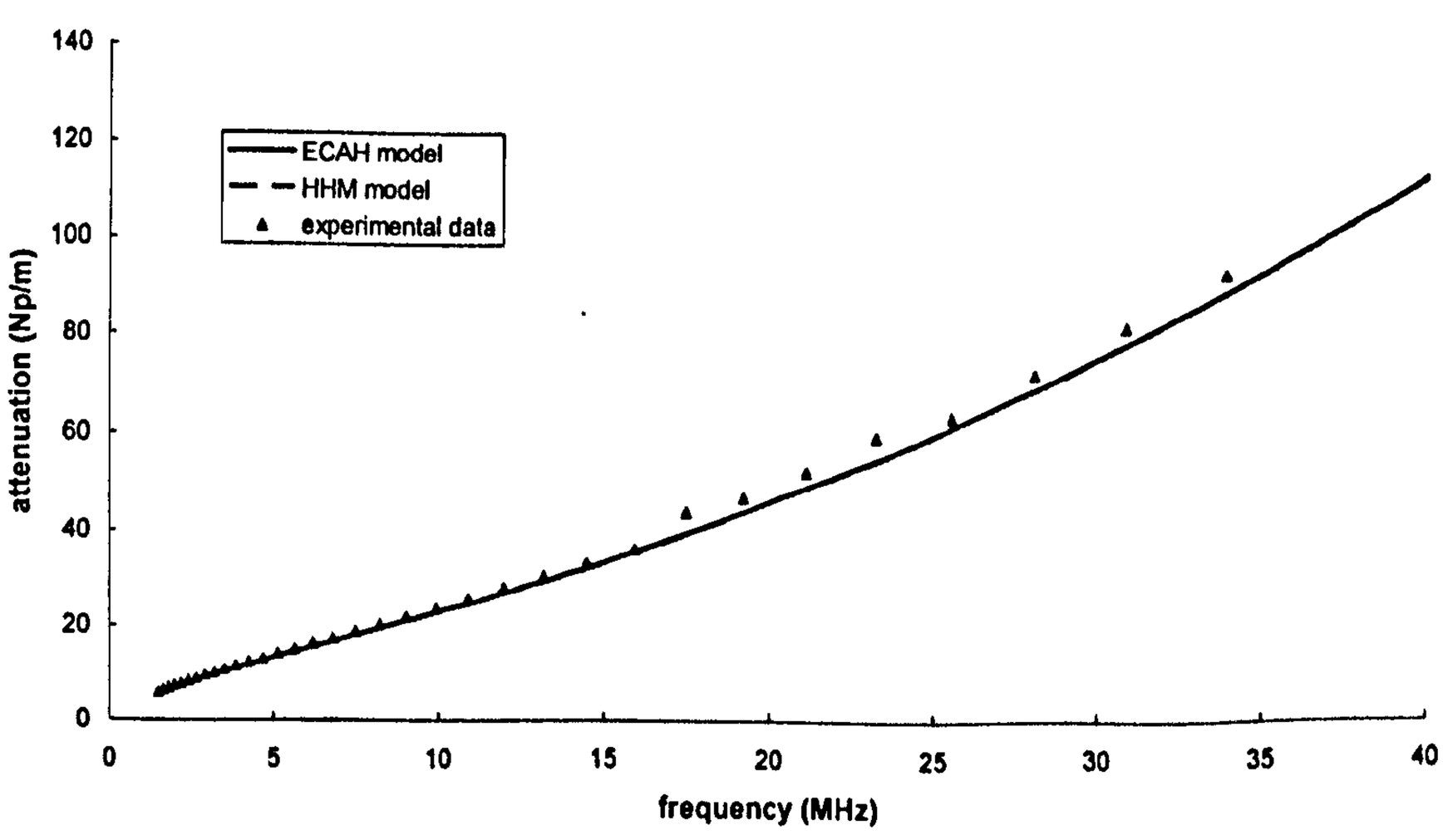

Figure 3.3a. Comparison of predicted and measured attenuation spectra for 5% corn oil-in-water emulsions with mean droplet radius of 600 nm, Line descriptions are the same as in figure 3.2a..

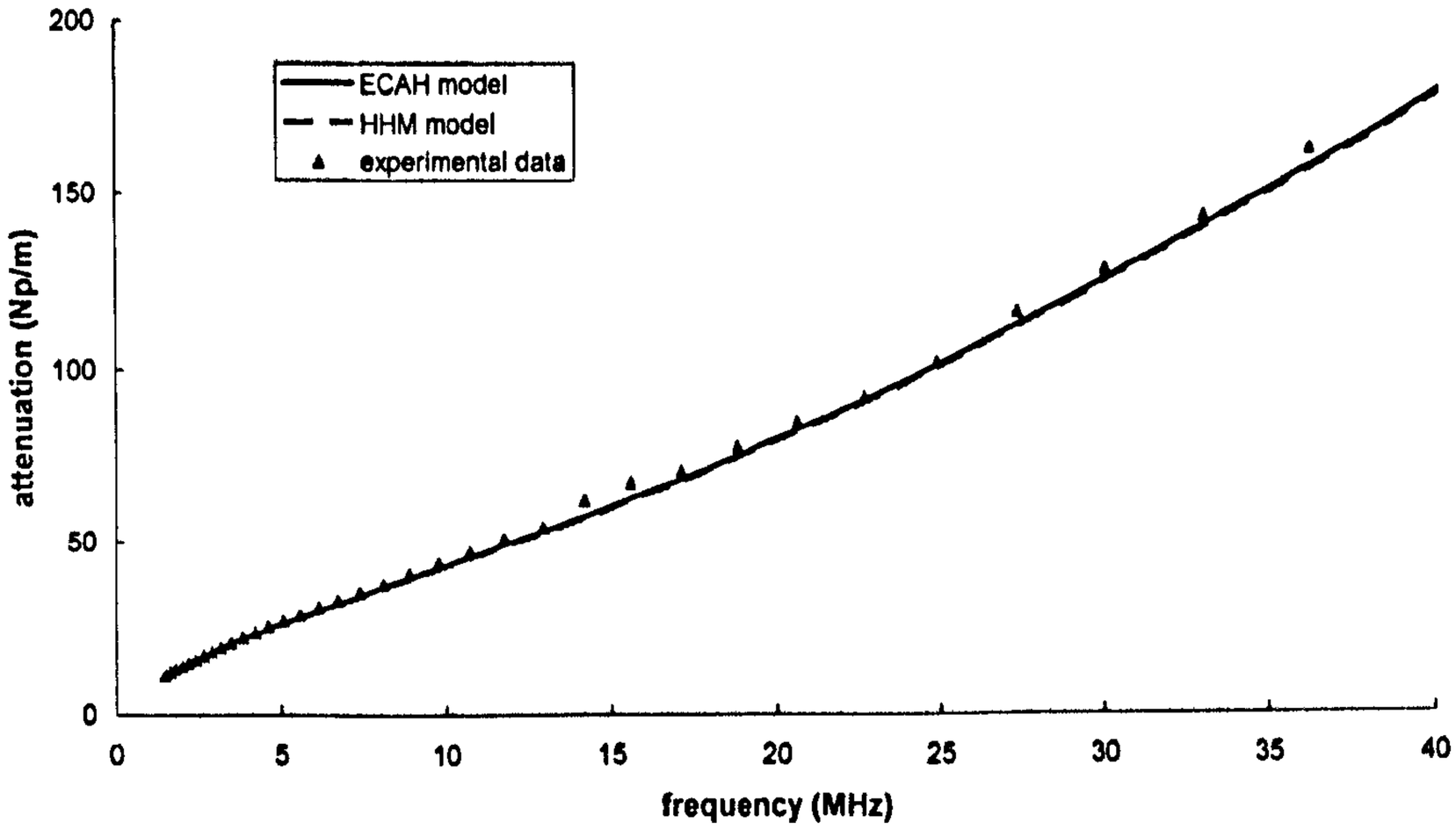

Figure 3.3b. Comparison of predicted and measured attenuation spectra for 10% corn oil-in-water emulsions with mean droplet radius of 600 nm. Line descriptions are the same as in figure 3.2a.

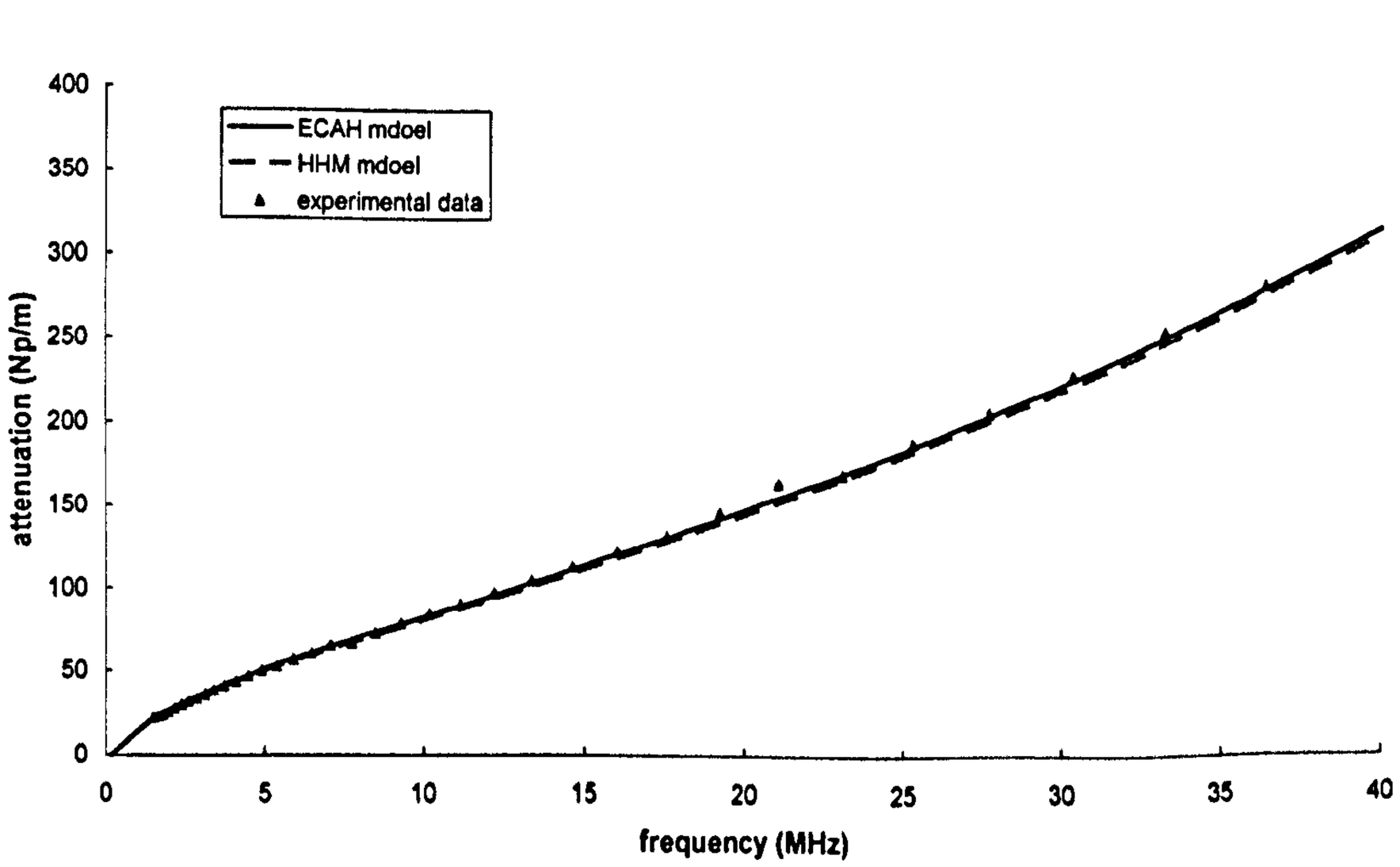

Figure 3.3c. Comparison of predicted and measured attenuation spectra for 20% corn oil-in-water emulsions with mean droplet radius of 600 nm. Line descriptions are the same as in figure 3.2a.

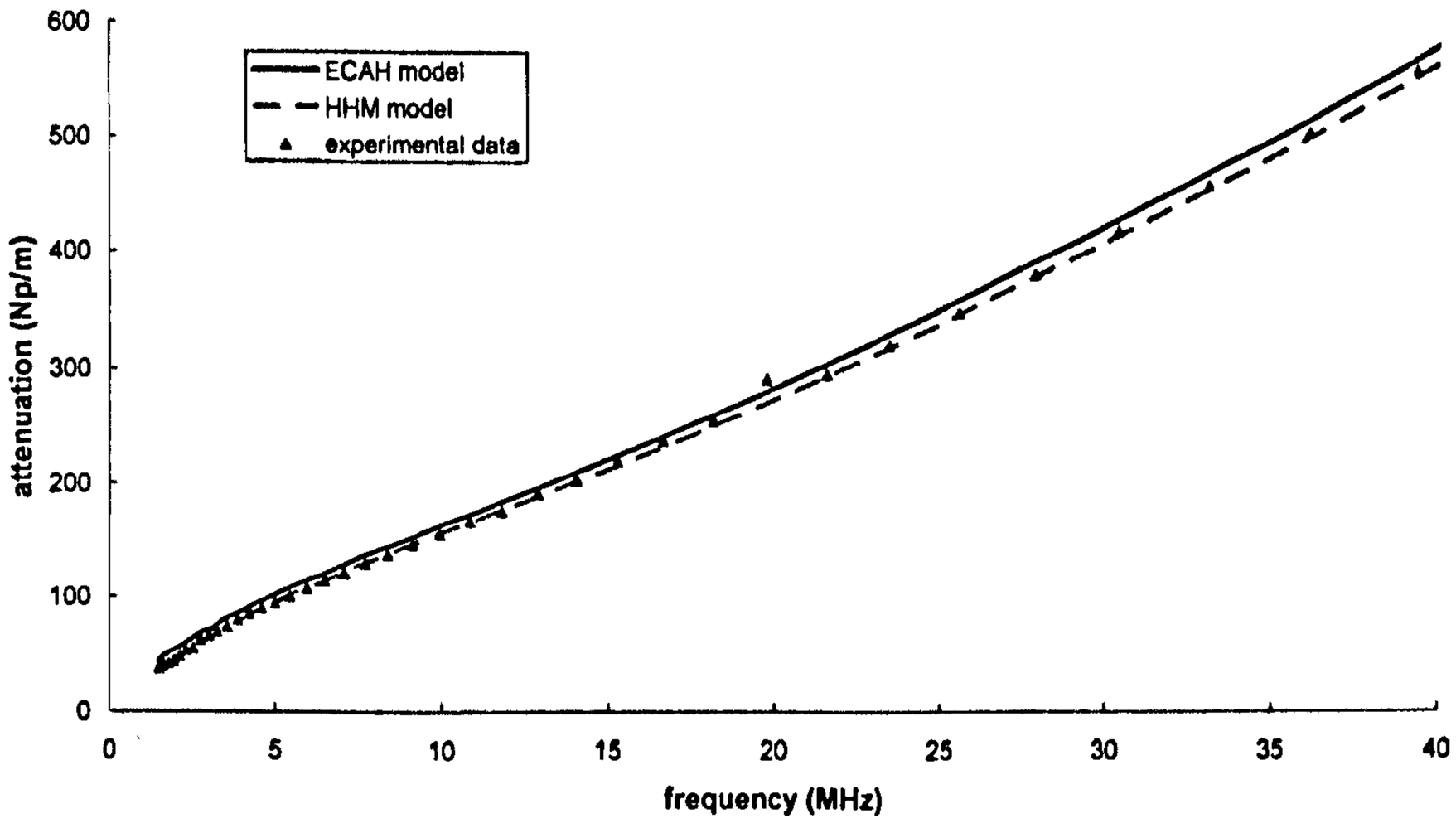

Figure 3.3d. Comparison of predicted and measured attenuation spectra for 40% corn oil-in-water emulsions with mean droplet radius of 600 nm. Line descriptions are the same as in figure 3.2a.

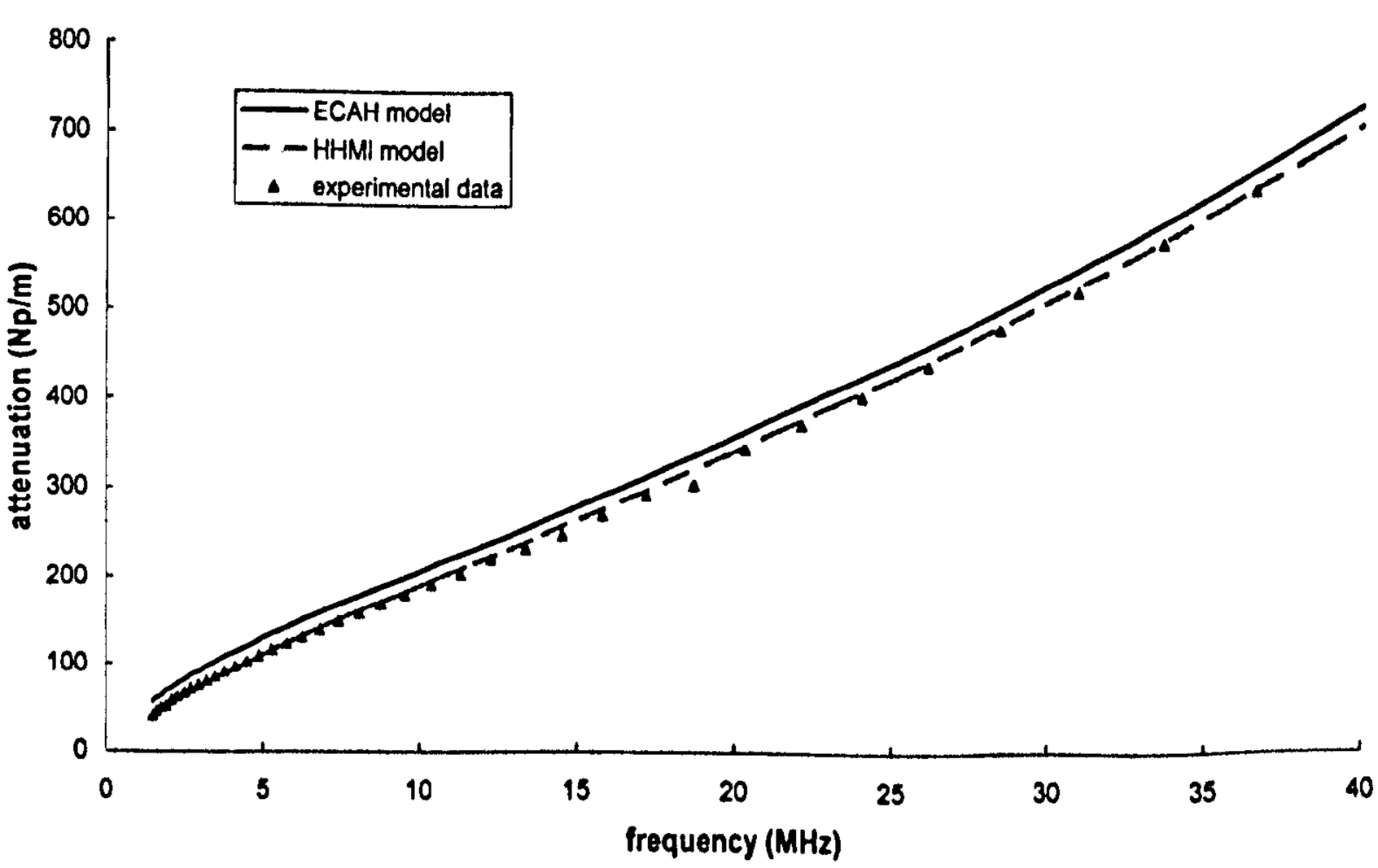

Figure 3.3e. Comparison of predicted and measured attenuation spectra for 50% corn oil-in-water emulsions with mean droplet radius of 600 nm. Line descriptions are the same as in figure 3.2a.

3.3 Coupled phase theory

At present there are three kinds of coupled phase theories. The first was suggested by Gumerov *et al* (1988) and Margulies and Schwartz, (1991 and 1994), who took into consideration heat transfer between the phases and assumed an incompressible particulate phase. Harker and Temple (1988) proposed a hydrodynamic model which allowed for a compressible particulate phase but neglected heat transfer between phases. Their model has proved to be successful for slurries. More recently, Evans and Attenborough (1996) combined the former two theories and allowed for both heat transfer and a compressible particulate phase, and as the result, the new coupled phase model can be used in both suspension and emulsion systems, at least in principle

The coupled phase model has proved successful for slurries, and there is also some evidence (Evans and Attenborough, 1996 and 2002) that it works for emulsions, but not enough to be sure. One of the purposes of this work is to determine whether it could be used for emulsions and also whether it could be used for concentrated emulsions. It will be tested later in this thesis as to whether or not it can give a better prediction of the volume fraction dependence of the attenuation compared to scattering theory.

3.3.1 Harker and Temple

In their paper, Harker and Temple (1988) constructed four differential equations: two continuity equations and two conservation of momentum equations. The transfer of momentum between phases was dealt with by

considering the drag force on one phase by the other. It is assumed that there is no gravitational field, and no heat or mass transfer between the phases.

$$\phi_j^0 \frac{\partial \rho_j^0}{\partial t} + i^{2j} \rho_j^0 \frac{\partial \phi}{\partial t} + \phi_j^0 \rho_j^0 \frac{\partial u_j}{\partial z} = 0, \qquad j = 1,2, \tag{3.13}$$

$$\rho_j^0 \phi_j^0 \frac{\partial u_j}{\partial t} = i^{2j-1} \omega \phi_2 \rho_1^0 S(u_2 - u_1) - \phi_j^0 \frac{\partial p}{\partial z}, \qquad j = 1,2, \tag{3.14}$$

where the subscripts 1 and 2 denote the dispersed phase and continuous phase, as usual. The subscript 0 denotes the constant equilibrium component of the variable. The complex quantity S is a factor representing momentum transfer between phases:

$$S = \frac{9i}{4}\frac{\delta^2}{r^2} + \frac{9}{4}(1+i)\frac{\delta}{r} + \frac{1+2\phi}{2(1-\phi)} \tag{3.15}$$

The assumptions implicit in the determination of S are that the particle is rigid and does not depend on relative fluid density. Observing equation 3.15 and equation 2.31b, It can be shown that the first two terms in these two equations are exactly the same, the difference between the two expressions is the third term on the right hand side, in equation 3.15, the third term represents the induced mass for a single rigid sphere, however, in equation 2.31b, the third term is a constant $\frac{1}{2}$, which applies to isolated spheres. When the particle volume fraction is quite low, the third term in equation 3.15 tends to $\frac{1}{2}$.

Since the suspension is compressible, the above equations cannot give a complete description of the system. It is assumed that the compressibility of the suspension is the volume average of the compressibility of the two phases. The density of the suspension will vary in response to the passage of a wave according to:

$$\rho_1 = \rho_1^0(1+\chi_1 p) \tag{3.16}$$

$$\rho_2 = \rho_2^0(1+\chi_2 p) \tag{3.17}$$

where χ is the adiabatic compressibility and ρ_j is the density of dispersed and continuous phase, ρ_j^0 is the steady state density of the two phases.

The velocities and densities for each phase, the pressure and particle phase volume fraction can all be specified by equations 3.13, 3.14, 3.16 and 3.17. If wave-like solutions are assumed, then they will be expressed in the following forms:

Velocity: $u = u^{'} \exp[i(kx-\omega t)]$;

Pressure: $p = p^{'} \exp[i(kx-\omega t)]$;

Volume fraction: $\phi = \phi^0 + \phi^{'} \exp[i(kx-\omega t)]$;

Density: $\rho = \rho^0 + \rho^{'} \exp[i(kx-\omega t)]$. **(3.18)**

The fluctuating parts of the field variables vary as $exp[i(kz-\omega t)]$, and are assumed to be small compared with their steady state values. The equations above were therefore expressed in linear form with respect to the variables. The transformations $\frac{\partial}{\partial t} \rightarrow -i\omega$ and $\frac{\partial}{\partial z} \rightarrow ik$ lead to the matrix equation:

$$\mathbf{Ax} = 0 \tag{3.19}$$

where $\mathbf{x} = (u_2, u_1, \rho_2, \rho_1, p, \phi)^T$

and

$$\mathbf{A} = \begin{bmatrix} 0 & 0 & 0 & 1 & -\chi_1\rho_1 & 0 \\ 0 & 0 & 1 & 0 & -\chi_2\rho_2 & 0 \\ -K\phi\rho_2 & 0 & \phi & 0 & 0 & \rho_2 \\ 0 & K\rho_1(1-\phi) & 0 & -(1-\phi) & 0 & \rho_1 \\ \phi(\rho_2+\rho_1 S) & \phi\rho_1 S & 0 & 0 & K\phi & 0 \\ \phi\rho_1 S & \rho_1((1-\phi)+\phi S) & 0 & 0 & K(1-\phi) & 0 \end{bmatrix} \tag{3.20}$$

A nontrivial solution to equation 3.20 is obtained by equating the determinant of the square matrix **A** to zero and expressing it in terms of the complex wave number $K(K = k/\omega)$. The expression was given by Challis *et al* (2005):

$$K^2 = \rho_3 \chi_3 \cdot \frac{\phi(1-\phi)(\rho_1\rho_2/\rho_3) - i(\gamma/\omega)}{\phi(1-\phi)(\phi\rho_1 + (1-\phi)\rho_2) - i(\gamma/\omega)} \tag{3.21}$$

where ρ_3 and χ_3 denotes effective density and compressibility of the mixture respectively. That is:

$$\rho_3 = \phi\rho_1 + (1-\phi)\rho_2$$

$$\chi_3 = \phi\chi_1 + (1-\phi)\chi_2$$

The velocity and attenuation of an elastic wave can be determined from the above expression using $\alpha = \mathrm{Im}(K)$ and $c = \omega/\mathrm{Re}(K)$. It was also noticed that in the limits $\phi = 0$ and $\phi = 1$, equation 3.21 reduces to $K^2 = \chi_1\rho_1$ and $K^2 = \chi_2\rho_2$ for each single phase respectively.

This model has certain advantages over the ECAH model in that it is mathematically simpler and it is self-consistent, as a result of the use of volume average field variables, which means that it should work for the whole range of possible volume fractions. It is also easier to stabilise computation against ill-conditioning in the matrices which require inversion. The Harker and Temple model does however have a major disadvantage in that it excludes the heat transfer between the two phases, which implies that it only applicable to the systems with a high density contrast between the two phases. Since most emulsions have a low density contrast between phases, it has been of great interest to develop the coupled phase theory of Harker and Temple to include the thermal transfer effects that are incorporated in the ECAH model. Evans

and Attenborough (1996) have achieved this with a new coupled phase model which could be used in emulsions; it will be discussed in the following section.

3.3.2 Evans and Attenborough

As noted above, the coupled phase model of Evans and Attenborough (1996) is a generalisation of the Harker and Temple coupled phase model in that it includes the effects of thermal transport between phases. This was achieved by including of two extra equations to describe heat transfer and energy conservation in each of the two phases. These equations are:

$$C_j\rho_j\frac{\partial T_j}{\partial t}+\frac{\rho_j(\gamma_j-1)C_j}{\beta_{Tj}}\frac{\partial u_j}{\partial z}=i^{2j-1}\omega\rho_1 S_h(T_2-T_1),\ j=1,2 \qquad \textbf{(3.22)}$$

T_1, T_2 are the temperatures of the dispersed and continuous phase respectively, and they can be written in the form:

$$T=T^0+T^{'}\exp[i(kx-\omega t)]$$

C_1, C_2 are constant volume specific heat capacities of the dispersed and continuous phases respectively, and S_h is the irreversible heat transfer term which is given by:

$$S_h=\frac{-3\kappa_2}{i\omega r^2\rho_2}\left[\frac{1}{1-iq_2r}-\frac{\kappa_2}{\kappa_1}\frac{\tan(q_1r)+3/(q_1r)-3\tan(q_1r)/(q_1r)^2}{\tan(q_1r)-q_1r}\right]^{-1} \qquad \textbf{(3.23)}$$

where $q_1=\frac{1+i}{\delta_{T,1}}$ and $q_2=\frac{1+i}{\delta_{T,2}}$. $\delta_{T,1}, \delta_{T,2}$ are thermal wavelengths for the dispersed and continuous phases respectively.

This expression for the irreversible heat transfer between the phases comes from Gumerov *et al* (1988). Comparing this equation with equation

2.31a, we find that the thermal term in equation 2.31a is analogous to the expression in equation 3.23 in the square bracket, i.e.

$$S_h \approx -\frac{3\kappa_2}{i\omega r^2 \rho_2} \cdot H \tag{3.24}$$

At low frequencies, the first term in equation 2.31a, which denotes the heat transfer to the continuous phase, tends to one: $\frac{1}{1-iq_2 r} \to 1$; however, the second term in equation 2.31a , which denotes the heat transfer to the particles tends to infinity; as a result, equation 2.31a tends to zero and the heat transfer disappears at low frequencies. We get the similar results in equation 3.23 at low frequencies: the heat transfer between the continuous phase tends to one, whilst the heat transfer between particles tends to $\frac{\kappa_2}{5\kappa_1}$, and the steady state heat transfer tends to $\left[1-\frac{\kappa_2}{5\kappa_1}\right]^{-1}$.

The thermodynamic equations of state for the two phases, in terms of the magnitudes of the fluctuating parts of the field variables are:

$$\rho_2^0 + \rho_2^0 \beta_{T2} T_2^0 - \gamma_2 \rho_2^0 \chi_2 p = 0 \tag{3.25}$$

$$\rho_1^0 + \rho_1^0 \beta_{T1} T_1^0 - \gamma_1 \rho_1^0 \chi_1 p = 0 \tag{3.26}$$

where β_{Ti} is the thermal volume expansion coefficient of the dispersed and continuous phases.

Solutions in the form given by equation 3.18 are assumed with $-i\omega$ and ik substituted for time and x-axis differential operators, and the matrix equation can be written in the same form of equation 3.20, where $\mathbf{x} = (u_2, u_1, \rho_2, \rho_1, p, \phi, T_2, T_1)^T$ and

$$\mathbf{A}=\begin{bmatrix} 0 & 0 & 0 & 1 & -\gamma_1\rho_1\chi_1 & 0 & 0 & \rho_1\beta_{11} \\ 0 & 0 & 1 & 0 & -\gamma_2\rho_2\chi_2 & 0 & \rho_2\beta_{12} & 0 \\ -K\rho_2\phi & 0 & \phi & 0 & 0 & \rho_2 & 0 & 0 \\ 0 & K\rho_1(1-\phi) & 0 & -(1-\phi) & 0 & \rho_1 & 0 & 0 \\ -(\rho_2+\rho_1 S) & \rho_1 S & 0 & 0 & K & 0 & 0 & 0 \\ \phi\rho_1 S & -\rho_1((1-\phi)+\phi S) & 0 & 0 & K(1-\phi) & 0 & 0 & 0 \\ K\dfrac{\rho_2 C_2(\gamma_2-1)}{\beta_{12}} & 0 & 0 & 0 & 0 & 0 & -(\rho_2 C_2+\rho_1 S_h) & \rho_1 S_h \\ 0 & \dfrac{K(1-\phi)\rho_1 C_1(\gamma_1-1)}{\beta_{11}} & 0 & 0 & 0 & 0 & \phi\rho_1 S_h & -\rho_1((1-\phi)C+\phi S_h) \end{bmatrix} \tag{3.27}$$

It can be seen that the top left six by six sub-matrix of equation 3.27 corresponds Harker and Temple's hydrodynamic matrix equation, i.e. equation 3.20 when $\gamma_1 = \gamma_2 = 1$. Columns 7 and 8 are related to the heat transfer terms from equation 3.22. Evans and Attenborough have solved this equation using *Mathematica* to obtain the attenuation and sound speed. The complex wave number K was found to be (Challis *et al*, 2005):

$$\begin{aligned} K^2 = &\left\{\frac{\omega^2(\gamma\chi)_3\rho_3}{\gamma_3}\left(\frac{\rho_1\rho_2\phi_1\phi_2}{\rho_3}-i\frac{\gamma}{\omega}-i\frac{\gamma}{\omega}\frac{(C\rho)_3}{\rho_3 C_1 C_2}-\frac{\gamma\sigma}{\omega^2}\frac{(C\rho)_3}{\rho_1\rho_2\phi_1\phi_2 C_1 C_2}\right)\right\} \\ &\times\left\{\frac{\rho_1\rho_2\phi_1\phi_2(\gamma/\rho)_3}{\gamma_3}-i\frac{\gamma}{\omega}-i\frac{\sigma}{\omega}\frac{(C\rho)_3(1/\rho)_3+\beta_3(C(\gamma-1)/\beta)_3}{\gamma_3 C_1 C_2}\right. \\ &\left.-\frac{\gamma\sigma}{\omega^2}\frac{(C\rho)_3+\beta_3(C(\gamma-1)/\beta)_3}{\rho_1\rho_2\phi_1\phi_2 C_1 C_2\gamma_3}\right\}^{-1} \end{aligned} \tag{3.28}$$

This is currently the most general form of the complex wave number for a coupled phase model. The inclusion of thermal effects results in additional complex terms in both the numerator and denominator, as well as new cross terms that depend on both the shear drag and the thermal coupling. If the thermal effects are removed from equation 3.28, for example, set $S_h = 0$, or set $\gamma_1 = \gamma_2 = 1$, then the solution reverts back to that of Harker and Temple.

3.3.3. Simulation using the coupled phase model

The Evans and Attenborough model was used to simulate ultrasonic wave propagation through a sunflower oil-in-water emulsion and a corn oil-in-water emulsion. The thermo-physical properties of these materials show in table 3.1. Figure 3.4 shows the result for the calculated excess attenuation (i.e. the intrinsic losses in liquids have been neglected) for sunflower oil-in-water emulsion as a function of volume fraction at frequency of 1.25 MHz. The experimental data come from McClements and Povey's (1989) measurement for sunflower oil-in-water emulsion. The particle radius is 0.27 μm and the frequency is 1.25 MHz. The coupled phase predictions are programmed using the results obtained by solving matrix equation 3.27 using *Maple*, the ECAH explicit expression was calculated using equations 2.30 and 2.31, and the HHM model was calculated using equation 3.6. It can be seen that there is quite good agreement between the coupled phase model and the HHM model at this low kr value ($k_c r = 0.0015$), both of them increase non-linearly as functions of volume fraction, and are in good agreement with the experimental data up to $\phi = 0.35$. Some discrepancies between theory and experimental data can be explained on the basis that we used the mean particle radius whilst the emulsion was polydispersed. The predictions using the coupled phase model and the HHM model are away from the ECAH model at above 10%, and the discrepancy becomes larger at higher volume fractions, this being due to thermal wave overlap effects.

Figures 3.6 and 3.7 show the attenuation data for different concentrations of corn oil-in-water emulsions as functions of frequency. The same three

models are used to predict the simulation results. In these calculations, the full particle size distribution (figure 3.5) was used; the mean particle radius was 600 nm. These two figures show that the coupled phase model agrees with the measured attenuation and the HHM model only at low values of kr, but tend to underestimate the attenuation as the frequency increases. This investigation shows that the coupled phase model is a very long wavelength limited model. Its validity can be defined by considering the value of the wavenumber-particle radius product. In figure 3.6 the $k_c r = 0.008$, in figure 3.7, the $k_c r = 0.008$ as well. From our experimental data the coupled phase model appears to be valid for frequencies less than 3 MHz, which for the mean particle radius 600 nm, corresponding to a maximum kr of 0.008.

property	Sunflower oil	Water	Corn oil
Ultrasonic velocity (m s^{-1})	1469.9	1497.0	1456.1
Attenuation coefficient (Np m^{-1})	$2.76\times10^{-11} f^{1.7}$	$2.5\times10^{-14} f^{2}$	$6.74\times10^{-12} f^{1.85}$
Density (kg m^{-3})	920.6	997.0	917.7
Viscosity (mPa s)	54	0.88	63
Specific heat (J $K^{-1}kg^{-1}$)	1980	4177.0	1923
Thermal conductivity (W m^{-1} s^{-1})	0.17	0.5952	0.166
Thermal expansivity (K^{-1})	0.00071	0.00026	0.00072

Table 3.1. Thermo-physical properties of sunflower oil, corn oil and water used in the calculations of the ultrasonic properties of the emulsions ($25.0^{o}C$). All the data are from McClements and Povey (1989).

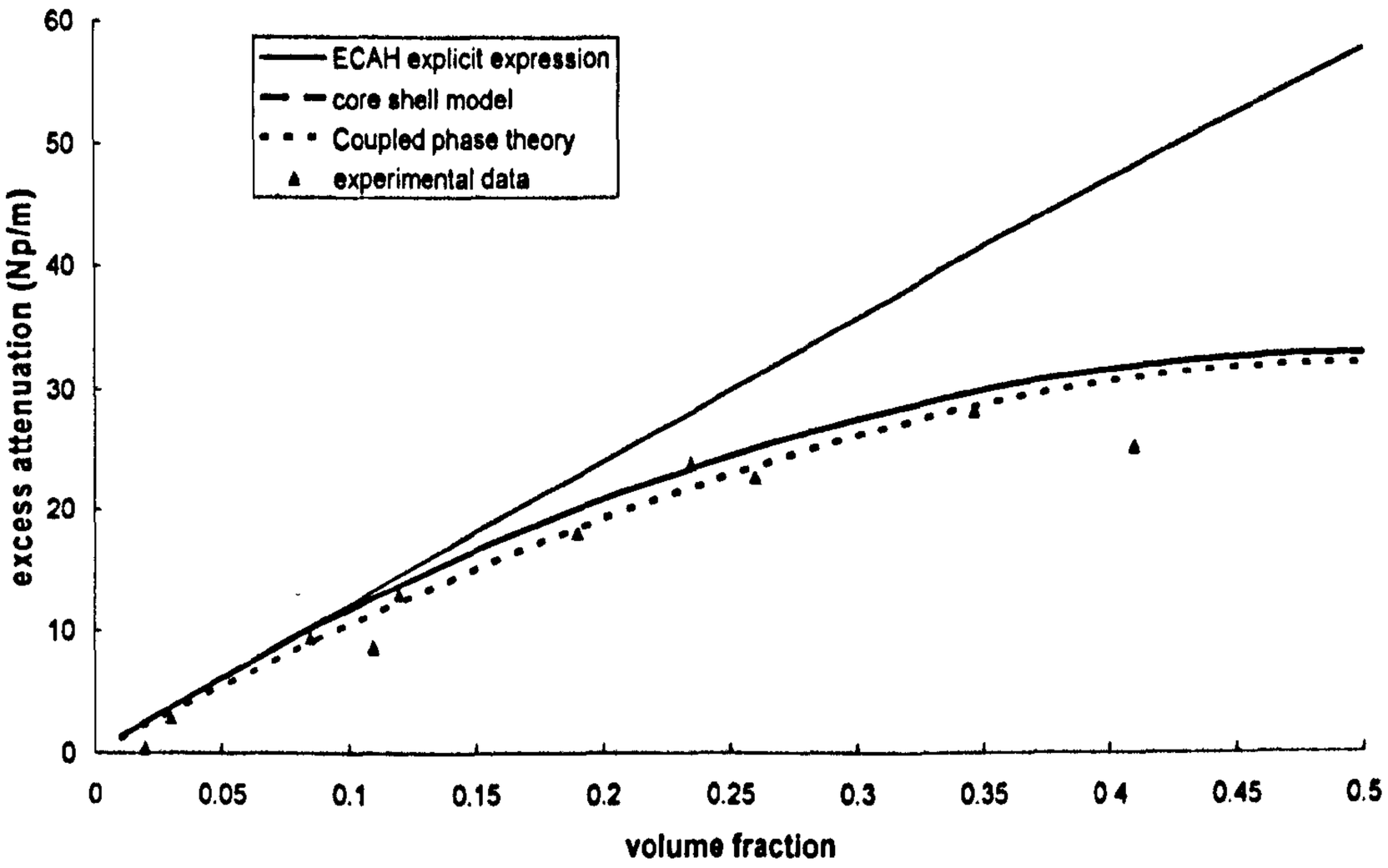

Figure 3.4. Excess attenuation in Np/m as a function of volume fraction for the sunflower oil-in-water emulsion using the coupled phase model (dash line), the ECAH explicit expression (solid line) and the HHM model (broken line). The frequency was 1.25 MHz and the mean particle radius 0.27 μm.

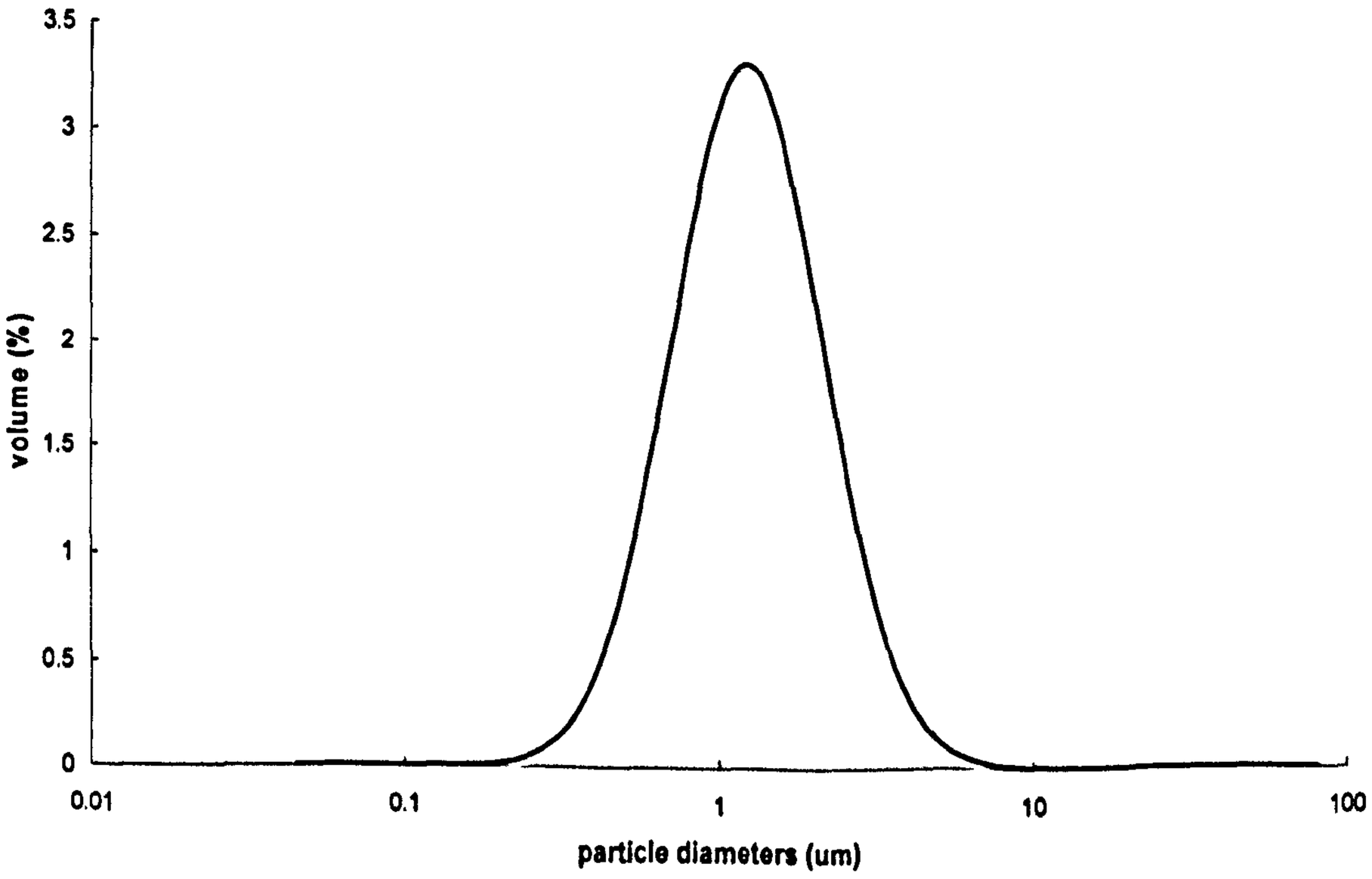

Figure 3.5. Particle size distribution for corn oil-in-water emulsion measured by Chanamai (1999), the mean particle radius is 600 nm.

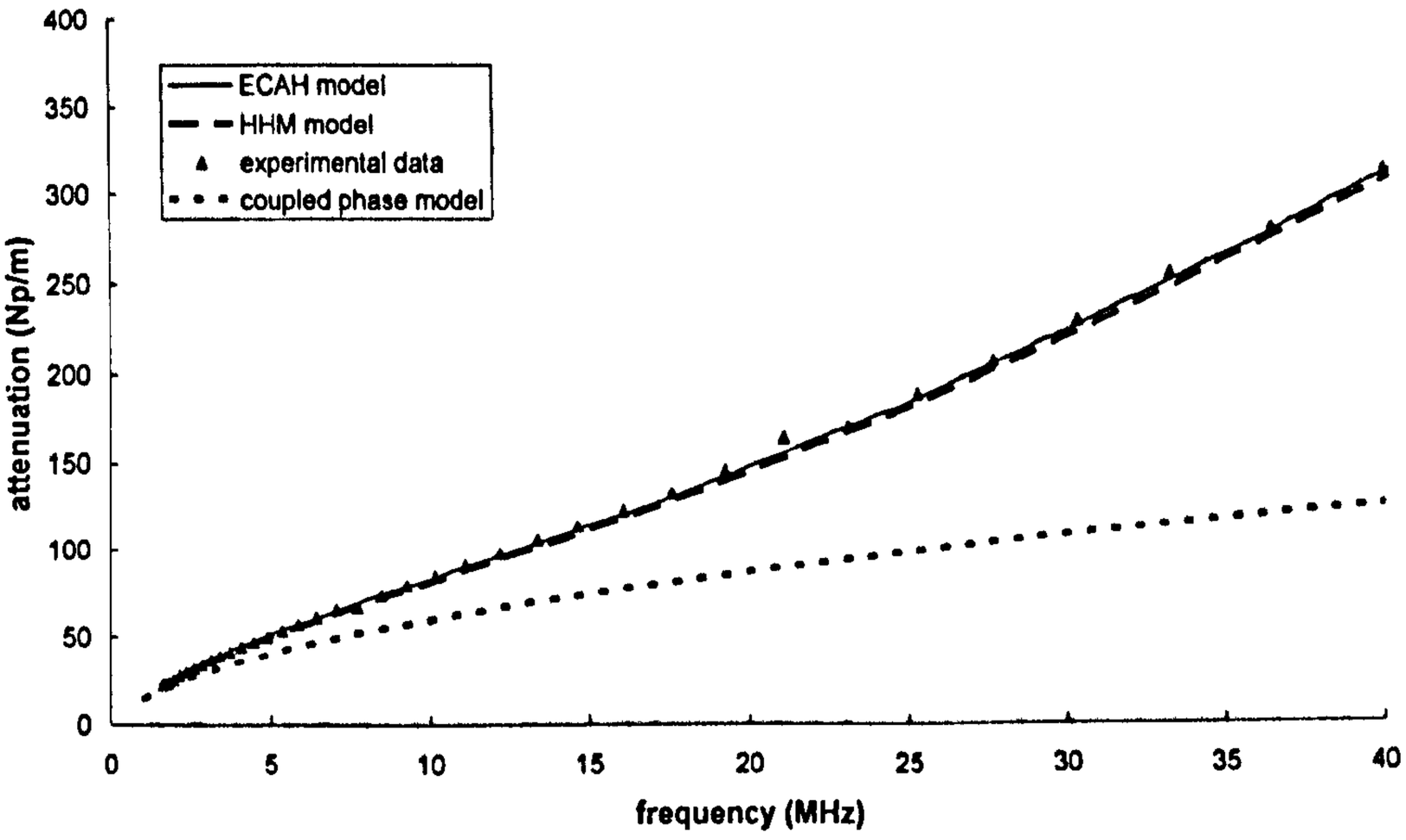

Figure 3.6. Attenuation as a function of frequency for the corn oil-in-water emulsion using the coupled phase model (dash line), the ECAH model (solid black line) and the HHM model (broken line). Volume fraction is 20%, using the PSD shown in figure 3.5.

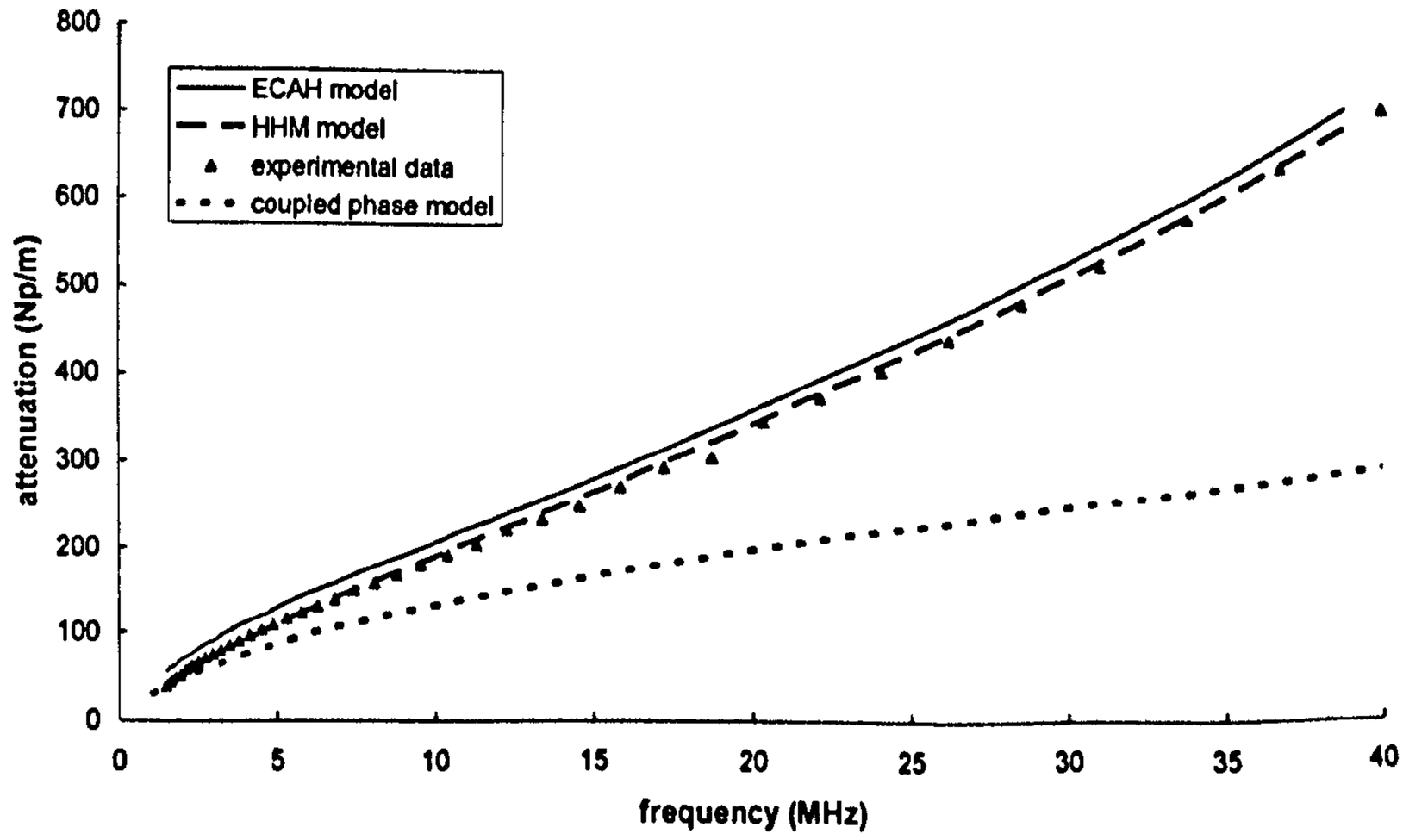

Figure 3.7. Attenuation as a function of frequency for the corn oil-in-water emulsion using the coupled phase model (dash line), the ECAH model (solid line) and the HHM model (broken line). Volume fraction is 50%, using the PSD shown in figure 3.5.

3.4. Conclusion

Two models — the HHM model and the Evans and Attenborough coupled phase model — for attenuation coefficient calculations in high particle concentrated systems have been presented in this chapter. The HHM model was developed to include thermal wave interactions and would expected to be applicable to concentrated emulsions. Our experiments and simulations in figures 3.2 and 3.3 show that this model is a good alternative to the scattering model, and can be used to predict the attenuation at high volume fractions. However, it has some limitations in that it really only applies to systems where the density contrast between the droplets and the surrounding liquids is low, that is where the dominant phenomena in the attenuation is the thermal loss. In systems where there is a relatively high density contrast it would also be necessary to take into account the effect of the overlap of the shear waves.

The Evans and Attenborough coupled phase theory has been derived to include heat transfer between the phases and compressibility in the particulate phase, as well as the viscous wave interaction. Evans and Attenborough applied this model to different emulsions of low density contrast between phases, allowing the hydrodynamic coupling to vanish. It can be used to determine the attenuation and phase velocity spectrum below a very long wavelength limit, that is when $kr < 0.01$.

In the previous chapter and this chapter, we have discussed some basic models for ultrasound propagation though emulsions and each of them has its own limits.

In the next chapter the problem of emulsions with a shell around them is addressed in more detail. The idea is to examine a comprehensive 'shell' scattering model for application not only to real encapsulated emulsions, but also as a possible alternative to the HHM formulation.

Chapter 4 Shell Theory for Encapsulated Emulsions

4.1 Introduction

In chapter 2, we introduced the basic theory of acoustic wave propagation in particulate dispersions — the ECAH model, applicable to fairly dilute systems. The model was extended to include the thermal overlap effects in concentrated emulsions (Hemar, 1997, McClements et al, 1999) in chapter 3. However, in this case the shell is not actually a real one — it is merely an outer face which enables us to deal with overlapping thermal wave fields. Moreover, it has limitations in that it did not include the viscous overlap effects, so it can only be used for low-density-contrast emulsions. There are situations in which the core shell idea can be applied to real physical shells. In many agrochemical, pharmaceutical and food products, many emulsions use a thin polymer shell, which is porous to the bioactive ingredient, and which controls its release rate. Such materials are known as microencapsulated emulsions. There is a requirement to investigate non-destructively both the droplet size and the properties of the shell, and it was thought that measurements of ultrasonic compression wave attenuation and phase velocity could provide a means to achieve this. A formal shell model was developed many years ago by Anson and Chivers (1993). In their paper an analysis is given for sound scattering and attenuation by shelled structures immersed in fluids, together with some comparisons with previous (limited) published

results. Their shell model deals with ultrasonic scattering from spherical shells including viscous and thermal effects, and showed be applicable to both suspensions and emulsions. Several years later, Hipp (2002a, 2002b) reviewed the Anson and Chivers' model and added some approximations which, according to the author, extended the model's flexibility. He used the same boundary conditions as did Anson and Chivers to set up the diffraction equation, but used a different method to solve it.

It was not clear in Hipp's original publication (Hipp 2002a, 2002b) whether or not he had followed the formulation of Anson and Chivers exactly; some utility was therefore to be gained from comparing Hipp's results with equivalent calculations using the Anson and Chivers model, and this comparison is included in this chapter. It is also shown that this formulation can be used in place of the HHM model to account for the thermal interactions between particles in highly concentrated emulsions. The Anson-Chivers model is finally applied to polymer encapsulated emulsions in a combined experimental-theoretical study.

4.2 Anson and Chivers shell model

There are a number of methods of calculating the scattering properties of a fluid-loaded elastic shell available in the literature: Werby and Green (1983) and Werby *et al* (1988) have considered elastic shells in fluids with fluid cores. Gaunaurd and Kalmins (1982) have considered a gas-filled elastic shell with a viscoelastic solid coating for kr values up 20. However these models were somewhat restricted in that they did not include all of the physical phenomena which constituted the ECAH model.

This was later achieved by Anson and Chivers (1993) who considered the scattering from a spherical particle surrounded by a concentric shell (figure 4.1). Whenever a compressional acoustic wave falls on a surface of discontinuity, waves of two kinds are excited on both sides of the surface in addition to the reflected and transmitted compressional waves. Hence, in each of the media arise a longitudinal wave, a highly damped shear/viscous wave and a highly damped thermal wave. The acoustic attenuation of a dispersion of shelled particles is determined by the behaviour of compressional waves in the continuous phase resulting from its interactions with particle and shell.

The following presents a summary of Anson and Chivers' formulation of this shelled system. The indices and dimensions used are as shown in figure 4.1. In each medium, i.e. the surrounding fluid material (medium 1), the shell material (medium 2) and the core material (medium 3), there are three kinds of waves present: compressional, shear and thermal. These waves are represented by three potentials ϕ_c, A_ψ and ϕ_t respectively, and can be obtained by using the wave equation 2.10 (chapter 2). Following a similar method to the ECAH model, using wave potential and partial wave analysis, the various wave modes can be expressed as follows:

The incident plane wave is represented by:

$$\phi_0 = \sum_{n=0}^{\infty} i^n (2n+1) j_n(k_{c1}R) P_n(\cos\theta) \qquad \textbf{(4.1 a)}$$

In the surrounding liquid medium (medium 1), reflected wave potentials are given by

$$\phi_{c1} = \sum_{n=0}^{\infty} i^n (2n+1) A_n h_n(k_{c1}R) P_n(\cos\theta) \qquad \textbf{(4.1 b)}$$

$$\phi_{t1} = \sum_{n=0}^{\infty} i^n (2n+1) B_n h_n (k_{t1} R) P_n (\cos\theta) \qquad \textbf{(4.1 c)}$$

$$\mathrm{A}_{\psi 1} = \sum_{n=0}^{\infty} i^n (2n+1) C_n h_n (k_{s1} R) P_n^1 (\cos\theta) \qquad \textbf{(4.1 d)}$$

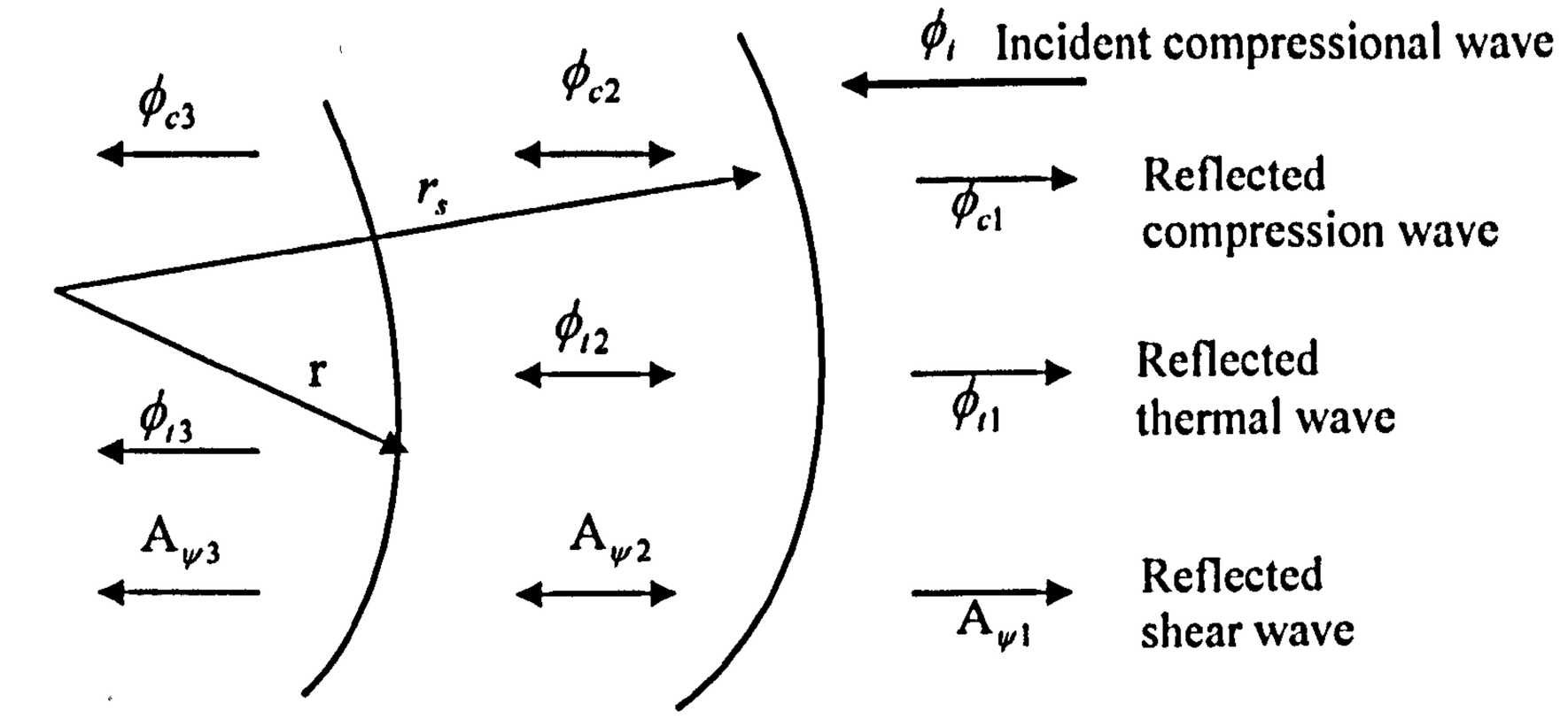

Figure 4.1. Scheme for the Anson and Chivers shell model.

In the core medium (medium 3):

$$\phi_{c3} = \sum_{n=0}^{\infty} i^n (2n+1) J_n j_n (k_{c3} R) P_n (\cos\theta) \qquad \textbf{(4.1 e)}$$

$$\phi_{t3} = \sum_{n=0}^{\infty} i^n (2n+1) K_n j_n (k_{t3} R) P_n (\cos\theta) \qquad \textbf{(4.1 f)}$$

$$\mathrm{A}_{\psi 3} = \sum_{n=0}^{\infty} i^n (2n+1) L_n j_n (k_{s3} R) P_n^1 (\cos\theta) \qquad \textbf{(4.1 g)}$$

In the shell medium (medium 2) the wave potential may host both outgoing (represented by using the Hankel function h_n) and incoming (represented by using the Bessel function j_n) waves, and therefore can be written as:

$$\phi_{c2} = \sum_{n=0}^{\infty} i^n (2n+1) \left[D_n j_n (k_{c2} R) + G_n h_n (k_{c2} R) \right] P_n (\cos\theta) \qquad \textbf{(4.1 h)}$$

$$\phi_{t2} = \sum_{n=0}^{\infty} i^n (2n+1) \left[E_n j_n (k_{t2} R) + H_n h_n (k_{t2} R) \right] P_n (\cos\theta) \qquad \textbf{(4.1 i)}$$

$$A_{\psi 2} = \sum_{n=0}^{\infty} i^n (2n+1)\left[F_n j_n(k_{s2}R) + I_n h_n(k_{s2}R)\right] P_n^1(\cos\theta) \qquad \textbf{(4.1 j)}$$

where A_n represents the scattered partial amplitude of compression wave

B_n represents the scattered partial amplitude of thermal wave

C_n represents the scattered partial amplitude of transverse wave

D_n and G_n represent the partial amplitude of compression wave inside the shell

E_n and H_n represent the partial amplitude of thermal wave inside the shell

F_n and I_n represents the partial amplitude of shear wave inside the shell

J_n represents the forward partial amplitude of compression wave

K_n represents the forward partial amplitude of thermal wave

L_n represents the forward partial amplitude of shear wave

The boundary conditions of the shell model are an extension of those of the ECAH model. The first boundary is between the core material and its shell ($R = r$). Compared to ECAH model, additional boundary conditions need to be applied at the outer limit of the shell and the continuous phase with the radius $R = r_s$. At each boundary, continuity is required for radial velocity and stress, tangential velocity and stress, heat flux and temperature. Therefore we can obtain a system of 12 equations with 12 unknown coefficients A_n to L_n. This can be written in matrix form as:

$$\begin{bmatrix} d_{11} & d_{12} & d_{13} & d_{14} & d_{15} & d_{16} & d_{17} & d_{18} & d_{19} & 0 & 0 & 0 \\ d_{21} & d_{22} & d_{23} & d_{24} & d_{25} & d_{26} & d_{27} & d_{28} & d_{29} & 0 & 0 & 0 \\ d_{31} & d_{32} & d_{33} & d_{34} & d_{35} & 0 & d_{37} & d_{38} & 0 & 0 & 0 & 0 \\ d_{41} & d_{42} & d_{43} & d_{44} & d_{45} & 0 & d_{47} & d_{48} & 0 & 0 & 0 & 0 \\ d_{51} & d_{52} & d_{53} & d_{54} & d_{55} & d_{56} & d_{57} & d_{58} & d_{59} & 0 & 0 & 0 \\ d_{61} & d_{62} & d_{63} & d_{64} & d_{65} & d_{66} & d_{67} & d_{68} & d_{69} & 0 & 0 & 0 \\ 0 & 0 & 0 & d_{74} & d_{75} & d_{76} & d_{77} & d_{78} & d_{79} & d_{7,10} & d_{7,11} & d_{7,12} \\ 0 & 0 & 0 & d_{84} & d_{85} & d_{86} & d_{87} & d_{88} & d_{89} & d_{8,10} & d_{8,11} & d_{8,12} \\ 0 & 0 & 0 & d_{94} & d_{95} & 0 & d_{97} & d_{98} & d_{99} & d_{9,10} & d_{9,11} & 0 \\ 0 & 0 & 0 & d_{10,4} & d_{10,5} & 0 & d_{10,7} & d_{10,8} & d_{10,9} & d_{10,10} & d_{10,11} & 0 \\ 0 & 0 & 0 & d_{11,4} & d_{11,5} & d_{11,6} & d_{11,7} & d_{11,8} & d_{11,9} & d_{11,10} & d_{11,11} & d_{11,12} \\ 0 & 0 & 0 & d_{12,4} & d_{12,5} & d_{12,6} & d_{12,7} & d_{12,8} & d_{12,9} & d_{12,10} & d_{12,11} & d_{12,12} \end{bmatrix} \begin{bmatrix} A_n \\ B_n \\ C_n \\ D_n \\ E_n \\ F_n \\ G_n \\ H_n \\ I_n \\ J_n \\ K_n \\ L_n \end{bmatrix} = \begin{bmatrix} M_1 \\ M_2 \\ M_3 \\ M_4 \\ M_5 \\ M_6 \\ 0 \\ 0 \\ 0 \\ 0 \\ 0 \\ 0 \end{bmatrix}$$

(4.2)

The first three columns of the matrix deal with the behaviour of compressional, thermal and shear waves in the surrounding fluid, whilst the last three columns, deal with the behaviour of the same kinds of waves in the core. The remaining six columns describe the waves spreading into the shell. After scaling, the expressions for the coefficients of this matrix are given in appendix 4.1.

Anson and Chivers model has some limitations: the first one is the assumption of concentric spherical geometry, and the second one is the requirement that the losses in the material are reasonably small (i.e. $\frac{\omega}{c} >> \alpha_c$). In fact, both of the requirements are met for the emulsions used in this project.

As for the input parameters, since we are only concerned with the fluid core with a polymer shell, the composite particle being suspended in the surrounding fluid phase in this thesis, there are 22 parameters needed as the input (see table 4.1). These parameters include the thermal properties: thermal conductivity κ, volume thermal expansion coefficient β_T, and specific heat

capacity at constant pressure C_p for all three materials; compressional properties: density ρ, compressional wave speed c and compressional wave attenuation α_c for all three media; shear/viscous properties: shear viscosity η for the fluid core and surrounding phase, the second Lame constant μ and the amplitude attenuation coefficient of shear wave α_s for the polymer shell.

	Compressional properties	Thermal properties	Shear/viscous properties
Medium 1	ρ_1, c_1, α_{C1}	$\kappa_1, \beta_{T1}, C_{p1}$	η_1
Medium 2	ρ_2, c_2, α_{C2}	$\kappa_2, \beta_{T2}, C_{p2}$	μ_2, α_{S2}
Medium 3	ρ_3, c_3, α_{C3}	$\kappa_3, \beta_{T3}, C_{p3}$	η_3

Table 4.1. Input parameters required for a polymer shell with a viscous fluid core, suspended in a viscous fluid.

With the knowledge of these input parameters, the other necessary variables can be calculated. These include the elastic modulus λ and the ratio of the specific heat γ:

$$\lambda = \rho.c^2 - \frac{4}{3}\mu \tag{4.3}$$

$$\gamma = 1 + \frac{\beta_T^2 T_0 c^2}{C_p} \tag{4.4}$$

4.2.1 Computational procedures

In this section, the computational procedures are described in detail together with the assumptions made and how the calculation was simplified. The most important procedure is scaling of each term inside the matrix equation. As in the ECAH model, A_n is the only term required for attenuation

as this is the only component that can be detected experimentally. Thus, all columns except the first can be divided by the same term without affecting the result. The following changes were made from column 2 to 12 following Tebbutt (1996) in his implementation of ECAH. The acoustic terms (i.e. the products of wavenumber and radius) were made to appear only in the denominator in the expressions of d_{ij}. This means column 2 was divided by x_{l1}^3, column 3 divided by x_{s1}, column 5 and column 8 divided by x_{l2}^3, column 6 and column 9 by x_{s2}, column 11 was divided by y_{l3}^3, and column 12 was divided by y_{s3}. Other columns remained unchanged. These modifications were made to reduce the complexity of the matrix in a simple way. For example, if we do not need to consider either the thermal or viscous effects, we can then simply set the reciprocal of the appropriate wavenumbers to zero, resulting in the whole columns equal to zero, and reducing the order of the matrix.

After establishing expressions for each element in the matrix equation, we now consider how to solve it to get the attenuation coefficient. As with the ECAH model, considerable care must be taken when solving the ill-conditioned matrix equation. First of all, the computation of scattering coefficients from the 12x12 matrix equation 4.2 relies on accurate and stable numerical computation of spherical Bessel and Hankel functions (see appendix 1.1). The arguments for these functions are compressive, shear and thermal wavenumber-particle radius products for the three media and in the general case all of them are complex. Computational experiments were carried out over frequency range of 100 kHz to 100 MHz and over the shell radius range of 100 nm to 50 mm. When using this range of sizes and frequencies it was found that the real parts of the wavenumber-radius products lie within the

range 10^{-5} to 10^{6}, and the imaginary parts of the wavenumber-radius products lie within the range 10^{-11} to 10^{6}.

$$10^{-5} \leq \mathrm{Re}(kr_s) \leq 10^{6} \tag{4.5}$$

$$10^{-11} \leq \mathrm{Im}(kr_s) \leq 10^{6} \tag{4.6}$$

where k denotes either compressive, shear or thermal wavenumber in either the continuous or the dispersed phase, and r_s denotes the shell radius.

According to Anson and Chivers, the Bessel and Hankel functions used in the calculation were put into the forms: $\frac{j_{n+1}(x)}{j_n(x)}$, $\frac{h_{n+1}(x)}{h_n(x)}$, $\frac{j_{n+1}(y)}{j_{n+1}(x)}$ and $\frac{h_{n+1}(y)}{h_n(x)}$, to reduce the numerical instability. However, there is an exception of the term in the final expression for A_n which is in the form: $\frac{j_n(x)}{h_n(x)}$. This term controls the convergence of the series obtained for A_n when calculating the forward and backward scattering, that is when the angle $\theta = 0$ or π respectively, where θ is defined as the angle between the scattering in the far field to the axis of wave propagation.

Numerical experiments to establish the stability map of Bessel and Hankel functions on the complex plane encompassed by equations 4.5 and 4.6 showed that when the imaginary part of the argument was larger than a certain threshold then overflow occurred in the computation of spherical Hankel functions. It followed that underflow occurred in the computation of the spherical Bessel functions. The computation was not sensitive to the size of the real part of the argument or the order of the function, within the limits of those sizes and orders of practical interest (n<1000). Within the frequency and

particle size ranges of interest it follows that the stability of the computation of Bessel and Hankel functions depends completely upon the imaginary part of the wavenumber-particle radius product argument. For polymer materials where the imaginary part of the shear wavenumber is large, the Hankel functions are proportional to the inverse of the exponent of the imaginary part. Bessel functions are directly proportional to the exponent of imaginary part. In the surrounding medium (medium 1) and the core medium (medium 3), the relevant terms are all in the form $\frac{h_{n+1}(x)}{h_n(x)}$ or $\frac{j_{n+1}(x)}{j_n(x)}$, so the exponentials cancelled. In the shell medium (medium 2), however, terms of the form $\frac{j_{n+1}(y)}{j_{n+1}(x)}$ and $\frac{h_{n+1}(y)}{h_n(x)}$ occur, and these are proportional to $e^{k'(r_s-r)}$, where k' is the imaginary part of the relevant wave number, and r_s and r are the shell radius and particle radius, respectively. It is terms of this type that can become very large for Hankel functions and very small for Bessel functions, leading to overflow/underflow problems. Assumptions were made follow the steps taken by Anson and Chivers: when $k'(r_s - r) \geq 10^4$, then set $e^{k'(r_s-r)} = 1$ in columns containing Hankel functions, whilst set $e^{k'(r_s-r)} = 0$ in the relevant columns involving Bessel functions. This is equivalent to assuming that the waves involved are totally damped after travelling a distance equal to or less than the thickness of the shell.

In addition, the thermal terms b_c and b_t for solid and liquid can also become very large at high frequencies, so these terms were normalized by dividing b_c:

$$\frac{b_t}{b_c} = \frac{\omega^2 - \left(\frac{c^2}{\gamma} + \frac{4\mu}{3\rho}\right)k_t^2}{\omega^2 - \left(\frac{c^2}{\gamma} + \frac{4\mu}{3\rho}\right)k_c^2} \text{ for solid} \qquad (4.7)$$

$$\text{and } \frac{b_t}{b_c} = \frac{\omega^2 - \left(\frac{c^2}{\gamma} - \frac{4i\omega\eta}{3\rho}\right)k_t^2}{\omega^2 - \left(\frac{c^2}{\gamma} - \frac{4i\omega\eta}{3\rho}\right)k_c^2} \text{ for liquid.} \qquad (4.8)$$

4.2.2. Program results

In order to test the accuracy of the program, we compared our program results with Anson and Chivers' original results. The materials are the same as they used in their simulation. The three materials used are water or olive oil for the surrounding fluid, polystyrene or aluminium for the shell and also water, olive oil or air for the core. The input parameters of these three materials are shown in table 4.2.

Shell materials

Substance	**Aluminium**	**polystyrene**
$c\ (m \cdot s^{-1})$	6420	2330
$c_s\ (m \cdot s^{-1})$	3040	1100
$\alpha_c / f\ (Npm^{-1}Hz^{-1})$	-	8.0×10^{-6}
$\alpha_s / f\ (Npm^{-1}Hz^{-1})$	-	38.0×10^{-6}
$\rho\ (kg \cdot m^{-3})$	2700	1050
$\kappa\ (W \cdot m^{-1} \cdot K^{-1})$	238	0.133
$C_p\ (J \cdot K^{-1} \cdot kg^{-1})$	904	1200
$\beta\ (K^{-1})$	6.9×10^{-5}	2.6×10^{-4}

Surrounding and core materials

Substance	water	Olive oil	air
$c\ (m \cdot s^{-1})$	1500	1440	344
$\alpha_c / f^2\ (Npm^{-1}Hz^{-2})$	2.5×10^{-14}	135×10^{-14}	1600×10^{-14}
$\eta\ (Pa \cdot S)$	1.0×10^{-3}	93.3×10^{-3}	0.02×10^{-3}
$\rho\ (kg \cdot m^{-3})$	1000	900	1.17
$\kappa\ (W \cdot m^{-1} \cdot K^{-1})$	0.59	0.19	0.024
$C_p\ (J \cdot K^{-1} \cdot kg^{-1})$	4182	2000	1000
$\beta\ (K^{-1})$	2.1×10^{-4}	7.2×10^{-4}	36.6×10^{-4}

Table 4.2. Input parameters for simulation: thermo-physical properties of different materials.

The following sections show some selected simulation results using our program compared to those of Anson and Chivers. The backscattering amplitude $f(\pi)$ (refer to chapter 2) was calculated for a range of wavenumber-particle radius products $k_c r$ from 0 to 30 with the step of 0.01. The particle radii in the following calculations are 49.5 mm and the ratio between the particle radius and shell radius is set to 0.99, which means that a very thin shell thickness was used.

4.2.2.1 Influence of surrounding material on backscattering

The influence of the surrounding fluid on the backscattering was examined here. The backscattering amplitudes of an air-filled spherical aluminium shell suspended in olive oil or water were calculated, respectively, shown in figure 4.3 (figure 4.2 shows Anson and Chivers' results). Comparing the top and bottom figures we see that the two curves have similar shapes: both have a very sharp initial ripple and the subsequent ripples happened at similar intervals in kr. Whereas the backscattering amplitude for the olive oil

is smaller than that of water, especially for the ripples at very low *ka* value, which means that the particle suspended in the olive oil has a strong absorption compared with water. It is concluded that the effect of the different surrounding fluids is mainly on the amplitude of the curve, and that the periodic native of the response did not change significantly.

4.2.2.2 Influence of core material on backscattering

Figures 4.4 to 4.7 show the influence of the core material on the backscattering. There is no doubt that for a very thin shell thickness, the core response is expected to be dominant. For this reason, the ratio between particle radius and shell radius was set to 0.99 to get a very thin shell thickness. Figures 4.4 (Anson and Chivers results) and 4.5 (our simulations) show the backscattering from a water-filled aluminium shell suspended in water together with an olive oil-filled aluminium shell suspended in water. We can see that the two curves have very similar shape at low *kr* (*kr* <10), and the two main sharp peaks occur at very similar *kr* value, but the shape differs more at higher values of *kr*. Comparing the two core materials, we find that for the water-filled aluminium shell in water, the shell material has significant influence on the backscattering, because without it, there would not have been any scattering at all. Replacing the inner water by olive oil means the scattering will be determined by both the core and the shell, therefore, the amplitude of the backscattering changed. It is interesting to compare figure 4.5 with the bottom curve in figure 4.3, which is the same situation but with air inside. The backscattering for air core in figure 4.3 has totally different shape, which has a high amplitude in backscattering as well as a very sharp initial

peaks. The scattering for the air core is much stronger than for the oil and water cores.

Figures 4.6 (Anson and Chivers results) and 4.7 (our simulation results) show the backscattering from a viscoelastic plastic shell (polystyrene) in water with a water core and olive oil core, respectively. The phenomenological model of viscoelasticity used here is Zener's model, which has been explained fully in one of Challis' papers (Challis, 1995). This time changing the core material to a more viscous and lossy liquid (olive oil) reduces the whole amplitude of the scattering, up to kr=23, and this effect appears to increase with increasing kr, but without significantly changing the values of kr at which the subsidiary maxima occur. When kr>23, there is a dramatic change on the backscattering curve — the amplitude of the backscattering for the olive oil becomes much higher than that of water till kr=28 then decreases sharply, and the subsidiary maxima occur at different kr values. We can conclude that larger kr value is sensitive to the core material.

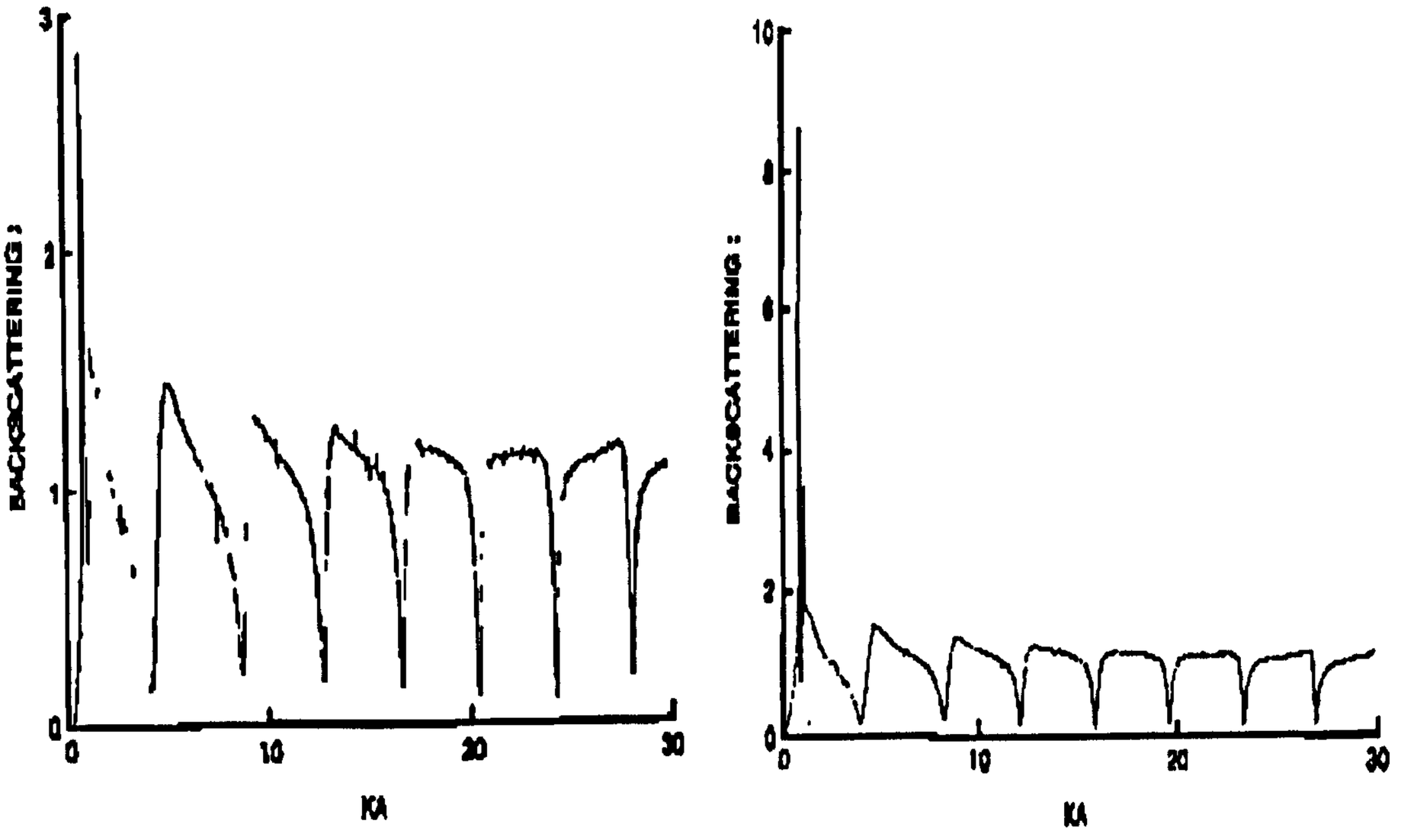

Figure 4.2. Anson and Chivers' results: Left: backscattering of an air-filled aluminium shell in olive oil; right: backscattering of an air-filled aluminium shell in water. Both have a particle radius of 49.5 mm, and the ratio of particle to shell radius was $r / r_s = 0.99$.

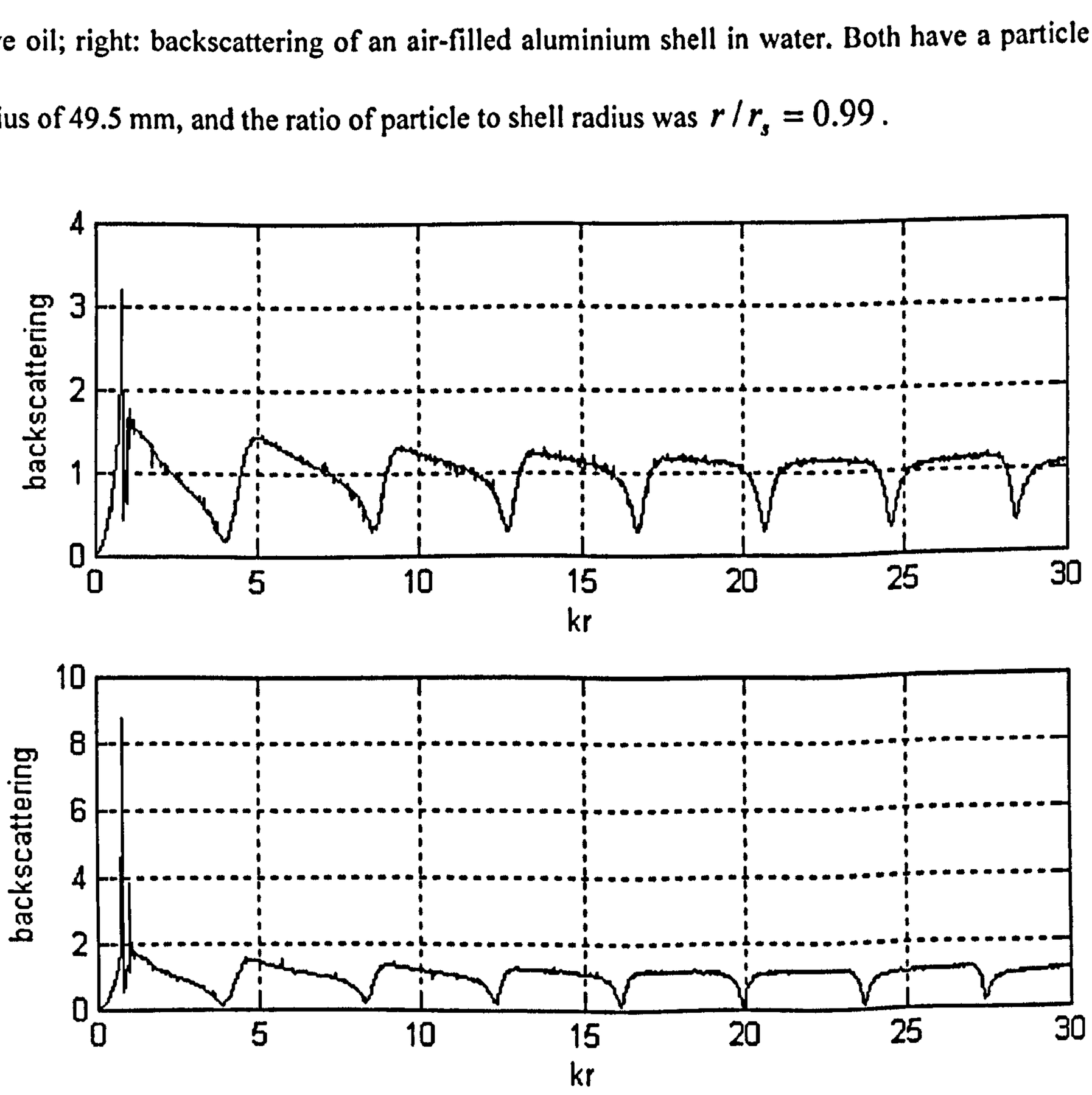

Figure 4.3. Computation in this project: Top: backscattering of an air-filled aluminium shell in olive oil; bottom: backscattering of an air-filled aluminium shell in water. Other descriptions are the same as in figure 4.2.

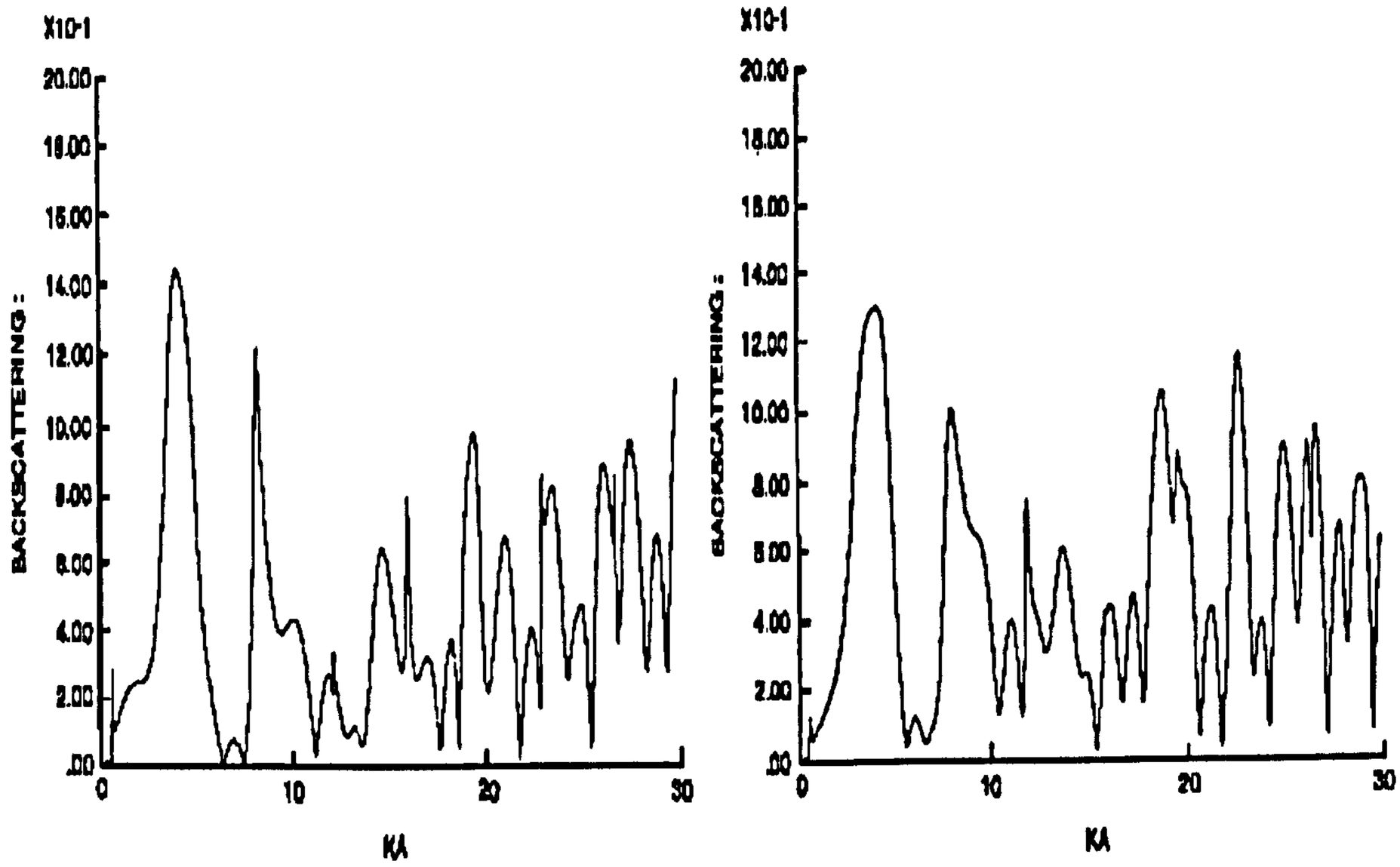

Figure 4.4. Anson and Chivers results. Left: backscattering from a water-filled aluminium shell in water; right: backscattering from an oil-filled aluminium shell in water. Other descriptions are the same as in figure 4.2.

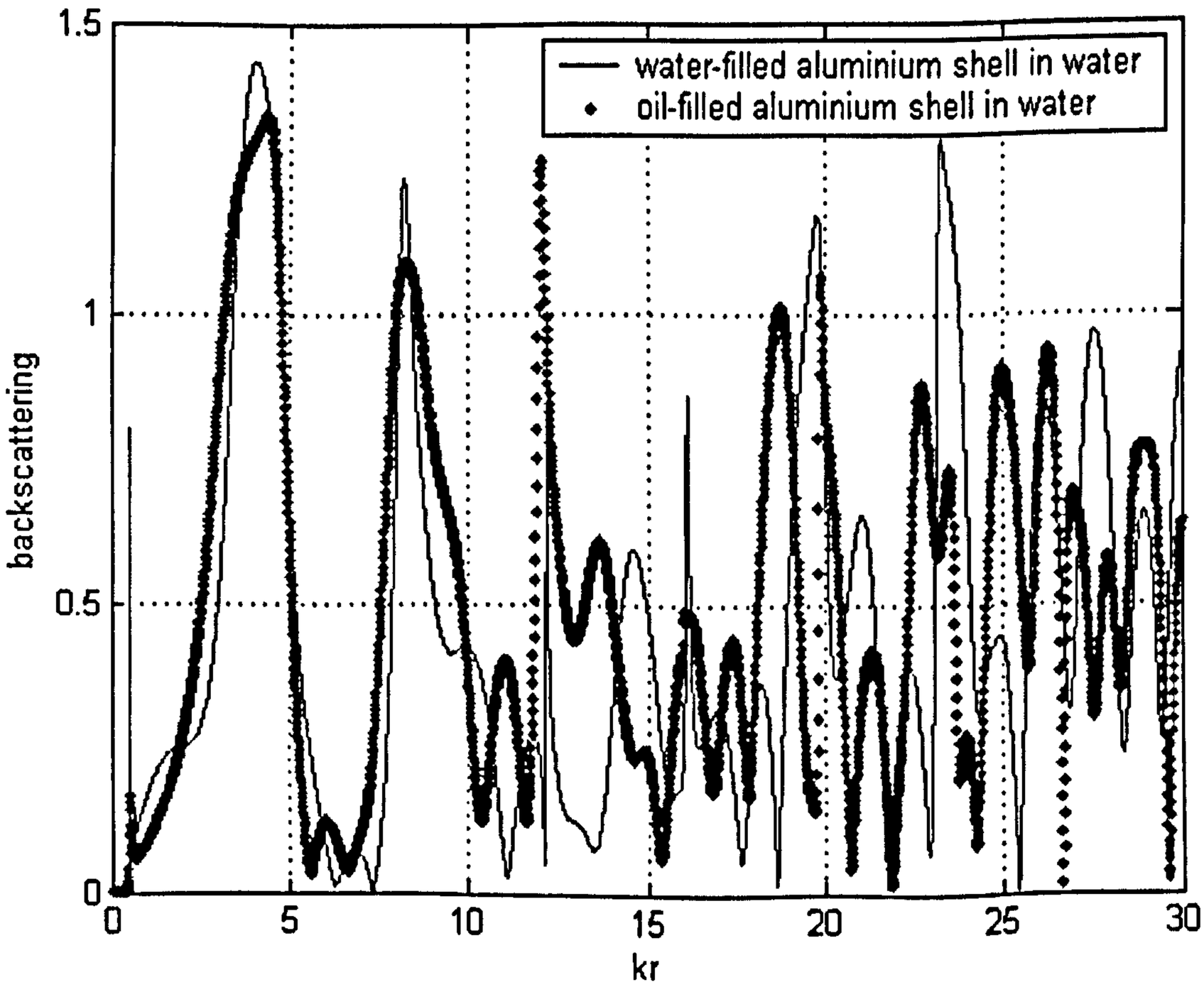

Figure 4.5. Our simulation results. Backscattering from a water-filled aluminium shell in water (the solid line); backscattering from an oil-filled aluminium shell in water (dotted line). Other descriptions are the same as in figure 4.2.

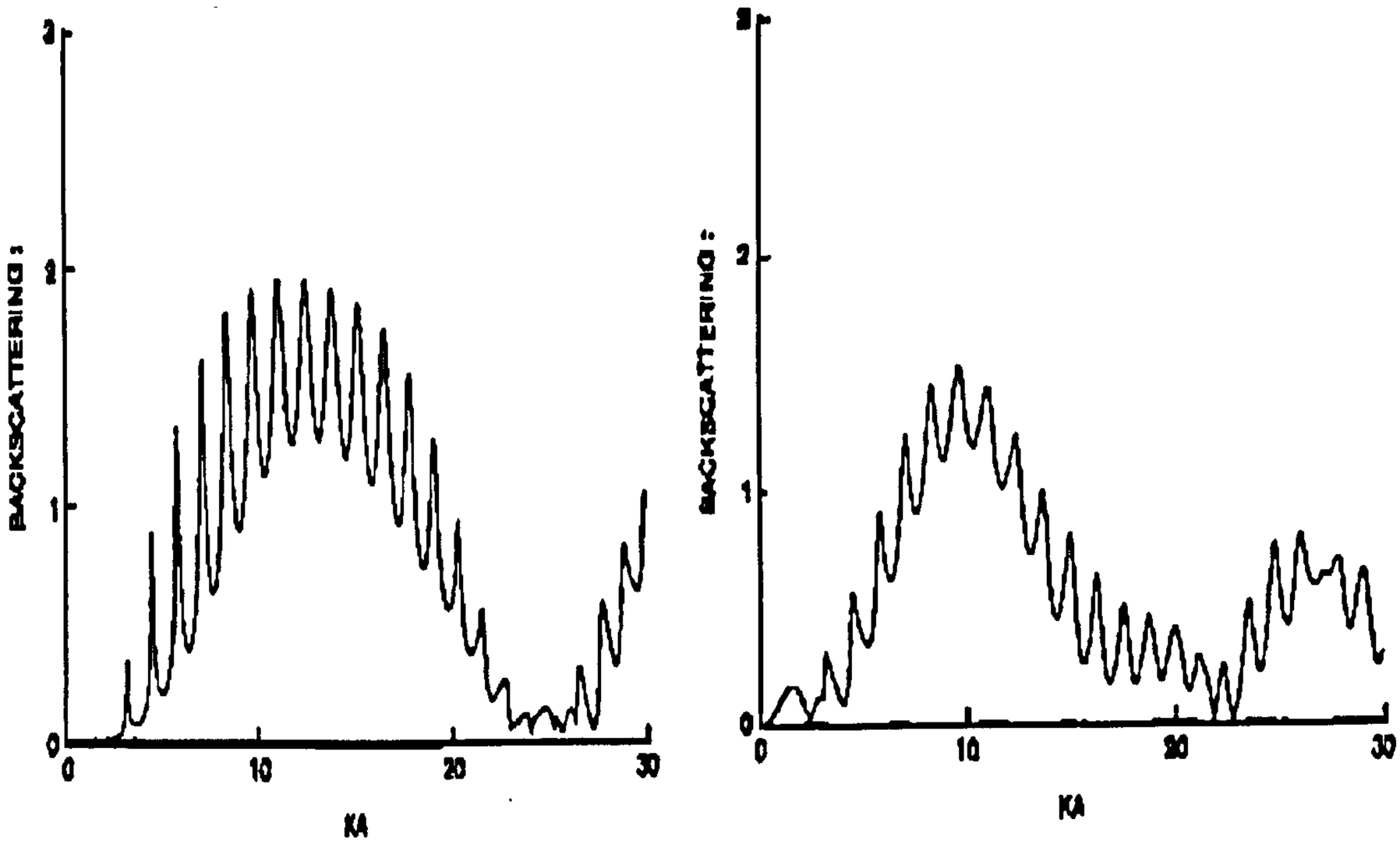

Figure 4.6. Anson and Chivers results. Left: backscattering from a water-filled polystyrene shell in water; right: backscattering from an oil-filled polystyrene shell in water.). Other descriptions are the same as in figure 4.2.

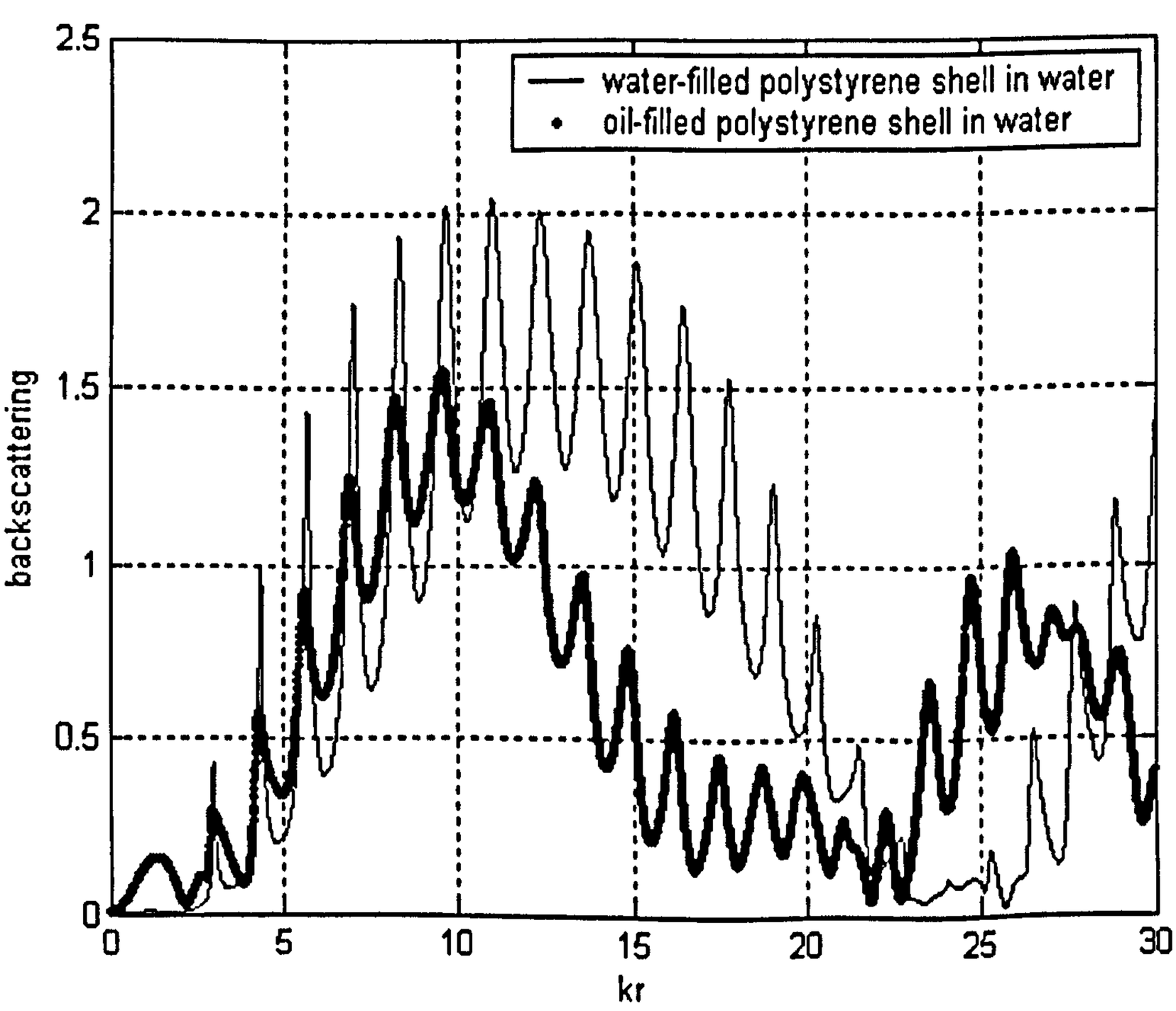

Figure 4.7. Our simulation result. Backscattering from a water-filled polystyrene shell in water (solid line); backscattering from an oil-filled polystyrene shell in water (dotted line). Other descriptions are the same as in figure 4.2.

4.2.2.3 Influence of shell material on backscattering

The influence of a viscoelastic plastic shell (polystyrene) and a solid shell (aluminium) is shown in figure 4.8, both with water core (for Anson and Chivers results please refer to figure 4.6 (left) and figure 4.4 (left)). Examination of the two curves showed the polystyrene shell gives a response which is completely different from that of the aluminium shell. As we mentioned above, when the core material has the same physical properties as the surrounding phase, the response of backscattering will mainly depend on the physical properties of the shell, and it is obvious that polystyrene is a vicoelastic plastic while aluminium is a solid, the properties of the two materials being completely different, and hence the backscattering response is different as well.

The influence of shell thickness on the backscattering is examined in figure 4.9. A water-filled polystyrene shell suspended in water was selected because the shell properties have significant influence on the scattering. The shell radius is fixed to 50 mm, and the ratio between particle and shell radius was reduced from 0.99 to 0.95, which means the shell thickness is increasing. It shows that the thicker shell is a much stronger scatterer; the amplitude of the backscattering increases as the shell thickness increases, especially at high kr values (kr >20). At low kr values (kr<7), the shape of the backscattering did not change much, and the values of kr at which the subsidiary maximum occurred remained the same, but the backscattering amplitude for thicker shell is large. For kr>7 the structure of the scattering changed significantly indicating increased sensitivity to the shell thickness for large kr.

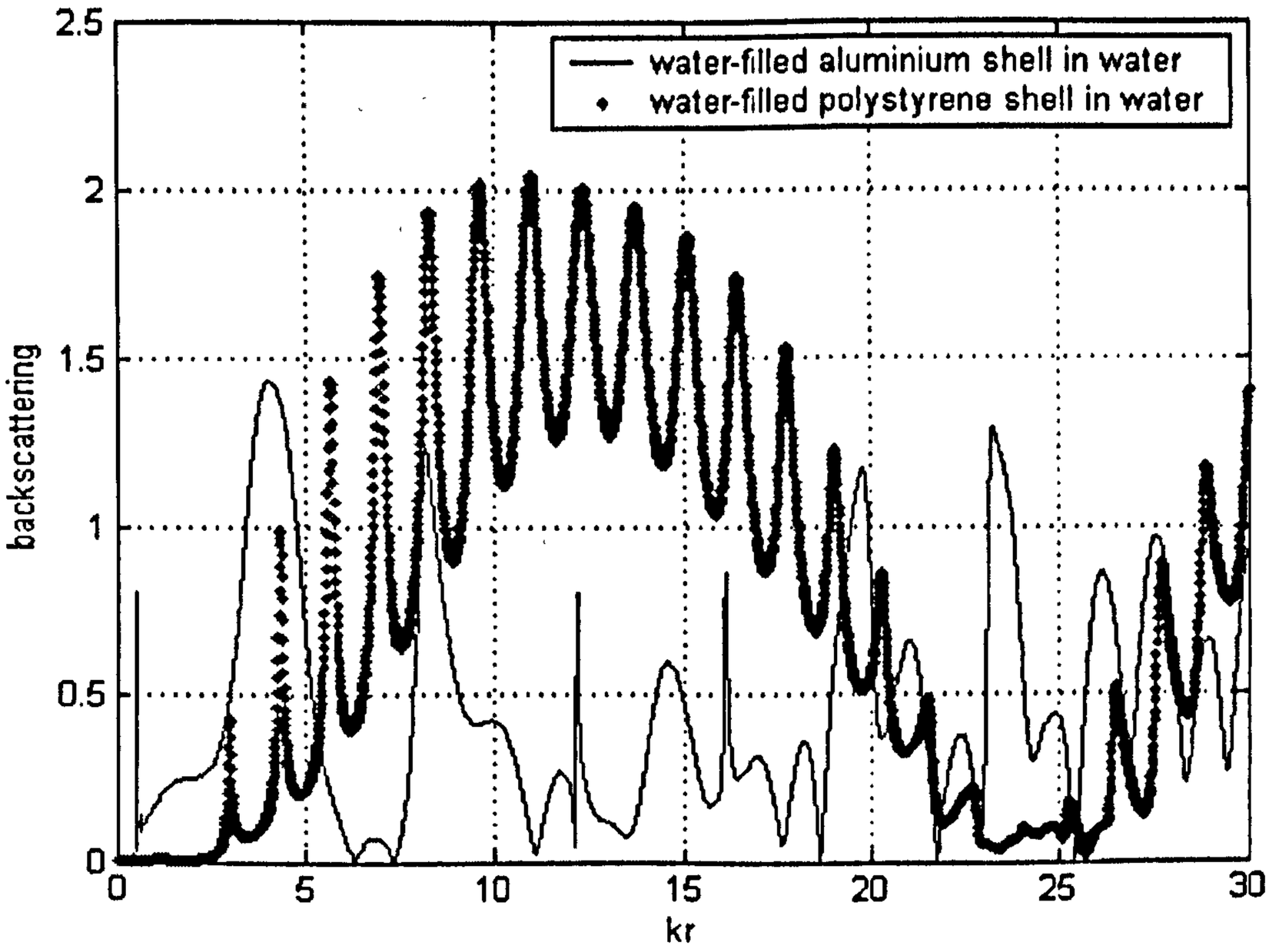

Figure 4.8. Our simulation result. Backscattering from a 50 mm radius water-filled aluminium shell in water (solid line); backscattering from a 50 mm radius water-filled polystyrene shell in water (dotted line). Other Other descriptions are the same as in figure 4.2.

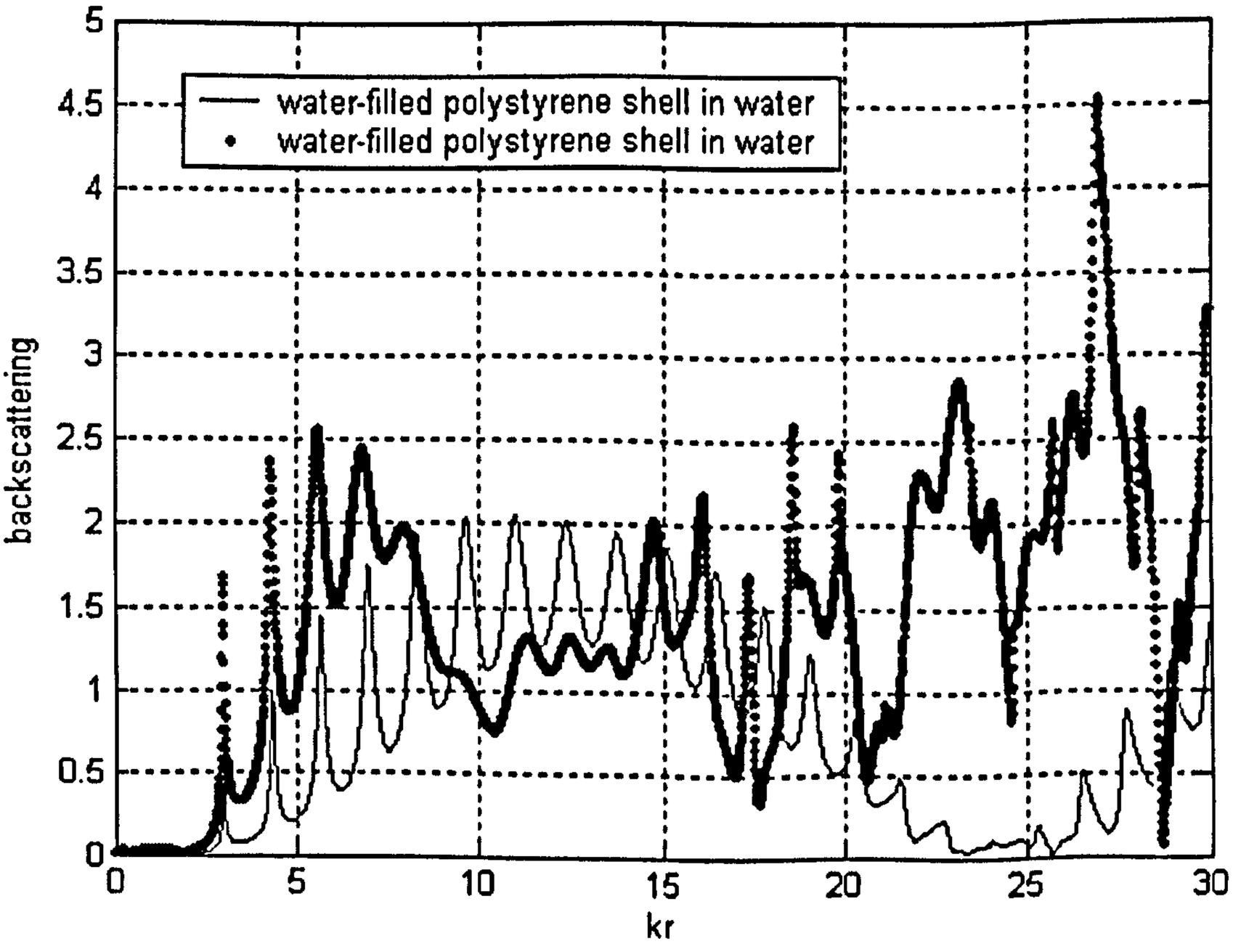

Figure 4.9. Backscattering from a water-filled polystyrene shell in water, with shell radius of 50 mm, core radius of 49.5 mm (solid line), and core radius of 47.5 mm (dotted line).

4.2.2.4 Influence of thermal and viscous effects on backscattering

The effects of thermal and viscous waves were investigated here. The backscattering from an air-filled aluminium shell in water was calculated using the particle radius and shell radius mentioned above. Figure 4.10 shows the backscattering including thermal and viscous effects (the upper figure), and the backscattering without thermal and viscous effects (the lower figure). The inclusion of thermal and viscous terms appears to have very little effect on the structure of the curve, but has some contributions in backscattering amplitudes, especially for the diminishing of the amplitude of the first two sharp peaks. A further investigation at low *kr* values is shown in figure 4.11, with a smaller *kr* step of 0.001. The thermal effect alone reduces the first amplitude by about 3% and reduces the second one by about 0.1%; whereas the viscous effect has more influence than the thermal one, which reduces the first amplitude by about 30%, and reduces the second one by about 4%. This confirms the previous comment on the effects of including viscosity and thermal terms.

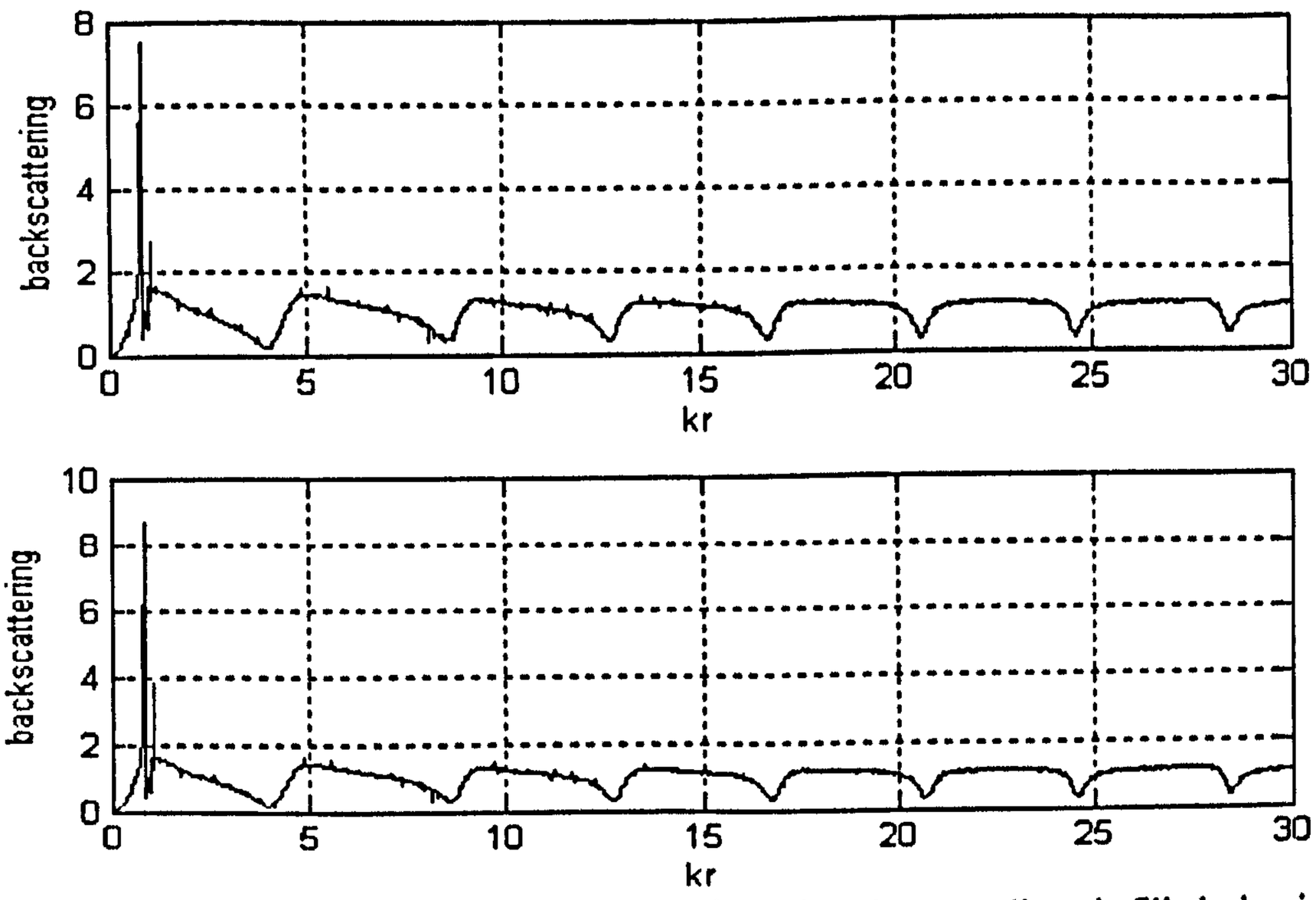

Figure 4.10. Our simulation results: Backscattering of a 50 mm radius air-filled aluminium shell in water, with particle radius of 49.5 mm and the ratio between particle and shell radius is 0.99. Top: backscattering including thermal and viscous effects; bottom: backscattering without thermal and viscous effects.

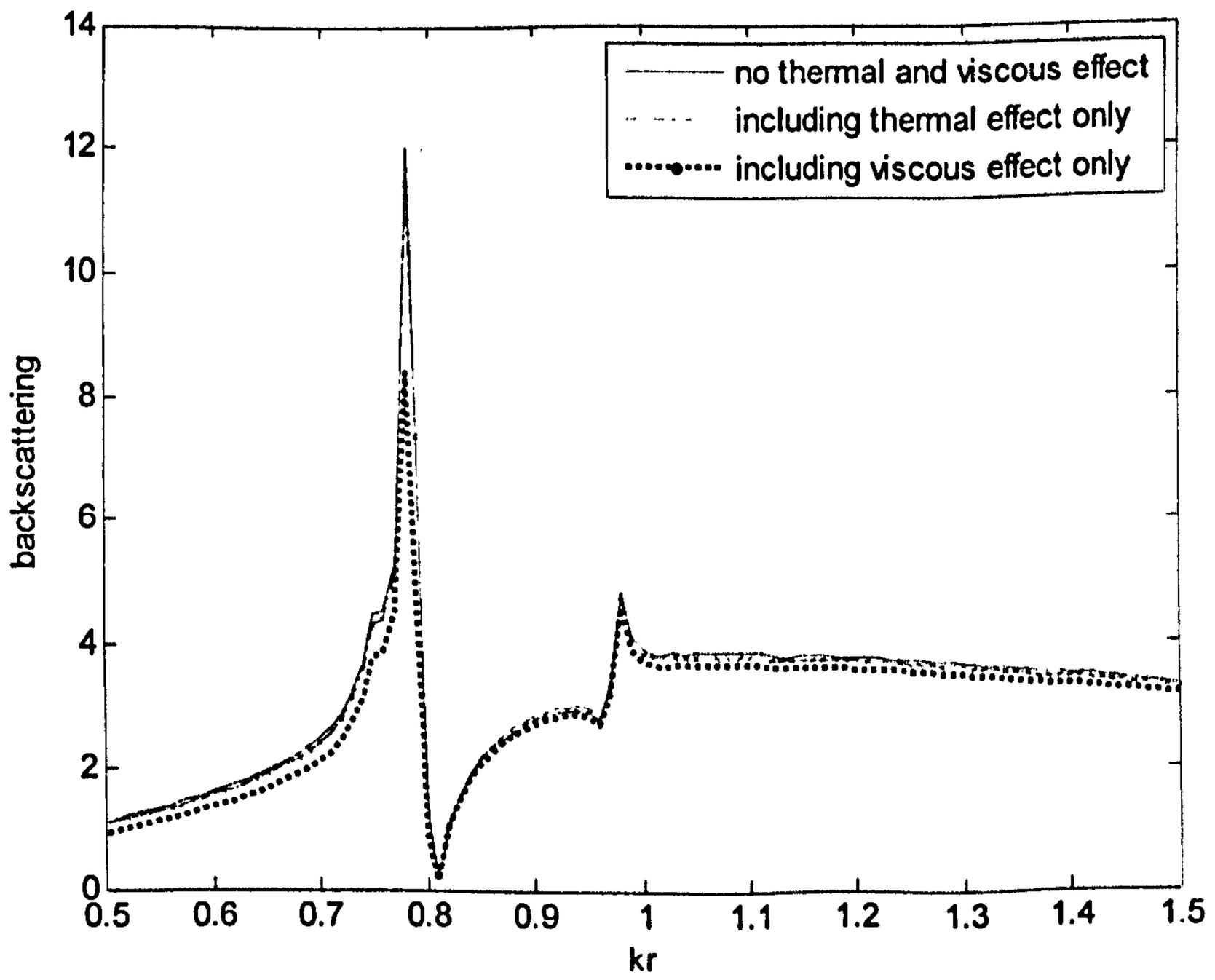

Figure 4.11. A further investigation about the backscattering curve shown in figure 4.10: the solid line is the backscattering without thermal and viscous effect, the broken line with stars is with thermal effects only, and the dash line is with viscous effect only.

4.2.2.5 Attenuation calculation for an encapsulated emulsion

In the above sections we compared our simulation data for backscattering with Anson and Chivers' results. The comparisons indicate that our simulation data are almost the same as theirs, which implies that our program is stable and gives confidence. What we are concerned in this thesis is not the backscattering calculation, but to calculate the attenuation and phase velocity as functions of frequency. The experiment for a kind of encapsulated emulsion (sugar-in-olive oil, with the added tripalmitin to form an imagined shell outside the sugar particles) has been done by Dr. Holmes in Applied Ultrasonics Laboratory. Our aim here is to use the developed Anson and Chivers shell model to calculate the attenuation and compare with the experimental result to see the applicability of this model. Moreover, we change the shell thickness in the simulation to see if the attenuation is sensitive to the shell thickness; and we also interested in checking when the thickness tends to zero, whether the shell model can give a same result as ECAH model.

The thermo-physical properties of the three media are shown in table 4.3. The suspended particle radius is 7.5 μm, particle concentration is 36.4% v/v, the shell radius is 10.5 μm (calculated using equation 3.8), and shell thickness is 3.0 μm, which means a very thick shell is used.

Substance	Sugar	Tripalmitin	Olive oil	silica	Corn oil
$c\ (m\cdot s^{-1})$	3800	2500	1424.4	5968	1456.1
α_c / f^2 $(Np\cdot m^{-1}Hz^{-2})$	1.72×10^{-16}	1.0×10^{-16}	135×10^{-14}	2.6×10^{-22}	6.47×10^{-12}
$\mu\ (N\cdot m^{-2})$	5.73×10^{9}	2.33×10^{9}	-	3.09×10^{10}	-
$\eta\ (Pa\cdot S)$	-	-	0.07	-	0.06
$\rho\ (kg\cdot m^{-3})$	1588	1036	909.0	2185	917.7
κ $(W\cdot m^{-1}\cdot K^{-1})$	0.245	0.088	0.1593	1.6	0.166
C_P $(J\cdot K^{-1}kg^{-1})$	1245	1625	1948	729	1923
$\beta\ (K^{-1})$	0.6×10^{-4}	5.55×10^{-4}	7.37×10^{-4}	1.35×10^{-6}	7.2×10^{-4}

Table 4.3. Thermo-physical properties of some materials used in this chapter.

Figure 4.12 shows the experimental attenuation data together with the simulation data as a function of frequency for the 36.4% sugar-in-oil emulsion with 4% tripalmitin. There is a good agreement between the experiment and the simulation up to 12 MHz, and after that there is an increasingly variant at frequencies above 13 MHz in the experimental data due to the effects of noise. This good agreement shows that our shell model can be applied in the attenuation calculation for encapsulated emulsions. The influence of shell thickness was also shown in figure 4.12. A very thin shell thicknesses compared to the particle radius was selected, 200 nm, to investigate the change in the attenuation with the decreasing in shell thickness. We can see that the attenuation does not change significantly with decreasing of shell thickness at low frequency, however at frequencies larger than 10 MHz, the attenuation is getting smaller as the shell thickness decreases, due to the attenuation caused by the shell getting smaller.

As we discussed above, when the shell thickness is setting to zero, the shell model can be treated as a single particle model, and therefore we should obtain the same result as that of ECAH model. Figure 4.13 shows the comparison between shell model and ECAH model, from which we see that the two curves are coincident when frequency is less than 25 MHz, at higher frequencies the shell model is slightly smaller than the ECAH model, but the difference is acceptable within the error limits. We conclude that our implementation of the Anson and Chivers model behaves in the limit of no shell exactly as the ECAH model.

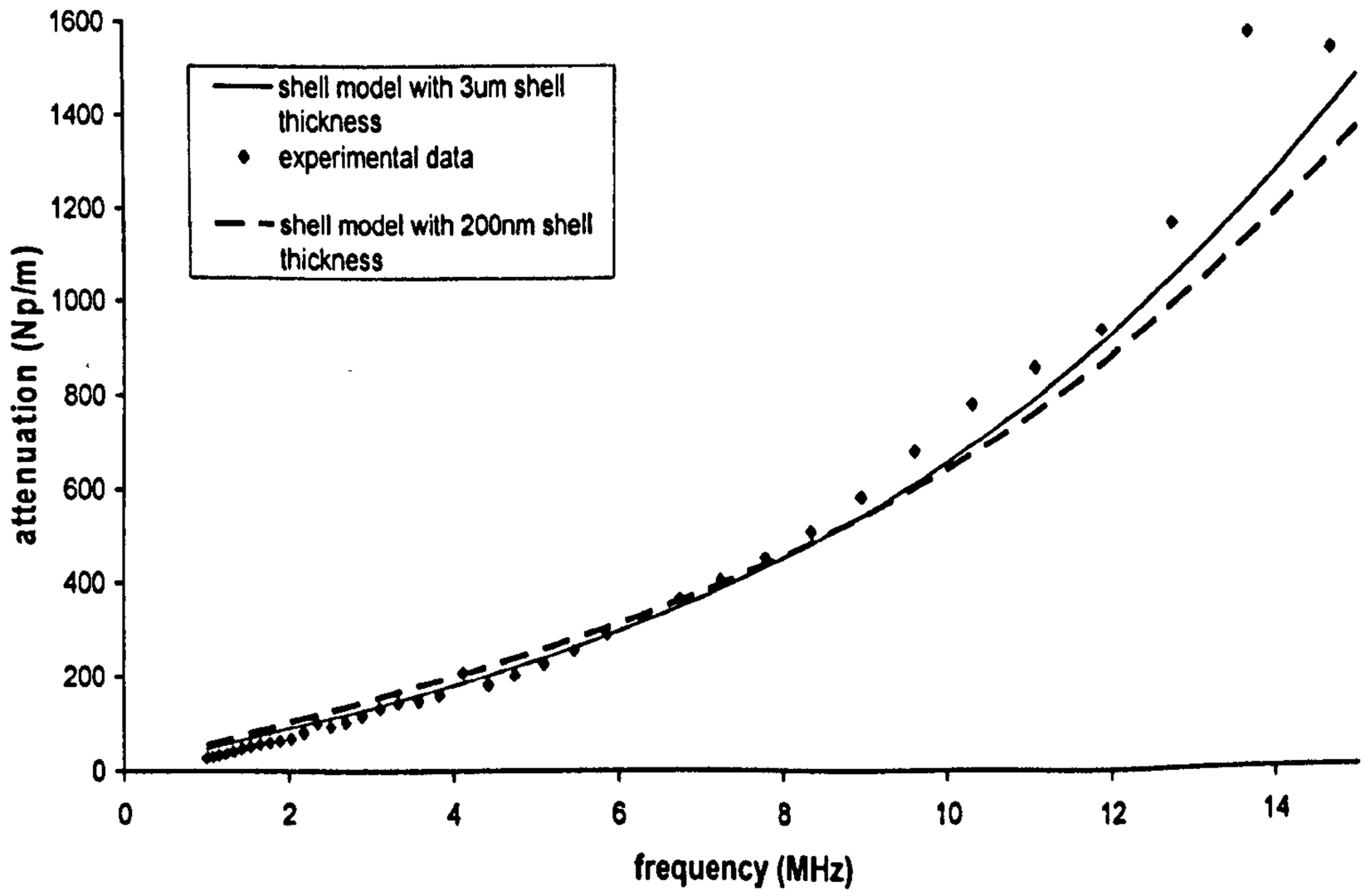

Figure 4.12. Attenuation as a function of frequency for 36.4% sugar-in-oil with 4% tripalmitin: experimental data (dots), simulation using the Anson and Chivers shell model with shell thickness of 3μm (solid line), and simulation using Anson and Chivers shell model with shell thickness of 0.2μm (broken line).

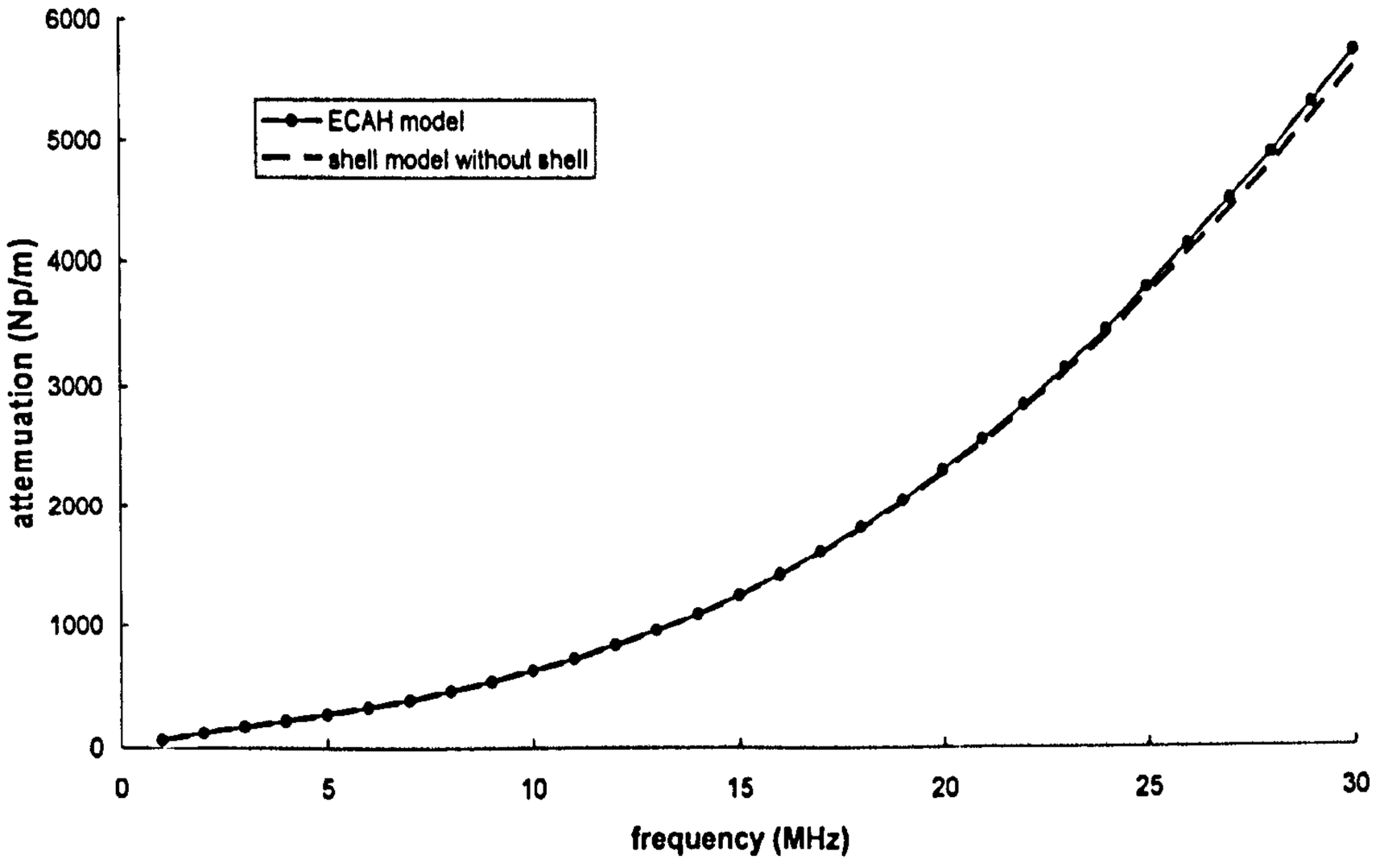

Figure 4.13. Attenuation simulation using the Anson and Chivers shell model without shell (the broken line) as well as the ECAH model (the dotted line) for 36.4% sugar-in-olive oil.

4.3 Concentrated emulsions and suspensions —the Hipp model

Hipp (2002a, 2002b) developed a shell model using the same boundary conditions as those of Anson and Chivers, only several years later. His model applied to both dilute or concentrated suspensions and emulsions because of the inclusion of thermal and viscous effects, and with no wavelength or frequency restrictions. Hipp's model was based on the assumption that a given particle was surrounded by a shell of original dispersant in its immediate vicinity, which in turn was immersed in an unlimited effective medium accounting in an effective way for the effect of neighbouring particles. The shell has the same thermal properties as those of original continuous phase, and the thermo-physical properties of the effective medium are calculated as

the volume average of both suspended particles and the shell. Hipp pointed out that the situation in the shell model is similar to that of the ECAH model, except that the particle and the outer phase are separated by an intermediate phase.

Hipp set up potentials for compression, shear and thermal waves in the three media just as Anson and Chivers had done. The resulting equations were solved for both boundaries at the surface of particle and at the surface of shell according to figure 4.1, the boundary conditions are exactly the same as that of Anson and Chivers' shell model, which results in a 12×12 matrix equation. This equation is also the same as that of Anson and Chivers (see equation 4.2, and appendix 4.1).

The calculation of the attenuation is based on the compression partial wave amplitude in the shell G_n, which is different from both the ECAH model and the Anson and Chivers model. In the original ECAH model, the observed attenuation is defined by the coefficient A_n of the scattered compressive waves, so does in the Anson and Chivers shell model. But in Hipp's shell model, where an imaginary shell is invoked, we find that only the coefficient G_n represents the wave in the shell and allows evaluation of how the wave is attenuated by the particle. The Hipp model will converge to ECAH model as the shell thickness tends to infinity, the particle is then immersed in the pure continuous phase again.

We have carried out a number of computational experiments to test the validity of Hipp's model in solid-in-liquid and liquid-in-liquid systems. The aim of these experiments was to investigate whether the Hipp model converges to the ECAH model at low particle concentrations, and secondly,

whether the Hipp model predicts lower attenuation at high particle concentrations. Tables 4.2 and 4.3 show the physical properties for the materials of water, corn oil and silica in the calculations used. Figures 4.14a to 4.14d show the attenuation for silica-in-water suspensions as a function of particle volume fraction, for a number of different frequencies in the range 2 MHz to 100 MHz. Experiments were made using a Perspex (PMMA) test cell in the Applied Ultrasonics Laboratory at frequencies of 5 MHz and 20 MHz. The experimental data at the higher frequencies 50 MHz and 100 MHz were given by Hipp, who did the experiments using *Ultrasizer* (Malvern Instruments Ltd.). Since the density difference between silica and water is relatively high ($\frac{\rho_3}{\rho_2} \approx 2.0$), viscoinertial effects are expected to dominate in determining the attenuation. From figure 4.14a we can see that the ECAH model predicts a linear increase in the attenuation with volume fraction. However, the experimental results show that the attenuation does not increase as rapidly with concentration as predicted. The non-linearly results in a much lower attenuation than the ECAH model would suggest. In this case, the attenuation reaches a peak at around 15% concentration and decreases at higher concentrations. It is believed that the reduction in attenuation compared with the ECAH model may be due to the interaction of shear waves in this case when particles are close together. The Hipp model accounts for such interactions and the figure shows that it predicts the attenuation with a greater success than the ECAH model. The Hipp model predicts a non-linear form for attenuation versus volume fraction and can produce a peak in the attenuation curve. Figures 4.14b to 4.14d show that the ECAH model is valid up to a

higher concentration as the frequency increasing, whilst Hipp model is in good agreement with the experimental data.

These results confirm Hipp's important findings — as concentration increases the increased attenuation is much less than that expected from the linear increase with concentration which would be expected from the original ECAH model; the difference between ECAH and experiment is more pronounced at low frequencies and much less pronounced at high frequencies.

Figures 4.15a to 4.15d show the attenuation for corn oil-in-water emulsions as a function of particle volume fraction, and this time the dominant part becomes thermal effects due to the low-density-contrast between corn oil and water ($\frac{\rho_3}{\rho_2} \approx 1.0$). Again, we observe an over prediction of attenuation by the ECAH model, the gap between the model and experiment reducing as frequency is increased.

From further observations of these figures, it is also clear that our implementation of the Hipp model provides a simulation that closely matches the experimental data. Compared with these two groups of figures, we see that the deviation between ECAH model and experiment is more significant for the solid-in-water suspension, and this is due to the fact that the thermal skin depth in the continuous phase is less than that the shear skin depth ($\delta_T \approx 0.4\delta_S$), as has been discussed earlier in chapter 2.

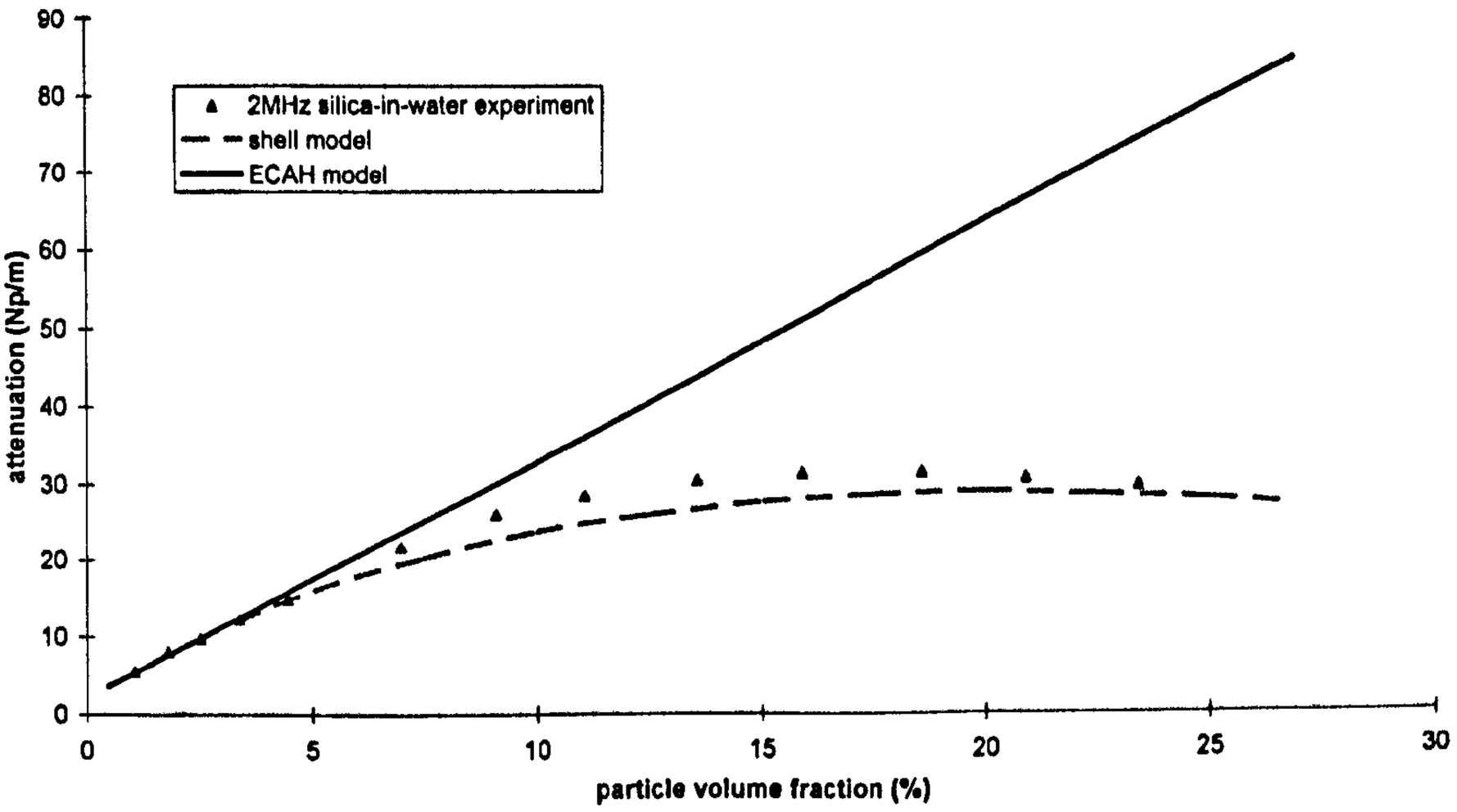

Figure 4.14a. Attenuation as a function of particle volume fraction for silica in water with mean particle radius 0.2 μm at 2 MHz. The curves in these figures are Hipp's shell model (dash line), the ECAH model (solid line) and the experimental data (dots).

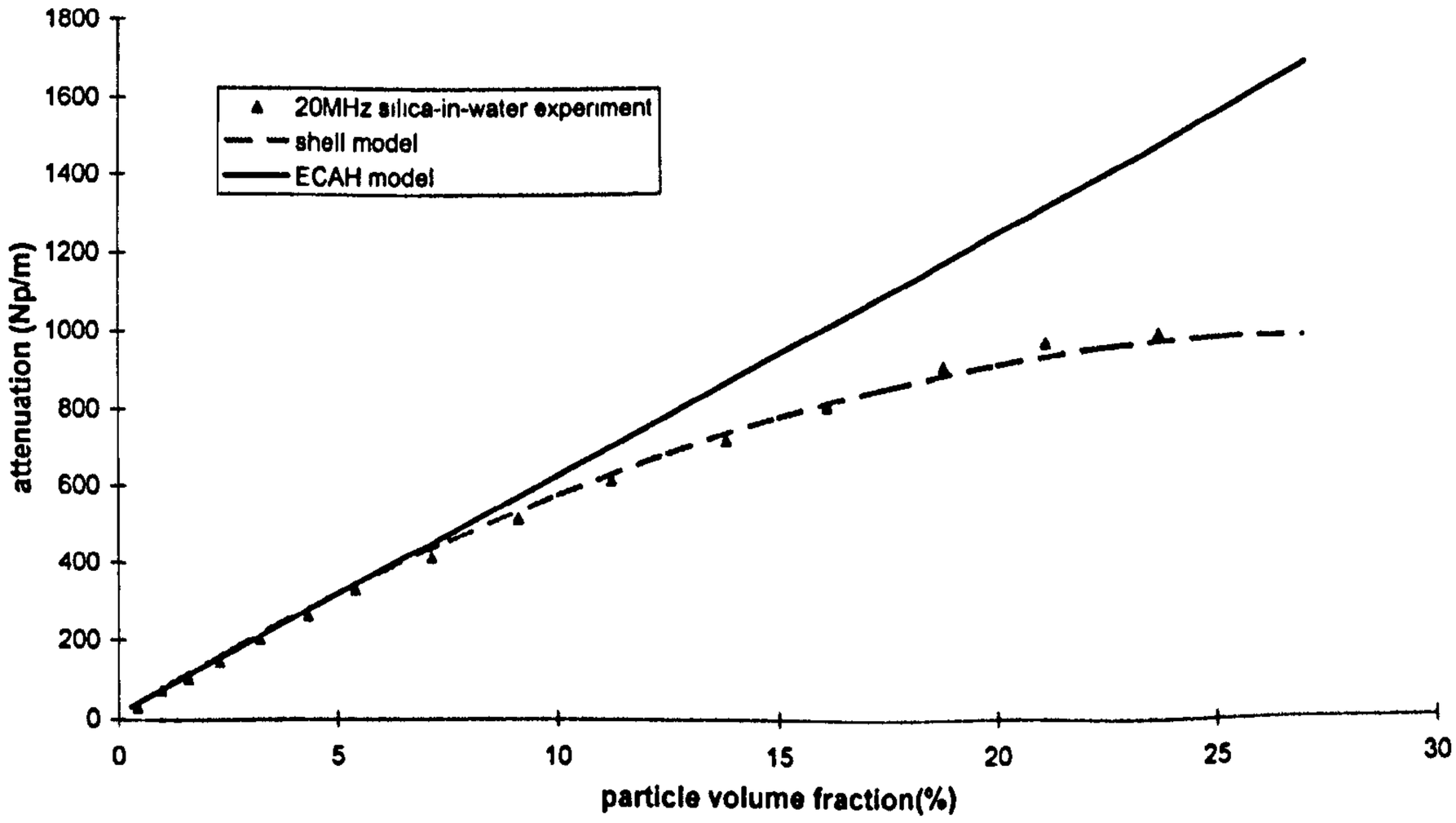

Figure 4.14b. Attenuation as a function of particle volume fraction for silica in water with mean particle radius 0.2 μm at 20 MHz. The curves in these figures are Hipp's shell model (dash line), the ECAH model (solid line) and the experimental data (red dots).

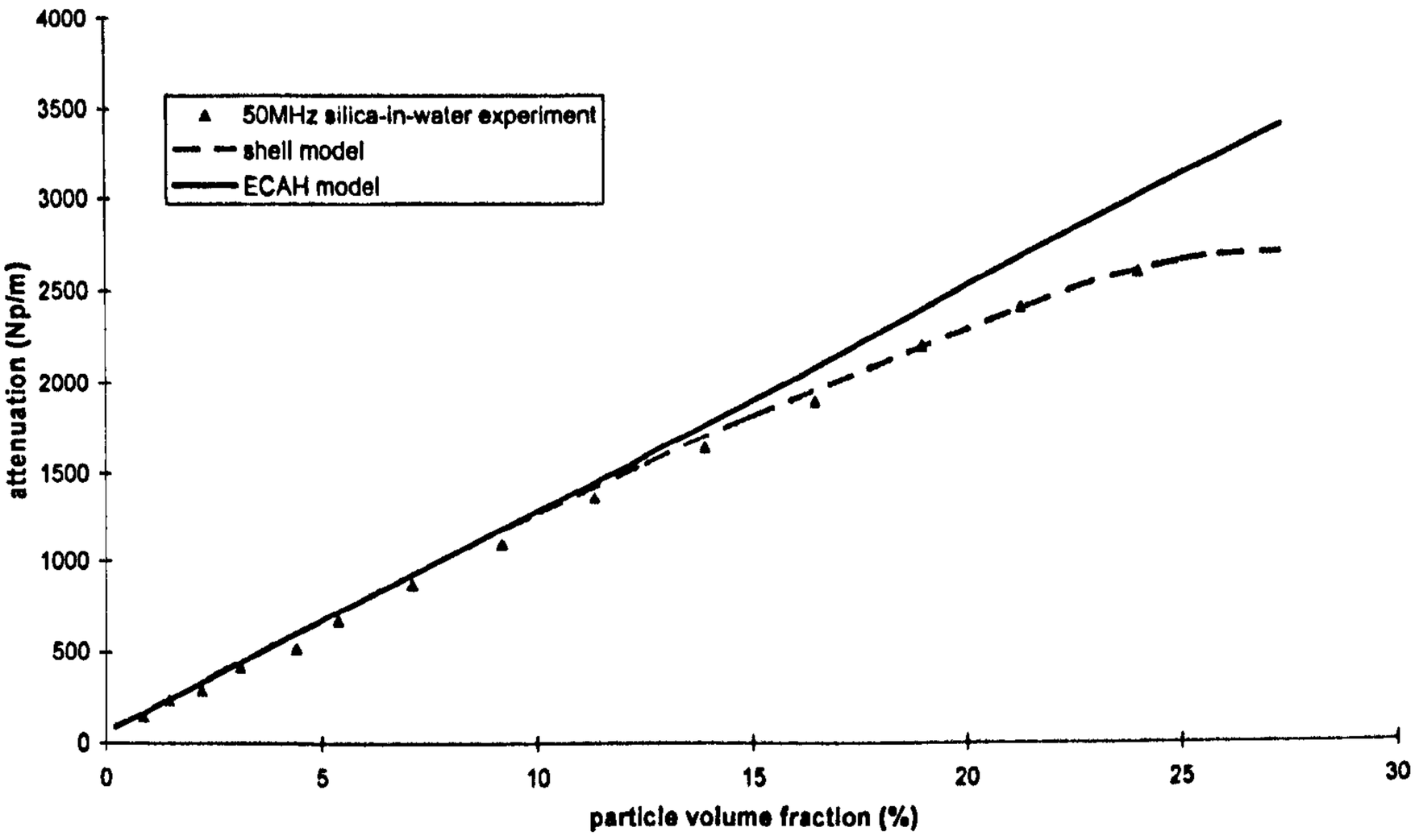

Figure 4.14c. Attenuation as a function of particle volume fraction for silica in water with mean particle radius 0.2 μm at 50 MHz. The curves in these figures are Hipp's shell model (dash line), the ECAH model (solid line) and the experimental data (dots).

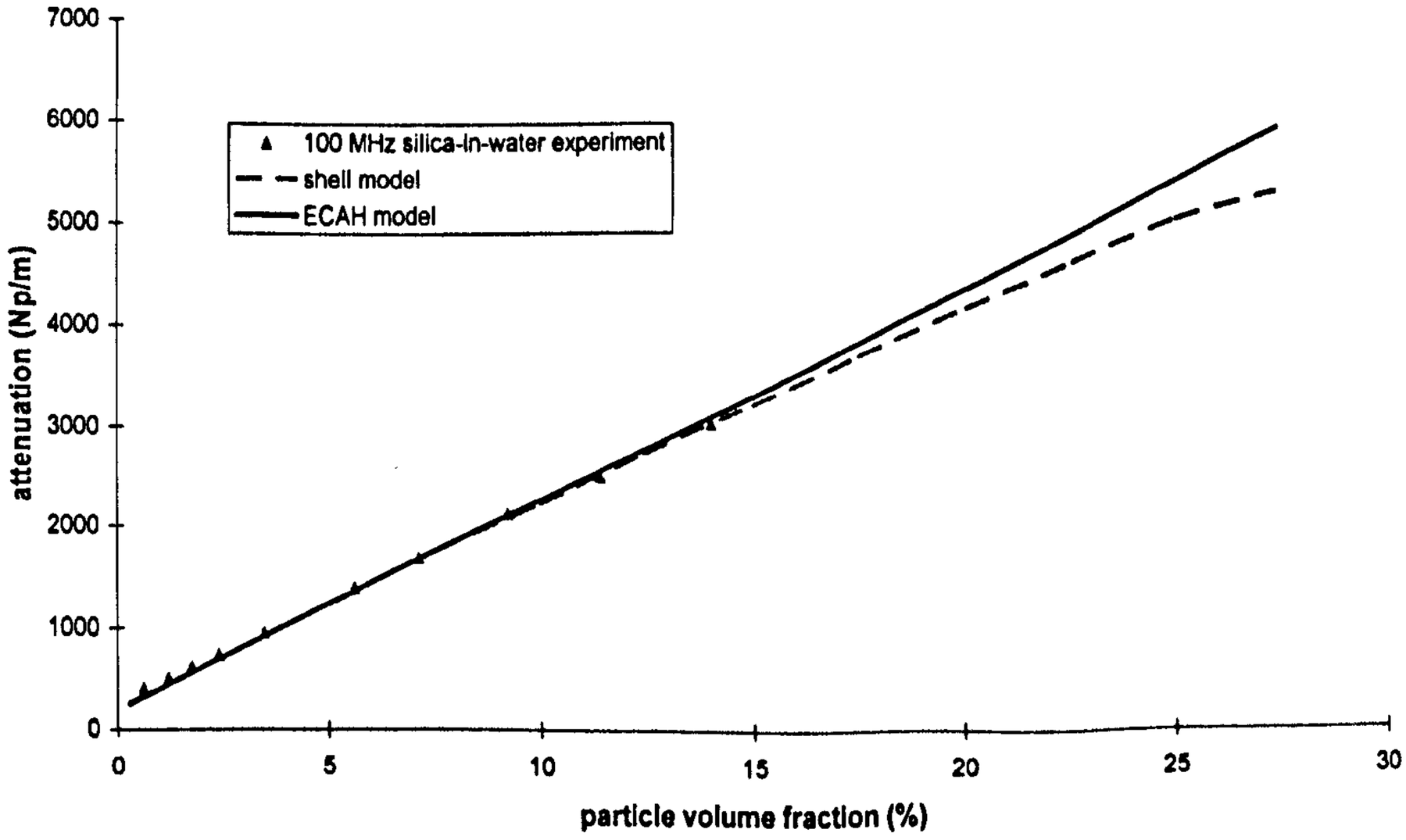

Figure 4.14d. Attenuation as a function of particle volume fraction for silica in water with mean particle radius 0.2 μm at 100 MHz. The curves in these figures are Hipp's shell model (dash line), the ECAH model (solid line) and the experimental data (dots).

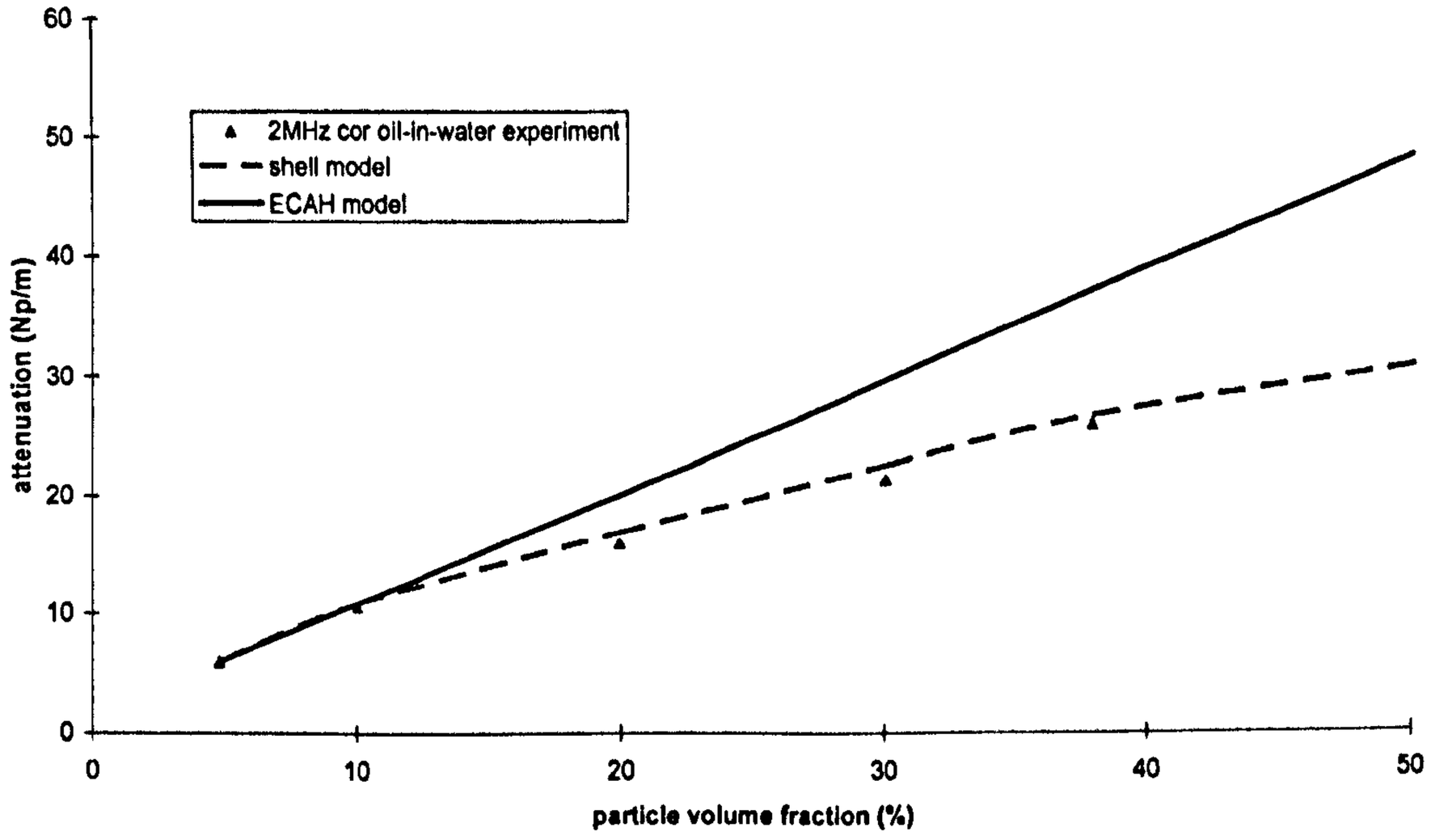

Figure 4.15a. Attenuation as a function of particle volume fraction for corn oil in water with mean particle radius 0.1 μm at 2 MHz. The curves in these figures are Hipp's shell model (dash line), the ECAH model (solid line) and the experimental data (dots).

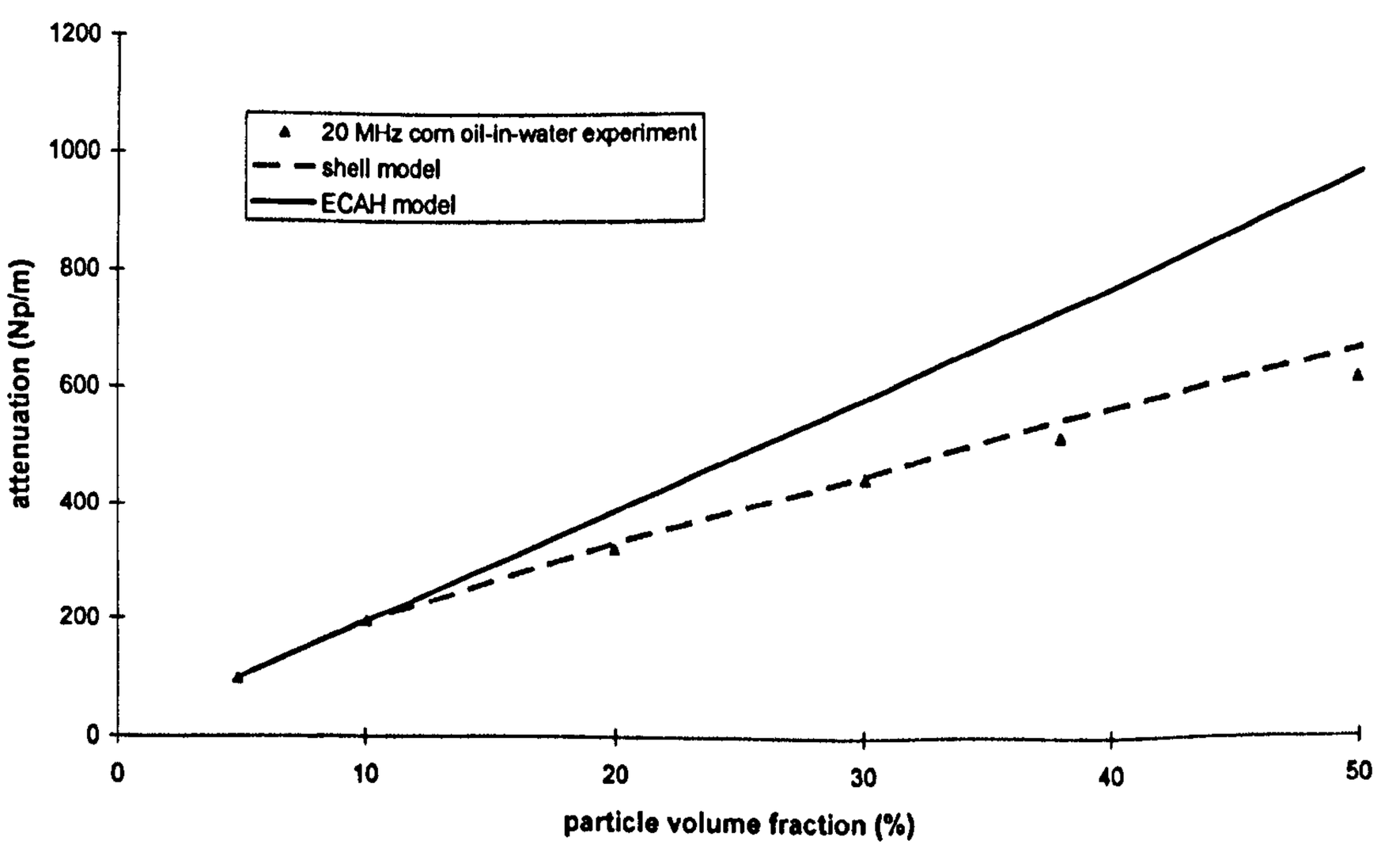

Figure 4.15b. Attenuation as a function of particle volume fraction for corn oil in water with mean particle radius 0.1 μm at 20 MHz. The curves in these figures are Hipp's shell model (dash line), the ECAH model (solid line) and the experimental data (dots).

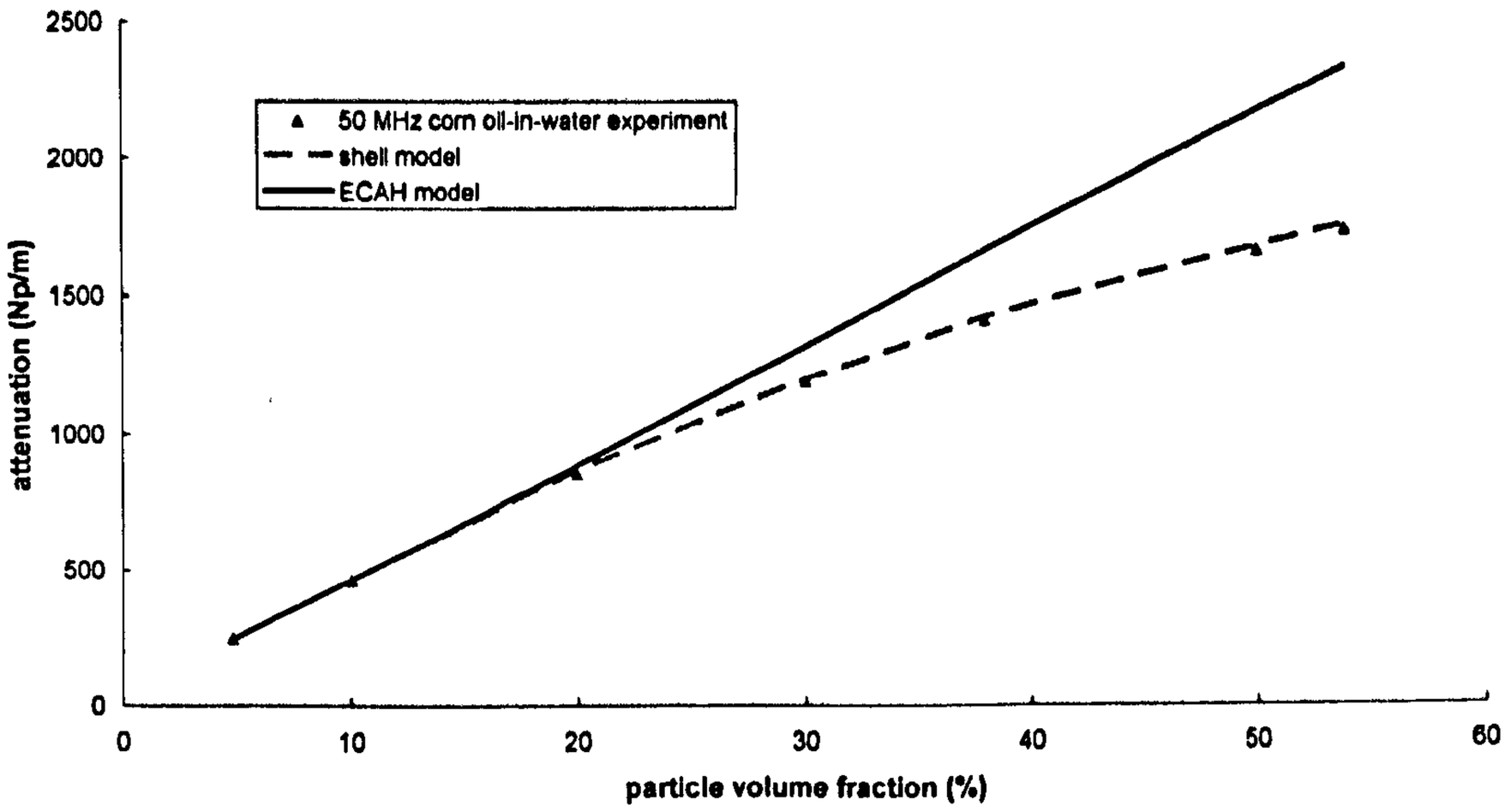

Figure 4.15c. Attenuation as a function of particle volume fraction for corn oil in water with mean particle radius 0.1 μm at 50 MHz. The curves in these figures are Hipp's shell model (dash line), the ECAH model (solid line) and the experimental data (dots).

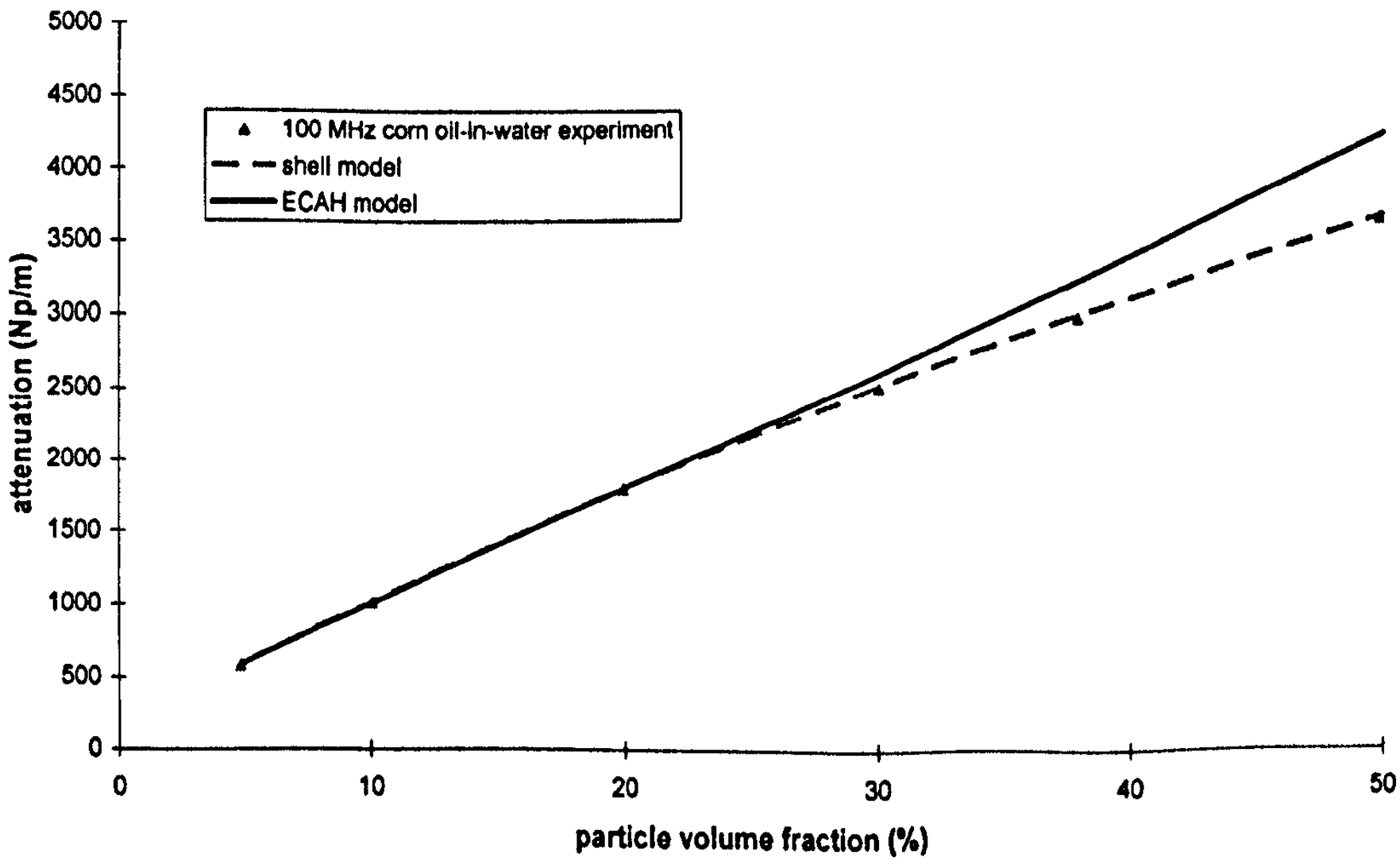

Figure 4.15d. Attenuation as a function of particle volume fraction for corn oil in water with mean particle radius 0.1 μm at 100 MHz. The curves in these figures are Hipp's shell model (dash line), the ECAH model (solid line) and the experimental data (dots).

The following figures examine whether the Anson and Chivers shell model is equivalent to the Hipp shell model for a comparable system. Simulations were done for both solid-in-water suspensions and liquid-in-water emulsions at relatively high particle concentrations. For both systems, we assumed that particles are suspended in a shell of water, and outside this shell, there is a continuous phase whose physical properties are determined by the volume average of the properties of the suspended particles and water, which is exactly the same as the assumption that Hipp made in his shell model. As to the Anson and Chivers shell model, these are a few changes: the shell changes to a liquid one, and the continuous phase becomes the volume average of both the particles and shell. The particle radius for silica is 0.2 μm, and for corn oil is 0.1 μm. From figures 4.16 and 4.17 we can see that Hipp's shell model gives the same prediction as that of Anson and Chivers shell model for both emulsions and suspension at high volume fractions.

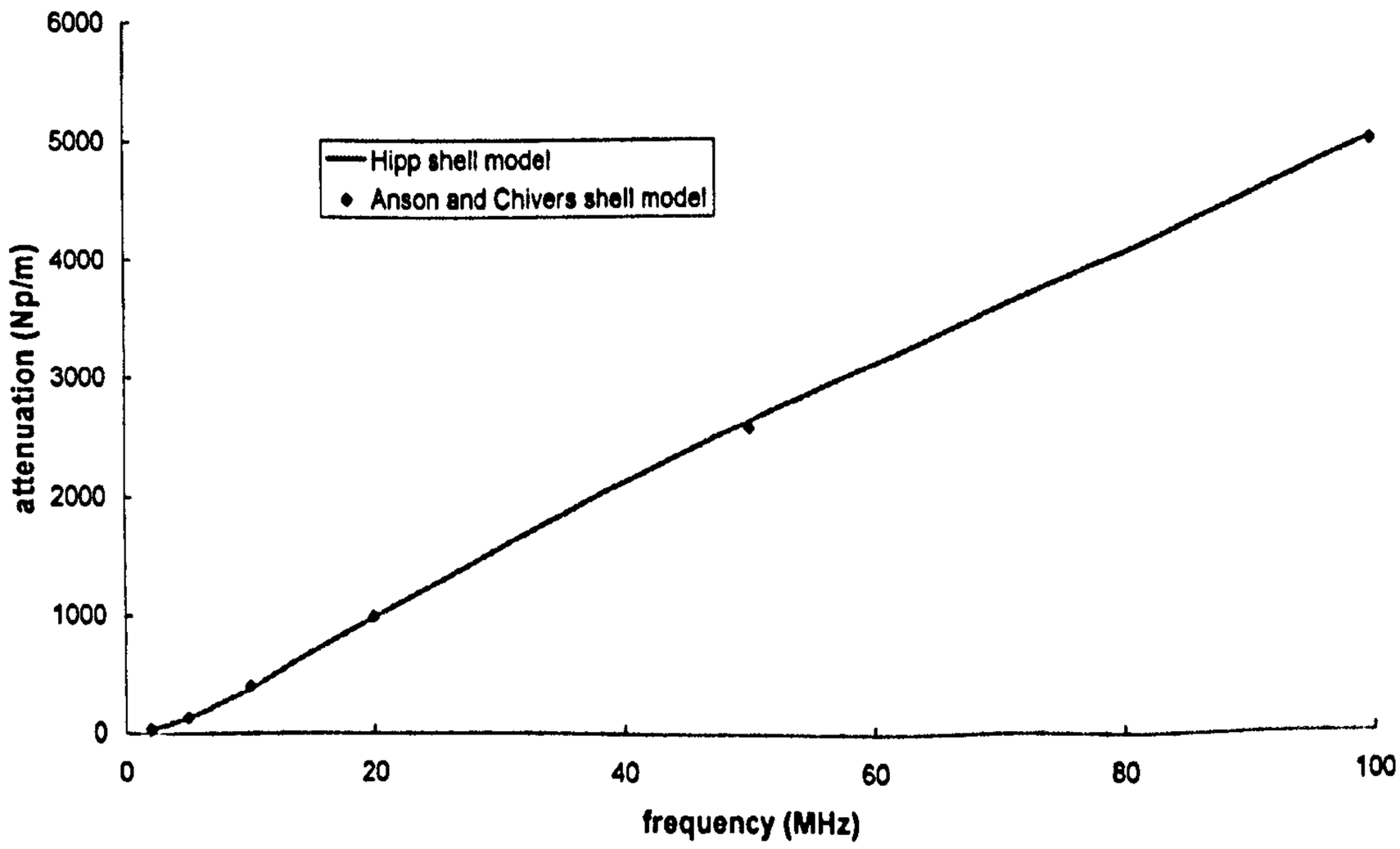

Figure 4.16. Simulations using Hipp shell model (solid line) and the Anson and Chivers shell model (dots) for silica-in-water suspensions with a volume fraction of 25%, the particle radius is 0.2 μm, and the shell thickness is 0.3μm.

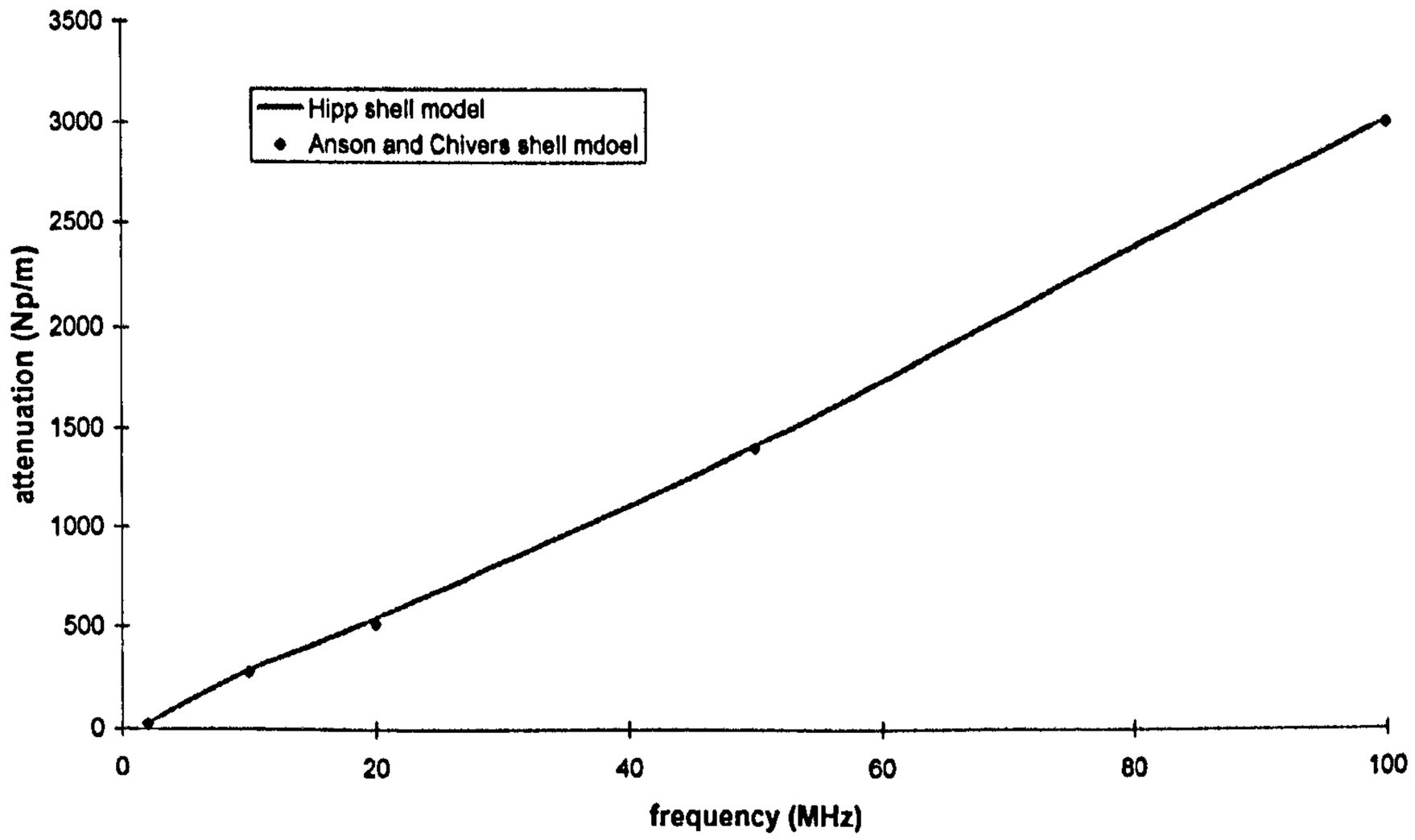

Figure 4.17. Simulations using Hipp shell model (solid line) and the Anson and Chivers shell model (dots) for corn oil-in-water emulsions, volume fraction is 38%, the particle radius is 0.1 μm, and the shell thickness is 0.14 μm.

4.4. Conclusion

A comprehensive shell model was presented in this chapter, which was first developed by Anson and Chivers, and several years later, Hipp propose a very similar formulation based on Anson and Chivers' boundary conditions to simulate the scattering in concentrated systems. This shell model can be used not only for concentrated emulsions but also for the concentrated suspensions due to the inclusion of viscous interactive effects.

We developed our own program based on the Anson and Chivers shell theory, and this works well when comparing with the backscattering results with those of Anson and Chivers. A number of implementations were carried out in order to examine the influence of core materials, shell materials and the shell thickness, and much useful information was obtained. Moreover, we

combined the simulations using our program with experiment for encapsulated emulsions, and showed that the shell model converges to the ECAH model when the shell thickness tends to zero.

We also included the Hipp shell model in this chapter, and this was possible because Hipp's idea was the application of the Anson and Chivers shell model in the calculation of acoustic attenuation and phase velocity in concentrated mixture. Hipp used Anson and Chivers shell model and extended it so that it can be widely used without any wavelength limit. We did some experiments to test Hipp's results and we also compared Hipp's shell model with the Anson and Chivers shell model, and found that they can exactly get the same results when given the same inputs.

In the next chapter the experimental systems used in this work are discussed. These will be used in chapter 6 to examine the performance of all of the theories discussed in chapters 2 to 4 with a view to determining (once and for all) when they are applicable and where they break down.

Chapter 5 Experiment and Methods

5.1 Introduction

This chapter provides a description of the wideband ultrasonic spectrometer used to investigate suspension and emulsion systems. The spectrometer is intended to characterise suspensions and emulsions in terms of attenuation and phase velocity as functions of frequency. The principal measured propagation variable is usually the ultrasonic wave attenuation coefficient as a function of frequency, sometimes known as the *attenuation spectrum.* In more sophisticated experiments the phase velocity dispersion is measured as a function of frequency (the *phase velocity spectrum*), although this requires carefully designed signal processing procedures for its extraction from raw data. All of these measures are linked through the Kramers-Kronig relationships (O'Donnell, 1981), although formal use of this theory is not straightforward. In most real practical situations the attenuation spectrum is the function generally used to elucidate material properties and the physical phenomena that underlie them.

In the following sections brief descriptions are provided for the experimental set-up for attenuation and phase velocity measurement. The functional elements include: the relatively high amplitude pulser which excites the transmitter transducer plus its timing and trigger arrangement, the transducers and the test cell onto which they are mounted and the digitisation and data capture techniques. An example experiment is presented to illustrate how the attenuation and phase velocity are obtained. At the end of the chapter,

we introduce electronic noise and discuss the problem of the experimental errors in the context of earlier work by Kalashnikov and Challis (2005).

5.2 Review of Previous Methods

Methods to measure ultrasonic properties (the attenuation and phase velocity) in liquids generally cover the frequency range between 20kHz to over 100 MHz, with most work being performed between 500kHz and 20 MHz, depending on the strength of the absorption being measured and its dependence on frequency. The methods are subdivided into two groups, namely resonator methods and pitch-catch propagation methods. The former method is mostly used in the lower part of the frequency range (<1 MHz), for which the ultrasonic attenuation is normally small (Schultz and Kaatze, 1998, Eggers and Kaatze, 1996). In resonator cells the effective path for the interaction of the ultrasonic wave with the test medium is substantially lengthened by multiple reflections. Resonator techniques require careful calibration to establish the inherent losses associated with the test cell, and, unfortunately, these in turn require calibration liquids of known-properties which are close to the properties of the liquid to be measured. It is not surprising that appropriate calibration liquids are frequently just not available. Calibration requires the attenuation coefficient of the reference to be precisely known, together with previous knowledge of the sound velocity and density of the reference liquid. In addition to these strict demands on the choice of the reference liquid there are also rigorous requirements on the mechanical stability of the cell, which should maintain its delicate adjustment during the

emptying, cleaning and refilling procedures when the sample is exchanged for the reference.

In pitch-catch methods the signals used can be short wide bandwidth pulses, gated sinewave bursts, tone-bursts or random codes (McClements, 1996, Chanamai et al, 1998). The signal processing required to extract attenuation can be based on simple deconvolution schemes or correlation concepts. At higher frequencies, these propagation methods are appropriate because the attenuation to be measured is likely to be high and the amplitude of the acoustic signal will be considerably reduced as it passes through the test medium. This implies that just one pass through the test medium will be sufficient to obtain a signal loss that is large enough to be quantified with usable precision. We shall see later that the optimum value for the total measured signal loss is 1 Neper. These methods have been applied widely with much success in the past and are still generally accepted today (Kao et al, 1990, Hsu and Hughes, 1992).

The pitch-catch technique involves fixed path or variable path length test cells designed for the absolute determination of the attenuation spectrum. A fixed system has the advantage of stable geometry which is required to maintain the faces of the transducers in parallel alignment, preventing the lowpass filtering effects which occur when waves strike a receiving transducer obliquely (Challis, 1982); it is also relatively cheap and can be applied to process plant pipe-work. It suffers the disadvantage that the wave propagation distance in the test medium cannot be adjusted to optimise the signal to noise conditions for the measurement. Variable geometry systems permit such optimisation and as a result they enable measurements on any given sample

over much wider bandwidths than possible with fixed systems. A commercial device with variable geometry, the *Ultrasizer* (Malvern Instruments Ltd., Malvern, Worcester, U.K.), measures over bandwidths between 1 MHz and more than 100 MHz; however, the measurements require considerable time and the apparatus is very expensive; it has now been removed from the market.

A second variation on the basic arrangement for the pitch-catch method is to combine the transmitting and receiving transducers into a single device which then acts as both transmitter and receiver; the transmitted wave passes through the test medium and is reflected back to the receiver by a solid (typically steel, glass, or quartz) reflector, the so-called pulse-echo method. In this case the propagation distance is doubled but all of the other arrangements remain the same.

A third variation concerns the manner in which the transducers are operated. High frequency transducers are both fragile and expensive and may not be affordable in some circumstances, particularly taking account of their fragility and the possibility that they may have to be replaced if damaged. It is possible to operate cheap low frequency devices in a transient thickness mode in which the exciting pulse is much shorter than the resonant period. This results in a very short transient with a bandwidth approaching 70 MHz being obtainable from a device with a fundamental resonant frequency which is below 1 MHz. Thus very high operating bandwidths can be obtained at low cost. A full discussion of this method is beyond the remit of the present work, and the reader is referred to Challis et al(1982 and 1991).

5.3 Measurement techniques employed in this work

5.3.1 Operating principles

Figure 5.1 shows diagram of the system used for measurement in this project. The blocks shown are the high voltage (HV) pulse generator (DUI, NDT Solutions Ltd, Chesterfield, UK), the commercial transmission and receiving transducers (V309, V311, V354, Panametrics Inc, Massachusetts, USA), Perspex test cell (based on an earlier design developed in the AU laboratory), the digital storage oscilloscope (DSO, LeCroy 9314, LeCroy Inc, NewYork, USA) and the personal computer. The signal pathway for the system starts from the HV pulse generator to the test cell, the wideband amplifier and the DSO, in that order, via 50 Ω coaxial cables. Where possible the input resistance of each item along the signal path is matched to 50 Ω to prevent reflections at the cable ends. The acoustic part of the signal pathway consists of the transmission and receiving transducers as well as the intervening test medium. The pulse generator excites the transmission transducer into a highly damped half-wave acoustic resonance which causes the radiating face of the device to emit ultrasound into the test medium, generally via a buffer layer to protect the transducer from chemical attack or the ingress of water. The acoustical signal then propagates across the test medium as a field that is generally assumed to be a workable approximation to a plane wave, although in reality it is not exactly so. This signal ultimately arrives at the receiving transducer (similar to the transmission transducer), which filters it according to its resonant characteristics and converts it into an equivalent electrical signal, which is amplified by the broadband amplifier and

digitised by the DSO. The acoustic signal in the test cell reflects back to the transmitter and then again back to the receiver, and so on, producing a series of reverberation components which are also digitised. These are of little use as a means to estimate attenuation of the reverberation waves because they become successively more distorted by diffraction effects as the reverberations proceed; they eventually die away due to attenuation in the test medium and radiation damping, the decay rate being faster at higher attenuation. However, the existence of these reverberations prevents rapid repetition of the measurement process — each measurement must be delayed until there are no observable reverberations from the previous one and this sets a limit to the minimum time between successive measurements, which is between 1 ms and 100 ms, although 10 ms is typical. An important outcome of this is that if coherent averaging is used to improve the signal to noise ratio (SNR) it could take several seconds to complete a measurement. In studies of non-stationary chemical systems, such long time intervals may not be available due to rapid chemical change or to flow.

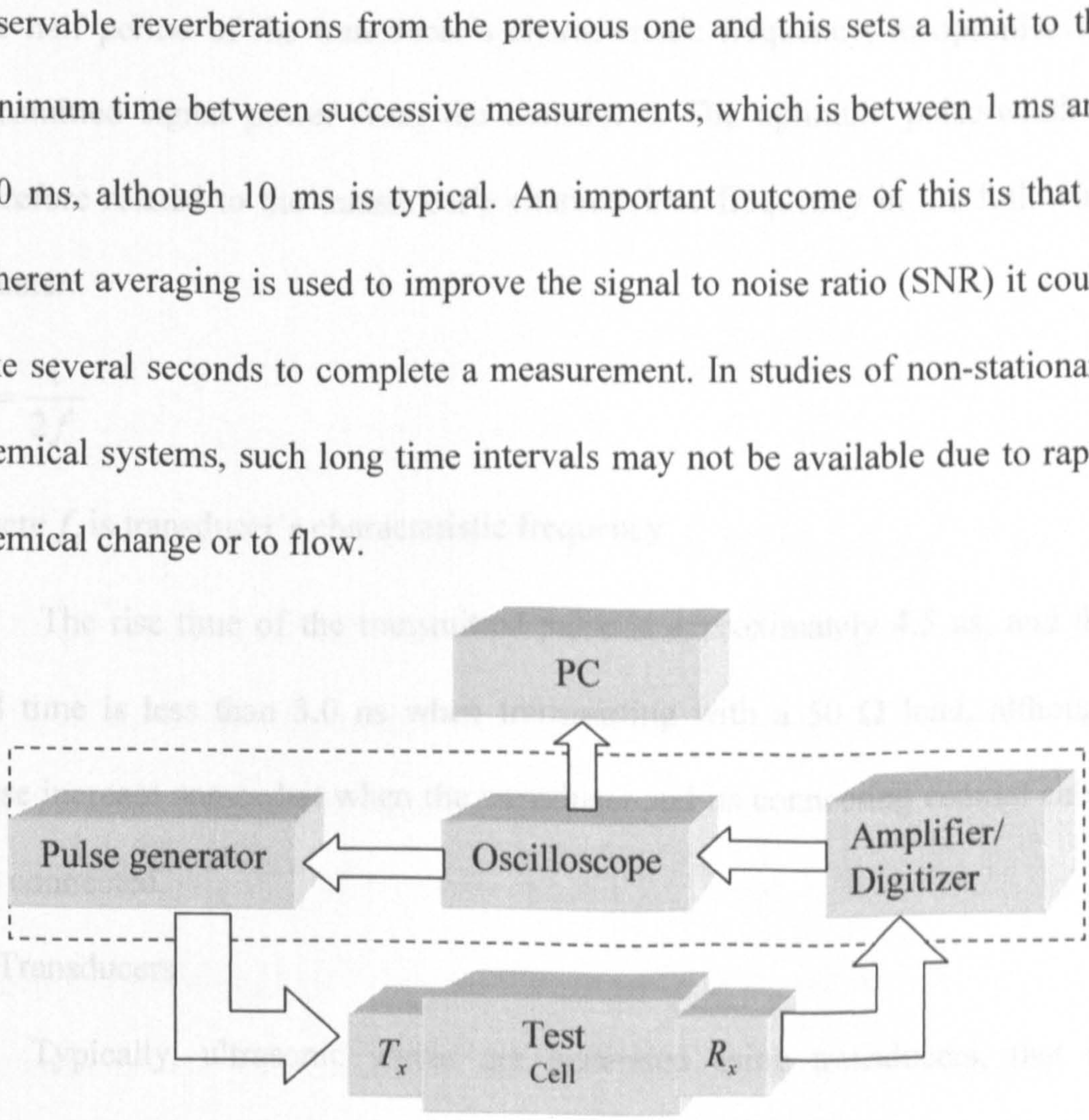

Figure 5.1. Schematic of experiment arrangement.

1) The high voltage pulse generator

The pulse generator and receiver amplifier were based on earlier designs developed in the Applied Ultrasonics Laboratory and which are now marketed by the spin-off company NDT Solutions Ltd (Chesterfield, UK). The receiver bandwidth (at 3 dB) of this device is 100Hz to 70 MHz, and the gain ranges from –20 dB to 60 dB in 0.5 dB step increments.

It excites a unipolar or bipolar pulse of amplitude between 10 V and 300 V and a duration that is short enough to provide adequate bandwidth, typically in the range of 5 ns to 1 μs. The width of the voltage pulse is normally tuned to one half period of the transducer's characteristic frequency, to optimise the transmitted signal power from the transducer. The optimum pulse-width is therefore related to the transducer's characteristic frequency in the following manner:

$$T = \frac{1}{2f_c}$$

where f_c is transducer's characteristic frequency

The rise time of the transmitted pulse is approximately 4.5 ns, and the fall time is less than 3.0 ns when transmitting with a 50 Ω load, although these increase somewhat when the transducer and its connecting coaxial cable are connected.

2) Transducers

Typically, ultrasonic waves are generated using transducers, that is, devices that convert one form of energy into another. An ultrasonic transducer generates ultrasonic waves (normally compression) by converting an electrical signal into a corresponding stress or displacement (Hocking, 1995), which can

then be propagated into a material under evaluation. It is also capable of doing the inverse, that is, convert mechanical stress or displacement into an equivalent electrical signal, which can then be recorded and processed.

The basic structure of the transducer is shown in figure 5.2. It consists of three layers, i.e. the piezoelectric element (i.e. active element), a lossy backing layer, and a radiating face element. The piezoelectric element is responsible for the transduction process of converting mechanical energy into acoustic and vice versa. The element has silvered electrodes wired to coaxial-style connectors for connection with transmitter and receiver electrodes. The thickness of the piezoelectric element is half-wavelength, at its centre resonant frequency. The backing layer is usually made from highly attenuating material with a high density. The layer controls the reverberation response of the transducer by absorbing energy radiating from the back face of the piezoelectric element. When the backing and piezoelectric layers are acoustically matched, the resultant transducer will have a heavily damped response and lower amplitudes, but with a usefully wide bandwidth. If the two layers are mismatched, more acoustic energy will be propagated into the test medium, and such a transducer will have a longer response time and higher sensitivity over a narrower range of frequencies.

The radiating face varies in its construction, and may be a thin layer of polymer material or a thicker buffer of a harder material such as glass. For applications where the transducer has direct contact with the test medium, the radiating face serves as a protective element for the piezoelectric layer; it must be durable and corrosion-proof in order to withstand friction and wear. In many applications the radiation face serves to match or at least partially match

the high acoustic impedance of the piezoelectic element to the lower impedances of the acoustic load.

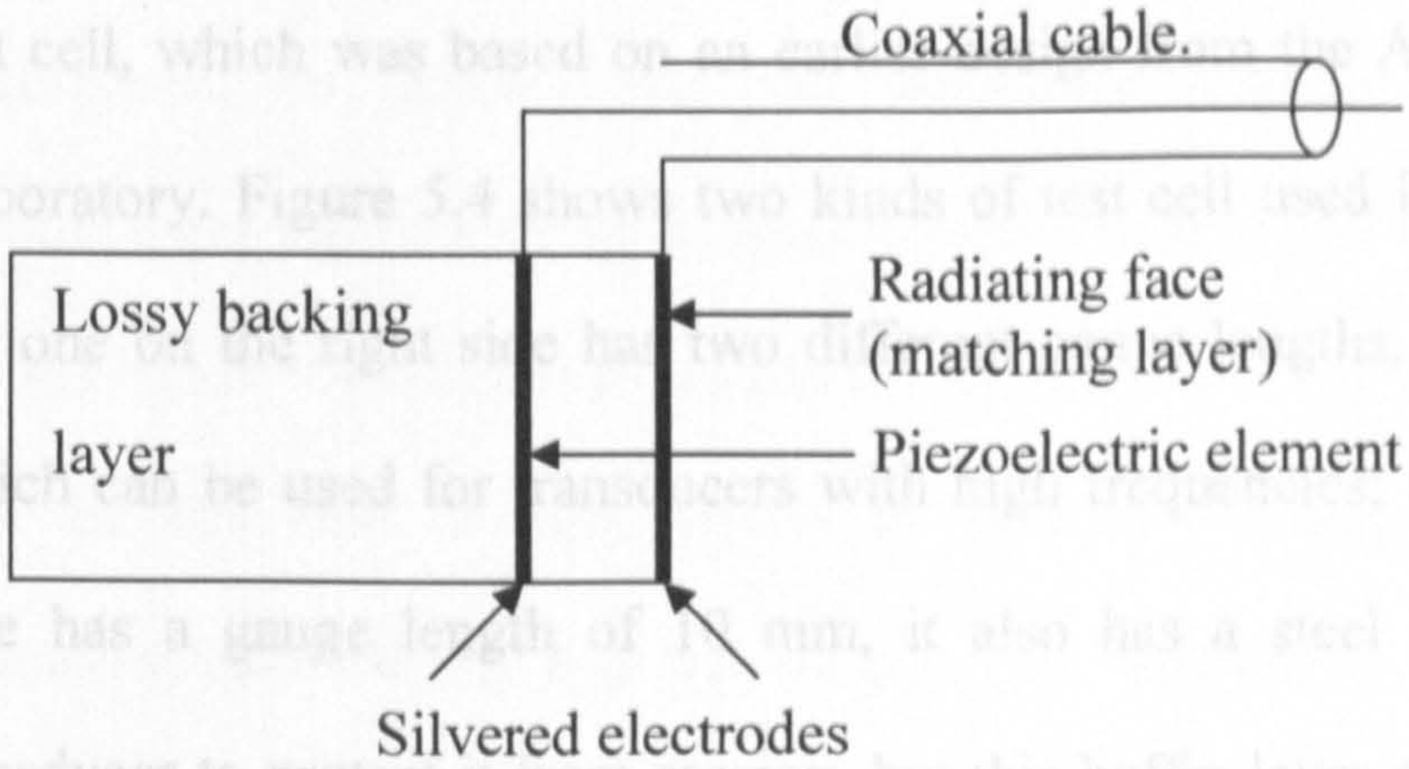

Figure 5.2. Basic structure of the transducer.

The transducers used were the Panametrics-NDT™ V309, V311, V354 and V356 immersion-type transducers with centre frequencies of 5 MHz, 10 MHz 20 MHz and 30 MHz respectively (Appendix 5.1). These transducers are single element longitudinal wave devices with a quarter wavelength layer acoustically matched to water (figure 5.3); they are all of 0.5 inch diameter and a length of 33 mm.

Figure 5.3. Immersion transducers used in the experiments.

3) Test cell

Experimental calibration measurements were carried out in pitch-catch mode, with the transducers co-axially aligned in a circular Perspex (PMMA) test cell, which was based on an earlier design from the Applied Ultrasonics Laboratory. Figure 5.4 shows two kinds of test cell used in the experiments, the one on the right side has two different gauge lengths, 4 mm and 8 mm, which can be used for transducers with high frequencies; the one on the left side has a gauge length of 10 mm, it also has a steel buffer outside the transducer to protect it from erosion, but this buffer layer adds an extra delay time into the system. The transducers are aligned coaxially with their faces parallel, one set on each side of a diametral line across the cell. The outer faces of the transducer are immersed in the test medium. Transducer response exhibits zeros at DC and even multiples of the centre frequency, as shown in figure 5.5. The 3dB operating bandwidth varies from device to device but typically extends from $0.3f_0$ to $1.6f_0$, a frequency bandwidth of $1.3f_0$.

Test cells with different gauge lengths are used to get an optimised signal to noise ratio for transducers with different central frequencies. That means the measurements at high frequency are best done with the transmitting and receiving transducers close together (small gauge length d) to compensate for high values of the attenuation coefficient and to bring the signal level above the system noise; measurements at low frequency are best done with the transducers farther apart in order to increase the total measured attenuation towards the optimum value of 1 Neper (Challis et al, 2005).

Figure 5.6 shows the modulus frequency responses for water at room temperature for propagation distances of 4 mm, 8 mm, 10 mm and 26 mm,

calculated using the equation: $|H_{REF}(\omega)| = \exp[-\alpha(\omega) \cdot d]$ (which means the modulus of the spectra is a function of the products of attenuation and transmission distance). A frequency range up to 320 MHz was used for the calculations, to ensure that all significant spectral components are encompassed and to prevent aliasing effects which would occur when a more limited frequency range is evaluated for the frequency response. It can be seen that the low-pass filtering effects in frequency responses increase with increasing path-lengths; this has the effect of widening the impulse response duration and dispersion in the time-domain.

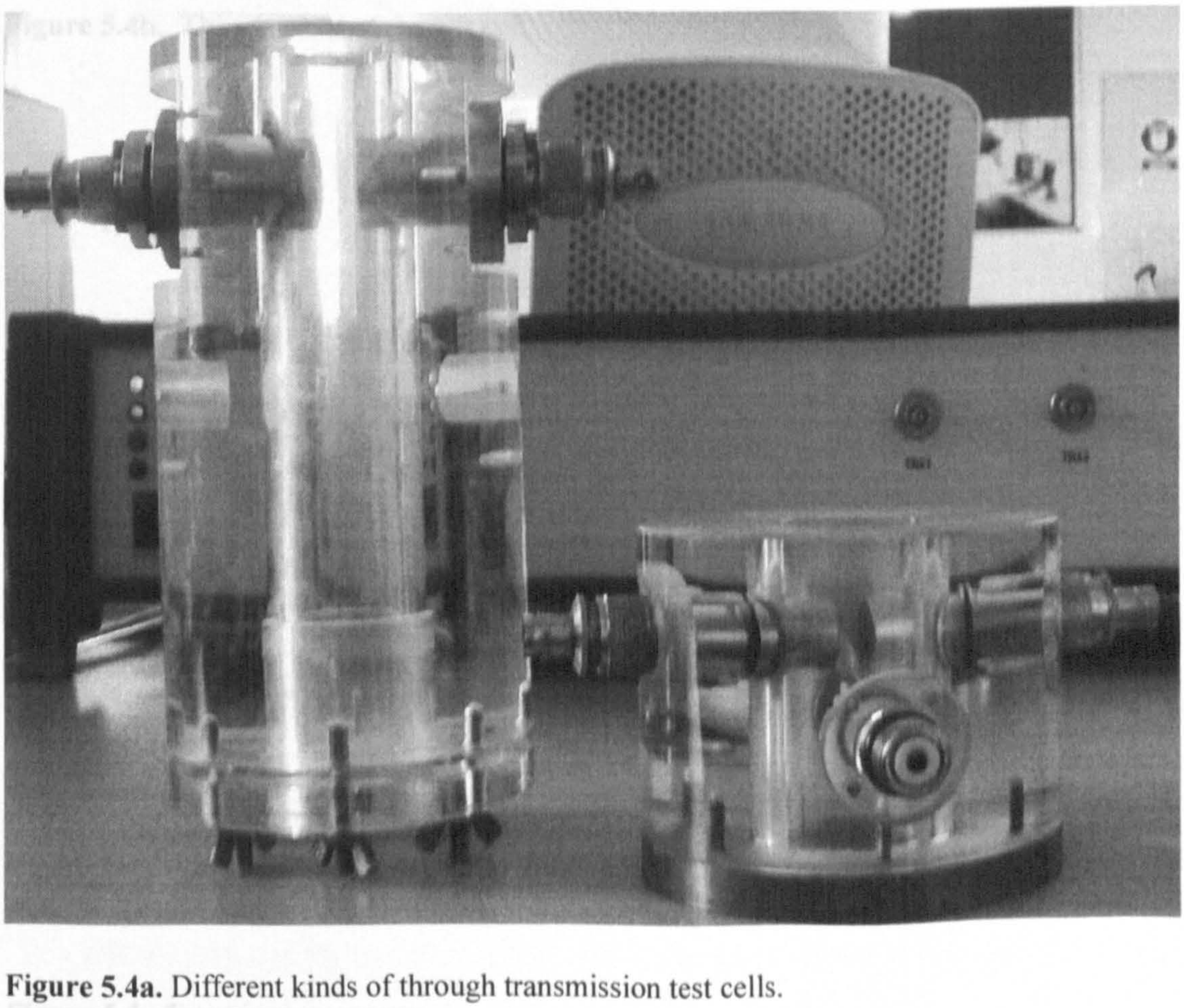

Figure 5.4a. Different kinds of through transmission test cells.

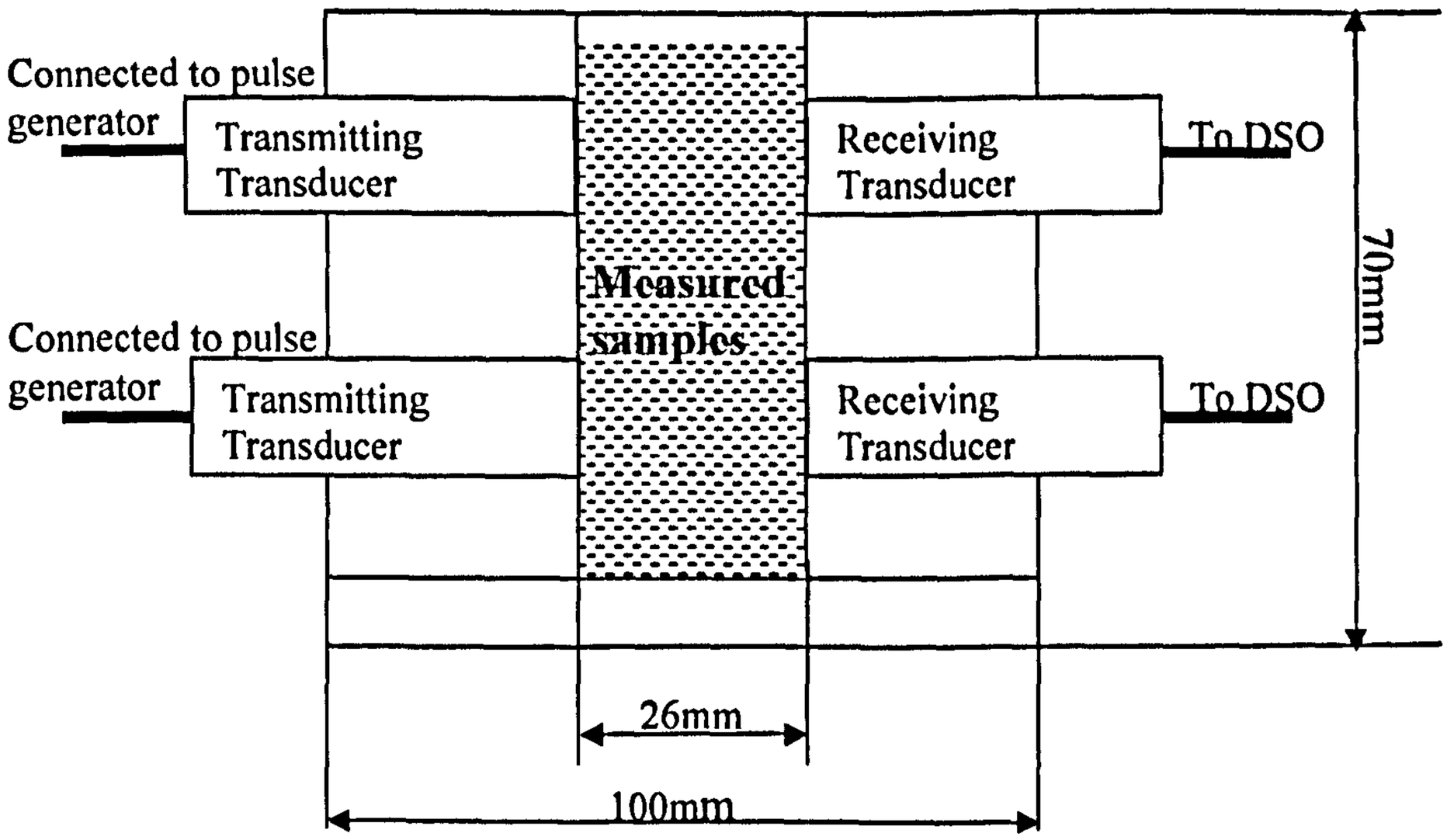

Figure 5.4b. The structure of the test cell.

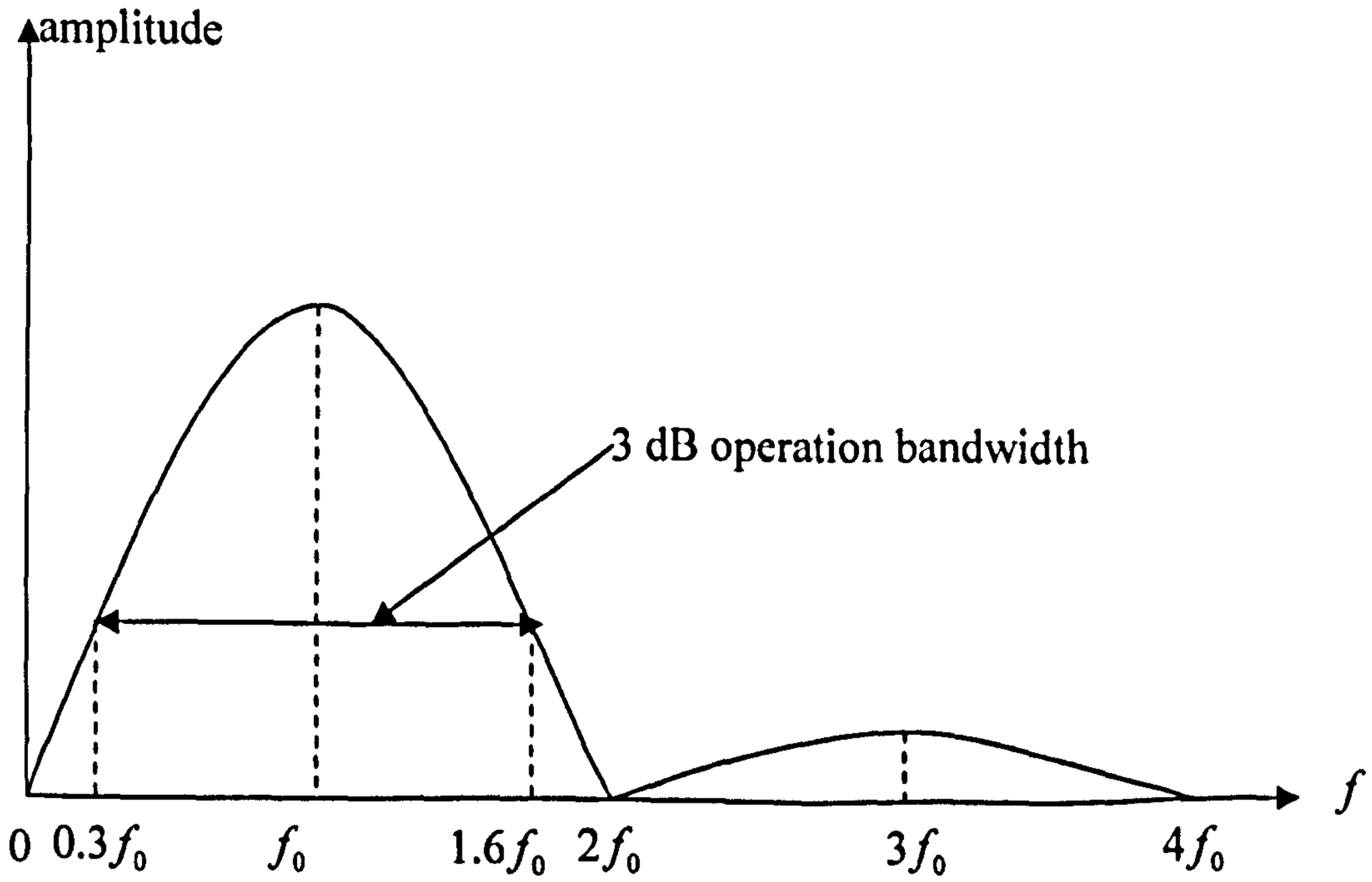

Figure 5.5. Transducer response.

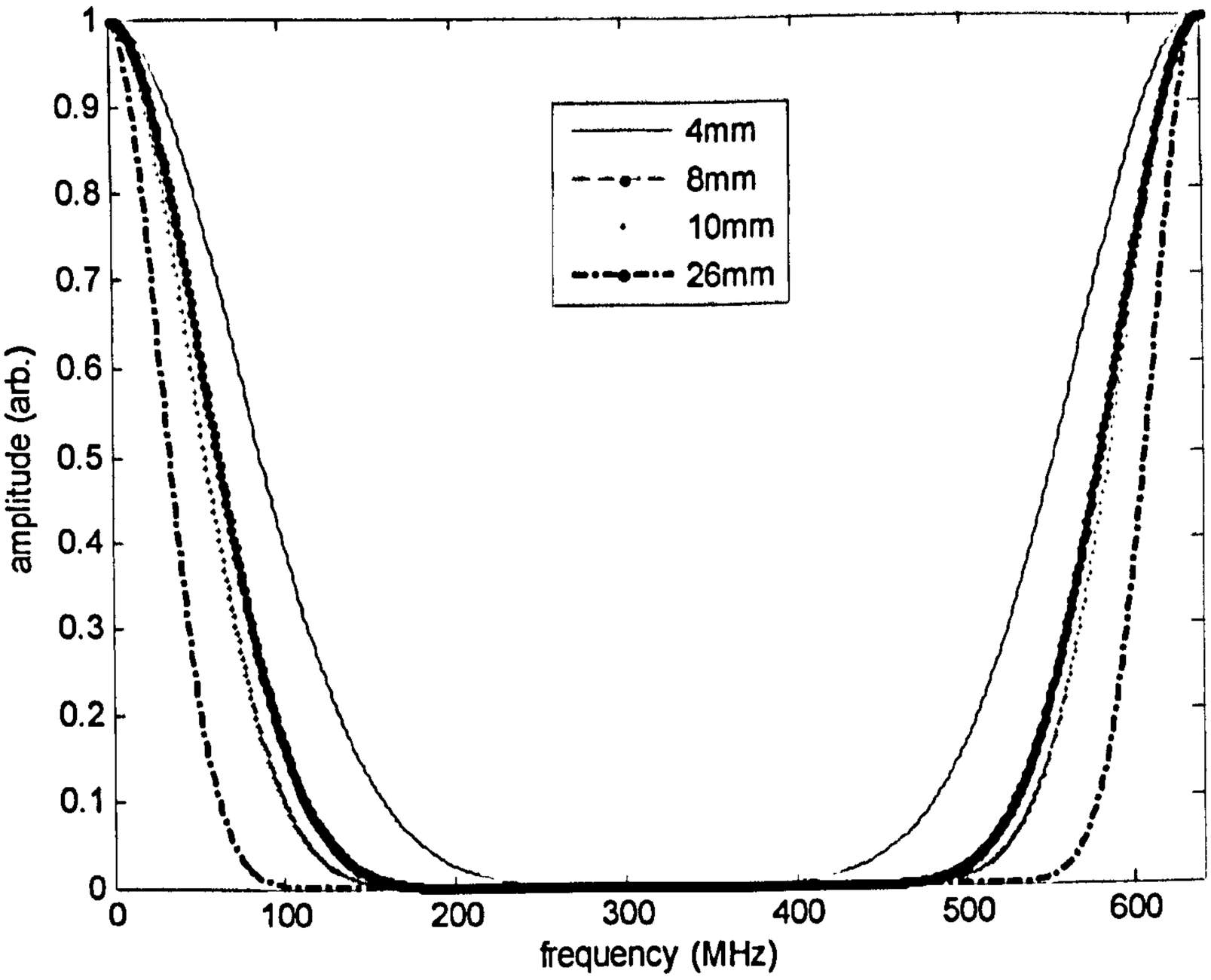

Figure 5.6. Modulus frequency responses of distilled water, for path-lengths of 4 mm, 8 mm, 10 mm and 26 mm.

4) The digital storage oscilloscope

The signal obtained at the output of the amplifier is monitored and digitised by a digital storage oscilloscope (DSO, LeCroy 9314) running at a sampling frequency of 320 MHz. The data recorded by the DSO is transmitted via a GPIB interface (IEEE 488) to a personal computer for further processing.

5.3.2 Computation of attenuation and phase velocity

Ultrasonic spectrometers usually characterise the test medium in terms of its attenuation and phase velocity as functions of frequency. The calculation of the attenuation coefficient takes into account the whole signal pathway through the system. This includes the transmitter excitation waveform, the responses of the two transducers and their buffer layers, the response of the test medium (required) and the response of the electronics. In the context of

spectrometering, ultrasonic compression wave propagation through an acoustic pathway may be regarded as a series of convolutions in the time domain and these convolutions are equivalent to the following multiplications in the frequency domain:

$$Y(\omega) = X(\omega) \cdot T(\omega) \cdot C_1(\omega) \cdot H(\omega) \cdot C_2(\omega) \cdot R(\omega) \cdot E(\omega) \qquad \textbf{(5.1)}$$

where ω is radial frequency,

$Y(\omega)$ = received signal;

$X(\omega)$ = electrical excitation signal;

$T(\omega)$ = frequency response of transmitting transducer;

$C_1(\omega)$ = coupling between transmitting transducer front face and test medium;

$H(\omega)$ = frequency response of test medium;

$C_2(\omega)$ = coupling between receiving transducer front face and test medium;

$R(\omega)$ = frequency response of receiving transducer;

$E(\omega)$ = frequency response of instrument electronics.

It is necessary to calibrate for the responses of the transducers and this is not straightforward. The normal procedure is to record the attenuation in a reference medium whose attenuation and other properties are well known, distilled degassed water being a common choice. A test on distilled water yields:

$$Y_{REF}(\omega) = X(\omega) \cdot T(\omega) \cdot C_{REF1}(\omega) \cdot H_{REF}(\omega) \cdot C_{REF2}(\omega) \cdot R(\omega) \cdot E(\omega) \qquad \textbf{(5.2)}$$

where $H_{REF}(\omega)$ = frequency response of water test medium;

$C_{REF1}(\omega)$ = coupling between transmitting transducer front face and water test medium;

$C_{REF2}(\omega)$ = coupling between transmitting transducer front face and water test medium.

All other responses in the water reference measurement, i.e. the excitation signal, transducer responses and the impulse response of the instrument electronics, are assumed to be identical to those in the test medium measurement. The water reference data is used to remove the responses of the excitation signal, transducers and instrument electronics, by means of frequency-domain division:

$$\frac{Y(\omega)}{Y_{REF}(\omega)} = \frac{X(\omega)\cdot T(\omega)\cdot C_1(\omega)\cdot H(\omega)\cdot C_2(\omega)\cdot Rx(\omega)\cdot E(\omega)}{X(\omega)\cdot T(\omega)\cdot C_{REF1}(\omega)\cdot H_{REF}(\omega)\cdot C_{REF2}(\omega)\cdot R(\omega)\cdot E(\omega)} \tag{5.3}$$

Cancelling the common terms and rearranging gives:

$$H(\omega) = \frac{Y(\omega)\cdot C_{REF1}(\omega)\cdot H_{REF}(\omega)\cdot C_{REF2}(\omega)}{Y_{REF}(\omega)\cdot C_1(\omega)\cdot C_2(\omega)} \tag{5.4}$$

The coupling terms C_n are calculated from the relevant transmission coefficients and the density and sound speed in the test medium, both of which are measured relatively simply, see below.

The ultrasonic wave attenuation in a medium can be calculated from the moduli of the complex frequency-domain data. Since the acoustic plane wave response of a test medium is expressed as:

$$H(\omega) = e^{-\alpha(\omega)\cdot d} e^{-j\frac{\omega x d}{c(\omega)}} \tag{5.5}$$

where α is the attenuation coefficient, ω is the angular frequency and d is the propagation distance. The modulus of the frequency response of the test medium is then:

$$|H(\omega)| = e^{-\alpha(\omega)\cdot d} \tag{5.6}$$

The ultrasonic attenuation can be calculated as:

$$\alpha(\omega) = \frac{1}{d}\log_e\left[\frac{1}{|H(\omega)|}\right] \tag{5.7}$$

Substituting for $H(\omega)$ from equation 5.4:

$$\alpha(\omega) = \frac{1}{d}\log_e\left[\frac{|Y_{REF}(\omega)| \cdot C_1(\omega) \cdot C_2(\omega)}{|Y(\omega)| \cdot H_{REF}(\omega) \cdot C_{REF1}(\omega) \cdot C_{REF2}(\omega)}\right] \tag{5.8}$$

The frequency response of distilled water can be calculated from literature values of α / f^2 at the specific temperature at which the water reference measurement was taken. Water can be considered as a dispersion-free medium that obeys Beer's law (Kalashnikov and Challis, 2005); for a water reference measurement at room temperature ($25°C$) for instance, the attenuation coefficient is

$$\alpha_w(\omega) = 2.5\times10^{-14} \cdot f^2\,(Nepers \cdot m^{-1} \cdot s^{-2}) \tag{5.9}$$

where f is the frequency in Hz.

Given the gauge length d, the frequency response of water is then:

$$|H_{REF}(\omega)| = \exp[-\alpha(\omega) \cdot d] \tag{5.10}$$

The coupling between the medium and transducer front face layers are represented by the transmission coefficients between the two materials, and this can be calculated from knowledge of the acoustic impedances of the test medium and the transducer front layer. The acoustic impedance, Z, of a test material is:

$$Z_{medium} = \rho_{medium} \times c_{medium} \quad \text{(Rayls)} \tag{5.11}$$

$$Z_{transducer} = \rho_{transducer} \times c_{transducer} \text{ (Rayls)} \tag{5.12}$$

for the transducer, where ρ is density ($Kg \cdot m^{-3}$)

and c is low-frequency velocity based on time of flight ($m \cdot s^{-1}$).

The transmission coefficients are then:

$$t_{01} = \frac{2 \cdot Z_{medium}}{Z_{medium} + Z_{transducer}} = C_1(\omega) \tag{5.13}$$

$$t_{10} = \frac{2 \cdot Z_{transducer}}{Z_{medium} + Z_{transducer}} = C_2(\omega) \tag{5.14}$$

The same applies for the water reference medium, and because the properties of water are well documented, the acoustic impedance for water could be calculated from established experimental results. The density and the velocity of distilled water can be expressed as follows (Kaye and Laby, 1995):

$$\rho(T) = \frac{\sum_{i=0}^{5} k_{iP} \cdot T^i}{1 + (A \cdot T)} \tag{5.15}$$

$$c = \sum_{i=0}^{5} k_{iT} \cdot T^i \tag{5.16}$$

where A is a constant $A = 16.887236 \times 10^{-3}$, and T is the water temperature in degrees Celsius. The constants k_{iP} and k_{iT} are given in table 5.1 (Del Grosso and Mader, 1972).

i	k_{iP}	k_{iT}
0	999.83952	$0.140238754 \times 10^{4}$
1	16.952577	$0.503711129 \times 10^{1}$
2	7.9905127×10^{-3}	$-0.580852166 \times 10^{-1}$
3	46.241757×10^{-6}	$0.334198834 \times 10^{-3}$
4	105.84601×10^{-9}	$-0.147800417 \times 10^{-5}$
5	$281.03006 \times 10^{-12}$	$0.314643091 \times 10^{-8}$

Table 5.1. Values of the constant k_{iP} in equation 5.15 and k_{iT} in equation 5.16.

The ultrasonic phase velocity of a test medium can be determined by taking the phase difference between test medium and water reference data, as well as the transmission distance. The phase spectrum is calculated as:

$$\angle Y(\omega) = \frac{\mathrm{Im}[Y(\omega)]}{\mathrm{Re}[Y(\omega)]} \tag{5.17}$$

where $Y(\omega)$ is the frequency-domain data. The phase velocity is then expressed as:

$$c(\omega) = \frac{d}{\left[\frac{\angle Y(\omega) - \angle Y_{REF}(\omega)}{\omega} + \tau_d + \tau_s\right]} \tag{5.18}$$

where $\angle Y(\omega)$ = phase spectrum of test medium data (rad.);

$\angle Y_{REF}(\omega)$ = phase spectrum of water reference data (rad.);

d = propagation distance (m);

τ_d = time from initial electromagnetic breakthrough to the start of recording window;

τ_s = amount of pulse time-shift imposed to minimise phase-wrapping;

ω = angular frequency (rad.).

This basic calculation works well in low noise environments, but in the majority of measurements the desired signal at the output of the digitiser is corrupted by electronic noise. Detection of wanted signals from unwanted noise is one of the most important topics in the theory and practice of ultrasonic measurements. A very simple technique for improving the signal-to-noise ratio (SNR) is coherent averaging. If the received signal has finite duration and repeats itself at particular instants of time, governed by the system clock, and if the background noise remains stationary in a statistical sense and uncorrelated with the signal, we may gain an increase in SNR by

averaging several consecutive notionally identical records of the received ultrasonic signal. In the averaging process the repeats of the desired signal add constructively whilst the noise components average to a progressively small value. This process can be viewed in the time domain by representing the signal at the output of the receiver amplifier $H_{out}(t)$ as:

$$H_{out}(t) = s(t) + n(t) \tag{5.19}$$

where $n(t)$ is the noise component, and $s(t)$ is the signal component. $n(t)$ has a Gaussian distribution with a variance of σ^2, so the amplitude of the noise is equivalent to the standard deviation σ.

If the input signal repeats N times,

$$H_N(t) = \sum_{n=1}^{N} [s_n(t) + n_n(t)] \tag{5.20}$$

From equation 5.20 we can see the signal term will increase by a factor of N, however, the noise component $n(t)$ is random and unrelated to the signal $s(t)$, therefore the noise will not combine coherently as the signal does. The summation of noise terms expressed in equation 5.20 is equivalent to the summation of N samples taken from a Gaussian distribution with a variance of σ^2. The variance of N samples taken from a Gaussian distribution of variance σ^2 is $N\sigma^2$. The amplitude of the averaged noise is equivalent to the standard deviation $\sqrt{N}\sigma$. If the signal to noise ratio of the system without averaging is defined as:

$$SNR = \frac{s(t)}{n(t)} = \frac{s(t)}{\sigma} \tag{5.21}$$

Then the signal to noise ratio after averaging is:

$$SNR_{aver} = \frac{s(t)}{n(t)} = \frac{Ns(t)}{\sqrt{N}\sigma} = \sqrt{N} \times SNR \qquad (5.22)$$

The signal to noise ratio has been increased by a factor of $\sqrt{N}$. If we take 1000 measurements into a coherent average, it will expect to have $\sqrt{1000}$ (=31.62) times better chance of seeing the required signal. In practice, the undesired noise is not always statistically ideal, spectrally white, and formally incoherent between successive signal records, and so the improvement in SNR will generally be slightly less than $\sqrt{N}$. A major disadvantage of coherent averaging is that the SNR is enhanced at the expense of processing time. In most acoustic experiments the acoustic disturbances continue to reverberate to and fro in the apparatus long after the signal of interest has been received, and these reverberations are picked up by the receiver system. It is therefore necessary to wait until these reverberations have died down before the transmitting transducer can be pulsed again. This waiting period slows down the coherent averaging procedure, for example, a typical set-up with 1000 averages will require around 10 seconds to complete, whereas the propagation time of the signal of interest can be as small as 10 μs. For studies on a stationary medium this time is insignificant but for studies in fast reacting or flowing chemical systems the averaging time is too great for meaningful data to be obtained. Therefore, an alternative method is needed, which is in some sense equivalent to averaging, but does not take so much time. There are many ways that this can be achieved and the majority can be categorised as correlation techniques, the details of which are beyond the scope of this work, and the user is referred to a thesis by Phang (2006).

5.3.3 An example of an experiment

5.3.3.1 Materials

Dow Corning 200 silicon oil with a viscosity of 350 centistokes (cSt.) used in this work was purchased from Dow Corning Ltd, U.K. The physical constants of water and the silicon oil are given in table 5.2. This silicon oil is chosen because its ultrasonic wave attenuation is high and it is useful as an analogue for ultrasonic measurements in highly attenuating, low SNR acoustic pathways; it is also chemically stable over time.

	Density ($kg \cdot m^{-3}$)	**Sound velocity ($m \cdot s^{-1}$)**
water	997.0	1497.0
Silicon oil	968.0	1000.0

Table 5.2. Physical constants of water and silicon oil at $25^{o}C$.

5.3.3.2 Ultrasonic measurements

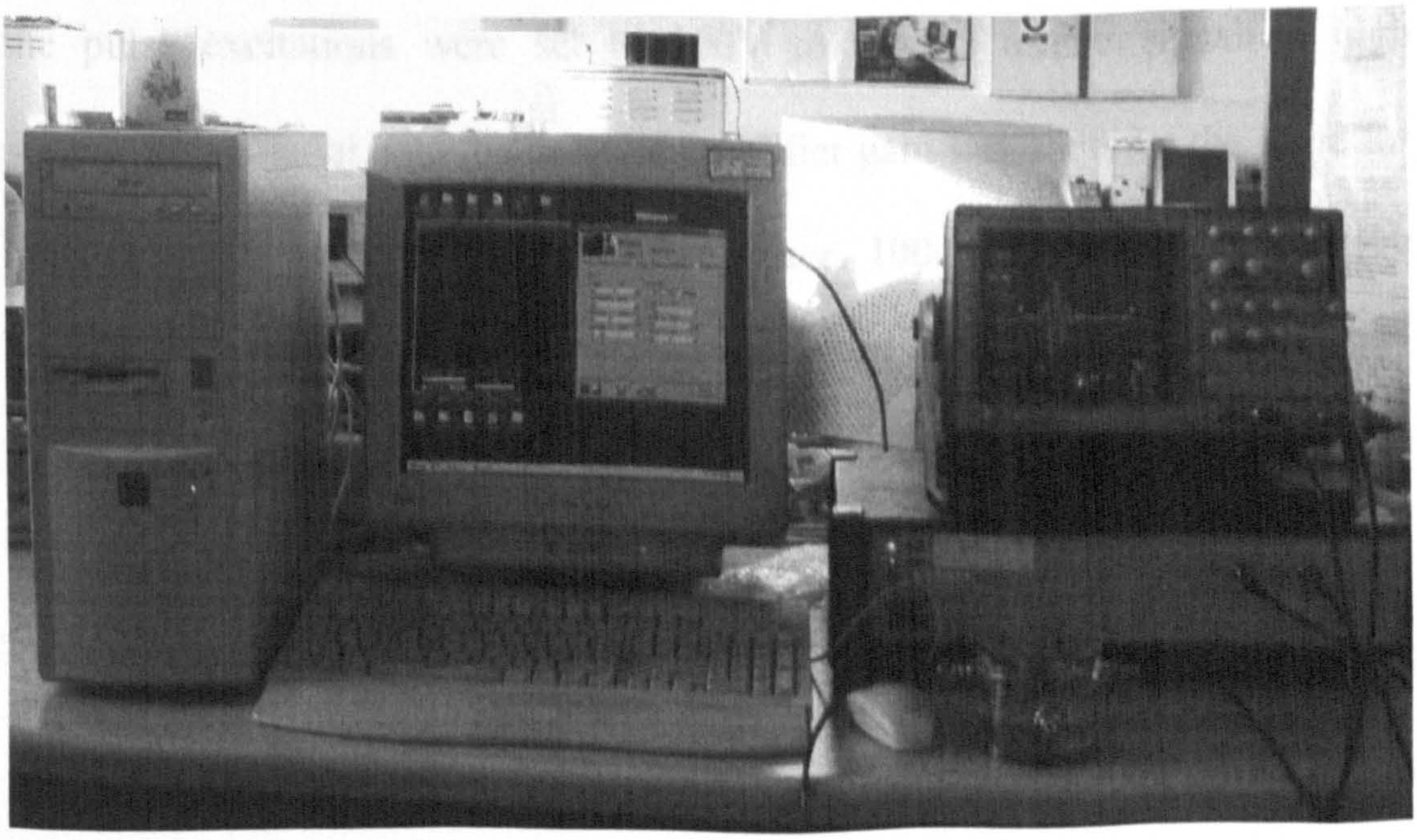

Figure 5.7. Photograph of the whole experimental system.

About 50ml of emulsions was degassed for 3 min using the sonic wave generator to get rid of the bubbles, then was placed in the test cell and allowed to reach thermal equilibrium for 5 min prior to making the measurement ($T = 25.0 \pm 0.3^{o} C$). The emulsions were stirred continuously at a speed of 250 rev min^{-1} during thermal equilibrium and measurement to ensure homogeneity. The emulsion stirring is a necessary step for ultrasonic measurement, without stirring, we are trying to measure the attenuation and phase velocity of a quiescent system.

The ultrasonic attenuation and phase velocity were measured over a range of frequencies using the method discussed above. Figure 5.7 shows a photograph of the practical system used and its functional structure follows the arrangements shown on figure 5.1. The pulse generator was controlled from a Windows environment using the *WinDUI* software, supplied by the manufacture (NDT solutions Ltd, Chesterfield, UK). The system clock repetition frequency was set to 9.9 kHz, given sufficient time to avoid distortion due to acoustic reverberations. For both calibration measurements the pulse excitations were set to 100V to give a usable signal in high attenuation material, and the receiver amplifier gain was set to be the same for both measured material and reference water. 1000 coherent averages were applied in each measurement to improve the SNR, and the received signal was digitised at 320 MHz.

The wide frequency range was achieved by using different transducers with different central frequency, for example, 5 MHz, 10 MHz, 20 MHz and 30 MHz transducers were used in this work. As discussed above, different path lengths were selected appropriate to these transducers.

After digitising, prior to computing FFTs of the time-domain data, the mean of the first 20 samples in each record is calculated and subtracted from the whole signal to remove any DC offsets that remain from the digitising process in order to avoid any spectral leakage from any spurious and unwanted zero-frequency components. The Fourier transform was used to get the frequency response of the sampled signal. Assuming the sampling frequency is f_s, and the length of the FFT is NPTS, which should be a power of 2 points, the time resolution must be $1/f_s$, and frequency resolution becomes $f_s / NPTS$. Since we use 1024 points in the FFT calculation, if the signal data points are less than 1024, we need to zero pad the signal data up to 1024 points for the FFT calculation. The zero padding stage causes the spacing of the frequency coefficients to decrease from 320MHz/640 (the output data length is 640) to 320MHz/1024, which improves the frequency domain resolution a little.

5.3.3.3 Experimental results

Figures 5.8 to 5.15 show the time domain signal and the frequency domain response after FFT for both distilled degassed water and silicon oil using different transducers. The time domain signal in which we are interested is the first disturbance to propagate through the test material, before any subsequent reverberations in the test cell, therefore there is some delay for the time domain signal due to the transducer front face layer and transmission distances between the transducers. As the transducer centre frequency increases, the bandwidth of the transducer amplitude increases as well, typically approximately to 1.5 times the transducer central frequency.

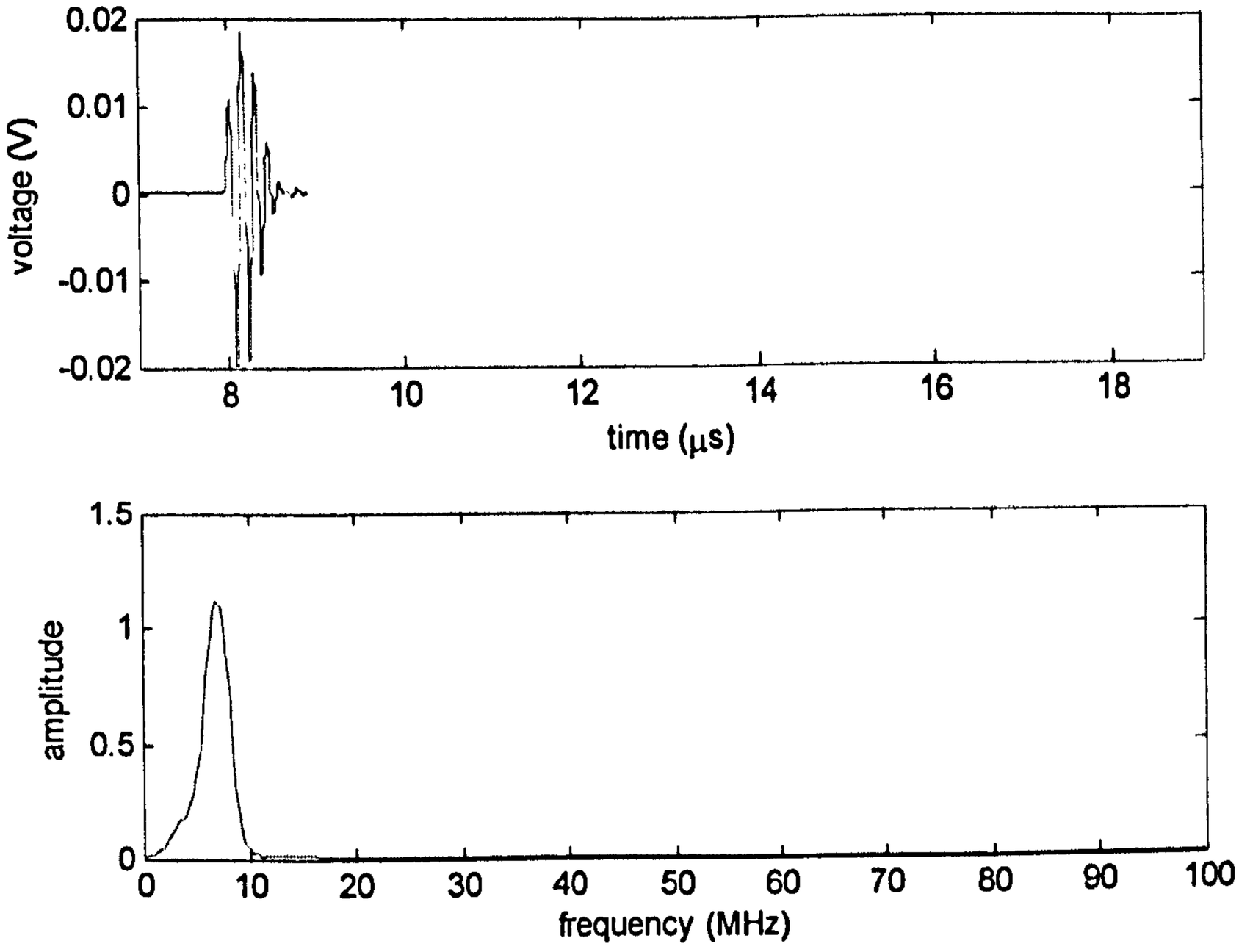

Figure.5.8. Experimental water calibration results using 5MHz transducer using a 10mm test cell with a stainless steel buffer, shown in time (top) and frequency (bottom) domains.

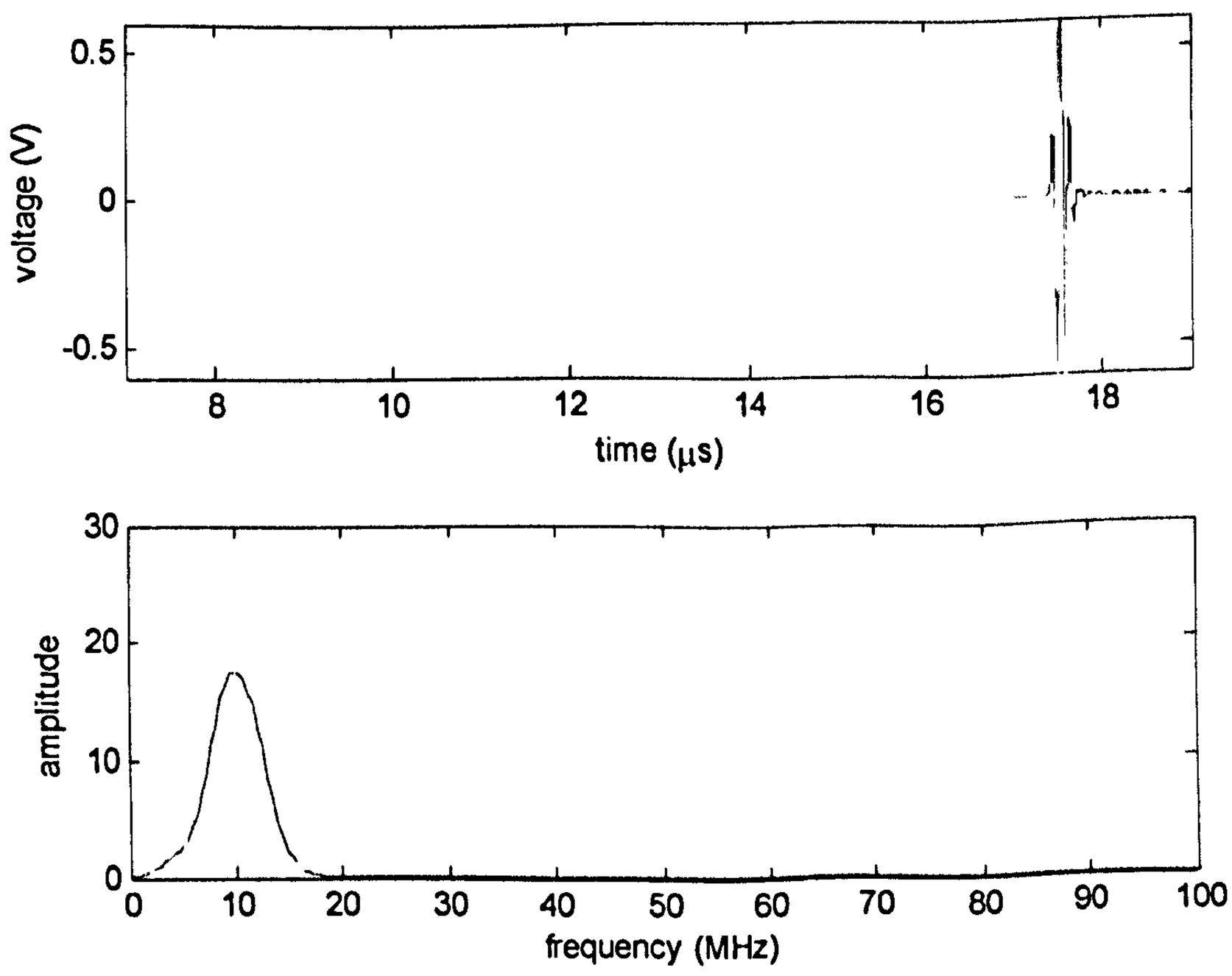

Figure.5.9. Experimental water calibration results using 10MHz transducer using 26mm transmission distance, shown in time (top) and frequency (bottom) domains.

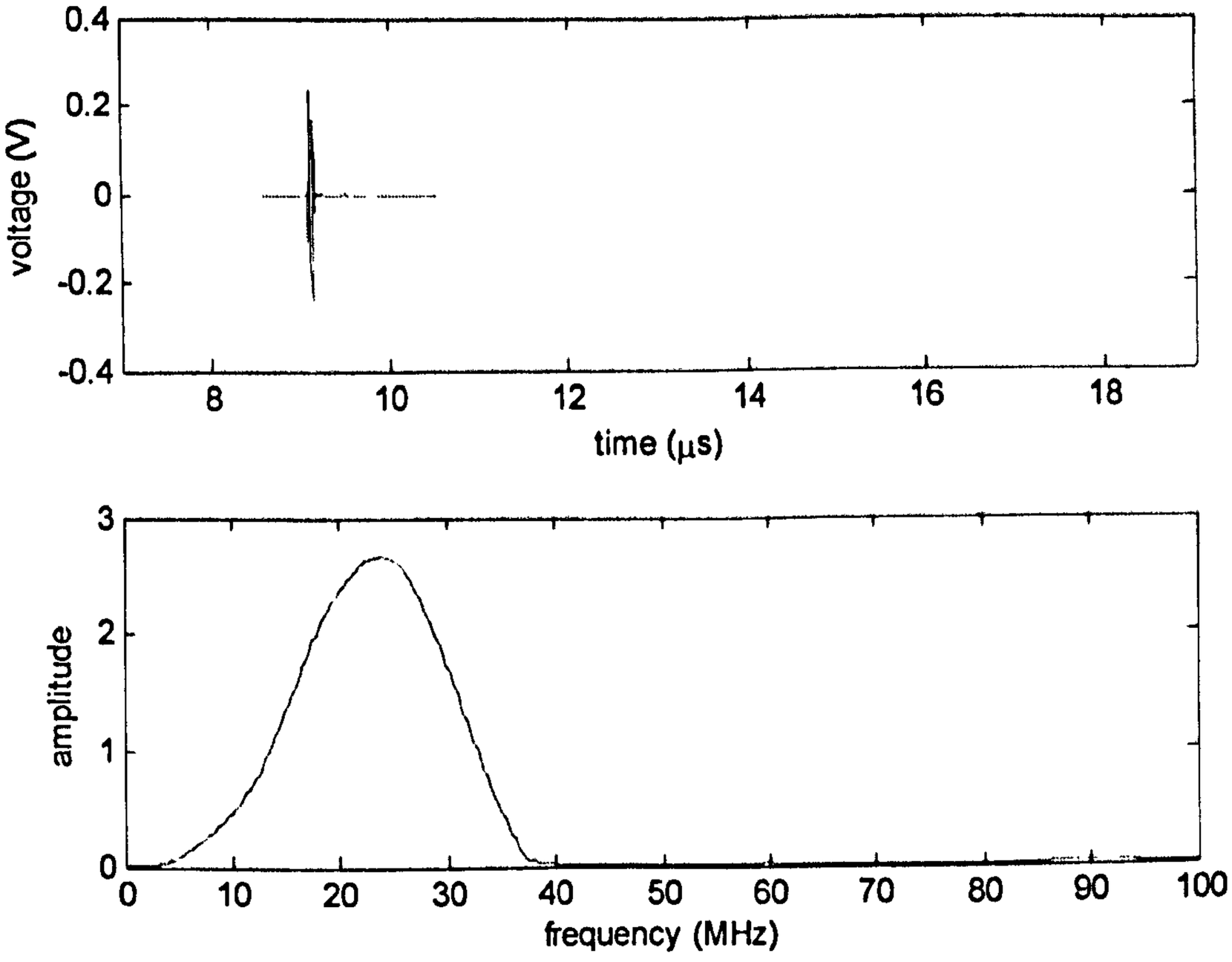

Figure.5.10. Experimental water calibration results using 20MHz transducer with plastic delay line using 8 mm transmission distance, shown in time (top) and frequency (bottom) domains.

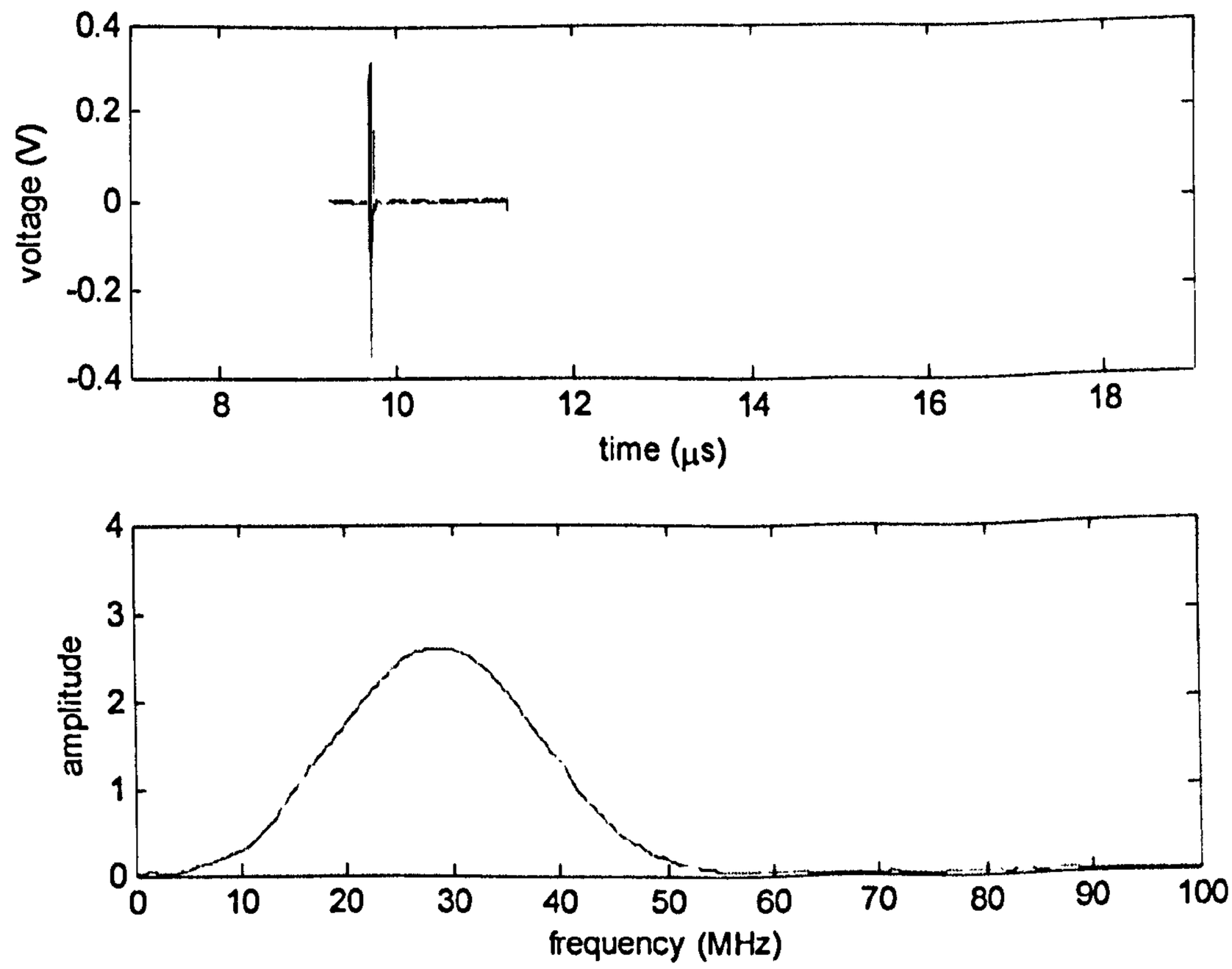

Figure.5.11. Experimental water calibration results using 30MHz transducer with silica delay line using 8mm transmission distance, shown in time (top) and frequency (bottom) domains.

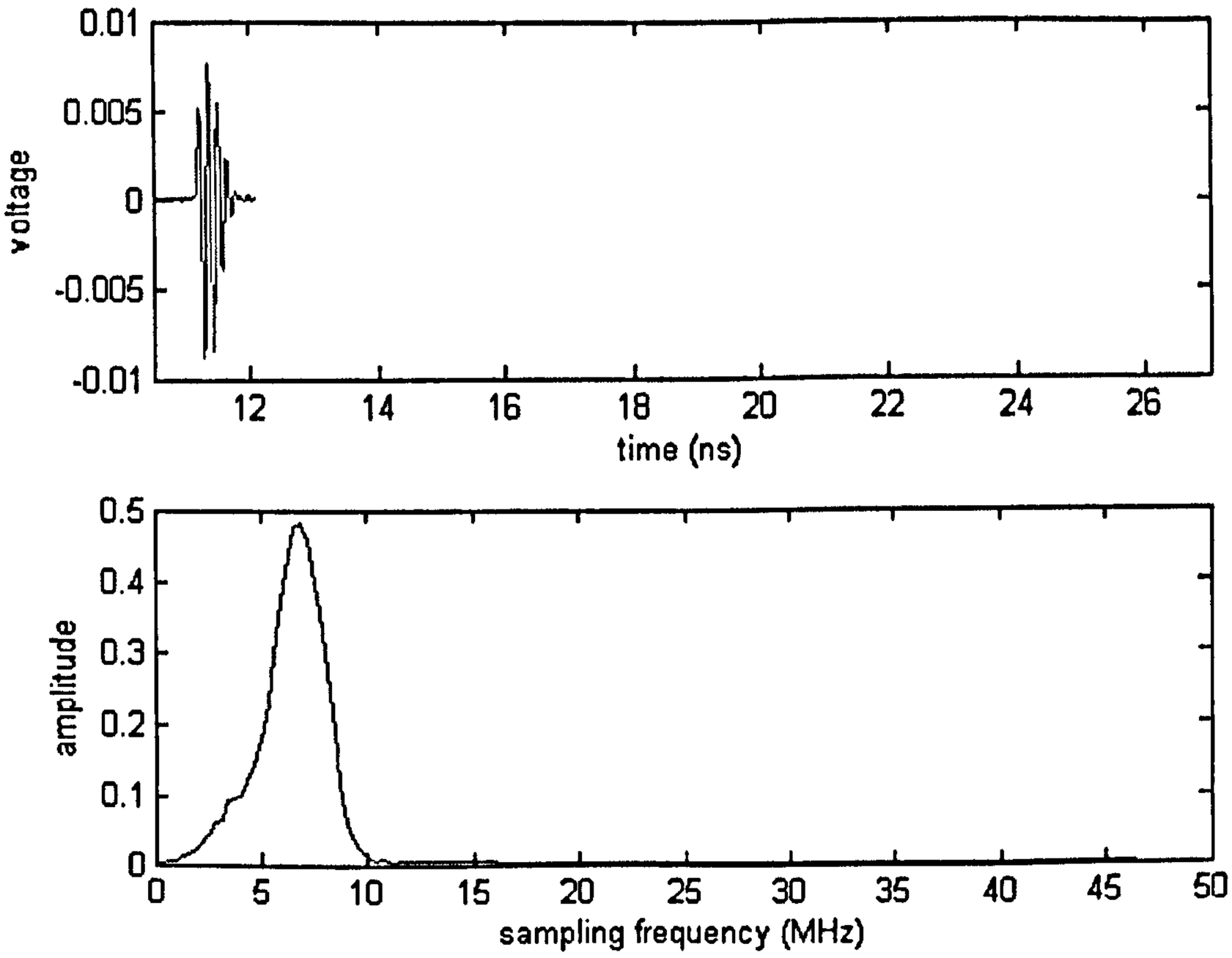

Figure.5.12. Experimental oil results using 5MHz transducer using a 10mm test cell with a stainless steel buffer, shown in time (top) and frequency (bottom) domains.

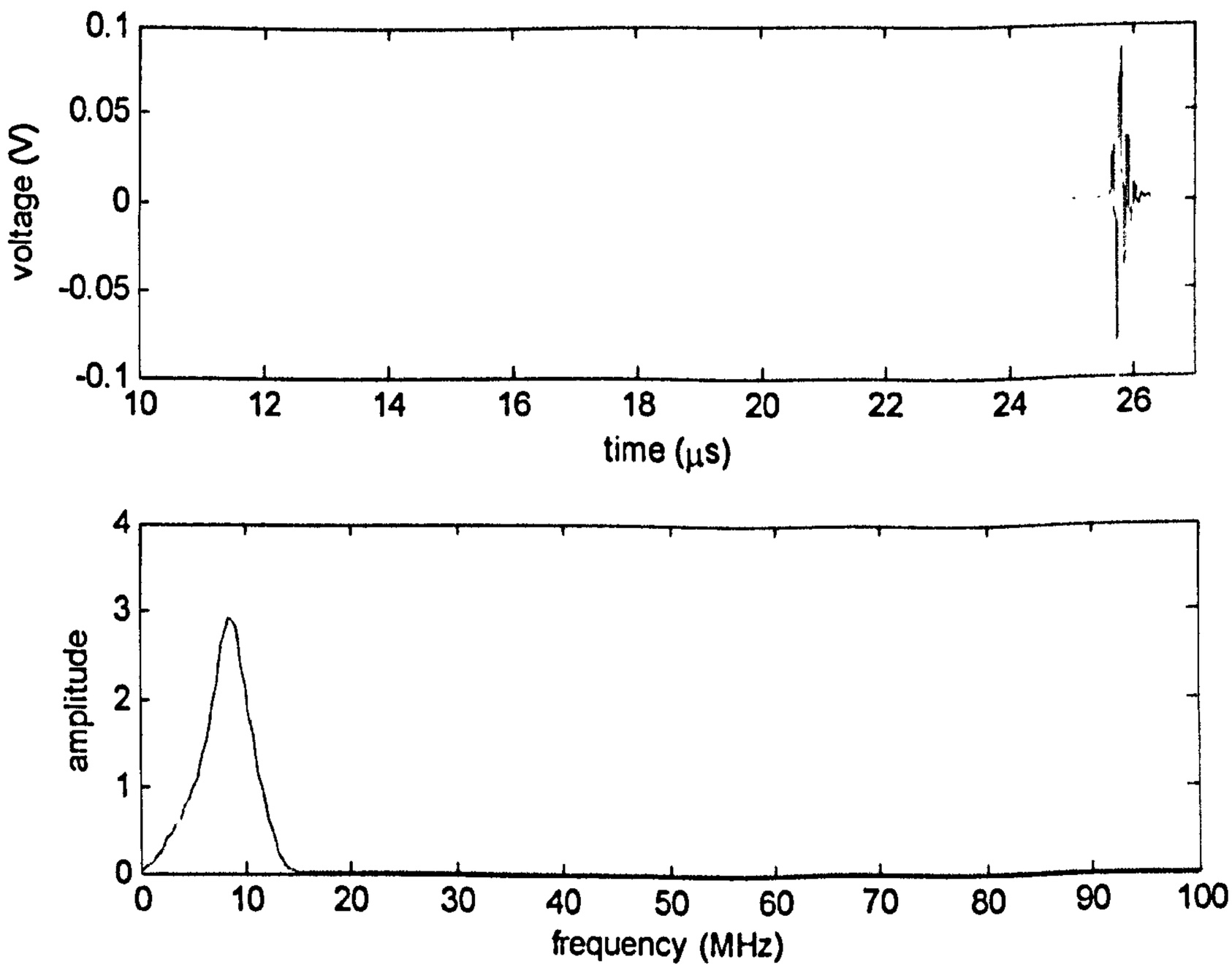

Figure.5.13. Experimental oil results using 10MHz transducer using 26 mm transmission distance, shown in time (top) and frequency (bottom) domains.

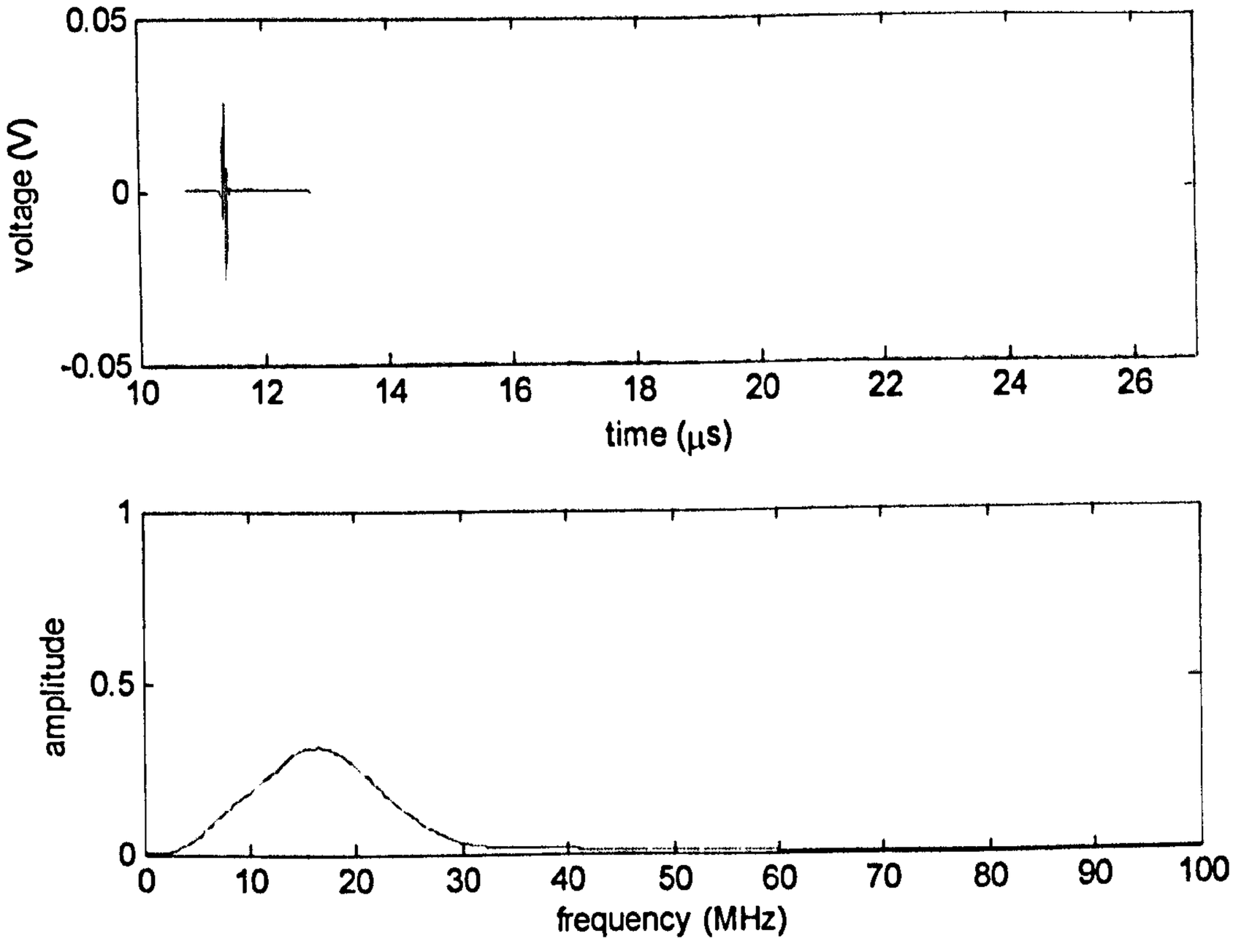

Figure.5.14. Experimental oil results using 20MHz transducer with plastic delay line using 8 mm transmission distance, shown in time (top) and frequency (bottom) domains.

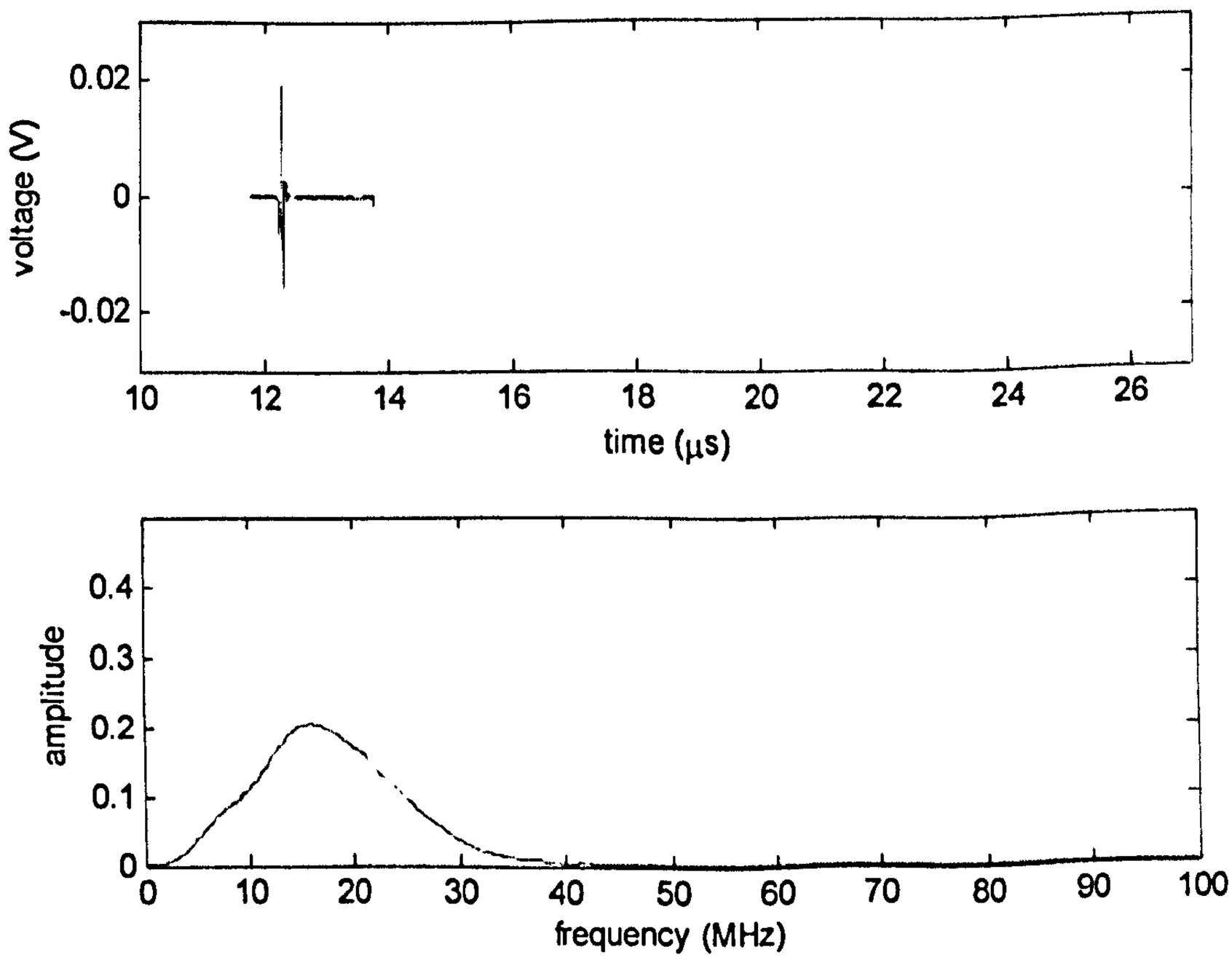

Figure.5.15. Experimental oil results using 30MHz transducer with silica delay line using 8 mm transmission distance, shown in time (top) and frequency (bottom) domains.

The requisite attenuation and phase velocity functions were obtained using a MATLAB program developed by the author. It computes the attenuation and phase velocity based on the computational procedure outlined in §5.3.2. The attenuation and phase velocity functions generated using this software are shown in figures 5.16 and 5.17. From the attenuation curve we can see that the attenuation results from the different transducers lie on a single isotonic curve. Attenuation of 500 $Np.m^{-1}$ over a path length 8 mm corresponds to a total signal loss in the test fluid of 4.0 Np. The smallest measurable loss was around 0.15 Np. In some measurements, the attenuation coefficient curves become more variant at the lower and higher frequency, which is because we are trying to measure very small changes on top of a large signal at lower attenuation whereas at high attenuations the signal is simply contaminated by noise, giving a low SNR; this will be discussed in detail in the next section.

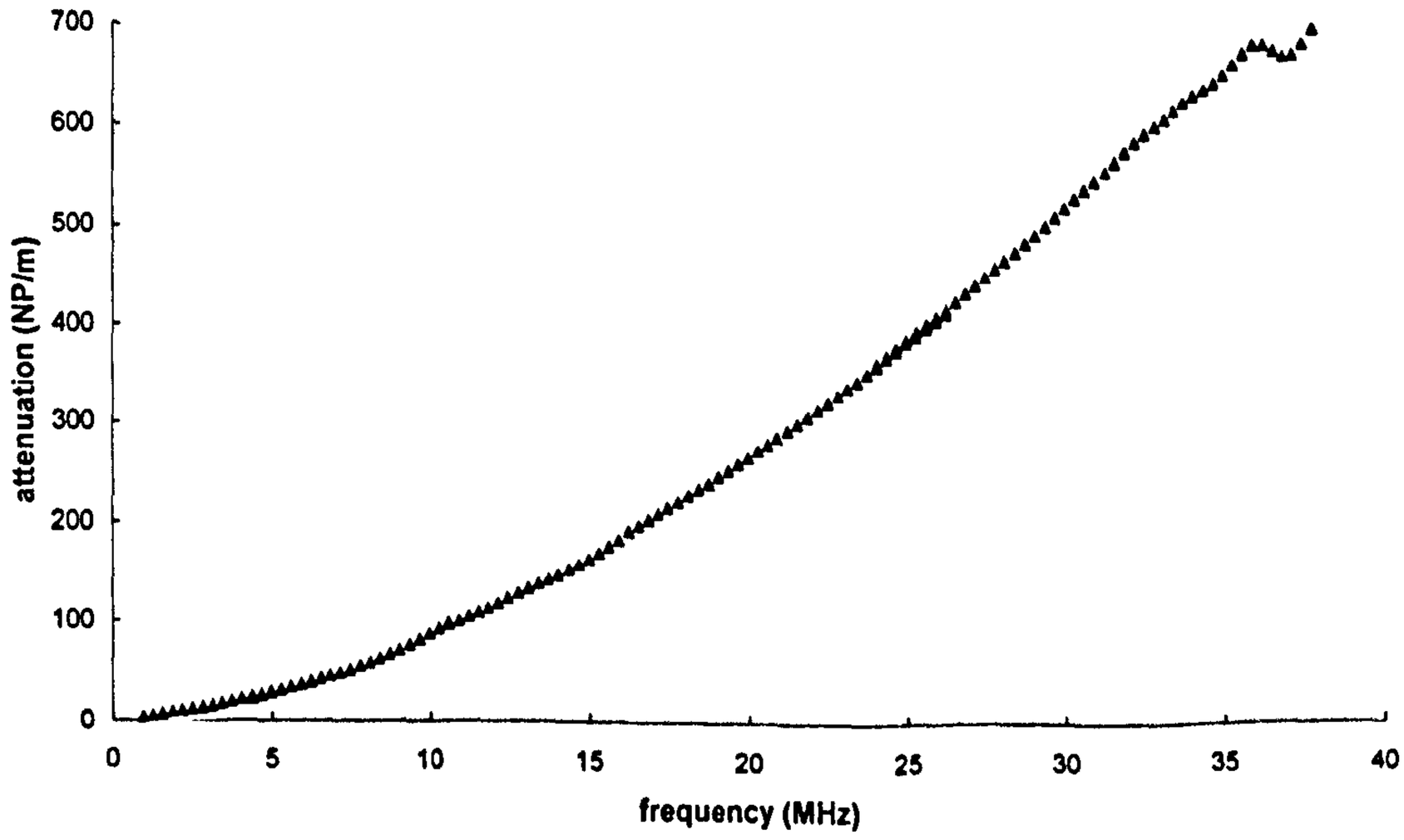

Figure 5.16. Measurement of ultrasonic attenuation for silicon oil.

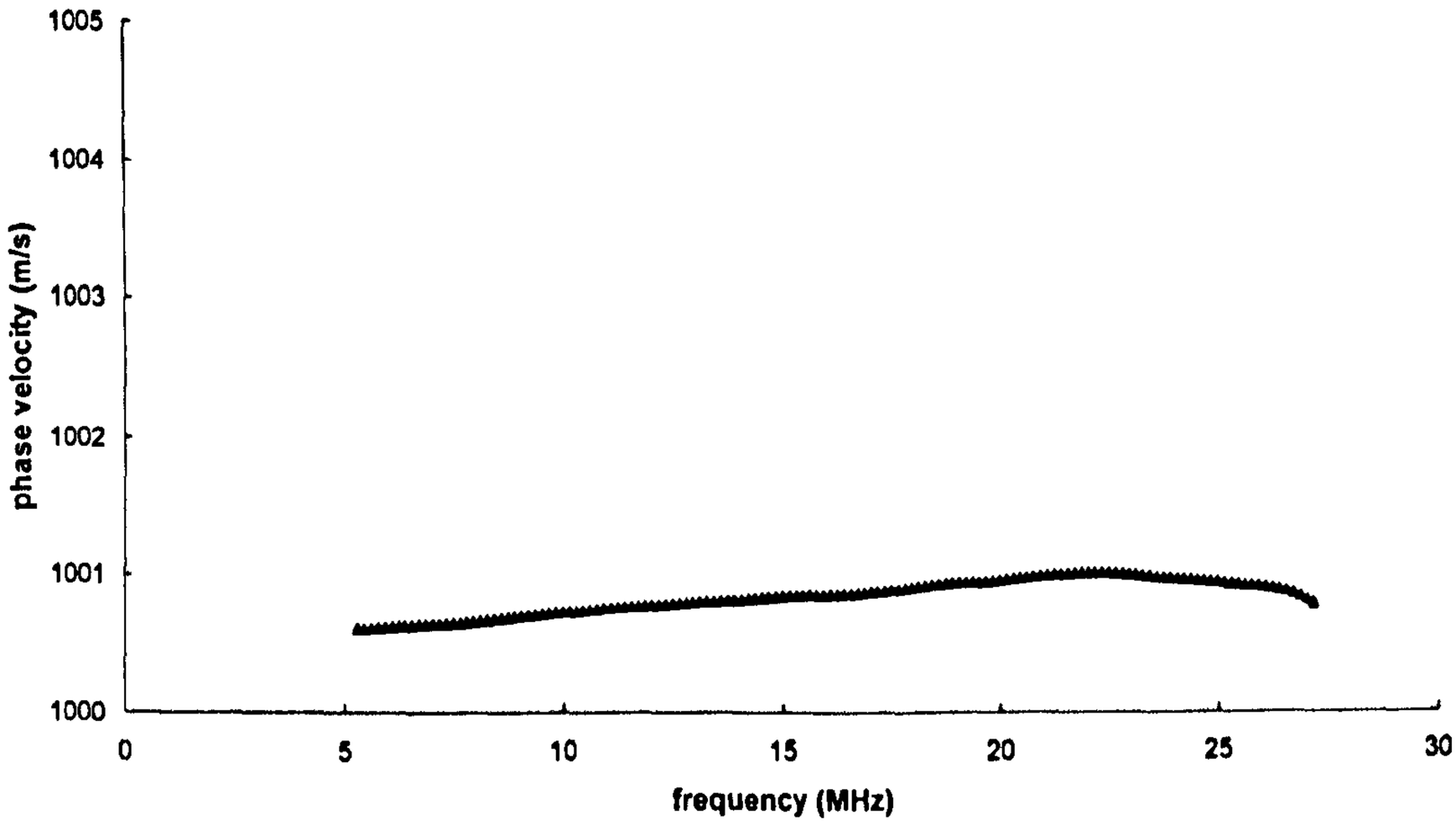

Figure 5.17. Measurement of ultrasonic phase velocity for silicon oil.

5.4. Errors and uncertainties

5.4.1 Errors calculation

The accuracy and precision of experimentally measured ultrasonic attenuation and phase velocity functions are usually compromised by noise. The presence of noise in experimentally obtained ultrasonic signals is undesirable but inevitable. In a typical ultrasonic signal pathway the unwanted noise arises primarily from electronic equipment involved in the measurements, the so-called electronic noise. In our ultrasonic measurement set-up, a signal generator produces excitation signals that drive the transmitting transducer, which then generates ultrasonic waves (usually compression) that propagate through the test medium. The propagated signal is captured by a receiving transducer that converts the ultrasonic waves into an electrical equivalent, which is then amplified, digitised and processed by a

computer or dedicated processor (see figure 5.18). In such an arrangement it was found that the principal determinants of noise are equipment electronic noise (additive, quantisation and frame jitter) and numerical/computational rounding (Kalashnikov and Challis, 2005).

The time-domain random noise maps into the frequency-domain in the manner stated by Blair (1998), and this frequency-domain noise then leads to errors in the attenuation and phase velocity coefficients subsequently derived. The frequency-domain noise maps to errors in the ultrasonic data in a highly non-linear way, with the errors increasing dramatically in measurements of both high and low attenuations (figure 5.19). Quantification of these errors will therefore provide a useful basis for controlling and optimising the design of ultrasonic spectrometers for both laboratory and industrial applications. These errors may be quantified using the statistical concepts of bias and variance, or for convenience of interpretation, relative bias and variance in percentages. The following is a summarised adaptation from Kalashnikov and Challis's work (2005), outlining the theoretical treatments for noise quantification in ultrasonic spectrometry measurements.

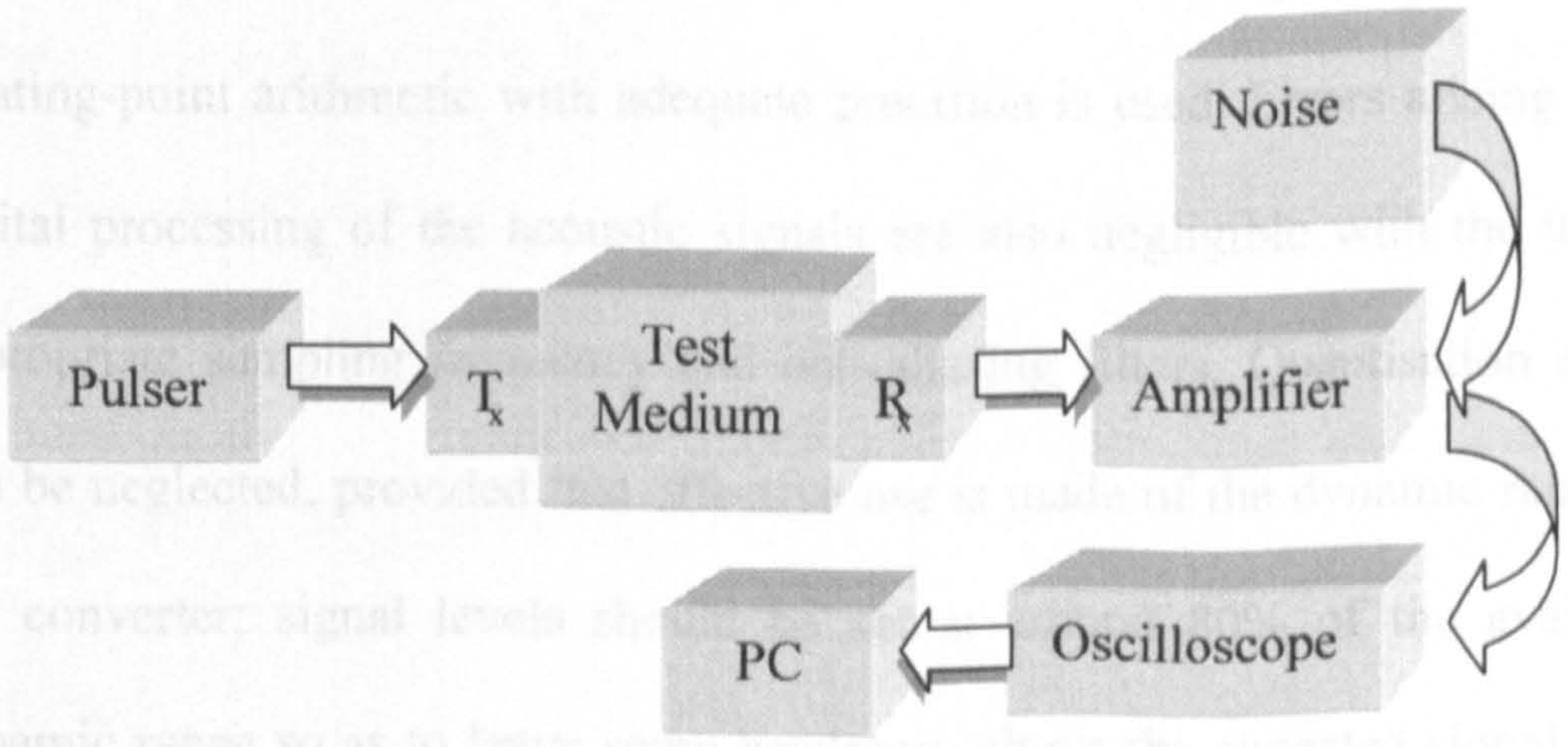

Figure.5.18. Schematic of a conventional attenuation measurement system with noise.

The ultrasonic compression wave attenuation and phase velocity functions are related to the response of the test medium in the following manner:

$$H(\omega) = e^{-\alpha(\omega)d} e^{-j\omega\left[\frac{d}{c(\omega)} - \tau\right]} \tag{5.23}$$

where d is the propagation distance and τ is the data acquisition delay. The attenuation is to be calculated from the modulus of $H(\omega)$, and the phase velocity calculated from its phase spectrum. The test medium response $H(\omega)$ contains:

1) The *true* test medium response $H_T(\omega)$, and

2) Errors/noise expressed as random numbers r with bias b and standard deviation σ.

The modulus and phase spectra of $H(\omega)$ are thus:

$$|H(\omega)| = |H_T(\omega)| + b_m + r_m\sigma_m \tag{5.24}$$

$$\angle H(\omega) = \angle H_T(\omega) + b_p + r_p\sigma_p \tag{5.25}$$

Generally numerical/computational errors are negligible provided floating-point arithmetic with adequate precision is used. Errors arising from digital processing of the acoustic signals are also negligible with the use of appropriate sampling frequency and anti-aliasing filters. Quantisation errors can be neglected, provided that effective use is made of the dynamic range of the converter; signal levels should be set at around 80% of the available dynamic range so as to leave some headroom above the expected signal level

to protect against transient saturation of the converter (Diebold, 1977, Challis and Kitney, 1991).

With these taken into account it may be concluded that the primary error components are additive noise and frame jitter. Additive noise contributes to errors in the attenuation data, while errors in the phase velocity result from both additive noise and frame jitter. By considering equipment noise as the primary source of errors, Kalashnikov and Challis adopted a statistical technique based on Lindley (1965) to derive the relative biases in the attenuation and phase velocity in relation to the equipment noise. These biases are expressed as follows:

Relative bias in attenuation, $B[\alpha(\omega)] = -b_m M_m[\alpha(\omega)d] + \sigma_m{}^2 M_m[2\alpha(\omega)d]$

(5.26)

Relative bias in phase velocity, $B[c(\omega)] = -b_p M_p + \sigma_p{}^2 M_p{}^2$ **(5.27)**

The authors subsequently showed that random electronic noise introduces no bias in the amplitude spectra, hence the above expressions could be rewritten as follows:

Relative bias in attenuation, $B[\alpha(\omega)] = \sigma_m{}^2 M_m[2\alpha(\omega)d]$ **(5.28)**

Relative bias in phase velocity, $B[c(\omega)] = \sigma_p{}^2 M_p{}^2$ **(5.29)**

The relative variances in the attenuation and phase velocity are calculated using equations 5.30 and 5.31, respectively:

$$\frac{\sigma^2[\alpha(\omega)]}{\alpha^2(\omega)} = \sigma_m{}^2 M_m{}^2[\alpha(\omega)d] \quad \textbf{(5.30)}$$

$$\frac{\sigma^2[c(\omega)]}{c^2(\omega)} = \sigma_p{}^2 M_p{}^2 \quad \textbf{(5.31)}$$

The terms $M_m[\alpha(\omega)d]$ and $M_m[2\alpha(\omega)d]$ are error magnification functions for the amplitude spectrum, which express the mapping of errors in the raw data domain into the domain of measured variables, and are expressed as:

$$M_m[\alpha(\omega)d] = \frac{e^{\alpha(\omega)d}}{\alpha(\omega)d} = M_1 \tag{5.32}$$

$$M_m[2\alpha(\omega)d] = \frac{e^{2\alpha(\omega)d}}{2\alpha(\omega)d} = M_2 \tag{5.33}$$

$M_m[\alpha(\omega)d]$ and $M_m[2\alpha(\omega)d]$ exhibit a minimum value of e=2.71828 when $\alpha(\omega)d = 1$ for equation 5.32, and $\alpha(\omega)d = 0.5$ for equation 5.33 respectively. The two functions are plotted in figure 5.19. As can be seen, the lowest relative error in measured attenuation occurs when M is at its minimum, that is at $\alpha(\omega)d = 0.5$ Np for $M_m[2\alpha(\omega)d]$ and at $\alpha(\omega)d = 1$ Np for $M_m[\alpha(\omega)d]$. The significant implication of figure 5.19 is that the best measurement condition occurs when measured attenuation is in the range 0.5 to 1 Np. The curve also shows that measurement errors rise dramatically when the measured attenuation is less than 0.4 Np or greater than 1.5 Np. This curve is very useful in the context of the design of experiments with specified error limits: if the maximum attenuation to be measured ($\alpha_{max}d$) is known, we can obtain the corresponding value of M from the curve; the relative error in the attenuation measurement will then be a multiplication of that value of M with the noise to signal ratio.

M_p is the error magnification function for the phase spectrum, and is expressed as:

$$M_p = \frac{c}{\omega d} \tag{5.34}$$

where c and ω respectively represent the measured velocity and the bandwidth, both of which are fixed for a particular test medium and experimental measurement. Errors in the phase velocity data, as represented by the magnification function, can therefore be reduced by increasing the experimental gauge length.

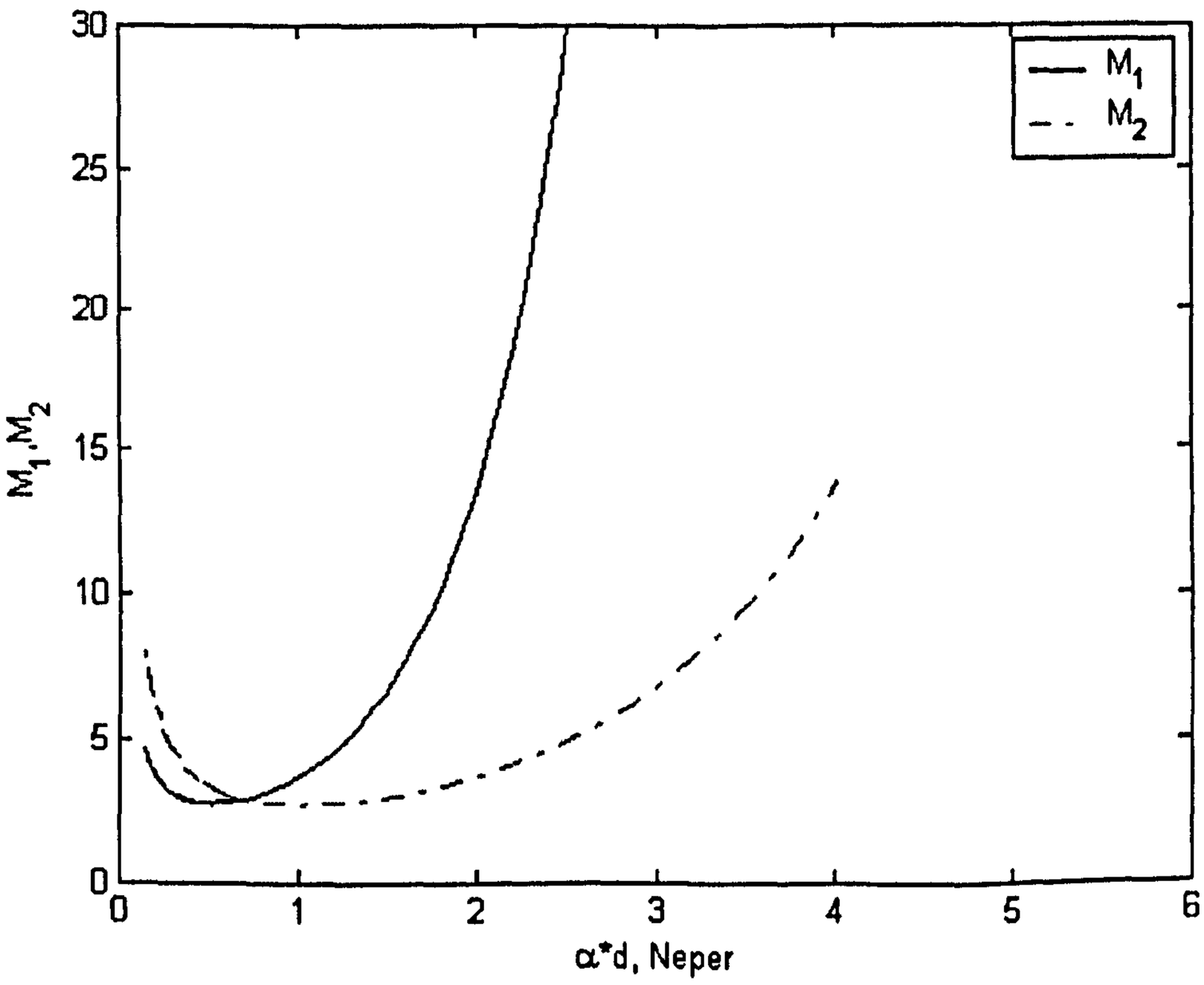

Figure.5.19. Error multiplier functions that magnify bias and variance in the amplitude spectra using equations 5.32 and 5.33, plotted against total signal loss expressed in Np (attenuation of distilled water was used for calculation).

5.4.2 Errors calculation in our experiment system

Experimental data were collected and recorded using the experimental equipment as discussed above. The test medium was silicone oil (350cst, Dow Corning 200), and the attenuation result was obtained using the 20MHz transducer with the plastic delay line at a 10 mm transmission distance. Data

consisting of 1000 frames of 640 samples each were collected. The raw signal records (figure 5.20a) exhibit noticeable noise that is significantly reduced by coherent averaging (figure 5.20b). The signal to noise ratio (SNR) of recorded signal is 30.2dB and 52dB before and after coherent averaging respectively (the SNR of the recorded time-domain signal was calculated by using the division between the output signal with power applied to the transmitter and the output signal without power). The SNR has been improved about 12 times after applying 1000 times coherent averaging. This is less than the theoretical improvement ($\sqrt{1000}$ =31.6) and this is due to the noise not being ideally random.

The Fourier transform of every record was calculated, and the amplitudes were averaged separately within the range 0-40MHz. The averaged spectra were regarded as the true received spectra $|Y_T(\omega)|$. The attenuation coefficient of the silicone oil (350cst, Dow Corning 200) at 25^oC (Povey, 1997) is:

$$\alpha_T(\omega) = 2.04\times10^{-10}\cdot f^{1.66} \quad (Nepers\cdot m^{-1}) \tag{5.35}$$

Theoretical attenuation can be defined as the ratio of the output amplitude and the input amplitude of the ultrasonic wave, and was given by:

$$|H(\omega)| = \frac{|A_o(\omega)|}{|A_i(\omega)|} = e^{-\alpha_T(\omega)d} \tag{5.36}$$

The calibration amplitude spectrum was derived as:

$$|X(\omega)| = \frac{|Y_T(\omega)|}{|H(\omega)|} \tag{5.37}$$

The theoretical attenuation ($H(\omega)$), averaged amplitude spectrum ($Y_T(\omega)$) and calculated calibration spectrum ($X(\omega)$) for this kind of silicon oil are shown as figure 5.21.

The additive noise was quantified by calculation of the standard deviation of the amplitude spectrum ($Y(\omega)$), and the averaged amplitude spectrum ($Y_T(\omega)$) was considered as true signal, so we could get the SNR as:

$$SNR = 10\log\frac{Y_T(\omega)}{std(Y(\omega))}(dB) \tag{5.38}$$

The SNR was greater than 27dB in the frequency range from 3 MHz to 40 MHz, and greater than 40dB in the frequency range from 5 MHz to 27 MHz (figure 5.22).

The attenuation and phase velocity for silicon oil was calculated for every record available, 1000 records in this experiment. Both the theoretical value and the values obtained by experiment have been included in figure 5.23. It is clear that there is a good agreement between the experimental results and theory for both attenuation and phase velocity. Figures 5.24 and 5.25 show the relative bias and variance for attenuation and phase velocity respectively, where the experimental relative bias and standard deviation are plotted together with the values calculated using the equations (equations 5.28 to 5.31) discussed above.

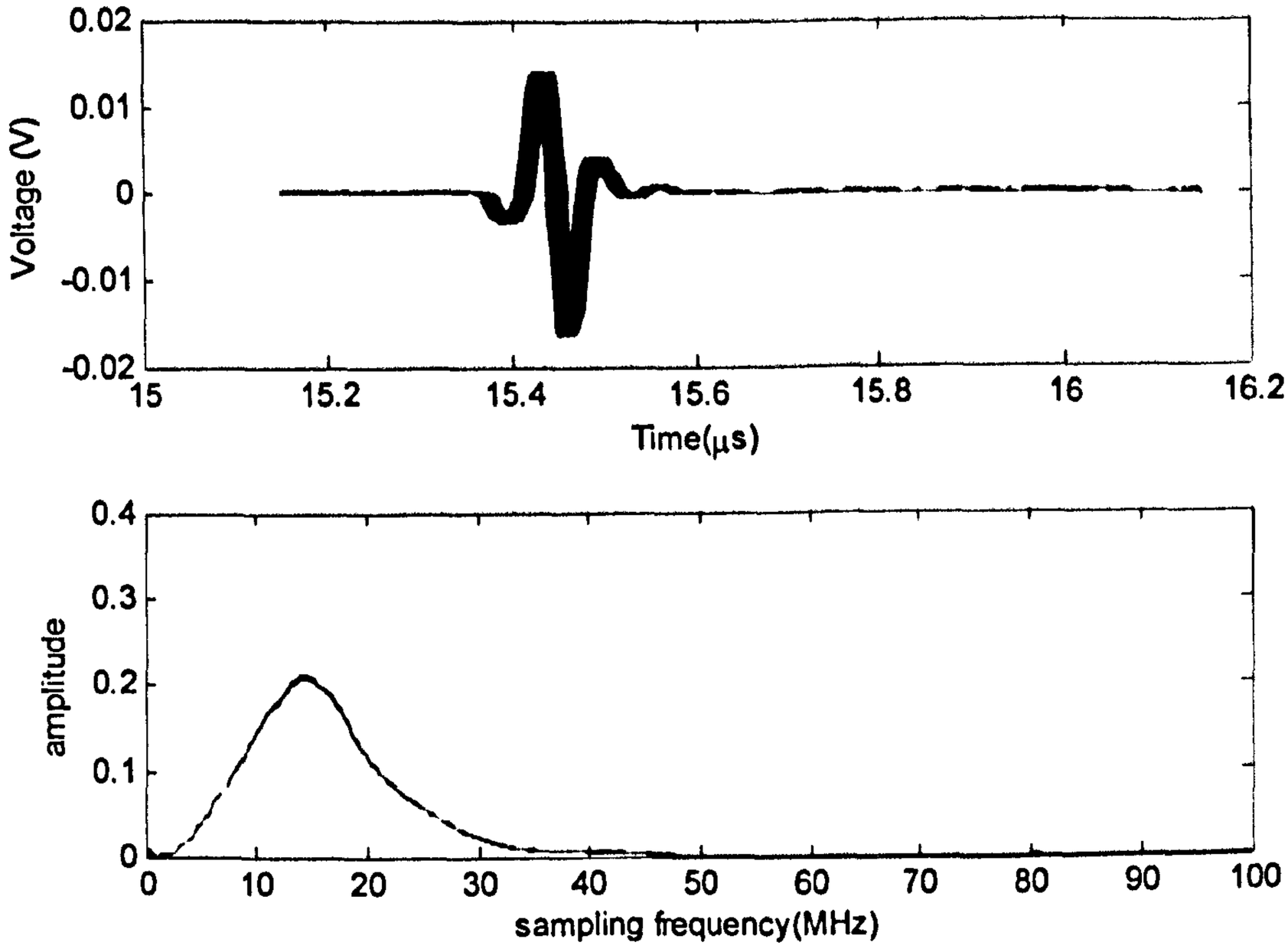

Figure.5.20a. Recorded oil signals superimposed in the time domain and frequency domain, using 20 MHz transducer with plastic delay line, at 10 mm gauge length.

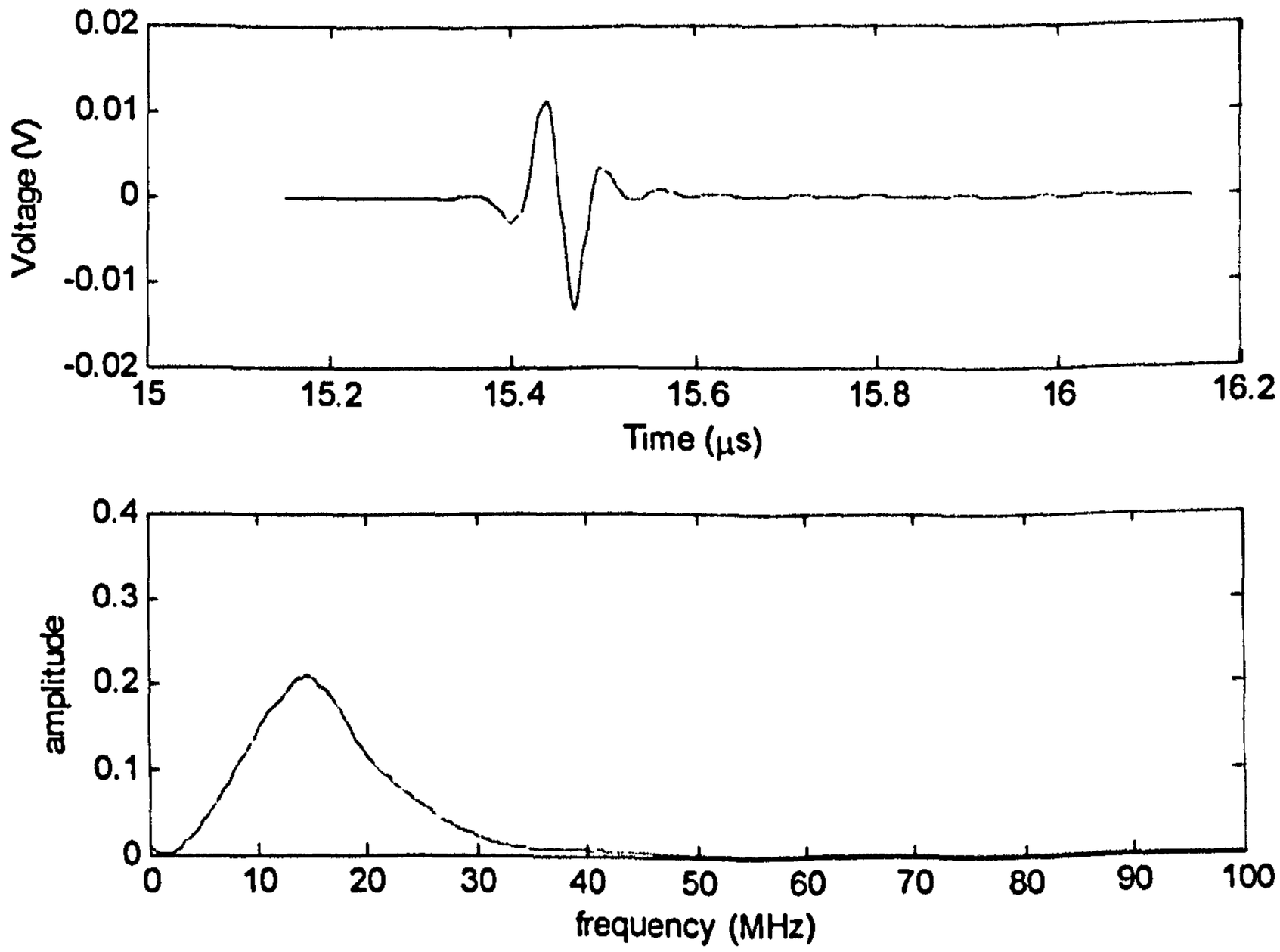

Figure.5.20b. Recorded oil signal after coherent averaging based on figure 5.20a.

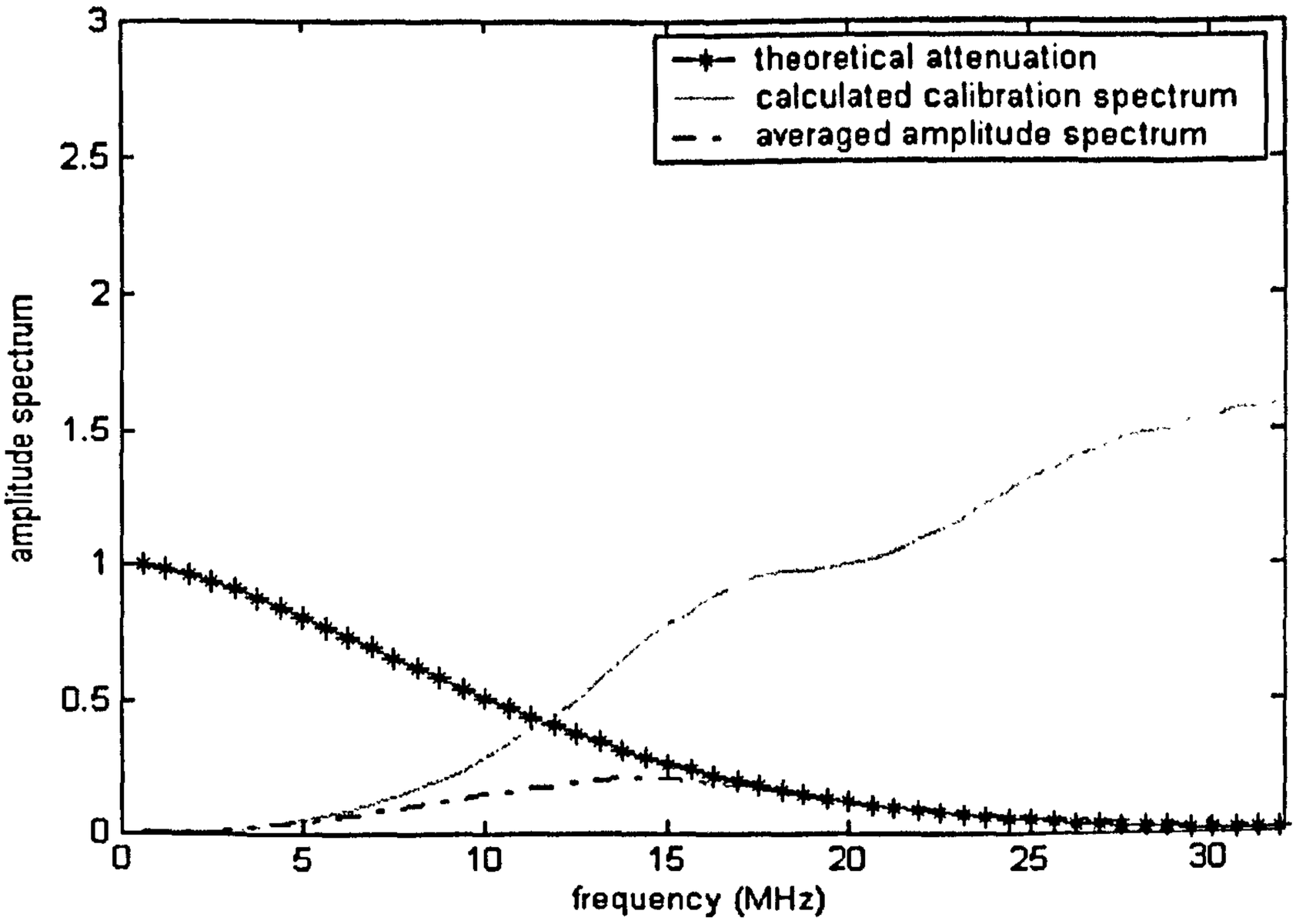

Figure 5.21. Frequency domain result for oil: Theoretical attenuation calculated use equation 5.36 (crosses), average amplitude spectrum (dash line) and calculated calibration spectrum using equation 5.37 (solid line). $d = 10$ mm.

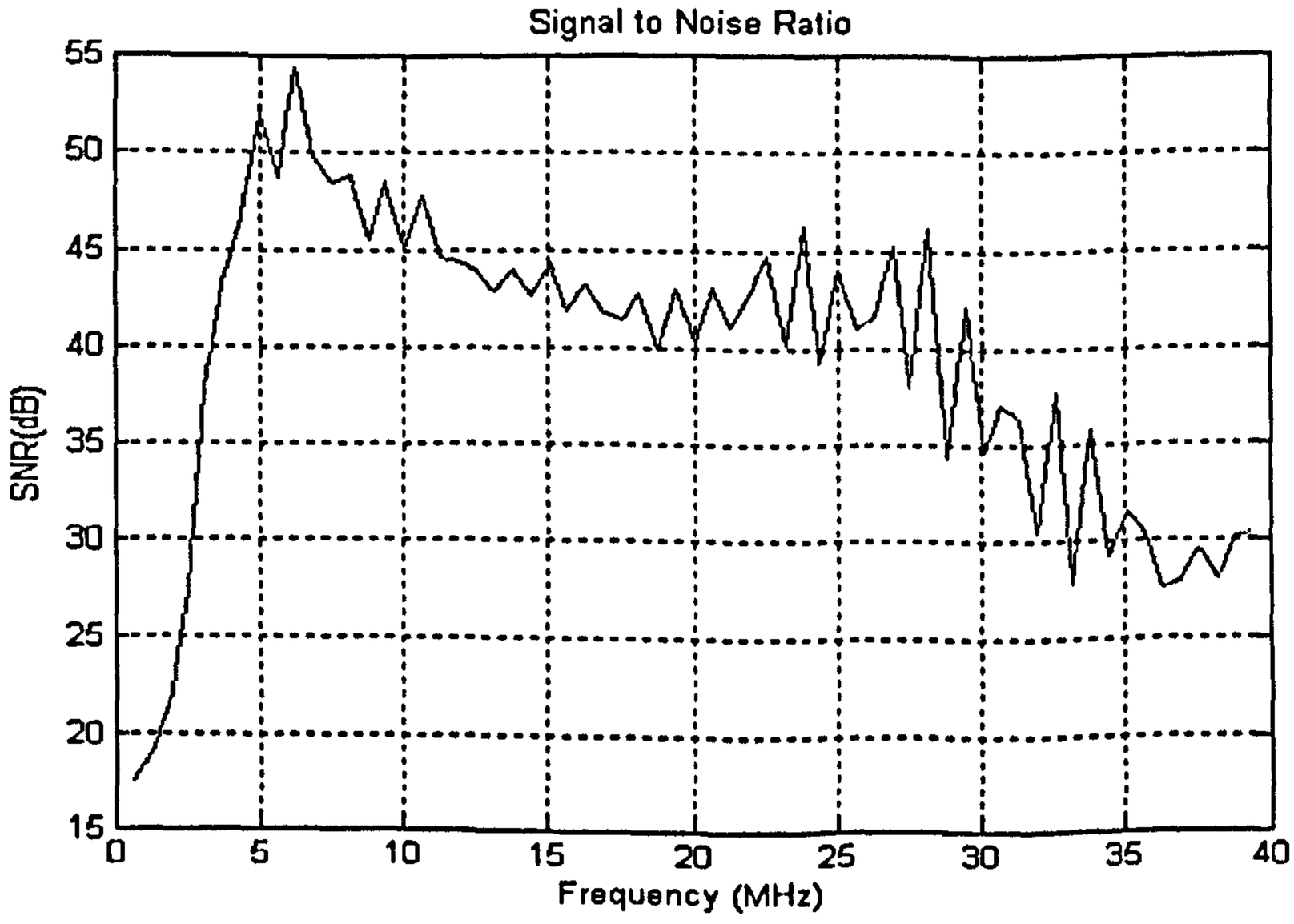

Figure 5.22. Signal to noise ratio for experiment.

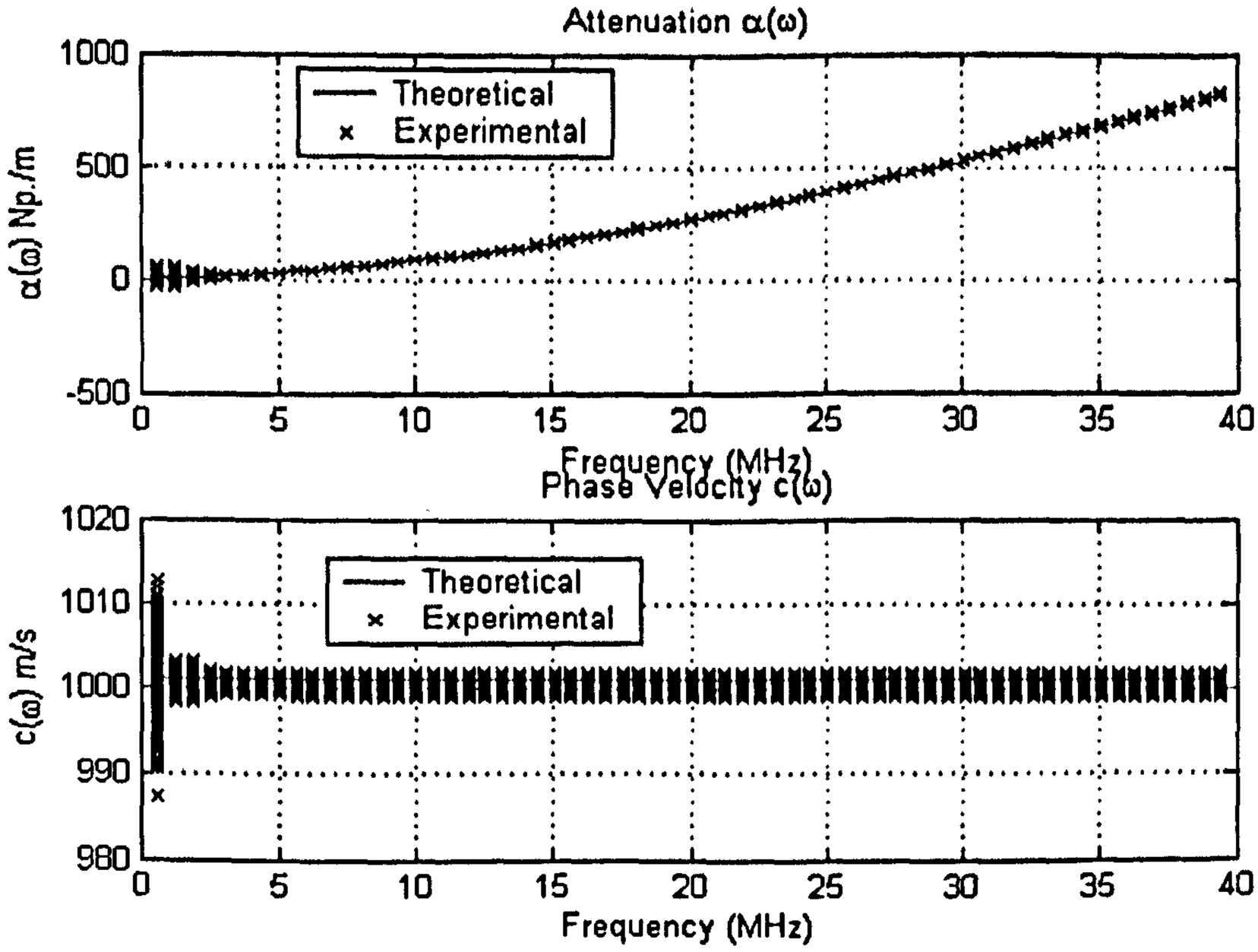

Figure 5.23. Ensemble of calculated attenuation (top) and phase velocity (bottom) values (points) and the theoretical values (solid line). 1000 samples were used in the experiment.

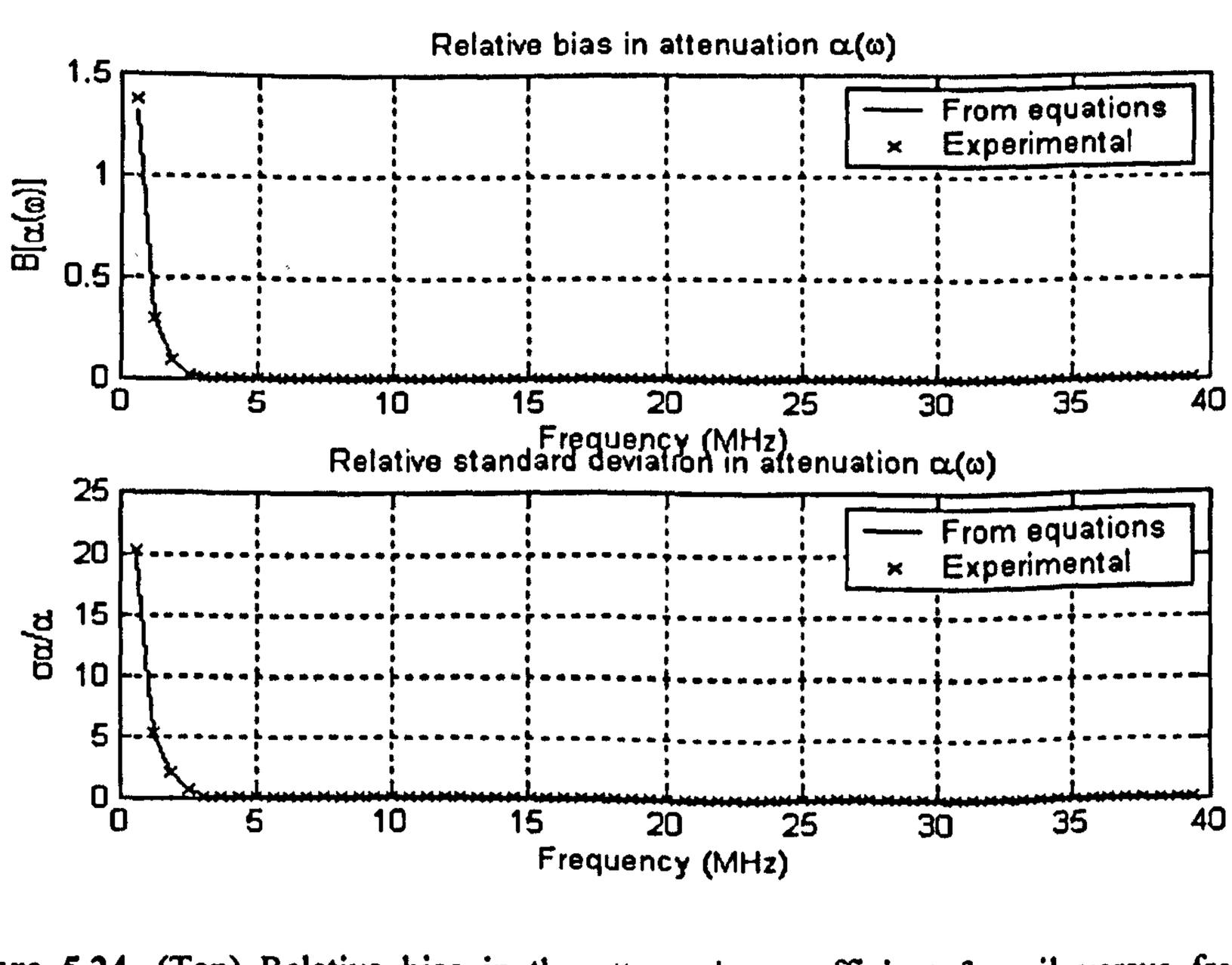

Figure 5.24. (Top) Relative bias in the attenuation coefficient for oil versus frequency: calculated from equation 5.28 (solid line) and experiment results (crosses). Bottom: relative standard deviation: calculated from equation 5.30 (solid line) and experiment results (crosses).

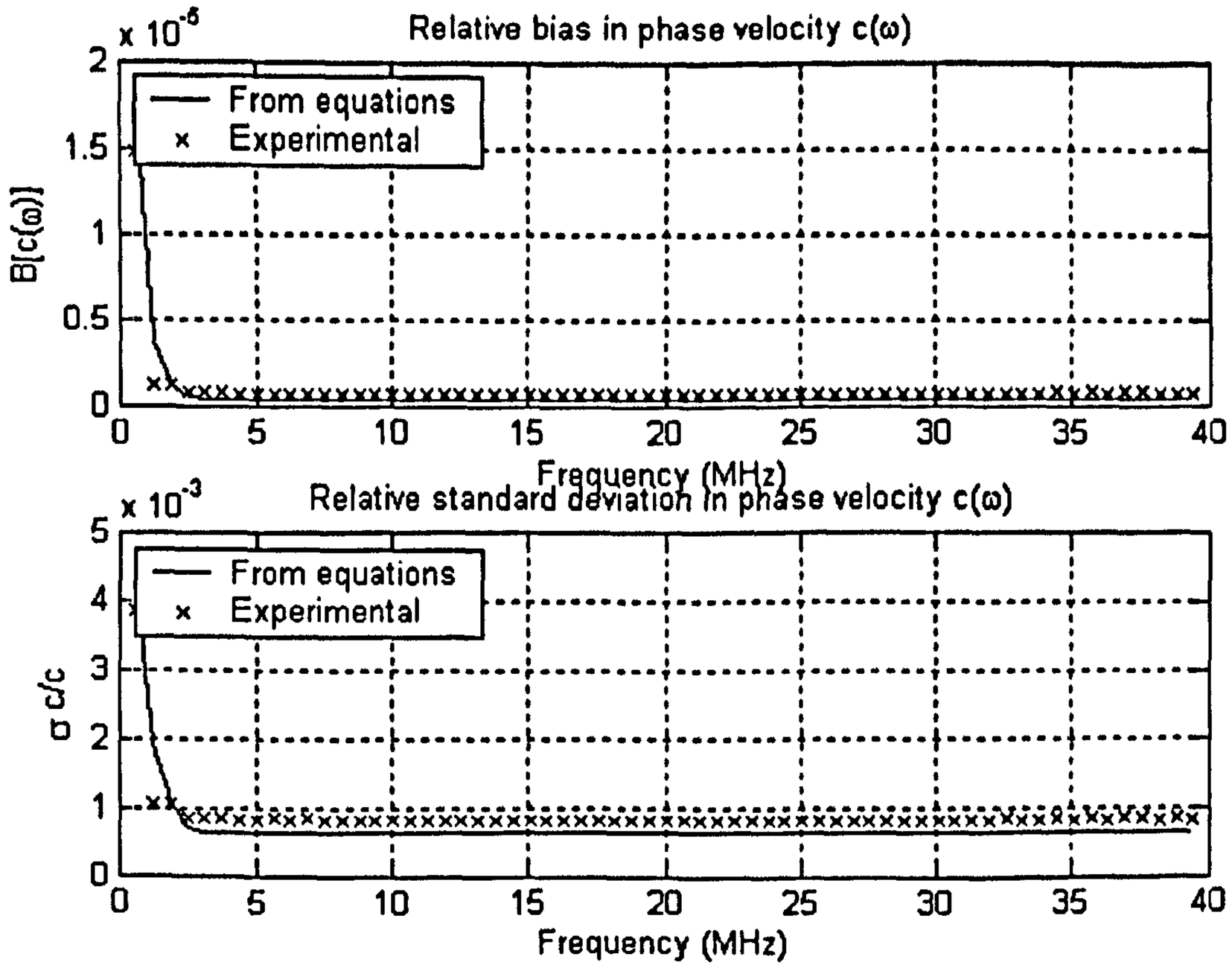

Figure 5.25. (Top) Relative bias in the phase velocity for oil versus frequency: Values calculated from equation 5.29 (solid line) and experiment results (crosses). Bottom: relative standard deviation: calculated from equation 5.31 (solid line) and experiment results (crosses).

5.5. Conclusion

The focus of this chapter concerned the experimental methods used in this research project. The experimental set-up was explained, followed by a discussion of the calculations of the attenuation and phase velocity of a given test medium. Experimental errors were analysed in terms of basic statistical theory and an example experiment was done using Dow Corning 200 silicon oil. The error calculations were based on Kalashnikov and Challis (2001, 2002 and 2005).

In the next chapter, we will use the methods described above in a series of experiments designed to investigate the applicability of the wave propagation theories described in chapters 2 to 4.

Chapter 6 Experiments and Simulations

6.1 Introduction

This chapter is mainly concerned with the experiments and simulations for emulsion systems with different particle concentrations as well as contrasting particle size distributions, using the experimental method discussed in chapter 5. These experimental data are compared with theoretical data predicted using the ECAH model, the ECAH explicit expression for A_0 and A_1 terms, HHM model, and Evans and Attenborough's coupled phase model. Besides the experiments on concentrated emulsions, also included are the experiments on encapsulated emulsions to test the Anson and Chivers shell model. These models have been discussed earlier in chapters 2 to 4.

The first experiment is the attenuation and phase velocity measurements on dilute emulsion systems, consisting of a 5% v/v n-hexadecane oil-in-water with different concentrations of surfactant in the continuous phase. This experiment provided a test as to whether our measurement strategy was correct or not. This was followed by experiments on a number of 1-bromohexadecane oil-in-water emulsions with different concentrations and particle sizes in order to test how and when the traditional ECAH model breaks down. Experiments were thus done at smaller particle sizes (around 90 nm), again to test how and when the ECAH model breaks down. In addition we also wished to determine if the HHM model and Evans and Attenborough's coupled phase model could be used for highly concentrated emulsions with small particle sizes.

Finally, there are included some experiments on encapsulated emulsions where these experimental data were compared with our simulations using the Anson and Chivers shell model, again in order to determine its applicability. We also changed the shell thickness and thermo-physical properties of the shell in the simulation in order to assess their influence on the attenuation.

6.2 Experiment 1: 5% v/v n-hexadecane in water emulsion with 1% Tween and 2% Tween

6.2.1 Emulsion preparation

These two kinds of n-hexadecane oil-in-water emulsions were prepared and characterized by the Procter Department of Food Science at the University of Leeds. The author is most grateful for this support. The two emulsions have different particle size distributions, which were measured by using an optical instrument, the *Mastersizer 2000* (Malvern Instruments Ltd., Malvern, Worcester, U.K.) at the University of Leeds (see figures 6.4a and 6.4b).

The disperse phase volume fractions of these emulsions are the same, namely 5% n-hexadecane, whereas the contents of the continuous phase is different; one of the continuous phases uses a surfactant solution containing 1 wt% Tween, the other uses 2 wt% Tween. This small amount of surfactant changes some of the properties of continuous phase slightly (such as phase velocity and attenuation), but we still use the properties of water as the continuous phase property in the following calculations because it is difficult to measure the properties of the continuous phase in our laboratory. It is recommended to do such measurement in the future work. The changes in the

properties may explain the divergences from the experimental data to the simulations. The thermo-physical properties of the dispersed phase and continuous phase are shown in table 6.1.

6.2.2 Ultrasonic measurements

Ultrasonic attenuation and phase velocity spectra of these emulsions were measured in the frequency range from 2 MHz to 25 MHz using a Perspex (PMMA) test cell and a single 20 MHz broadband ultrasonic transducer. The details of the measurement methods and calculations have been described in chapter 5. The signal was averaged 1000 times prior to analysis to improve the signal-to-noise ratio (also see chapter 5). Each analysis was carried out on five separate samples, and the average of all five results for attenuation was calculated.

Figures 6.1 and 6.2 give the measured ultrasonic attenuation and phase velocity for the two n-hexadecane emulsions. We see that the attenuations for n-hexadecane emulsions are not high compared to that of the oil alone. There is increasing variance at frequencies above 22 MHz for both of the emulsions. This corresponded to attenuation of 170 Npm^{-1}, which with a test cell gauge length of 10 mm, convert to a total loss of 1.7 Np, which corresponded to a mapping factor $M(\alpha d) = 3.5$. It was shown in chapter 5 that the error in the attenuation is $M(\alpha d) \cdot NSR$.The low signal levels were due to the use of steel buffers and to high attenuation. The phase velocity data are shown in figure 6.2, and again, there is an increasing variance at frequencies above 22 MHz for both of the emulsions.

Properties	n-hexadecane	Water	1-bromohexadecane
Ultrasonic velocity ($m\ s^{-1}$)	1357.9	1497.0	1299.4
Attenuation coefficient ($Np\ m^{-1}\ Hz^2$)	$9.35\times10^{-14}\ f^2$	$2.5\times10^{-14}\ f^2$	$1.45\times10^{-13}\ f^2$
Density ($kg\ m^{-3}$)	773.0	997.0	1000.0
Viscosity (mPa s)	3.44	0.88	6.63
Specific heat ($J\ K^{-1}kg^{-1}$)	2215.0	4177.0	2090.8
Thermal conductivity ($W\ m^{-1}\ s^{-1}$)	0.143	0.611	0.141
Thermal expansivity (K^{-1})	0.00091	0.00026	0.000775

Table 6.1. Thermo-physical properties of the n-hexadecane, water and 1-bromohexadecane used in the calculation (25°C). These data were obtained from Hemar and Herrmann(1997), Chanamai (1999) and Holmes (1999).

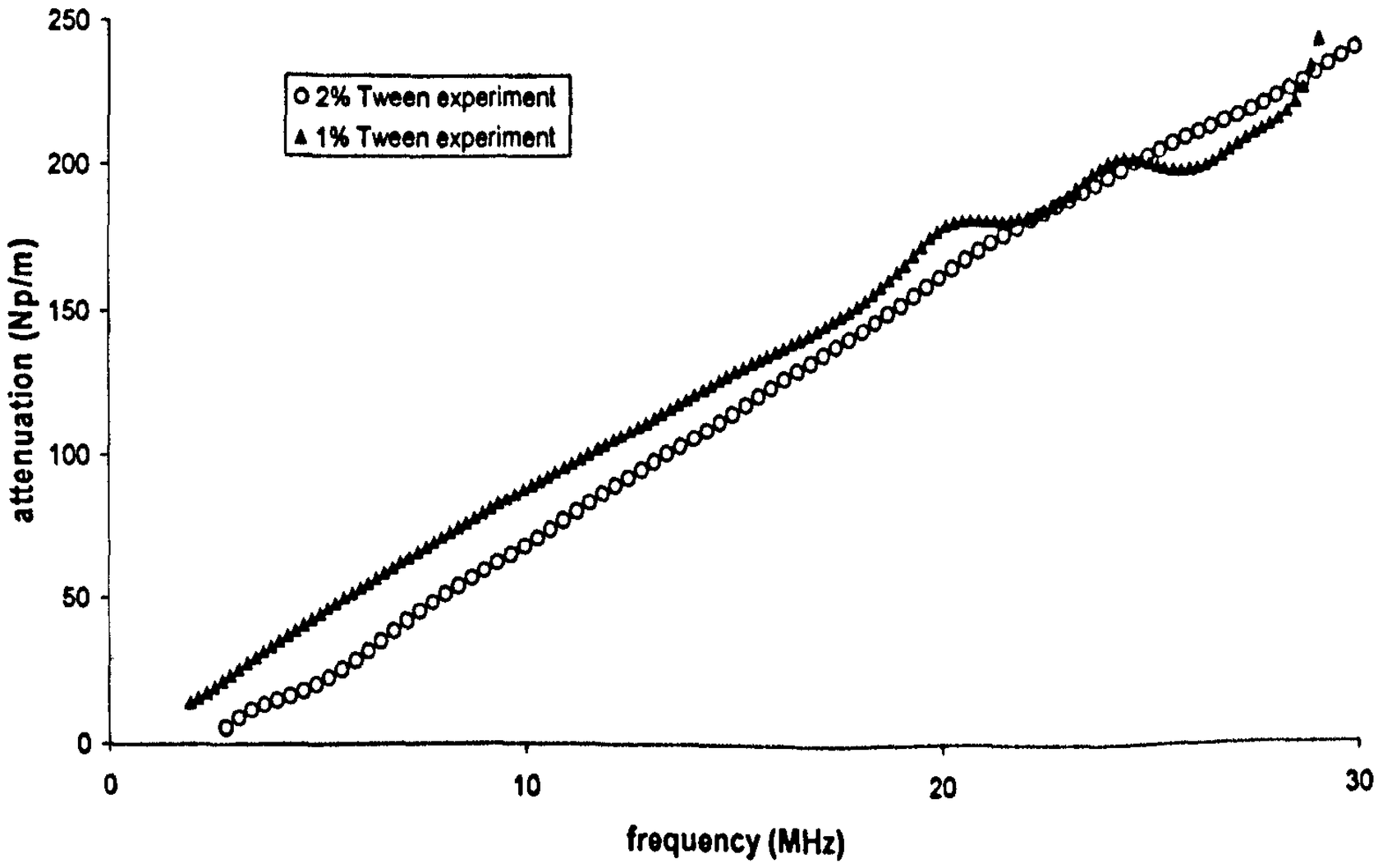

Figure 6.1. Experimental results for attenuation in 5% v/v n-hexadecane oil-in-water emulsions. The triangle line is the result for the emulsion with 1% Tween; the circled line is the result for the emulsion with 2% Tween.

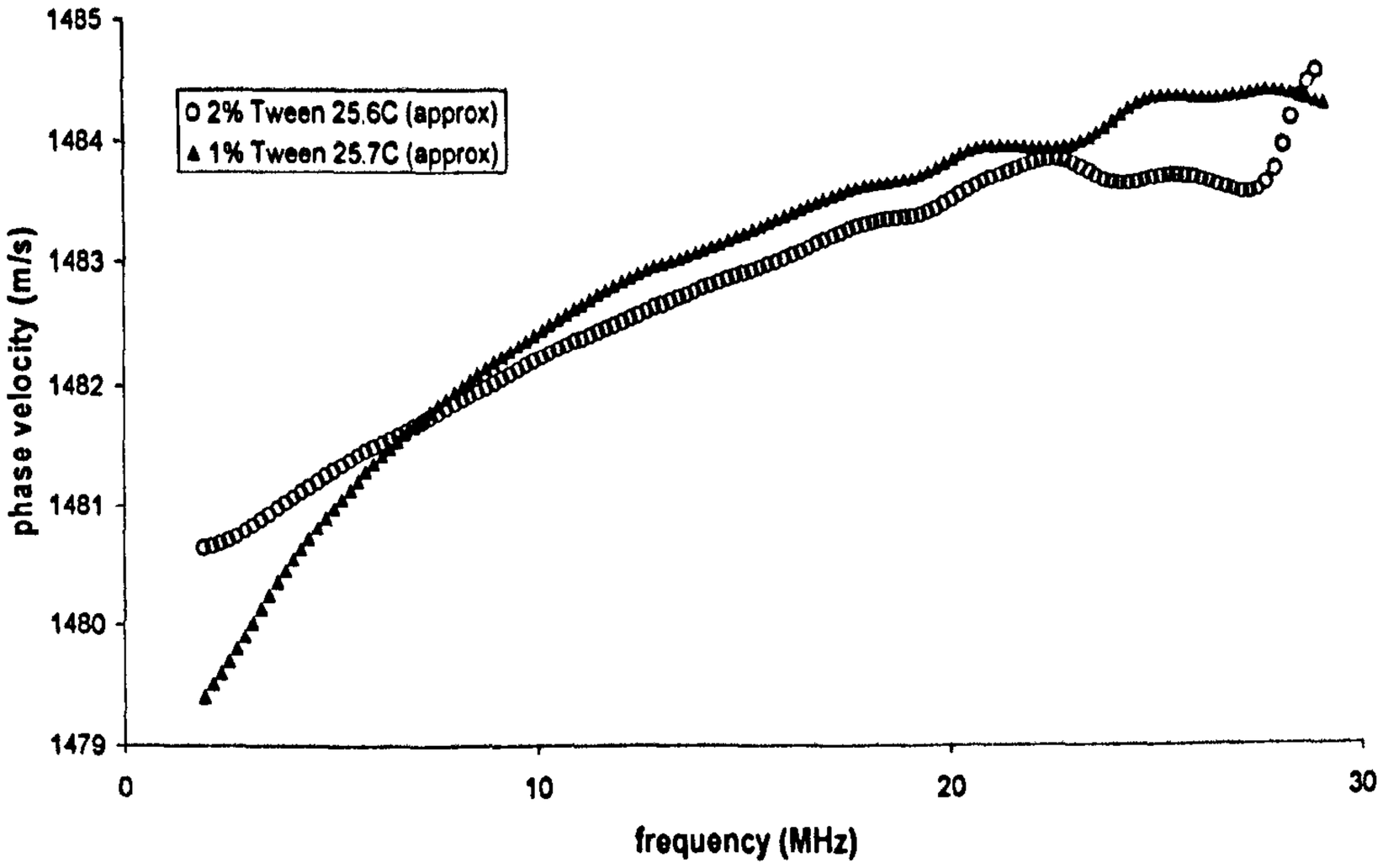

Figure 6.2. Experimental results for phase velocity in 5% v/v n-hexadecane oil-in-water emulsions. The triangle line is the result for the emulsion with 1% Tween; the circled line is the result for the emulsion with 2% Tween.

6.2.3 Simulations using ECAH model

In order to characterize the properties of these emulsions, it was necessary to measure the particle size distributions (PSDs) without disturbing the mixture. The PSDs of these emulsions are generally expressed in log-normal form because this reduces the number of parameters required in the fitting procedure (Challis et al, 2005) when using ultrasound for particle size analysis. The particles contained in the size range r to $r+dr$ in these mixtures are given by:

$$dN = Np(r)dr \tag{6.1}$$

where N is the number per unit volume, and

$$p(r) = \frac{1}{\sqrt{2\pi}\sigma r}\exp\left[-\frac{1}{2}\left(\frac{\ln r - \mu}{\sigma}\right)^2\right] \tag{6.2}$$

where μ is the logarithmic mean, and corresponds to the particle mean radius, and σ is the logarithmic standard deviation, a measure of the width of the distribution. It affects the maximum total particle concentration which can be achieved.

The basis of measuring the PSD using ultrasound spectrometry is to use the appropriate scattering model to predict ultrasonic attenuation as functions of frequency and with particle radius and volume fraction as its parameters. It can be calculated as follows: a first estimate of the mean droplet size μ and the standard deviation σ is used to calculate the ultrasonic attenuation using the appropriate scattering theory. The most commonly used model is that of ECAH, equation 2.25. The predicted values are then compared with the experimental values, the difference between predicted and measured data was determined, and then the sum of the squares of the differences (SSD) is calculated (McClements, 1996). For example, the SSD calculation using ultrasonic attenuation measurements as a function of frequency is given by:

$$SSD = \sum_i \left(\alpha_{theory}(f_i) - \alpha_{exp}(f_i)\right)^2 \tag{6.3}$$

where $\alpha_{theory}(f_i)$ is the predicted ultrasonic attenuation coefficient at a particular frequency f_i using the scattering theory, and $\alpha_{exp}(f_i)$ is the experimentally measured value.

Varying mean μ and standard deviation σ, the attenuation calculated and compared with experimental data until the SSD error is minimised. Once the values of the mean particle size and the standard deviation have been determined, the particle size distribution $p(r)$ can be calculated using

equation 6.2. In some complex cases, a bimodal distribution is used to increase the reliability of the distribution curve.

As we mentioned above, the ECAH model is widely used in determining the PSDs, it requires discrete values of particle radius as input whereas the log-normal distribution is a continuous function; there is thus a problem in deciding on the number of size bins used to discretize the continuous distribution. Figure 6.3 shows the influence of different numbers of size bins in the particle size distribution, where 9, 11 and 15 bins were used in the calculation, we can see the mean particle radius is nearly the same value, and the standard deviation is similar as well. This figure shows that the number of bins has little influence on the distribution curve, and 9 bins are enough to describe the particle distribution. For the distribution of the bins in particle size, Challis *et al* (2005) suggested that a simple logarithmic progression centred on a modal value μ is enough, so the bin sizes are:

$$r = \frac{\mu}{x^4}, \frac{\mu}{x^3}, \frac{\mu}{x^2}, \frac{\mu}{x}, \mu, x\mu, x^2\mu, x^3\mu, x^4\mu \tag{6.4}$$

where x represents the logarithmic increment in particle radius r. Given the value μ, the bin heights can be calculated using the following equation:

$$\phi(r) = \frac{p(r)r^3}{\exp\left(3\mu + \frac{9}{2}\sigma^2\right)} \tag{6.5}$$

Previous experience has indicated that a value of $x = 3$ works well in most situations, although in cases where an unacceptable fitting error arises the value of x itself can be taken into the fitting procedure and set to values greater or less than three (see Challis et al, 2005).

The PSDs measured in these experiments are compared with those obtained using the *Mastersizer* instrument in figures 6.4a and 6.4b. There are two curves in each figure, one corresponds to measurement on the *Mastersizer 2000*, and the other from the attenuation fit. From figures 6.4a and 6.4b we see that the values of the mean particle radius are similar for both curves; however the standard deviation was larger when determined by the ultrasound method than by *Mastersizer*, resulting in a broader distribution curve, which means that around the mean diameters, there is a smaller frequency of sizes of particles. The difference of the width of the distribution curves could be caused by many reasons: such as, the different thermo-physical properties used in the two methods, the different frequency range measured in the two methods, the different number of input parameters and the different measured attenuation accuracy between the two methods.

The PSDs measured using ultrasound spectrometry were obtained by adapting the ECAH model to measured attenuation data in a least squared error sense. We note here that in the case of ECAH the adaptation process was based on the full matrix form of ECAH with the extension of Lloyd and Berry (1967). The question now arises as to whether the resulting PSD would in reality give rise to the attenuation that was initially measured. In order to test this we have recalculated attenuation using these PSDs and compared the results with the original experimental data. The accuracy of the measured attenuation for all the frequencies is given by the merit quality (the lower merit, the better fit). The merit quality is defined (Malvern 1998) as:

$$Meritquality(\%) = \frac{1}{N}\sqrt{\sum_{i=1}^{N}\left(\frac{\alpha_{theory}(f_i)-\alpha_{exp}(f_i)}{\alpha_{exp}(f_i)}\right)^2} \times 100\% \qquad (6.6)$$

where N is the number of point in the attenuation spectrum.

Figure 6.5 shows the experimental attenuation spectra and the simulation data predicted using the ECAH model of Lloyd and Berry by using the PSDs measured by ultrasound spectrometry. Also shown in this figure is the ECAH model simulation data with the PSDs obtained by the *Mastersizer*. We can see there is a good agreement between these simulation data, and both of them closely follow the experimental data from about 3 MHz to nearly 25 MHz. The merit qualities calculated from equation 6.6 are 1.3% and 2.7% for the *Mastersizer* and the ultrasound method, respectively. This factor represents the precision of the fit and is related to the accuracies of the predicted attenuation, obtained from the determined PSD, in comparison with the measured one. We therefore can conclude that the particle size distributions calculated using the ultrasonic method are as accurate as those obtained by the *Mastersizer*.

The *Mastersizer 2000* is used as a reference technique for the particle size distribution measurement and can provide precise distribution data. Therefore, in the following experiments, all the simulations are calculated using the PSDs measured by the *Mastersizer* instead of the ultrasound method, in order to test the applicability of different models. However, this technique needs sample dilution and not suitable for working in-line, the ultrasound spectrometry is then used in the PSD measurement for emulsions with different concentrations as a comparison with the *Mastersizer* results.

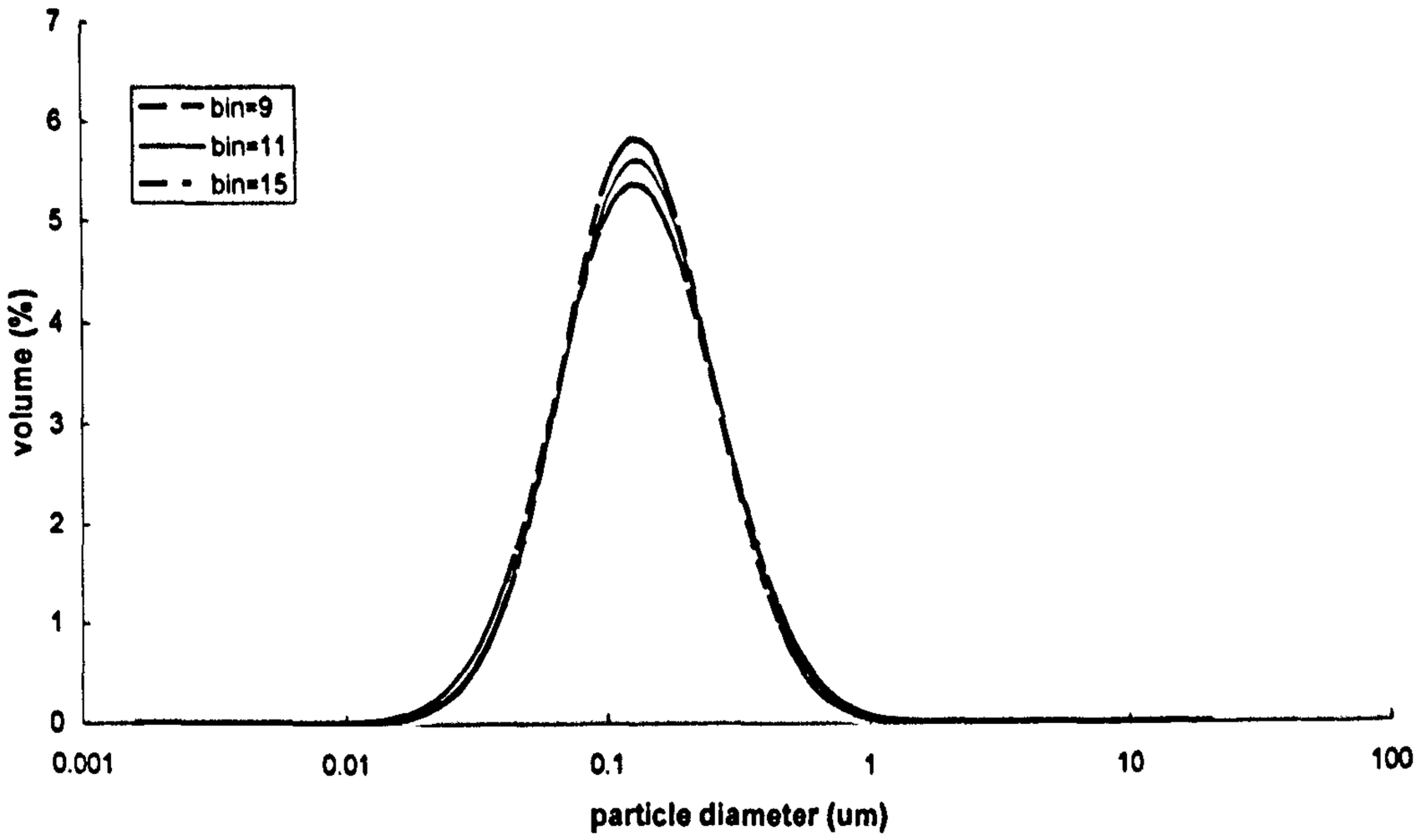

Figure 6.3. Particle size distribution for 5% n-hexadecane oil-in-water emulsion with 2% Tween using different bins. The broken line is for 9 bins; the solid line for 11 bins, and dash line for 15 bins.

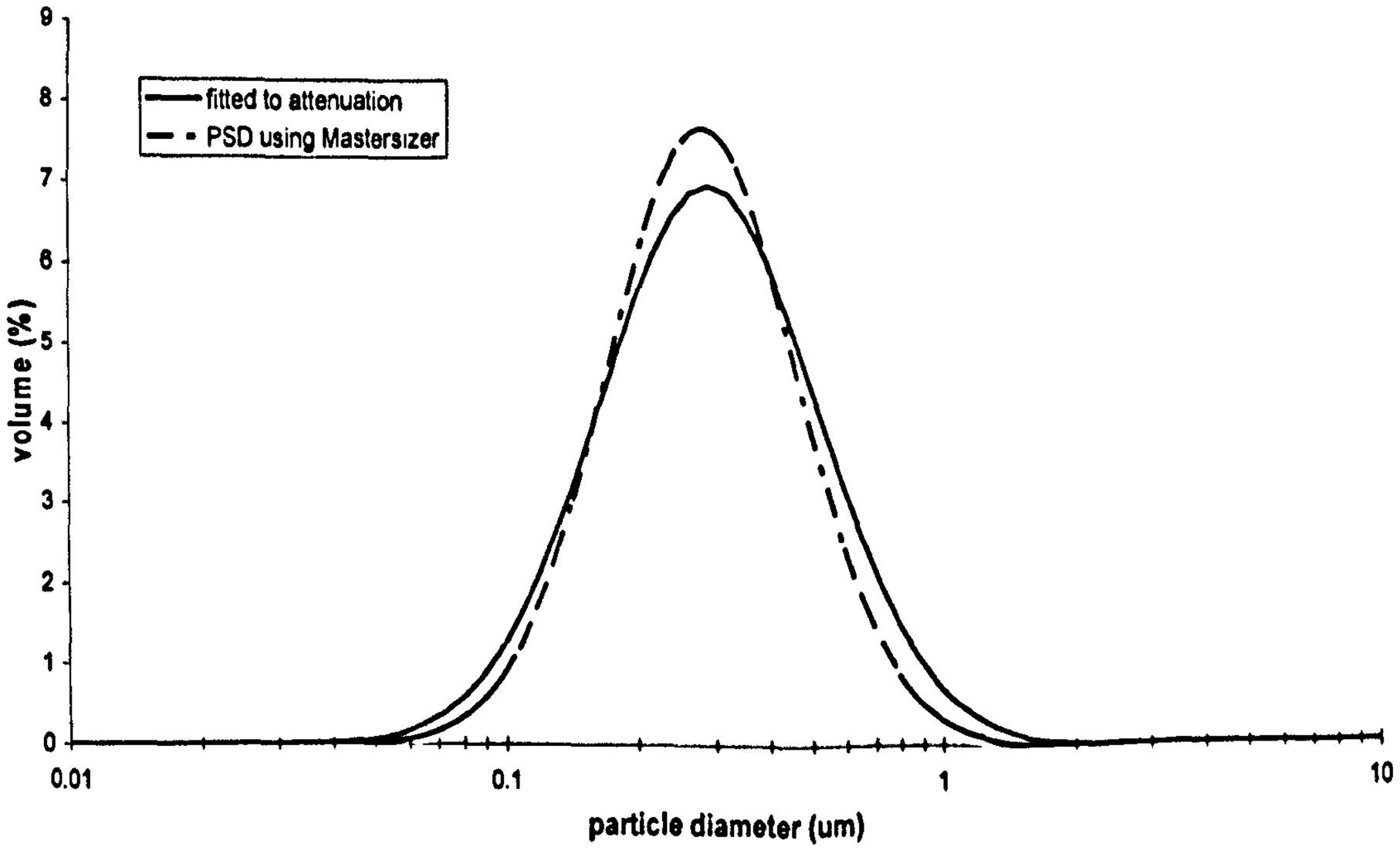

Figure 6.4a. Particle size distribution for 5% n-hexadecane in water emulsion with 1% Tween. The broken line is the measurement using *Mastersizer*; the solid line is the measurement using attenuation data.

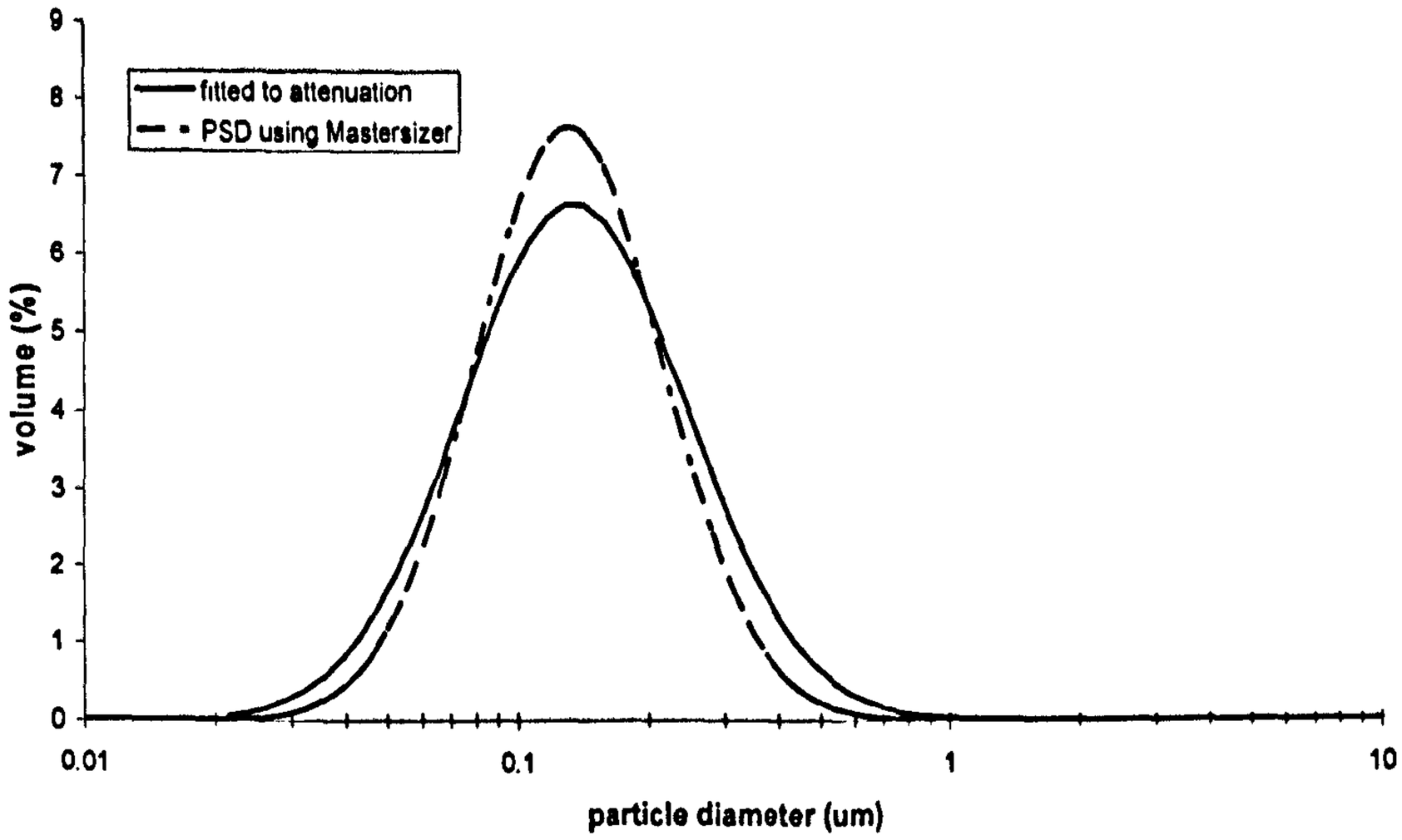

Figure 6.4b. Particle size distribution for 5% n-hexadecane in water emulsion with 2% Tween. The broken line is the measurement using *Mastersizer*; the solid line is the measurement using attenuation data.

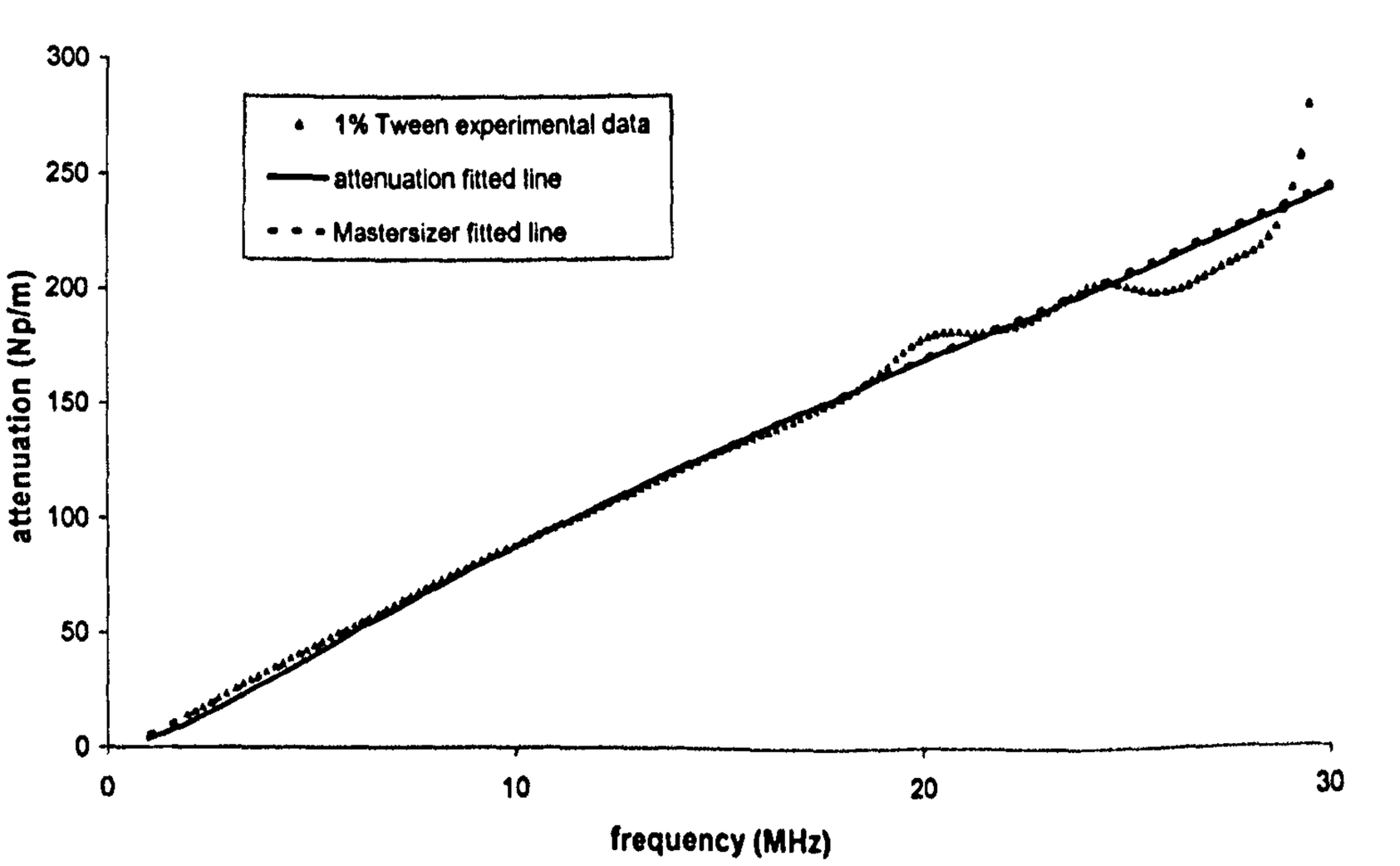

Figure 6.5a. Experimental data (triangles) and simulation with ECAH model for 5% n-hexadecane in water with 1% Tween using the particle size distribution shown in figure 6.4a. The solid line is the attenuation fitted data, and the dash line is the *Mastersizer* PSD fitted data.

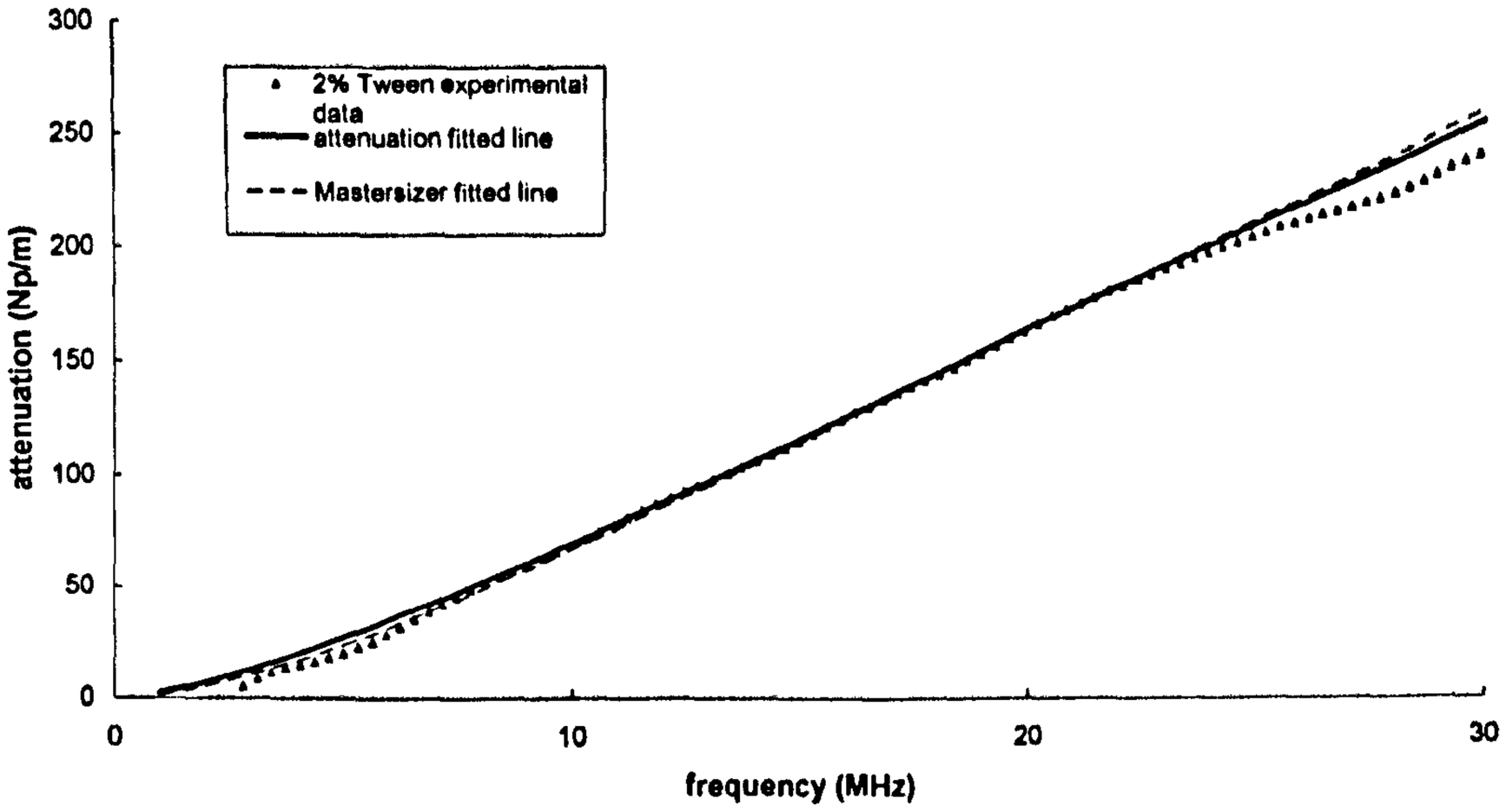

Figure 6.5b. Experimental data (triangles) and simulation with ECAH model for 5% n-hexadecane in water with 2% Tween using the particle size distribution shown in figure 6.4b. The solid line is the attenuation fitted data, and the dash line is the *Mastersizer* PSD fitted data.

6.3 Experiment 2: 1-bromohexadecane oil-in-water emulsions with large particle radius at different concentrations

6.3.1 Emulsion preparation

The aim of the following experiments was to investigate the applicability of the ECAH model to the study of density-matched oil-in-water emulsions of low (6.25% v/v) and high (50% v/v) concentration and with small (0.09 μm) and large (1.2 μm) particle radii. The match with the density of water is expressed as the ratio of densities $\frac{\rho_{water}}{\rho_{bhex}} = 0.997$. Thermal phenomena will be dominant in the attenuation mechanism, and viscoinertial effects can be neglected. The ECAH explicit expressions for A_0 and A_1 terms are enough in

the attenuation calculation, although it is likely that A_1 can be neglected. The thermo-physical properties of the continuous phases and dispersed phase are shown in table 6.1.

To obtain emulsions with other particle concentrations, the 50% v/v emulsion was diluted. For example, for a 200 ml 25% v/v emulsion, 100 ml distilled water is added to 100 ml 50% v/v emulsion then blended it to make it uniformly dispersed. Other concentrations were prepared in the same way.

The size of the droplets in the emulsions was measured using a commercial particle-sizing instrument based on static light scattering (Horiba, LA-900, Irvine, CA). For a very dilute (< 0.01%) 1-bromohexadecane oil-in-water emulsion, the PSD is shown in figure 6.6, which is not a log-normal distribution. The median droplet radius measured by the light scattering technique was 1.2 μm.

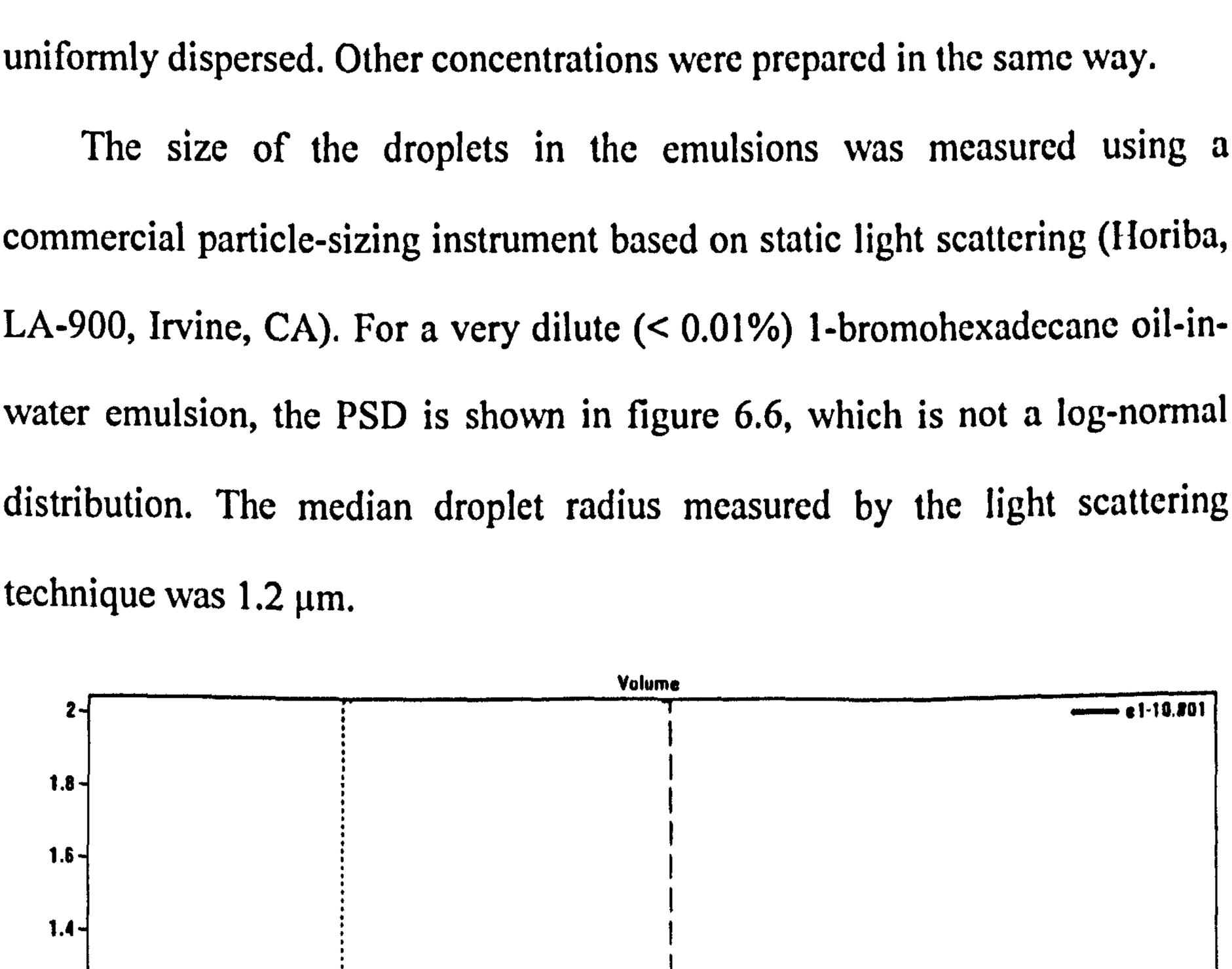

Figure 6.6. The particle size distribution of the diluted (<0.01% v/v) 1-bromohexadecane oil-in-water emulsion estimated using the optical method. Median particle radius is 1.2μm.

6.3.2 Experimental results

The same experimental method is used as described in section §6.2.2. The only difference here is the extension of the frequency range. In this experiment, the ultrasonic attenuation spectra were measured in the frequency range from 3 MHz to 37 MHz using two different Perspex test cells and three different broadband ultrasonic transducers (10 MHz, 20 MHz and 30 MHz) to cover the whole range. The first test cell was used for low frequency measurements (10 MHz transducer), which had a 26 mm gauge length; the second test cell was used for middle to high frequency measurements (20 MHz and 30 MHz) with options for 8 mm or 4 mm gauge lengths. Again, the average of five separate samples was calculated as the final attenuation.

Figures 6.7 to 6.10 show the experimental attenuation data obtained for emulsions at different concentrations. There are three lines in each figure, each line corresponds to an attenuation result for different centre-frequency transducers. These figures show that the attenuation results from the different transducers coincide or are close to a single isotonic curve. This coincidence gives confidence in the experimental techniques. All of the attenuation curves showed a discontinuity between 37 MHz and 40 MHz. This is attributed to the effects of noise mapping nonlinearly into the measurements at high attenuations (see chapter 5, section §5.4.1, figure 5.19). It is concluded here that the working limits for all of the measurement frequencies were in the range from 3 MHz to 37 MHz.

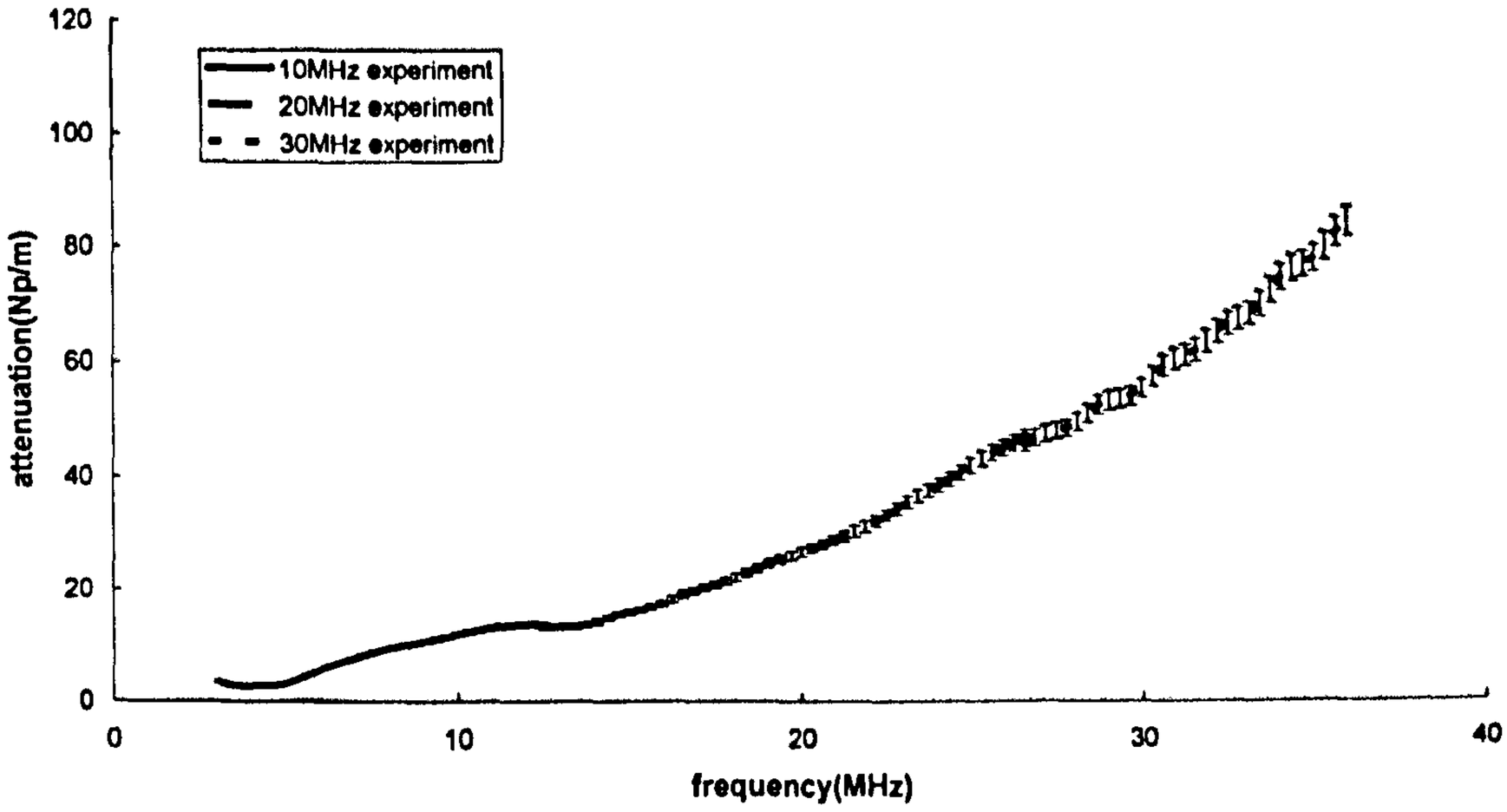

Figure 6.7. Experimental attenuation for 6.25 % 1-bromohexadecane oil-in-water emulsion, using different centre frequency transducers, with the error bars ($\pm 5\%$) shown on the attenuation curve. The solid line is the measurement for 10 MHz transducer with 26 mm gauge length, the broken line for the 20 MHz transducer with 8 mm gauge length, and the dotted line for the 30 MHz transducer with 4 mm gauge length.

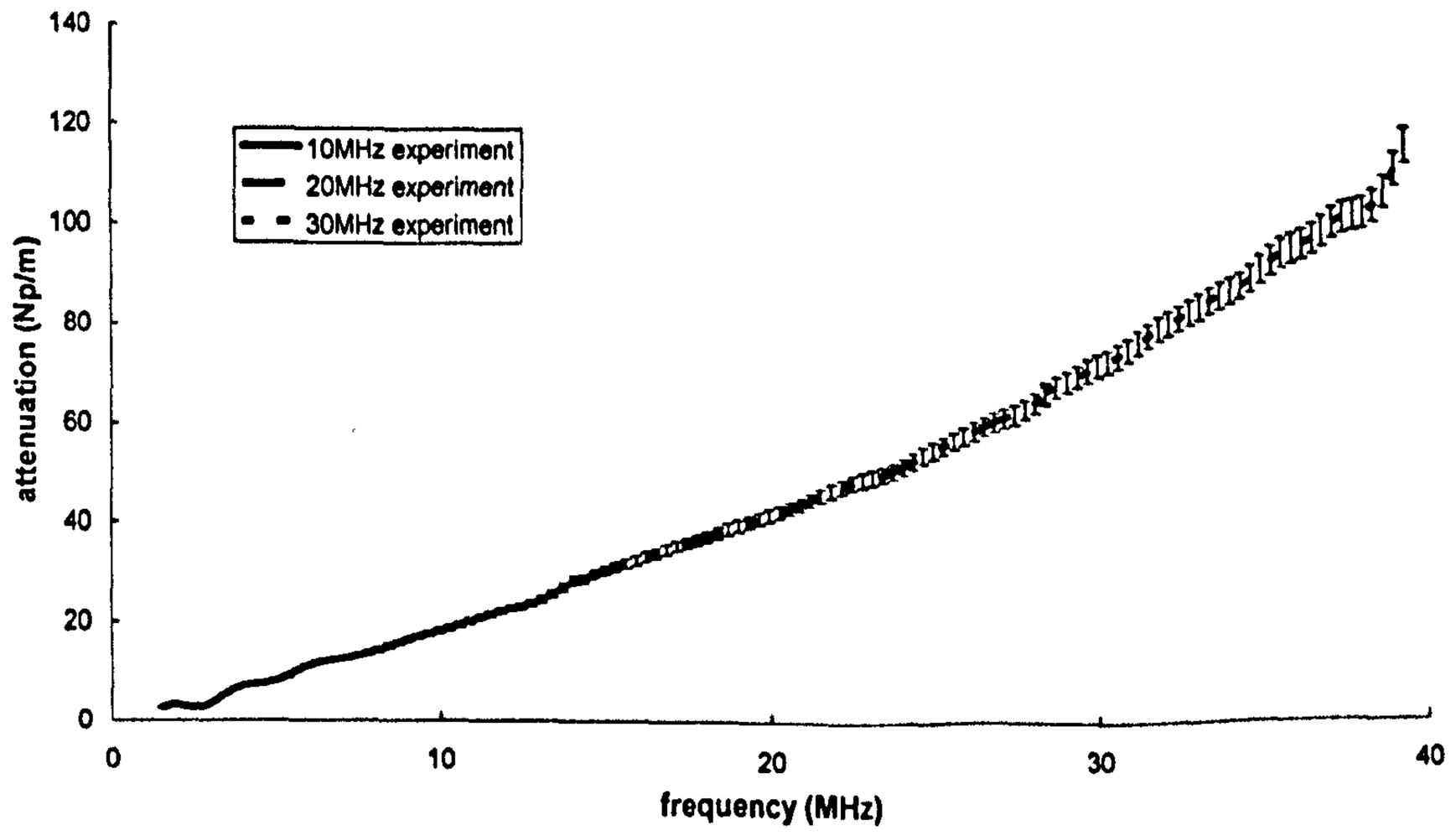

Figure 6.8. Experimental attenuation for 12.5 % 1-bromohexadecane oil-in-water emulsion, using different centre frequency transducers. The line descriptions are the same as those in figure 6.7.

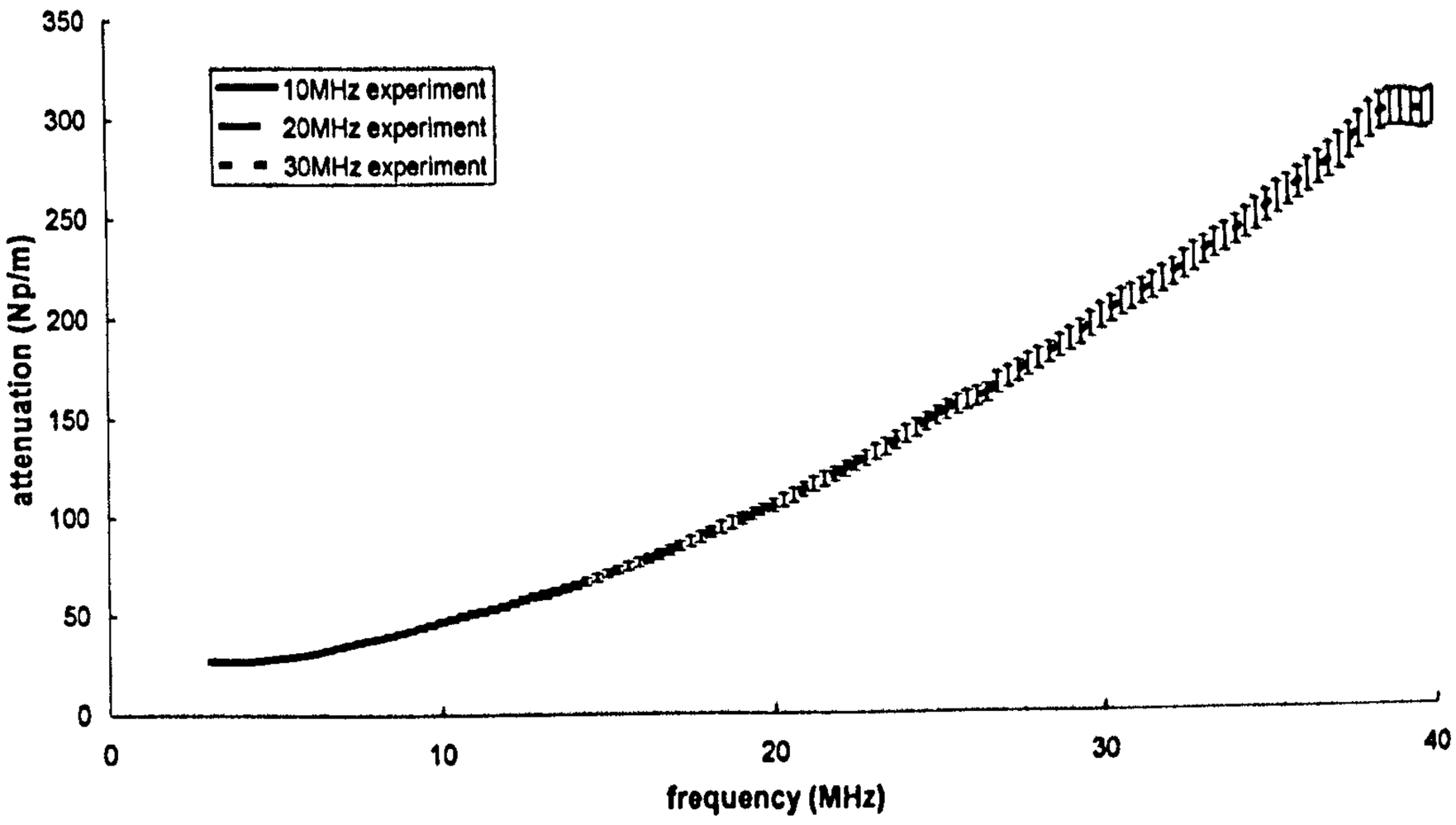

Figure 6.9. Experimental attenuation for 25 % 1-bromohexadecane oil-in-water emulsion, using different centre frequency transducers. The line descriptions are the same as those in figure 6.7.

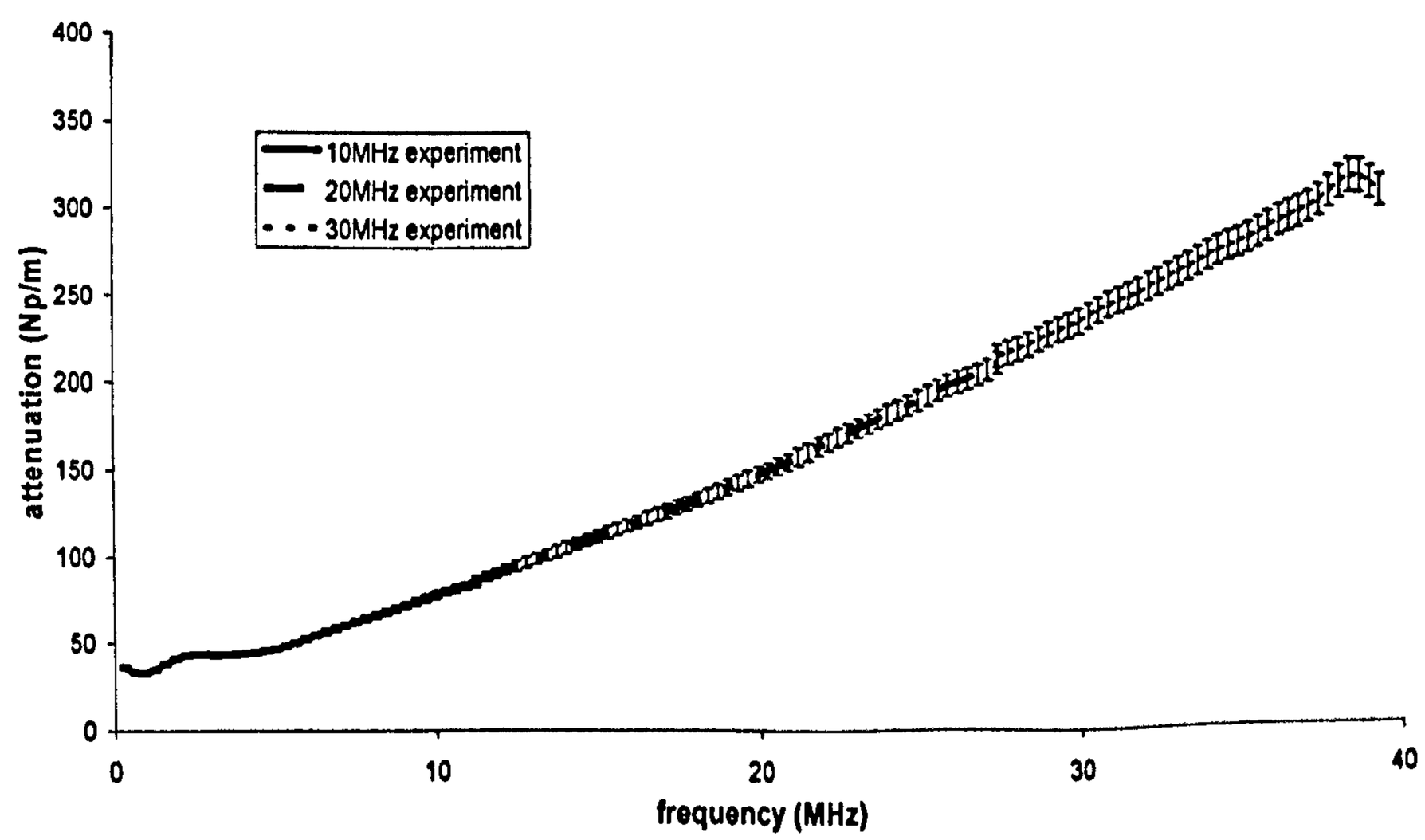

Figure 6.10. Experimental attenuation for 50 % 1-bromohexadecane in water emulsion, using different centre frequency transducers. The line descriptions are the same as those in figure 6.7.

6.3.3 PSD measurement and simulations

The PSDs for all emulsions with different concentrations are measured using the method discussed in section §6.2.3 and are plotted in figure 6.11. Two models were used in the PSD calculations: the full ECAH model with Lloyd and Berry and the HHM model. The first observation from figure 6.11 is that the mean particle diameters have nearly the same value after dilution, which means that the mean particle diameter is relatively insensitive to the droplet concentration. The second observation is for higher concentrated emulsions, there is a slight difference in the standard deviation compared to that at the lower concentrations, which implies that the maximum value of the concentrations was different as well. Now we are trying to compare the PSD results calculated using the ECAH model and the HHM model. We can see that the mean particle diameters gave the same result for the same particle concentration even at high volume fraction, which gives the confidence that the ECAH model still can be used for emulsions with large particle radius even at high concentrations. However, the standard deviation is larger when determined by the HHM model than by the ECAH model, resulting in a broader distribution curve, which means that around the mean diameters, there is a wider range of particle sizes. The main reason for this difference is because the ECAH model requires more independent parameters than the HHM model.

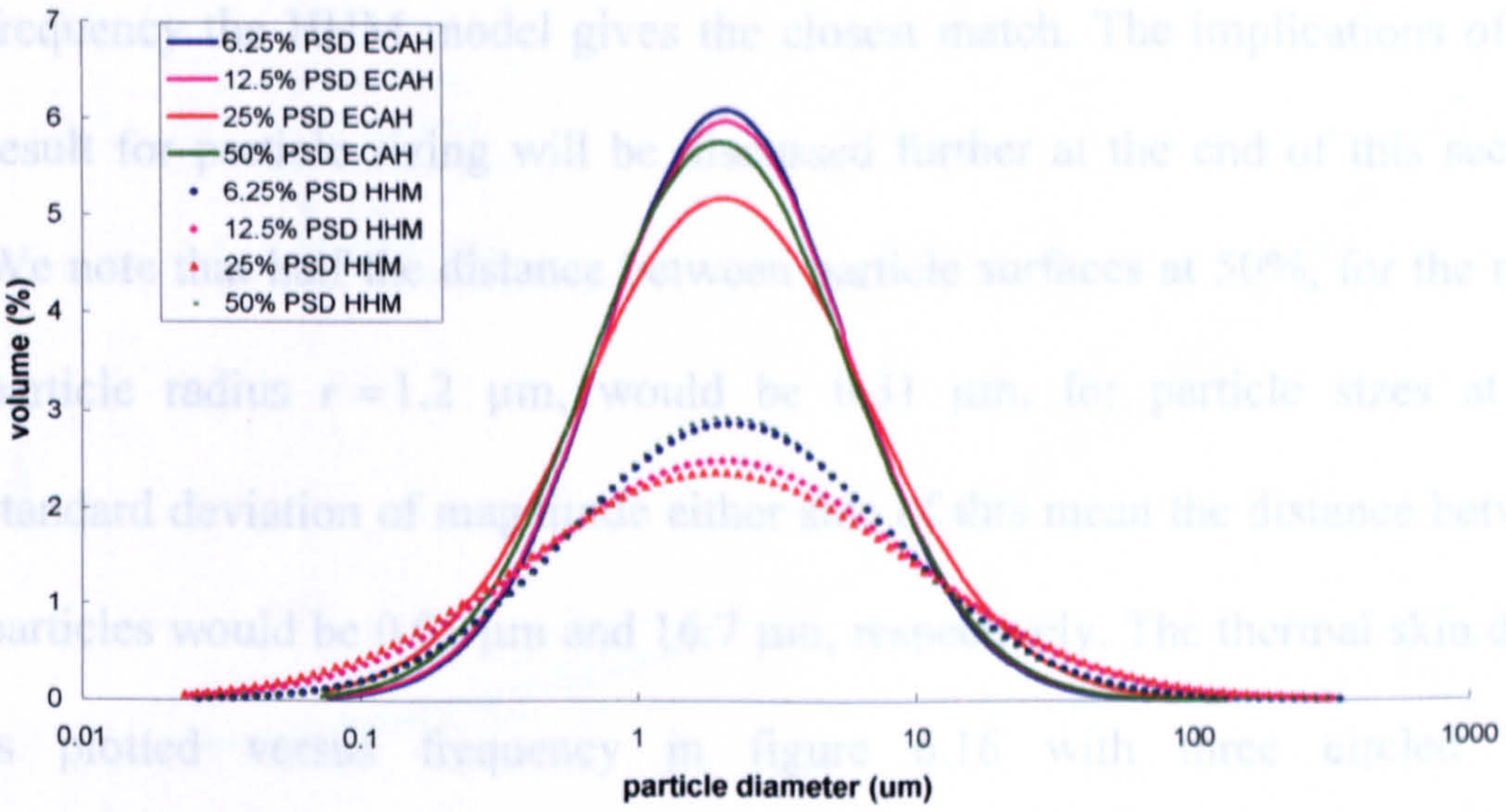

Figure 6.11. The PSDs of the 1-bromohexadecane oil-in-water emulsions, calculated using the full ECAH model and the HHM model. The blue lines represent the PSDs for 6.25%, the pink lines for 12.5%, the red lines for 25%, and the green lines for 50%.

The simulation data were calculated using four different models — the 'full' ECAH model with Lloyd and Berry, the ECAH model simplified to its explicit approximations, the HHM model, and the CP model of Evans and Attenborough. All the calculations are based on the particle size distribution obtained by the optical method, and the results for a series of oil concentrations are shown at figures 6.12 to 6.15.

The first observation is that the three models based on the ECAH formulation give results that are very close to each other and that they are also close to the experimental data. The second observation is that the coupled phase theory of Evans and Attenborough gives attenuations that are very much smaller than these observed experimentally — except at the very low frequencies, below 7 MHz for the 6.25% and 12.5% concentrations, and below 3 MHz for the 25% and 50% concentrations. Turning now to the small difference between the ECAH based models we note that all three give similar

predictions up to approximately 25 MHz for all concentrations; above that frequency the HHM model gives the closest match. The implications of this result for particle sizing will be discussed further at the end of this section. We note that half the distance between particle surfaces at 50%, for the mean particle radius $r = 1.2$ μm, would be 0.31 μm, for particle sizes at one standard deviation of magnitude either side of this mean the distance between particles would be 0.01 μm and 16.7 μm, respectively. The thermal skin depth is plotted versus frequency in figure 6.16 with three circled lines corresponding to the three half-interparticle spacings. We note that for the majority of the particle sizes the half distance between particles is greater than the thermal skin depth, although there will be some smaller particles where this half distance is less than the skin depth. We would thus expect the ECAH model to apply quite well but not perfectly.

We also note that the earlier assumption that only partial wave coefficients A_0 and A_1 would be required in the analysis has been borne out in practice. As we showed in figure 2.6a for 12.5% 1-bromohexadecane oil-in-water emulsion in chapter 2, the dominant part is A_0, the higher order terms of partial wave coefficients are much smaller than A_0, and they can be neglected in the attenuation calculation.

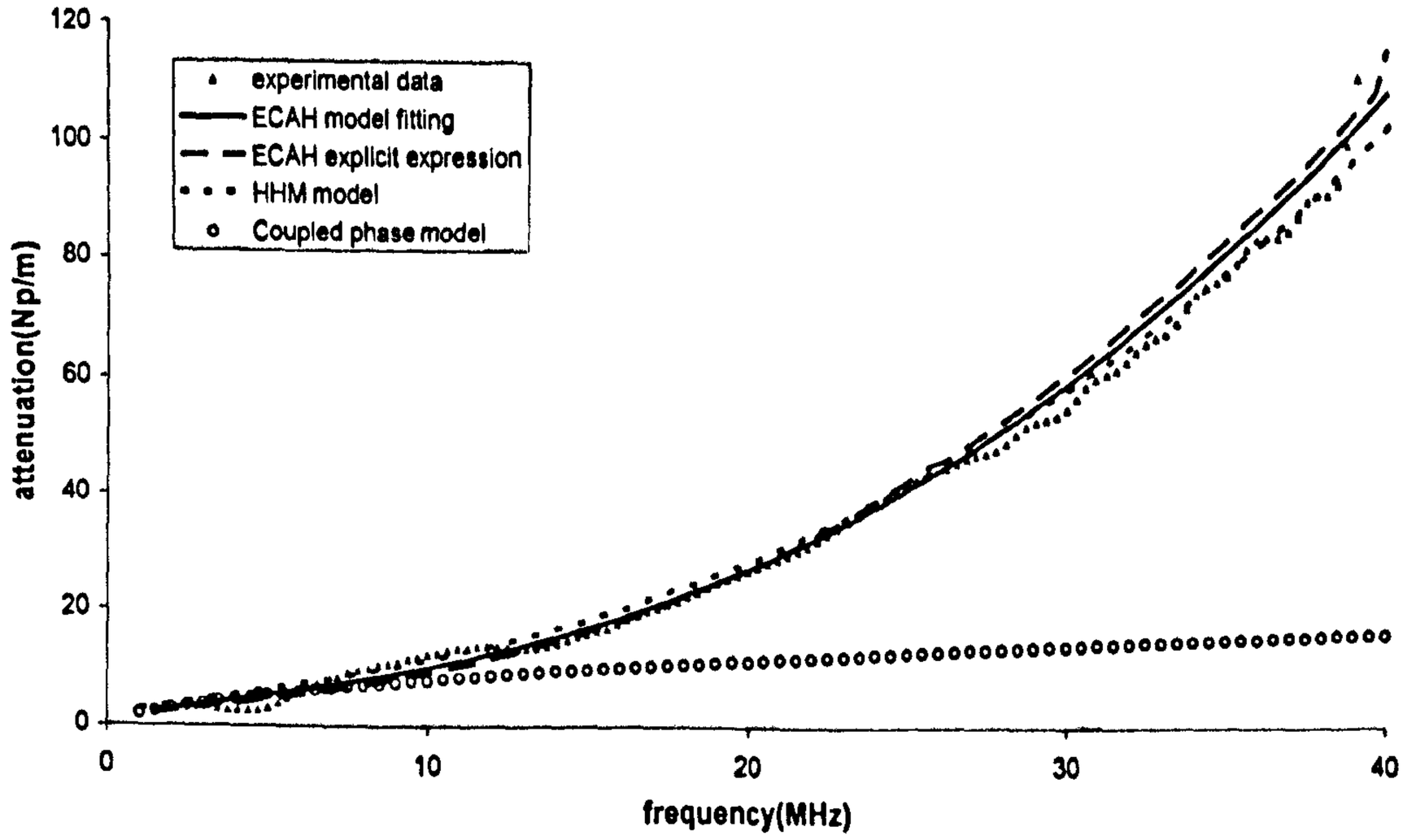

Figure 6.12. Attenuation and simulation data for 6.25% 1-bromohexadecane oil-in-water emulsion, calculated using the PSD obtained by optical method.

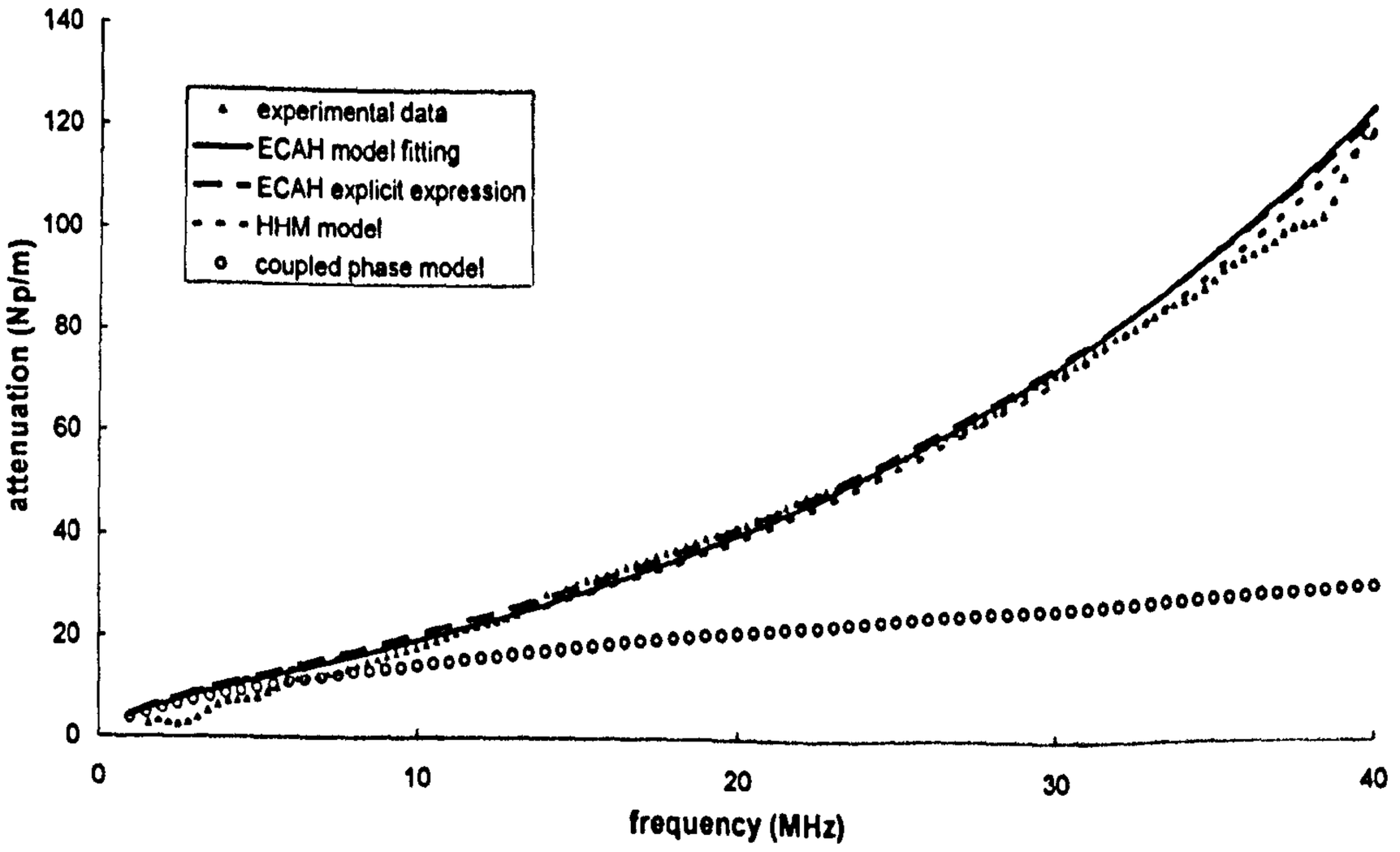

Figure 6.13. Attenuation and simulation data for 12.5% 1-bromohexadecane oil-in-water emulsion, calculated using the PSD obtained by optical method.

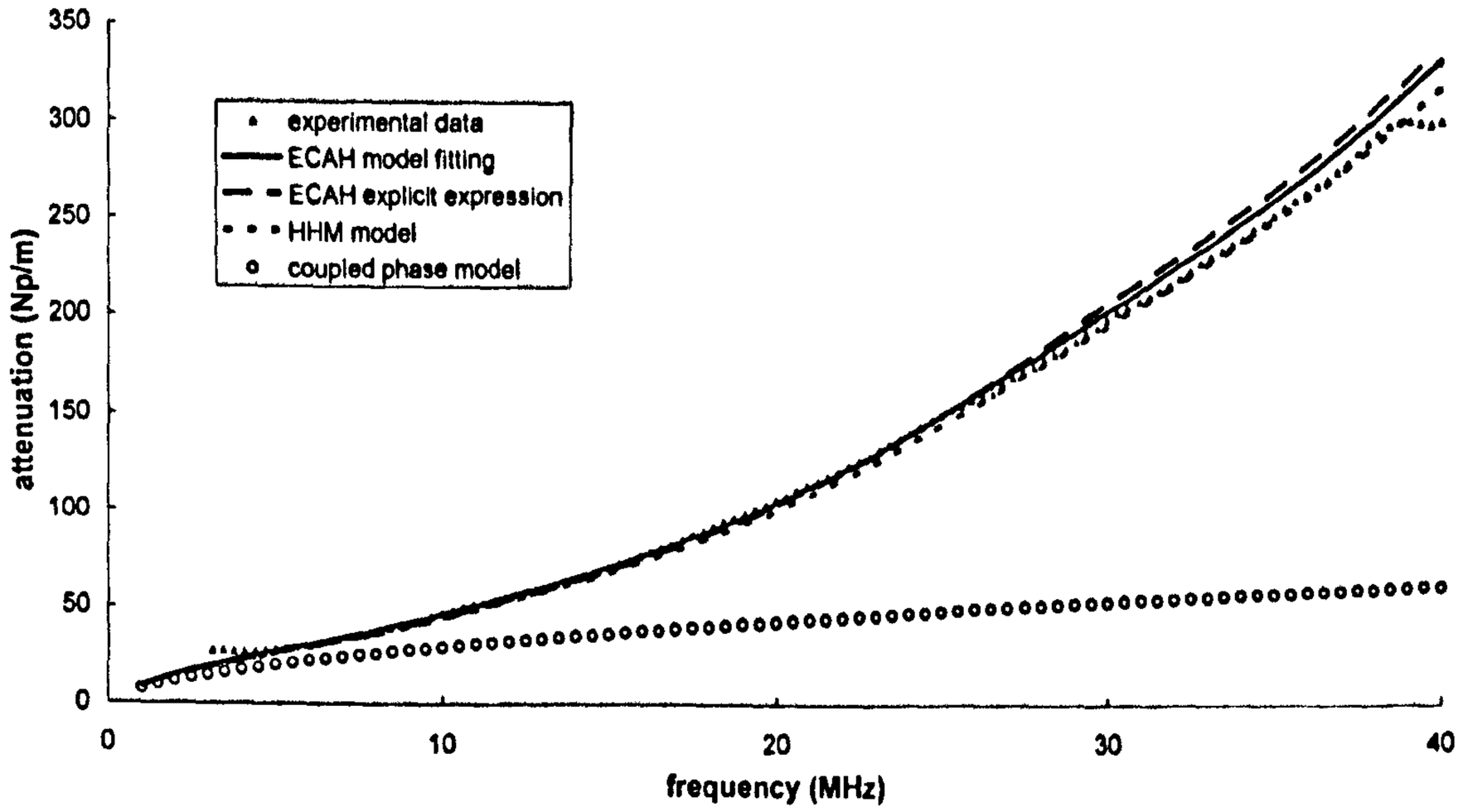

Figure 6.14. Attenuation and simulation data for 25% 1-bromohexadecane oil-in-water emulsion, calculated using the PSD obtained by optical method.

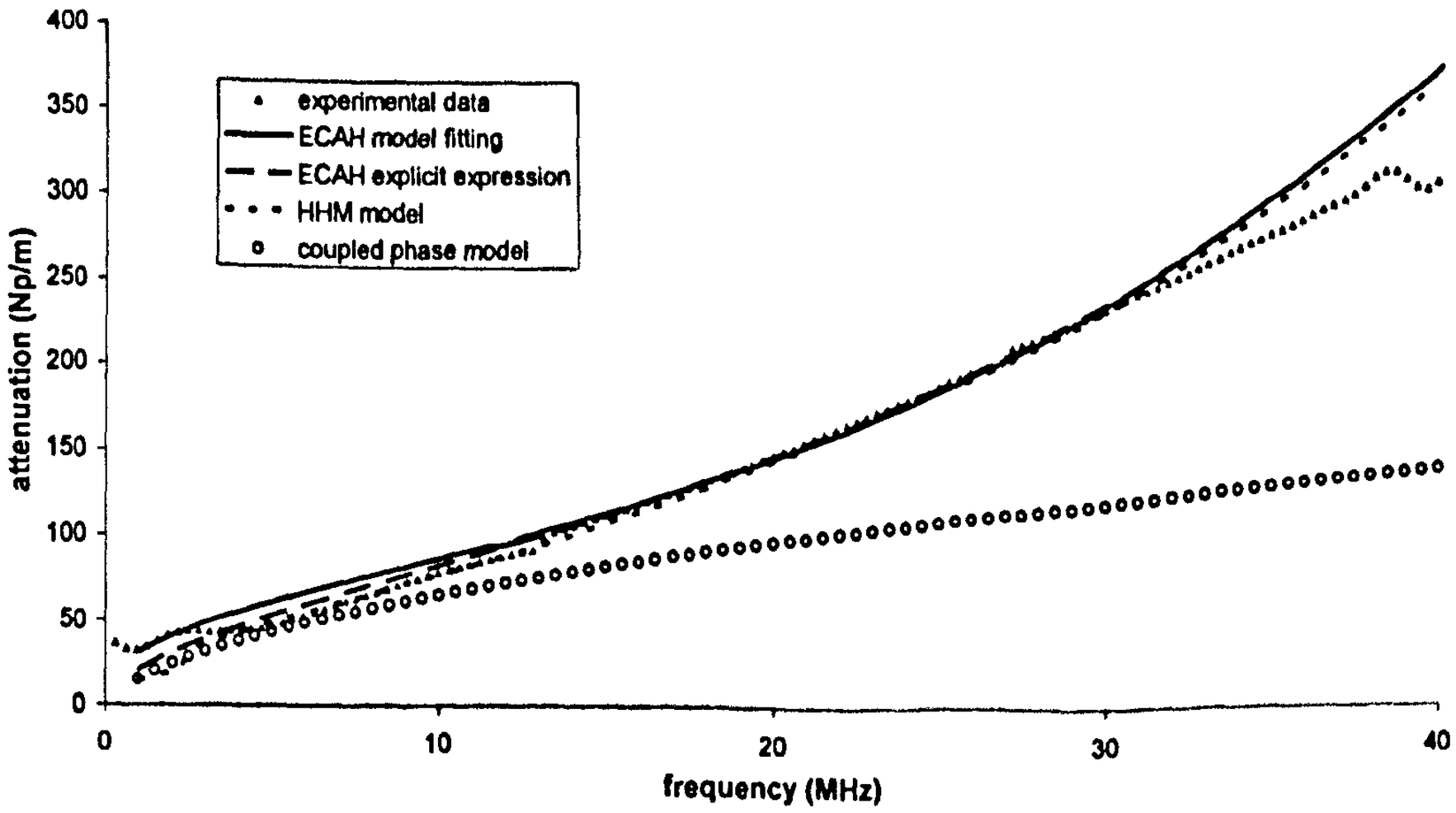

Figure 6.15. Attenuation and simulation data for 50% 1-bromohexadecane oil-in-water emulsion, calculated using the PSD obtained by optical method.

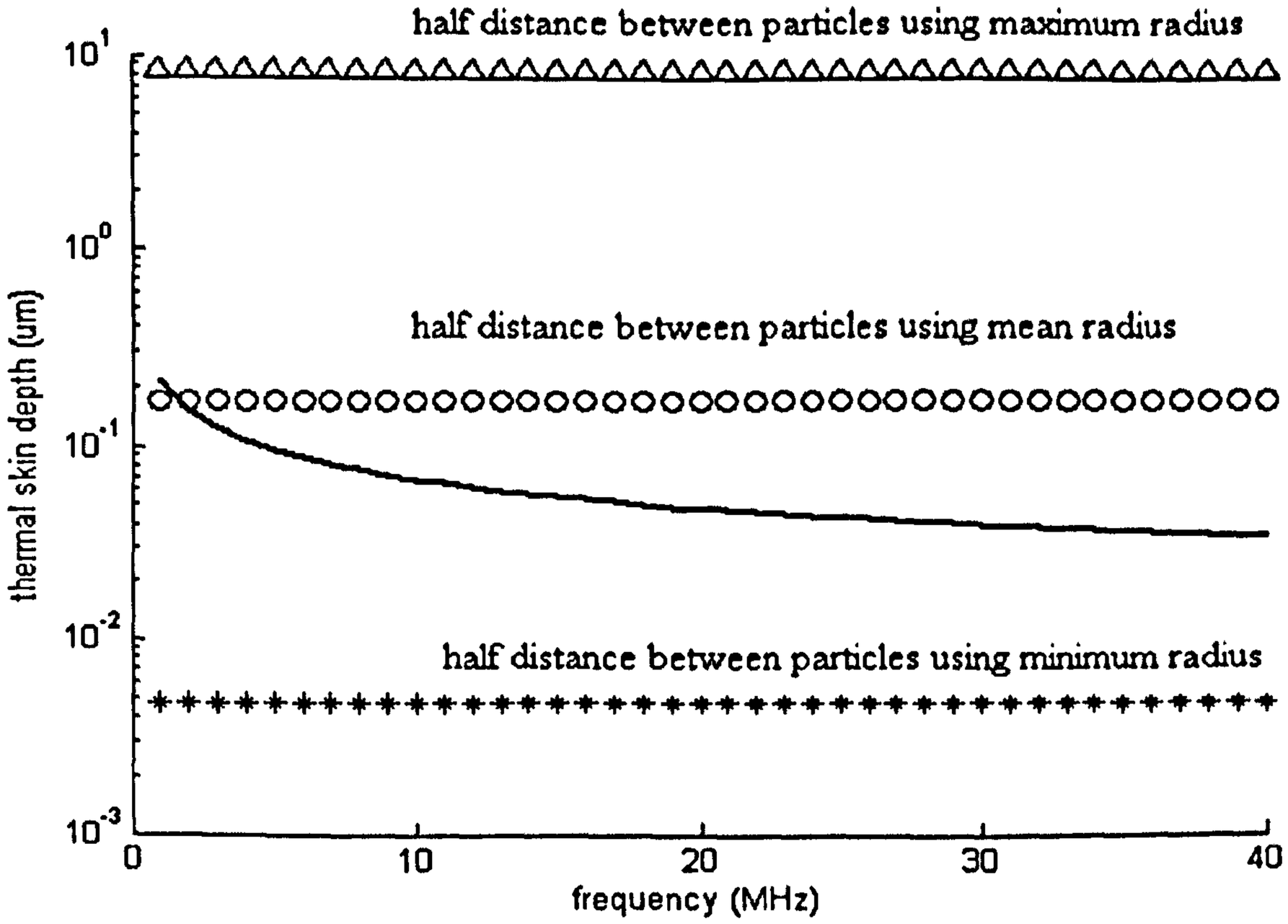

Figure 6.16. Thermal skin depth (solid line) versus frequency, also shown is the half-distance between particles at selected radii: the triangles for the maximum particle radius, circles for mean particle radius and the stars for the minimum particle radius.

6.4 Experiment 3: 1-bromohexadecane oil-in-water emulsion with small particle radius at different concentrations

6.4.1 Emulsion preparation

Emulsions of 1-bromohexadecane in water for different concentrations were prepared, this time with smaller particle radius. These emulsions were prepared by the Procter Department of Food Science at the University of Leeds and the particle size distributions were measured using the *Mastersizer* instrument (see figures 6.17 and 6.18) at that institution as before. For these experiments, both the aqueous and dispersed phase are exactly the same

materials as those in section 6.3, but the particle radius is much smaller, around 90 nm for the low concentrated emulsions, and around 120 nm for 50% emulsion. Because the 50% oil emulsion was made separately from the lower concentration emulsions, there is a slight difference in the mean particle sizes. This group of experiments was used to test the applicability of the ECAH model at small particle sizes, especially at high concentrations. Again, it was required to determine whether the ECAH explicit expression could be used to replace the full ECAH model in this situation, and also whether or not the McClements CS model and the Evans and Attenborough CP model are applicable.

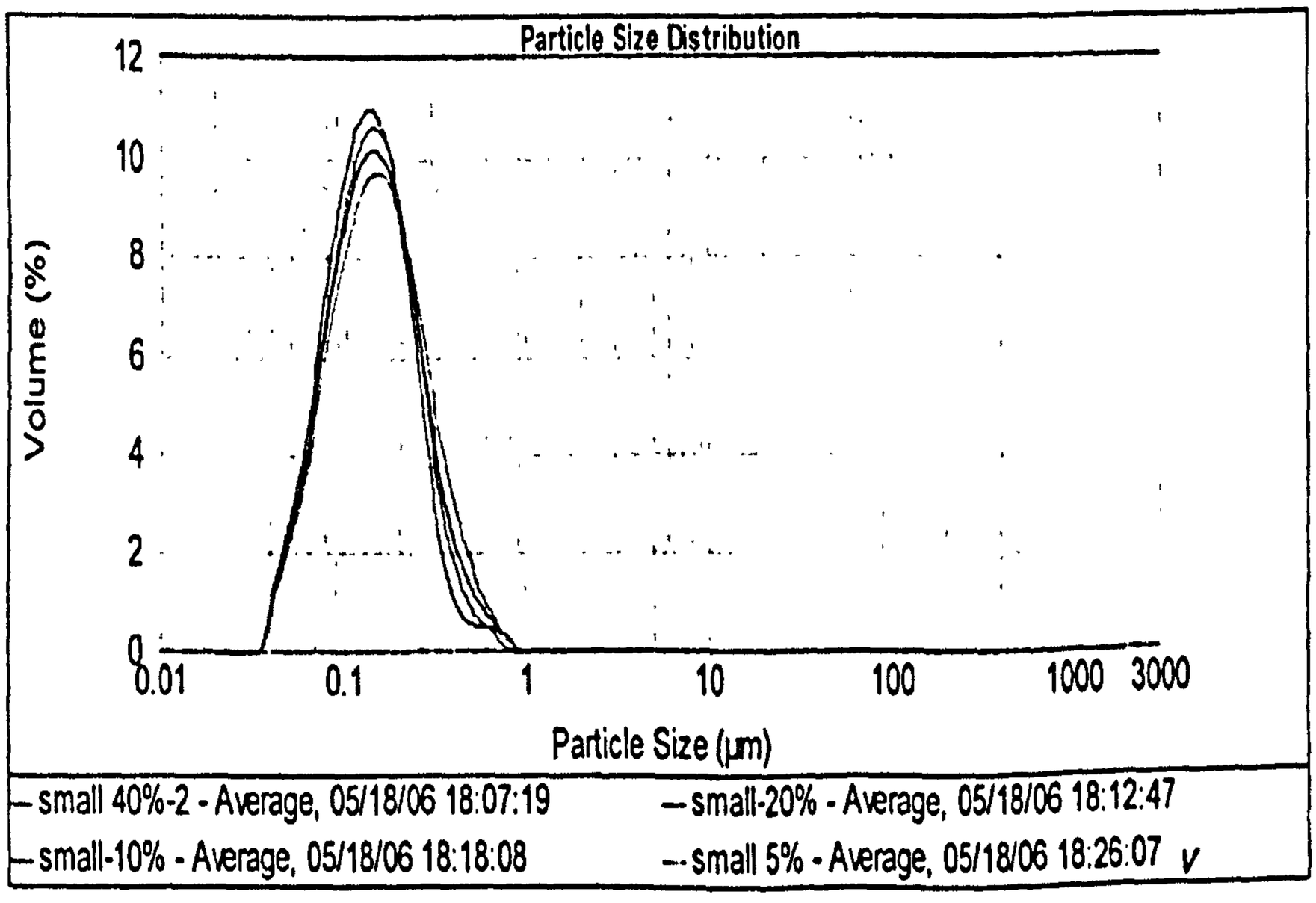

Figure 6.17. PSD for 5%,10%, 20% and 40% 1-bromohexadecane oil-in-water emulsion using the *Mastersizer*, calculated in Leeds University.

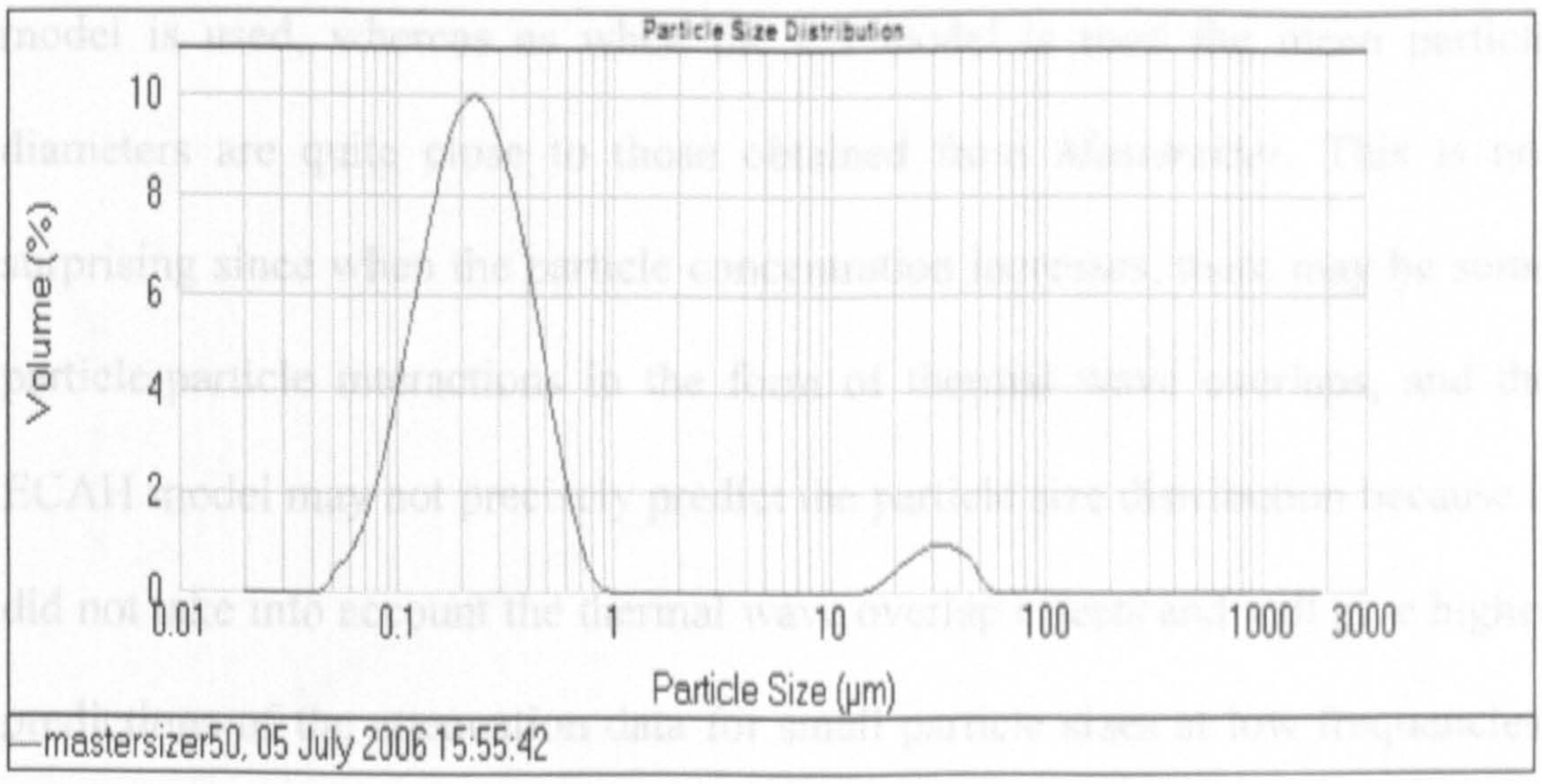

Figure 6.18. PSD for 50% 1-bromohexadecane oil-in-water emulsion using the *Mastersizer*, calculated in Leeds University.

6.4.2 Experiment results

The same test cell and transducers were used as in the previous experiment, section §6.3.2. Figures 6.19 to 6.23 give the experimental results for the 1-bromohexadecane oil-in-water emulsion with small particle sizes at different particle concentrations. The attenuation results from the different transducers lie close to a single isotonic curve, and the useable frequency range extended from 2 MHz to 37 MHz for emulsions up to 20%, and up to over 30 MHz for the high concentrations of 40% and 50%.

Figures 6.24 to 6.28 show the PSDs for each emulsion using the full ECAH model, and the McClements CS model, in comparison with the *Mastersizer* results. For particle concentrations smaller than 10%, the two models gave same values for both the mean particle diameter and the standard deviation, which are identical to the Mastersizer mean radius. For higher concentrations, the difference in PSDs using the two models becomes significant: the mean particle diameter appears to be larger when the ECAH

model is used, whereas as when the CS model is used the mean particle diameters are quite close to those obtained from *Mastersizer*. This is not surprising since when the particle concentration increases, there may be some particle-particle interactions in the form of thermal wave overlaps, and the ECAH model may not precisely predict the particle size distribution because it did not take into account the thermal wave overlap effects and will give higher predictions of the attenuation data for small particle sizes at low frequencies. The ECAH model may not be the best model for emulsions with small particle sizes. Observing figure 6.28, the PSD curves for 50% emulsion, there is a different shape between the PSDs using ultrasound spectrometry and the *Mastersizer* method, it seems the second lobe in the *Mastersizer* PSD is due to the influence of bubbles.

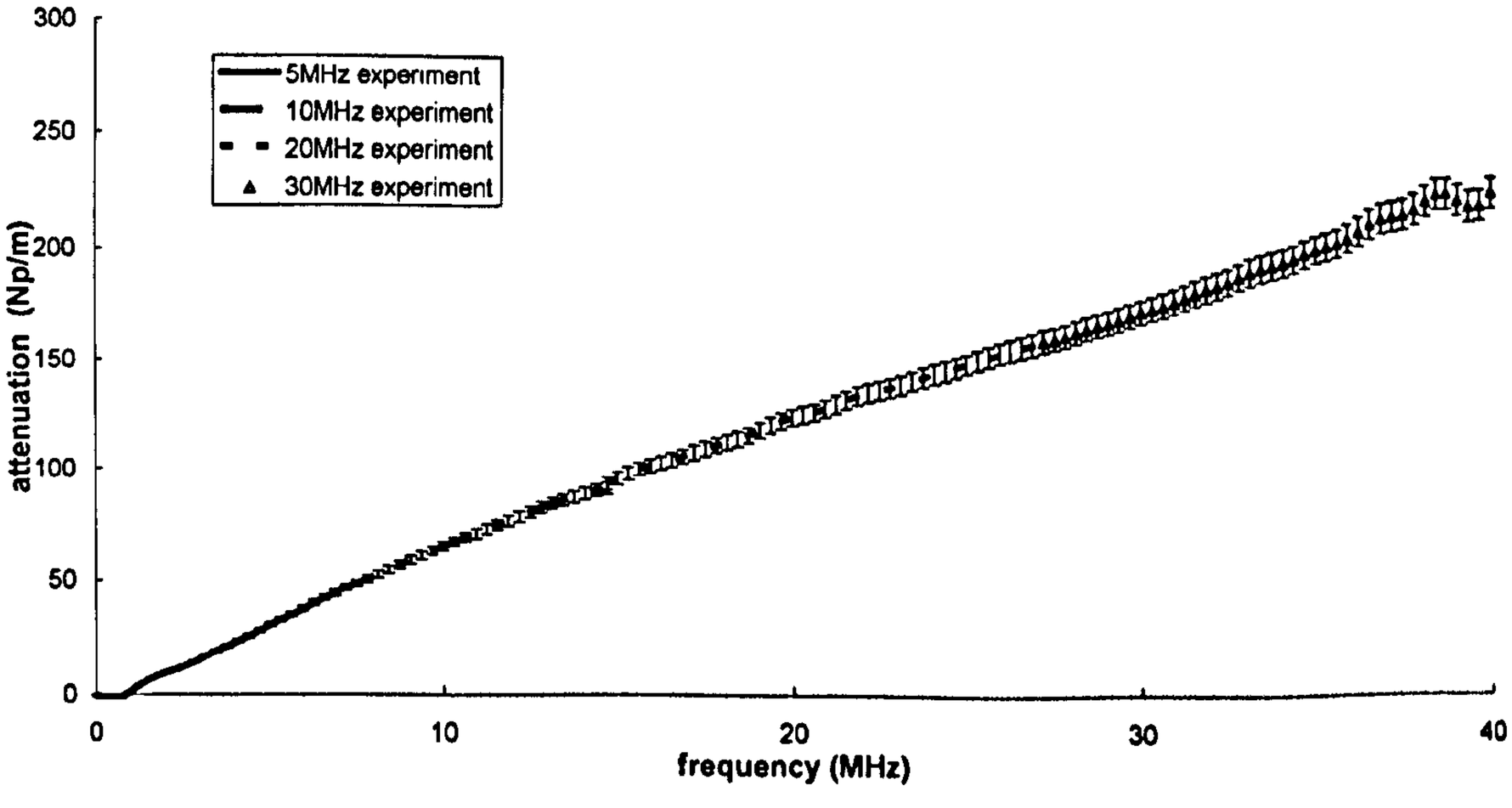

Figure 6.19. Attenuation experiment for 5% 1-bromohexadecane oil-in-water emulsion with small particle sizes using different transducers. The solid line represents the attenuation measurement using the 5 MHz transducer at 26 mm gauge distance, the dash line is the measurement using the 10 MHz transducer at 26 mm, the dotted line is the measurement using the 20 MHz transducer at 8 mm, and the triangles is 30 MHz transducer at 4 mm.

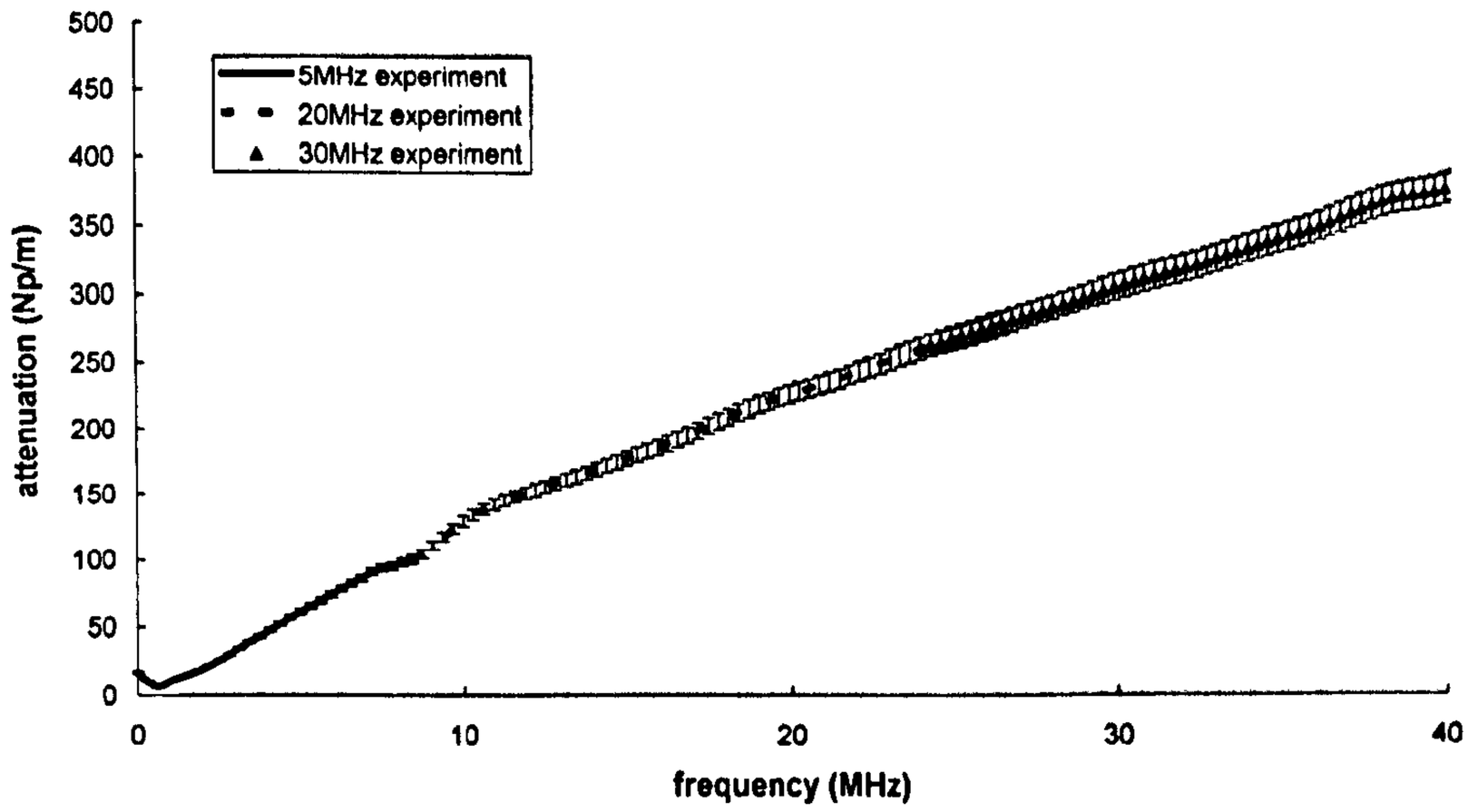

Figure 6.20. Attenuation experiment for 10% 1-bromohexadecane oil-in-water emulsion with small particle sizes using different transducers. Line descriptions are the same as figure 6.19.

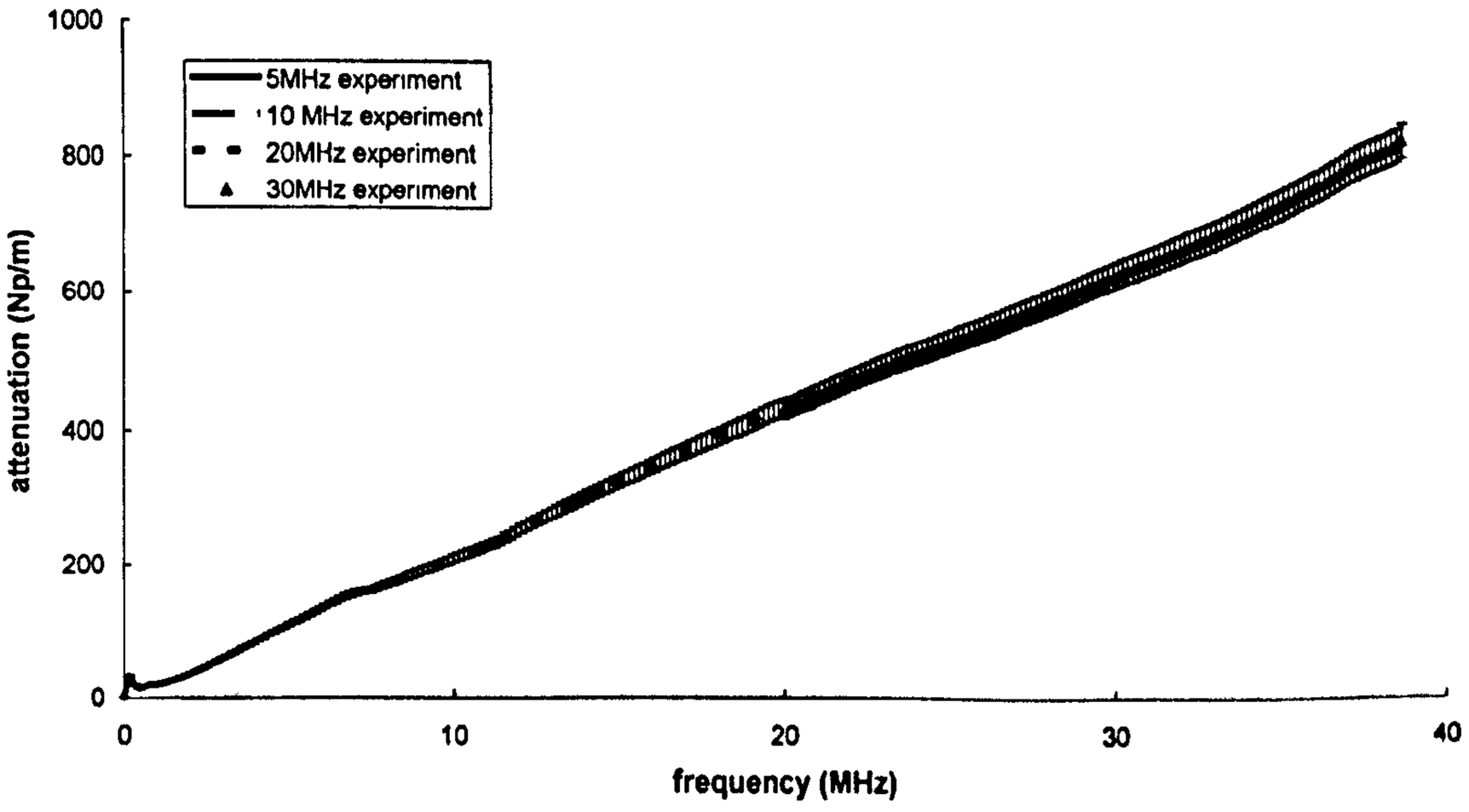

Figure 6.21. Attenuation experiment for 20% 1-bromohexadecane oil-in-water emulsion with small particle sizes using different transducers. Line descriptions are the same as figure 6.19.

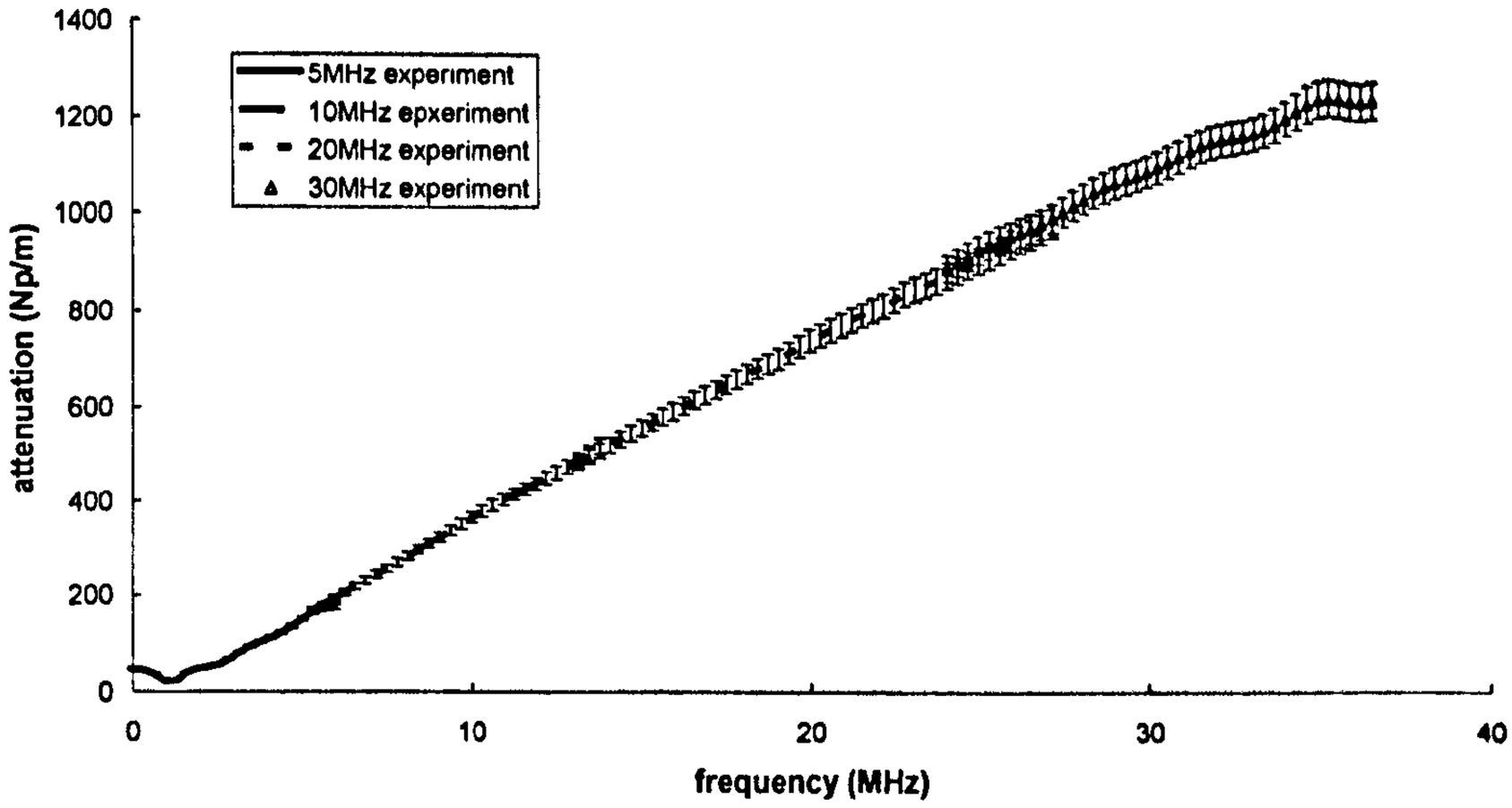

Figure 6.22. Attenuation experiment for 40% 1-bromohexadecane oil-in-water emulsion with small particle sizes using different transducers. Line descriptions are the same as figure 6.19.

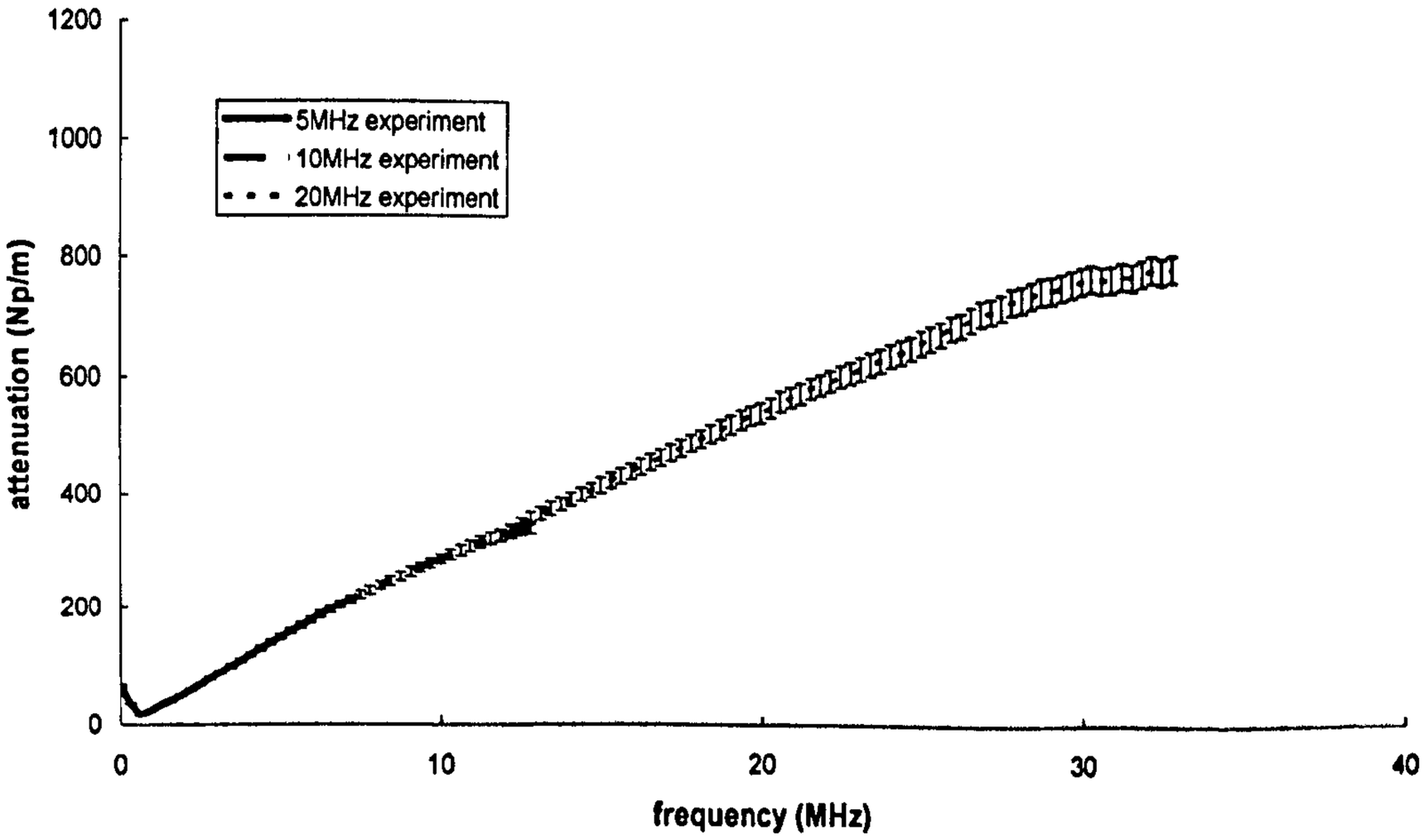

Figure 6.23. Attenuation experiment for 50% 1-bromohexadecane oil-in-water emulsion with small particle sizes using different transducers. Line descriptions are the same as figure 6.19.

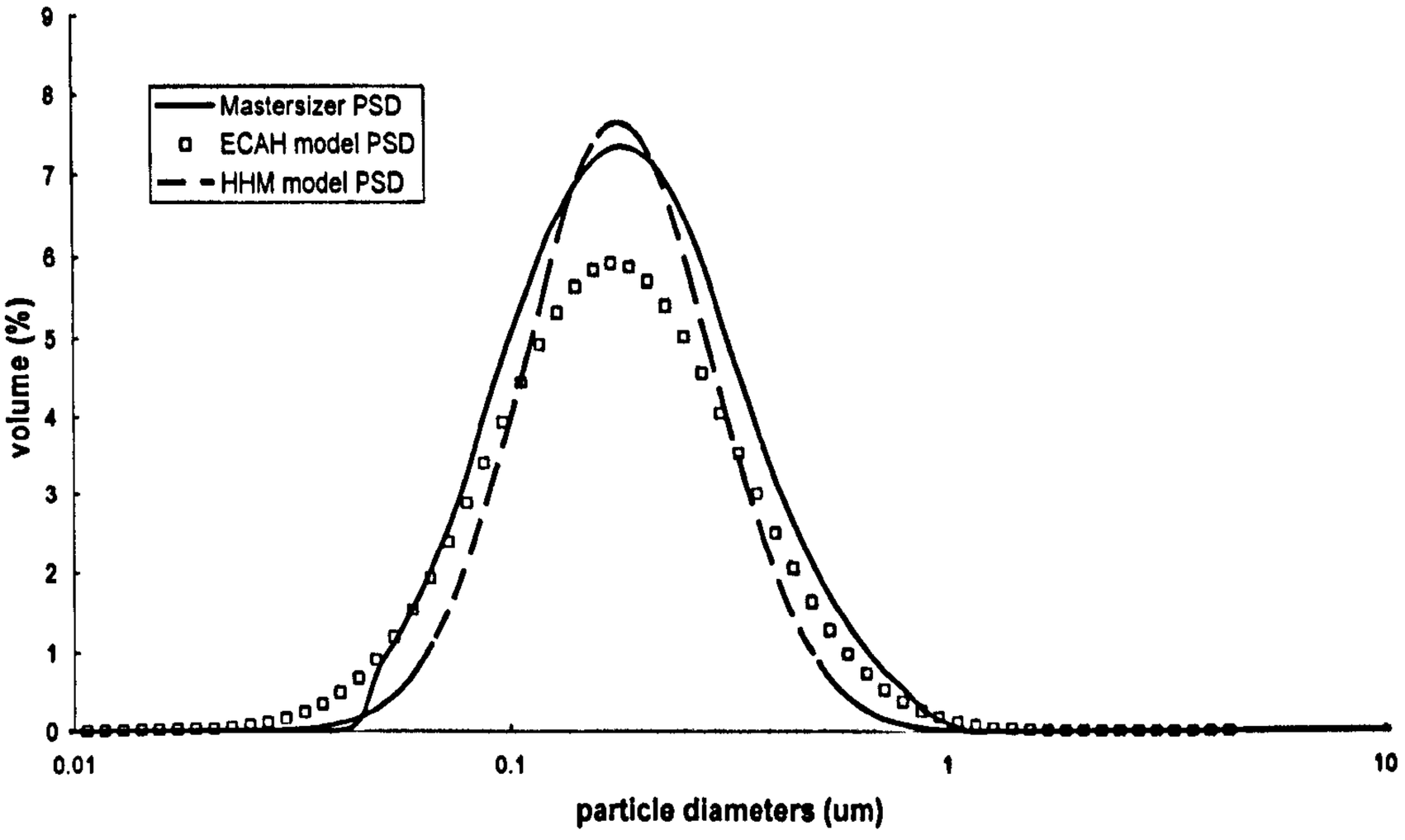

Figure 6.24. Particle size distribution for 5% 1-bromohexadecane in water emulsion. Volume fraction contribution is plotted against particle sizes. The solid line is the *Mastersizer* result, the square line is the ECAH result, and the dash line is the HHM model result.

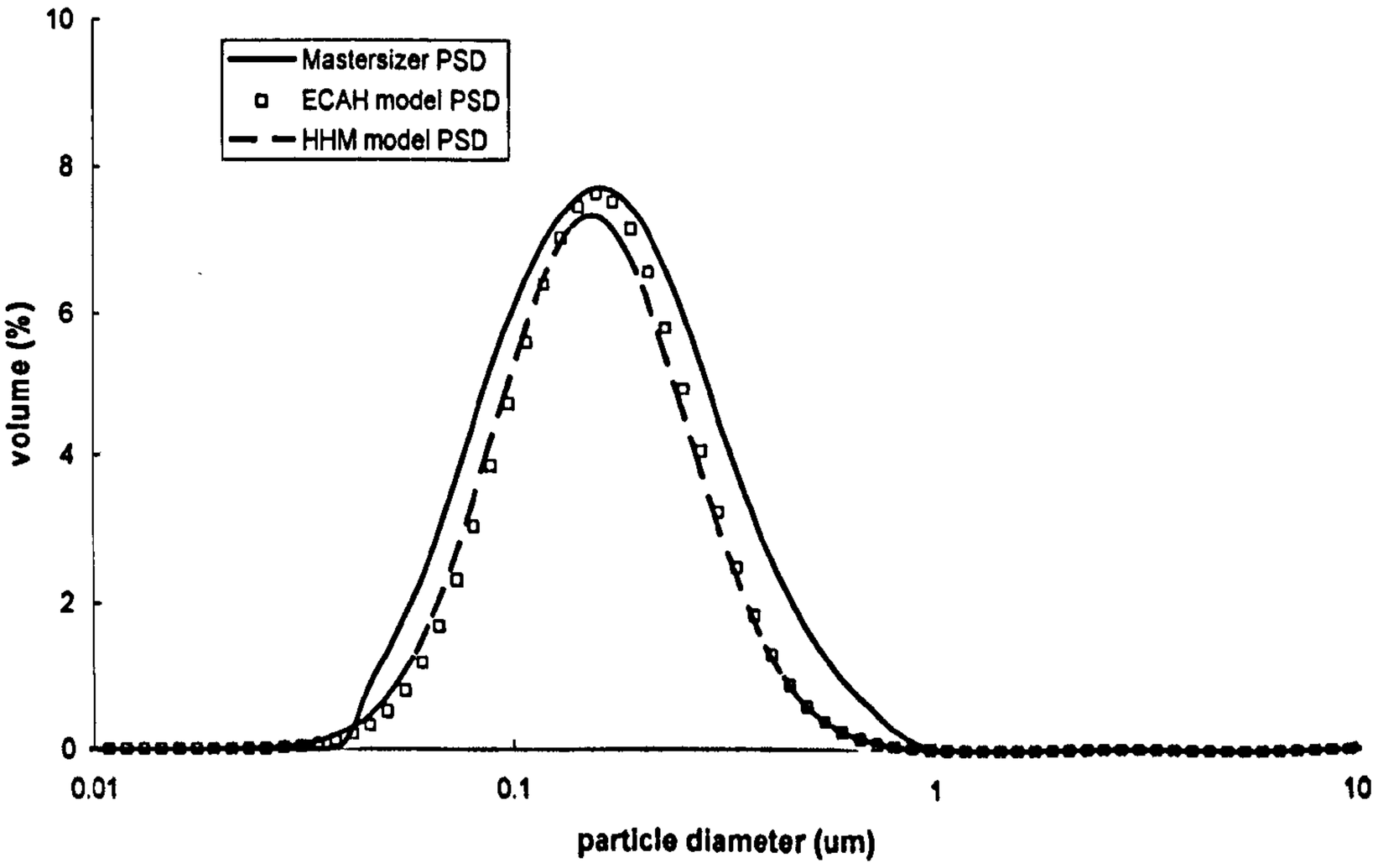

Figure 6.25. Particle size distribution for 10% 1-bromohexadecane in water emulsion. Volume fraction contribution is plotted against particle sizes. The solid line is the *Mastersizer* result, the square line is the ECAH result, and the dash line is the HHM model result.

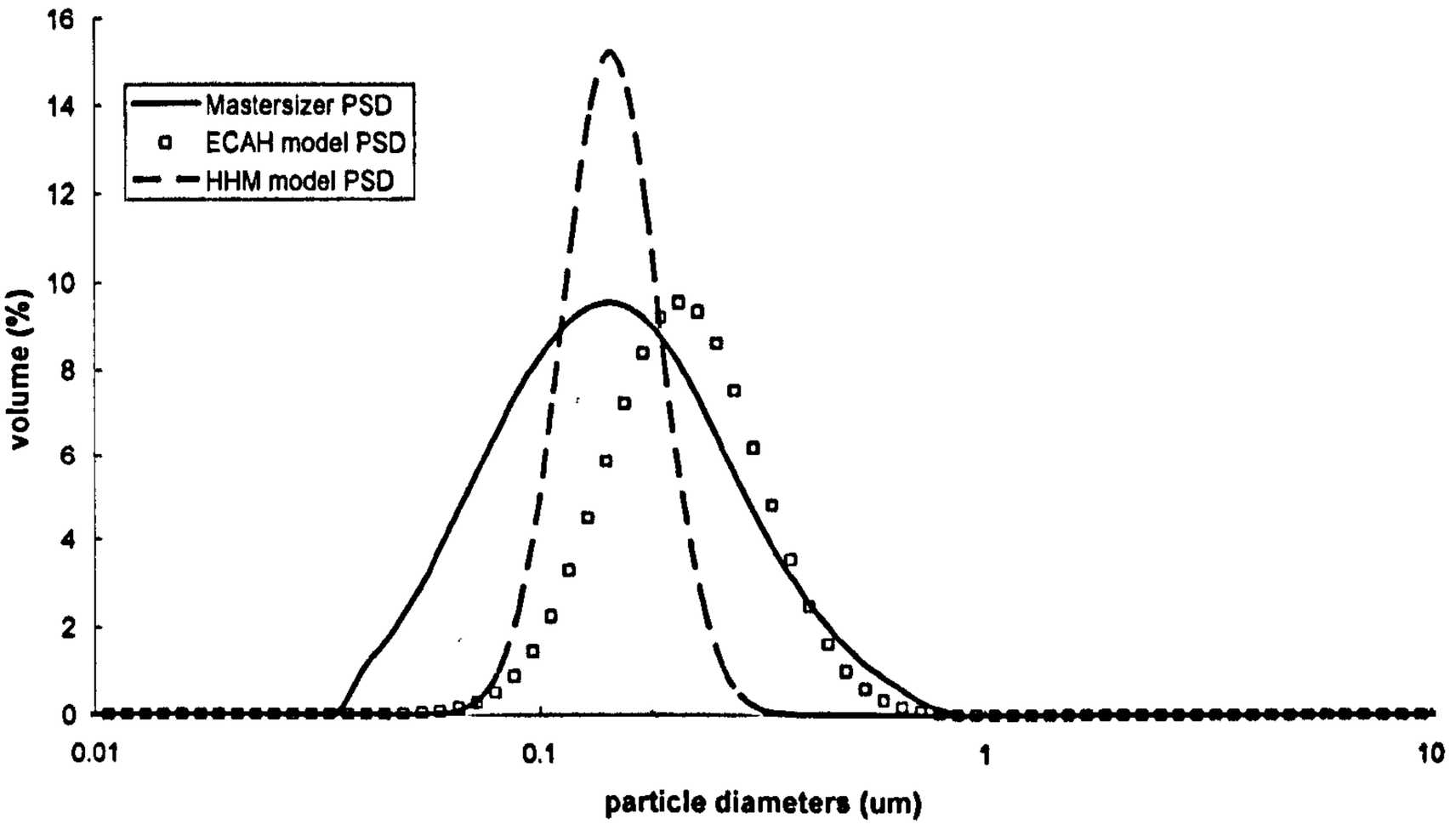

Figure 6.26. Particle size distribution for 20% 1-bromohexadecane in water emulsion. Volume fraction contribution is plotted against particle sizes. The solid line is the *Mastersizer* result, the square line is the ECAH result, and the dash line is the HHM model result.

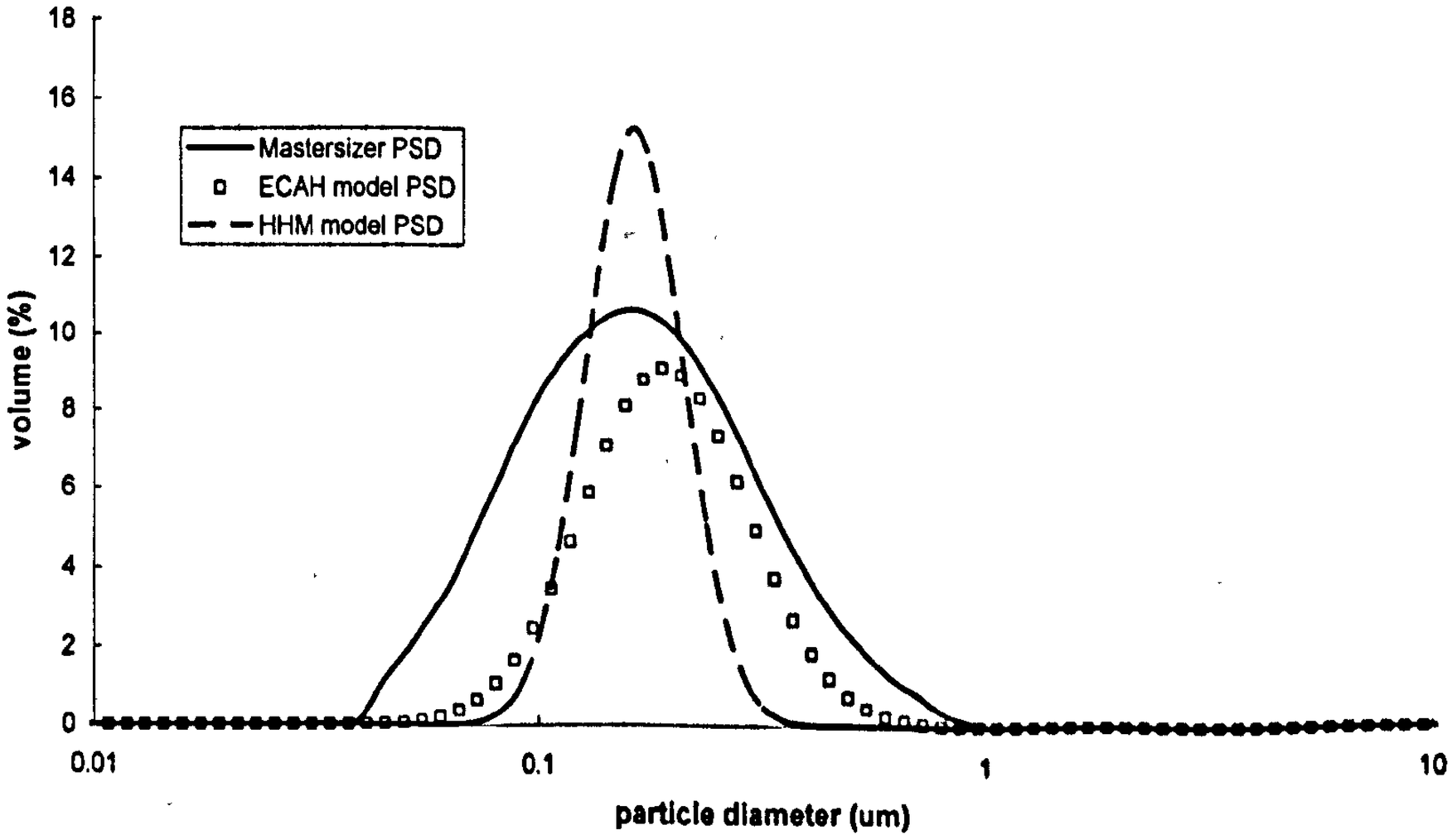

Figure 6.27. Particle size distribution for 40% 1-bromohexadecane in water emulsion. Volume fraction contribution is plotted against particle sizes. The solid line is the *Mastersizer* result, the square line is the ECAH result, and the dash line is the HHM model result.

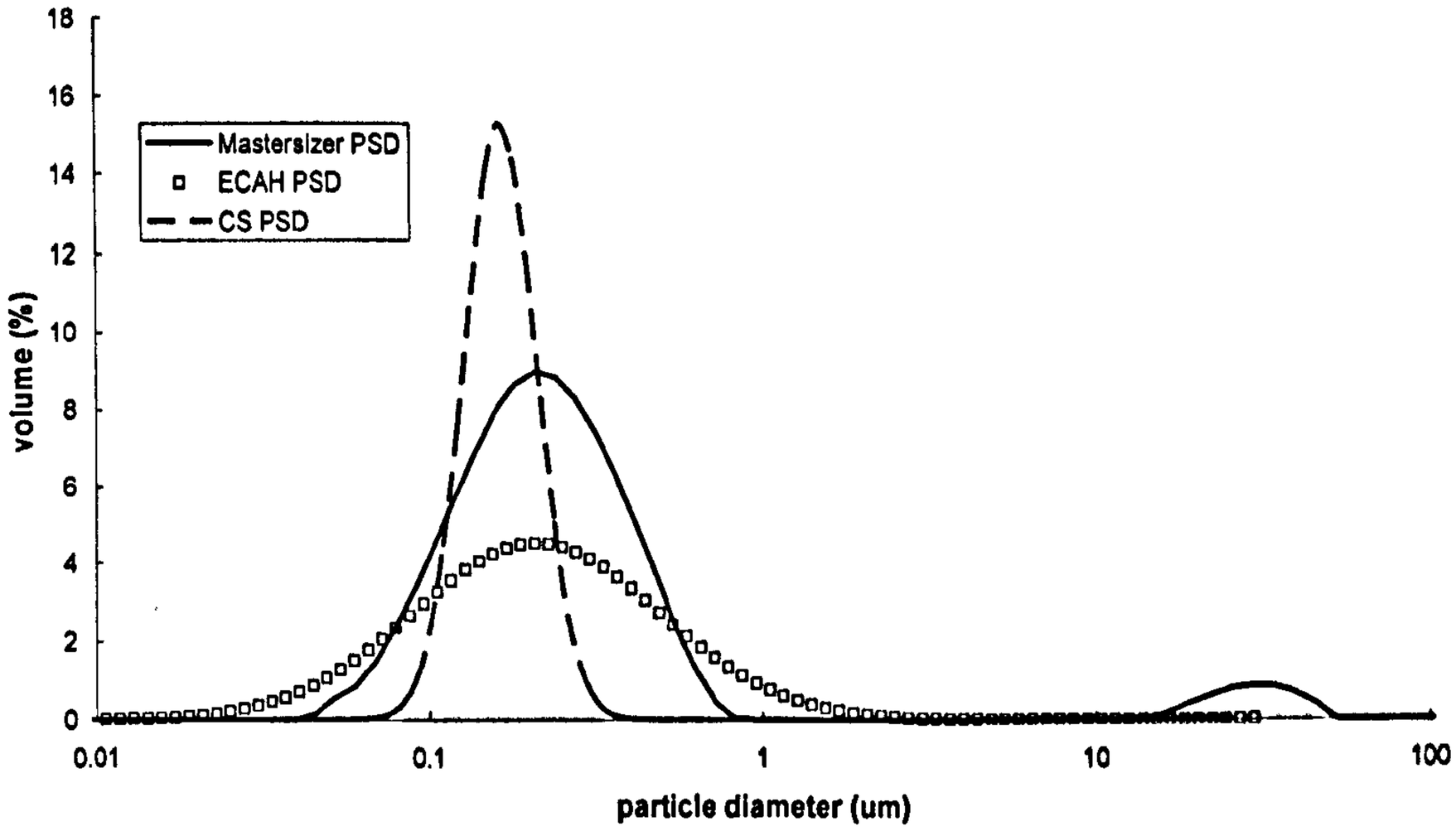

Figure 6.28. Particle size distribution for 50% 1-bromohexadecane in water emulsion. Volume fraction contribution is plotted against particle sizes. The solid line is the *Mastersizer* result, the square line is the ECAH result, and the dash line is the HHM model result.

6.4.3 Simulations

Figures 6.29 to 6.34 show the simulation results for attenuations versus frequency for 1-bromohexadecane emulsion with small particle sizes, using the PSDs obtained by the *Mastersizer*. Each figure gives the experimental data together with the simulations for the full ECAH model, its explicit expressions, the HHM model, and Evans and Attenborough's CP model. The fitting procedure has been discussed above in section §6.3.3. Figure 6.29 is the 5% 1-bromohexadecane in water emulsion with the mean particle radius of 90 nm, at this low particle concentration, the half particle-particle distance ($d = 0.15\,\mu m$) is large compared to the thermal skin depth ($\delta_T = 0.1\,\mu m$) at 2 MHz. It is clear that there are no thermal wave interactions, and the ECAH model works well over the whole frequency range. In the long wavelength regime (the particle radius is much smaller than the compressional wave length 150 μm at 10

MHz), we can see that the explicit expressions gives good prediction compared with the experimental data, and it closely follows the full ECAH result. The simulation result using HHM model is also in good agreement with the experimental data as well as the ECAH model, as we discussed in chapter 3, the thermal term in HHM model tends to give same value as that in ECAH model at very low concentration. We can conclude that all the three ECAH based models gave similar results, and all of them agreed with the experimental data for the whole frequency range. However the Evans and Attenborough's CP model predicts a much lower attenuation than the experimental data for the whole frequency range.

Increasing the particle concentration to 10% roughly doubles both the experimental and the simulated results, as can be seen in figure 6.30. The same comments apply as for the 5% attenuation.

As we discussed in chapter 2, the ECAH model will break down for small particle sizes at high particle concentrations because of the thermal and viscous wave interactions. In these experiments, the density of 1-bromohexadecane is almost the same as that of water. Therefore, thermal absorption is the dominant attenuation mechanism. From the former discussion (equation 2.39), calculation shows that the critical volume fraction, for emulsions with a particle sizes of 100 nm, is 11%, which means below this concentration, half the average distance between the particles is larger than the thermal skin depth, as a result, there is no thermal wave overlap effect, and the ECAH model can be used; on the contrary, above this concentration, there are thermal wave interactions between neighbouring particles, and the ECAH

model is expected to give a higher prediction than the experimental data at low frequencies.

The simulation data for 20% emulsion using the *Mastersizer* PSD is shown in figure 6.31. Both the ECAH model and its explicit expression predicted a slightly higher prediction than the experimental data at low frequencies (say $f < 15MHz$); above this frequency, the predictions using these two models converged to the experimental data. The HHM model prediction closely followed the experimental data from 2 MHz to 37 MHz. The CP model still gave lower predictions compared with the experimental results. The merit qualities of the ECAH model and its explicit expression are 6.2% and 6.4%, respectively, and the merit quality of the HHM model is 1.6%.

With a further increase in concentration up to 40%, these phenomena become much clearer, figure 6.32; we see that both the ECAH model and its explicit expression gave a much higher attenuation (about 13% higher) compared with the measurement along the whole frequency range. At higher frequencies ($f > 30$ MHz), the ECAH model and its explicit expression kept increasing and converged to the experimental data. The HHM model took into account the thermal wave overlap effects, and was in good agreement with the experimental data across the frequency range.

For the 50% emulsion, the mean particle radius increases to 120 nm, obtained using the *Mastersizer*. Although the particle radius becomes larger, there are still particle-particle interactions in this emulsion, both the ECAH model and its explicit expression gave a higher prediction (about 18% higher) for the whole frequency range; at large frequencies, it began to converge to the experimental data. The HHM model still closely followed the measurement

data for the whole frequency range and again the CP model gave a lower prediction across the whole frequency range.

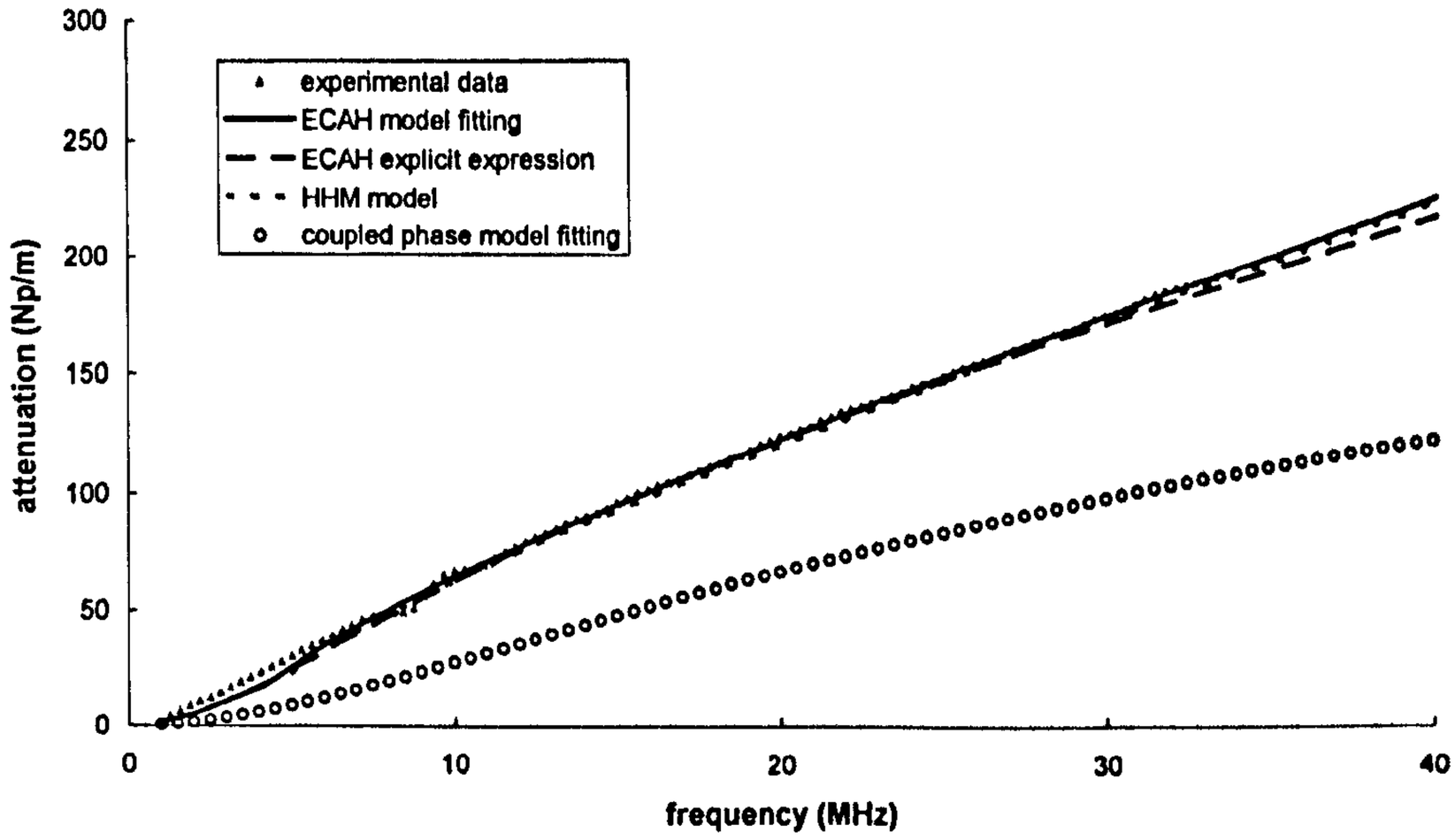

Figure 6.29. Attenuation and simulation data for 5% 1-bromohexadecane oil-in-water emulsion, using the PSDs in figure 6.17.

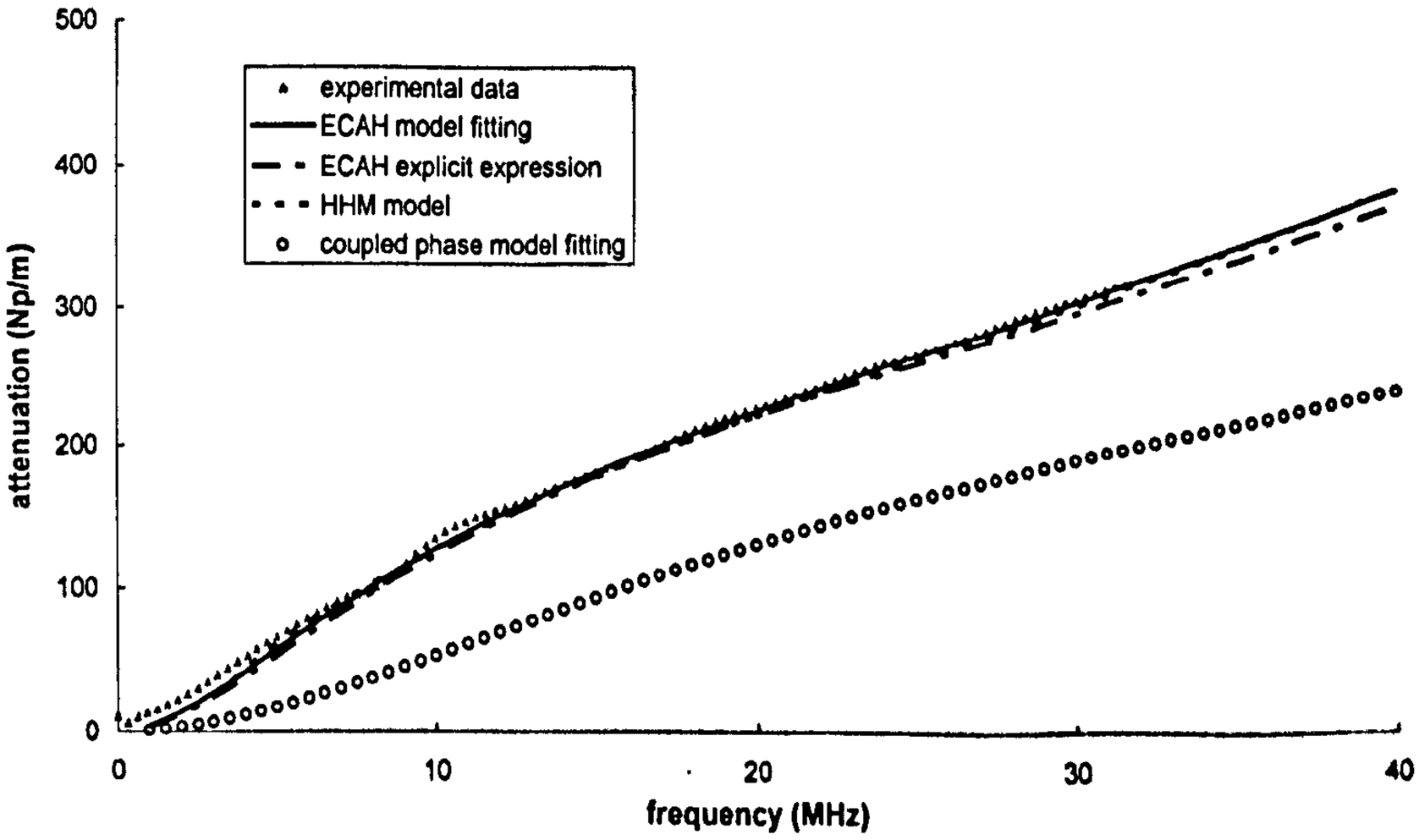

Figure 6.30. Attenuation and simulation data for 10% 1-bromohexadecane oil-in-water emulsion, using the PSDs in figure 6.17.

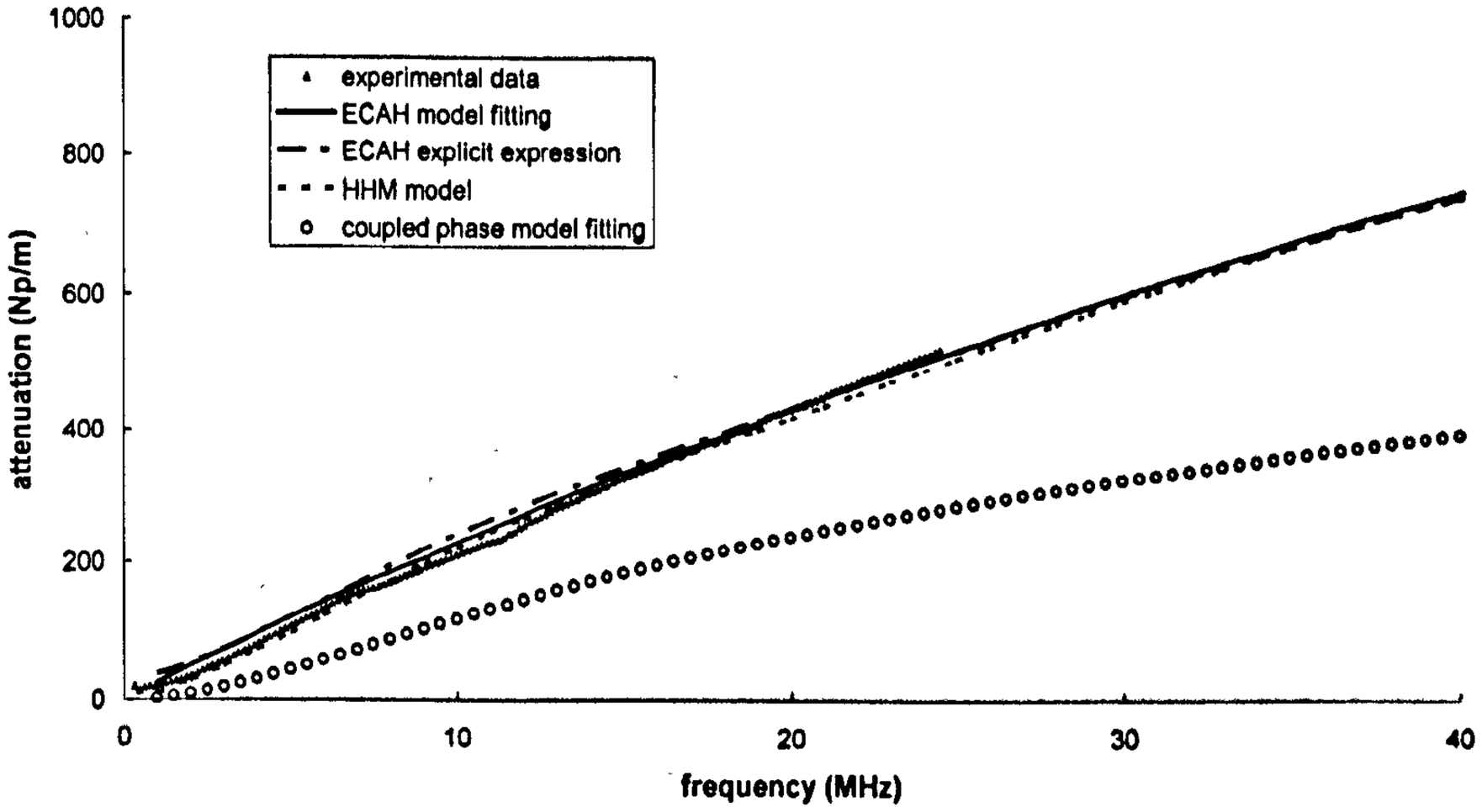

Figure 6.31. Attenuation and simulation data for 20% 1-bromohexadecane oil-in-water emulsion, using the PSDs in figure 6.17.

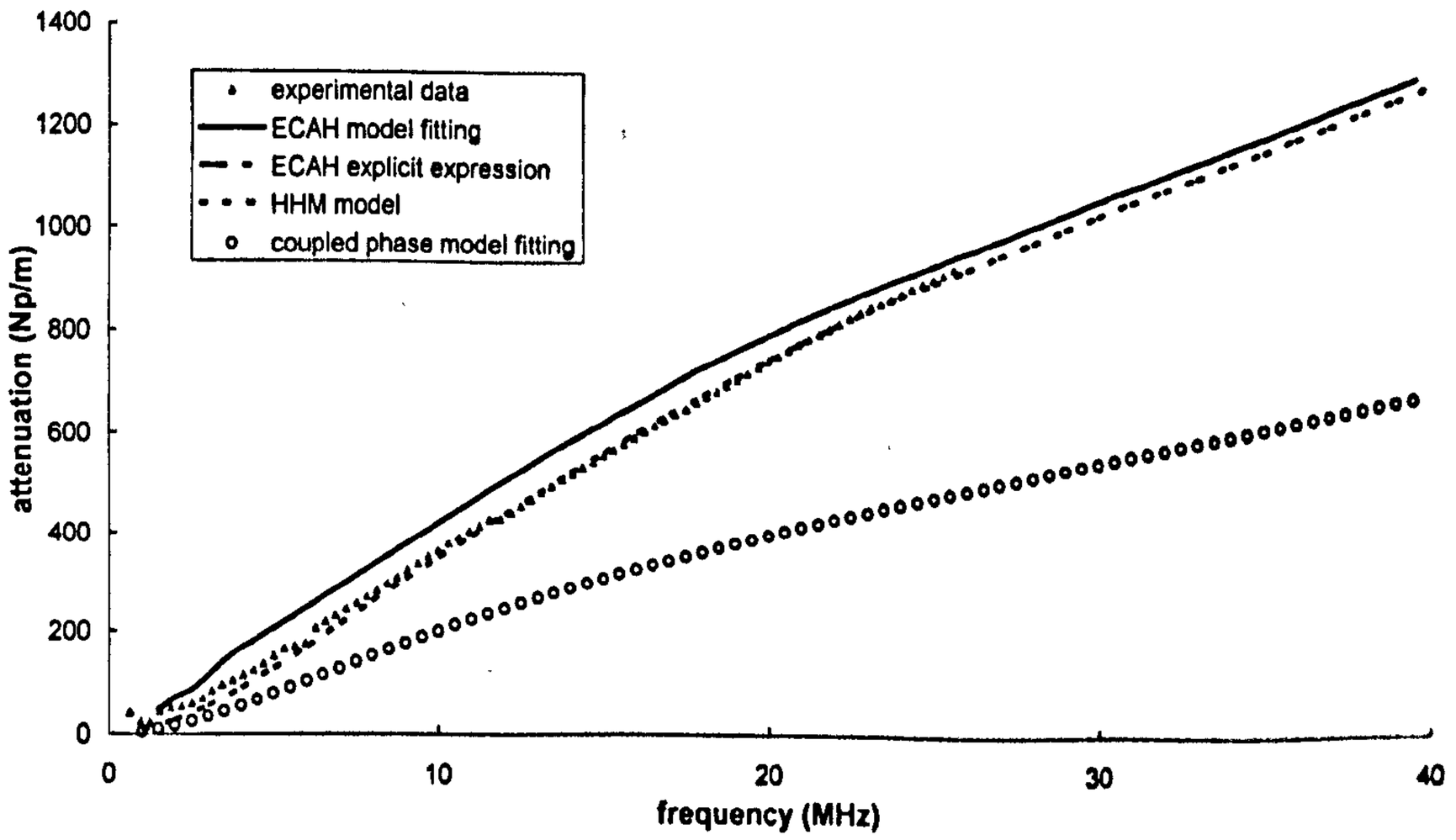

Figure 6.32. Attenuation and simulation data for 40% 1-bromohexadecane oil-in-water emulsion, using the PSDs in figure 6.17.

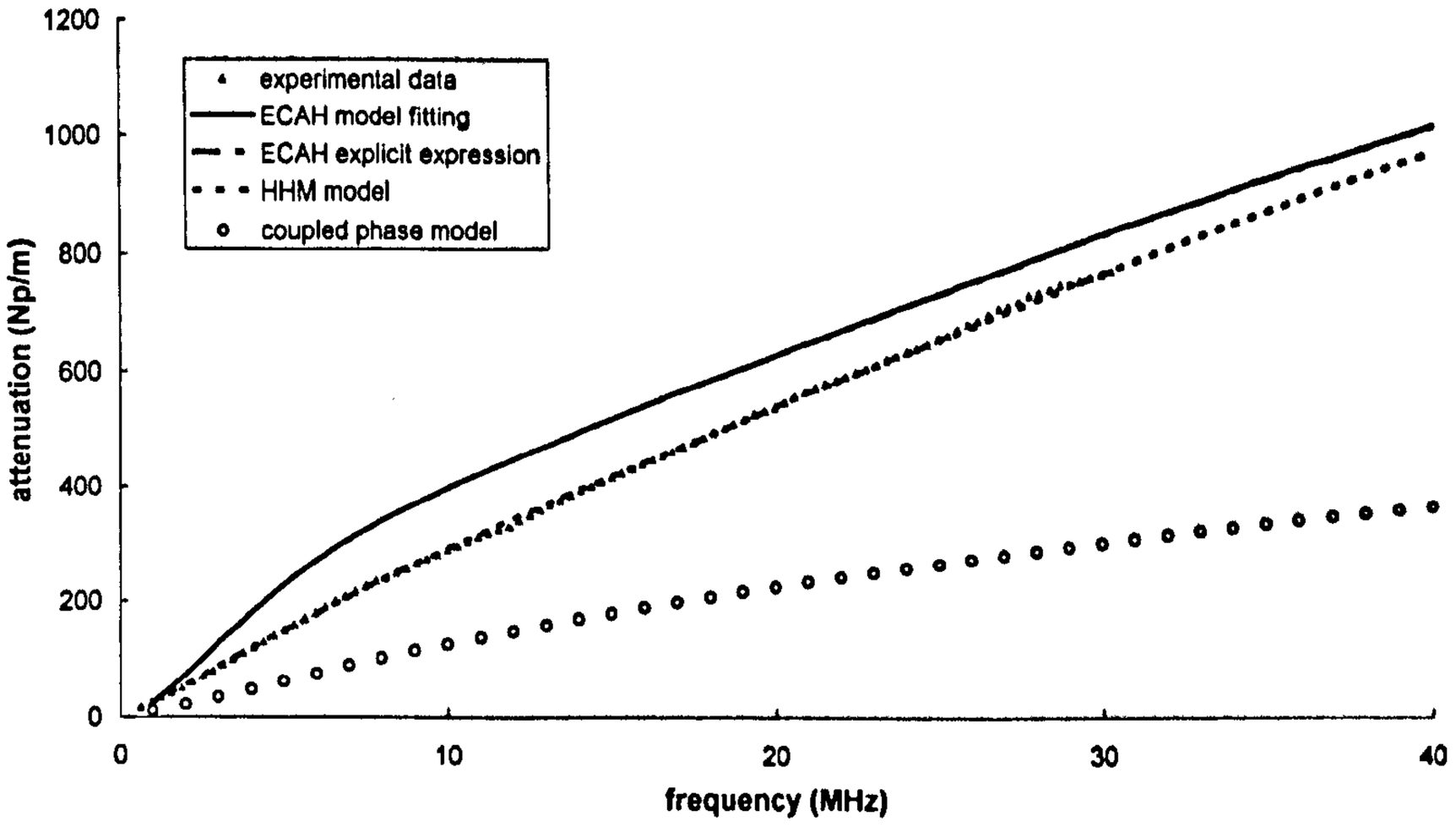

Figure 6.33. Attenuation and simulation data for 50% 1-bromohexadecane oil-in-water emulsion, using the PSDs in figure 6.18.

6.5 Experiment 4: encapsulated emulsions

6.5.1 Emulsions preparation

A set of encapsulated emulsions and their unencapsulated precursors was supplied by Dow AgroSciences Ltd, Kings Lynn, UK. The encapsulated emulsions were prepared to give the combinations of concentrations and particle size, and the precursor emulsions were prepared to give a guide to the initial state of the encapsulated ones, see table 6.2. 20% v/v (sample 16-C) and 40% v/v (sample 17-A). Solvesso 100S unencapsulated emulsions were prepared by weighing 30 or 60 ml of Solvesso 100S oil and 120 ml aqueous solution into a glass beaker and blending with a high speed blender for 1 min. The continuous phase consisted of distilled water with 4 wt% Gonsenol G103 (PVA) as the surfactant in solution. The thermo-physical properties of the continuous phase are the same as those of water, table 6.3. The Solvesso 100S

is a petroleum-derived complex substance used in agrochemicals. The particle size distributions of these emulsions were measured using a *Mastersizer* instrument by Dow AgroSciences (see appendix 6.1). This was done three times. The first measurement was made just after the emulsion was made, the second one day later, and the third after 10 days. The first two measurements gave PSDs which were identical within the limits of experimental error, whilst the 10 day result indicated the mean particle radius of the unencapsulated emulsions increased significantly (see table 6.3). This indicates that the unencapsulated emulsions are not stable with time, and most probably flocculated over a period of days. However, they could be redispersed by vigorous stirring before each experiment. This can be demonstrated by figure 6.34, when shows the measured attenuation for 20% unencapsulated emulsion (sample 16-C) with the change of time, using 5 MHz transducer at a 26 mm gauge distance. The blue line shows the attenuation measured after receiving the sample; several days later, this emulsion is flocculated, and the attenuation changed because of the flocculation, as the black line shows; after redispersing, the flocculation was reversed and the attenuation was measured again, see the red line, which is identical to the first one within the limits of experimental error.

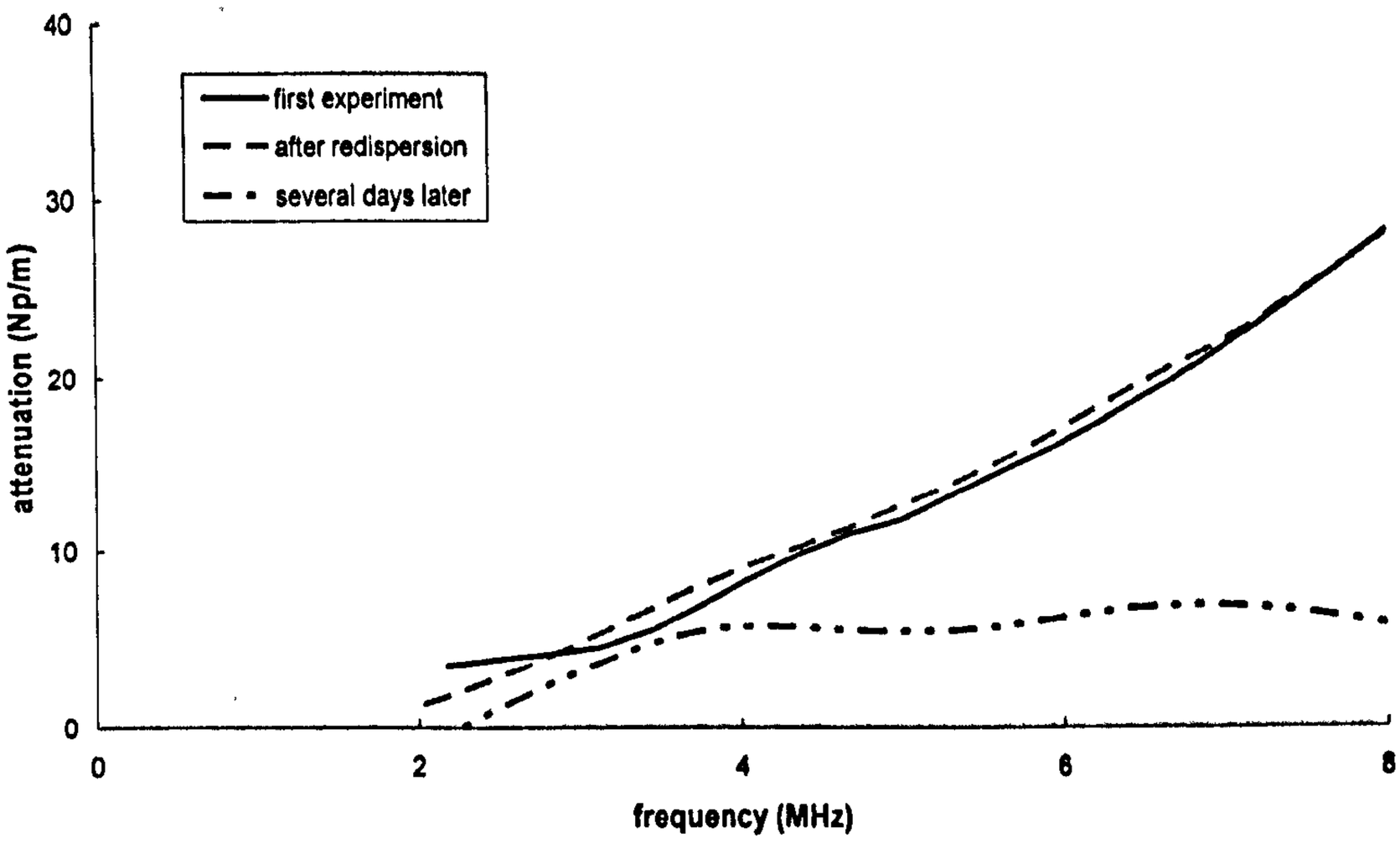

Figure 6.34. The experimental attenuation for 20% Solvesso 100S oil-in-water emulsion, with mean particle diameter of 1.64 μm. The attenuation was measured over a period of days: the solid line shows the first experimental data, the dash line shows the attenuation data several days later, when the emulsion become flocculated; and the broken line shows the experimental data after stirring the flocs.

The encapsulation process was as follows: an oil emulsion without shell is first made with the desired droplet size; 0.24% EDA (Ethylene diamine) was added into the emulsion to form capsules and 0.4% Atlox (a blend of polyoxymethylene surfactant) was added as a dispersant. All the three samples of the encapsulated emulsions were made using these procedures. Sample 16-D (20% encapsulated emulsion) was made using sample 16-C (20% unencapsulated emulsion), and they have the same particle radius. Sample 16-B was also made using sample 16-C, but this time further processing was applied to give a smaller particle radius before encapsulation. Sample 17-B (40% encapsulated emulsion) was made on the basis of the 40%

unencapsulated emulsion (sample 17-A), with the same particle sizes. All the samples and particle sizes are listed in table 6.2.

For the encapsulated emulsions, the oil phase is the mixture of 1% Voranate M-220 (a polyisocyanate) and 20% Solvesso 100S, the aqueous phase is distilled water with the surfactant, and the shell phase is a kind of polyurethane, which results from a reaction of the Voronate M-220 with EDA (Ethylene diamine). The thermo-physical properties of these three media are shown in table 6.3. For the oil phase, the inclusion of small amount (1%) of Voranate M-220 does not change the thermo-physical properties significantly, so we assumed that it has the same properties as Solvesso 100S; the properties of the continuous phase is the same as water. The density, shear rigidity and heat capacity of the shell were stated by Dow AgroSciences Ltd; to be quite similar to those of polystyrene, hence, the other properties, such as velocity, the attenuation coefficient, thermal conductivity and thermal expansivity of the shell were taken to be those of polystyrene.

Sample	Type of emulsions	Volume fraction (v/v)	Mean particle diameters (measured after made)	Mean particle diameters (10 days later)
16-B	encapsulated emulsion	20%	1.46 μm	1.75 μm
16-D	encapsulated emulsion	20%	1.64 μm	1.84 μm
17-B	encapsulated emulsion	40%	1.64 μm	1.79 μm
16-C	Unencapculated emulsion	20%	1.64 μm	8.54 μm
17-A	Unencapculated emulsion	40%	1.64 μm	15.25 μm

Table 6.2. Particle sizes and concentrations of Dow emulsions.

Properties	Oil phase	Aqueous phase	Shell
Ultrasonic velocity ($m\ s^{-1}$)	1357.1	1497.0	2330.0
Attenuation coefficient ($Np\ m^{-1}$)	$2.48\times10^{-13} f^2$	$2.5\times10^{-14} f^2$	$1.0\times10^{-13} f^2$
Shear rigidity	-	-	1.27×10^{9}
Density ($kg\ m^{-3}$)	878.0	997.0	1053.0
Viscosity (Pa s)	8.341×10^{-4}	8.8×10^{-4}	-
Specific heat ($J\ K^{-1}kg^{-1}$)	1740.5	4177.0	1193
Thermal conductivity ($W\ m^{-1}\ s^{-1}$)	0.162	0.5952	0.14
Thermal expansivity (K^{-1})	6.1×10^{-4}	2.6×10^{-4}	2.6×10^{-4}

Table 6.3. Thermo-physical properties of three different phases at 25°C.

6.5.2 Experiment results and simulations

Figure 6.35 shows the attenuation experiment for the 20% Solvesso 100S oil-in-water emulsion together with the predictions using the ECAH model. The particle size distribution for this emulsion was determined using ultrasound spectrometry and compared with the *Mastersizer* result in figure 6.36; the particle sizes are nearly the same but with a slightly different standard deviation. The frequency working limit for the measurement is from 2 MHz to 27 MHz, obtained using three different transducers. The three sets of data appeared to be consistent in that they formed a smooth continuous line. The prediction using the ECAH model with the PSDs calculated by the *Mastersizer* showed very good agreement with the experimental data. It is not surprising that no thermal or viscous wave interactions are expected in this emulsion since half the average distance between the particles (0.58 μm) is

larger than both the thermal ($\delta_T = 0.13\,\mu m$) and viscous ($\delta_S = 0.28\,\mu m$) skin depths. The ECAH model results agree well with experiment.

Similar results were obtained for the 40% v/v emulsion (sample 17-A), and these are shown in figure 6.37, with the PSDs shown as figure 6.38. We note that the model and experiment were in good agreement up to 15 MHz and, after that, the model slightly underpredicted the attenuation between 15 and 22 MHz. The increasing variance above 22 MHz is typical of a measurement system when the effects of noise become significant.

The equivalent results for the encapsulated emulsions are shown in figures 6.39 and 6.40. In these experiments, the same three transducers and gauge lengths were used as before. Figure 6.39 shows the results for sample 16-B and sample 16-D, both are 20% encapsulated emulsions with 0.17 μm shell thickness, but the mean particle diameter is different, for sample 16-B the mean diameter is 1.46 μm, while the mean diameter is 1.64 μm for sample 16-D. Comparing the two experimental data we can see that the slight difference in particle radius changes the attenuation curve a little: for sample 16-B, the emulsion with a smaller suspended particle, its attenuation is slightly larger than that of sample 16-D, the emulsion with at larger particle radius. This phenomenon is much clearer at higher frequencies ($f > 17$ MHz) when the effects of the noise become significant. The attenuation for these samples was calculated with the PSDs from *Mastersizer* using the Anson and Chivers model. These two attenuation results are quite close to each other, which means the slightly difference in the core radius has little influence on the attenuation curve.

Figure 6.40 shows the experimental result for sample 17-B, 40% encapsulated emulsion, and the simulation data using Anson and Chivers model with the PSD from *Mastersizer* (mean particle diameter 1.64 μm and shell diameter 1.97 μm). The simulation data gave a good prediction at high frequencies.

Comparing the attenuation result of sample 16-C with that of sample 16-D in figure 6.41a, each having the same particle concentration and suspended particle sizes, we see that there is a dramatic increase in the attenuation when the emulsion undergoes encapsulation; it is about three times greater than that without shell. Figure 6.41b shows the ratio of the attenuation in the encapsulated and unencapsulated systems as function of frequency. This increase of the attenuation depends on the properties of the shell. If the thermo-physical properties of the shell were similar to those of the continuous phase, the increase would be small, but, on the contrary, the increase is large. A similar result was obtained in the case of the 40% v/v emulsion where, again, the attenuation of encapsulated emulsion at high frequencies is nearly three times larger than the attenuation of emulsion without a shell.

On the basis that the theory and techniques described here could lead to a means to non-destructively estimate the properties of encapsulated emulsions, it is of interest to investigate the sensitivity of the theoretical formulations to some of the key properties of the encapsulated particles. To this end a brief analysis has been done to assess the effects of shell thickness, shell density and thermal properties on the attenuation data. The influence of the shell thickness on the attenuation is shown in figure 6.42. It is clear that when we decrease the shell thickness, the attenuation decreases as well; however, the

extent of the decrease depends on the properties of shell. When the shell thickness was set to zero, which means there is no shell around the particles, the attenuation is greatly decreased, and the result converged to the ECAH model. This convergence indicates that for a well-defined emulsion system, the attenuation could be used to estimate the shell thickness.

The changes in the shell density lead to a dramatic change in the attenuation, see figure 6.43. There is an inverse proportion between the shell density and the attenuation. The influence of thermal properties (such as the thermal conductivity, thermal expansivity and specific heat) on the attenuation is quite small, shown in figure 6.44. The changes of the ultrasonic properties, such as the velocity and the attenuation coefficient have no influence on the attenuation curve. The implication of this result for the non-destructive evaluation of encapsulated emulsions is that it is possible to estimate shell thickness or density from ultrasonic attenuation measurement, but not both at the same time.

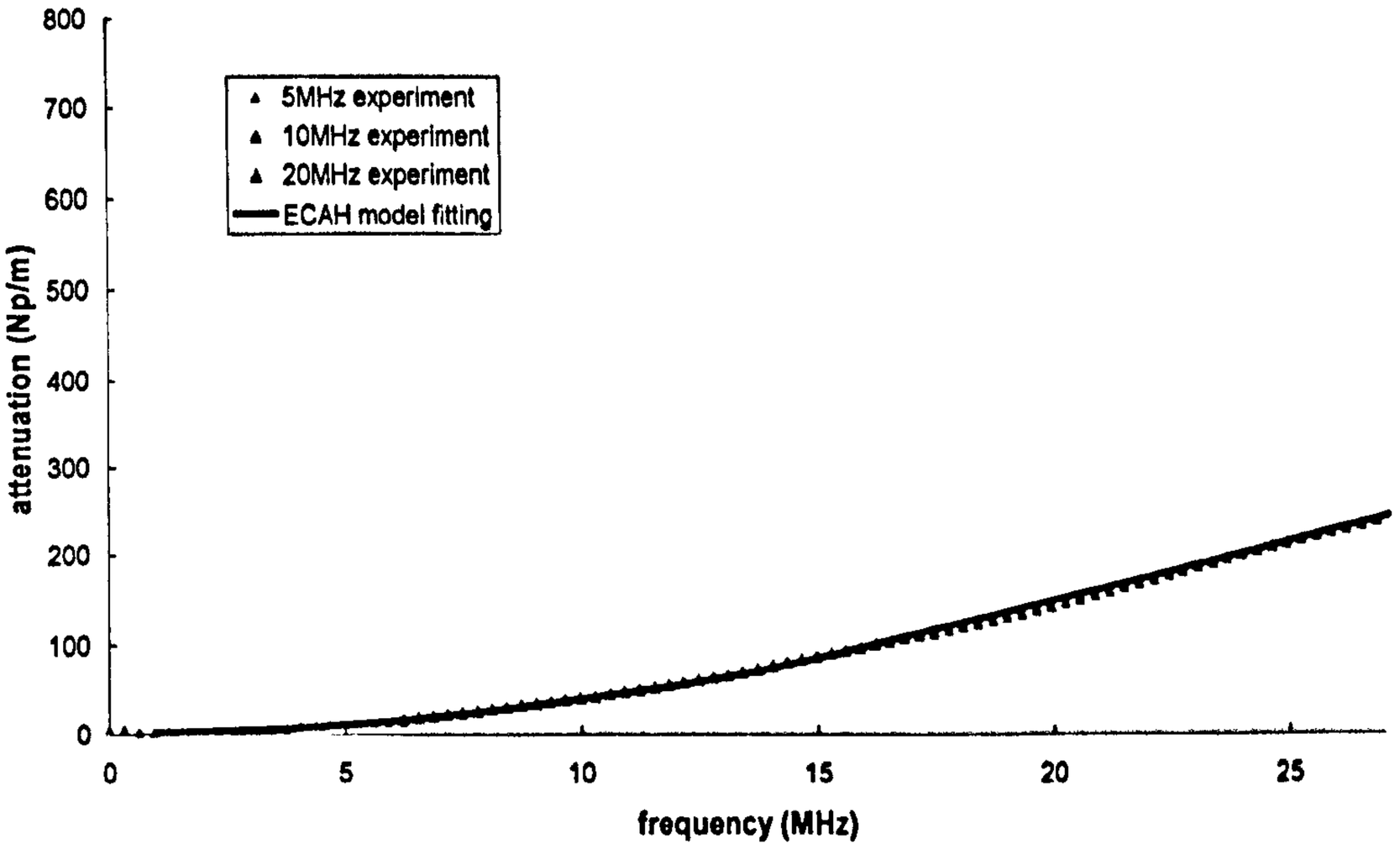

Figure 6.35. Attenuation experiment data for 20% Solvesso 100S oil-in-water emulsion (sample 16-C), the simulation data was predicted using the ECAH model with the PSDs obtained by the *Mastersizer*.

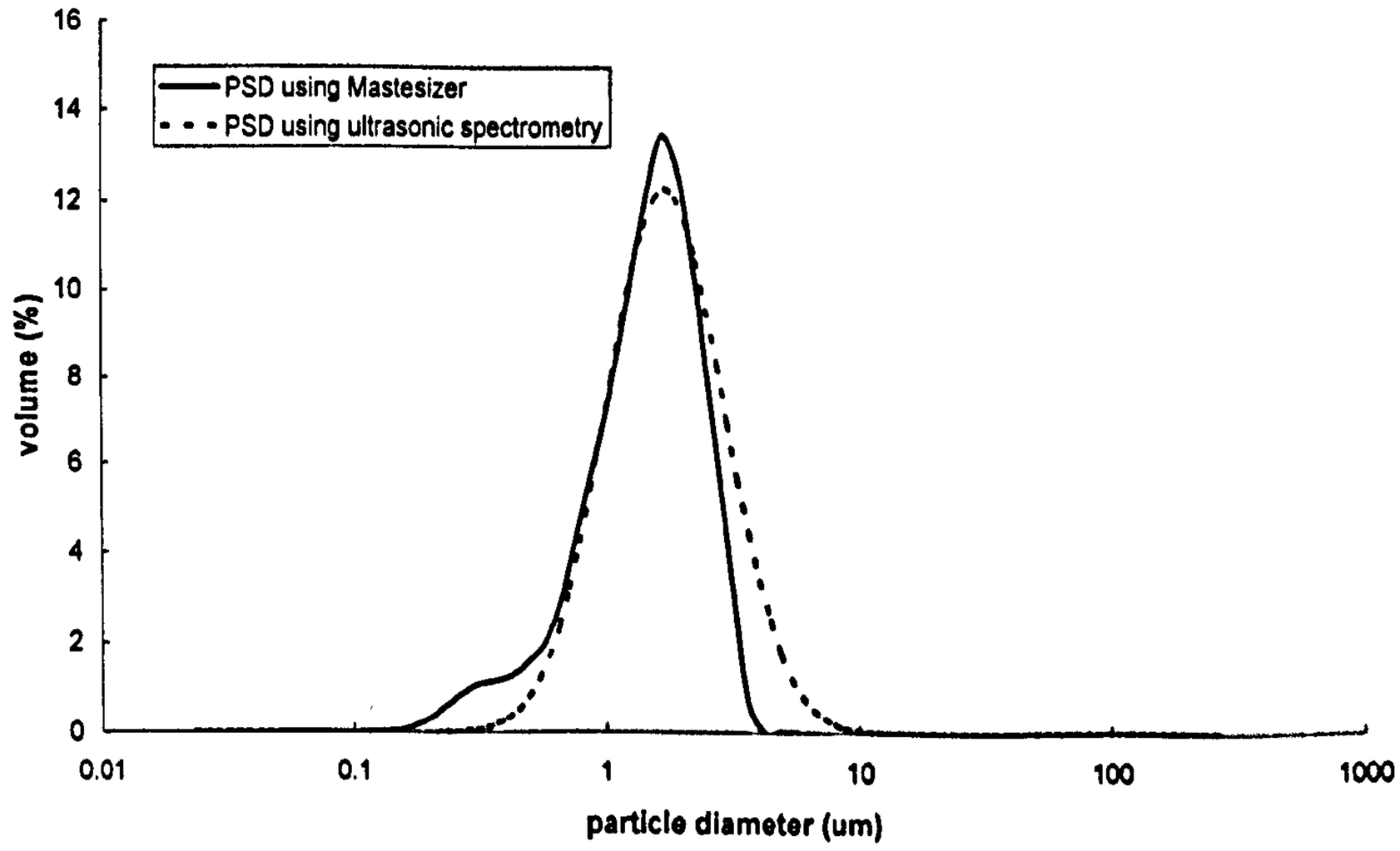

Figure 6.36. PSDs for 20% Solvesso 100S oil-in-water emulsion (sample 16-C). The solid line is PSD by *Mastersizer* (just after the emulsion was made) and the dash line is using the ultrasound spectrometry (just after receiving this sample).

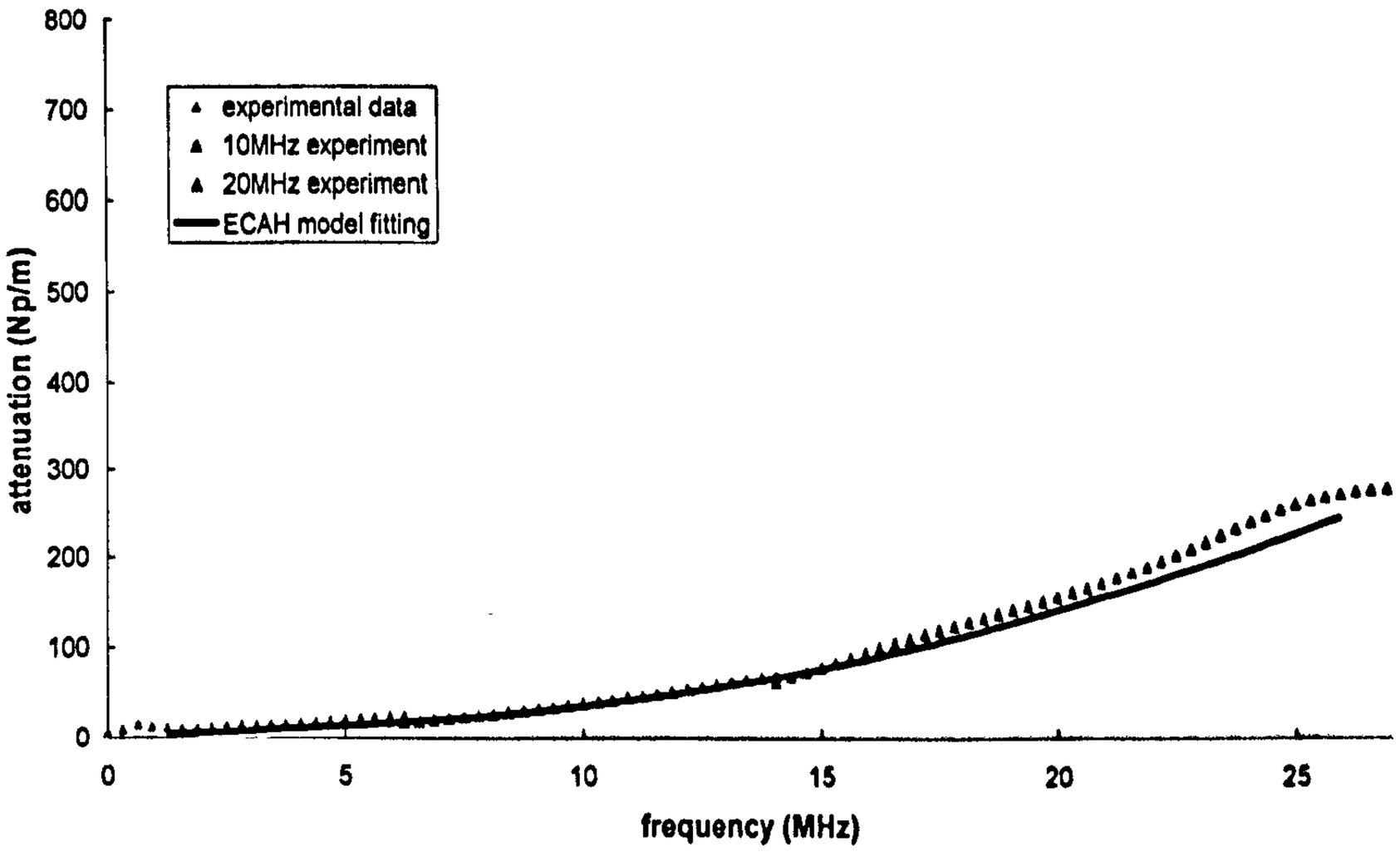

Figure 6.37. Attenuation experiment data for 40% Solvesso 100S oil-in-water emulsion (sample 17-A), the simulation data was predicted using the ECAH model with the PSDs obtained by the *Mastersizer*.

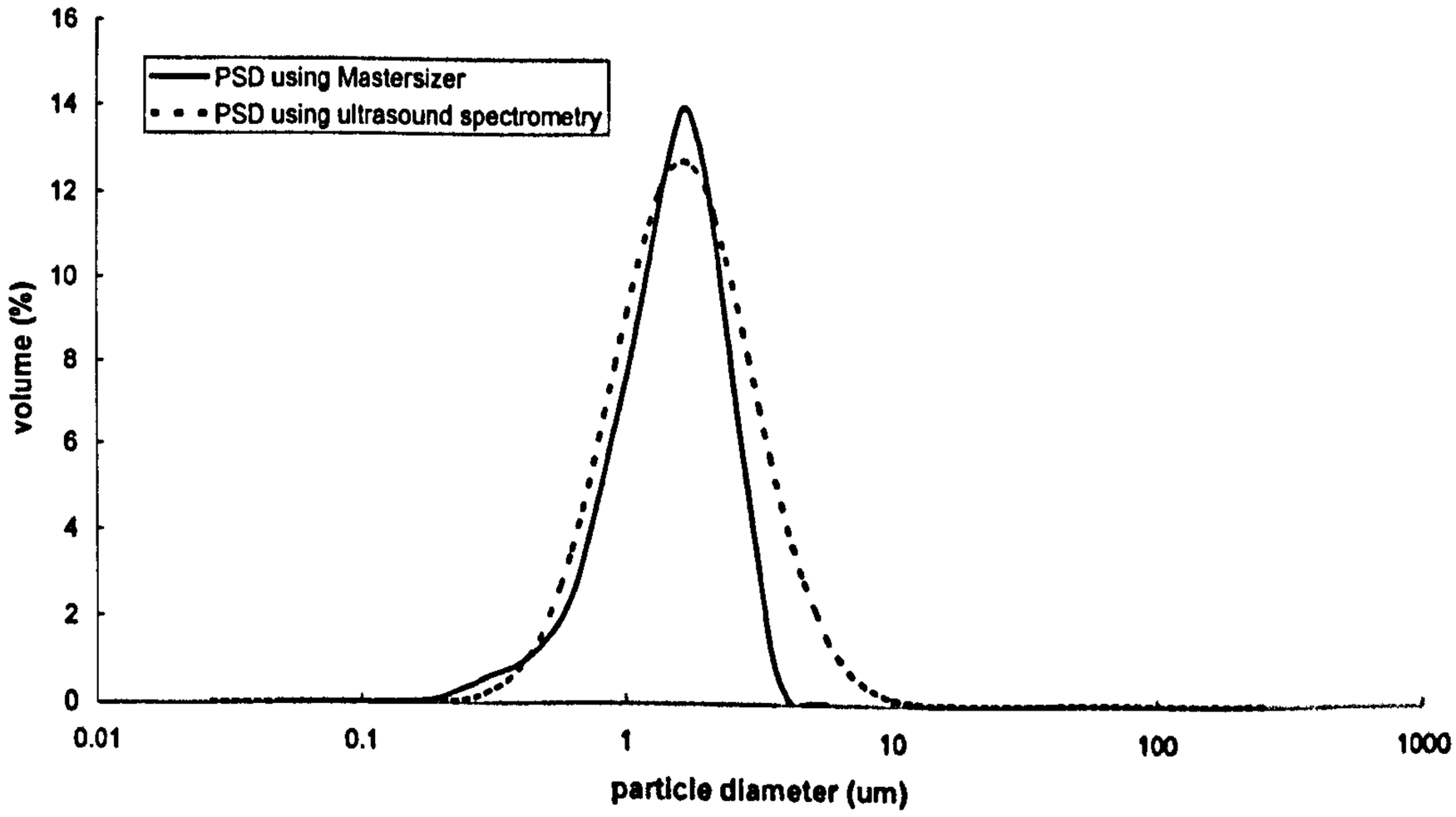

Figure 6.38. PSDs for 40% Solvesso 100S oil-in-water emulsion (sample 17-A). The solid line is PSD by *Mastersizer* (just after the emulsion was made) and the dash line is using the ultrasound spectrometry (just after receiving this sample).

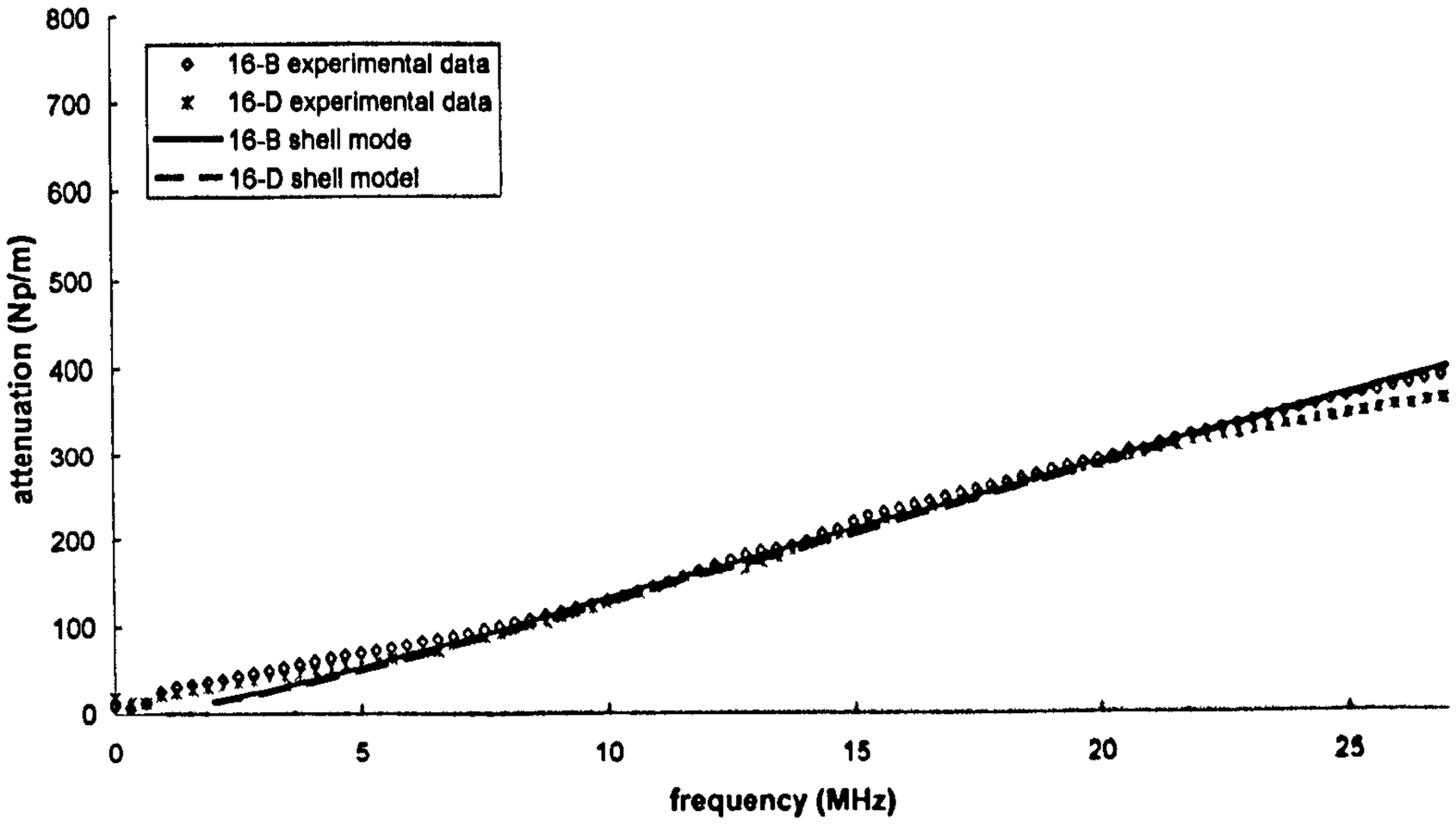

Figure 6.39. Attenuation experiment data for 20% encapsulated emulsions: sample 16-B with particle diameter of 1.46μm (dots) and sample 16-D with particle diameter of 1.64μm (stars), the shell thicknesses for both of the emulsions are 0.165 μm. The simulation data was predicted using the Anson-Chivers shell model using the PSDs by the *Mastersizer*. The solid line for sample 16-B and the broken line for sample 16-D.

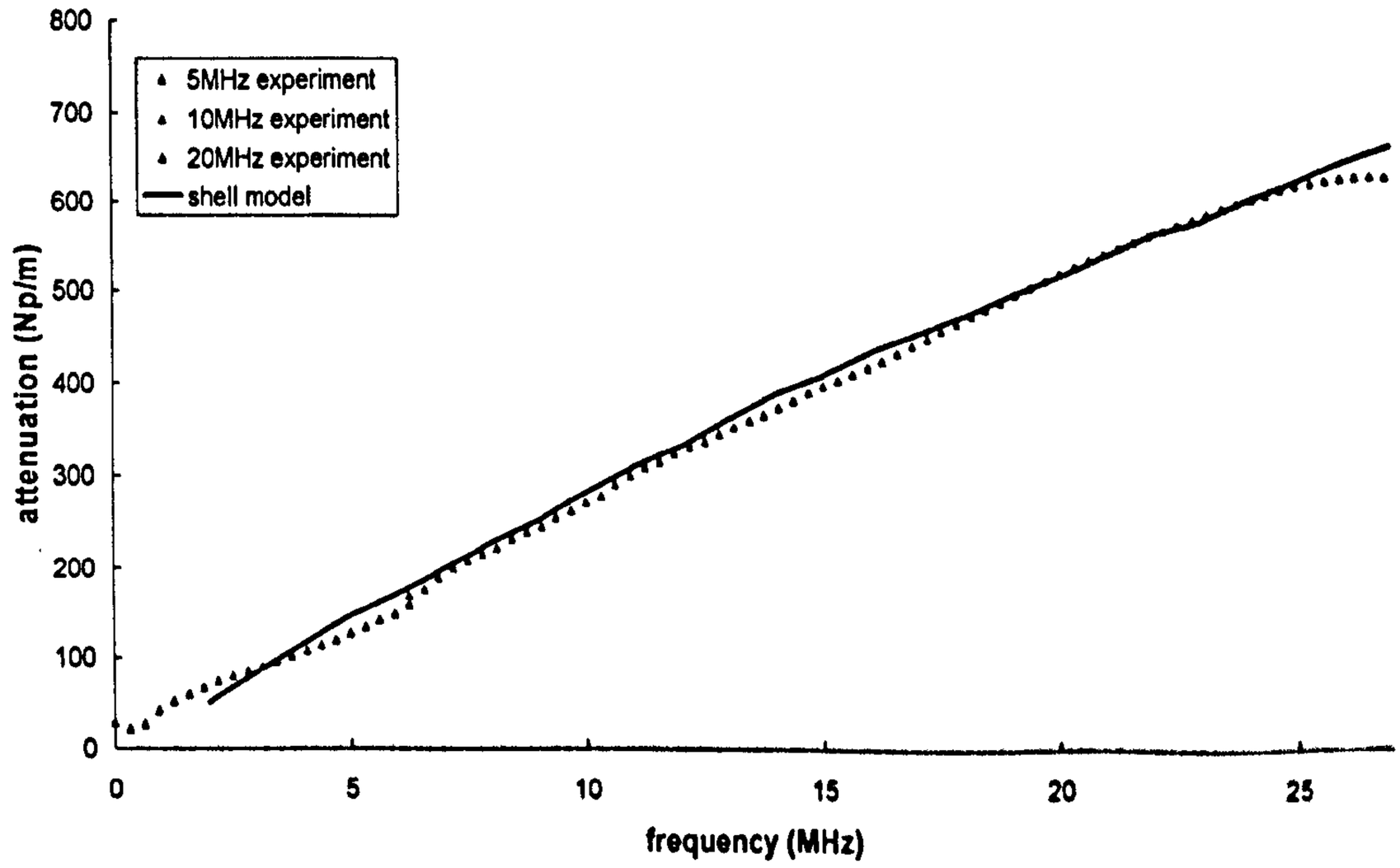

Figure 6.40. Attenuation experiment data for 40% Solvesso oil-in-water encapsulated emulsion (sample 17-B), particle diameter is 1.64 μm, and shell diameter is 1.97μm. The simulation data was predicted using the Anson and Chivers shell model.

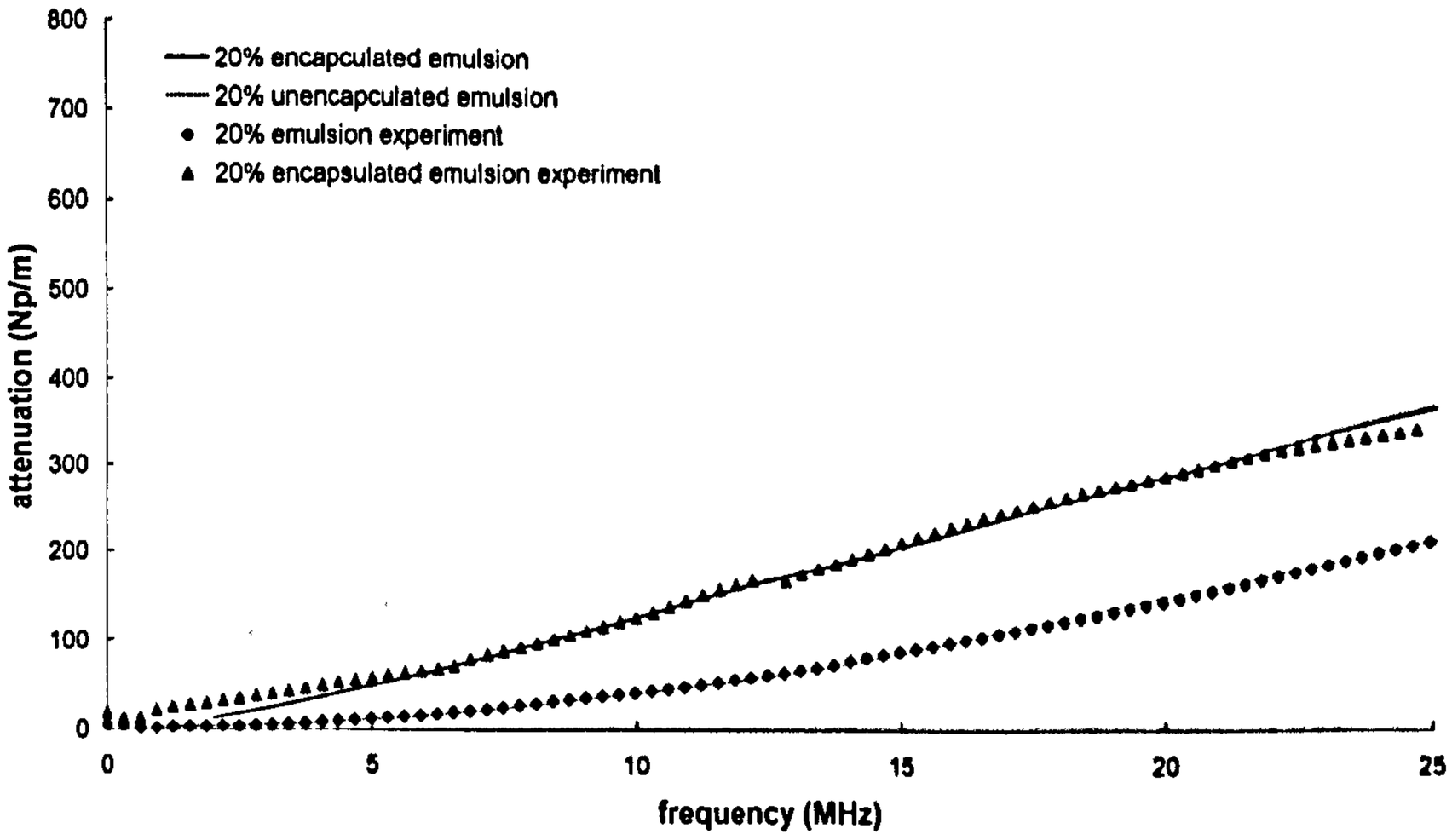

Figure 6.41a. The comparison of attenuation as functions of frequency for 20% oil in-water emulsion (sample 16-C) (the blue dots and blue line) and the 20% encapsulated emulsion (sample 16-D) (red dots and pink line), which have the same suspended particle radius.

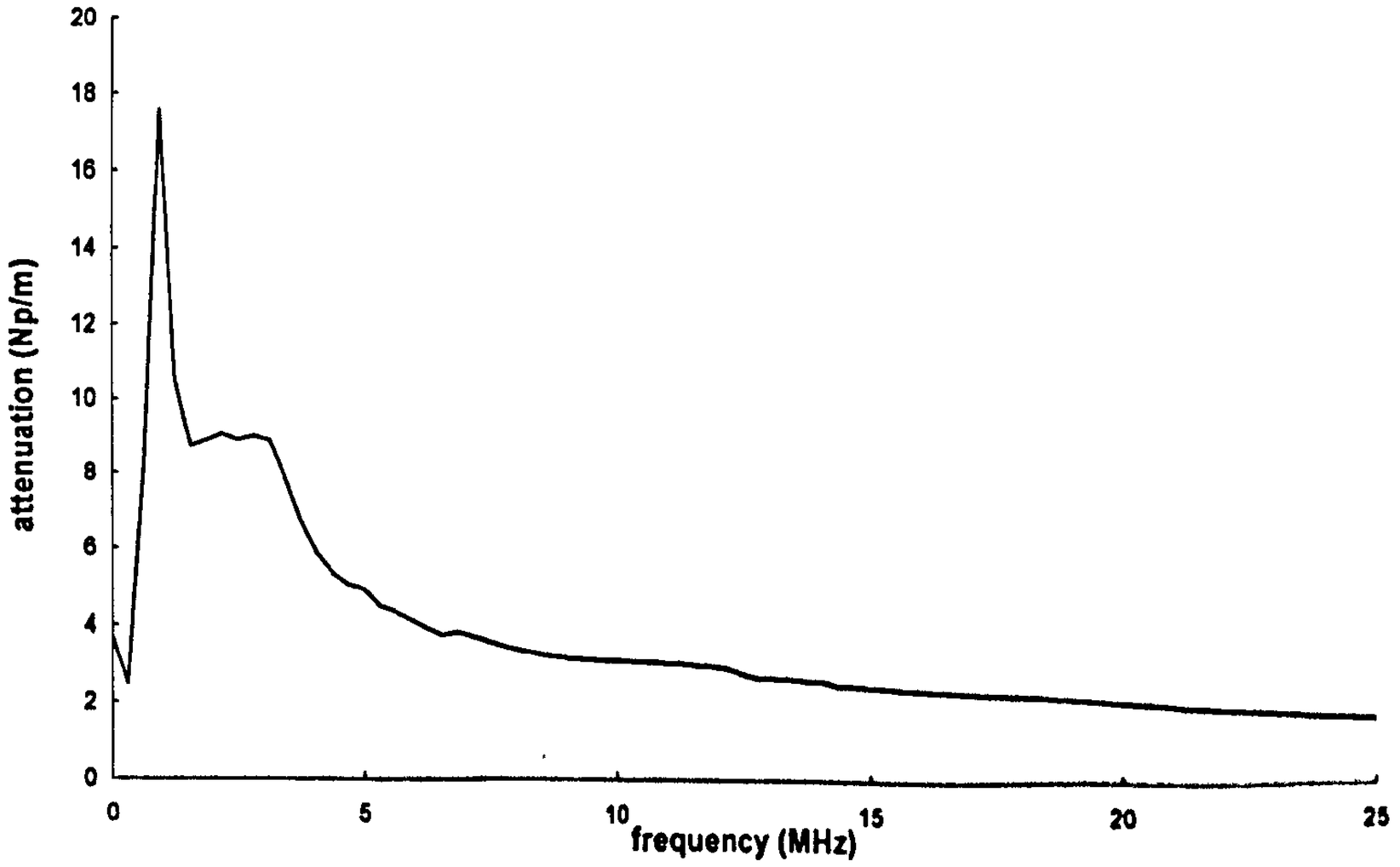

Figure 6.41b. The ratio of the attenuation in the two emulsions (sample 16-C and 16-D) shown in figure 6.41a: both have the same suspended particle radius and concentration.

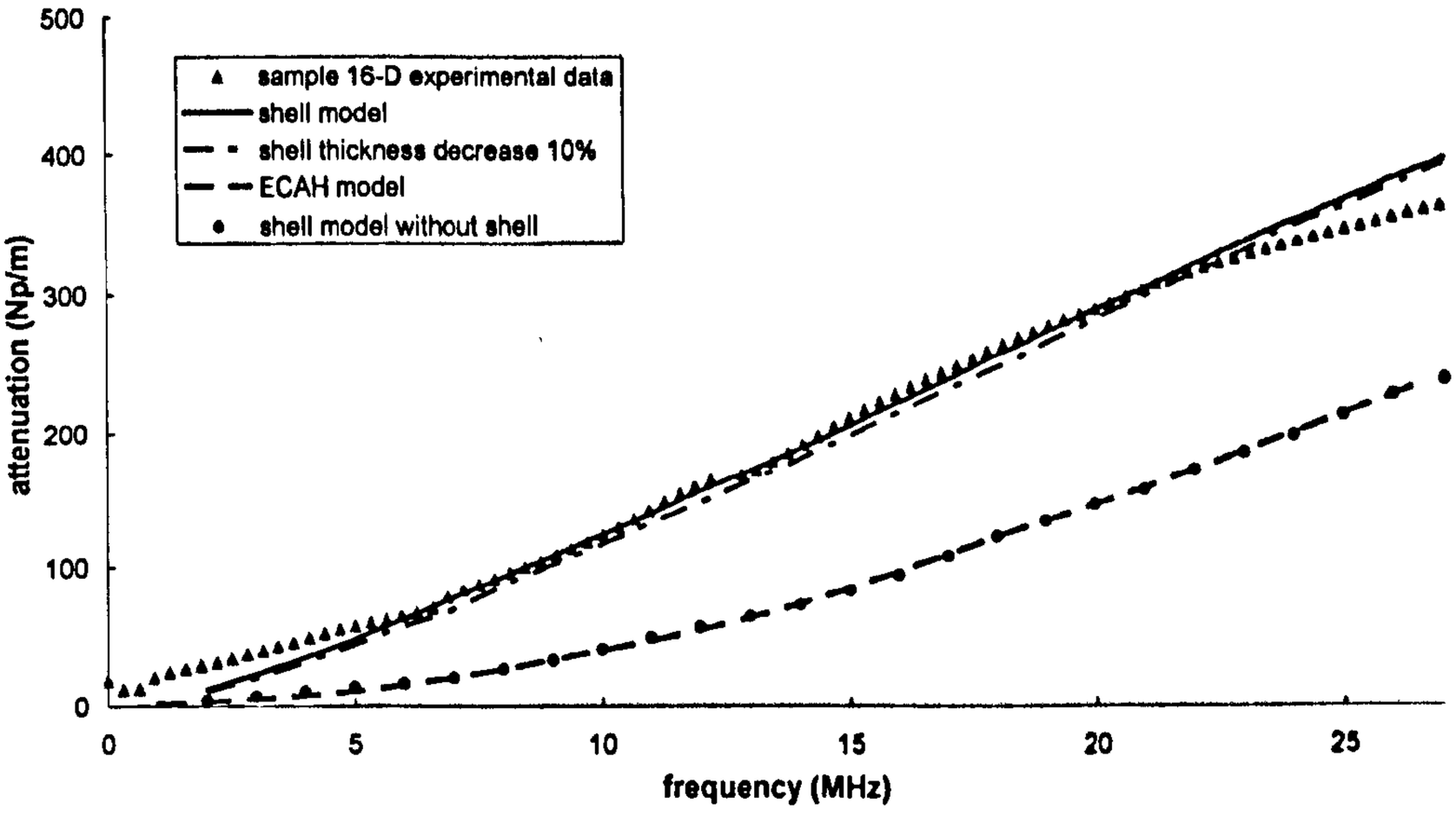

Figure 6.42. The influence of shell thickness on the attenuation for encapsulated emulsions (sample 16-D). The triangles are the experimental data, black line is the shell model fit, the dash line is the shell model results when the shell thickness decreases 10%, and the broken line is the ECAH model result, the dots are the shell model result when the shell thickness is zero.

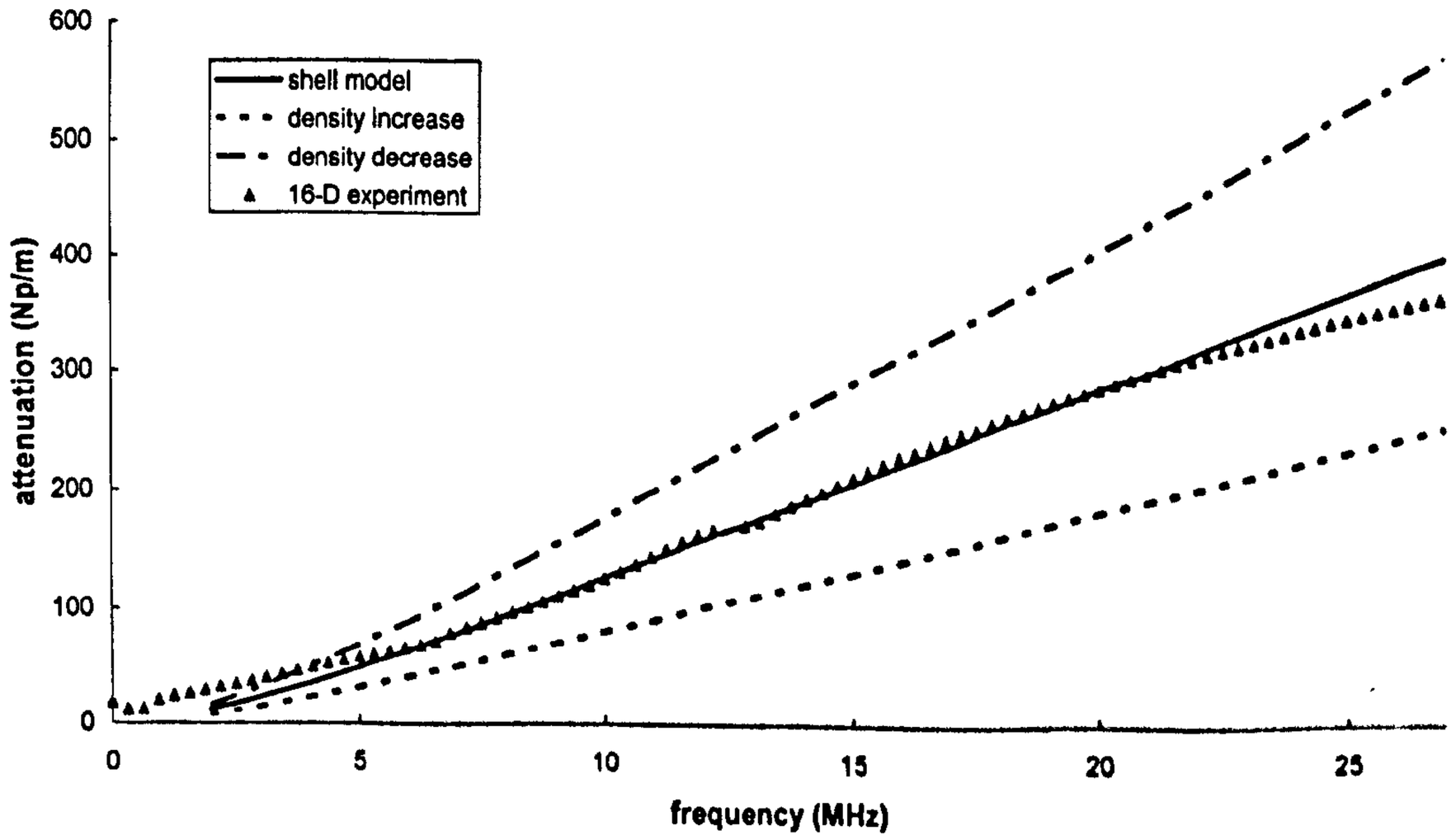

Figure 6.43. The influence of density on attenuation for encapsulated emulsion (sample 16-D). The triangles are experimental data, the solid line is the shell model fit result, and the dash line and broken line represent for the shell model results when density of shell decrease or increase, respectively.

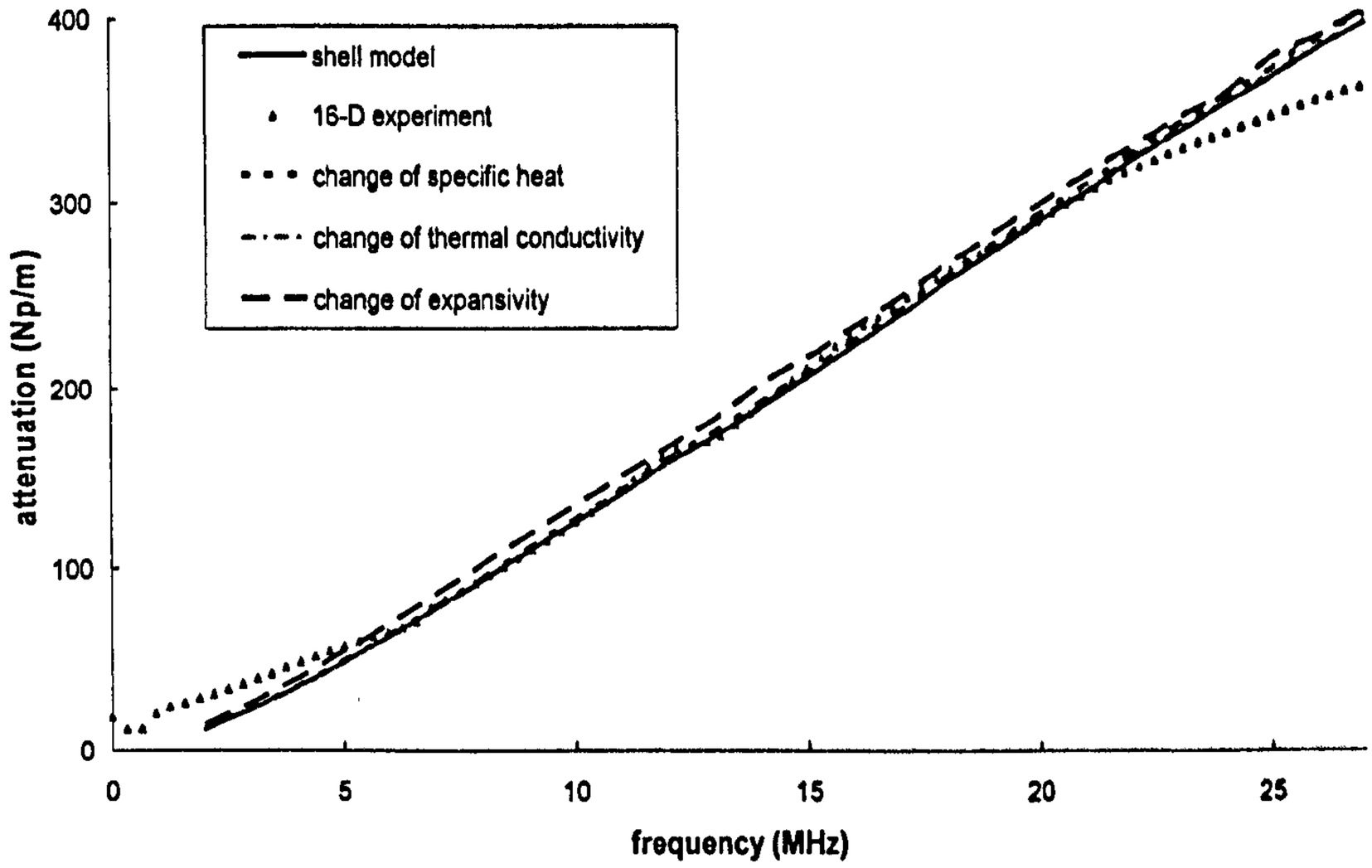

Figure 6.44. The influence of thermal properties on attenuation for encapsulated emulsion (sample 16-D). The triangles are experimental data, the solid line is the shell model fit result, broken represents the result when specific heat changes, dash line represents the result when thermal conductivity changes, and dots is the change of expansivity.

6.6 Conclusion

The aim of the work described in this chapter was to evaluate the range of applicability of the ECAH model and associated explicit expressions in the long wavelength limit and also to test the IHM model for higher concentrations when thermal overlaps could be expected. Also included here was a test of the validity of Evans and Attenborough's coupled phase theory when applied to emulsions. In line with the commercial significance of encapsulated emulsions we also examined the applicability of the Anson and Chivers extension of the ECAH model to these materials. In all of the subprogrammes experiments to measure attenuation over as wide a bandwidth

as possible were performed on carefully prepared emulsion samples. It is hoped that the data from these experiments will go some way to a 'once and for all' benchmark of the various propagation theories. This will enable designs of ultrasonic spectrometers and process monitors to be as robust as the hardware technology would allow and for them to use software that derives from the simplest propagation model that successfully simulates measured data. In this respect the principal conclusions of this chapter are:

1. The basic ECAH formulation as interpreted by Lloyd and Berry (equation 2.25) works well for concentrations as high as 50% for mean particle diameters 2.4 μm up to a frequency of 37 MHz. Importantly the explicit approximations in the ECAH theory give results identical with the full model. This is particularly significant because it will lead to much simpler software embedded into process instruments, avoiding the computations and ill-conditioning associated with the full boundary condition matrix.

2. Around the wavelength-particle size region where thermal wave overlaps could become significant, the basic ECAH model begins to overpredict attenuation, as expected. In these circumstances the HHM model was shown to give accurate simulations of measured results. In the dilute limit this model gives results equivalent to the ECAH model, and it is not complex from a computational point of view. So, returning now to the issue of a process instrument to measure PSD, it would make sense to use the HHM model as the basis of the instrument, using long wavelength approximations to aid computation, since this would cover both the dilute and the concentrated regions.

3. The coupled phase model of Evans and Attenborough has been shown to underpredict attenuation by a considerable margin; it is thought that this is due to the absence of a true elastic scattering term. The failure of this model is somewhat of a disappointment as it initially appeared to have potential for a much simplified computational kernel for a process instrument.

4. The problem of encapsulated emulsions was addressed and it was shown that the Anson and Chivers model gives good simulations of measured attenuation. It was also shown that the attenuation was sensitive to the thickness of the encapsulating shell, an important factor in the determination of the proper functionality of the emulsion. It is therefore concluded that the techniques of bulk wave ultrasonic spectrometry can be extended to include encapsulated emulsions. This may be significant for the agrochemical, pharmaceutical and food industries.

Chapter 7 Discussion

7.1 Introduction

This thesis has formed part of an ongoing programme of which the aim is to develop low cost and robust instrumentation to estimate the PSD of emulsions in an on-line situation. The overall programme includes low cost test cells which can be connected to pipework, electronic pulser-receiver platforms which are compact, robust, and also of low cost, and software to interpret raw compression wave data. This thesis focuses on part of the software development, namely on the mathematical and computational modelling of bulk wave attenuation in emulsions. This area is important because of the way in which PSD is determined from experimental data: the measured attenuation as a function of frequency is calculated and compared with the attenuation predicted by a mathematical model which has as one of its inputs a parameterized analytic function to represent the PSD, the log-normal function being the most common.

The error between experimental and predicted attenuations is calculated in a least mean square sense and the parameters of the analytic PSD are adjusted until this error is minimized. The resulting PSD is then taken as representing the PSD of the test material. This procedure requires many computations of the predicted attenuation and because of this it was thought worthwhile to focus attenuation on mathematical/computational models in order to determine the applicability of the various models available (i.e. are they good predictors) and also to arrive at the simplest model possible. Here

advantage would be gained in avoiding where possible the matrix operations associated with the full ECAH model. There were a number of problem spaces in which the models were to be evaluated, for example, small or large particles, high and low emulsion concentrations, and also special cases such as the encapsulated emulsions.

At the beginning of the project, there was much evidence in the literature to suggest that the ECAH model and extensions to it gave good prediction across a broad range of emulsion types. The alternative coupled phase model of Evans and Attenborough had the advantage that it was computationally simple and might provide a valid predictor. The question was which forms of the model(s) should be used in each problem space. These considerations form the basis of this discussion.

7.2 Coupled phase theory versus scattering theory

According to the models discussed in this thesis for the emulsion systems, they can be divided into two groups: scattering theory and coupled phase theory. Scattering theory describes the ultrasonic wave propagation on a system of isolated single-particles in the long wavelength limit. Examples are the ECAH model, which had been widely used in the semi-dilute systems; and the HHM model, which accounts for the thermal wave overlap effects, encountered on high concentrated emulsions. The coupled phase model was derived by Evans and Attenborough, and was based on the former hydrodynamic model by Harker and Temple with added the thermal effects. It took the ensemble of all particles as one imaginary 'phase' and the continuous phase as another, and used the conservation of mass and momentum to

account for the viscoinertial losses and the conservation of energy to account for the thermal losses. As far as our experimental results and simulation data are concerned, the coupled phase theory can not give accurate predictions for emulsions either with small particle sizes or with large particle sizes, at any volume fractions. Table 7.1 shows the difference between scattering model and the coupled phase model.

	Scattering model	**Coupled phase model**
Main difference	Scattering (thermal and elastic), non-self consistent,	Not scattering, use self-consistent: i.e. volume averaging for variables
Set up of equations	Conservation equations, Stress-strain relationship, Thermodynamic equations (temperature and pressure coupling)	Conservation equations (energy, mass and momentum) for each phase
Attenuation mechanisms	Intrinsic absorption, visco-inertial and thermal losses, and scattering losses	Intrinsic absorption, visco-inertial and thermal losses
Heat fluxes and hydrodynamic	Evaluated from gradients at the particle boundary	Evaluated from differences between phases

Table 7.1. Differences between scattering theory and coupled phase theory.

Figure 7.1 is a typical example, which shows the attenuation predicted using ECAH model and coupled phase model for a 25% 1-bromohexadecane oil-in-water emulsion, with a particle mean radius of 1.2 μm, together with the experimental data. It shows clearly that the ECAH model gave good fit to the experimental result whilst the coupled phase model diverged from the ECAH model from 3 MHz and underpredicted the attenuation compared with the experimental data. It is to be noted that the coupled phase model is attractive due to its computational simplicity, notwithstanding the fact that, in its current form, it is not a good simulator. It therefore warrants further study which, due to time constraints, could not be included in this project. Its mathematical

formulation should be thoroughly checked in the first instance. This should be followed by careful computations using the ECAH model with scattering phenomena removed to check whether the lack of these in the coupled phase model is the cause of the discrepancy.

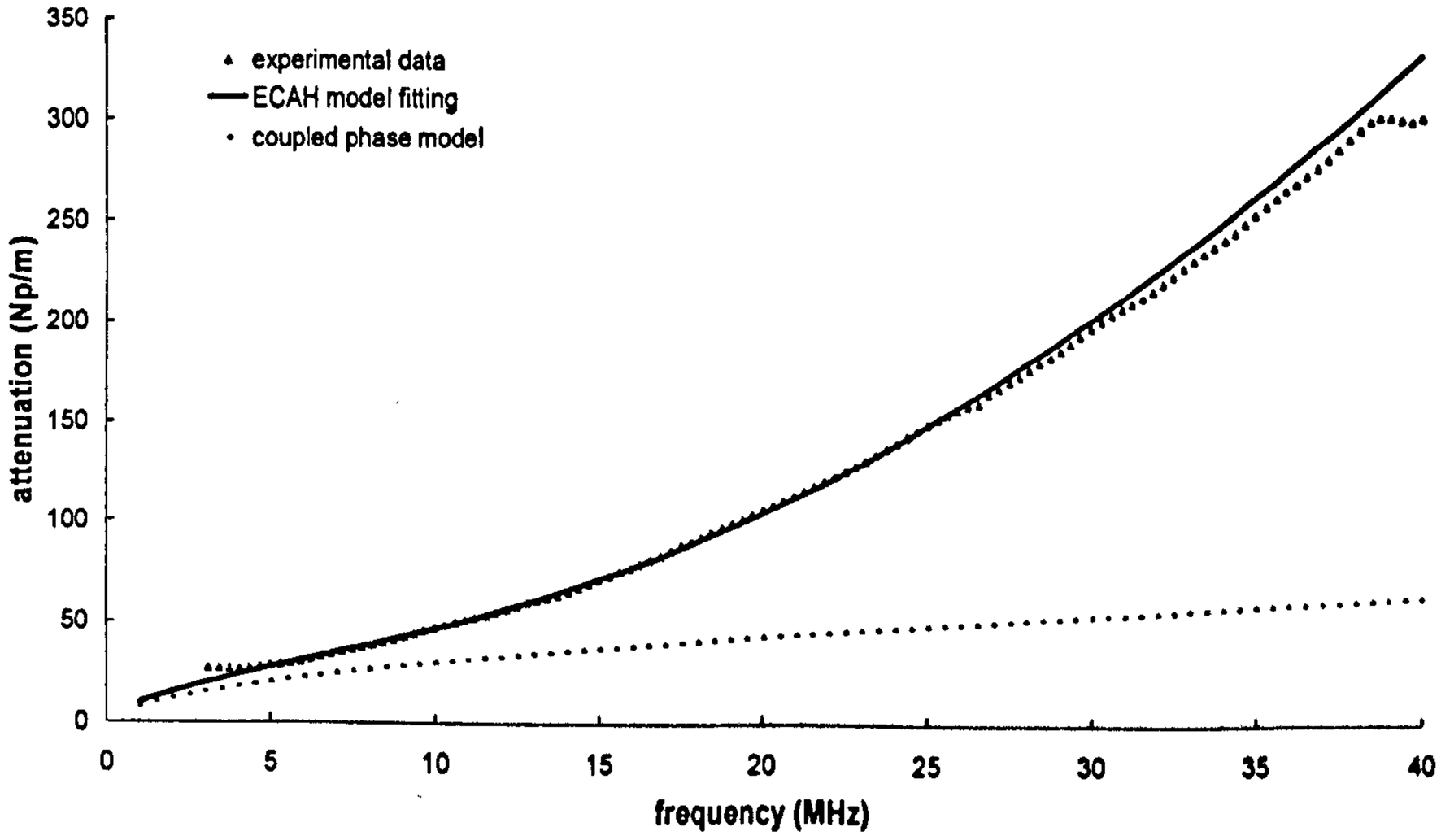

Figure 7.1. ECAH (the solid line) and coupled phase (the dotted line) predictions of attenuation compared to experimental data (triangles) for a 25% v/v 1-bromohexadecane oil-in-water emulsion, with particle radius 1.2 μm.

7.3 The ECAH model: computation of wavenumber

There are three established ways in which the partial wave solutions in the ECAH model are summed to get the composite wavenumber; these are the single scattering formulation of Foldy (1961), the multiple scattering formulation of Waterman and Truell (1961), and the multiple scattering model of Lloyd and Berry (1967) which according to its authors overcome errors in the approximates used by Waterman and Truell. The differences between these have been discussed by Challis *et al* (1998). All of the computations were

done in chapter 2 (see figure 2.4) using all three for comparison purpose and it was found that the results did not differ significantly between the models. The majority of the graphs in the rest of this thesis show the Lloyd and Berry computation. It is thought that this alignment between the models arose because the emulsions under study exhibited a low contrast in the density of the dispersed phase with respect to that of the continuous phase. It should not be assumed that the three methods will always give similar results, and so all three should always be tested in any given situation.

7.4 The explicit approximations to the ECAH model

The ECAH explicit expression for liquid-in-liquid systems was first derived by Epstein and Carhart (1953), as shown in equations 2.26 and 2.27, these equations then modified by Povey and Pinfield (1997) to get a simpler form, but the same result. Povey's simplifications for A_0 and A_1 terms were used in this thesis, leading to equation 2.30. Since the emulsions are polydispersed, Lloyd and Berry's multiple scattering formulation (equation 2.25) was modified to calculate the complex wavenumber, setting the higher order terms of attenuation coefficients to zero, the equation then becomes:

$$\frac{\beta^2}{k_c^2} = 1 - \sum_{j=1}^{J} \frac{3i\phi_j}{k_c^3 r_j^3}\left(A_{0j} + A_{1j}\right) - \sum_{j=1}^{J} \frac{27\phi_j^2}{k_c^6 r_j^6}\left(A_{0j}A_{1j}\right) - \sum_{j=1}^{J} \frac{54\phi_j^2}{k_c^6 r_j^6}\left(A_{1j}^2\right) \qquad (7.1)$$

Equation 7.1 was evaluated using the full ECAH model and using the explicit expressions for attenuations for a range of 1-bromohexadecane emulsions with large and small particle sizes (see chapter 6 sections §6.3 and §6.4, the mean sizes are 1.2 μm for large particle and 90 nm for small particle) and over a range of concentrations. Figures 7.2, 7.3, 7.4 and 7.5 show attenuation versus

frequency for large particles at 6.25%, 50%, and for small particles at 5% and 50%. These figures showed that the full ECAH model and the explicit expressions for all particle sizes and concentrations gave virtually identical results. This has the important implication that the complex computation associated with the full ECAH model can be avoided and the explicit expressions used instead for emulsions of this type. It is expected that the same will be true for other emulsions with different contrast in physical properties, although it is recommended that test computations are carried out in each new case.

A brief analysis of the data used shows that the compressional wave length is much greater than the particle radius (in the long wavelength domain), for example, at 25 °C and 40 MHz, the wavelength of the compressional wave is $\lambda = \frac{c}{f} = 37.5$ μm, which is much larger than the particle radius (1.2 μm or 90 nm). Moreover, the attenuation in dispersed and continuous phases was $1.45e^{-13} f^2$ and $2.5e^{-14} f^2$, respectively, which can be neglected compared with the real part of the compressional wavenumber ($\frac{2\pi f}{c}$). The velocity of the compressional wave is much larger than the velocity of the shear and thermal waves, which means thermal wavelength and shear wavelength smaller than the compressional wavelength. These factors provide conditions for successful application of the explicit approximations to the ECAH theory.

Pinfield (1996) pointed out that the explicit expressions have different formulations depending on different thermal and viscous wavelengths. For emulsions with similar densities between the dispersed phase and continuous phase, the dominant phenomenon is thermal transport, and so the zero-order

coefficient A_0 is important. The different analytical expressions for this term depended on whether the thermal wavelength is smaller than the particle size or not. In our calculations, the thermal wavelength was always much shorter than the particle radius during the whole frequency range from 1 to 40 MHz for large particle sizes $r = 1.2$ μm, but for small particle sizes $r = 90$ nm, the thermal wavelength is always larger than the particle radius. Because of this we did choose a different formulation based on particle radius in the calculation. For emulsions with different density contrast, both the zero-order and the first-order coefficients should be taken into account. Therefore, different expressions for the first-order coefficient A_1 should be determined depend on whether the shear wavelength is smaller than the particle size or not. As a result, it is necessary to calculate the thermal and viscous wavelengths and then choose which approximation should be used.

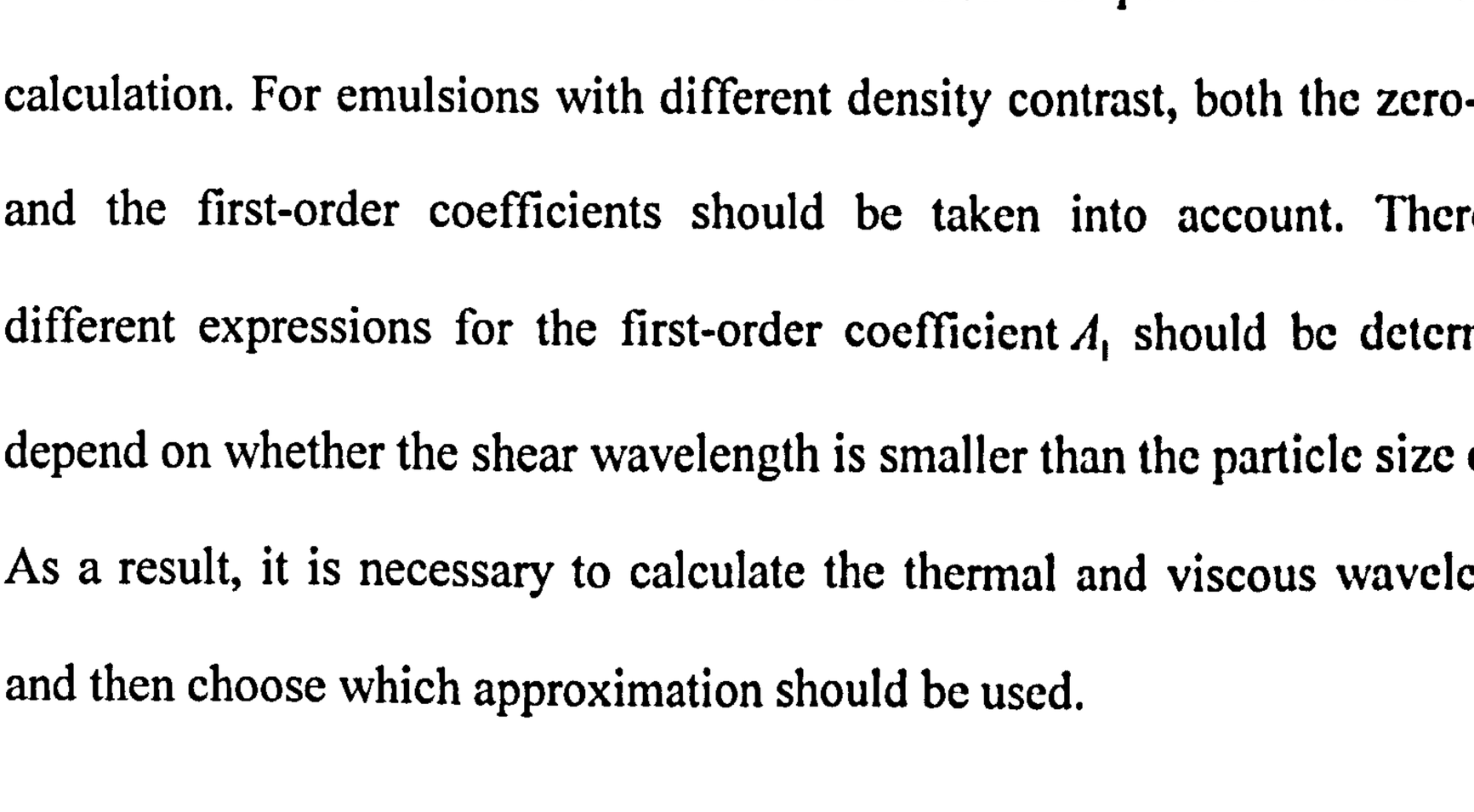

Figure 7.2. Attenuation versus frequency for 6.25% 1-bromohexadecane emulsion, using the *Mastersizer* PSD, predicted using full ECAH model (solid line) and its explicit expression (broken line).

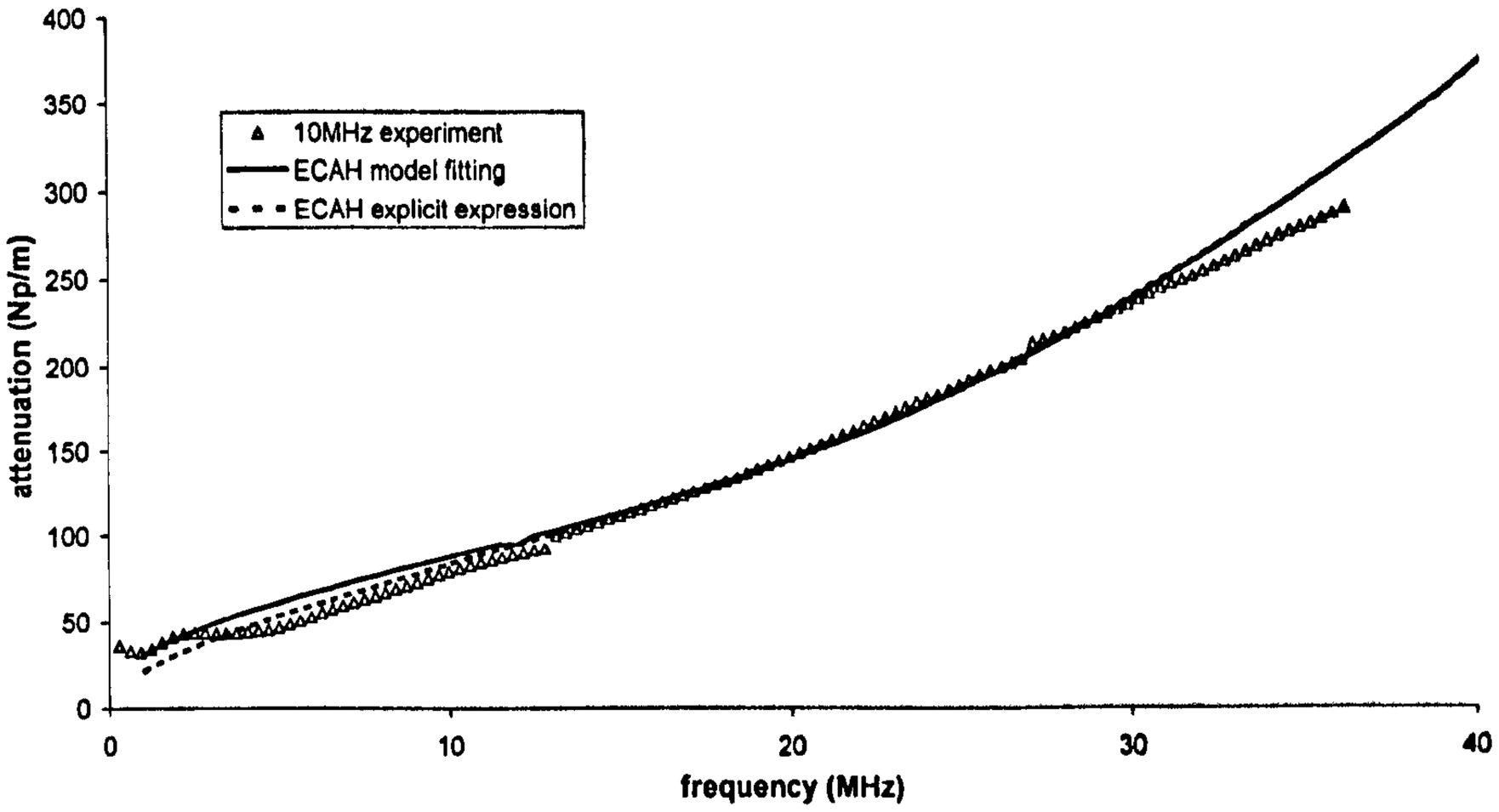

Figure 7.3. Attenuation versus frequency for 50% 1-bromohexadecane emulsion, with the *Mastersizer* PSD, predicted using full ECAH model (solid line) and its explicit expression (broken line).

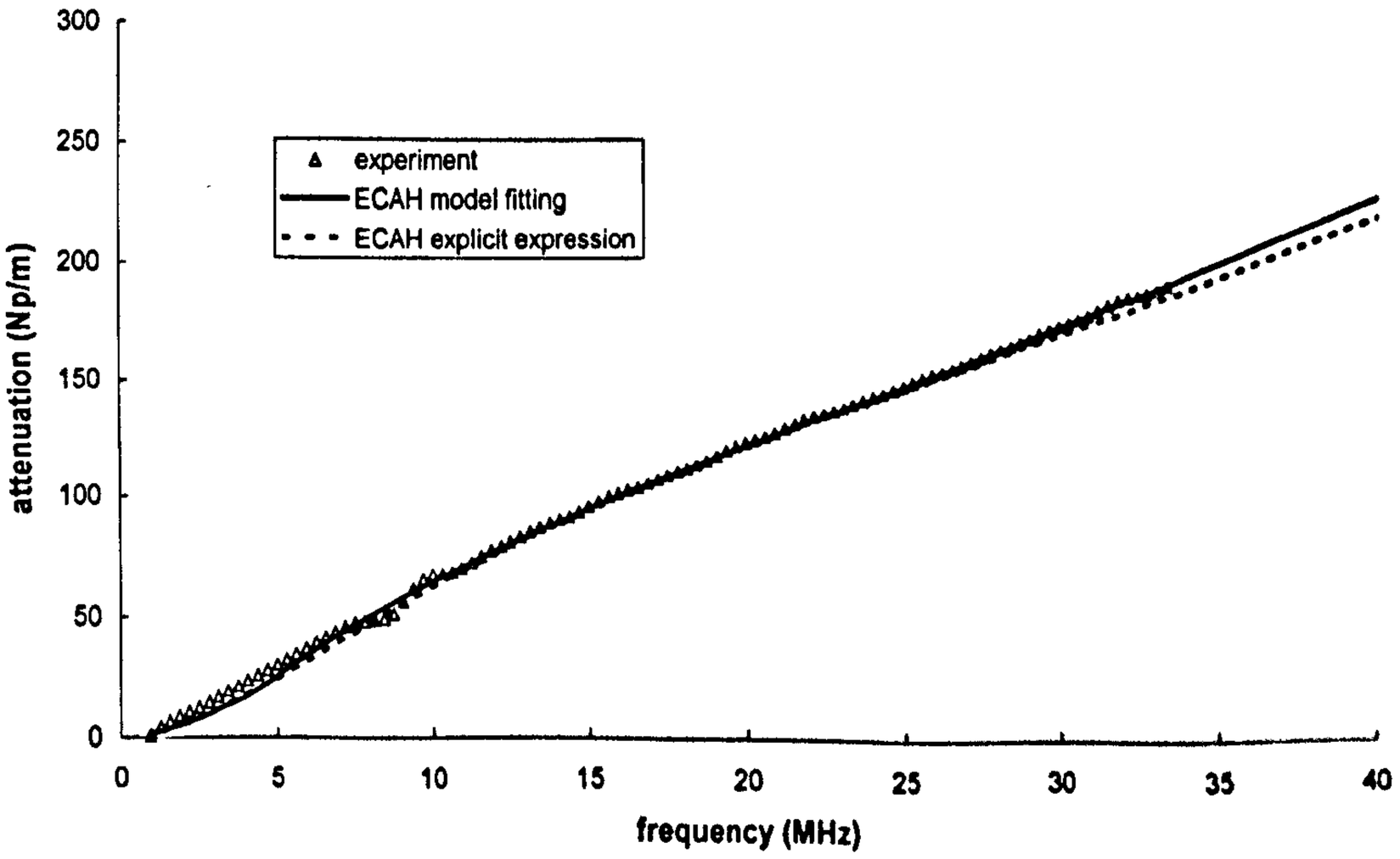

Figure 7.4. Attenuation versus frequency for 5% 1-bromohexadecane emulsion, with the *Mastersizer* PSD, predicted using full ECAH model (solid line) and its explicit expression (broken line).

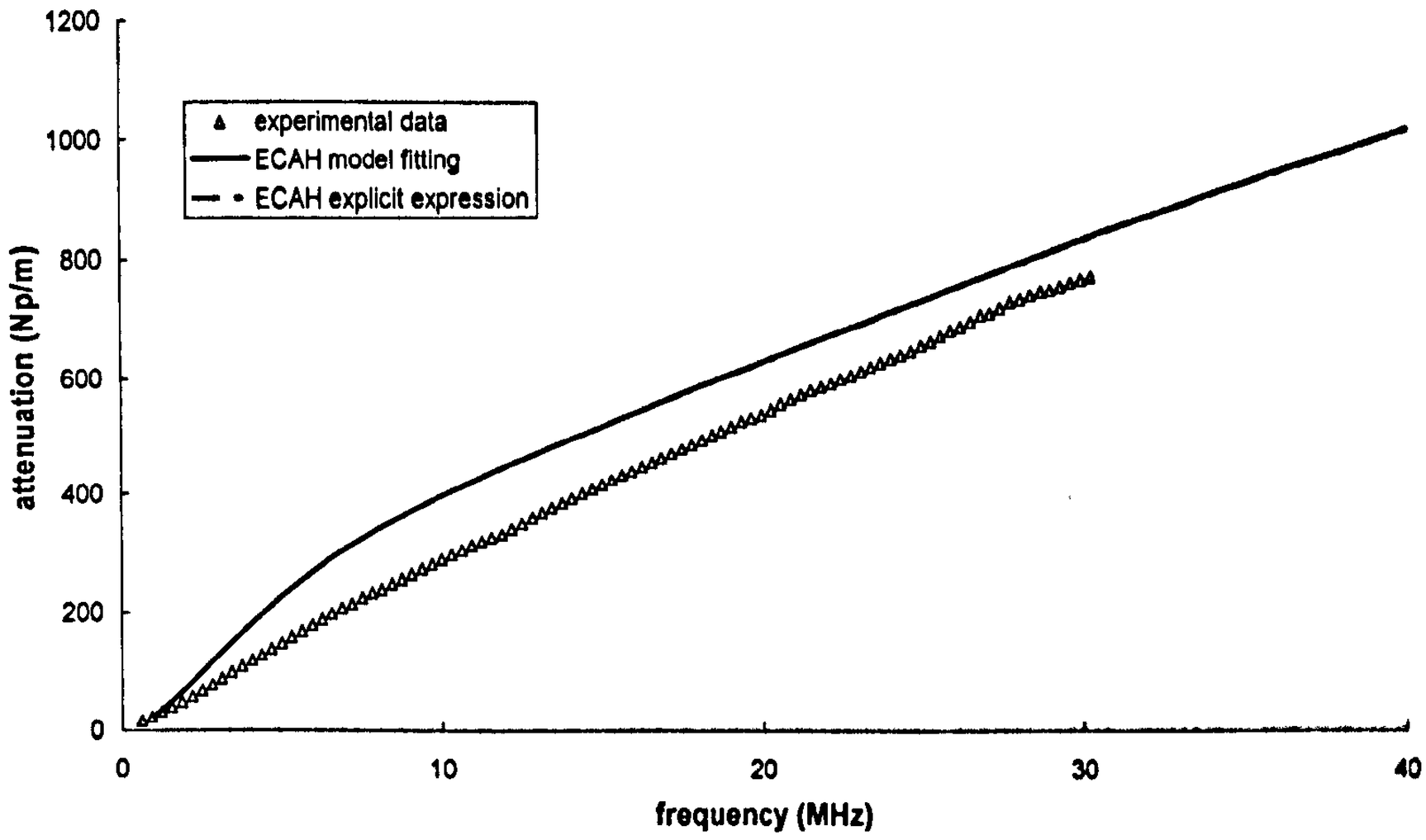

Figure 7.5. Attenuation versus frequency for 50% 1-bromohexadecane emulsion, with the *Mastersizer* PSD, predicted using full ECAH model (solid line) and its explicit expression (broke line).

7.5 ECAH model at high concentrations

It is well known that the ECAH model when applied to emulsions breaks down at high concentrations due to the overlapping of the thermal waves evanescent from adjacent particles in close proximity. The HHM model has been shown to overcome this problem. The model invokes a shell of continuous phase around each particle, with a volume equivalent to the mean free volume in the mixture. Outside of this 'shell' a new continuous phase is invoked as an equivalent medium with thermo-physical properties calculated as the volume or mass averages of the two phases. The model yields a new form for the partial coefficient A_0, which can then be used to compute the attenuation using the ECAH explicit expression. The question to be answered in this work was what particle size-concentration space we should use the HHM model. In chapter 6, experiments were performed to examine this.

Figures 6.27 to 6.31 show attenuation versus frequency for the small particle emulsions (90nm) for concentration of 5% to 50% v/v, and figures 6.12 to 6.15 give corresponding data for the large particle emulsions. All of these graphs also show the attenuation simulated using the basic ECAH model in the explicit approximation and the simulations using the HHM model. On each figure there is a frequency at which the HHM model and the experimental results, diverge from the basic ECAH model. Since this divergence is quite subtle and all experimental data has same variance, it is difficult to exactly quantify the divergence frequency. It makes more sense to identify a divergence frequency from the fundamental relationship between half the separation distance between particles and the thermal skin depth. Figure 7.6 shows the relationship between the diverged frequency and the volume fraction for large (1.2 μm) and small (90 nm) particle sizes, respectively. The points in this figure show the frequencies when the thermal skin depth equals to the half particle distance according to each volume fraction, above this frequency, there is no thermal wave interactions. For example, at 40% v/v, when frequency is smaller than 40 MHz, there is thermal overlap between particles, the ECAH model overpredicted the attenuation and the CS model can give a close prediction compared to the experimental data, see figure 6.30. At higher frequencies, the ECAH model will converge to the HHM model and the experimental data. It can be concluded that the HHM model can replace the ECAH model for concentrated emulsions with small particle radius at low frequency. At low concentrations or at high frequencies, it converges to the basic ECAH model. For emulsions with high particle concentration, it is suggested that the HHM model is used to calculate the PSD

instead of using the ECAH model, because the ECAH model can not give an accurate prediction in this situation.

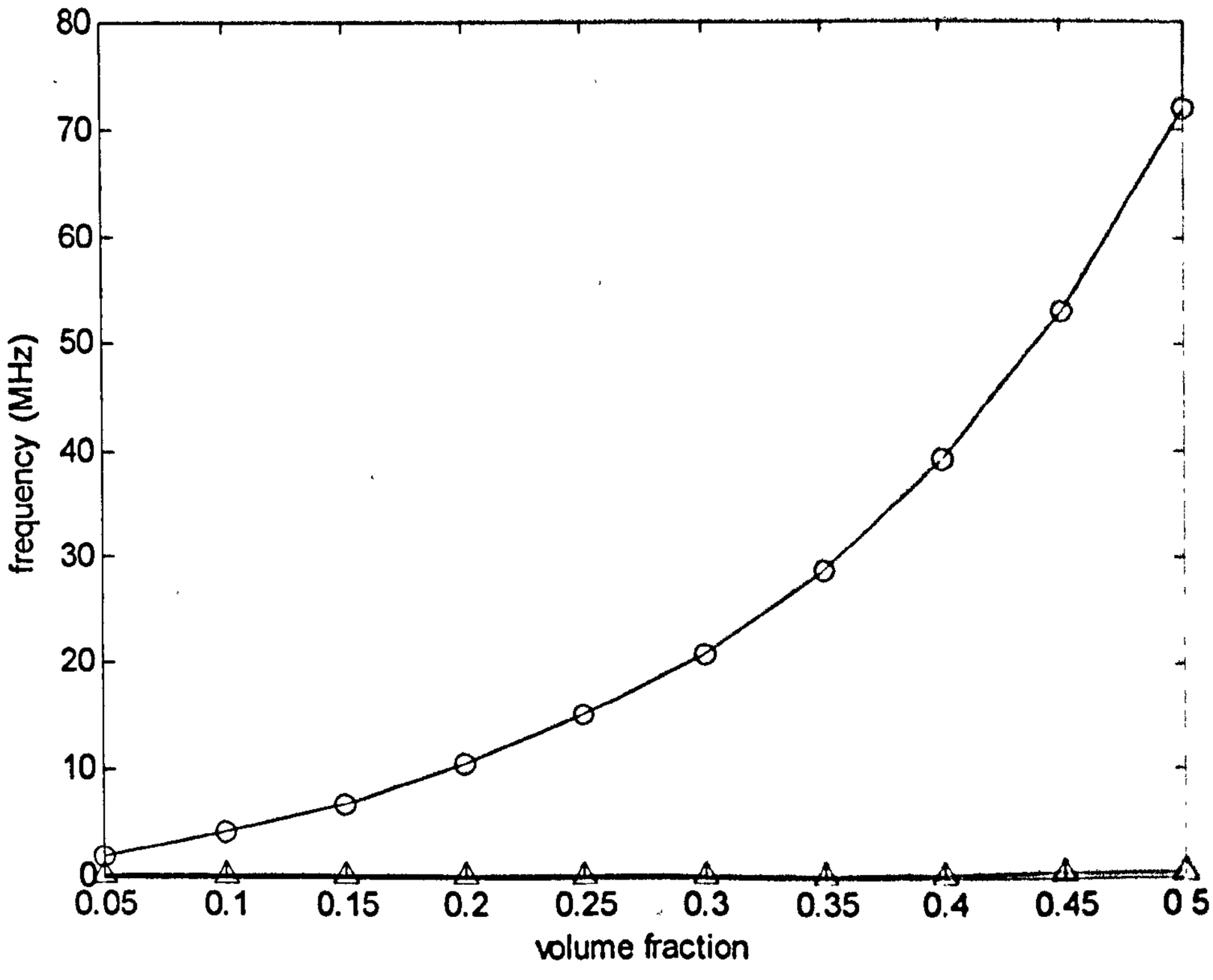

Figure 7.6. Diverged frequencies versus volume fraction for large 1.2 μm (the line with triangles) and small 90 nm (the line with circles) particle sizes.

7.6 An anomalous result for small particle emulsions

Figure 7.7 shows attenuation versus concentration for the small particle emulsion at 40 MHz calculated using the ECAH, IIIM model and from experiment. The calculation was based on the PSD for each emulsion. There is a steadily rising curve at first, whereas the attenuation measured appeared to fall dramatically between $\phi = 40\%$ and $\phi = 50\%$. An estimation of the PSD at 50% using the *Mastersizer* instrument at Leeds showed that it was different from the PSD at lower concentrations. The PSDs showed in figures 6.17 and 6.18 for lower concentrations and 50%, respectively.

Recalculation using the PSD of 40% gave the result in figure 7.8, where the ECAH model formed a straight line, and the HHM model has a drop at high concentration, which matched well with the measured data. Clearly, the emulsion had ripened, the increase in particle size causing the fall in attenuation at high concentrations. This result does show that ultrasonic attenuation measurements can be used effectively to estimate PSDs at high concentrations of dispersed phase, provided that one can 'believe' the underpinning mathematical models. This is necessary because optical techniques can not be used at high concentrations.

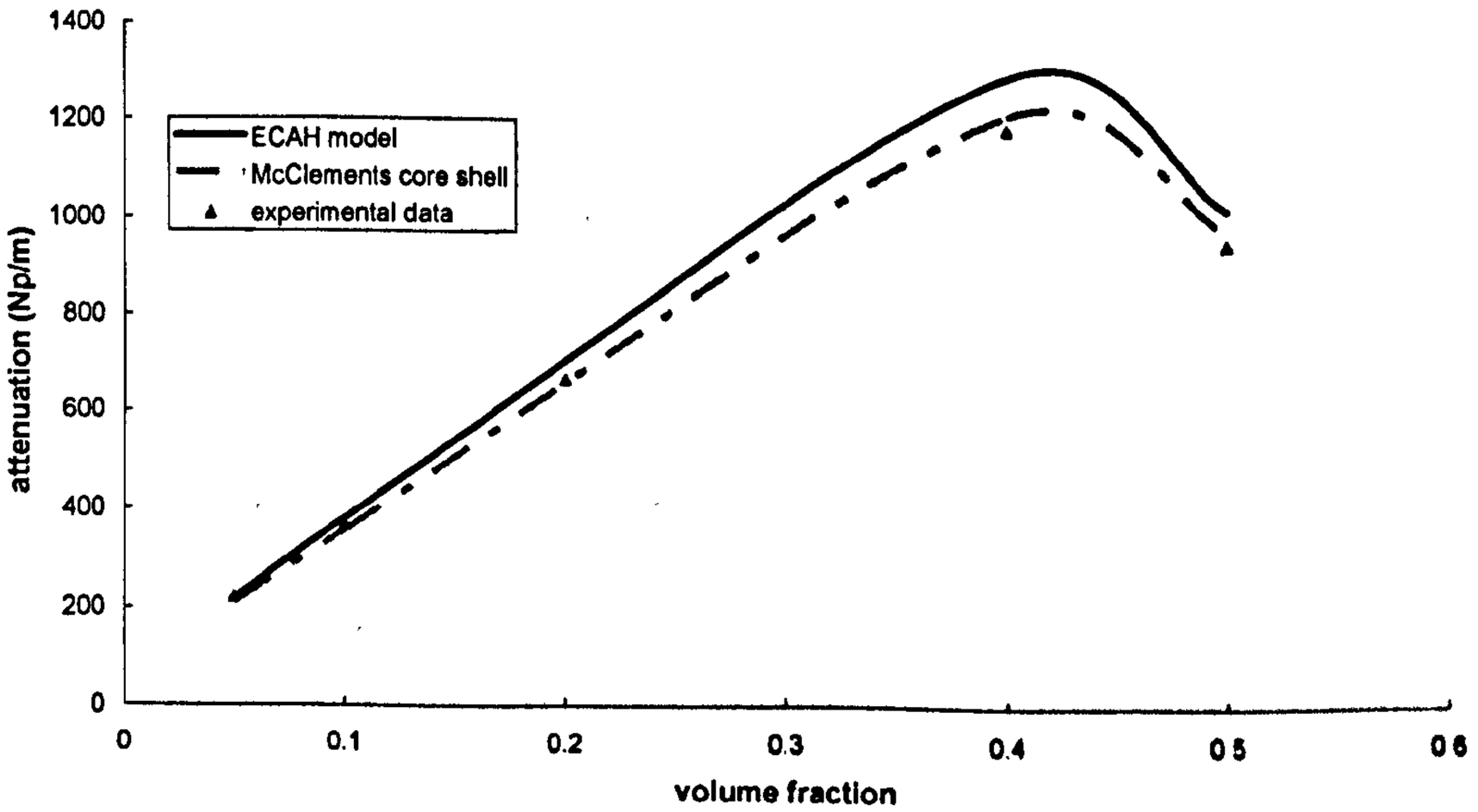

Figure 7.7. Attenuation versus volume fraction for 1-bromohexadecane in water emulsion, using PSDs calculated for each emulsion at 40MHz.

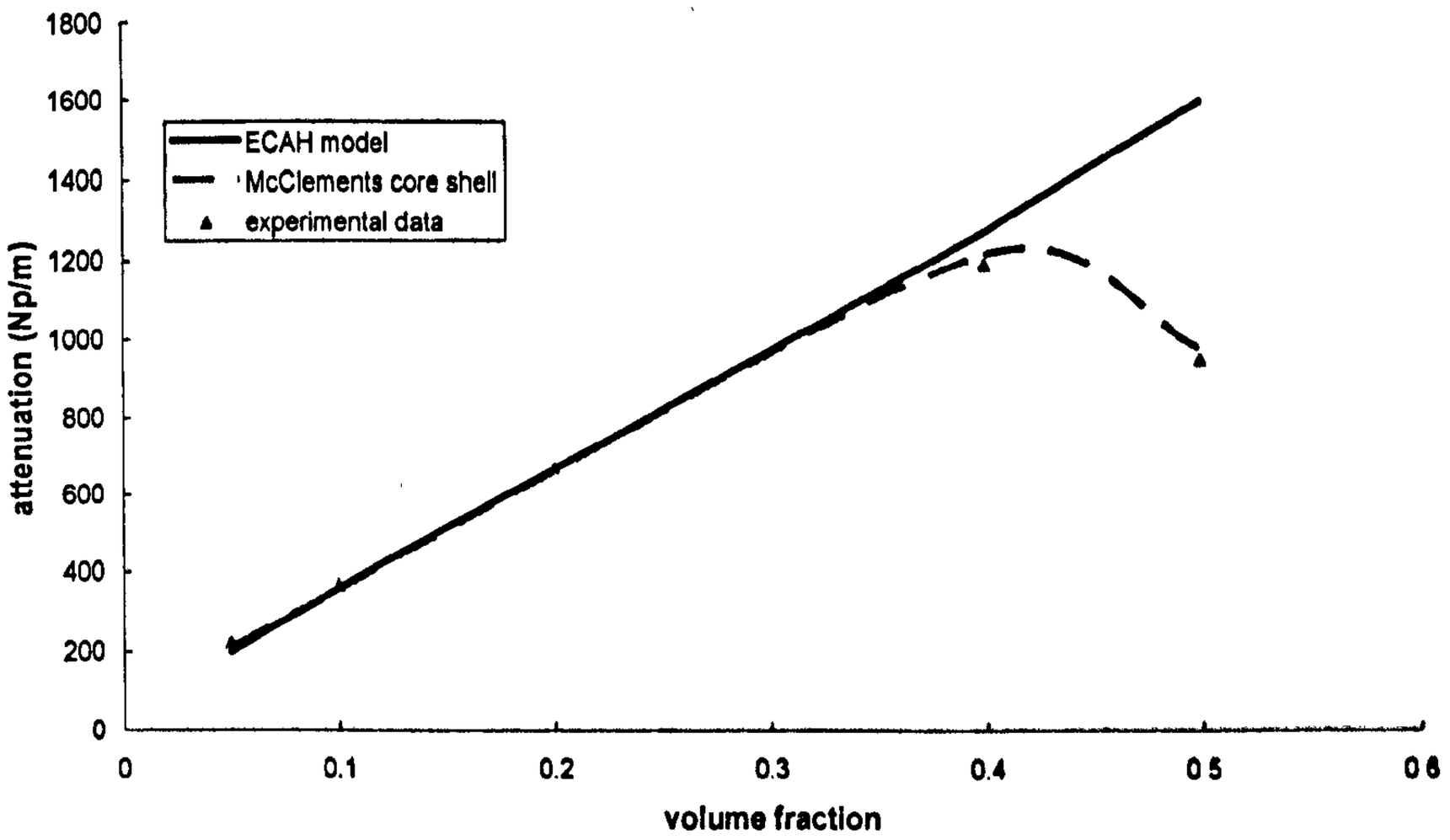

Figure 7.8. Attenuation versus volume fraction for 1-bromohexadecane in water emulsion, using PSD for the 40% emulsion at 40MHz.

7.7 Encapsulated Emulsions

The simulation of ultrasonic wave propagation in encapsulated emulsions requires some kind of shell model to represent the encapsulated particle. The relatively simple model of Hemar McClements, whilst appropriate for use with emulsions as we have shown, is not applicable in a general sense to complex particles in which either the base particle, the shell, or both exhibit strong contrasts with the continuous phase in respect of their densities and elastic properties, as distinct from their thermal properties as was Hemar McClements' case. There was a requirement to develop an inspection tool for agrochemical products which were emulsions with oil droplet particles encapsulated by polymer and suspended in an aqueous continuous phase, and so a more comprehensive shell model was required. The shell model of Anson and Chivers was chosen as the most appropriate for use with the emulsion

materials. Its appropriateness derived from the fact that it incorporated all of the loss mechanisms associated with the ECAH model — thermal, inertial and scattering. The many other shell models available in the literature tended to focus on metal shells, probably because their basis way have been in the area of target recognition in marine warfare. We have shown that the model works as well as the Hipp model (chapter 4) in the case of concentrated non-encapsulated emulsions and suspensions. For encapsulated emulsions we have shown that the model successfully simulates the unencapsulated and the encapsulated emulsions. It is also sensitive to the thickness and density of the shell and so, in principle, could be used as the basis for examining this dimension in real systems nondestructively. Figures 6.39 to 6.42 give representative results.

7.8 Concluding Remarks

Overall the work described in this thesis has answered the principal questions associated with the use of ultrasonic attenuation measurements to estimate the PSD of emulsions. Most of these questions were associated with the applicability of the theoretical models to emulsions of various particle sizes and concentrations. Excepting the encapsulated emulsions, the emulsions used were mainly based on 1-bromohexadecane as the dispersed phase. It is recognized that this is slightly limiting in relation to the range of emulsion products that might be tested, but this limit was accepted for the following reason: The Applied Ultrasonics Laboratory at Nottingham does not have advanced expertise in emulsion preparation, and so the emulsions used have to be prepared elsewhere, characterised and then transported to Nottingham. The

stability of the emulsions is therefore paramount, and so density matched mixtures like 1-bromohexadecane oil-in-water, were preferred. Within the above limitation, the work has shown that the ECAH model in its explicit approximation form is applicable across a wide range of particle sizes and concentrations, and that above a certain concentration limit the HHM model can be used. The coupled phase model of Evans and Attenborough is rejected for the time being. The HHM model can also be used with confidence for low concentrations and therefore could form a singular basis for an emulsion particle sizing instrument, particularly if a fast and stable algorithm is developed to represent it computationally. In summary the working limit for $\sqrt{f}r$ can be derived from formula 2.39:

$$\sqrt{f}r \le \frac{\sqrt{\frac{\kappa}{\pi\rho C_P}}}{\frac{1}{\phi^3}-1} = D \qquad (7.2)$$

which means given the particle concentrations, when the products of $\sqrt{f}r$ is less than the constant D, the HHM model is applicable.

The utility of the Anson-Chivers model has been demonstrated in the context of encapsulated emulsions. It requires high computational effort which could be reduced at a later date if it could be reduced to a form of explicit approximation along the lines of the basic ECAH model.

Chapter 8 Summary, Conclusion and Future Work

8.1 Summary

Chapter 1 presented a brief introduction of the background of this work and a framework to this thesis.

Chapter 2 gave an in depth examination of the wave propagation in emulsions. The most widely used scattering theory in suspensions and emulsions is due to Epstein and Carhart (1953) and Allegra and Hawley (1972) (known as the ECAH model), which incorporates both thermal and visco-inertial loss mechanisms in a single scattering system. The wave equations, boundary conditions, and the matrix equations were discussed in this chapter. The single scattering theory by Foldy (1961), and the multiple scattering theories by Waterman and Truell (1961), and Lloyd and Berry (1967) were presented. In order to avoid solving the complex matrix equation, Epstein and Carhart and Allegra and Hawley developed the explicit expressions for attenuation coefficients A_0 and A_1 terms for both fluid particles and solid particles, these terms were revised by Pinfield (1996) and Povey (1997) to obtain a simpler formulation. At the end of this chapter, we investigated the reasons why this model fails in the case of high particle concentrations. The problem is that in concentrated systems, each suspended particle cannot be regarded as independent of its neighbours. For instance, in the case of emulsions, thermal flux away from a particle is affected by a corresponding

flow of heat away from adjacent particles. The basic ECAH model did not take account of these interactions.

Chapter 3 investigated the theories which can be used in concentrated emulsions. They are HHM model and Evans and Attenborough's coupled phase model. The HHM model attempted to deal with the heat flux problem by imposing a shell of pure continuous phase around the particle, outside the shell there is a continuous phase with properties averaged to take account of both suspended particles and continuous phase. Heat transport away from the particle and its shell is then determined by the boundary condition at the shell boundary — an interface between pure continuous phase and the averaged continuous phase. This model was developed to take into account of the thermal overlap effect. It has been shown in this thesis that it can be used in highly concentrated emulsions with low density contrast.

The coupled phase theory of Evans and Attenborough includes both hydrodynamic and thermal effects and can be used for a wide range of mixture types. It does not incorporate effects due to the crowding of adjacent particles, but due to the self-consistent property, it could in principle be used for a wide range of concentrations. The advantage of the coupled phase model is there are no complex Bessel and Hankel functions, and it is very easy to solve for the complex wavenumber. Besides this, it can be used in any mixture with different concentration. However it was shown to seriously underpredict attenuation.

Chapter 4 investigated the Anson and Chivers (1993) shell model, which considered the sound scattering and attenuation by shell structures immersed in fluids. There maybe different combinations of the three media. This thesis

examined is a fluid core sheathed in a layer of polymer shell, suspended in a fluid. It took into consideration of viscoelasticity in the shell, thermal and viscous effects in the core and the surrounding fluid. A software based on the Anson-Chivers shell model was developed, which is stable at very low *kr* value when considering the thermal effects. The result was compared with previous results obtained by Anson and Chivers on the basis of $f(0)$ (the far field scattering amplitude when $\theta = \pi$), and showed good agreement. We also calculated the attenuation for the encapsulated emulsions and then compared with the experimental data. The work done by Hipp (2002a, 2002b) was also included in this chapter, who used Anson and Chivers boundary conditions to set up a 12×12 matrix equation for the HHM model, which is the case of an imaginary shell of pure continuous phase around the particle, outside the shell there is an effective medium, whose properties can be calculated using the volume average relationships. At the last part of this chapter, the comparison of Hipp's model with Anson and Chivers' model showed that they gave identical results.

Chapter 5 gave a brief description of the wide bandwidth ultrasonic spectrometer that was used for all the experimental measurements. The electronic apparatus that was used and the construction of the test cell were presented, along with the procedures that were utilised for data capture and digitization of the received acoustic signals. The methods by which ultrasonic attenuation and phase velocity were calculated from the frequency spectra were also presented. We presented an example experiment to measure the attenuation and phase velocity of pure oil, the result was successfully compared with the previous results from others. The errors and uncertainties in

this experiment were investigated. It was found that the electronic noise, expressed in the frequency domain, maps into errors in attenuation in a highly nonlinear way, which suggested that the minimum error can be obtained when the product of attenuation and gauge length is around 1 Np.

Chapter 6 presented the comparisons of experimental data and simulations using the models we discussed in chapter 2 and 3 for emulsions with different concentrations. The samples chosen to be examined encompassed both the large and small suspended particle sizes. Four models were compared with the experimental data for all the samples. It was found that the full ECAH model gave good predictions for all the volume fractions at large particle sizes, whereas, for the small particle sizes, it began to give a discrepancy with respect to the experimental data at high concentrations, due to the thermal wave interaction effects between the neighbouring particles. The ECAH explicit expression closely followed the results of ECAH model for all samples, therefore, we can use it to replace the full ECAH model in the long wavelength region. However, the explicit expression has some limitations, it can be used when the following conditions were met:

1. It can only be used in the long wavelength region;
2. The imaginary part of compressional wavenumber can be neglected for both particles and continuous phase;
3. Both the thermal wavelength and shear wavelength must less than the compressional wavelength.

All the three conditions were met in this work, with the frequency range from 1 to 40 MHz and particle size between 0.09 μm to 1.2 μm. At high particle concentrations, the ECAH explicit expression also gave a higher prediction for

small particle size systems, and this was expected because it did not take into account the particle interactions. Our simulations showed that the IIIM model worked well at high volume fraction (for example 50% v/v). This is because this model considered the thermal overlap effects, reducing the attenuations at a high concentration and at low frequencies. The coupled phase model did not give the correct attenuation in any of the experiments, although it can be used for all volume fractions, it seemed to give a much smaller prediction than the experimental result. The experiments for the encapsulated emulsions showed good agreements with our simulations using the Anson and Chivers shell model, which means that we can use this model in the future to predict the attenuation for the encapsulated emulsions without wavelength and frequency limit. Examining the parameters of the media, we found that the attenuation is very sensitive to the density and thickness of shell.

In chapter 7, the experimental results and simulation results were analysed. From the initial investigations, it was concluded that the IIIM model is a good alternative for measuring the emulsions with high volume fraction. The Anson and Chivers shell model can be used for both emulsions and suspension, either with shell or without shell.

8.2 Conclusions

The principal group of conclusions are that the ECAH model works well for density matched emulsions with concentrations up to around 20% v/v, the exact figure depending on the particle sizes in suspension. The explicit approximations to the ECAH model, as modified by Povey and Pinfield work equally well and are to be preferred due to their computational simplicity.

Above the concentration limit cited above, the HHM model is appropriate for use in particle sizing, and it can also be used for lower concentrations. It is therefore the preferred basis for a particle sizing algorithm.

The second group of conclusions concern the Anson-Chivers shell model: this can be used both for emulsions and suspensions, as demonstrated by Hipp. More significantly, it has been experimentally verified that it applies to encapsulated emulsions and could usefully form the basis of an ultrasonic characterization tool for these materials.

8.3 Potential areas for future development

Perhaps the most important of these is to repeat the work on non-encapsulated emulsions using all phases which differ in densities from the continuous phase. It would also be worthwhile to try to extend the work to emulsions of ultra-high concentration, say 60-70% v/v. Given the framework already set up, this could be done relatively rapidly provided that preparation and characterisation of the emulsions could take place in the laboratory.

In terms of the engineering of instruments it will be important to develop a fast and robust algorithm for the HHM model, and to embed this into an over arching particle sizing algorithm. The same could apply to the Anson-Chivers shell model, and here it would be useful to apply analytical methods in order to arrive at an explicit approximation so as to reduce its computational complexity.

The problems of small and large particles in low and high concentrations apply equally to suspensions of solid particles with a high density contrast with respect to the continuous phase. It would therefore make good sense to

carry out a very similar programme of work for these materials. Here the high concentration problem arises due to overlapping of viscosity wave fields between adjacent particles, and some kind of shell model could be developed here. At the end of this PhD programme the Anson-Chivers model was applied to concentrated suspensions. The shell was pure water phase, as with the IIIM model, whilst the continuous phase was given properties volume averaged between the materials of both phases. The simulation of attenuation versus frequency and concentration was much better than the basic ECAH model. Figure 8.1 shows the attenuation simulation and experimental results for a Ludox-in-water suspension, with particle radius around 16.5 nm and concentration of 33.6% v/v, using ECAH model, the Anson-Chivers shell model (Homles et al, 2007). This figure shows that there are exciting prospects for the future.

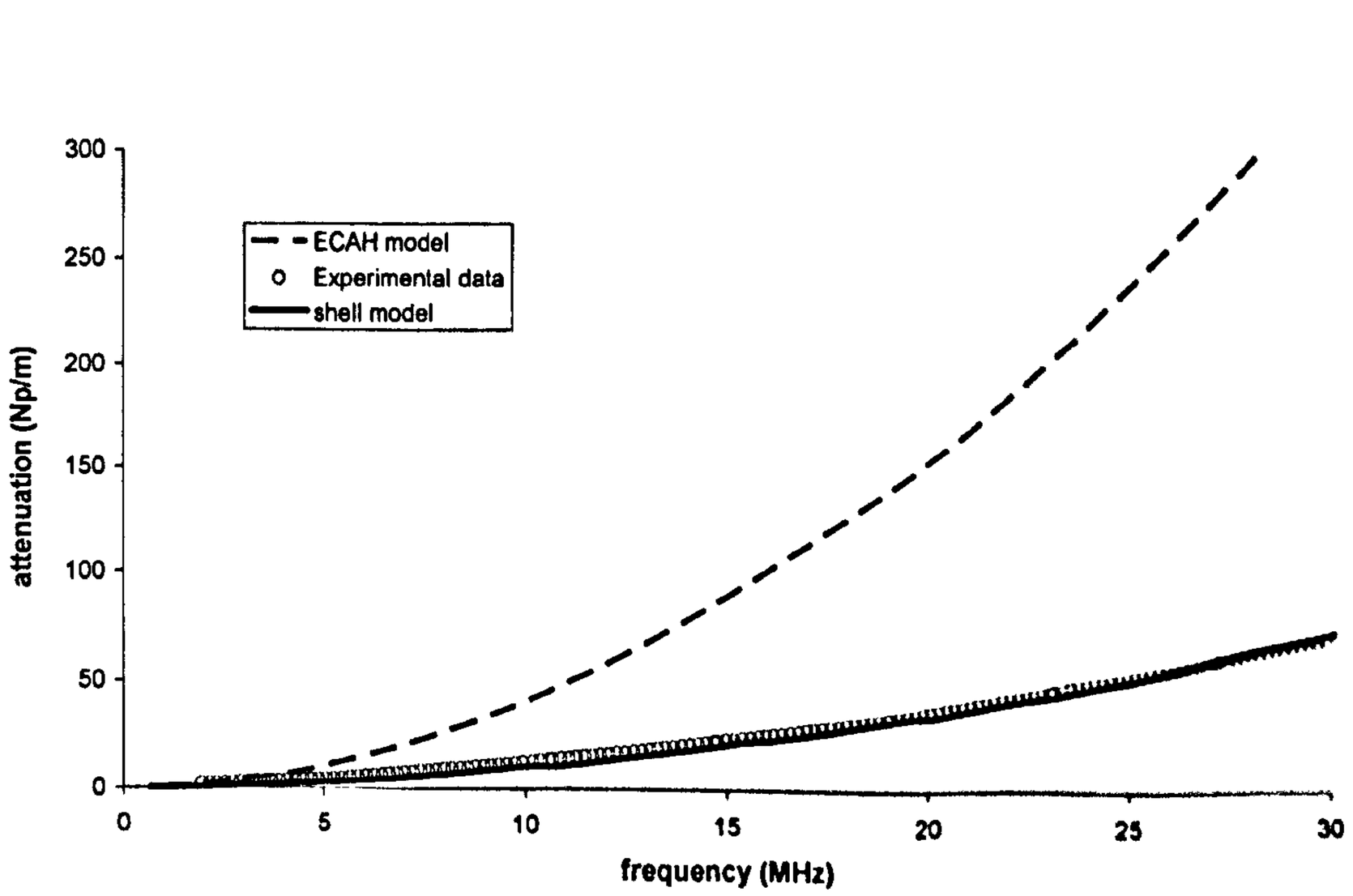

Figure 8.1. The experimental attenuation results (the red circles) and prediction using ECAH model (broken line), and Anson-Chivers shell model (solid line) for Ludox-in-water suspension with particle radius of 16.5 nm and concentration of 33.6% v/v.

References

Ahuja A S (1973) J. Appl. Phys. Vol.44 pp 4863

Allegra J R and Hawley S A 1972 Attenuation of sound in suspensions and emulsions: theory and experiments J.Acoust.Soc.Am. vol.51 1545-1564

Ament W S (1953) Sound propagation in gross mixtures J. Acoust. Soc. Am. 25 pp 638–641

Ament W S (1959) US Naval Research Lab. Tech. Rept. 5307

Anson L W and Chivers R C (1993) Ultrasonic scattering from spherical shells including viscous and thermal effects, J. Acoust. Soc. Am., Vol. 13, No 4, Part 1 pp1687

Berryman J G (1980) Confirmation of Biot's theory Appl. Phys. Lett. Vol.37 pp 382–384

Biot M A (1962) Generalised theory of acoustic propagation in porous dissipative media J. Acous. Soc. Am. 34 1254-64

Blair J J (1998) Error estimates for frequency response calculated from time-domain measurements, IEEE Trans. Ultrason., Ferroelect., Freq. Contr., vol 49 pp475-483

Challis R E (1982) The Effect of Transducer-Reflector Angulation on Echos Received from Targets Using Ultrasonic Pulse-Echo Equipment. Acoustica.Vol.50. No 3, pp.221

Challis R E and Kitney R I (1991) Biomedical signal processing (in four parts), Part 2 "The frequency transforms and their inter relationships", Med. & Biol. Eng. & Comput., 29, pp1-17

Challis R E, Harrison J A, Holmes A K and Cocker R P (1991) A wide bandwidth spectrometer for rapid ultrasonic absorption measurements in liquids J. Acoust.Soc.Am.Vol.90, No 2, Part.1

Challis R E, Freemantle R.J and Holmes A K (1995) On ultrasonic compression wave absorption in unfilled and filled polymers, Proc.I.O.A vol17 Part6 pp 23-30

Challis R E, Tebbutt J S and Holmes A K (1998) Equivalence between three scattering formulations for ultrasonic wave propagation in particulate mixtures, J. Phys., D: Appl. Phys. 31 pp 3481-3497

Challis R E, Povey M J (2005) Ultrasonic techniques for characterizing colloidal dispersions Rep. Prog.Phys. 68 pp 1541-1637

Chanamai R, Herrmann N and McClements D J (1999) "Influence of thermal overlap effects on the ultrasonic attenuation spectra of polydisperse oil-in-water emulsions" Langmuir Vol.15. No.10, pp 3418-3423

Davis M C (1979) Attenuation of sound in highly concentrated suspensions and emulsions J. Acoust. Soc. Am. 65(2) pp 387-390

Diebold G J (1977) Effects of A/D converter resolution in signal averaging, Rev. Sci. Instrum., Vol. 48, pp1689-1694

Dukhin A. S, Goetz P J and Hamlet C W (1996 a) Acoustic spectroscopy for concentrated polydisperse colloids with high density contrast Langmuir 12, pp 4987-4997

Dukhin A. S, Goetz P J and Hamlet C W (1996 b) Acoustic spectroscopy for concentrated polydisperse colloids with low density contrast Langmuir 12, pp 4998-5005

Eggers F and Kaatze U (1996) Broad-band ultrasonic measurement technique for liquids, Meas. Sci. Technol. 7, pp.1-19

Epstein P S and Carhart R (1953) The absorption of sound in suspension and emulsions: I. Water fog in air J.Acoust.Soc.Am. vol.25 553-65

Evans J M and Attenborough K (1996) A coupled phase theory for sound propagation in an emulsion of heat-conducting, compressible liquids, 15th International Congress on Acoustics

Evans J M and Attenborough K (1997) Coupled phase theory for sound propagation in emulsions J. Acoust. Soc. Am. 102(1) pp 278-282

Evans J M and Attenborough K (2002) Sound propagation in concentrated emulsions: Comparison of coupled phase model and core-shell model J. Acoust. Soc. Am. 112(5) pp 1911-1917

Fikioris J G and Waterman P C (1964) Multiple scattering of waves II. Hole correctios in the scalar case J. Math. Phys. 5 pp 1413-1420

Foldy (1961) Multiple scattering of waves J. Math. Phys. 2 pp512-537

Fox L and Wilkinson J H (2001) The NAG Fortran Library Manual, Mark 20, The numerical algorithm group Ltd

Gaunaurd G C and Kalmins A (1982) Resonances in the sonar cross sections of coated sherical shells, Int. J. Solids Struct. 18, 1083-1102

Goodman R R (1982) Reflection and transmission f sound by elastic spherical shells, J. Acoust. Soc. Am. 34, 338-344

transition J. Acoust. Soc. Am. Vol.72 pp 556–65

Kaye G. W. C and Laby T H Tables of physical and chemical constants, 16th edition

Kalashnikov A N and Challis R E (2002) Errors in the measurement of ultrasonic absorption for materials evaluation, Review of Quantitative Nondestructive Evaluation, Vol.21, pp 1997-2004

Kao I Y, Hete B and Shung K K (1990) A novel method for the measurement of acoustic speed J. Acoust. Soc. Am. 88, pp 1679–1682

Kirchhoff G (1868) Uber den Einfluss der Warmteleitung in einem Gase auf die Schallbewegung. Pogg. Ann. 134 (6), pp177-193

Lamb H (1945) Hydrodynamics. New York: Dover

Lindley D V (1965) An Introduction to probability and statistics, Cambridge University Press, Cambridge UK

Lloyd P and Berry M V (1967) Wave propagation through an assembly of spheres Part IV. Relations between different scattering theories Proc. Phys. Soc. Vol.91 pp 678–688

Malvern User Manual (1998)

Margulies T S and Schwartz W H (1994) A multiphase continuum theory for sound wave propagation through dilute suspensions of particles, J. Acoust. Soc. Am. 96, 319-331

Marquardt D W An algorithm for least-square estimation of nonlinear parameters J. Soc. Indust. Appl. Math. Vol.11 pp 431

McClements D J and Povey M J W (1989) Scattering of ultrasound by emulsions J.Phys. D:Appl.Phys. vol.22 pp 38-47

McClements D J, Fairley P and Povey M J (1990) Comparison of effective medium and multiple-scattering theories of predicting the ultrasonic properties of dispersions J. Acoust. Soc. Am. 87(5) pp2244-2246

McClements D J (1992) Comparison of multiple scattering theories with experimental measurements in emulsions J. Acoust. Soc. Am. Vol 91(2) pp 849-853

McClements D J (1996) Principles of ultrasonic droplet size determination in emulsions Langmuir Vol. 12 No14, pp 3454-3461

McClements D J, Herrmann N and Hemar Y (1998 a) Influence of flocculation on the ultrasonic properties of emulsions: theory J. Phys. D:Appl.Phys. 31, pp 2950-2955

McClements D J, Herrmann N and Hemar Y (1998 b) Influence of flocculation on the ultrasonic properties of emulsions: experiment J. Phys. D:Appl.Phys. 31, pp 2956-2963

McClements D J and Hemar N (1999) Incorporation of thermal overlap effects into multiple scattering theory J.Acoust.Soc. Am. 105 (2), Pt.1 pp 915-918

Murphy J, George J, Nagl A and Uberall H (1979) Isolation of the resonant components in acoustic scattering from fluid loaded elastic spherical shells, J. Acoust. Soc. Am. 65, 368-373

O'Donnell M (1981) Kramers-Kronig relationship between ultrasonic attenuation and phase velocity, J. Acoust. Soc. Am. 69(3), pp 696-701

O'Neill T J (1998) Extended computation of ultrasonic wavenumber in particulate dispersions PhD Thesis University of Keele

Phang A P R (2006) PhD thesis, University of Nottingham

Pinfield V J (1996) Ph.D thesis, University of Leeds

Pinfield V J (2007) Acoustic scattering in dispersions: improvements and approximations for the ECAH method, J. Acoust. Soc. Am. in press

Povey M J W (1997) Ultrasonic techniques for fluid characterization Academic, San Diego, CA

Releigh Lord (1871) Phil. Mag.41 107, pp 274

Releigh Lord (1894) Theory of Sound 2nd edn. Macmillan, London (first published 1877)

Roberts D (1996) Ultrasound analysis of particle size distribution, Materials World. Vol. 4, no. 1, pp 12-14

Schultz J and Kaatze U (1998) A continuous wave transmission method for the ultrasonic spectrometry of liquids, Meas. Sci. Technol. 9, pp.1266-1276

Sewell C J T (1910) On the extinction of sound in viscous atmospheres by small obstacles of cylindrical form Phil.Trans. R. Soc. A 210 239–70

Strokes G G (1851) Mathematical and physical Papers I Trans. Camb. Phil. Soc.8 287

Strutt J W and Rayleigh (1896) The Theory of Sound. London: Macmillan

Tebbutt J S (1996) Ultrasonic absorption and phase velocity spectra colloids: theory, simulation and measurement Ph.D Thesis University of Keele

Torquato S (1985) J. Appl. Phys. 68 5486-5493

Urick R J (1947) A sound velocity method for determining the compressibility of finely divided substances J. Appl. Phys. Vol.18 983–7

Urick R J and Ament W S (1949) The propagation of sound in suspensions of irregular particles J. Acoust. Soc. Am. 20 283-289

Wang Y(1999) The characterization of food emulsions using ultrasound PhD Thesis 28-72 Leeds University

Waterman P C and Truell R (1961) Multiple scattering of waves J. Math. Phys. Vol.2 512-37

Werby M F and Green L H (1983) An extended unitary approach for acoustic scattering from elastic shells immerses in a fluid, J. Acoust. Soc. Am. 74

Werby M F and Green L H (1984) A comparison of acoustical scattering from fluid loaded elastic shells and sound soft objects, J. Acoust. Soc. Am. 76, 1227-1230

Wood A B (1941) A Textbook of Sound. London: G Bell and Sons

Ying C F and Truell R (1956) Scattering of a plane longitudinal wave by a spherical obstacle in an isotropically elastic solid, J . Appl. Phys. 27 1086-97

http://mathworld.wolfram.com/

Appendix

Appendix 1.1. Bessel and Hankel functions and Legendre Polynomials:

The solution to of equation 2.20 requires evaluation of spherical Bessel and Hankel functions, the arguments of which takes the form of particle radius times wavenumber products for the six partial wave types in the system — compression, transverse and thermal waves inside and outside of particles.

1.1. The spherical Bessel function of the first kind with the order n is given as:

$$J_n(x) = \frac{x^n}{2^n n!}\left(1 - \frac{x^2}{2\cdot 2n+2} + \frac{x^4}{2\cdot 4\cdot 2n+2\cdot 2n+4} - \ldots\right)$$

which converges for all values of x, real or complex, see figure A1.1.

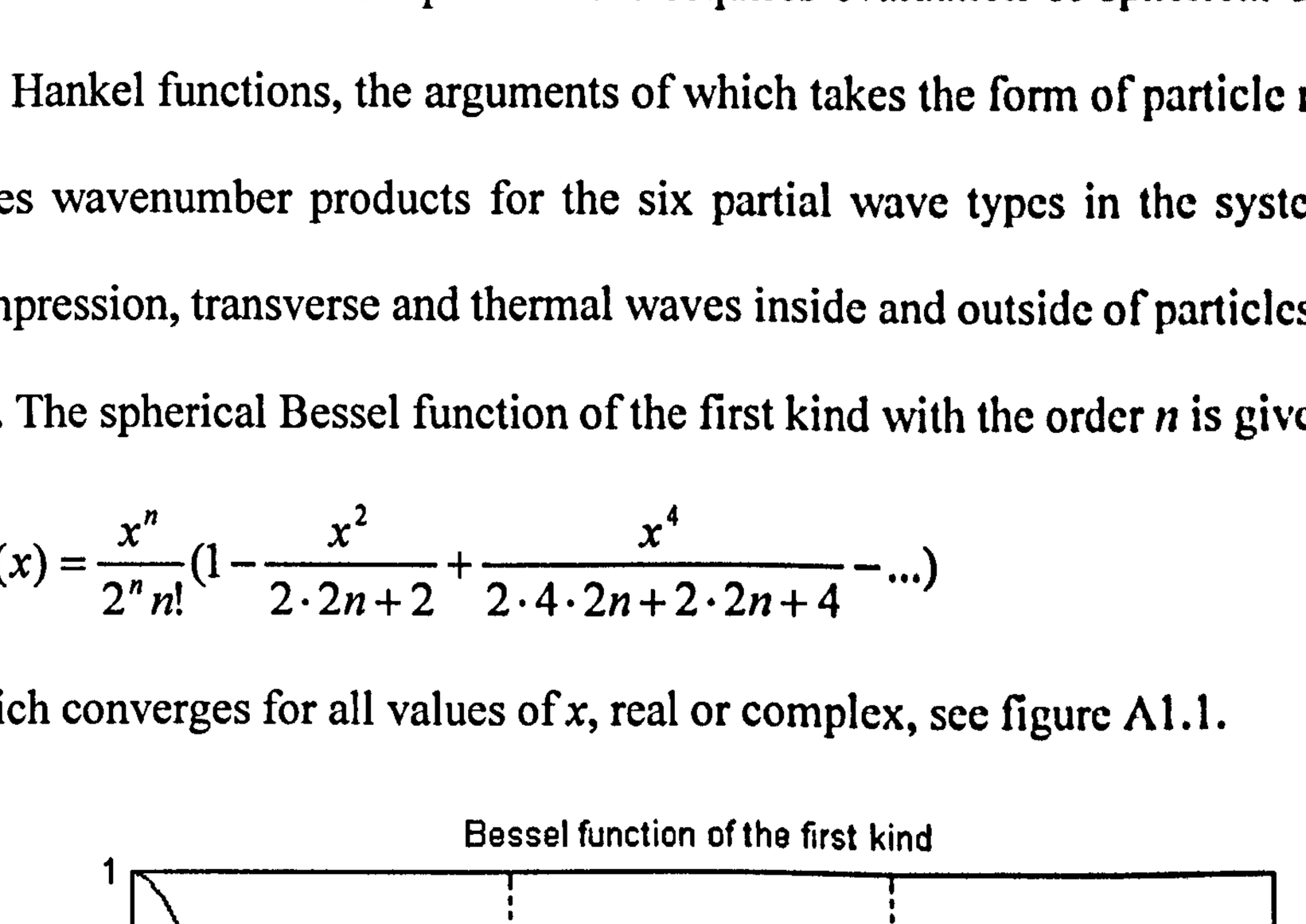

Figure A.1.1. Spherical Bessel function of the first kind when the order n=0, 1, 2, 3 (the red line is for n=0, the yellow line is for n=1, the green line is for n=2, and the blue line is for n=3).

Epstein and Carhart gave the approximate expressions for Bessel function with small arguments in the calculation of the matrix equation 2.20. The function can be simplified for the zero, first and second order:

$$j_0(x)=\frac{\sin x}{x},\quad j_1(x)=\frac{1}{x}\left(\frac{\sin x}{x}-\cos x\right),$$

$$j_2(x)=\frac{1}{x}\left[\left(\frac{3}{x^2}-1\right)\sin x-\frac{3}{x}\cos x\right]$$

1.2. The spherical Hankel function used here is the second kind of Bessel function, which is defined as:

$$H_n(x)=J_n(x)+iY_n(x);$$

where $Y_n(x)$ is the Neumann's function, which is spherical Bessel function of the second kind. And the function can be simplified by using Epstein and Carhart formulations for small arguments:

$$h_0(x)=-\frac{ie^{ix}}{x},\ h_1(x)=-\frac{e^{ix}}{x}(1+i/x),\ h_2(x)=i\frac{e^{ix}}{x}\left(1+\frac{3i}{x}-\frac{3}{x^2}\right);$$

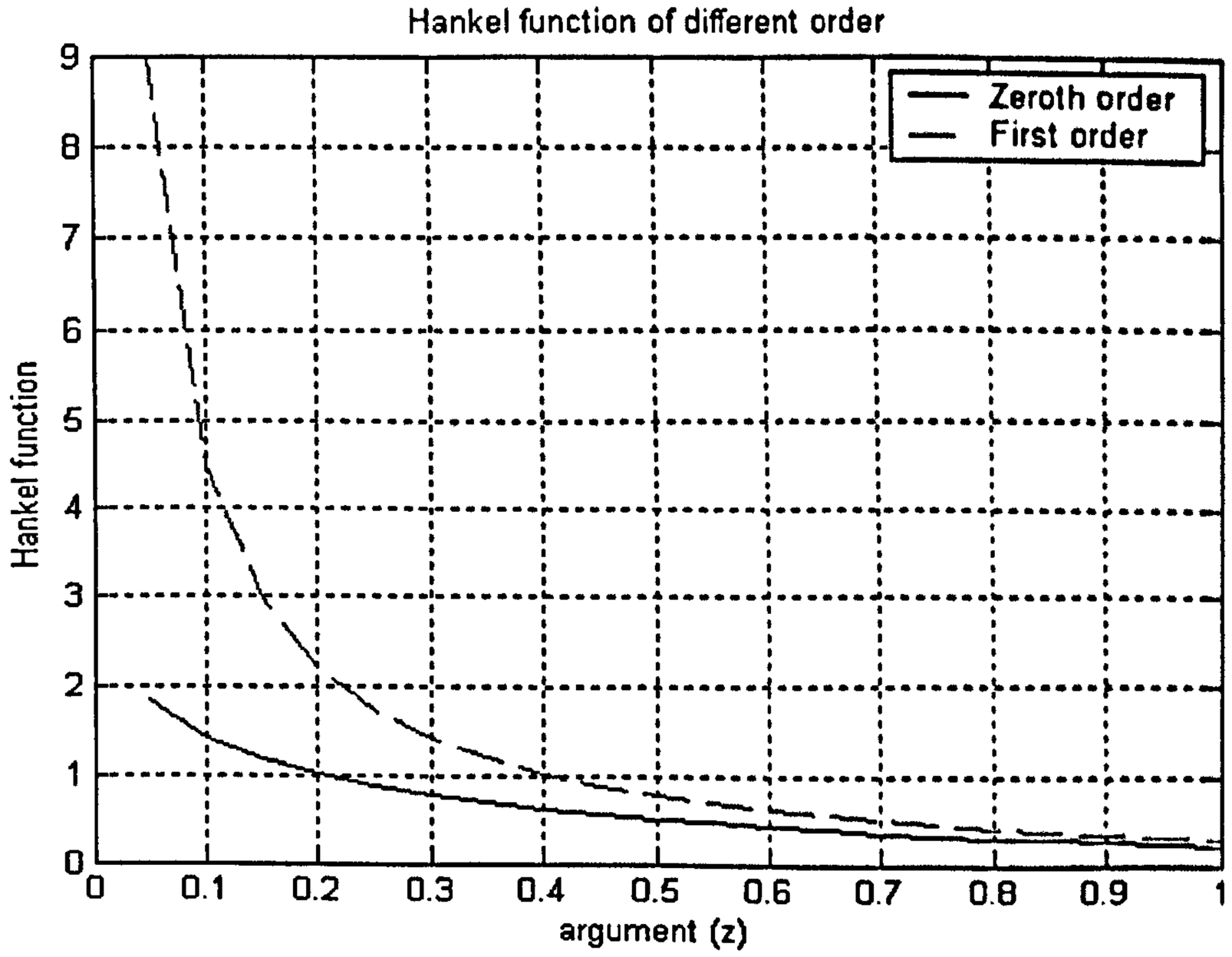

Figure A.1.2. Spherical Hankel function when order n=0,1.

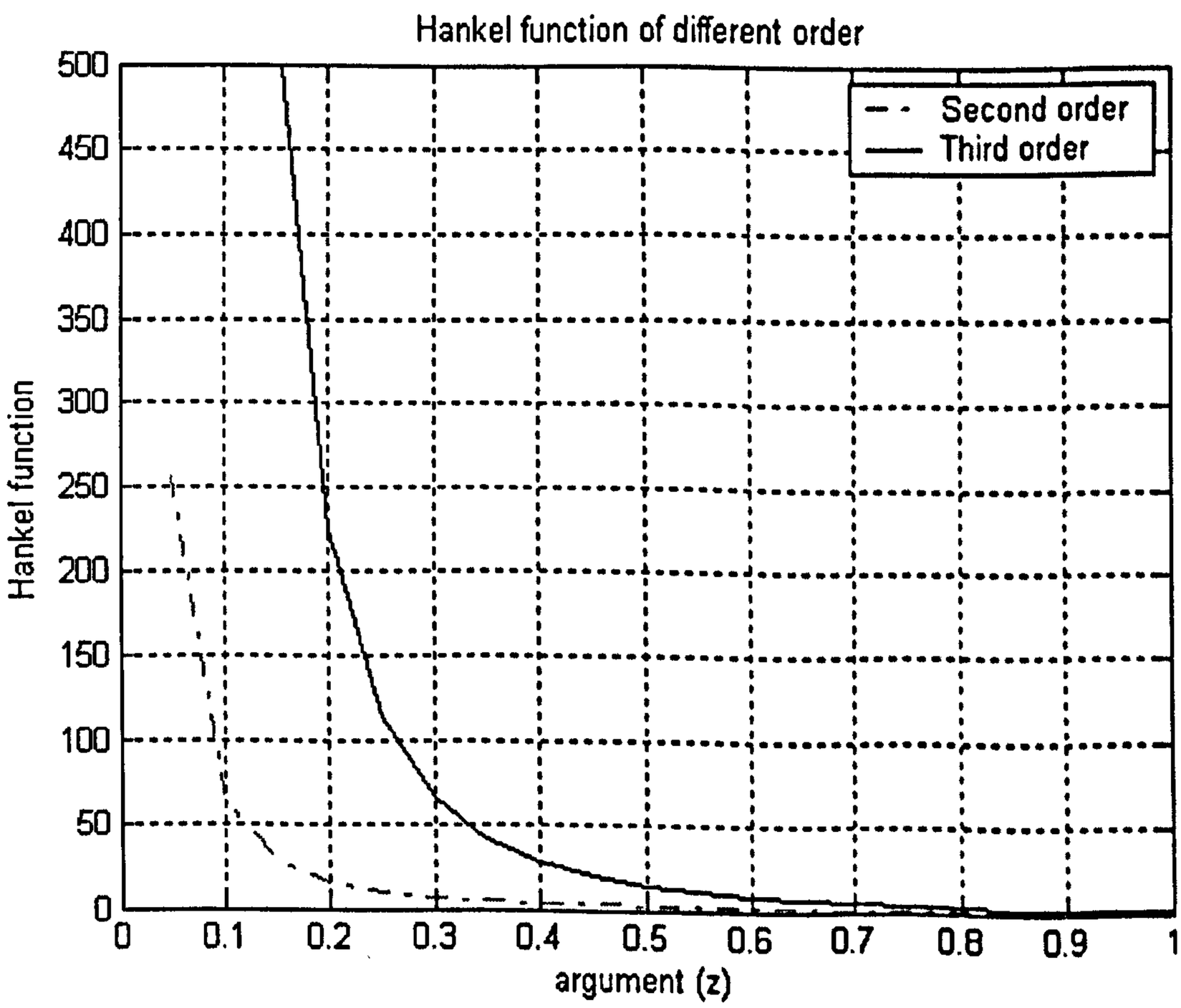

Figure A.1.3. Spherical Hankel function when order n=2,3

1.3. Legendre Polynomials of different order

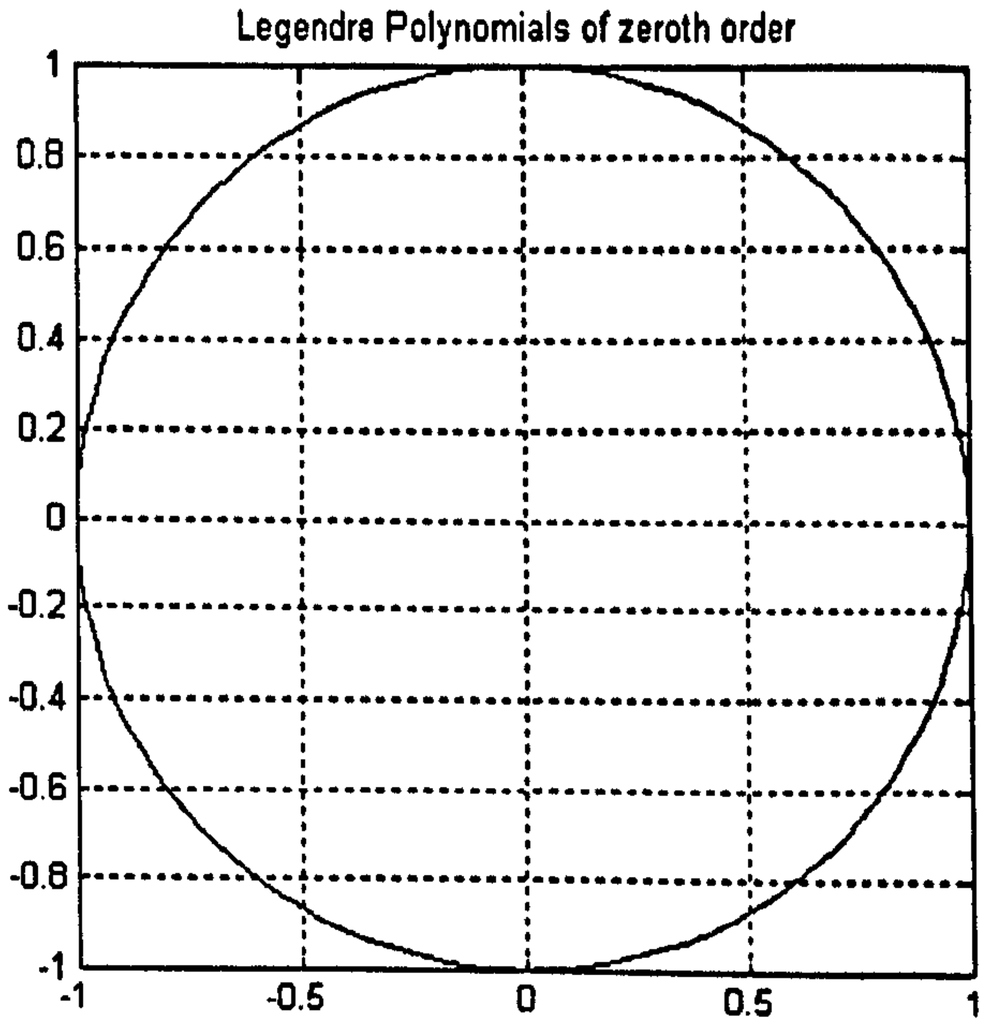

Figure A.1.4. Polar diagram of the magnitude of $P_0(\cos\theta)$

$$P_0(\cos\theta) = 1$$

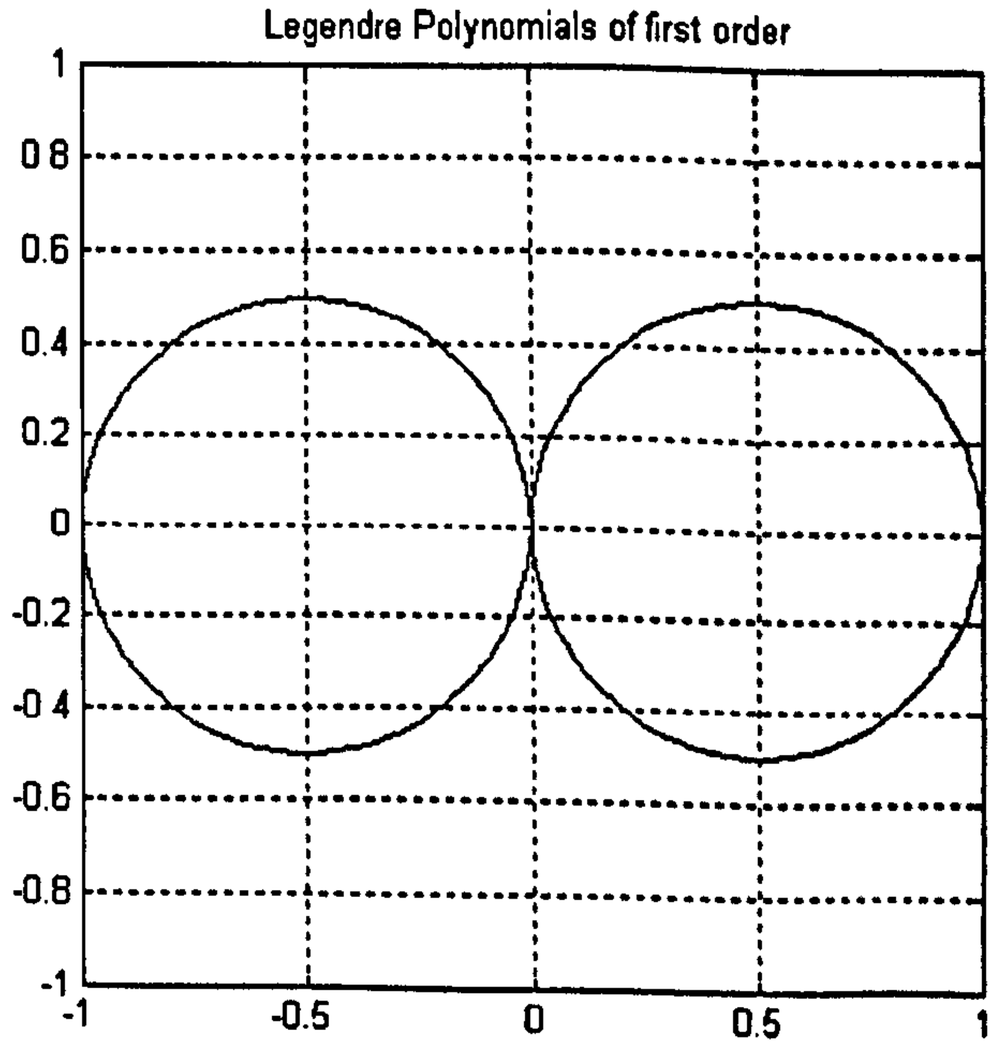

Figure A.1.5. Polar diagram of the magnitude of $P_1(\cos\theta)$

$$P_1(\cos\theta) = \cos\theta$$

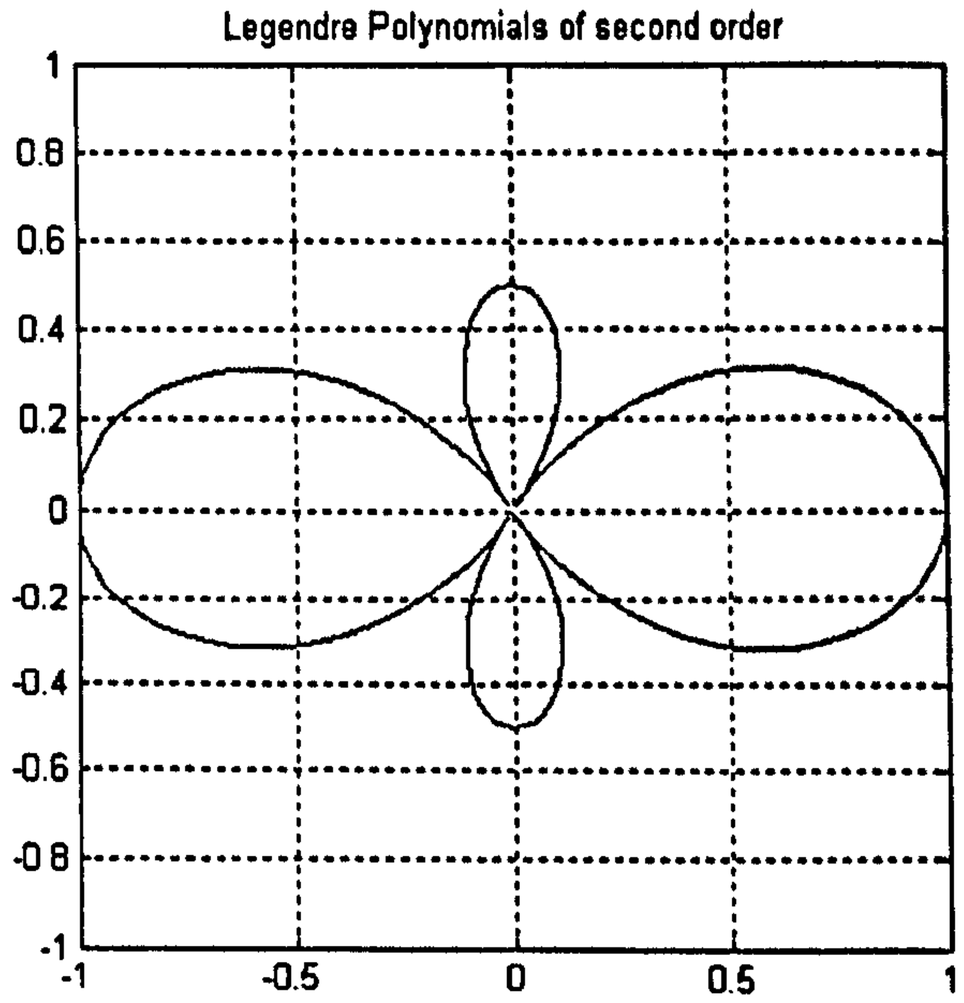

Figure A.1.6. Polar diagram of the magnitude of $P_2(\cos\theta)$

$$P_2(\cos\theta) = \frac{3}{2}\cos(\theta)^2 - \frac{3}{2}\cos(\theta)$$

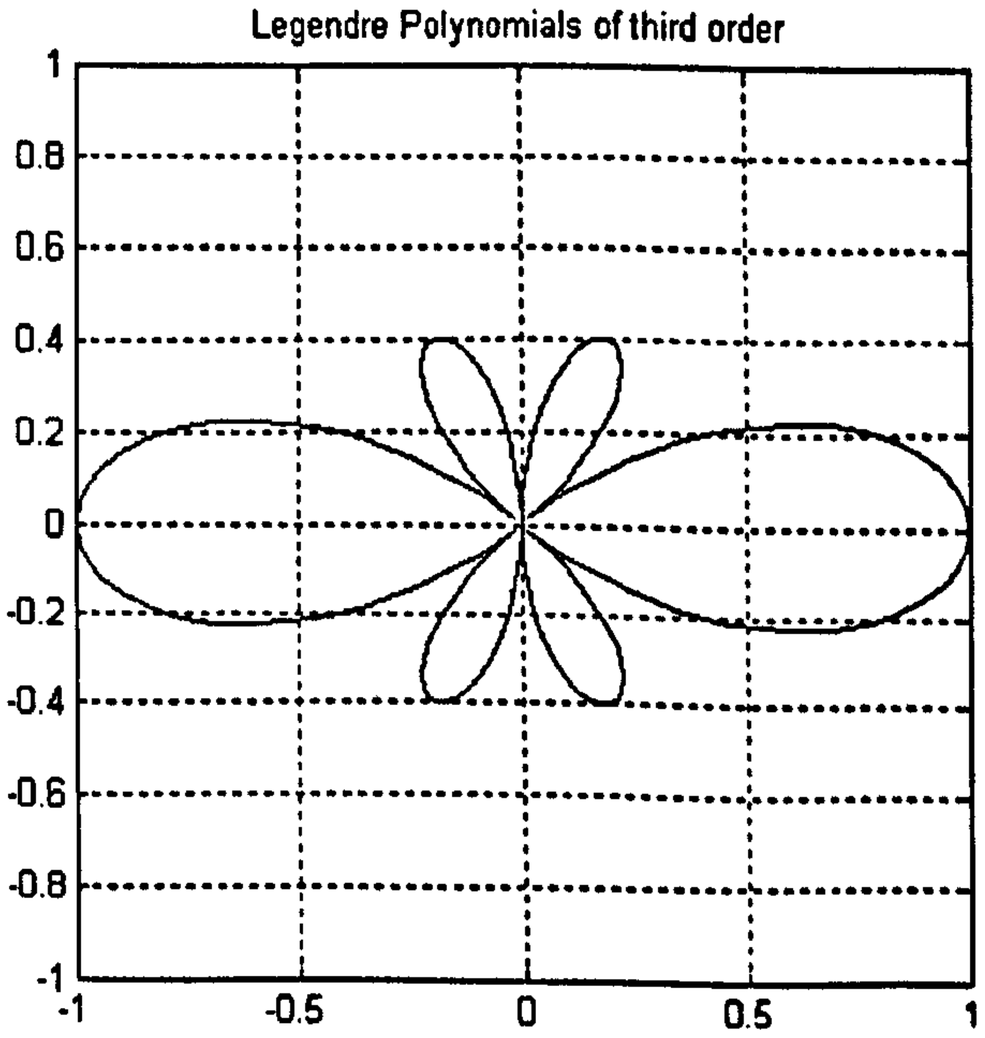

Figure A.1.7. Polar diagram of the magnitude of $P_3(\cos\theta)$

$$P_3(\cos\theta) = \frac{5}{2}\cos(\theta)^3 - \frac{3}{2}\cos(\theta)$$

Appendix 2.1. Terms in the Matrix Equation 2.20

The left hand side of six by six matrix $[M]_{EC}$ in equation 2.20 is as follow, see Challis *et al* (1998)

$$M_1^1 = a_{c2} h_n^{'}(a_{c2})$$

$$M_1^2 = h_n(a_{c2})$$

$$M_1^3 = b_{c2} h_n(a_{c2})$$

$$M_1^4 = \kappa_2 a_{c2} b_{c2} h_n^{'}(a_{c2})$$

$$M_1^5 = -\eta_2 \left\{ \left[h_n(a_{c2})(a_{s2}^2 - 2a_{c2}^2) \right] - 2a_{c2}^2 h_n^{''}(a_{c2}) \right\}$$

$$M_1^6 = -\eta_2 \left\{ a_{c2} h_n^{'}(a_{c2}) - h_n(a_{c2}) \right\}$$

$$M_2^1 = a_{t2} h_n^{'}(a_{t2})$$

$$M_2^2 = h_n(a_{t2})$$

$$M_2^3 = b_{t2} h_n(a_{t2})$$

$$M_2^4 = \kappa_2 a_{t2} b_{t2} h_n^{'}(a_{t2})$$

$$M_2^5 = -\eta_2 \left\{ \left[h_n(a_{t2})(a_{s2}^2 - 2a_{t2}^2) \right] - 2a_{t2}^2 h_n^{''}(a_{t2}) \right\}$$

$$M_2^6 = -\eta_2 \left\{ a_{t2} h_n^{'}(a_{t2}) - h_n(a_{t2}) \right\}$$

$$M_3^1 = -n(n+1) h_n(a_{s2})$$

$$M_3^2 = -[h_n(a_{s2}) + a_{s2} h_n^{'}(a_{s2})]$$

$$M_3^3 = 0$$

$$M_3^4 = 0$$

$$M_3^5 = -\eta_2 2n(n+1)[a_{s2} h_n^{'}(a_{s2}) - h_n(a_{s2})]$$

$$M_3^6 = -\frac{\eta_2}{2}[a_{s2}^2 h_n^{''}(a_{s2}) + (n-1)(n+2)h_n(a_{s2})]$$

$$M_4^1 = i\omega a_{c1} j_n^{'}(a_{c1})$$

$$M_4^2 = i\omega j_n(a_{c1})$$

$$M_4^3 = i\omega b_{c1} j_n(a_{c1})$$

$$M_4^4 = i\omega \kappa_1 a_{c1} b_{c1} j_n^{'}(a_{c1})$$

$$M_4^5 = -j_n(a_{c1})(\omega^2 r^2 \rho_1 - 2\eta_1 a_{c1}^2) + 2\eta_1 a_{c1}^2 j_n^{''}(a_{c1})$$

$$M_4^6 = -\eta_1[a_{c1} j_n^{'}(a_{c1}) - j_n(a_{c1})]$$

$$M_5^1 = i\omega a_{t1} j_n^{'}(a_{t1})$$

$$M_5^2 = i\omega j_n(a_{t1})$$

$$M_5^3 = i\omega b_{t1} j_n(a_{t1})$$

$$M_5^4 = i\omega \kappa_1 a_{t1} b_{t1} j_n^{'}(a_{t1})$$

$$M_5^5 = -j_n(a_{t1})(\omega^2 r^2 \rho_1 - 2\eta_1 a_{t1}^2) + 2\eta_1 a_{t1}^2 j_n^{''}(a_{t1})$$

$$M_5^6 = -\eta_1[a_{t1} j_n^{'}(a_{t1}) - j_n(a_{t1})]$$

$$M_6^1 = -i\omega n(n+1) j_n^{'}(a_{s1})$$

$$M_6^2 = -i\omega[j_n(a_{s1}) + a_{s1} j_n^{'}(a_{s1})]$$

$$M_6^3 = 0$$

$$M_6^4 = 0$$

$$M_6^5 = -2n(n+1)\eta_1[a_{s1} j_n^{'}(a_{s1}) - j_n(a_{s1})]$$

$$M_6^6 = \frac{\eta_1}{2}[a_{s1}^2 j_n^{''}(a_{s1}) + (n-1)(n+2) j_n(a_{s1})]$$

The right hand side of a six by one vector C_6 :

$$C_1 = -a_{c2} j_n^{'}(a_{c2})$$

$$C_2 = -j_n(a_{c2})$$

$$C_3 = -b_{c2} j_n(a_{c2})$$

$$C_4 = -\kappa_2 a_{c2} b_{c2} j_n^{'}(a_{c2})$$

$$C_5 = \eta_2 \left\{ \left[j_n(a_{c2})(a_{s2}^2 - 2a_{c2}^2) \right] - 2a_{c2}^2 j_n^{''}(a_{c2}) \right\}$$

$$C_6 = \eta_2 \left\{ a_{c2} j_n^{'}(a_{c2}) - j_n(a_{c2}) \right\}$$

Appendix 4.1 Analytical form of the matrix elements

The left hand side of twelve by twelve matrix equation 4.2 is as follow, see Anson and Chivers (1993):

First column:

$$d_{11} = nh_n(x_{c_1}) - x_{c_1}h_{n+1}(x_{c_1})$$

$$d_{21} = h_n(x_{c_1})$$

$$d_{31} = \frac{b_{c_1}}{b_{c_2}}h_n(x_{c_1})$$

$$d_{41} = \frac{b_{c_1}}{b_{c_2}}\left[nh_n(x_{c_1}) - x_{c_1}h_{n+1}(x_{c_1})\right]$$

$$d_{51} = \frac{\rho_1}{\rho_2}\left[TX1.h_n(x_{c_1}) - \frac{4x_{c_1}h_{n+1}(x_{c_1})}{x_{s_1}^2}\right]$$

$$d_{61} = \frac{1}{x_{s_1}^2}\left[(n-1)h_n(x_{c_1}) - x_{c_1}h_{n+1}(x_{c_1})\right]\frac{\rho_1}{\rho_2}$$

Second column:

$$d_{12} = \frac{1}{x_{t_1}^3}\left[nh_n(x_{t_1}) - x_{t_1}h_{n+1}(x_{t_1})\right]$$

$$d_{22} = \frac{1}{x_{t_1}^3}h_n(x_{t_1})$$

$$d_{32} = \frac{b_{t_1}}{b_{c_2}}\frac{1}{x_{t_1}^3}h_n(x_{t_1})$$

$$d_{42} = \frac{b_{t_1}}{b_{c_2}}\frac{1}{x_{t_1}^3}\left[nh_n(x_{t_1}) - x_{t_1}h_{n+1}(x_{t_1})\right]$$

$$d_{52} = \frac{\rho_1}{\rho_2}\frac{1}{x_{t_1}^3}\left(TX1.h_n(x_{t_1}) - \frac{4x_{t_1}h_{n+1}(x_{t_1})}{x_{s_1}^2}\right)$$

$$d_{62} = \frac{1}{x_{t_1}^3}\frac{1}{x_{s_1}^2}\left[(n-1)h_n(x_{t_1}) - x_{t_1}h_{n+1}(x_{t_1})\right]\frac{\rho_1}{\rho_2}$$

Third column:

$$d_{13} = -\frac{1}{x_{s_1}}n(n+1)h_n(x_{s_1})$$

$$d_{23} = -\frac{1}{x_{s_1}}\left[n(n+1)h_n(x_{s_1}) - x_{s_1}h_{n+1}(x_{s_1})\right]$$

$$d_{53} = \frac{\rho_1}{\rho_2}\frac{1}{x_{s_1}^3}2n(n+1)\left((n-1)h_n(x_{s_1}) - x_{s_1}h_{n+1}(x_{s_1})\right)$$

$$d_{63} = -\frac{1}{x_{s_1}^3}\left[\left(n^2 - 1 - \frac{x_{s_1}^2}{2}\right)h_n(x_{s_1}) + x_{s_1}h_{n+1}(x_{s_1})\right]\frac{\rho_1}{\rho_2}$$

Fourth column:

$$d_{14} = nj_n(x_{c_2}) - x_{c_2}j_{n+1}(x_{c_2})$$

$$d_{24} = j_n(x_{c_2})$$

$$d_{34} = j_n(x_{c_2})$$

$$d_{44} = \frac{\kappa_2}{\kappa_1}\left[nj_n(x_{c_2}) - x_{c_2}j_{n+1}(x_{c_2})\right]$$

$$d_{54} = TX2j_n(x_{c_2}) - \frac{4x_{c_2}j_{n+1}(x_{c_2})}{x_{s_2}^2}$$

$$d_{64} = \frac{1}{x_{s_2}^2}\left[(n-1)j_n(x_{c_2}) - x_{c_2}j_{n+1}(x_{c_2})\right]$$

$$d_{74} = nj_n(y_{c_2}) - y_{c_2}j_{n+1}(y_{c_2})$$

$$d_{84} = j_n(y_{c_2})$$

$$d_{94} = j_n(y_{c_2})$$

$$d_{10,4} = \frac{\kappa_2}{\kappa_3}\left[nj_n(y_{c_2}) - y_{c_2} j_{n+1}(y_{c_2})\right]$$

$$d_{11,4} = TY2 j_n(y_{c_2}) - \frac{4y_{c_2} j_{n+1}(y_{c_2})}{y_{s_2}^2}$$

$$d_{12,4} = \frac{1}{y_{s_2}^2}\left[(n-1) j_n(y_{c_2}) - x_{y_2} j_{n+1}(y_{c_2})\right]$$

Fifth column:

$$d_{15} = \frac{1}{x_{t_2}^3}\left[nj_n(x_{t_2}) - x_{t_2} j_{n+1}(x_{t_2})\right]$$

$$d_{25} = \frac{1}{x_{t_2}^3} j_n(x_{t_2})$$

$$d_{35} = \frac{b_{t_2}}{b_{c_2}} \frac{1}{x_{t_2}^3} j_n(x_{t_2})$$

$$d_{45} = \frac{\kappa_2}{\kappa_1} \frac{b_{t_2}}{b_{c_2}} \frac{nj_n(x_{t_2}) - x_{t_2} j_{n+1}(x_{t_2})}{x_{t_2}^3}$$

$$d_{55} = \frac{1}{x_{t_2}^3}\left[TX2.j_n(x_{t_2}) - \frac{4x_{t_2} j_{n+1}(x_{t_2})}{x_{s_2}^2}\right]$$

$$d_{65} = \frac{1}{x_{t_2}^3} \frac{1}{x_{s_2}^2}\left[(n-1) j_n(x_{t_2}) - x_{t_2} j_{n+1}(x_{t_2})\right]$$

$$d_{75} = \frac{1}{x_{t_2}^3}\left[nj_n(y_{t_2}) - \frac{b}{a} x_{t_2} j_{n+1}(y_{t_2})\right]$$

$$d_{85} = \frac{1}{x_{t_2}^3} j_n(y_{t_2})$$

$$d_{95} = \frac{1}{x_{t_2}^3} \frac{b_{t_2}}{b_{c_2}} j_n(y_{t_2})$$

$$d_{10,5} = \frac{\kappa_2}{\kappa_3} \frac{b_{t_2}}{b_{c_2}} \frac{1}{x_{t_2}^3}\left[nj_n(y_{t_2}) - \frac{b}{a} x_{t_2} j_{n+1}(y_{t_2})\right]$$

$$d_{11,5} = \frac{1}{x_{t_2}^3}\left[TY2.j_n(y_{t_2}) - \frac{4(b/a)x_{t_2}j_{n+1}(y_{t_2})}{y_{s_2}^2}\right]$$

$$d_{12,5} = \frac{1}{x_{t_2}^3}\frac{1}{y_{s_2}^2}\left[(n-1)j_n(y_{t_2}) - \frac{b}{a}x_{t_2}j_{n+1}(y_{t_2})\right]$$

Sixth column:

$$d_{16} = -\frac{1}{x_{s_2}}n(n+1)j_n(x_{s_2})$$

$$d_{26} = -\frac{1}{x_{s_2}}\left[(n+1)j_n(x_{s_2}) - x_{s_2}j_{n+1}(x_{s_2})\right]$$

$$d_{56} = \frac{1}{x_{s_2}^3}2n(n+1)\left((n-1)j_n(x_{s_1}) - x_{s_2}j_{n+1}(x_{s_2})\right)$$

$$d_{66} = -\frac{1}{x_{s_2}^3}\left[\left(n^2 - 1 - \frac{x_{s_2}^2}{2}\right)j_n(x_{s_2}) + x_{s_2}j_{n+1}(x_{s_2})\right]$$

$$d_{76} = -\frac{1}{x_{s_2}}n(n+1)j_n(y_{s_2})$$

$$d_{86} = -\frac{1}{x_{s_2}}\left[n(n+1)j_n(y_{s_2}) - \frac{b}{a}x_{s_2}j_{n+1}(y_{s_2})\right]$$

$$d_{11,6} = \frac{1}{x_{s_2}}\frac{1}{y_{s_2}^2}2n(n+1)\left[(n-1)j_n(y_{s_2}) + y_{s_2}j_{n+1}(y_{s_2})\right]$$

$$d_{12,6} = -\frac{1}{x_{s_2}}\frac{1}{y_{s_2}^2}\left[\left(n^2 - 1 - \frac{y_{s_2}^2}{2}\right)j_n(y_{s_2}) + y_{s_2}j_{n+1}(y_{s_2})\right]$$

Seventh column:

$$d_{17} = nh_n(x_{c_2}) - x_{c_2}h_{n+1}(x_{c_2})$$

$$d_{27} = h_n(x_{c_2})$$

$$d_{37} = h_n(x_{c_2})$$

$$d_{47} = \frac{\kappa_2}{\kappa_1}\left[nh_n(x_{c_2}) - x_{c_2}h_{n+1}(x_{c_2})\right]$$

$$d_{57} = TX2h_n(x_{c_2}) - \frac{4x_{c_2}h_{n+1}(x_{c_2})}{x_{s_2}^2}$$

$$d_{67} = \frac{1}{x_{s_2}^2}\left[(n-1)h_n(x_{c_2}) - x_{c_2}h_{n+1}(x_{c_2})\right]$$

$$d_{77} = nh_n(y_{c_2}) - y_{c_2}h_{n+1}(y_{c_2})$$

$$d_{87} = h_n(y_{c_2})$$

$$d_{97} = h_n(y_{c_2})$$

$$d_{10,7} = \frac{\kappa_2}{\kappa_3}\left[nh_n(y_{c_2}) - y_{c_2}h_{n+1}(y_{c_2})\right]$$

$$d_{11,7} = TY2h_n(y_{c_2}) - \frac{4y_{c_2}h_{n+1}(y_{c_2})}{y_{s_2}^2}$$

$$d_{12,7} = \frac{1}{y_{s_2}^2}\left[(n-1)h_n(y_{c_2}) - x_{y_2}h_{n+1}(y_{c_2})\right]$$

Eighth column:

$$d_{18} = \frac{1}{x_{t_2}^3}\left[nh_n(x_{t_2}) - x_{t_2}h_{n+1}(x_{t_2})\right]$$

$$d_{28} = \frac{1}{x_{t_2}^3}h_n(x_{t_2})$$

$$d_{38} = \frac{b_{t_2}}{b_{c_2}}\frac{1}{x_{t_2}^3}h_n(x_{t_2})$$

$$d_{48} = \frac{\kappa_2}{\kappa_1}\frac{b_{t_2}}{b_{c_2}}\frac{nh(x_{t_2}) - x_{t_2}h_{n+1}(x_{t_2})}{x_{t_2}^3}$$

$$d_{58} = \frac{1}{x_{t_2}^3}\left[TX2.h_n(x_{t_2}) - \frac{4x_{t_2}h_{n+1}(x_{t_2})}{x_{s_2}^2}\right]$$

$$d_{68} = \frac{1}{x_{t_2}^3}\frac{1}{x_{s_2}^2}\left[(n-1)h_n(x_{t_2}) - x_{t_2}h_{n+1}(x_{t_2})\right]$$

$$d_{78} = \frac{1}{x_{t_2}^3}\left[nh_n(y_{t_2}) - \frac{b}{a}x_{t_2}h_{n+1}(y_{t_2})\right]$$

$$d_{88} = \frac{1}{x_{t_2}^3}h_n(y_{t_2})$$

$$d_{98} = \frac{1}{x_{t_2}^3}\frac{b_{t_2}}{b_{c_2}}h_n(y_{t_2})$$

$$d_{10,8} = \frac{\kappa_2}{\kappa_3}\frac{b_{t_2}}{b_{c_2}}\frac{1}{x_{t_2}^3}\left[nh_n(y_{t_2}) - \frac{b}{a}x_{t_2}h_{n+1}(y_{t_2})\right]$$

$$d_{11,8} = \frac{1}{x_{t_2}^3}\left[TY2.h_n(y_{t_2}) - \frac{4(b/a)x_{t_2}h_{n+1}(y_{t_2})}{y_{s_2}^2}\right]$$

$$d_{12,8} = \frac{1}{x_{t_2}^3}\frac{1}{y_{s_2}^2}\left[(n-1)h_n(y_{t_2}) - \frac{b}{a}x_{t_2}h_{n+1}(y_{t_2})\right]$$

Ninth column:

$$d_{19} = -\frac{1}{x_{s_2}}n(n+1)h_n(x_{s_2})$$

$$d_{29} = -\frac{1}{x_{s_2}}\left[(n+1)h_n(x_{s_2}) - x_{s_2}h_{n+1}(x_{s_2})\right]$$

$$d_{59} = \frac{1}{x_{s_2}^3}2n(n+1)\left((n-1)h_n(x_{s_1}) - x_{s_2}h_{n+1}(x_{s_2})\right)$$

$$d_{69} = -\frac{1}{x_{s_2}^3}\left[\left(n^2 - 1 - \frac{x_{s_2}^2}{2}\right)h_n(x_{s_2}) + x_{s_2}h_{n+1}(x_{s_2})\right]$$

$$d_{79} = -\frac{1}{x_{s_2}}n(n+1)h_n(y_{s_2})$$

$$d_{89} = -\frac{1}{x_{s_2}}\left[n(n+1)h_n(y_{s_2}) - \frac{b}{a}x_{s_2}h_{n+1}(y_{s_2})\right]$$

$$d_{11,9} = \frac{1}{x_{s_2}}\frac{1}{y_{s_2}^2}2n(n+1)\left[(n-1)h_n(y_{s_2}) + y_{s_2}h_{n+1}(y_{s_2})\right]$$

$$d_{12,9} = \frac{1}{x_{s_2}}\frac{1}{y_{s_2}^2}\left[\left(n^2 - 1 - \frac{y_{s_2}^2}{2}\right)h_n(y_{s_2}) + y_{s_2}h_{n+1}(y_{s_2})\right]$$

Tenth column:

$$d_{7,10} = nj_n(y_{c_3}) - y_{c_3}j_{n+1}(y_{c_3})$$

$$d_{8,10} = j_n(y_{c_3})$$

$$d_{9,10} = \frac{b_{c_3}}{b_{c_2}}j_n(y_{c_3})$$

$$d_{10,10} = \frac{b_{c_3}}{b_{c_2}}\left[nj_n(y_{c_3}) - x_{c_3}j_{n+1}(y_{c_3})\right]$$

$$d_{11,10} = \frac{\rho_3}{\rho_2}\left[TY3.j_n(y_{c_3}) - \frac{4y_{c_3}j_{n+1}(y_{c_3})}{y_{s_3}^2}\right]$$

$$d_{12,10} = \frac{1}{y_{s_3}^2}\left[(n-1)j_n(y_{c_3}) - y_{c_3}j_{n+1}(y_{c_3})\right]\frac{\rho_3}{\rho_2}$$

Eleventh column:

$$d_{7,11} = \frac{1}{y_{t_3}^3}\left[nj_n(y_{t_3}) - y_{t_3}j_{n+1}(y_{t_3})\right]$$

$$d_{8,11} = \frac{1}{y_{t_3}^3}j_n(y_{t_3})$$

$$d_{9,11} = \frac{b_{t_3}}{b_{c_2}}\frac{1}{y_{t_3}^3}j_n(y_{t_3})$$

$$d_{10,11} = \frac{b_{t_3}}{b_{c_2}}\frac{1}{y_{t_3}^3}\left[nj_n(y_{t_3}) - y_{t_3}j_{n+1}(y_{t_3})\right]$$

$$d_{11,11} = \frac{\rho_3}{\rho_2}\frac{1}{y_{t_3}^3}\left(TY3.j_n(y_{t_3}) - \frac{4y_{t_3}j_{n+1}(y_{t_3})}{y_{s_3}^2}\right)$$

$$d_{12,11} = \frac{1}{y_{t_3}^3}\frac{1}{y_{s_3}^2}\left[(n-1)j_n(y_{t_3}) - y_{t_3}j_{n+1}(y_{t_3})\right]\frac{\rho_3}{\rho_2}$$

Twelfth column:

$$d_{7,12} = -\frac{1}{y_{s_3}}n(n+1)j_n(y_{s_3})$$

$$d_{8,12} = -\frac{1}{y_{s_3}}\left[n(n+1)j_n(y_{s_3}) - y_{s_3}j_{n+1}(y_{s_3})\right]$$

$$d_{11,12} = \frac{\rho_3}{\rho_2}\frac{1}{y_{s_3}^3}2n(n+1)\left((n-1)j_n(y_{s_3}) - y_{s_3}j_{n+1}(y_{s_3})\right)$$

$$d_{12,12} = -\frac{1}{y_{s_3}^3}\left[\left(n^2 - 1 - \frac{y_{s_3}^2}{2}\right)j_n(y_{s_3}) + y_{s_3}j_{n+1}(y_{s_3})\right]\frac{\rho_3}{\rho_2}$$

Terms on the right hand side of the matrix equation:

$$M_1 = -\left[nj_n(x_{c1}) - x_{c1}j_{n+1}(x_{c1})\right]$$

$$M_2 = -j_n(x_{c1})$$

$$M_3 = -\frac{b_{c1}}{b_{c2}}j_n(x_{c1})$$

$$M_4 = -\frac{b_{c1}}{b_{c2}}\left[nj_n(x_{c1}) - x_{c1}j_{n+1}(x_{c1})\right]$$

$$M_5 = -\frac{\rho_1}{\rho_2}\left(TX1j_n(x_{c1}) - 4\frac{x_{d1}}{x_{s1}^2}j_{n+1}(x_{c1})\right)$$

$$M_6 = -\frac{\rho_1}{\rho_2}\frac{1}{x_{s1}^2}\left((n-1)j_n(x_{c1}) - x_{C1}j_{n+1}(x_{c1})\right)$$

where the products of wavenumber and radius for the core and the shell are defined as:

$$x_{c_j} = k_{c_j} r_c \qquad y_{c_j} = k_{c_j} r_s$$

$$x_{s_j} = k_{s_j} r_c \qquad y_{s_j} = k_{s_j} r_s$$

$$x_{t_j} = k_{t_j} r_c \qquad y_{t_j} = k_{t_j} r_s$$

j=1, 2, and 3 represents the surrounding medium, the shell medium and the core medium, respectively, and

$$TX_j = \left(1 - \frac{2n(n-1)}{x_{s_j}^2}\right)$$

$$TY_j = \left(1 - \frac{2n(n-1)}{y_{s_j}^2}\right)$$

where j=1, 2 and 3.

Appendix 5.1 Transducer descriptions

The transducers used in the experiments were the Panametrics-NDT™ V309, V311, V354 and V356 immersion-type transducers with centre frequencies of 5 MHz, 10 MHz, 20 MHz and 30 MHz respectively. The following figures show the description of these transducers:

PANAMETRICS
221 Crescent St Waltham, MA 02453-3497
Tel: 800-225-8330, 781-899-2719
Fax: 781-899-1552

TRANSDUCER DESCRIPTION

PART NO.: V309 FREQUENCY: 5.00 MHz
SERIAL NO.: 279517 ELEMENT SIZE: .5 IN. DIA.
DESIGNATION: IMMERSION

TEST INSTRUMENTATION

PULSER/RECEIVER: 5052 UA #1
DIGITAL OSCILLOSCOPE: LeCroy LT342 / SN: LT34201114
TEST PROGRAM: TP103-3 VER. 1009BE
CABLE: RG-58/U 4 FT.

TEST CONDITIONS

PULSER SETTING: ENERGY: 1 ; DAMPING: 50 ohm
RECEIVER SETTING: ATTN: 44dB ; GAIN: 40dB
TARGET: 2 IN SILICA; WATER PATH; 1in
JOB CODE: TP200

MEASUREMENTS PER ASTM E1065

WAVEFORM DURATION:
-14DB LEVEL -- .344US
-20DB LEVEL -- .488US
-40DB LEVEL -- 0.85US

SPECTRUM MEASURANDS:
CENTER FREQ. ----- 5.10MHz
PEAK FRECUENCY -- 4.62MHz
-6DB BANDWIDTH -- 67.841 %

COMMENTS:

F#: 5.15

** ACCEPTED.

TECHNICIAN: (6) _____ DATE: 09-21-2000

SIGNAL WAVEFORM

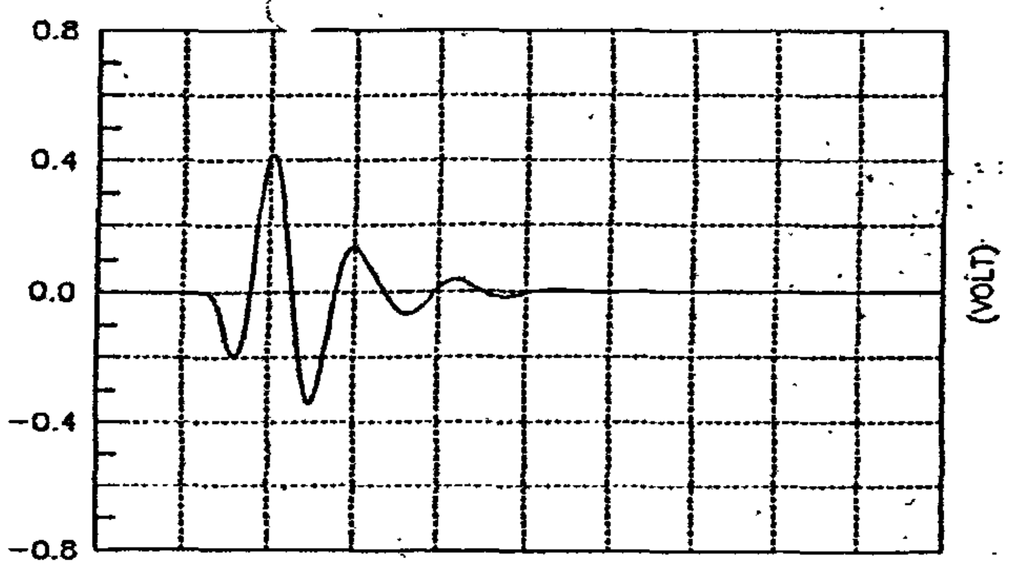

(.2 USEC / DMSION)

FREQUENCY SPECTRUM

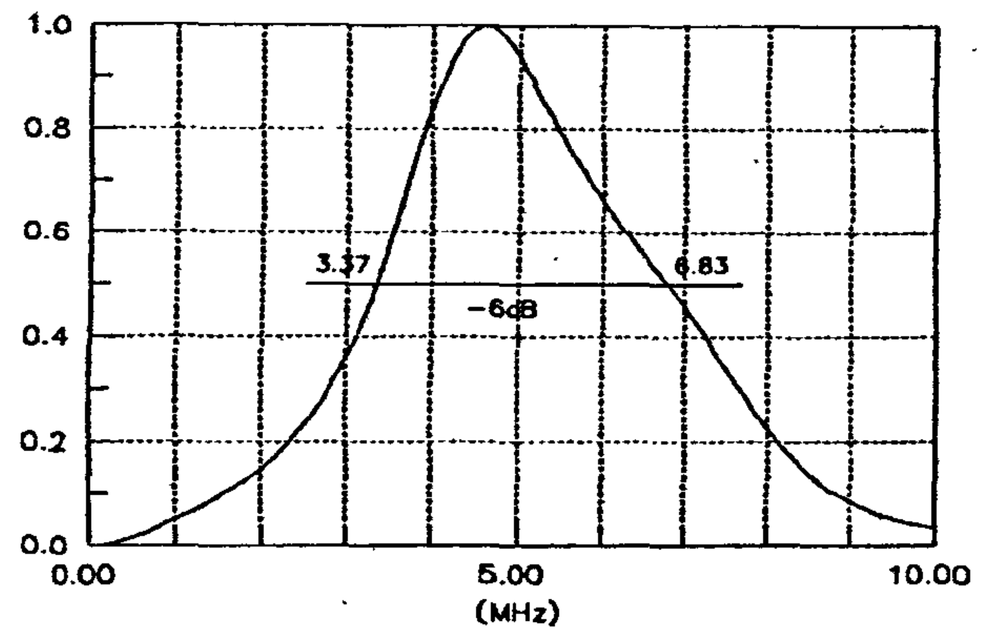

TP103-2 REV.A 8/27/93 PREPARED BY PQ-ENGINEERING

PANAMETRICS
221 Crescent St Waltham MA 02453-3497
Tel: 800-225-8330, 781-899-2719
Fax: 781-899-1552

TRANSDUCER DESCRIPTION

PART NO.: V311 FREQUENCY: 10.00 MHz
SERIAL NO.: 306441 ELEMENT SIZE: .5 in. DIA.
DESIGNATION: NON-FOCUSED IMMERSION

TEST INSTRUMENTATION

PULSER/RECEIVER: PANAMETRICS 5052 UA #1
DIGITAL OSCILLOSCOPE: LECROY 9400 - V 2.08FT 3E0321
TEST PROGRAM: TP103-1 VER. 995R2 SETUP: DWG. #5978
CABLE: RG-58/U LENGTH: 4 FT.

TEST CONDITIONS

PULSER ENERGY: 1
PULSER DAMPING: 50 ohm
RECEIVER SETTING: 40 dB GAIN / 50dB ATTENUATION
TARGET: FRONT SURFACE OF 2.0 in. SILICA; WATER PATH 1.063 in

MEASUREMENTS PER ASTM E1065

WAVEFORM DURATION:
-14DB LEVEL -- .231US
-20DB LEVEL -- .248US
-40DB LEVEL -- .464US

SPECTRUM MEASURANDS:
CENTER FREQ. ---- 9.40MHz
PEAK FREQUENCY -- 9.05MHz
-6DB BANDWIDTH -- 61.70 %

COMMENTS:

F. 9.5

** ACCEPTED
TECHNICIAN: (3) David Santoro DATE: 12-10-01

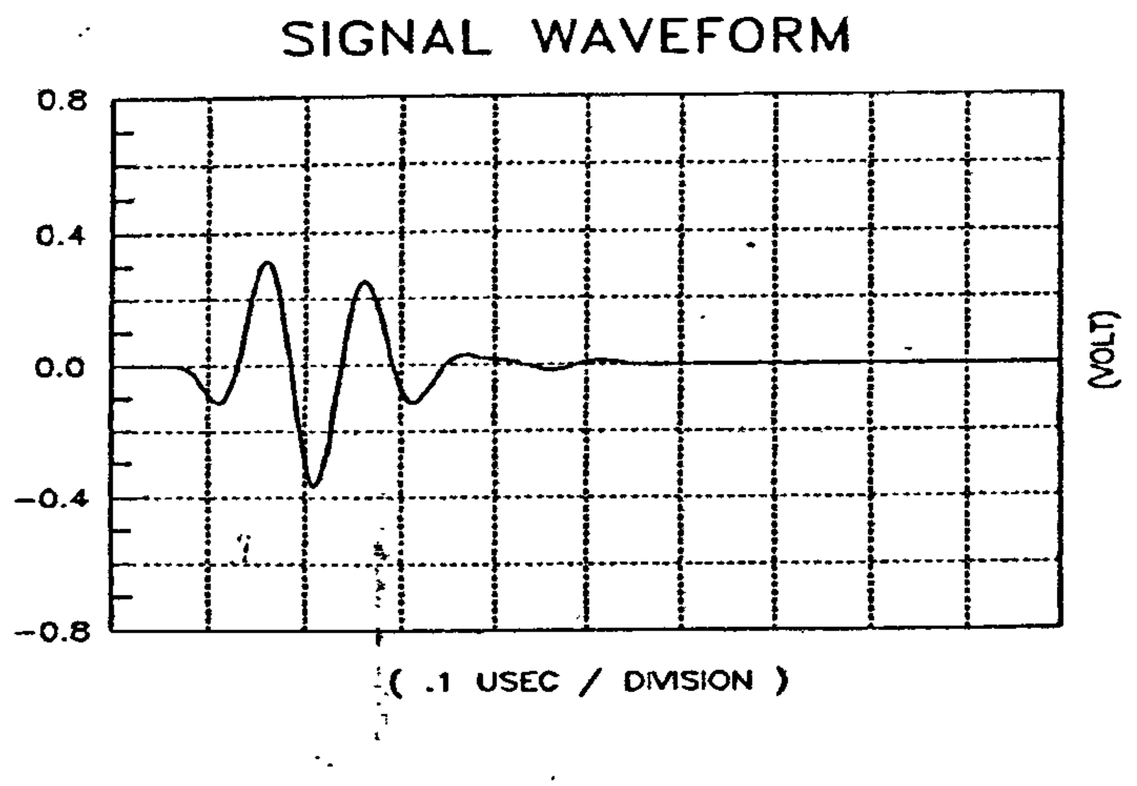

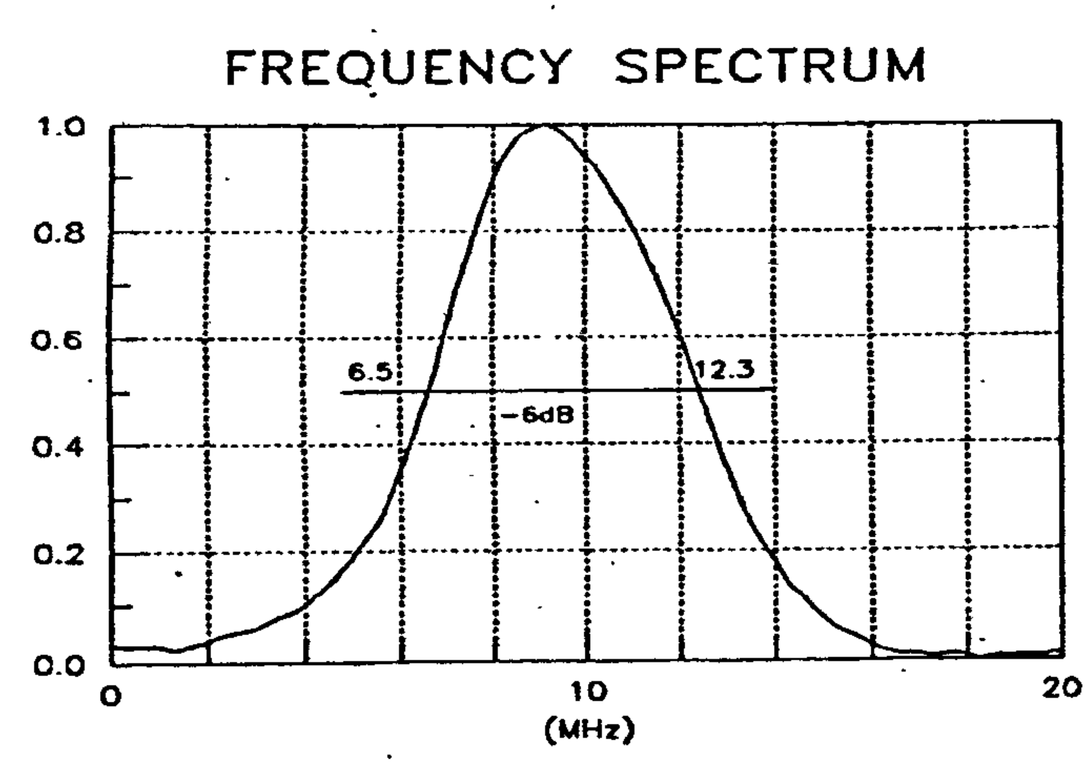

-8 REV A 8/27/93 PREPARED BY P3-ENGINEERING

PANAMETRICS
221 Crescent St Waltham, MA 02453-3497
Tel: 800-225-8330, 781-899-2719
Fax: 781-899-1552

TRANSDUCER DESCRIPTION

PART NO.: V354 FREQUENCY: 20.00 MHz
SERIAL NO.: 277128 ELEMENT SIZE: .25 in. DIA.
DESIGNATION: IMMERSION

TEST INSTRUMENTATION

PULSER/RECEIVER: 5052#494
DIGITAL OSCILLOSCOPE: LECROY 9450 S/N 3325-CH2
TEST PROGRAM: TP103-2 VER. 9958
CABLE: RG-58A/U 4FT

TEST CONDITIONS

PULSER SETTING: ENERGY:1 ; DAMPING:50
RECEIVER SETTING: ATTN:30dB; GAIN:40dB
TARGET: 2.0 IN SILICA; WATER PATH: 1.005in
JOB CODE: TP200

MEASUREMENTS PER ASTM E1065

WAVEFORM DURATION:
-14DB LEVEL -- .070US
-20DB LEVEL -- .080US
-40DB LEVEL -- .151US

SPECTRUM MEASURANDS:
CENTER FREQ. ---- 21.6MHz
PEAK FREQUENCY ---- 21.8MHz
-6DB BANDWIDTH ---- 98.206 %

COMMENTS:

4.337us SILICA DELAY LINE
F#: 28

** ACCEPTED.

TECHNICIAN: (7) _____ DATE: 12-28-1999

SIGNAL WAVEFORM

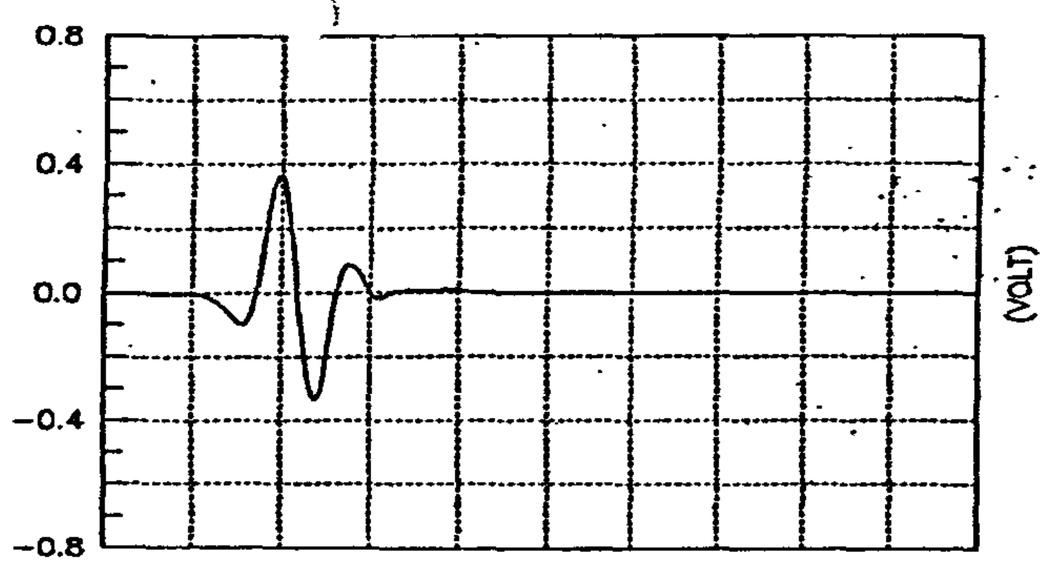

FREQUENCY SPECTRUM

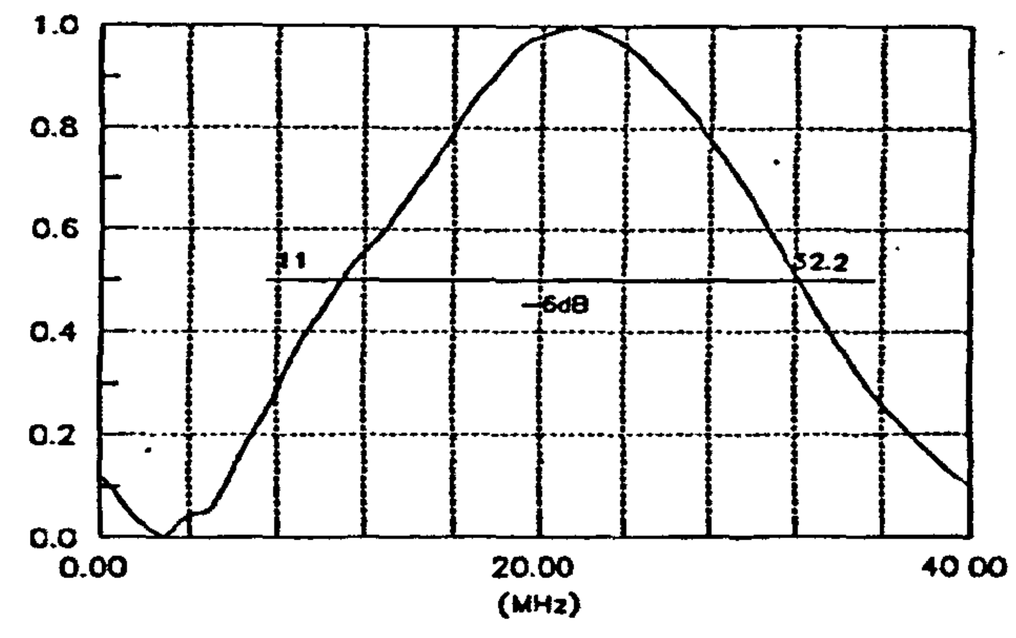

TP103-8 REV.A 9/27/93 PREPARED BY PI-ENGINEERING

GE Panametrics

221 Crescent St, Waltham, MA 02453-3497
Tel: 800-225-8330, 781-899-2719
Fax: 781-899-1552

TRANSDUCER DESCRIPTION

PART NO.: V356 FREQUENCY: 30.00 MHz
SERIAL NO.: 334246 ELEMENT SIZE: .25 in. Dia.
DESIGNATION: FLAT IMMERSION

TEST INSTRUMENTATION

PULSER/RECEIVER: PANAMETRICS 5601
DIGITAL OSCILLOSCOPE: LeCroy LC564A / SN: LC56410253
TEST PROGRAM: TP103-3 VER. 102A0H
CABLE: RG-58A/U LENGTH: 2FT.

TEST CONDITIONS

PULSER SETTING: ENERGY: 1 ; DAMPING: 50
RECEIVER SETTING: ATTN: 42dB ; GAIN: 46dB
TARGET: 2.0 in. SILICA; WATER PATH: .103in
JOB CODE: TP200

MEASUREMENTS PER ASTM E1065

WAVEFORM DURATION:
-14DB LEVEL -- .054US
-20DB LEVEL -- .058US
-40DB LEVEL -- .154US

SPECTRUM MEASURANDS:
CENTER FREQ. ----- 30.9MHz
PEAK FREQUENCY -- 31.0MHz
-6DB BANDWIDTH -- 77.534 %

COMMENTS:

4.299 us SILICA DELAY LINE
F#: 31.92

** ACCEPTED.
TECHNICIAN: (7) _____ DATE: 04-10-2003

SIGNAL WAVEFORM

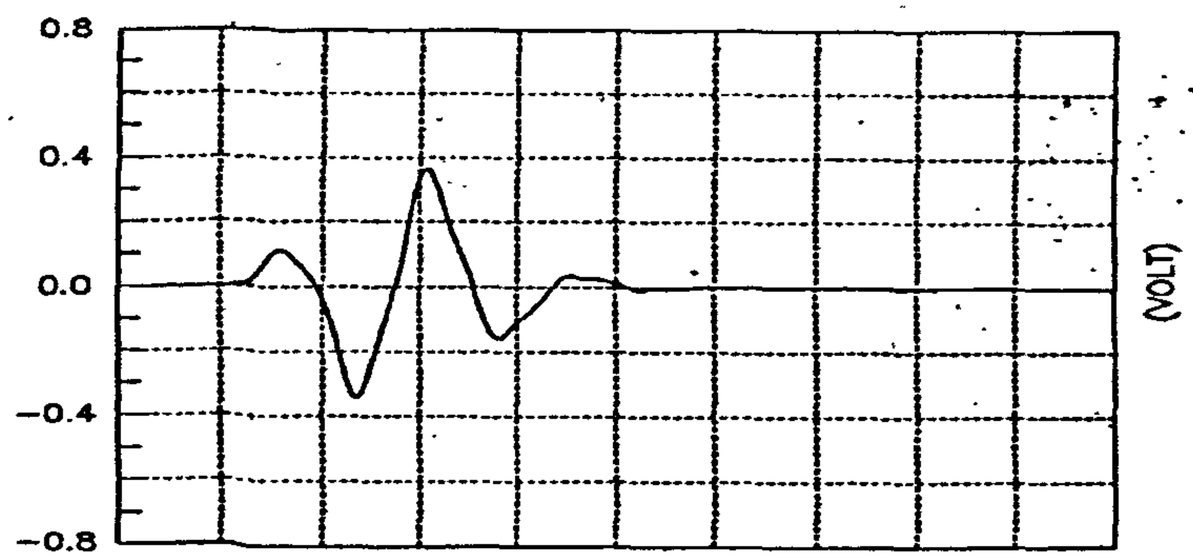

(.02 USEC / DIVISION)

FREQUENCY SPECTRUM

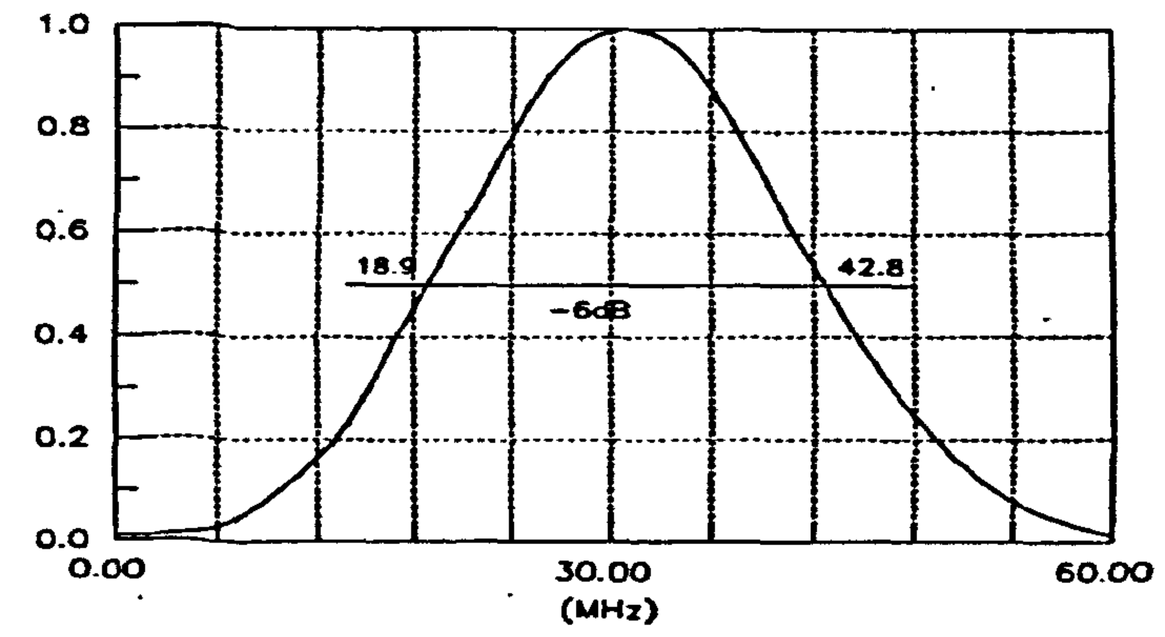

P103-3 REV.B 12/5/02 PREPARED BY P3 ENGINEERING

Appendix 6.1 PSDs calculated using *Mastersizer 2000*

MASTERSIZER 2000

Result Analysis Report

Sample Name: small 5% - Average | SOP Name: 1-Bromohexadecane | Measured: 05/18/06 18 26 07

Sample Source & type: Factory = Paris | Measured by: USERNAME | Analysed: 05/18/06 18 26 08

Sample bulk lot ref: 123-ABC | Result Source: Averaged

Particle Name: 1-Bromohexadecane | Accessory Name: Hydro 2000G (A) | Obscuration: 13 21 %

Particle RI: 1.461 | Absorption: 0 0 .. | Analysis model: General purpose

Dispersant Name: Water | Size range: 0 020 to 2000.000 um | Weighted Residual: 2 795 %

Dispersant RI: 1.330

Concentration: 0 0373 %Vol | Vol. Weighted Mean D[4,3]: 0.185 um | Specific Surface Area: 46 9 m²/g

Span (10% - 90%): 1 757 | Uniformity: 0 555 | Surface Weighted Mean D[3,2]: 0 128 um

Result units: Volume | d(0.5): 0.183 um

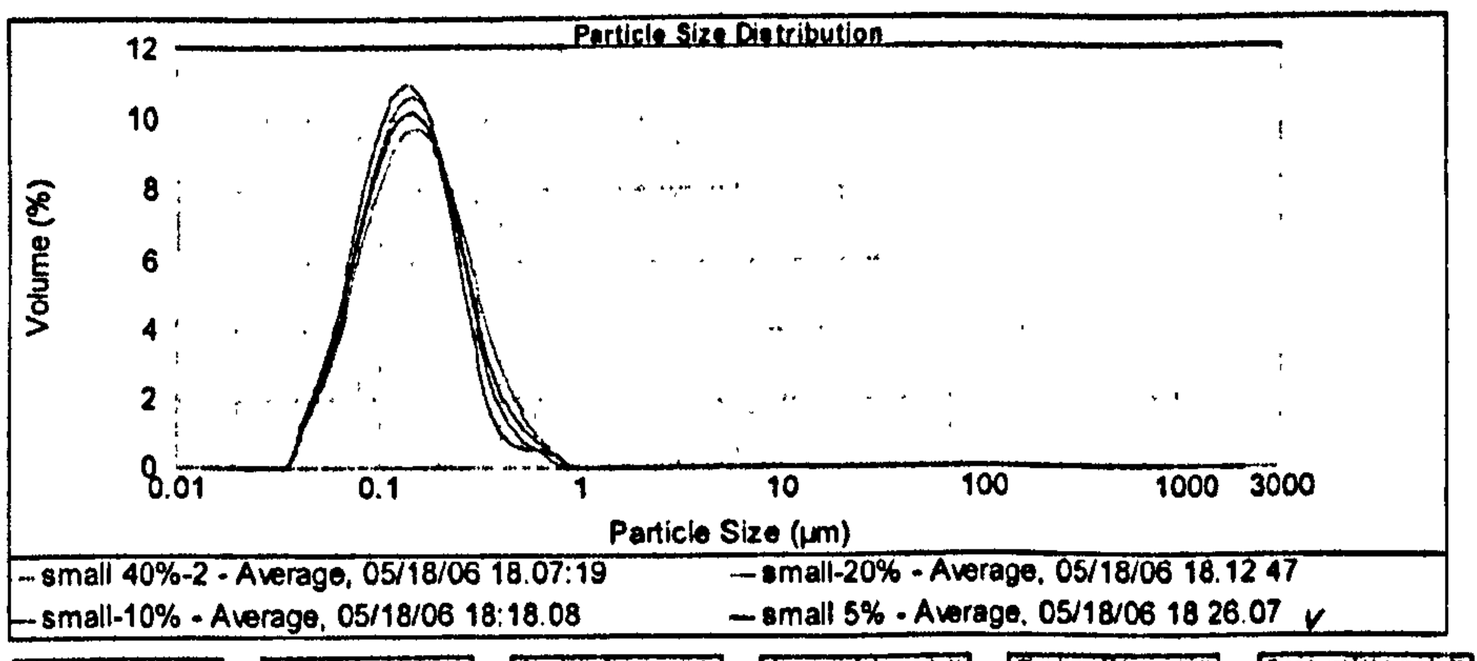

Size (µm)	Volume In %
0.020	0.00
0.022	0.00
0.025	0.00
0.028	0.00
0.032	0.00
0.036	0.13
0.040	0.78
0.045	1.24
0.050	1.79
0.056	2.41
0.063	3.26
0.071	4.14
0.080	4.99
0.089	5.75
0.100	6.38
0.112	6.87
0.126	7.20
0.142	7.34
0.159	7.28
0.178	6.97
0.200	6.45
0.224	5.78
0.252	4.98
0.283	4.11
0.317	3.31
0.356	2.60
0.399	2.01
0.448	1.52
0.502	1.12
0.564	0.78
0.632	0.53
0.710	0.25
0.796	0.11
0.893	0.00
1.002	0.00
1.002	0.00
1.125	0.00
1.262	0.00
1.416	0.00
1.589	0.00
1.783	0.00
2.000	0.00
2.244	0.00
2.518	0.00
2.825	0.00
3.170	0.00
3.557	0.00
3.991	0.00
4.477	0.00
5.024	0.00
5.637	0.00
6.325	0.00
7.098	0.00
7.098	0.00
7.962	0.00
8.934	0.00
10.024	0.00
11.247	0.00
12.619	0.00
14.159	0.00
15.887	0.00
17.825	0.00
20.000	0.00
22.440	0.00
25.179	0.00
28.251	0.00
31.698	0.00
35.566	0.00
39.905	0.00
44.774	0.00
50.238	0.00
50.238	0.00
56.368	0.00
63.246	0.00
70.963	0.00
79.621	0.00
89.337	0.00
100.237	0.00
112.468	0.00
126.191	0.00
141.589	0.00
158.866	0.00
178.250	0.00
200.000	0.00
224.404	0.00
251.785	0.00
282.508	0.00
316.979	0.00
355.699	0.00
355.699	0.00
399.092	0.00
447.744	0.00
502.377	0.00
563.677	0.00
632.466	0.00
709.627	0.00
796.214	0.00
893.357	0.00
1002.374	0.00
1124.683	0.00
1261.916	0.00
1415.892	0.00
1588.666	0.00
1782.502	0.00
2000.000	0.00

Operator notes:

Malvern Instruments Ltd
Malvern UK
Tel: +(44) (0) 1684-892456 Fax +(44) (0) 1684-892789

Mastersizer 2000 Ver 3 01 C:\Program Files\Malvern Instruments\Mastersizer 2000\Measurement 18-HD report.mea
Serial Number 34035-57
19 May 2006 14 18 18

Figure A.6.1. PSDs for small particle sizes 1-bromohexadecane emulsions with 5%,10%, 20% and 40% volume fraction, calculated using *Mastersizer* 2000 in University of Leeds.

MASTERSIZER 2000

Result Analysis Report

Sample Name: mastersizer50	**SOP Name:** 20% n-hexadecane,Ran Huo, one time	**Measured:** 05 July 2006 15:55:42
Sample Source & type: Factory = Paris	**Measured by:** USERNAME	**Analysed:** 05 July 2006 15:55:44
Sample bulk lot ref: 123-ABC	**Result Source:** Measurement	

Particle Name: n-hexadecane	**Accessory Name:** Hydro 2000G (A)	**Analysis model:** General purpose	**Sensitivity:** Normal
Particle RI: 1.434	**Absorption:** 0.005	**Size range:** 0.020 to 2000.000 um	**Obscuration:** 11.05 %
Dispersant Name: Water	**Dispersant RI:** 1.330	**Weighted Residual:** 3.932 %	**Result Emulation:** Off

Concentration: 0.0208 %Vol	**Span :** 1.773	**Uniformity:** 7.07	**Result units:** Volume
Specific Surface Area: 29.8 m?g	**Surface Weighted Mean D[3,2]:** 0.202 um	**Vol. Weighted Mean D[4,3]:** 1.815 um	

d(0.1): 0.110 um **d(0.5):** 0.235 um **d(0.9):** 0.526 um

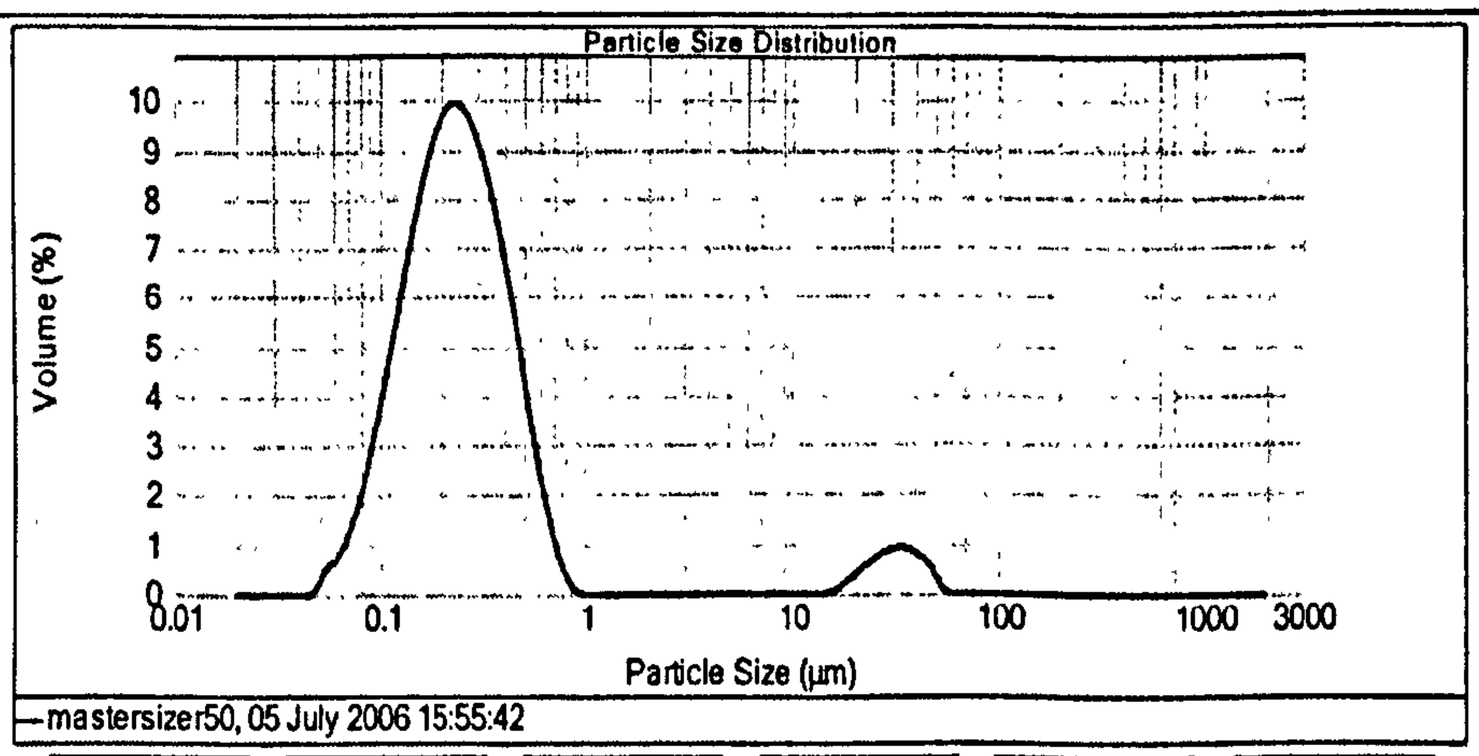

Size (µm)	Volume In %	Size (µm)	Volume In %	Size (µm)	Volume In %	Size (µm)	Volume In %	Size (µm)	Volume In %	Size (µm)	Volume In %
0.010	0.00	0.105	4.49	1.096	0.00	11.482	0.00	120.226	0.00	1258.925	0.00
0.011	0.00	0.120	6.73	1.259	0.00	13.183	0.00	138.038	0.00	1445.440	0.00
0.013	0.00	0.138	6.93	1.445	0.00	15.136	0.07	158.489	0.00	1659.587	0.00
0.015	0.00	0.158	7.95	1.660	0.00	17.378	0.26	181.970	0.00	1905.461	0.00
0.017	0.00	0.182	8.67	1.905	0.00	19.953	0.43	208.930	0.00	2187.762	0.00
0.020	0.00	0.209	8.98	2.188	0.00	22.909	0.62	239.883	0.00	2511.886	0.00
0.023	0.00	0.240	8.84	2.512	0.00	26.303	0.77	275.423	0.00	2884.032	0.00
0.026	0.00	0.275	8.30	2.884	0.00	30.200	0.84	316.228	0.00	3311.311	0.00
0.030	0.00	0.316	7.43	3.311	0.00	34.674	0.81	363.078	0.00	3801.894	0.00
0.035	0.00	0.363	6.33	3.802	0.00	39.811	0.68	416.869	0.00	4366.158	0.00
0.040	0.00	0.417	5.04	4.366	0.00	45.709	0.39	478.630	0.00	5011.872	0.00
0.046	0.17	0.479	3.70	5.012	0.00	52.481	0.01	549.541	0.00	5754.399	0.00
0.052	0.53	0.550	2.37	5.754	0.00	60.256	0.00	630.957	0.00	6606.934	0.00
0.060	0.85	0.631	1.26	6.607	0.00	69.183	0.00	724.436	0.00	7585.776	0.00
0.069	1.47	0.724	0.44	7.586	0.00	79.433	0.00	831.764	0.00	8709.636	0.00
0.079	2.30	0.832	0.05	8.710	0.00	91.201	0.00	954.993	0.00	10000.000	0.00
0.091	3.32	0.955	0.00	10.000	0.00	104.713	0.00	1096.478	0.00		
0.105		1.096		11.482		120.226		1258.925			

Operator notes:

Figure A.6.2. PSDs for small particle sizes 1-bromohexadecane emulsions with 50% volume fraction, calculated using Mastersizer 2000 in University of Leeds.

NOTTINGHAM'S PROJECT

Composition of :

Capsules CS

✓

C1544-	16-B	16-D	17-B
	% w/w	% w/w	% w/w
Solvesso 100S	20.00	20.00	40.00
Voronate	1.01	1.01	2.02
EDA	0.24	0.24	0.49
Propylene Glycol	4.34	4.34	3.68
Antifoam C	0.07	0.07	0.11
Surfactant*	4.00	4.00	3.00
Water	69.94	69.94	49.90
Atlox	0.40	0.40	0.80
Total	100.00	100.00	100.00

Emulsion EW

C1544-	16-C	17-A
	% w/w	% w/w
Solvesso 100S	20.00	40.00
Propylene Glycol	4.34	3.68
Antifoam C	0.07	0.11
Surfactant*	4.00	3.00
Water	71.19	52.41
Atlox	0.40	0.80
Total	100.00	100.00

* Gonsenol G-03 (PVA)

20-Jul-06	Particle Size Determinationwith code: NAD						
D[v,0.5]	1.18 EW 1.48 CS	1.30EW 1.46 CS	1.31 EW 1.43 CS			1.40	1.33
D[v,0.9]	2.63 EW 3.06 CS	3.17 EW 3.47 CS	3.30 EW 3.37 CS			2.68	2.68
20-Jul-06	**Particle Size Determinationwith code: NHD**						
D[v,0.5]	1.46 EW 1.75 CS	1.66 EW 3.13 EW	1.64 EW 1.75 CS			1.64	1.64
D[v,0.9]	2.66 EW 3.16 CS	1.80 CS 3.48 EW	3.16 EW 3.42 CS			2.73	2.72
21-Jul-06	**Particle Size Determinationwith code: NHD**						
D[v,0.5]	1.81	1.86	1.77			2.23	2.38
D[v,0.9]	3.06	3.39	3.54			4.49	5.74

31-Jul-06	Particle Size Determinationwith code: NAD						
D[v,0.5]	1.46	1.51	1.41			9.11	9.9
D[v,0.9]	3.07	3.55	3.26			15.78	20.12
31-Jul-06	**Particle Size Determinationwith code: NHD**						
D[v,0.5]	1.75	1.84	1.79			8.54	15.25
D[v,0.9]	3.16	3.54	3.38			8.92	19.16

Note:

For making CS,a EW is made first to the desired (like EW's made) droplet size oil (droplet size determination) at that stage oil phase is Voranate&Solvesso.Once the droplet size is attained, addition of EDA 10% to form capsules and Atlox to disperse CS (dropletsize determination after addition of EDA - 20-Jul 06) then 1 day after and after 11 days.

EW's as shown above are not stable with time, the droplet size determination of 31-Jul-06 have been determined after shaking by hand the flask.

CS's flasks HAVE TO BE SHAKEN by hand in order to well disperse CS's.

Figure A.6.3. PSDs for encapsulated emulsions and unencapsulated emulsions, tested with delay of days.

MALVERN INSTRUMENTS

MASTERSIZER

Result: Analysis Report

Sample Details

Sample ID: C1544-16-C
Sample File: JUL06
Sample Path: C:\SIZERS\DATA\
Sample Notes: blank Ew from Steve Wilson with 4%gohsenol 03-20% oil
EW de C1544-16B
9mn HS
VD+NF

Run Number: 270
Record Number: 16

Measured: 20 Jul 2006 14 33
Analysed: 20 Jul 2006 14 33
Result Source: Analysed

System Details

Range Lens: 300RF mm
Presentation: 3NHD
Analysis Model: Polydisperse
Modifications: None

Beam Length: 2.40 mm
[Particle R.I. = (1.4564, 0.1000); Dispersant R.I. = 1.3300]

Sampler: MS17

Obscuration: 19.5 %
Residual: 0.845 %

Result Statistics

Distribution Type: Volume
Mean Diameters:
D [4, 3] = 1.68 um

Concentration = 0.0052 %Vol
D (v, 0.1) = 0.72 um
D [3, 2] = 1.22 um

Density = 1.000 g / cub. cm
D (v, 0.5) = 1.64 um
Span = 1.233E+00

Specific S.A. = 4.8992 sq. m / g
D (v, 0.9) = 2.73 um
Uniformity = 3.803E-01

Size Low (um)	In %	Size High (um)	Under%	Size Low (um)	In %	Size High (um)	Under%
0.05	0.00	0.06	0.00	6.63	0.00	7.72	100.00
0.06	0.00	0.07	0.00	7.72	0.00	9.00	100.00
0.07	0.00	0.08	0.00	9.00	0.00	10.48	100.00
0.08	0.00	0.09	0.00	10.48	0.00	12.21	100.00
0.09	0.00	0.11	0.01	12.21	0.00	14.22	100.00
0.11	0.01	0.13	0.01	14.22	0.00	16.57	100.00
0.13	0.02	0.15	0.03	16.57	0.00	19.31	100.00
0.15	0.05	0.17	0.09	19.31	0.00	22.49	100.00
0.17	0.13	0.20	0.22	22.49	0.00	26.20	100.00
0.20	0.30	0.23	0.52	26.20	0.00	30.53	100.00
0.23	0.56	0.27	1.08	30.53	0.00	35.56	100.00
0.27	0.86	0.31	1.94	35.56	0.00	41.43	100.00
0.31	1.05	0.36	2.99	41.43	0.00	48.27	100.00
0.36	1.13	0.42	4.11	48.27	0.00	56.23	100.00
0.42	1.24	0.49	5.36	56.23	0.00	65.51	100.00
0.49	1.53	0.58	6.89	65.51	0.00	76.32	100.00
0.58	2.03	0.67	8.92	76.32	0.00	88.91	100.00
0.67	2.91	0.78	11.82	88.91	0.00	103.58	100.00
0.78	4.51	0.91	16.34	103.58	0.00	120.67	100.00
0.91	6.08	1.06	22.42	120.67	0.00	140.58	100.00
1.06	7.81	1.24	30.22	140.58	0.00	163.77	100.00
1.24	9.89	1.44	40.12	163.77	0.00	190.80	100.00
1.44	11.92	1.68	52.04	190.80	0.00	222.28	100.00
1.68	13.42	1.95	65.46	222.28	0.00	258.95	100.00
1.95	12.64	2.28	78.10	258.95	0.00	301.68	100.00
2.28	10.23	2.65	88.34	301.68	0.00	351.46	100.00
2.65	7.06	3.09	95.40	351.46	0.00	409.45	100.00
3.09	3.89	3.60	99.28	409.45	0.00	477.01	100.00
3.60	0.72	4.19	100.00	477.01	0.00	555.71	100.00
4.19	0.00	4.88	100.00	555.71	0.00	647.41	100.00
4.88	0.00	5.69	100.00	647.41	0.00	754.23	100.00
5.69	0.00	6.63	100.00	754.23	0.00	878.67	100.00

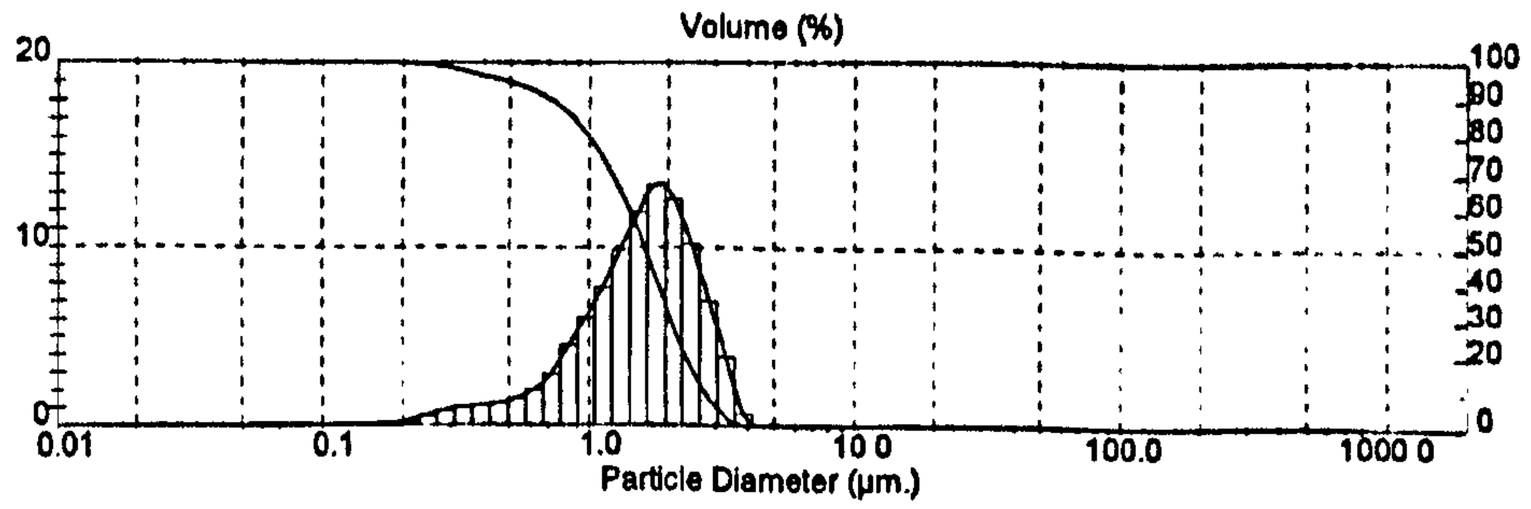

Malvern Instruments Ltd.
Malvern, UK
Tel =+[44] (0)1684-892456 Fax +[44] (0)1684-892789

Mastersizer S Ver. 2.17
Serial Number:

p. 174
20 Jul 06 14 33

Figure A.6.4. PSDs for sample 16-C 20% unencapsulated emulsion calculated using the *Mastersizer 2000* in Dow AgroSciences Ltd just after this emulsion made.

MALVERN MASTERSIZER

Result: Analysis Report

Sample Details

Sample ID: C1544-17-A
Sample File: JUL06
Sample Path: C:\SIZERS\DATA\
Sample Notes: blank Ew from Steve Wilson with 3%gohsenol 03-40% oil
1.6um aimed
4mn HS
VD+NF

Run Number: 274
Record Number: 20

Measured. 20 Jul 2006 15.22
Analysed: 20 Jul 2006 15.22
Result Source. Analysed

System Details

Range Lens: 300RF mm
Presentation: 3NHD
Analysis Model: Polydisperse
Modifications: None

Beam Length: 2 40 mm
[Particle R.I. = (1.4564, 0.1000); Dispersant R I. = 1.3300]

Sampler: MS17

Obscuration: 20 6 %
Residual. 0.750 %

Result Statistics

Distribution Type: Volume
Mean Diameters:
D [4, 3] = 1.71 um

Concentration = 0.0056 %Vol
D (v, 0.1) = 0.80 um
D [3, 2] = 1.32 um

Density = 1.000 g / cub. cm
D (v, 0.5) = 1.64 um
Span = 1.170E+00

Specific S.A. = 4 5531 sq. m / g
D (v, 0.9) = 2.72 um
Uniformity = 3 637E-01

Size Low (um)	In %	Size High (um)	Under%
0.05	0.00	0.06	0.00
0 06	0.00	0 07	0.00
0.07	0.00	0.08	0.00
0.08	0.00	0.09	0.00
0.09	0.00	0.11	0.00
0.11	0 00	0.13	0.00
0.13	0.01	0.15	0.01
0 15	0.02	0.17	0.03
0.17	0.05	0.20	0.08
0.20	0.12	0.23	0.20
0.23	0.26	0.27	0.46
0.27	0.43	0.31	0.89
0.31	0.60	0.36	1.49
0.36	0 75	0 42	2.23
0.42	0.97	0.49	3.20
0.49	1.37	0.58	4.57
0.58	1.98	0.67	6 55
0.67	2.95	0.78	9.50
0.78	4.60	0.91	14.10
0.91	6.33	1.06	20.43
1.06	8.28	1.24	28.71
1.24	10.54	1.44	39.24
1.44	12.58	1.68	51.82
1.68	13.95	1.95	65.77
1.95	12.79	2.28	78.56
2.28	10.10	2.65	88 66
2.65	6.74	3.09	95.40
3.09	3.64	3.60	99.04
3.60	0 96	4 19	100 00
4.19	0.00	4.88	100.00
4.88	0.00	5.69	100 00
5.69	0.00	6 63	100.00

Size Low (um)	In %	Size High (um)	Under%
6 63	0.00	7.72	100.00
7.72	0 00	9.00	100 00
9.00	0 00	10 48	100 00
10.48	0.00	12.21	100 00
12 21	0.00	14.22	100.00
14.22	0.00	16.57	100.00
16.57	0.00	19.31	100.00
19.31	0.00	22.49	100.00
22.49	0.00	26.20	100 00
26.20	0.00	30.53	100.00
30.53	0 00	35.56	100 00
35.56	0.00	41.43	100.00
41.43	0.00	48.27	100 00
48.27	0 00	56.23	100.00
56.23	0.00	65.51	100.00
65.51	0 00	76.32	100.00
76.32	0.00	88 91	100.00
88.91	0 00	103 58	100.00
103.58	0.00	120.67	100.00
120.67	0.00	140.58	100.00
140.58	0 00	163.77	100.00
163.77	0.00	190.80	100.00
190.80	0.00	222.28	100.00
222.28	0.00	258.95	100.00
258.95	0.00	301.68	100.00
301.68	0.00	351.46	100.00
351.46	0 00	409 45	100.00
409.45	0.00	477.01	100.00
477.01	0.00	555.71	100.00
555.71	0.00	647.41	100.00
647.41	0.00	754.23	100.00
754 23	0 00	878.67	100.00

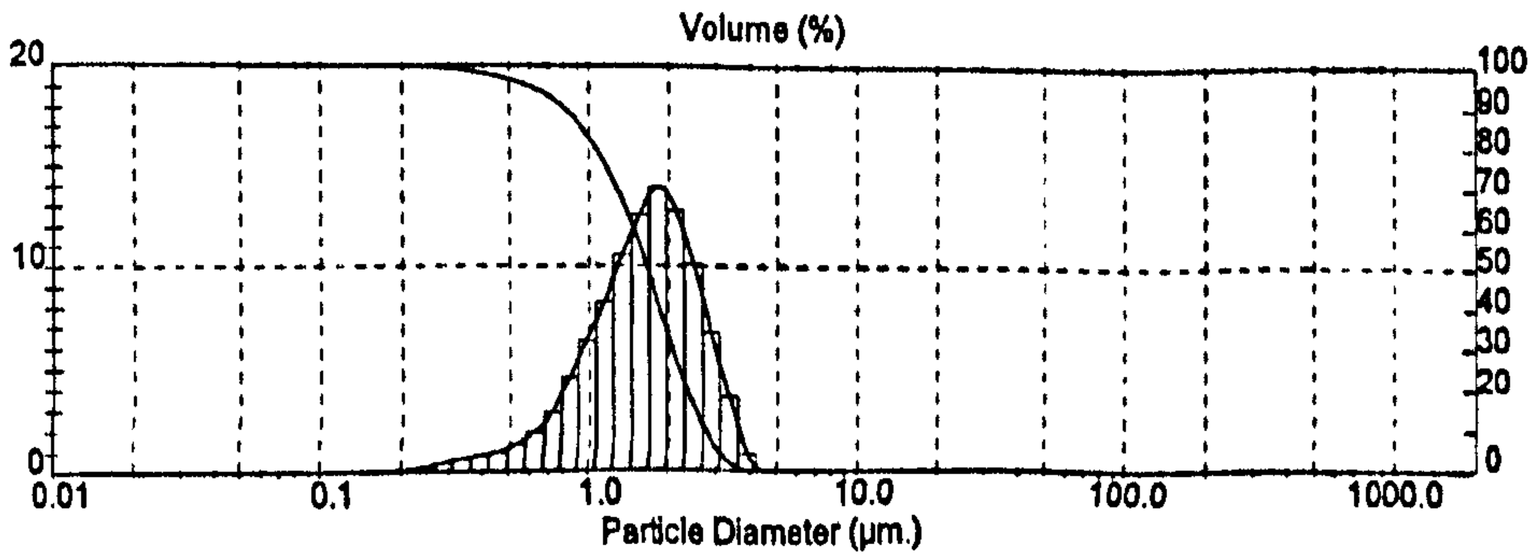

Malvern Instruments Ltd
Malvern, UK
Tel.=+[44] (0)1684-892456 Fax:+[44] (0)1684-892789

Mastersizer S Ver. 2.17
Serial Number:

p 177
20 Jul 06 15 22

Figure A.6.5. PSDs for sample 17-A 40% unencapsulated emulsion calculated using the *Mastersizer 2000* in Dow AgroSciences Ltd just after this emulsion made.

MALVERN MASTERSIZER

Result: Analysis Report

Sample Details

Sample ID: C1544-16-B 0% 1
Sample File: JUL06
Sample Path: C:\SIZERS\DATA\
Sample Notes: blank Ew from Steve Wilson with 4%gohsenol 03-20% oil

VD+NF

Run Number: 266
Record Number: 12

Measured: 20 Jul 2006 13 49
Analysed: 20 Jul 2006 13 49
Result Source: Analysed

System Details

Range Lens: 300RF mm
Presentation: 3NHD
Analysis Model: Polydisperse
Modifications: None

Beam Length: 2.40 mm
[Particle R.I. = (1.4564, 0.1000); Dispersant R.I. = 1.3300]

Sampler: MS17

Obscuration: 20 8 %
Residual 0 532 %

Result Statistics

Distribution Type: Volume
Mean Diameters:
D [4, 3] = 1.85 um

Concentration = 0.0059 %Vol
D (v, 0.1) = 0.68 um
D [3, 2] = 1.28 um

Density = 1.000 g / cub. cm
D (v, 0 5) = 1.75 um
Span = 1.416E+00

Specific S.A. = 4 6844 sq m / g
D (v, 0.9) = 3.16 um
Uniformity = 4 361E-01

Size Low (um)	In %	Size High (um)	Under%	Size Low (um)	In %	Size High (um)	Under%
0 05	0.00	0.06	0.00	6 63	0 00	7.72	100 00
0.06	0.00	0 07	0 00	7.72	0.00	9 00	100 00
0 07	0 00	0.08	0.00	9.00	0 00	10 48	100.00
0 08	0 00	0.09	0.00	10 48	0 00	12.21	100 00
0.09	0 00	0.11	0 00	12.21	0 00	14 22	100 00
0.11	0 00	0 13	0 01	14.22	0.00	16 57	100.00
0.13	0.01	0.15	0.02	16.57	0 00	19 31	100.00
0.15	0.03	0.17	0.05	19 31	0 00	22 49	100.00
0.17	0.08	0.20	0.12	22.49	0 00	26 20	100 00
0 20	0 19	0.23	0.31	26.20	0 00	30.53	100 00
0.23	0 39	0.27	0.70	30.53	0 00	35.56	100.00
0 27	0 68	0 31	1.38	35.56	0.00	41.43	100.00
0.31	0.98	0 36	2.36	41.43	0 00	48 27	100.00
0.36	1.25	0.42	3.61	48.27	0.00	56.23	100 00
0 42	1.59	0 49	5 20	56.23	0 00	65.51	100.00
0.49	2 04	0.58	7.23	65.51	0.00	76.32	100 00
0.58	2.54	0 67	9.77	76.32	0 00	88.91	100.00
0.67	3.23	0.78	13.00	88 91	0.00	103.58	100.00
0.78	4 33	0 91	17.34	103 58	0 00	120 67	100.00
0.91	5 45	1.06	22.79	120.67	0 00	140 58	100 00
1.06	6 67	1.24	29 45	140 58	0.00	163 77	100.00
1.24	8 08	1.44	37.54	163.77	0.00	190.80	100 00
1.44	9.47	1 68	47.01	190 80	0.00	222.28	100.00
1.68	10 61	1.95	57.62	222.28	0.00	258 95	100.00
1.95	11 64	2.28	69 26	258.95	0.00	301.68	100 00
2.28	10 83	2 65	80.09	301.68	0 00	351.46	100 00
2.65	8.79	3 09	88 88	351.46	0.00	409 45	100.00
3 09	6.25	3.60	95.13	409.45	0.00	477.01	100.00
3.60	3.71	4.19	98 84	477.01	0 00	555.71	100.00
4.19	1 16	4 88	100 00	555.71	0.00	647.41	100.00
4 88	0.00	5.69	100.00	647.41	0 00	754.23	100.00
5 69	0 00	6 63	100 00	754 23	0 00	878 67	100 00

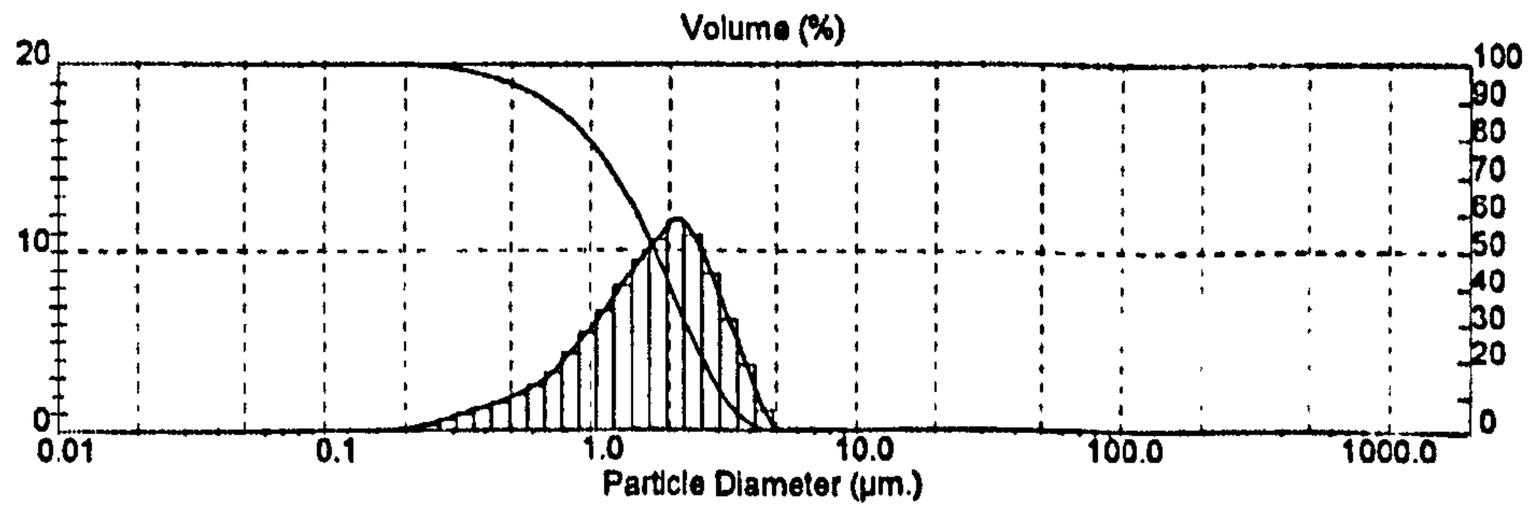

Malvern Instruments Ltd.
Malvern, UK
Tel = +[44] (0)1684-892456 Fax +[44] (0)1684-892789

Mastersizer S Ver. 2.17
Serial Number:

p 172
20 Jul 06 13 49

Figure A.6.6. PSDs for sample 16-B 20% encapsulated emulsion calculated using the *Mastersizer 2000* in Dow AgroSciences Ltd just after this emulsion made.

MALVERN INSTRUMENTS MASTERSIZER

Result: Analysis Report

Sample Details

Sample ID: C1544-16-D cs
Sample File: JUL06
Sample Path: C:\SIZERS\DATA\
Sample Notes: blank Ew from Steve Wilson with 4%gohsenol 03-20% oil
=C1544-16B for 1.6um aimed
2mn HS
VD+NF

Run Number: 272
Record Number: 18

Measured: 20 Jul 2006 15 00
Analysed: 20 Jul 2006 15 00
Result Source: Analysed

System Details

Range Lens: 300RF mm
Presentation: 3NHD
Analysis Model: Polydisperse
Modifications: None

Beam Length: 2.40 mm
[Particle R.I. = (1.4564, 0.1000); Dispersant R.I. = 1.3300]

Sampler: MS17

Obscuration: 20 9 %
Residual: 0 583 %

Result Statistics

Distribution Type: Volume
Mean Diameters:
D [4, 3] = 1.95 um

Concentration = 0.0060 %Vol
D (v, 0.1) = 0.66 um
D [3, 2] = 1.29 um

Density = 1.000 g / cub cm
D (v, 0.5) = 1.80 um
Span = 1.566E+00

Specific S.A. = 4.6439 sq. m / g
D (v, 0.9) = 3 48 um
Uniformity = 4 824E-01

Size Low (um)	In %	Size High (um)	Under%	Size Low (um)	In %	Size High (um)	Under%
0.05	0.00	0.06	0.00	6.63	0 00	7.72	100 00
0.06	0.00	0.07	0.00	7.72	0.00	9.00	100.00
0.07	0.00	0.08	0.00	9.00	0.00	10 48	100.00
0.08	0.00	0.09	0.00	10.48	0.00	12 21	100.00
0.09	0.00	0.11	0.00	12.21	0.00	14.22	100.00
0.11	0.00	0.13	0.01	14.22	0.00	16 57	100.00
0.13	0.01	0.15	0.02	16.57	0.00	19.31	100.00
0.15	0.03	0.17	0.05	19.31	0.00	22.49	100.00
0.17	0.07	0.20	0.12	22.49	0.00	26.20	100.00
0.20	0.17	0.23	0.29	26.20	0.00	30.53	100 00
0.23	0.35	0.27	0.65	30.53	0.00	35.56	100.00
0.27	0.63	0.31	1.28	35.56	0.00	41.43	100.00
0.31	0.96	0.36	2.24	41.43	0.00	48.27	100.00
0.36	1.31	0.42	3 55	48.27	0.00	56.23	100.00
0.42	1.74	0.49	5.30	56.23	0.00	65.51	100.00
0.49	2.29	0.58	7.58	65.51	0.00	76.32	100 00
0.58	2.85	0 67	10.43	76.32	0.00	88.91	100.00
0.67	3.53	0.78	13.97	88 91	0.00	103.58	100.00
0.78	4.43	0.91	18.39	103.58	0 00	120.67	100.00
0.91	5.34	1.06	23.73	120.67	0.00	140.58	100.00
1.06	6.31	1.24	30.04	140.58	0.00	163.77	100.00
1.24	7.37	1.44	37.41	163.77	0.00	190.80	100.00
1.44	8.37	1.68	45.78	190 80	0 00	222.28	100 00
1.68	9.24	1.95	55.02	222.28	0.00	258.95	100.00
1.95	10.17	2.28	65.19	258.95	0.00	301.68	100 00
2.28	10.06	2.65	75.26	301.68	0.00	351.46	100.00
2.65	9 00	3.09	84.26	351.46	0.00	409.45	100.00
3.09	7.17	3.60	91.43	409.45	0.00	477.01	100.00
3.60	5.02	4.19	96.45	477.01	0.00	555.71	100.00
4.19	2.86	4.88	99.30	555.71	0.00	647.41	100.00
4.88	0.70	5.69	100.00	647.41	0 00	754.23	100 00
5.69	0 00	6 63	100 00	754.23	0.00	878 67	100.00

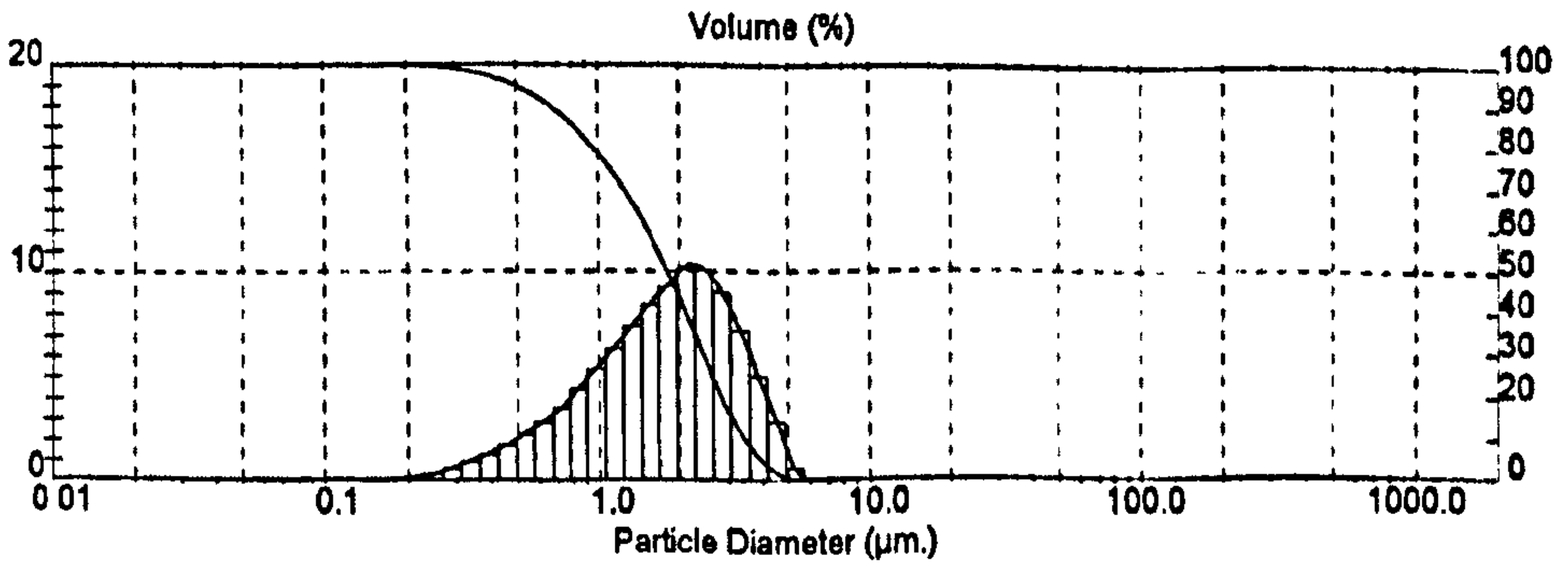

Malvern Instruments Ltd.
Malvern, UK
Tel:=+[44] (0)1684-892456 Fax:+[44] (0)1684-892789

Mastersizer S Ver. 2.17
Serial Number:

p 176
20 Jul 06 15 01

Figure A.6.7. PSDs for sample 16-D 20% encapsulated emulsion calculated using the *Mastersizer* 2000 in Dow AgroSciences Ltd just after this emulsion made.

MALVERN MASTERSIZER

Result: Analysis Report

Sample Details

Sample ID: C1544-17-B
Sample File: JUL06
Sample Path: C:\SIZERS\DATA\
Sample Notes: blank Ew from Steve Wilson with 3%gohsenol 03-40% oil
1.6um aimed
1.5mn HS before vaddition eda+atlox
VD+NF

Run Number: 275
Record Number: 21

Measured: 20 Jul 2006 15.35
Analysed: 20 Jul 2006 15.35
Result Source: Analysed

System Details

Range Lens: 300RF mm
Presentation: 3NHD
Analysis Model: Polydisperse
Modifications: None

Beam Length: 2.40 mm
[Particle R.I. = (1.4564, 0.1000); Dispersant R.I. = 1 3300]

Sampler: MS17

Obscuration: 18 7 %
Residual: 0.380 %

Result Statistics

Distribution Type: Volume
Mean Diameters:
D [4, 3] = 1.89 um

Concentration = 0.0052 %Vol
D (v, 0.1) = 0.58 um
D [3, 2] = 1.18 um

Density = 1.000 g / cub. cm
D (v, 0.5) = 1.70 um
Span = 1.713E+00

Specific S.A. = 5.0773 sq m / g
D (v, 0.9) = 3 49 um
Uniformity = 5.307E-01

Size Low (um)	In %	Size High (um)	Under%	Size Low (um)	In %	Size High (um)	Under%
0.05	0.00	0.06	0.00	6 63	0 00	7.72	100 00
0.06	0.00	0.07	0.00	7 72	0.00	9.00	100 00
0.07	0 00	0.08	0.00	9 00	0 00	10 48	100 00
0.08	0.00	0 09	0.01	10.48	0 00	12 21	100.00
0.09	0.01	0.11	0.01	12.21	0.00	14 22	100.00
0.11	0.02	0 13	0.03	14.22	0.00	16.57	100.00
0.13	0.03	0.15	0.06	16.57	0 00	19.31	100.00
0.15	0.08	0.17	0.14	19.31	0 00	22.49	100 00
0.17	0.16	0.20	0.30	22.49	0.00	26.20	100.00
0.20	0.31	0.23	0.61	26.20	0.00	30.53	100.00
0.23	0.56	0.27	1.17	30.53	0.00	35.56	100.00
0.27	0 91	0.31	2.08	35.56	0.00	41.43	100 00
0.31	1.28	0.36	3.37	41.43	0.00	48.27	100 00
0.36	1.67	0.42	5.03	48.27	0.00	56.23	100.00
0 42	2.11	0.49	7.15	56.23	0.00	65.51	100.00
0.49	2.66	0.58	9 81	65.51	0.00	76.32	100 00
0.58	3.23	0.67	13.04	76.32	0 00	88 91	100 00
0.67	3.91	0.78	16 94	88.91	0.00	103.58	100.00
0.78	4.75	0.91	21.69	103.58	0.00	120 67	100.00
0.91	5.59	1.06	27.28	120.67	0 00	140.58	100.00
1.06	6.46	1.24	33.74	140.58	0.00	163.77	100 00
1.24	7.36	1.44	41.10	163 77	0.00	190 80	100.00
1.44	8.15	1.68	49.25	190.80	0 00	222 28	100 00
1.68	8 78	1.95	58.03	222.28	0.00	258.95	100.00
1.95	9.40	2.28	67.44	258.95	0.00	301.68	100 00
2.28	9.09	2 65	76.53	301.68	0.00	351.46	100 00
2.65	8.08	3.09	84.61	351.46	0.00	409 45	100.00
3.09	6.52	3.60	91.13	409.45	0.00	477.01	100 00
3.60	4.72	4.19	95.85	477.01	0.00	555.71	100.00
4.19	2.96	4 88	98.80	555.71	0.00	647.41	100.00
4.88	1.20	5.69	100.00	647.41	0.00	754.23	100 00
5 69	0 00	6.63	100.00	754.23	0 00	878.67	100.00

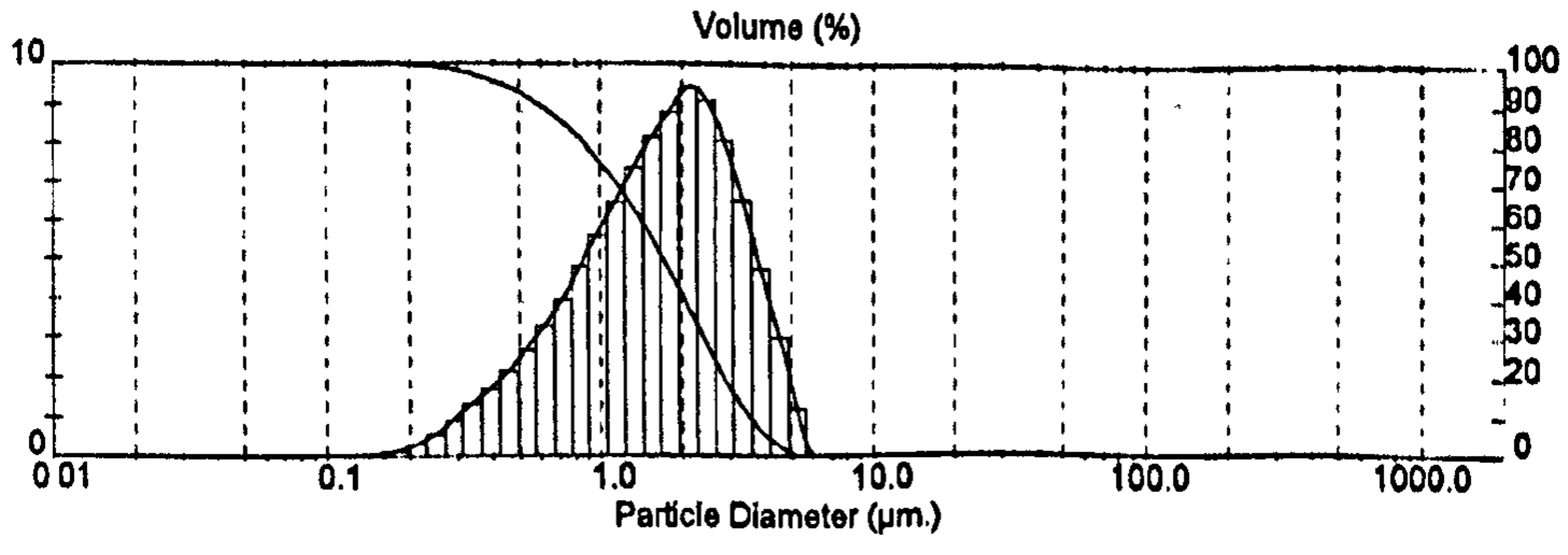

Malvern Instruments Ltd
Malvern, UK
Tel:=+[44] (0)1684-892456 Fax:+[44] (0)1684-892789

Mastersizer S Ver. 2.17
Serial Number:

p. 178
20 Jul 06 15 35

Figure A.6.8. PSDs for sample 17-B 40% encapsulated emulsion calculated using the *Mastersizer 2000* in Dow AgroSciences Ltd just after this emulsion made.

MALVERN MASTERSIZER

Result: Analysis Report

Sample Details

Sample ID: C1544-16-C EW
Sample File: OCT 05
Sample Path: C:\SIZERS\DATA\
Sample Notes: 20% SOLVESSO
PUMP 4 SPEED 3 ULTRASON 2
11DAYS
31/07/2006

Run Number: 17
Record Number: 87

Measured: 31 Jul 2006 15:14
Analysed: 31 Jul 2006 15:14
Result Source: Analysed

System Details

Range Lens: 300RF mm
Presentation: 3NHD
Analysis Model: Polydisperse
Modifications: None

Beam Length: 2.40 mm
[Particle R.I. = (1.4564, 0.1000); Dispersant R.I. = 1.3300]

Sampler: MS17

Obscuration: 19.0 %
Residual: 0.464 %

Result Statistics

Distribution Type: Volume
Mean Diameters:
D [4, 3] = 8.38 um

Concentration = 0.0120 %Vol
D (v, 0.1) = 0.75 um
D [3, 2] = 2.53 um

Density = 1.000 g / cub. cm
D (v, 0.5) = 8.54 um
Span = 1.698E+00

Specific S.A. = 2.3717 sq. m / g
D (v, 0.9) = 15.25 um
Uniformity = 5.041E-01

Size Low (um)	In %	Size High (um)	Under%
0.05	0.00	0.06	0.00
0.06	0.00	0.07	0.00
0.07	0.00	0.08	0.00
0.08	0.00	0.09	0.00
0.09	0.00	0.11	0.00
0.11	0.00	0.13	0.00
0.13	0.00	0.15	0.00
0.15	0.00	0.17	0.00
0.17	0.01	0.20	0.01
0.20	0.04	0.23	0.05
0.23	0.15	0.27	0.21
0.27	0.41	0.31	0.62
0.31	0.78	0.36	1.39
0.36	1.15	0.42	2.55
0.42	1.55	0.49	4.10
0.49	1.97	0.58	6.07
0.58	2.19	0.67	8.26
0.67	2.31	0.78	10.56
0.78	2.18	0.91	12.74
0.91	2.00	1.06	14.74
1.06	1.80	1.24	16.54
1.24	1.62	1.44	18.16
1.44	1.36	1.68	19.52
1.68	1.04	1.95	20.56
1.95	0.78	2.28	21.34
2.28	0.39	2.65	21.73
2.65	0.41	3.09	22.14
3.09	0.63	3.60	22.78
3.60	1.13	4.19	23.91
4.19	2.05	4.88	25.96
4.88	3.57	5.69	29.53
5.69	5.66	6.63	35.19

Size Low (um)	In %	Size High (um)	Under%
6.63	8.14	7.72	43.34
7.72	10.49	9.00	53.82
9.00	12.23	10.48	66.06
10.48	11.37	12.21	77.43
12.21	9.24	14.22	86.67
14.22	6.56	16.57	93.23
16.57	4.00	19.31	97.23
19.31	2.02	22.49	99.25
22.49	0.75	26.20	100.00
26.20	0.00	30.53	100.00
30.53	0.00	35.56	100.00
35.56	0.00	41.43	100.00
41.43	0.00	48.27	100.00
48.27	0.00	56.23	100.00
56.23	0.00	65.51	100.00
65.51	0.00	76.32	100.00
76.32	0.00	88.91	100.00
88.91	0.00	103.58	100.00
103.58	0.00	120.67	100.00
120.67	0.00	140.58	100.00
140.58	0.00	163.77	100.00
163.77	0.00	190.80	100.00
190.80	0.00	222.28	100.00
222.28	0.00	258.95	100.00
258.95	0.00	301.68	100.00
301.68	0.00	351.46	100.00
351.46	0.00	409.45	100.00
409.45	0.00	477.01	100.00
477.01	0.00	555.71	100.00
555.71	0.00	647.41	100.00
647.41	0.00	754.23	100.00
754.23	0.00	878.67	100.00

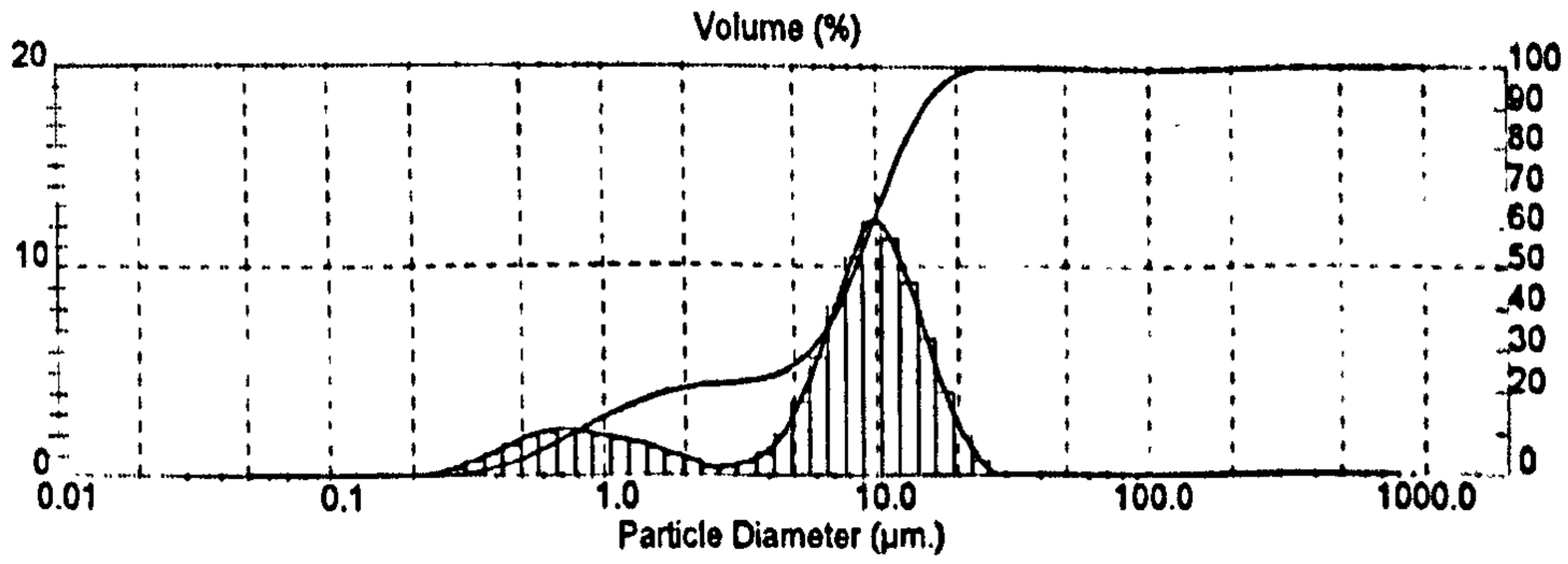

Figure A.6.9. PSDs for sample 16-C 20% non-encapsulated emulsion calculated using *Mastersizer 2000* in Dow AgroSciences Ltd, measured 10 days later.

MALVERN MASTERSIZER

Result: Analysis Report

Sample Details

Sample ID: C1544-17-A EW
Sample File: (Result Not Saved)
Sample Path: C:\SIZERS\DATA\
Sample Notes: 40% SOLVESSO
PUMP 4 SPEED 3 ULTRASON 2
11DAYS
31/07/2006

Run Number: 16

Measured: 31 Jul 2006 15 11
Analysed: 31 Jul 2006 15 11
Result Source: Analysed

System Details

Range Lens: 300RF mm
Presentation: 3NHD
Analysis Model: Polydisperse
Modifications: None

Beam Length: 2.40 mm
[Particle R.I. = (1.4564, 0.1000); Dispersant R.I. = 1.3300]

Sampler: MS17

Obscuration: 19.3 %
Residual: 0.446 %

Result Statistics

Distribution Type: Volume
Mean Diameters:
D [4, 3] = 9.61 um

Concentration = 0.0126 %Vol
D (v, 0.1) = 0.78 um
D [3, 2] = 2.58 um

Density = 1.000 g / cub. cm
D (v, 0.5) = 8.92 um
Span = 2.060E+00

Specific S.A. = 2.3222 sq. m / g
D (v, 0.9) = 19.16 um
Uniformity = 6.222E-01

Size Low (um)	In %	Size High (um)	Under%	Size Low (um)	In %	Size High (um)	Under%
0.05	0.00	0.06	0.00	6.63	6.64	7.72	42.49
0.06	0.00	0.07	0.00	7.72	7.97	9.00	50.46
0.07	0.00	0.08	0.00	9.00	8.84	10.48	59.30
0.08	0.00	0.09	0.00	10.48	9.34	12.21	68.63
0.09	0.00	0.11	0.00	12.21	8.52	14.22	77.15
0.11	0.00	0.13	0.00	14.22	7.28	16.57	84.42
0.13	0.00	0.15	0.00	16.57	5.84	19.31	90.26
0.15	0.00	0.17	0.01	19.31	4.34	22.49	94.60
0.17	0.02	0.20	0.03	22.49	2.96	26.20	97.56
0.20	0.07	0.23	0.10	26.20	1.80	30.53	99.36
0.23	0.20	0.27	0.30	30.53	0.64	35.56	100.00
0.27	0.46	0.31	0.76	35.56	0.00	41.43	100.00
0.31	0.80	0.36	1.56	41.43	0.00	48.27	100.00
0.36	1.11	0.42	2.67	48.27	0.00	56.23	100.00
0.42	1.45	0.49	4.12	56.23	0.00	65.51	100.00
0.49	1.80	0.58	5.92	65.51	0.00	76.32	100.00
0.58	2.01	0.67	7.93	76.32	0.00	88.91	100.00
0.67	2.14	0.78	10.07	88.91	0.00	103.58	100.00
0.78	2.08	0.91	12.15	103.58	0.00	120.67	100.00
0.91	1.96	1.06	14.11	120.67	0.00	140.58	100.00
1.06	1.81	1.24	15.92	140.58	0.00	163.77	100.00
1.24	1.63	1.44	17.55	163.77	0.00	190.80	100.00
1.44	1.38	1.68	18.93	190.80	0.00	222.28	100.00
1.68	1.07	1.95	20.01	222.28	0.00	258.95	100.00
1.95	0.83	2.28	20.83	258.95	0.00	301.68	100.00
2.28	0.69	2.65	21.53	301.68	0.00	351.46	100.00
2.65	0.72	3.09	22.25	351.46	0.00	409.45	100.00
3.09	0.98	3.60	23.24	409.45	0.00	477.01	100.00
3.60	1.52	4.19	24.76	477.01	0.00	555.71	100.00
4.19	2.39	4.88	27.14	555.71	0.00	647.41	100.00
4.88	3.62	5.69	30.76	647.41	0.00	754.23	100.00
5.69	5.09	6.63	35.85	754.23	0.00	878.67	100.00

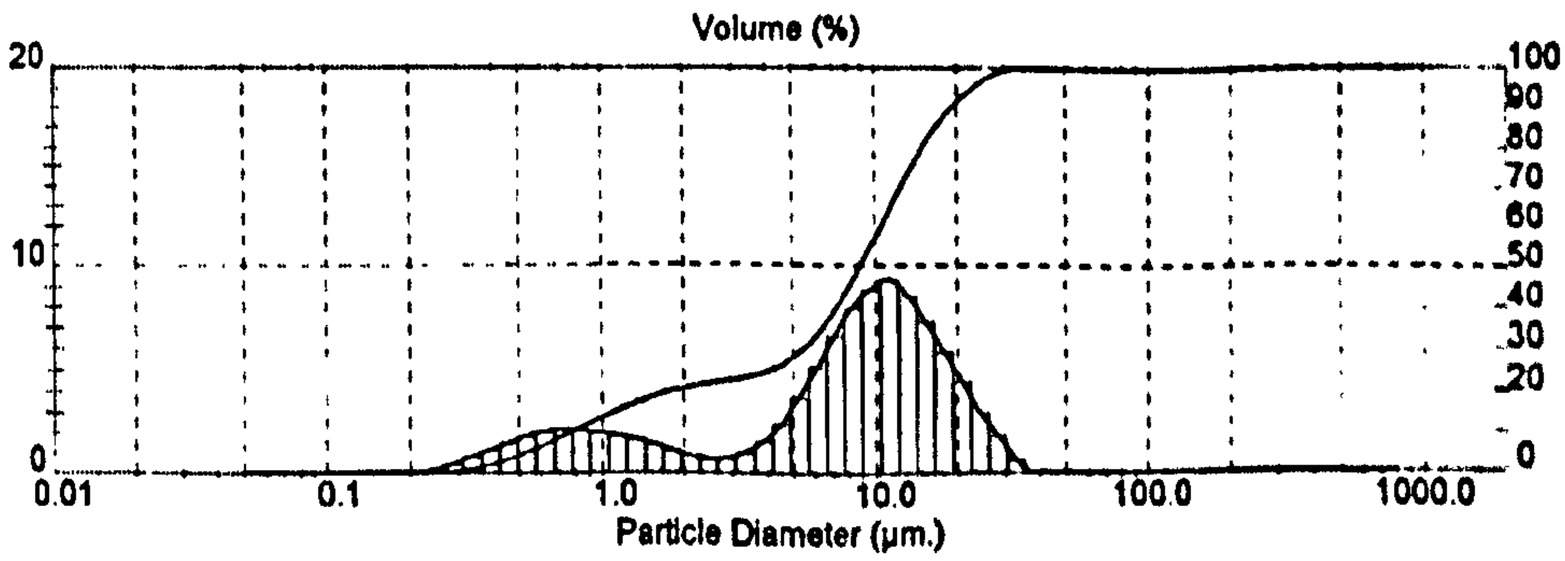

Figure A.6.10. PSDs for sample 17-A 40% non-encapsulated emulsion calculated using *Mastersizer 2000* in Dow AgroSciences Ltd, measured 10 days later.